Nikolay N. Nikitenkov

MODERN TECHNOLOGIES for Creating the Thin-film Systems and Coatings

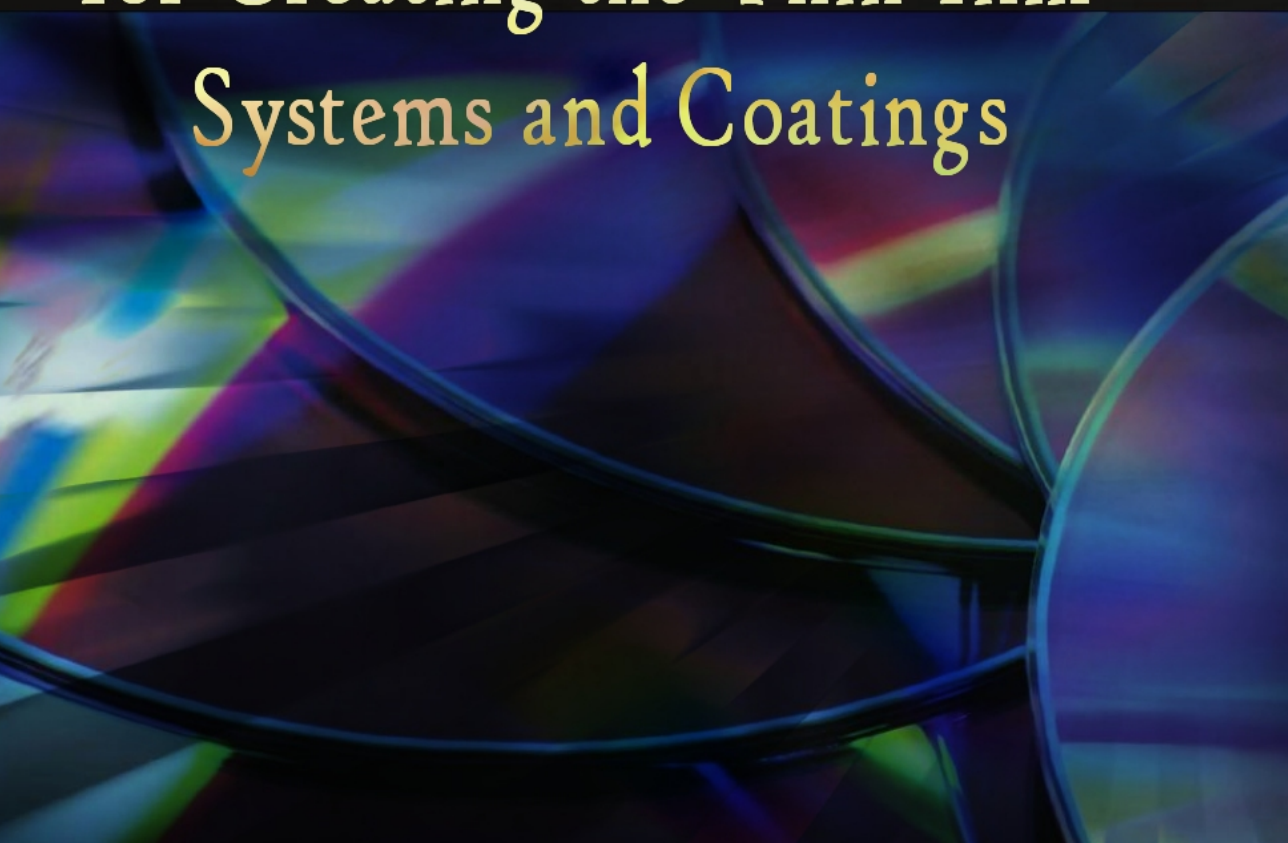

Modern Technologies for Creating the Thin-film Systems and Coatings

Edited by Nikolay N. Nikitenkov

Modern Technologies for Creating the Thin-film Systems and Coatings

Edited by Nikolay N. Nikitenkov

Published by ExLi4EvA
Copyright © 2017

All chapters are Open Access distributed under the Creative Commons Attribution 3.0 license, which allows users to download, copy and build upon published articles even for commercial purposes, as long as the author and publisher are properly credited, which ensures maximum dissemination and a wider impact of our publications. After this work has been published, authors have the right to republish it, in whole or part, in any publication of which they are the author, and to make other personal use of the work. Any republication, referencing or personal use of the work must explicitly identify the original source.

As for readers, this license allows users to download, copy and build upon published chapters even for commercial purposes, as long as the author and publisher are properly credited, which ensures maximum dissemination and a wider impact of our publications.

Notice
Statements and opinions expressed in the chapters are these of the individual contributors and not necessarily those of the editors or publisher. No responsibility is accepted for the accuracy of information contained in the published chapters. The publisher assumes no responsibility for any damage or injury to persons or property arising out of the use of any materials, instructions, methods or ideas contained in the book.

Publishing Process Manager
Technical Editor
Cover Designer AvE4EvA MuViMix Records

ISBN-10: 953-51-3004-8
ISBN-13: 978-953-51-3004-8

Print
ISBN-10: 953-51-3003-X
ISBN-13: 978-953-51-3003-1

Contents

Preface

Chapter 1 Molecular Precursor Method for Fabricating p-Type Cu2O and Metallic Cu Thin Films
by Hiroki Nagai and Mitsunobu Sato

Chapter 2 Modification of Oxide Thin Films with Low-Energy Ion Bombardment
by Oscar Rodríguez de la Fuente

Chapter 3 Conventional and Un-Conventional Lithography for Fabricating Thin Film Functional Devices
by Abdelhanin Aassime and Frederic Hamouda

Chapter 4 In Situ Engineering and Characterization of Correlated Materials with Integrated OMBE–ARPES
by Dawei Shen, Haifeng Yang and Zhengtai Liu

Chapter 5 Anomalous Rashba Effect of Bi Thin Film Studied by Spin-Resolved ARPES
by Akari Takayama

Chapter 6 Electrochemical Deposition of P3AT Films Used as a Probe of Optical Properties in Polymeric System
by Sankler Soares de Sá, Fernando Costa Basílio, Henrique de Santana, Alexandre Marletta and Eralci Moreira Therézio

Chapter 7 Magnetic Properties of Hausmannite Thin Films
by Petya Petkova

Chapter 8 Advance Deposition Techniques for Thin Film and Coating
by Asim Jilani, Mohamed Shaaban Abdel-wahab and Ahmed Hosny Hammad

Chapter 9 Vanadium Oxide Thin Films Obtained by Thermal Annealing of Layers Deposited by RF Magnetron Sputtering at Room Temperature
by Hernan M. R. Giannetta, Carlos Calaza, Liliana Fraigi and Luis Fonseca

Chapter 10 Smart Thermoresponsive Surfaces Based on pNIPAm Coatings and Laser Method for Biological Applications
by Laurentiu Rusen, Valentina Dinca, Cosmin Mustaciosu, Madalina Icriverzi, Livia Elena Sima, Anca Bonciu, Simona Brajnicov, Natalia Mihailescu, Nicoleta Dumitrescu, Alexandru I. Popovici, Anca Roseanu and Maria Dinescu

Chapter 11 Controlled Rate Thermal Analysis (CRTA) as New Method to Control the Specific Surface in Hydroxyapatite Thin Coatings
by E. Peón, A. El hadad, F.R. García‐Galván, A. Jiménez‐Morales and J.C. Galván

Chapter 12 Radio Frequency Magnetron Sputter Deposition as a Tool for Surface Modification of Medical Implants
by Roman Surmenev, Alina Vladescu, Maria Surmeneva, Anna Ivanova, Mariana Braic, Irina Grubova and Cosmin Mihai Cotrut

Chapter 13 Thin Films for Immobilization of Complexes with Optical Properties
by Joana Zaharieva and Maria Milanova

Chapter 14 Silicon Oxycarbide Thin films and Nanostructures: Synthesis, Properties and Applications
by Spyros Gallis, Vasileios Nikas and Alain E. Kaloyeros

Chapter 15 Growth and Characteristics of High-quality InN by Plasma- Assisted Molecular Beam Epitaxy
by Chen-Chi Yang, Ikai Lo, Cheng-Hung Shih, Chia-Hsuan Hu, Ying-Chieh Wang, Yu-Chiao Lin, Cheng-Da Tsai, Hui-Chun Huang, Mitch M. C. Chou, Cheng-Chang Yu and Der-Jun Jang

Chapter 17 Modern Technologies for Creating Nanostructures in Thin‐Film Solar Cells
by Yang Tang

Chapter 18 Close‐Spaced Sublimation (CSS): A Low‐Cost, High‐Yield Deposition System for Cadmium Telluride (CdTe) Thin Film Solar Cells
by Nowshad Amin and Kazi Sajedur Rahman

Chapter 19 Effects of CdCl2 Treatment on Physical Properties of CdTe/CdS Thin Film Solar Cell
by Nazar Abbas Shah, Zafran Rabeel, Murrawat Abbas and Waqar Adil Syed

Chapter 20 Silver-Based Low-Emissivity Coating Technology for Energy- Saving Window Applications
by Guowen Ding and César Clavero

Preface

Development of the thin film and coating technologies (TFCT) made possible the technological revolution in electronics and through it the revolution in IT and communications in the end of the twentieth century.

Now, TFCT penetrated in many sectors of human life and industry: biology and medicine; nuclear, fusion, and hydrogen energy; protection against corrosion and hydrogen embrittlement; jet engine; space materials science; and many others. Currently, TFCT along with nanotechnologies is the most promising for the development of almost all industries.

The 20 chapters of this book present the achievements of thin-film technology in many areas mentioned above but more than any other in medicine and biology and energy saving and energy efficiency.

Chapter 1

Molecular Precursor Method for Fabricating *p*-Type Cu_2O and Metallic Cu Thin Films

Hiroki Nagai and Mitsunobu Sato

Additional information is available at the end of the chapter

http://dx.doi.org/10.5772/66476

Abstract

Functional thin films are used in various fields of our life. Many different methods are used to fabricate these films including physical vapor deposition (PVD) and chemical processes. The chemical processes can be used to manufacture thin films in a relatively cheap way, as compared to PVD methods. This chapter summarizes the procedures of the molecular precursor method (MPM), a chemical process, for fabrication of both metal oxide semiconductor Cu_2O and metallic Cu thin films by utilizing Cu(II) complexes in coating solutions. The MPM, recently developed and reported by the present authors, represents a facile procedure for thin film fabrication of various metal oxides or phosphates. This method pertinent to the coordination chemistry and materials science including nanoscience and nanotechnology has provided various thin films of high quality. The MPM is based on the design of metal complexes in coating solutions with excellent stability, homogeneity, miscibility, coatability, etc., which are practical advantages. The metal oxides and phosphates are useful as the electron and/or ion conductors, semiconductors, dielectric materials, etc. This chapter will describe the principle and recent achievement, mainly on fabricating the *p*-type Cu_2O and metallic Cu thin films of the MPM.

Keywords: molecular precursor method, thin film, *p*-type Cu_2O, copper

1. Introduction

A sustainable society requires innovative technology where many disciplines interact. Highly functionalized thin films in various devices such as computers, which were developed mainly for the semiconductor industry in the last century, are now widely used in various fields of our daily life. For example, the touch panel in mobile phone uses a transparent conductive thin film and an antireflection thin film on the glass. A product with various thin films makes

life more comfortable. Many different methods are used to fabricate such thin films including physical vapor deposition (PVD) such as laser ablation, molecular beam epitaxy, sputtering, and chemical processes [1]. The chemical processes can be used to manufacture thin films in a relatively cheap way compared to PVD methods. The chemical process is a processing technique for preparing thin films, ceramic coatings, and powders. However, it is usually difficult to fabricate high-quality thin films using chemical processes.

Transparent metal oxide thin films of *p*-type semiconductors deposited directly on various substrates offer several advantages in the design of heterojunctions with *n*-type oxide films for fabricating thin film devices [2, 3]. Over the past years, the quest to obtain high-quality cuprous oxide films has fueled the development of many physical processing techniques including sputtering, thermal oxidation, vacuum evaporation, molecular beam epitaxy, and electrodeposition [4–9]. However, reproducible formation of cuprous oxide films, uncontaminated by copper or the CuO phase, is a formidable challenge from the technical perspective. Most of the aforementioned physical processing techniques are not economically viable in large area applications. The chemical procedures, which save both energy and resources, have therefore emerged as an attractive alternative because of cost-effective production capabilities.

Recently, we achieved the fabrication of *p*-type Cu_2O transparent thin films by means of a chemical process, the molecular precursor method (MPM), using the thermal reaction of molecular precursor films spin-coated on a Na-free glass substrate. A stable precursor solution for the spin-coating process was facilely prepared by reacting an isolated Cu(II) complex of ethylenediamine-*N, N, N′, N′*-tetraacetic acid (EDTA, H_4edta) with dibutylamine in ethanol [10, 11]. The MPM is one of the chemical processes used for thin film formation of metal oxides or phosphates [12–22]. The method is based on the formation of excellent precursor films involving anionic metal complexes and the alkylammonium cation. The stability, homogeneity, miscibility, and other characteristics of the precursor solutions, which can be used for various coating methods, are practical advantages, in contrast to the conventional sol-gel method.

This chapter summarizes the procedures used in the MPM for the fabrication of both metal oxide semiconductor Cu_2O and metallic Cu thin films by utilizing Cu(II) complexes in coating solutions.

2. Molecular precursor method

The decision by the Nobel Prize committee to award the Nobel Prize for chemistry in 1913 to Alfred Werner met with worldwide approval. In a statement, the committee said that Alfred Werner received the prize in recognition of his work on the linkage of atoms in molecules by which he has thrown new light on earlier investigations and opened up new fields of research especially in inorganic chemistry [23]. Today, the metal complexes are used in various applications such as catalysts, luminescence, and medicine. In 1996, one of the authors, M.S., focused on the thin film fabrication of various metal oxides and phosphate compounds

http://dx.doi.org/10.5772/66476

using the metal complexes of stable [10–22]. This is the MPM, which is one of the chemical processes used for thin film fabrication. In those days, most of the researchers in the field of thin film formation by chemical processes preferred to use rather unstable metal complexes. It is easy to imagine the capability of polymers to form films because we use polymer films every day. In fact, well-adhered precursor films can be formed on various substrates by coating the solution dispersing the produced oligomers and polymers including metallic species provided by hydrolyzing the unstable metal complexes. These results led us to believe for a long time that only the oligomers and polymers can form precursor films, but the stable metal complexes having discrete molecular weight would not be useful in the formation of such thin films. The MPM was a challenge to this central belief.

The MPM, pertinent to coordination chemistry and materials science including nanoscience and nanotechnology, has been used to fabricate various high-quality thin films with appropriate film thicknesses. As a result, the MPM represents a facile procedure for thin film fabrication of various metal oxides or phosphates, which are useful as electron and/or ion conductors, semiconductors, dielectric materials, etc [24, 25].

Figure 1 shows the Co_3O_4 thin films, which were first fabricated using the molecular precursor solutions. To date, more than 40 kinds of metal oxides or phosphates have been easily fabricated. **Figure 2** shows the general protocol for fabricating the titanium dioxide thin films. First, a water-resistant coating solution was prepared by the reaction of a neutral $[Ti(H_2O)(edta)]$ complex with dipropylamine in ethanol, where edta represents ethylenediamine-*N, N, N′, N′*-tetraacetate anion. Molecular precursor solutions can be used in spin, dip, or spray coating on various material surfaces to form precursor thin films. To obtain the precursor film, the coated film was dried at around 70°C. The precursor films involving metal complexes should be amorphous, just as with the metal/organic polymers in the sol-gel processes; otherwise, it would not be possible to obtain the resulting metal oxide thin films spread homogeneously on substrates by using the following heat treatment. After this, the precursor film was heat-treated at appropriate temperatures for eliminating the components in the organic ligand from the metal complexes involved in the precursor films and to fabricate thin films of crystallized metal oxides or phosphates. The heat treatment of a well-adhered precursor film at 450°C in air is useful for the fabrication of transparent titania thin films.

Figure 1. The Co_3O_4 thin films which were first time to fabricate the thin film using the molecular precursor solutions.

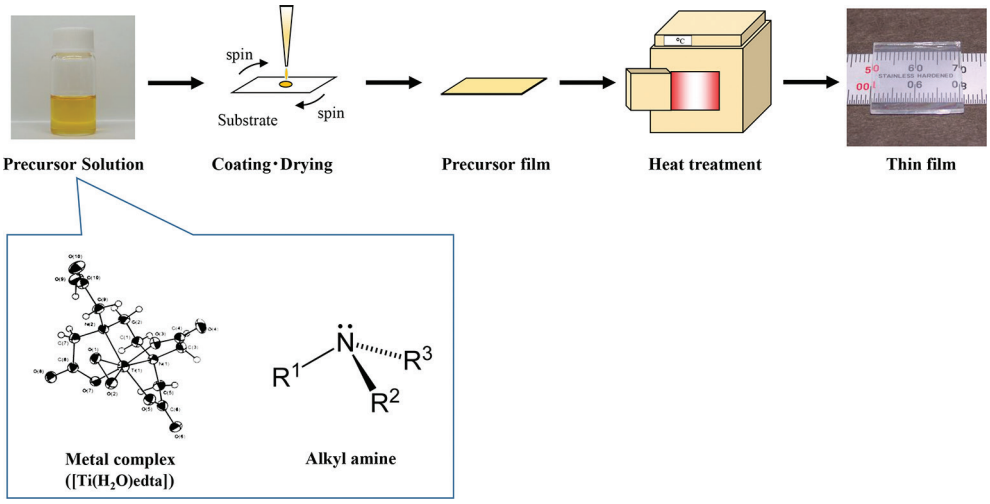

Figure 2. Protocol for fabricating the thin film using the molecular precursor method.

Cuprous oxide, Cu_2O, with a cubic structure is a potential candidate for *p*-type semiconductors having a band gap of 2.0 eV, which is the band gap of its single crystal. The thin films of Cu_2O can be grown generally by dry processes in a vacuum chamber at high temperature, such as sputtering, thermal oxidation, and pulsed laser deposition [26–28]. Over the past years, the quest to obtain high-quality Cu_2O films has fueled the development of many physical processing techniques including sputtering, thermal oxidation, vacuum evaporation, molecular beam epitaxy, and electrodeposition. However, reproducible formation of Cu_2O films uncontaminated by the CuO phase is a formidable challenge from the technical perspective [29, 30]. In addition, most of the aforementioned physical processing techniques are not economically viable in large area applications. Solution-based processes have, therefore, emerged as attractive alternatives because of the ability for cost-effective production [31]. Armelao and coworkers have successfully employed a sol-gel solution containing dissolved copper acetate to produce a Cu_2O thin film [32]. The semiconductive nature of the thin film was, however, unclear owing to the lack of Hall effect measurements in their work.

Recently, *p*-type Cu_2O transparent thin films were fabricated using the thermal reaction of molecular precursor films spin-coated on a Na-free glass substrate [10]. A stable precursor solution for the spin-coating process was facilely prepared by reacting an isolated Cu(II) complex of EDTA with dibutylamine in ethanol. The 50-nm-thick Cu_2O thin film resulting from heat treatment of the precursor film at 450°C for 10 min in Ar gas at a flow rate of 1.0 L min^{-1} was characterized by X-ray diffraction (XRD). **Figure 3** shows the XRD pattern of the resultant thin film deposited on the Na-free glass substrate after heat treating the precursor film. The XRD pattern of the resultant thin film indicated a precise cubic lattice cell parameter with a = 0.4265(2) nm, with a crystallite size of 8(2) nm. No additional peaks from any possible contaminants such as Cu and CuO appeared in the XRD pattern of the Cu_2O film. X-ray

http://dx.doi.org/10.5772/66476

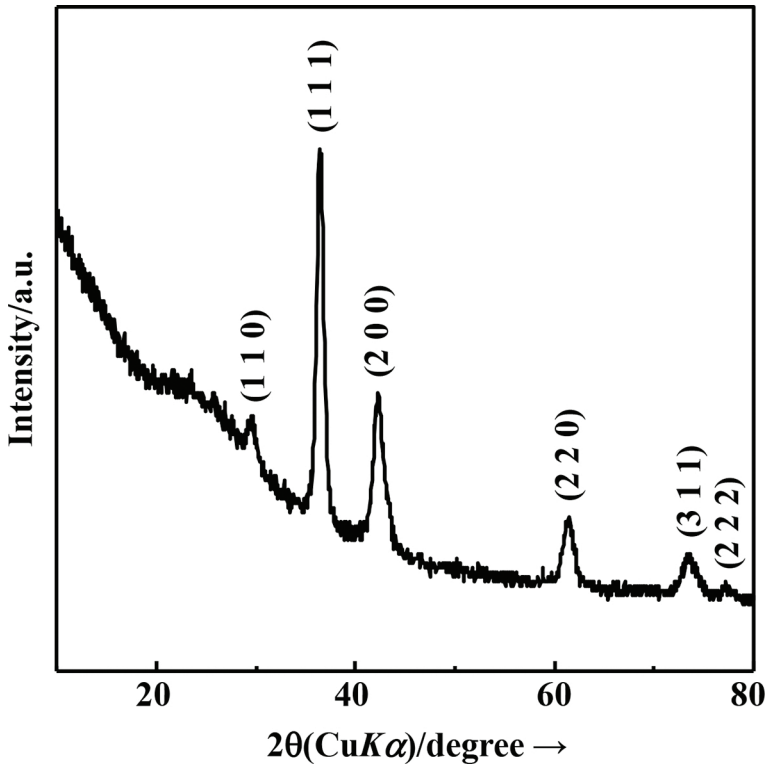

Figure 3. XRD pattern of the thin film adhered to a Na-free glass substrate after heat treatment at 450°C for 10 min in Ar gas at a flow rate of 1.0 L min^{-1}.

photoelectron spectroscopy (XPS) peaks attributed to the O 1s and Cu $2p_{3/2}$ level of the Cu_2O film were observed at 532.6 and 932.4 eV, respectively. The peak position of the Cu $2p_{3/2}$ level is identical to the reported values, which were observed for Cu_2O thin films prepared by other methods [31, 33]. In addition, no peak for the CuO phase was observed at its typical value of 944 eV [31]. The average grain size of the deposited Cu_2O particles was ~200 nm, observed via field-emission scanning electron microscopy (FE-SEM). The optical band edge evaluated from the absorption spectrum of the transparent Cu_2O thin film was 2.3 eV, assuming a direct transition semiconductor. The tensile strength of the films on the glass substrate was measured by a stud pull adhesion test. The tensile strength of the adhesion of the Cu_2O thin film to the substrate was 83(2) MPa, indicating strong adhesion to the glass substrate.

Figure 4 shows the Arrhenius plot of the Cu_2O thin film on the Na-free glass substrate over the temperature range 160–300 K. Hall effect measurements of the thin film indicated that the single phase Cu_2O thin film is a typical *p*-type semiconductor with a hole concentration of 1.7×10^{16} cm^{-3} and hole mobility of 4.8 cm^2 V^{-1} s^{-1} at ambient temperature. The activation energy from the valence band to the acceptor level was determined as 0.30 eV by least-square fitting using the free carrier concentration spectroscopy (FCCS) method [34].

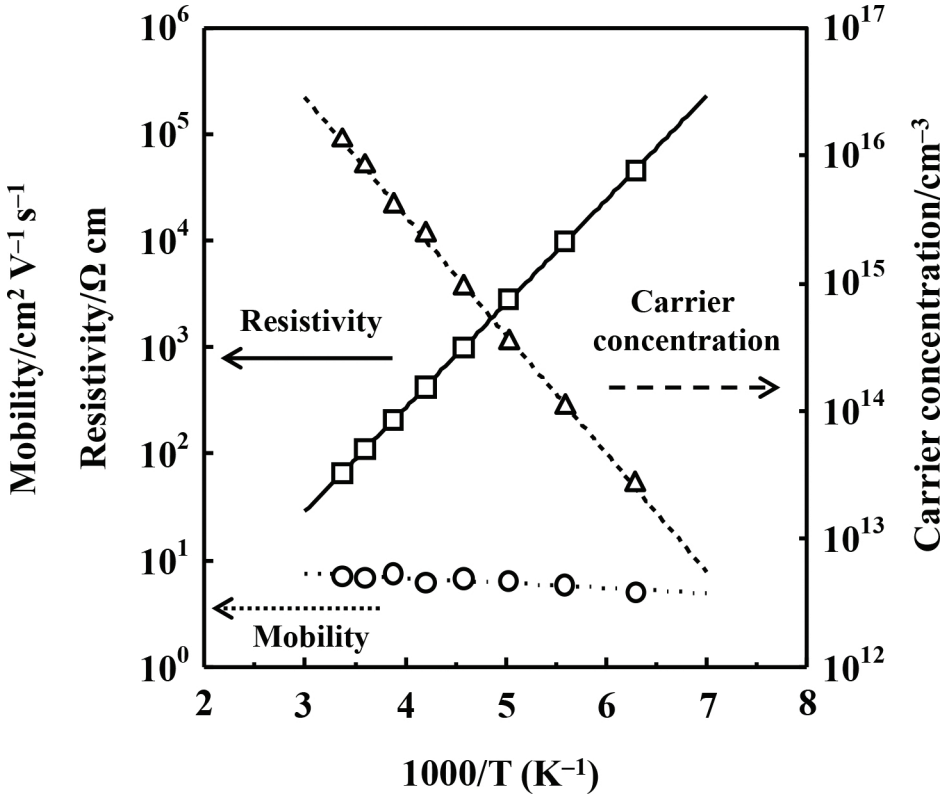

Figure 4. Temperature dependency of the resistivity (— ◊ —), carrier mobility (…o…), and carrier concentration (… Δ …) of the thin film. Film was formed by heat treatment at 450°C for 10 min in Ar gas at a flow rate of 1.0 L min^{-1} on a 10 × 10 × 1.1 mm^3 Na-free glass substrate.

The resistivity of the Cu_2O thin film fabricated using the MPM was lower than that of both films obtained by the oxidation of a copper film and by the dc reactive magnetron sputtering process [26–28]. It was observed that the carrier concentration tends to be high and the carrier mobility is low for the Cu_2O thin film fabricated by the MPM, compared to the thin films formed by previously reported processes (**Table 1**).

The method described is the first example of fabrication and characterization of *p*-type Cu_2O transparent thin films using a coating solution prepared from a starting Cu^{2+} complex of the H_2edta^{2-} ligand. Reduction of the Cu^{2+} species occurred unambiguously through the heating process under Ar gas flow. The CuO phase could be found in the thin film by the prolonged reactions after fabricating the Cu_2O thin film at the identical atmospheric condition and temperature. This result indicates that the formation mechanism of Cu_2O in the MPM differs from that of the sol-gel method, in which the Cu_2O phase was derived from the CuO phase in N_2 atmosphere at 90°C. It is notable that the quality of the resultant thin film fabricated

http://dx.doi.org/10.5772/66476

Method	Annealing condition			Thickness	Carrier concentration	Mobility	Resistivity
	Temperature	Atmosphere	Time	nm	(cm^{-3})	($cm^2\ V^{-1}\ s^{-1}$)	Ω cm
Molecular precursor method	450	Ar gas flow	10 min	50	4.8	76	4.8
Oxidation method [26]	400	10% O_2 in Ar gas	5 min	230	6.1	370	6.1
Magnetron sputtering [27]	200	O_2 gas pressure of 1.1×10^{-3} torr in vacuum	–	130	0.36	1.8	0.36
Pulsed laser deposition [28]	500	In vacuum	6 h	100	32	100	32

Table 1. Comparison of electrical properties of the thin film fabricated herein using a 0.3 mmol g^{-1} precursor solution under Ar gas at a flow rate of 1.0 L min^{-1}, versus those of the films formed by other methods. All values were measured at 300 K.

by the MPM is excellent, but that fabricated by the CuO reduction was not sufficient for Hall effect measurement.

3. Kinetic study of Cu_2O thin film fabrication

In order to clarify the precise mechanism of Cu_2O formation from the Cu(II) complex, a kinetic study was performed using XRD [11]. In the study, it was clarified that the thermal reaction of the precursor film, which consists of a dibutylammonium salt of a $[Cu(edta)]^{2-}$ complex ion, first produced metallic Cu species in Ar gas containing <10 ppm of air as an impurity. The Cu phase appeared gradually, and the amount of the phase could be determined from the area of the (111) peak of Cu. The activation energy (1.5×10^2 kJ mol^{-1}) of the reduction reaction from the Cu(II) complex to metallic Cu species was obtained by an Arrhenius plot over the temperature range 230–250°C. Above this temperature range, the Cu_2O phase was formed by the oxidation of the Cu phase under Ar gas flow. The amount of the Cu_2O phase could be determined from the area of the (111) peak. The activation energy (1.4×10^2 kJ mol^{-1}) of Cu_2O formation from the Cu phase was obtained by the Arrhenius plot over the temperature range 400–450°C. In order to examine the stability of the formed Cu_2O phase, the oxidation reaction rate from Cu_2O to the CuO phase in an identical atmosphere was also measured over the temperature range 450–475°C. The activation energy of the oxidation reaction from Cu_2O to the CuO phase was determined to be 1.0×10^2 kJ mol^{-1}. It was observed that the quality of the *p*-type Cu_2O thin film is strongly dependent on the mechanism of the low-temperature formation.

The XPS spectra of the films are shown in **Figure 5**. The peak positions of the Cu $2p_{3/2}$ level in spectra (a)–(d) are 933.5, 932.7, 932.5, and 933.2 eV in **Figure 5**A, respectively. The peaks observed in (a) and (d) can be assigned to the Cu^{2+} ion, and the broad peak at 944 eV observed in (d) is typical of CuO. In contrast, the peaks observed in (b) and (c) can be assigned to metallic Cu and/or Cu^+ ions. These XPS results are consistent with the XRD results.

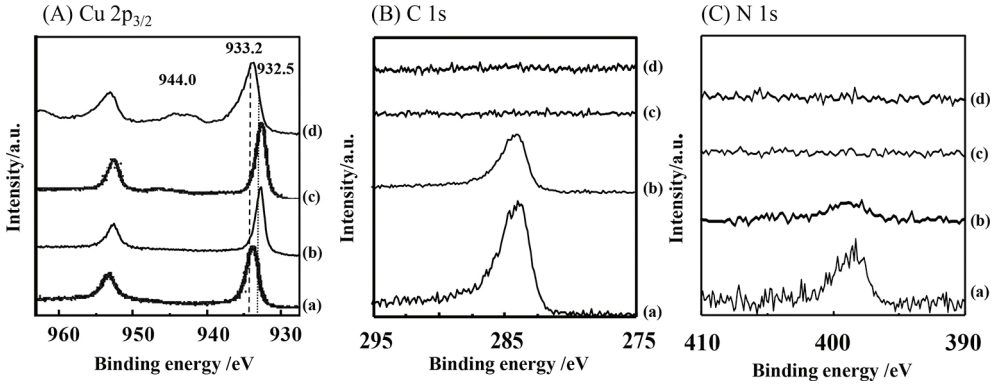

Figure 5. XPS spectra of (A) Cu $2p_{3/2}$, (B) C 1s, and (C) N 1s of the thin films heat-treated in Ar gas flow. The films were fabricated by heat treating the precursor film at (a) 200°C for 10 min, (b) 400°C for 0 min, (c) 450°C for 10 min, and (d) 450°C for 60 min.

In **Figure 5**B and C, the XPS spectra of the C1s and N1s peaks, respectively, are shown. No impurities such as nitrogen or carbon atoms can be found in the XPS spectra of the resultant Cu_2O thin films, although the metallic Cu^0 thin film includes a certain amount of nitrogen and carbon atoms. It was thus clarified that single phase Cu_2O formation was completed by the removal of organic residues in the Cu^0 thin film. The co-presence of nitrogen and carbon atoms was thus shown to have an important role in preventing the oxidation of the produced Cu_2O phase. The presence of nitrogen and carbon atoms may also help in organizing the stepwise reactions.

In the sol-gel method for Cu_2O thin film formation, the CuO film is annealed at 900°C for 5 h in nitrogen for the partial removal of oxygen atoms from the initial oxide thin film. In contrast, the MPM eliminates the organic components in order to form the Cu_2O thin film at the abovementioned lower temperature. It is interesting that the difference between these two methods is in the kind of atoms that must be removed. Furthermore, it is important that the formation route of the *p*-type Cu_2O thin films determines the quality of the thin films, as mentioned above. The MPM is additionally preferable in terms of saving energy by reducing the formation temperature.

It was first shown that the expected Cu_2O formation using the MPM occurred via an unexpected intermediate Cu^0 phase formed by the thermal decomposition of the molecular precursor involving a Cu(II) complex salt. The XRD measurement of the crystallized thin films was useful in determining the activation energies of the redox reactions from the Cu(II) complex to Cu^0, from Cu^0 to Cu_2O, and from Cu_2O to CuO (**Figure 6**). The redox reactions of the metals and organic ligands occurred stepwise with annealing of the thin films under moderate conditions. Consequently, the ligand in the molecular precursor plays an important role in fabricating excellent *p*-type Cu_2O thin films. It is also suggested that kinetic studies on the thermal reactions of metal complexes in the solid state are essential for revealing the reaction mechanism of thin film fabrication.

http://dx.doi.org/10.5772/66476

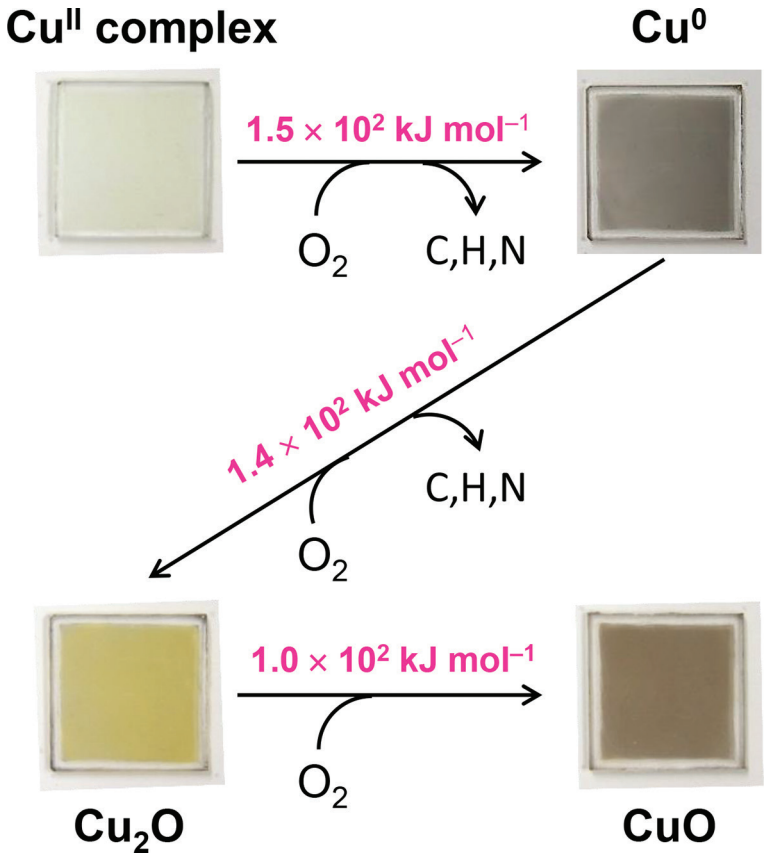

Figure 6. A kinetics study was performed in order to clarify the reaction mechanism for fabricating the excellent p-type Cu_2O thin films by using the molecular precursor method.

4. Fabrication of copper thin films

From the kinetic study of the Cu_2O thin film formation, it was elucidated that the Cu^0 species formed as an intermediate was oxidized to the resultant Cu_2O thin film during the heat treatment, and the oxidizing agent is the oxygen present in the commercially available Ar gas as an impurity (<2 ppm) [11]. However, the intermediate Cu thin film obtained through the reaction using the precursor film is not electrically conductive. Therefore, in order to fabricate transparent metal copper thin films, we examined novel precursor solutions [35, 36]. A novel precursor solution containing a Cu^{2+} complex of EDTA and a Cu^{2+} complex of propylamine derived from formic acid, and the amine was prepared by mixing the two precursor solutions. The concentration of total copper in the ethanolic precursor solution was adjusted to 0.35 mmol g^{-1}. The spin-coating method was used for precursor film formation on a Na-free glass substrate. The spin-coated precursor films were preheated in a drying oven at 70°C for 10 min

and then, heat-treated at 350°C for 15 min under an Ar gas flow of 1.5 L min^{-1} to fabricate thin films in a tubular furnace with a quartz glass tube. The resultant thin film is hereby denoted as **A**. The rate of temperature increase was controlled by a proportional-integral-derivative program preinstalled in the furnace. Before increasing the temperature, the tubular furnace was filled with Ar gas. The thickness of the resultant films was measured using a stylus profilometer. A flat- and same-sized quartz glass plate was placed on the resulting thin film **A** in the tubular furnace and then post-annealed at 350°C for 20 and 40 min in an Ar gas flow of 1.5 L min^{-1}. The resulting thin film is hereby denoted as **APn** (n = post-annealing time). The XRD patterns of the resultant thin films **A, AP20**, and **AP40** with a thickness of 40 nm over the 2θ range 30°–50° are shown in **Figure 7**. The peaks at 2θ = 36.6° and 42.5° for **A** can be assigned to the (111) and (200) phases of Cu_2O, respectively, and an additional peak at 43.5° for **A** is assigned to the (111) phase of copper (JCPDS card No. 04–0836). The peak at 2θ = 36.9° for **AP20** is assigned to the (111) phase of Cu_2O and that at 43.7° can be assigned to the (111) phase of copper.

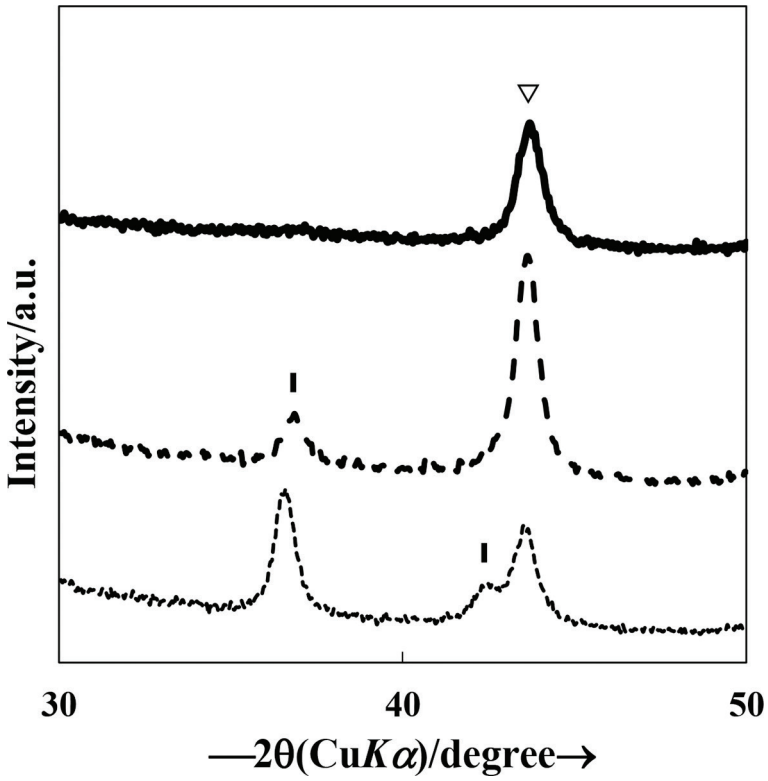

Figure 7. XRD patterns of A, AP20, and AP40 thin films. Parallel beam optics (θ = 0.3°) was employed for calculations. The lines indicate the following: ……A, ----AP20, and — AP40. The peaks are denoted as follows: ▽ Cu; | Cu_2O.

http://dx.doi.org/10.5772/66476

The single peak at 2θ = 43.7° for **AP40** is attributed the (111) phase of copper. Thus, the Cu_2O phase decreased gradually with increasing post-annealing time, and no peak owing to any impurity phase such as Cu_2O and CuO could be detected in the annealed **AP40** film. The cell parameter of the Cu cubic lattice in **A**, which was determined by the Wilson & Pike method, is a = 3.71(3) Å, and the crystallite size of Cu crystals formed in the film can be determined as 11(1) nm; the estimated standard deviations are presented in parentheses. The cell parameter of the Cu cubic lattice in **AP40** is a = 3.72(3) Å, and the crystallite size of the Cu crystals can be determined as 13(1) nm. The surface morphology of the **A** and **AP40** thin films was observed using FE-SEM. The grain size of the Cu particles also increased from 50 nm (A) to 70 nm (AP40) upon annealing. **Figure 8** shows the Auger spectra of **A, AP20**, and **AP40** thin films. Broad peaks were observed at 264 eV for carbon, 509 eV for oxygen, and 764, 835, and 914 eV for copper atoms. The kinetic energies of the copper atoms are identical to those in other films fabricated by the MPM. The result indicates that the amount of carbon atoms in the **AP40** thin film was reduced to half by the post-annealing treatment of **A**. **Figure 9** shows

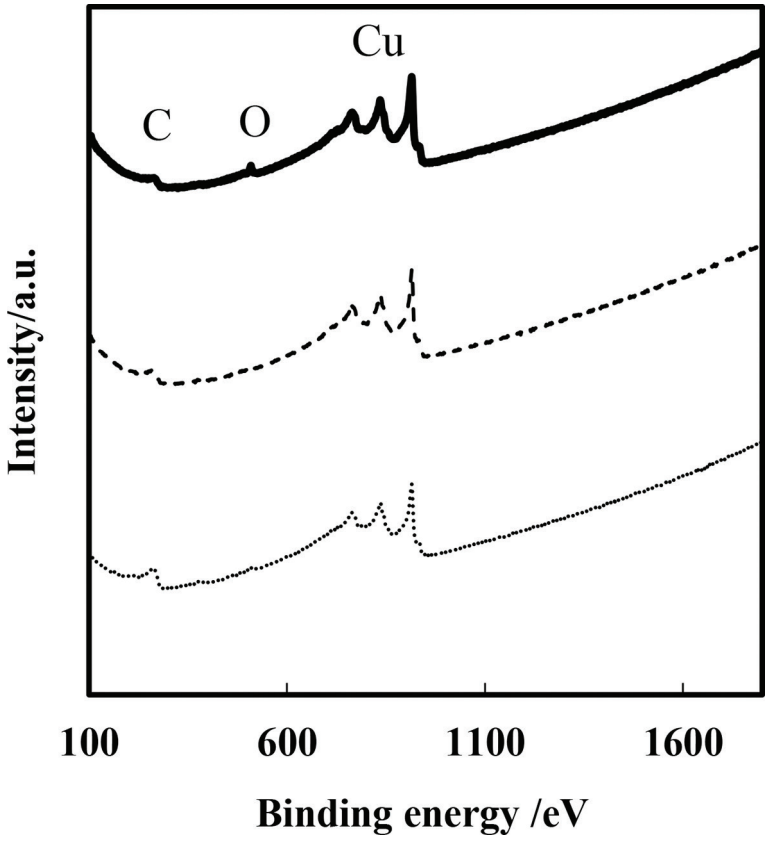

Figure 8. The Auger spectra of A and A20, and AP40 thin films. The lines indicate the following: ……A, ----AP20, and —AP40, respectively.

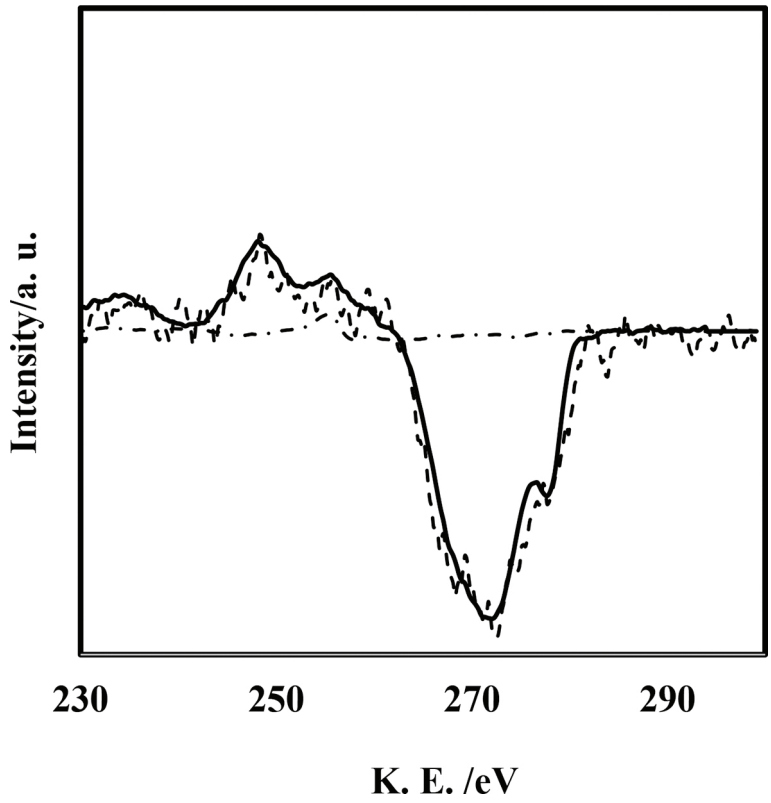

Figure 9. The curve fitting results of carbon state in AP40 thin film. The lines indicate the following: ……A, —Carbon (neutral), -·-·-·Carbon (tetravalent), respectively.

the curve fitting results of the Auger spectrum for **A** over the range 230–300 eV, corresponding to the carbon atoms, along with the curves of the neutral and tetravalent carbon atoms. The curve fitting results suggest that the carbon atom in **A** was 85% agreement to the neutral. The electrical resistivity of the **A, AP20**, and **AP40** thin films is 7.5×10^{-4}, 2.8×10^{-4}, and 4.7×10^{-5} Ω cm, respectively. Thus, highly conductive translucent copper thin films could be obtained in commercially available Ar gas. A plausible scheme for copper lattice formation, which can be deduced from the XRD and Auger spectra, is presented in **Scheme 1**.

$$4(\text{Cu-complexes}) \xrightarrow{<2\ \text{ppm}\ O_2} 4\left(\alpha\text{Cu} + \frac{1-\alpha}{2}\text{Cu}_2\text{O} + \beta\text{C}\right) \xrightarrow{\frac{\beta}{2}\text{COx}} 4\left(\text{Cu} + \frac{\beta}{2}\text{C} + \frac{1-\alpha-\beta}{4}\text{O}_2\right)$$

$\xrightarrow{\text{COx, NOx}}$ **A** **AP40**

Scheme 1. Plausible scheme for the formation of a Cu thin film from the precursor film.

http://dx.doi.org/10.5772/66476

The scheme indicates that four Cu complexes are required to construct one FCC copper unit cell. During the heat treatment of the precursor complexes in Ar gas flow containing <2 ppm of oxygen as impurity, neighboring complexes react with each other. The valency of copper was reduced from +2 to 0 by the thermal decomposition of the complexes of EDTA and butylamine ligands in Ar gas. In the process, Cu_2O involving Cu and the neutral carbon atom is produced in the **A** thin film. During the reaction from the **A** thin film to the resultant **AP40** thin film by post-annealing, when the oxygen content is below 2 ppm in the Ar gas, it cannot react with the film, because the quartz glass plate placed on the **A** thin film can prevent the film from encountering the oxygen molecule. In fact, the copper thin film, which was separately prepared by a vacuum plating method, was not oxidized by post-annealing under an identical condition. Thus, it is accepted that the reduction reaction occurred because of the materials inside the **A** thin film. Under these conditions, only one candidate that can act as a reductant for Cu^{2+} ion remains on the carbon atoms in film **A**.

The polycrystalline Cu lattices were gradually structured by reducing the valency of the Cu^{2+} ion with carbon atoms, and the Cu grains were simultaneously grown by annealing. This reaction mechanism involving the reduction reaction caused by carbon atoms may be comparable to the modern and indirect steel-making system using corks. The tensile strength of the **AP40** adhered onto the Na-free glass substrate was 36(12) MPa as determined from the stud pull adherence tests, indicating strong adhesion to the glass substrate. The tensile strength of the Cu film deposited onto an identical Na-free glass substrate by a vacuum plating method was 1.7(5) MPa after an identical heat treatment of the **AP40** thin film. Thus, the tensile strength of the **AP40** thin film on the Na-free substrate was more than 20 times higher than that of the Cu thin film deposited by the vacuum plating method. The covalent bonds between the trace amounts of Cu^{2+} ion present locally at the interface between the thin film **AP40** and the O^{2-} ions belonging to the Na-free glass molecules may assist in the formation of a robust interface between the Na-free glass substrate and the **AP40** thin film. In fact, the tensile strength of the adhesion of the Cu_2O thin film to the substrate fabricated using the MPM was 83(2) MPa.

Figure 10 presents the transmittance and reflectance spectra of the thin films. The transmittance spectra of **A, AP20**, and **AP40** are not significantly different in the UV-Vis region, and the transparency of **AP40** is more than ~30% in the visible region. The infrared reflectance of **AP40** is higher than 40% and reached 100% in the far-infrared region, whereas the reflectance of **A** was low, 20–30%, over this region. The MPM can facilely control the film thickness by adjusting the concentration of Cu ion in the precursor solution under identical spin-coating conditions. When the Cu thin film is 100-nm-thick, the conductivity is 1.8×10^{-5} Ω cm, and the transparency in the visible region is below 5%. Thus, a thicker film indicates higher conductivity, but reduced transparency.

Recently, we attempted to embed copper in narrow trenches (0.2–1.0 μm wide and 5.0 μm deep) by using the MPM. A new precursor solution was prepared by dispersing the Cu nanopowder (20–40 nm) into the abovementioned Cu precursor solution. Si substrates with the trenches were immersed in this precursor solution under ultrasonic vibration for 1 min and then slowly withdrawn from the solution. The dip coating and heat treatment steps were repeated twice. The cross-sectional FE-SEM images of the treated substrate indicate that the embedded copper fills the trenches without voids.

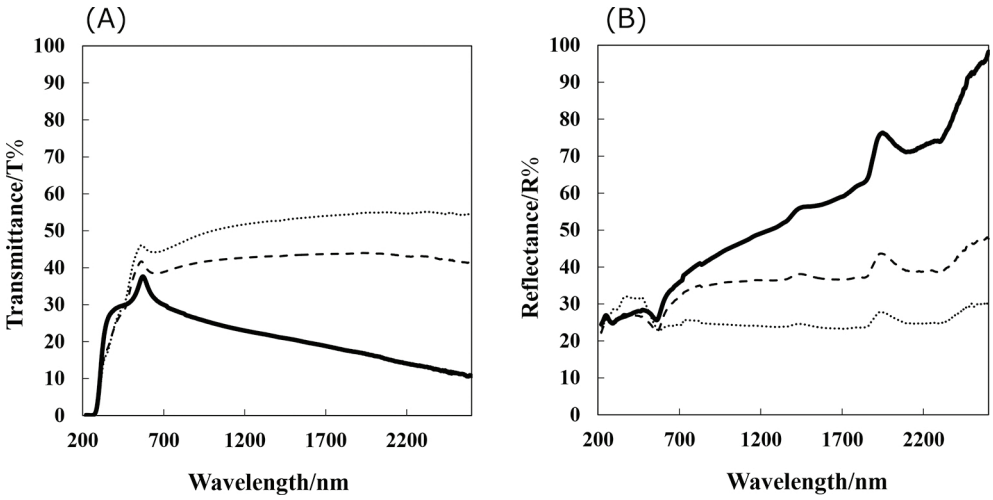

Figure 10. (A) The transmittance spectra of the resulting thin films. The lines indicate the following: ……A, ----AP20, and —AP40, respectively. (B) The reflectance spectra of the resulting thin films. The lines indicate the following: ……A, ----AP20, and —AP40, respectively.

5. Conclusion

Thermal reactions of metal complex films useful for ceramic thin film production such as Cu_2O did not attract much attention for a long time, with the exception of the CVD procedure. However, we indicated that the MPM provides facile and unique routes to obtain *p*-type Cu_2O and metallic Cu thin film with excellent adhesion to glass substrates, through the thermal reactions of metal complexes.

The importance of the metal complex in the MPM was presented by using the unprecedented thin film fabrication of *p*-type Cu_2O, along with the recently elucidated reaction mechanism. In general, impurities such as nitrogen and carbon atoms interfere seriously with the functions of semiconductor devices. However, the present molecular precursor involving nitrogen and carbon atoms is necessary for fabricating an excellent *p*-type Cu_2O thin film using this solution-based process. Additionally, in the chemical fabrication of copper thin films with high conductivity, an organic ligand that reacts with the central Cu(II) ion is essential, and the atoms derived from the ligand, which can act as a reductant, prevent the produced copper from oxidation.

It is important that most of the originally included atoms in the MPM system are not involved in the resultant thin films if the amounts and treatment are appropriate. Therefore, the role of the ligand of the metal complex resembles that of auxiliary lines to solve geometrical problems in mathematics. In the sol-gel process, the similarity of the gel composition and the final oxides is desirable and is supposed to be an advantage of the method, though the rearrangement of the polymerized amorphous species to the crystalline requires much energy. From this point of view, the concept of the MPM is quite different from that of the conventional sol-gel method and has many potential applications.

Author details

Hiroki Nagai and Mitsunobu Sato*

*Address all correspondence to: ft10302@ns.kogakuin.ac.jp

Department of Applied Physics, School of Advanced Engineering, Kogakuin University, Tokyo, Japan

References

[1] Werner K. Vossen JL., ed. Thin Film Processes. New York:Academic Press; 1978. pp.564.

[2] Minami T., Nishi Y., Miyata T. High-efficiency Cu_2O-based heterojunction solar cells fabricated using a Ga_2O_3 thin film as n-type layer. Appl. Phys. Express. 2013;6:044101.

[3] Ichimura M., Kato Y. Fabrication of TiO_2/Cu_2O heterojunction solar cells by electrophoretic deposition and electrodeposition. Mater. Sci. Semicond. Process. 2013;16:1538–1541.

[4] Chen JW., Perng DC., Fang JFD. Nano-structured Cu_2O solar cells fabricated on sparse ZnO nanorods. Sol. Energy Mater. Sol. Cells. 2011;95:2471–2477.

[5] Seung KB., Ki RL., Hyung KC. Oxide p-n heterojunction of Cu_2O/ZnO nanowires and their photovoltaic performance. J. Nanomater. 2013;2013:421371–421378.

[6] Chun-Hong K., Michael H. Morphologically controlled synthesis of Cu_2O nanocrystals and their properties. Nano Today. 2010;5:106–116.

[7] Toth RS., Kilkson R., Trivich D. Preparation of large area single-crystal cuprous oxide. J. Appl. Phys. 1960;31:1117–1121.

[8] Fortin E., Masson D. Photovoltaic effects in Cu_2O solar cells grown by anodic oxidation. Solid State Electron. 1982;25:281–283.

[9] Drobny VF., Pulfrey L. Properties of reactively-sputtered copper oxide thin films. Thin Solid Films. 1979;61:89–98.

[10] Nagai H., Suzuki T., Hara H., Mochizuki C., Takano I, Honda T., Sato M. Chemical fabrication of p-type Cu_2O transparent thin film using molecular precursor method. Mater. Chem. Phys. 2012;137:252–257.

[11] Nagai H., Suzuki T., Hara H., Mochizuki C., Takano I., Honda T., Sato M. Formation mechanism of p-type Cu_2O thin films via intermediate Cu^0 species derived from Cu(II) complex of ethylenediamine-N,N,N'N'-tetraacetic acid. Sci. Adv. Mater. 2014;6:603–611.

[12] Sato M., Hara H., Niside T., Sawada Y. A Water-resistant precursor in a wet process for TiO_2 thin film formation. J. Mater. Chem. 1996;6:1767–1770.

[13] Nishide T., Sato M., Hara H. Crystal structure and optical property of TiO_2 gels and films prepared from Ti-edta complexes as titania precursors. J. Mater. Sci. 2000;35:465–469.

[14] Sato M., Hara H., Kuritani M., Nishide T. Novel route to Co_3O_4 thin films on glass substrates via N-alkyl substituted amine salt of Co(III)-EDTA complex. Sol. Energy Mater. Sol. Cells. 1997;45:43–49.

[15] Sato M., Tanji T., Hara H., Nishide T., Sakashita Y. $SrTiO_3$ film fabrication and powder synthesis from a non-polymerized precursor system of a stable Ti(IV) complex and Sr(II) salt of edta. J. Mater. Chem. 1999;9:1539–1542.

[16] Nagai H., Mochizuki C., Hara H., Takano I., Sato M. Enhanced UV-sensitivity of Vis-responsive anatase thin films fabricated by using precursor solutions involving Ti complexes. Sol. Energy Mater. Sol. Cells. 2008;92:1136–1144.

[17] Nagai H., Hasegawa M., Hara H., Mochizuki C., Takano I., Sato M. An important factor controlling the photoreactivity of titania: O-deficiency of anatase thin film. J. Mater. Sci. 2008;43:6902–6911.

[18] Nagai H., Aoyama S., Hara H., Mochizuki C., Takano I., Baba N., Sato M. Rutile thin film responsive to visible light and with high UV light sensitivity. J. Mater. Sci. 2009;44:861–868.

[19] Nagai H., Aoyama S., Hara H., Mochizuki C., Takano I., Honda T., Sato M. Photoluminescence and photoreactivity affected by oxygen defects in crystal-oriented rutile thin film fabricated by molecular precursor method. J. Mater. Sci. 2010;45:5704–5710.

[20] Likius DS., Nagai H., Aoyama S., Mochizuki C., Hara H., Baba N., Sato M. Percolation threshold for electrical resistivity of Ag-nanoparticle/titania composite thin films fabricated using molecular precursor method. J. Mater. Sci. 2012;47:3890–3899.

[21] Mochizuki C., Sasaki Y., Hara H., Sato M., Hayakawa T., Yang F., Hu X., Shen H., Wang S. Crystallinity control of apatite through Ca-EDTA complexes and porous composites with PLGA. J. Biomed. Mater. Res. Part B. 2009;90:290–301.

[22] Honda T., Oda T., Mashiyama Y., Hara H., Sato M. Fabrication of c-axis oriented Ga-doped MgZnO-based UV transparent electrodes by molecular precursor method. Phys. Status. Solidi. 2010;7:2471–2473.

[23] Werner HA. A forerunner to modern inorganic chemistry. Angew. Chem. Int. Ed. 2013;52:6146–6153.

[24] Nagai H., Sato M. Heat Treatment in Molecular Precursor Method for Fabricating Metal Oxide Thin Films. In: Czerwinski F., editor. Heat Treatment – Conventional and Novel Applications. Rijeka:InTech; 2012. pp. 103–124.

[25] Nagai H., Sato M. Highly Functionalized Lithium-Ion Battery. In: Yang D., editor. Alkali-Ion Batteries. Rijeka: InTech; 2016. pp. 111–124.

[26] Jayatissa HA., Guo K., Jayasuriya CA. Fabrication of cuprous and cupric oxide thin films by heat treatment. Appl. Surf. Sci. 2009;255:9474–9479.

[27] Chu CL., Lu CH., Lo YC., Lai YC., Wang HY. Physical properties of copper oxide thin films prepared by dc reactive magnetron sputtering under different oxygen partial pressures. Phys. B. 2009;404:4831–4834.

[28] Kikuchi N., Tonooka K., Kusano E. Mechanisms of carrier generation and transport in Ni-doped Cu_2O. Vacuum. 2006;80:756–760.

[29] Ogwu AA., Bouquerel E., Ademosu O., Moh S., Crossan E., Placido F. The influence of rf power and oxygen flow rate during deposition on the optical transmittance of copper oxide thin films prepared by reactive magnetron sputtering. J. Phys. D: Appl. Phys. 2005;38:266–271.

[30] Ishizuka S., Kato S., Maruyama T., Akimoto K. Nitrogen doping into Cu_2O thin films deposited by reactive radio-frequency magnetron sputtering. Jpn. J. Appl. Phys. 2001;40:2765–2768.

[31] Chen A., Long H., Li X., Li Y., Yang G., Li P. Controlled growth and characteristics of single-phase Cu_2O and CuO films by pulsed laser deposition. Vacuum. 2009;83:927–930.

[32] Armelao L., Barreca D., Bertapelle M., Bottaro G., Sada C., Tondello E. A sol-gel approach to nanophasic copper oxide thin films. Thin Solid Films. 2003;442:48–52.

[33] Moulder FJ, Stickle FW, Sobol EP, Bomben DK. Handbook of X-ray photoelectron spectroscopy. 2nd ed. Waltham: Perkin-Elmer Corp.; 1992. 81 p.

[34] Matsuura H., Sonoi K. A simple graphic method for evaluating densities and energy levels of impurities in semiconductor from temperature dependence of majority-carrier concentratio. Jpn. J. Appl. Phys. 1996;35:555–557.

[35] Nagai H., Suzuki T., Nakano T., Sato M. Embedding of copper into submicrometer trenches in a silicon substrate using the molecular precursor solutions with copper nano-powder. Mater. Lett. 2016;182:206–209.

[36] Nagai H., Mita S., Takano I., Honda T., Sato M. Conductive and semi-transparent Cu thin film fabricated using molecular precursor solutions. Mater. Lett. 141;2015:235–237.

Chapter 2

Modification of Oxide Thin Films with Low-Energy Ion Bombardment

Oscar Rodríguez de la Fuente

Additional information is available at the end of the chapter

http://dx.doi.org/10.5772/66651

Abstract

We review in this chapter the use of low-energy ion bombardment (LEIB) in oxide thin films. In most cases, radiation effects in oxides are ultimately based on the preferential sputtering of the oxygen anions, yielding a chemically reduced oxide. The physics governing the processes in the low ion energy range will be briefly commented here. Also, general uses and applications of LEIB are reviewed here, focusing later in those specific applications on oxide layers. LEIB in oxides has supported, for instance, the fabrication of conductive transparent layers on top of semiconductors or the formation of self-organized morphological surface patterns. Finally, we show a novel application of LEIB when applied on single-crystalline surfaces of some oxides, which is the formation of an epitaxial thin film of the corresponding suboxide. For instance, we show how ion bombardment transform the surface of TiO_2(110) into an epitaxial TiO(001) thin film.

Keywords: low-energy ion bombardment, oxide, thin film, defect, epitaxy

1. Introduction

Ion irradiation of solids has been a research topic for decades. In the keV range, the maximum penetration depth in the material does not exceed a few nanometers, and ions in this range of energies have traditionally assisted in the preparation and analysis of surfaces: it has served as a cleaning tool in vacuum conditions and, combined with surface analysis techniques, in compositional depth analysis or to assist in the growth of thin films. But low-energy ion bombardment (LEIB) has been also a tool to controllably modify surfaces or thin films. It has several advantages over other surface modification methods: (a) its low penetration depth, which allows the modification of a shallow surface layer or a thin film, (b) the high degree of control by choosing the type of ion, energy, flux, and dose received by the sample, and (c) the possibility of modifying very small surface areas by using masks or focused beams.

We focus in this chapter in this low-energy range (from a few hundred eV to a few keV), showing the capabilities of the technique for a specific family of systems: thin oxide films. Oxides are materials which display a huge plethora of physical and chemical properties, and in the form of thin films, they have been extensively studied in the last two decades. Its ample tolerance to defects favors the availability of compounds with different stoichiometries and properties. This is a source of complexity but also provides opportunities to explore many different properties in various fields, such as catalysis, magnetism, sensors, or electronics. LEIB stands as a very attractive experimental technique to modify the properties of oxide thin films by creating defects or inducing structural and compositional transitions.

Oxides are present in a large number of technological devices, and a growing number of applications will probably be found in the coming decades. For this to occur, a broad insight of their properties and a deep understanding of the role played by defects will be required. As in the case of silicon technology, where defect engineering is responsible for the precise and powerful control of electronic properties, defect engineering in oxides is for sure the tool to be exploited to enhance the performance of any present or potential device based in oxides. This is by no means a novel statement, for it has been well known for many decades that the presence of defects in oxides determines many of their properties. However, two challenges nowadays are (a) to acquire a more profound knowledge of defects properties in oxides and (b) to be able to introduce them in the surface of the material in a controlled way. LEIB is a good tool for this purpose but goes beyond the simple generation of defects. It also induces the formation of new structural phases or the generation of textured and nanostructured surfaces, as we will describe in this chapter.

1.1. Historical remarks

Ion sputtering, or the ejection of atoms from surfaces with energetic ions, is a phenomenon reported more than 150 years ago. The effect of sputtering was already described in 1853 by Grove [1], when he observed that the cathode metal located inside discharge tubes gradually coated the inner walls. The coating was caused by the positive ions of the discharges hitting the negatively charged metal cathode, sputtering atoms away from it subsequently coating the glass. However, this was not unambiguously verified until 1902, about 50 years later, when Goldstein [2] performed the correct experiments. In the meantime, other hypotheses were considered (such as that thermal evaporation induced by the discharge). But the effect of atomic collisions from positively charged ions was finally acknowledged. It was in the mid-1900s that a quantitative description of the sputtering process was reached and a sound theory was developed. Since then, hundreds of works have continued improving the existing theories and performing new experiments about surface sputtering. Some of these works are reviewed in the excellent work by Sigmund [3]. The purpose of many of these investigations has been the application of low-energy ion bombardment on a growing number of materials, where of course we can meet oxides.

1.2. Organization of the chapter

In this work, we start introducing the most important theoretical concepts related to ion bombardment, focusing around the low-energy range. As we are dealing with oxides, the

http://dx.doi.org/10.5772/66651

concept of preferential sputtering of multicomponent materials is discussed. Then, we present some of the many applications or current uses of the technique for all types of materials, such as the modification of the surface topography or the controlled introduction of surface defects. Next, we invoke those uses reported in the literature about oxide surfaces and thin films, grouped in two big sets: (a) those examples exclusively describing morphological, structural, and chemical changes of the surfaces and (b) those works reporting other associated physicochemical properties, such as electrical conductivity. Finally, we present two applications recently carried out in our research group, which is the formation of single-crystalline epitaxial thin films of a suboxide when the surface of the corresponding oxide is ion bombarded: we report the formation of a TiO(001)/TiO_2(110) thin film and a Fe_3O_4(111)/α-Fe_2O_3(0001) bilayer.

2. Theoretical background

We present in this section a few theoretical concepts about some of the most relevant physical processes taking place during the collision of ions with solid surfaces. For a more profound study of the physics involved, the reader is referred to other works in the literature [3, 4].

2.1. Ion stopping

Several mechanisms are active when an ion enters a solid material, dissipating its initial energy. Ion stopping in a solid can take place by interactions with both the electrons and ions of the crystal. The physical quantity describing the interaction of the ion with the solid is the stopping power or cross section $S(E)$, which depends on the ion energy, and so it can be divided into two terms, an electronic (e) and a nuclear (n) term:

$$S(E) = S_e(E) + S_n(E) = -\frac{1}{N}\left(\left(\frac{dE}{dx}\right)_e + \left(\frac{dE}{dx}\right)_n\right) \quad (1)$$

As Eq. (1) states, $S(E)$ can be also described in terms of the energy loss rate dE/dx, being N the number density of atoms in the crystal. It is interesting to note that, as a universal reference, energy losses are typically of several hundreds of eV/nm in the low-energy range.

Collisions of the incident ion with electrons are more frequent, but in the range of low-to-medium energies, they have a little effect on the main trajectory of the ion (because of their small mass). In these ranges, electronic stopping has a comparable effect to that of a viscous flow continuously reducing the kinetic energy of the ion. In contrast, the interaction with the ions is more discrete, taking place between elastic consecutive collisions. For these nuclear losses, a simple elastic model using conservation of momentum describes the maximum transferred energy T_{max} from an incident atom to the struck atom as

$$T_{\max} = \frac{4 E_0 M_1 M_2}{(M_1 + M_2)^2} \quad (2)$$

where M_1 and M_2 are the masses of both atoms and E_0 is the kinetic energy of the incident one.

Depending on the nature of the collision, the effect produced has been typically classified in three regimes. In the *single knock-on* regime, the incident ion generates a small cascade of events, where atoms sequentially transfer their energy. Eventually, one of the atoms surpasses the lattice binding forces and is ejected out of the solid. But if the ion is sufficiently energetic, secondary cascades are generated, each of which can produce their own sputtered atoms. But the whole process can still be described as a sum of individual events. This is called the *linear cascade* regime. If, instead, the energy density of the collision is very high and most of the atoms located in a region are severely displaced from their equilibrium positions, looking more like a melted fluid, the regime is called *thermal spike*. The range where a given event is placed depends not only on the ion energy but also on the ion mass. As can be deduced from Eq. (2), a light ion (H^+, He^+, etc.) is very inefficient in its energy transfer T_{max} and enters the spike regime at very high ion energies. Most of the cases considered in this chapter, with medium-mass ions (mostly Ar^+) with up to a few keV of energy, lie in the *single knock-on* or *linear cascade* regime.

2.1.1. Ion range

To evaluate the spatial range of the area of the ion-bombarded material, the most important concept is that of the ion range *R*. The ion range in a solid is the integrated distance traveled by the ion before it stops after reducing its energy to zero, and so it is defined as

$$R = \int_{E_i}^{0} \frac{dE}{dE/dx} \tag{3}$$

Another useful magnitude is the projected range R_p, defined as the distance of *R* projected along the incoming direction of the ion before entering the solid. In the case of normal incidence, R_p is just the depth at which the ion remains implanted, which is not necessarily the distance traveled *R*. **Figure 1** shows schematically these parameters.

2.2. Partial sputtering yield

The sputtering yield is the average number of atoms leaving the solid per incoming ion. An atom is sputtered off the solid when it receives an impact which overcomes the threshold energy and has the possibility to exit the solid and enter the vacuum region. While the former condition is achieved by many atoms involved in cascade collisions, the last condition is only fulfilled by a few atoms close to the surface with their linear momentum pointing away toward vacuum.

As we are dealing with oxides, the concept of preferential sputtering is the most important one. Ion irradiation of multicomponent surfaces always involves compositional changes. Many works in the literature deal with these types of processes, which we will briefly expose here (the reader is referred to Ref. [5] for an excellent review of the topic). The most important physical quantity in a multicomponent material is the partial sputtering yield Y_i of element *i*, which is the average number of ejected *i* atoms per incoming ion. Mathematically, it can be defined as

$$Y_i = \int_0^{-\infty} p_i(z)\, N_i(z)\, dz \tag{4}$$

http://dx.doi.org/10.5772/66651

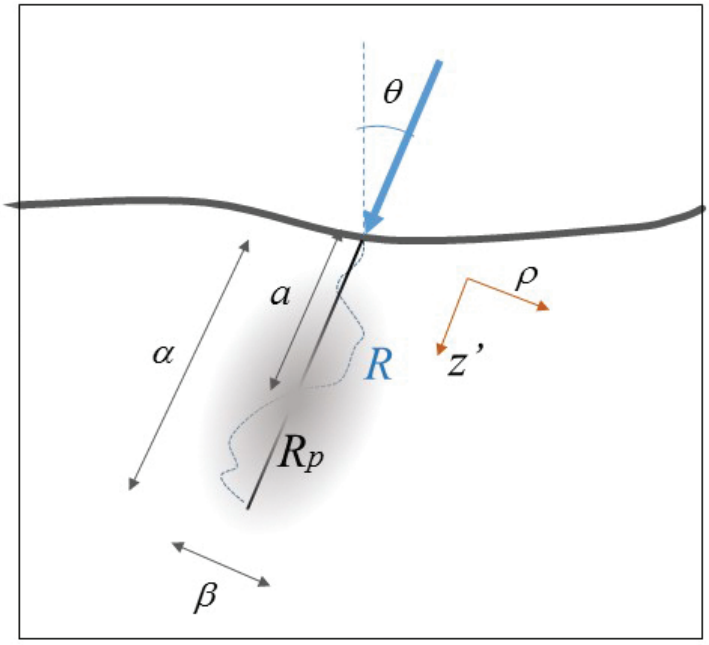

Figure 1. Scheme of the main parameters from Eqs. (3) to (6) for an ion impinging a surface at an angle θ. The center of the ellipsoid represents the region where the ion deposits most of its energy.

where the partial sputtering yield depends on the density $N_i(z)$ of atoms of type i (in atoms per unit volume) at a given depth z below the surface and with a sputtering probability $p_i(z)$, which decays to zero with increasing depth.

2.2.1. *Preferential sputtering of oxygen*

In a simple binary oxide, the ratio between the partial sputtering yields can be described as Eq. (4)

$$\frac{Y_M}{Y_O} = \frac{N_M}{N_O}\left(\frac{M_O}{M_M}\right)^{2m}\left(\frac{U_O}{U_M}\right)^{1-2m} \tag{5}$$

where N_i are the atomic densities, M_i are the masses, and U_i are the binding energies of the species (M stands for the metal cation and O for the oxygen anion). m is an exponent which characterizes the type of interatomic potential describing the collision and varies from 1 to 0 in the range from high to very low energies, respectively. Eq. (5) predicts that oxygen atom (the lightest atom and also frequently the most weakly bound to the crystal lattice) will be more easily ejected off the solid. However, Eq. (5) only describes a transient state. If the ion penetration depth is much smaller than the thickness of the sample bombarded, a steady state (after a sufficiently large ion fluence) will be reached where the bombarded material loses elements

in a ratio equal to its bulk composition. That is a simple consequence of mass conservation, and it is achieved if mass diffusion to long distances is not relevant.

According to the effects previously addressed, a clear consequence of ion sputtering is the formation of a modified layer, not only in terms of its structure or its density of defects but also in terms of chemical composition. A fact to take into account is that the depth of the altered layer may be larger than the penetration depth of the incoming ions. The reason can rely on thermal or bombardment-induced diffusion. Dissipated energy, either from the ion beam or from mechanical agitation from collisions, enhances diffusion. The diffusion is driven by a chemical gradient, which can be present even from many atomic layers below R_p (so, relatively far from the direct influence of the impinging ion).

3. Applications of low-energy ion bombardment

3.1. Surface cleaning and sample preparation

Probably, the most extended application of ion bombardment is the cleaning of the surfaces prior to their analysis or before another physical or chemical process. For instance, those surfaces of hard drilling tools which are to be coated with nitrides by means of physical vapor deposition (PVD) are usually exposed to Ar^+ prior to the coating. The reasons are the cleaning of the surface and the enhancement of atomic rugosity, which will favor mechanical adhesion of the coating, and thus will warrant a longer life of the tool. This process is one of the many examples in surface science and engineering which requires LEIB. Another extended use occurs for transmission electron microscopy (TEM), which requires thin (electron transparent) samples. The final stage is usually carried out with ion bombardment, usually named ion milling.

3.2. Secondary ion mass spectroscopy (SIMS)

Ion bombardment, sometimes in conjunction with surface analysis techniques, has been traditionally used to obtain surface composition. Secondary ion mass spectroscopy (SIMS) analyses, with the help of a mass spectrometer, the nature of the atoms sputtered from a surface with an ion beam [6]. It is a useful technique to carry out depth profiling studies, especially if combined with XPS or Auger spectroscopy. However, the change in the chemical state of the surface, induced by the ion beam, must always be taken into account (except if the surface layer or layers to be analyzed are single component).

3.3. Improvement of thin-film growth

The simultaneous combination of thin-film growth (by means of any vacuum technique) and LEIB has been frequently employed to explore different states of the film grown and to improve the required properties. The effect of the incoming energetic ions has a profound influence in the morphology of the film, as well as in its defect density, which in turn modifies

many other properties. The technique, usually called ion-beam-assisted deposition (IBAD), can produce a number of beneficial changes in several characteristics of the film, such as density, texture, residual stresses, adhesion, or crystalline order. Of course, this technique has been applied to thin films of oxides [7]. In most cases, the main role of the ions of the beam is to deposit energy, creating defects and inducing diffusion and mobility. But in some other cases (this is usually named reactive IBAD), the second role of the atoms in the beam is to chemically react with surface species to form compounds.

3.4. Controlled generation of surface defects

If bulk defects control many properties of solids (dislocations in the case of mechanical properties of metals or point defects in the case of optical properties of many oxides, to mention two time-honored examples), surface defects may as well control some surface physicochemical properties. The most paradigmatic example is that of the so-called active centers [8], which control some catalytic conversions and which have been proposed to be surface steps [9] or vacancies. A profound knowledge of the physical and chemical properties of surface defects requires a well-known process to generate them controllably, and LEIB is a good tool for that purpose [10–12]. Under the correct parameters (energy, dose, temperature, etc.), it can generate a broad spectrum of surface defects (surface vacancies, adatoms, linear steps, vacancy islands, etc.), which can be subsequently studied for whatever phenomenon of interest [13, 14]. Also, the kinetics of flattening of an initially rough surface, with the roughness induced with LEIB, has been studied for different types of materials (among them, also oxides). For instance, for the case of TiO_2(110) and after low ion doses (only 0.5 monolayers were sputtered), a power scaling law has been found for the high-temperature evolution of the width w of the surface terraces as $w \sim t^{0.24}$ [15].

3.5. Surface nanopatterning

One of the first phenomena observed on ion-bombarded surfaces was the formation, in some cases, of ordered structures with a well-defined periodicity of a few tens of nanometers [16]. These patterns, usually in the form of ripples, may develop spontaneously from an initially flat surface as a result of several competing mechanisms which are active in a wide variety of materials. This phenomenon soon caught the attention of the scientific community for its interest and potential applications. The method just requires an ion beam homogeneously irradiating a surface and can easily pattern macroscopic areas of the order of mm^2 or cm^2 (once the correct processing conditions have been achieved). Thus, the absence of masks, complicated nanolithographic methods, or focused ion beams is very attractive from the technological point of view.

As already mentioned, the self-organized nanostructures spontaneously emerge under those experimental conditions which promote a clearly balanced competition between opposed kinetic processes occurring at the surface. Ion bombardment induces surface disordering and roughening, while surface diffusion favors smoothing and defect annihilation. These two main opposed trends, acting under nonequilibrium conditions and summed with other

mechanisms or condition characteristic of each type of surface, determine the evolution and the final morphology of the surface.

The family of theories describing surface patterning is too ample to be mentioned here, but we can briefly comment here on the most acknowledged model, which accounts for the formation of ripples under an off-normal incident ion beam. This is the Bradley-Harper (BH) model [17], which successfully explains the dynamics of ripple formation in isotropic and amorphous surfaces: the ripples are parallel to the incident direction of the beam under high incidence angles and perpendicular to the beam direction under angles close to be grazing. To understand the BH model, one must consider the distribution of surface defects created by ion collisions. This is described by the Sigmund model [18], which accounts, under a continuum model approach, for an ellipsoidal average distribution of energy deposited under ion impacts formulated as

$$E(z', \rho) = \frac{\varepsilon}{(2\pi)^{1.5}\,\alpha\,\beta^2} \exp\left(-\frac{(z'-a)^2}{2\,\alpha^2} - \frac{\rho^2}{2\,\beta^2}\right) \tag{6}$$

Under cylindrical coordinates, z' and ρ are the radial and longitudinal components, oriented along the initial incidence ion direction. α and β are the longitudinal and lateral spreadings of the spatial distribution, a is the center of the ellipsoidal distribution, and ε represents the total energy deposited. **Figure 1** graphically displays these parameters. That part of the energy deposited close to the surface will create a surface vacancy by sputtering an atom off the solid. Bradley and Harper used the Sigmund distribution to account for the creation of surface defects, describing their effect on surface topography $h(x,y,t)$ with a partial differential rate equation, where x represents the direction parallel to the projection of the ion beam on the surface:

$$\frac{\partial h(x,y,t)}{\partial t} = -Y_0(\theta) + \frac{\partial Y_0}{\partial \theta}\frac{\partial h}{\partial x} + v_{\parallel}\frac{\partial^2 h}{\partial x^2} + v_{\perp}\frac{\partial^2 h}{\partial y^2} - K(\nabla^2)^2 h \tag{7}$$

The first term in Eq. (7) is the erosion rate Y_0 for a flat surface, whose explicit dependency with the incidence angle θ is considered in the second term. The third and fourth terms take into account the contribution to roughening with the most important mechanism: the curvature-dependent sputtering yield. The concave regions of the surface have a larger probability to be even more eroded by the ion beam. Surface atoms at the valleys are more easily sputtered than those at the crests, so that once a valley is initiated, its height difference with the crests continues growing. This is, very naively described, the surface instability necessary to start the formation of ripples. The last term considers surface smoothing by atomic self-diffusion.

The BH model is relatively simple, and more advanced equations, including higher order terms or surface anisotropy, have been developed in the last two decades. But the BH model, as described by Eq. (7), agrees well with many experimental results, including the rotation of the ripples depending on the incidence angle of the ion beam. The BH theory only considers amorphous and isotropic solids and ignores the existence of crystallographic directions and surface steps. Surprisingly, the BH theory has proven successful in many crystalline surfaces

and has been a good starting point in other cases. However, surface anisotropy induces new effects and mechanisms to be taken into account. For instance, surface steps may limit diffusion via Ehrlich-Schwöbel barriers, or may determine etching rates at low grazing angles, as we will see later. In any case, ion beam patterning has been observed in different types of materials, including oxides. We will refer to those works on surface nanopatterning of oxides in a specific section later.

4. LEIB of oxide surfaces and thin films

Oxides are a colossal family of materials, both in the sense of the existing diversities and of the properties displayed. The specific and complex nature of the bond between the oxygen and the metallic cation favors the existence of a vast set of functionalities in oxides. Complicated interactions are present, which cross-link the different properties of the oxide. Also, there is a huge variety of defects in oxides, which are rather abundant, on the other hand. This circumstance enormously obscures the profound understanding of the physical mechanisms involved in oxide properties but also assists in the modification or control of these properties.

Oxide thin films lie at the core of many technological devices [19]. Indium-tin-oxide (ITO) conductive and transparent coatings are a good example of this statement. The modification of the surface morphology and the controlled introduction of defects in thin oxide films are tools to improve their response in their respective applications. LEIB can assist in this task.

4.1. Modification of the morphology

Oxides have been also used to spontaneously generate ordered nanostructures in their surfaces with LEIB. Indeed, the first reported example took place for a glass surface bombarded with Ar^+ at 4 keV by Navez in 1956 [16]. The authors discovered at that moment the formation of ripples separated by tens of nanometers. For incidence angles close to normal incidence and up to $\theta = 80°$, the direction of the ripples was perpendicular to the incidence angle. For grazing angles, in contrast, the direction of the ripples was parallel to the ion beam. This was probably the first time that the ripple rotation mechanism, later explained in the BH theory, was observed. Recent works on amorphous SiO_2 have found that, while the quantitatively results are similar [20], there are differences depending on the type of silica (fused silica, amorphized silica, or thermally grown SiO_2). The wavelength dependence on the energy and the wavelength coarsening vary with the substrate, which in turn depends on their surface energies (see **Figure 2**). It is interesting to note that, for low incidence angles, the surfaces remain smooth.

Although we focus in this chapter in the use of low-energy ions, medium energies have been used to nanostructure oxide surfaces too, and we would like to briefly mention it. However, in those cases where the energy is of the order of 10–100 keV, new mechanisms arise in the

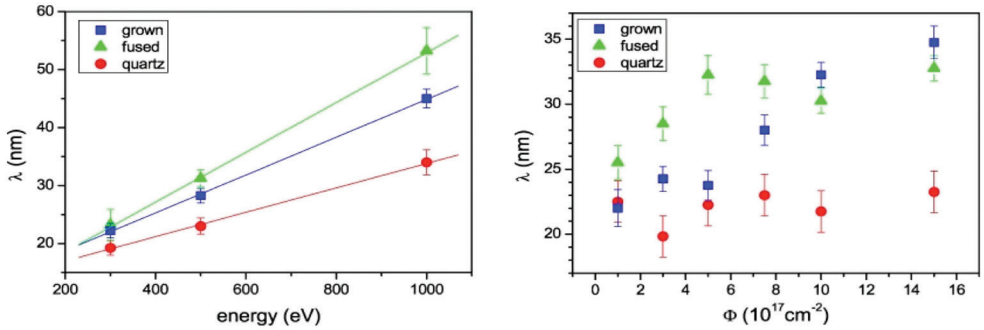

Figure 2. Ripple wavelength dependence on ion energy (left) and total ion dose (right) for three different SiO_2 surfaces. The total dose for the graph on the left is $\Phi = 1 \times 10^{18}$ cm^{-2}. The incidence angle for both graphs is 45°. Reproduced with permission from Ref. [20].

evolution of the surface morphology, which are far from the mechanisms invoked by BH theories and similar. That is the case of anatase TiO_2, for example, where different types of ions have been used to bombard the samples at different temperatures [21]. At these energies, the ion projected range *Rp* lies deep below the surface (of the order of tens of nanometers), and the agglomeration of point defects evolves into small voids in the first stages of ion bombardment. Further bombardment and void growth transform the initially flat surface into a morphology of void and mounds or nanorods aligned with the ion beam. In contrast, for the case of low-energy ions, the evolution of morphology does not include void formation, but is more limited to the formation and evolution of defects in the upper layers of the material.

Since TiO_2(110) is the most studied oxide surface, it can be understood that the nanopatterning of this surface has been addressed several times. In the case of low-energy ions, the morphology of the surface is, in many cases, rough and disordered if the bombardment takes place at room temperature. Diffusion is more limited in oxides than in metals, and there is no active mechanism to induce self-ordering at low T. In the case of TiO_2(110) bombarded with Ar^+ with an energy between 0.5 and 1.5 eV at room temperature, a disordered set of mounds is distributed across the surface [22]. These mounds are proposed to be chemically reduced oxide Ti_2O_3 regions, which align themselves along a given crystallographic direction under a thermal treatment between 700 K and 900 K.

However, at higher temperatures, the formation of ordered ripples in TiO_2(110) at grazing incidence has been reported in Ref. [23]. The TiO_2(110) orientation has two nonequivalent in-plane surface directions: (001) and (1–10). At low incidence angles, the existence of surface steps is determinant in ripple formation. Indeed, sputtering from terraces is about one order of magnitude smaller than from step edges. Also, the sputtering yield or erosion rate of the different steps differs, and the consequence is that the total sputtering yield is larger when the beam is directed along the [1–10] direction than when it is oriented along the [001] direction. Despite all, at sufficiently long bombardment times, the beam direction does not affect too

http://dx.doi.org/10.5772/66651

much the morphology of the formed ripples, somehow demonstrating the universality of the method for patterning large areas in different materials.

Another phenomenon which also recalls universality is the temperature-dependent reorientation of the ripples observed in TiO_2(110) [24], in the same way as for many metal surfaces. While at low (150 K) and high (620 and 720 K) temperatures ripples are aligned along the beam direction, at 300 K they are aligned perpendicularly, as illustrated in **Figure 3**. The same group has used LEIB as a tool to prepare TiO_2(110) surfaces with steps aligned along special orientations [25]. The method can be viewed as the equivalent to surface texturing with ion beams when the grains with higher sputtering yields destabilize. In this case, the ion beam under a low incidence angle preferentially erodes some specific steps, creating [1–10] steps. These are thermodynamically unstable but kinetically stabilized within this approach.

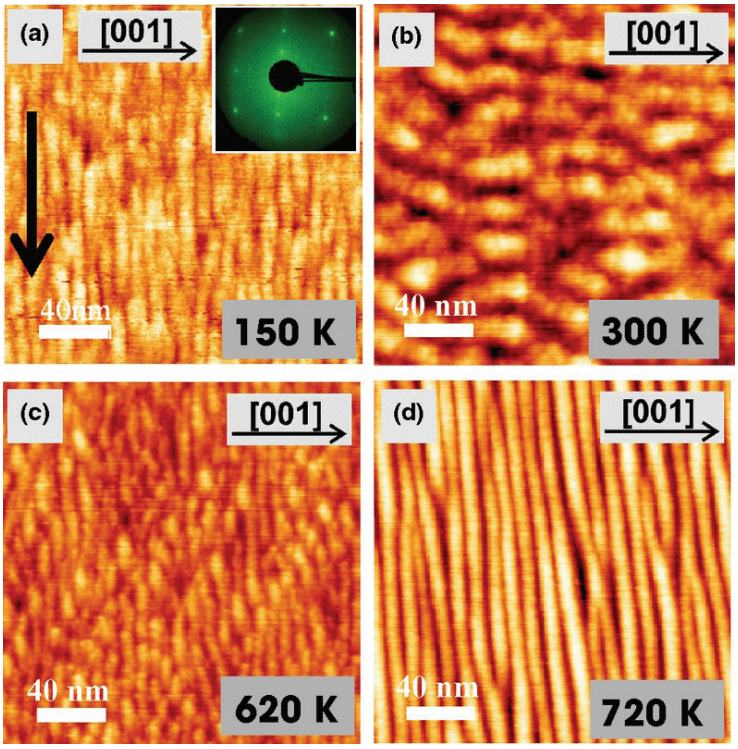

Figure 3. (a), (b), (c) and (d): STM images (200 × 200 nm^2) of Ar^+-modified TiO_2(110) surfaces, where the bombardment has been carried out at different temperatures under an incidence angle of 75°, an ion energy of 2 keV, and a total dose of 9 × 10^{16} ions/cm^2. The LEED pattern in (a) shows the crystalline order of the surface even after ion bombardment. All ripples are elongated along the beam projection, except for the case where bombardment has been done at RT. The black vertical arrow in (a) marks the projection of the beam on the surface and the horizontal black arrows mark the indicated crystallographic direction. Reproduced with permission from Ref. [24].

This work illustrates how grazing LEIB can be used to tune and texture certain surface steps, which can be relevant for applications sensitive to specific step orientations.

4.2. Modification of the electronic properties

Oxygen vacancy creation has been traditionally used to modify electronic properties of oxides. It is indeed a route to doping, since excess electrons (due to oxygen vacancies) can be transferred to the conduction band, transforming the material into a better conductor. This type of approaches has been sometimes referred to as vacancy engineering. The control to achieve the desired vacancy concentration can be gained through post-growth thermal annealings or during the growth, controlling experimental parameters such as the oxygen partial pressure or the laser energy if the material is grown by sputtering or by pulsed laser epitaxy (PLE) [26]. As already discussed, LEIB can be also helpful to control oxygen vacancies. Indeed, many of the most recent applications of LEIB on oxide surfaces are related to the modification of electronic and transport properties for different applications. In turn, other fundamental properties, such as the optical response, are modified as well. Most of the studies about oxides modified with LEIB have been accomplished on $SrTiO_3$ and TiO_2.

It is easy to understand that one of the oxides where LEIB has been most often employed to exploit its properties is $SrTiO_3$ (STO), a transparent insulating perovskite with many intriguing characteristics and also frequently used as a substrate to grow other materials on it. A very interesting phenomenon is that LEIB can generate a conductive layer at its surface, and that has been the subject of several studies. There is a clear correlation between conductivity and the concentration of oxygen vacancies created by ion bombardment in STO [27]. The resistivity values of a modified nanometric layer obtained after bombarding a $SrTiO_3(100)$ surface can follow a ~ $T^{2.5}$ law, dominated by the mobility of the carriers, and attain very low values (between 2×10^{-4} and 6×10^{-4} Ω cm at room temperature) without losing transparency [28]. In order to compare, some of the best conducting STO samples were previously produced by boron implantation at 100 keV, resulting in relatively thick and nontransparent conducting layers with resistivity values of about 0.01 Ω cm [29]. Thus, LEIB on STO is able to produce transparent conductive layers competitive with ITO layers, with an even smaller thickness.

This type of conductive layers formed by LEIB has also been reported in rutile TiO_2 [30], reporting again high carrier densities and mobilities. The authors account for a high crystallographic order in the ion-bombarded region of the $TiO_2(100)$ surface, which is not compatible with the rutile structure and which is attributed to the ordering of the vacancies produced by ion bombardment.

With respect to optical properties, hole levels in self-trapped states localized in the gap can be stabilized by conduction carriers (generated by oxygen deficiency) in Ar^+-bombarded single-crystalline STO [31]. Their recombination generates the emission of blue light at room temperature, and the emitting regions can be conveniently patterned. Cross-sectional TEM images show the formation of amorphous and modified (oxygen deficient) layers under the action of the ion beam (**Figure 4**).

http://dx.doi.org/10.5772/66651

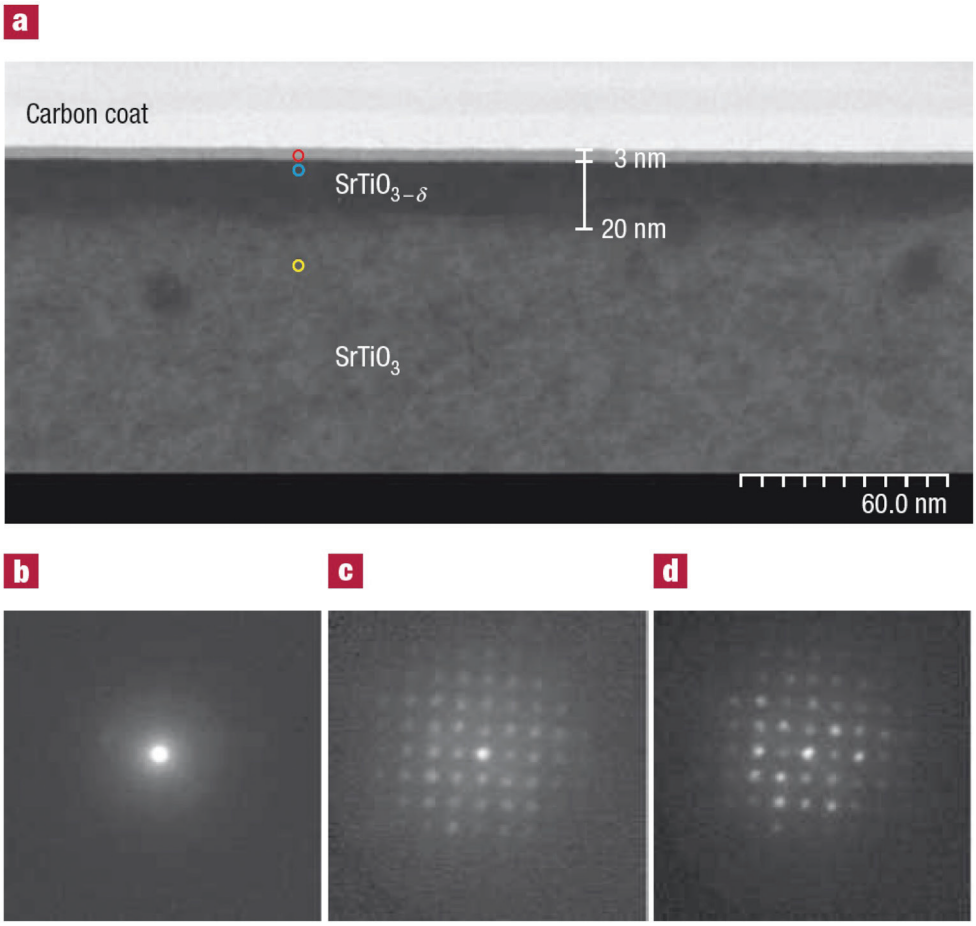

Figure 4. (a) TEM cross-sectional image from an Ar^+-modified STO single crystal. (b)–(d) electron diffraction images of the (b) red, (c) blue, and (c) yellow regions of the material. Diffraction patterns from (c) to (d) are qualitatively similar, but the contrast in the real space image suggests that a modification indeed exists: the ion beam transforms the upper layer of pristine STO into an amorphous film (red region) and induces the formation of an oxygen-deficient $SrTiO_{3-x}$ region with a thickness around 15–20 nm (blue region). Reproduced with permission from Ref. [31].

Under certain conditions, LEIB can also modify the optical properties of TiO_2(110) substrates, greatly enhancing its absorbance in the visible range and its luminescence [32]. The formation of self-organized crystalline nanodots at the surface and the generation of Ti interstitials justify this optical response. In general, this type of investigations opens a path to explore the field of oxide optoelectronics.

Another potential application where LEIB on oxides has found a niche is the generation of substrates suitable for resistive switching (RS) processes, which lie at the core of the nonvolatile

data-storage memristor technology. This technology, which is still in its exploratory stages, is based in the existence of on/off states which depend on the electrical resistance level of the bit (rather than on the electrostatic or magnetic state). The state can be switched with external electric fields in oxides, which force a metal-insulator transition (MIT). TiO_2 is a good candidate for this purpose, but it has been found that a previous forming step involving LEIB radically improves the RS process [33]. The conductive 2D layer generated consists in a set of self-organized grains with a locally reduced chemical composition. This distribution of grains is a kind of template where bipolar switching between a semiconductor and a metallic state (induced with a conductive atomic force microscopy (AFM) tip) is localized at the grains. **Figure 5** illustrates a progressive chemical reduction and a declining electrical resistance of the TiO_2 surface during ion bombardment. The same type of mechanism has been found in STO substrates [34] with rather low-energy Ar^+ ions (66–200 eV). LEIB greatly improves the resistive memory effect, if compared with pristine STO. In these cases, thermal annealings would create vacancies and would also improve the electrical conductance for RS processes. But the influence of LEIB is limited to the upper layers of the material and can be thus combined with focused ion beam methods or shadow masking to pattern surfaces.

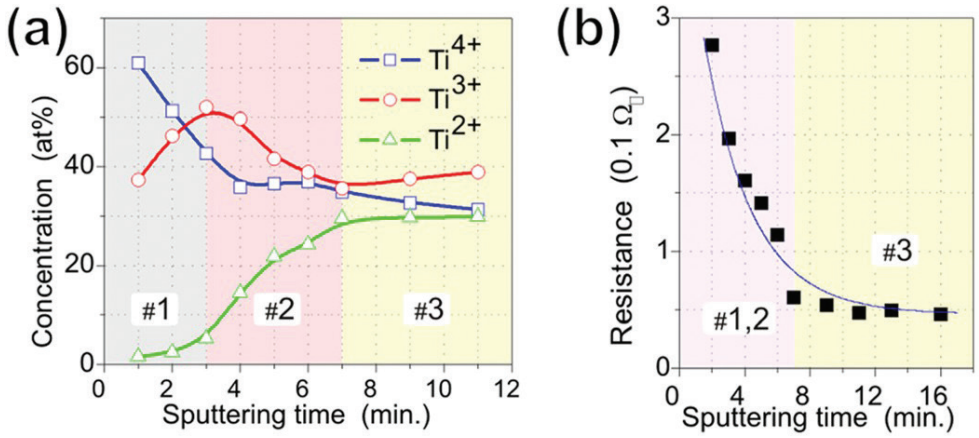

Figure 5. (a) Quantitative changes in the concentration of Ti cations with the sputtering time, as measured with XPS. (b) Behavior of the resistance (in Ω/μm²) of the modified layer with sputtering time. Adapted with permission from Ref. [33].

Oxides exhibit outstanding magnetic properties, and in this respect, LEIB can be employed to modify the microstructure and consequently the magnetic response of the oxide layer. Bilayers of $Ni_{80}Fe_{20}/\alpha$-Fe_2O_3 grown on SiO_2 exhibit, for instance, a different coercivity depending on the growth mode [35]. If ion bombardment is carried out on the α-Fe_2O_3 layer before the growth of the $Ni_{80}Fe_{20}$ film, the uniaxial anisotropy of this layer is reduced, exhibiting a lower coercivity. This is a clear example of how the coupling between a ferromagnetic layer and an antiferromagnetic layer can be tuned with LEIB.

Regarding the modification of interfaces, we can mention that STO, in combination with other insulating oxides such as $LaAlO_3$ (LAO), forms a heterostructure with remarkable conductive,

http://dx.doi.org/10.5772/66651

magnetic, and superconductive properties at the interface. The surprising origin is the stabilization of an emerging 2D electron gas (2DEG). There are examples of the modification of the 2DEG in LAO/STO interfaces [36]. They have shown that the conducting state at the interface can be completely suppressed with Ar^+ bombardment at 150 eV. The conductivity can be then restored with a high-temperature annealing in the presence of oxygen. The authors suggest that the strain induced by Ar implantation causes local destabilization and partial amorphization. These disordered regions localize defect states where charges are trapped, in the same way as in other types of semiconductors. The annealing eliminates the Ar and heals defects, restoring the initial conductivity. The LEIB approach has been also used to create a 2D electron gas in an Ar^+-bombarded $SrTiO_3(100)$ surface [37], which shows an increase of the low-temperature magnetoresistance when the magnetic field H points away from the surface. This and other effects are closely related to electron confinement, generated in this latter case by the modifications induced by ion bombardment.

5. Formation of epitaxial thin films of oxides

We present, in this final section of the chapter, a rather specific but quite surprising capability of ion bombardment, which we have successfully proven in a rutile $TiO_2(110)$ substrate. As we have seen in previous sections, LEIB is a commonly used process to modify the physicochemical properties of oxide surfaces. In this respect, the literature has usually described the resulting material as a defective and chemically reduced version of the oxide, lacking a profound knowledge of the real structure. As all properties ultimately depend on the structure, the situation is highly undesirable. We show here a case where the structure of the abovementioned ion-bombarded surface is well defined after the modification.

The purpose of this section is to show that the use of LEIB on a surface of a single-crystalline oxide can induce the formation of a single-crystalline and epitaxial thin layer of the corresponding suboxide. For the case of $TiO_2(110)$, we show here that high doses of Ar^+ bombardment of the single crystal produces a 10 nm thick film of TiO(001) [38].

It is well known that the progressive depletion of oxygen in polycrystalline materials during ion bombardment can, in some cases, induce the formation of a new phase with the cation in a lower oxidation state. In other words, the formation of a crystalline suboxide (i.e., with well-defined Bragg reflections) can be promoted. The main message of this section is that if the starting point is a single-crystalline surface (instead of ion bombarding a polycrystalline material) and if there is some kind of structural affinity or matching with a particular crystallographic orientation of the suboxide, this suboxide can nucleate and grow epitaxially coupled to the original oxide, being a thin epitaxial film the outcome of the process.

5.1. Formation of a TiO(001) thin film on $TiO_2(110)$

Titanium dioxide is, with its different structures, a wideband semiconductor with many applications in technology. It has been also, along the years, a benchmark for the fundamental study of oxide surfaces. In fact, as we mentioned before, $TiO_2(110)$ is the most studied oxide surface

[39]. Regarding its optical properties, it is very transparent and has a high refractive index, which together with its stability, non-toxicity and the easy synthesis of small particles, justifies its extensive use as a white pigment. It also displays a very interesting photocatalytic activity. This property, along with its particular interaction with water, has fostered the investigation and the use of TiO_2 as a self-cleaning coating [40]. As we have previously discussed, also in the field of resistive switching, the investigation with TiO_2 has found a satisfactory feedback.

The starting point of the modification we describe here is a rutile TiO_2(110) clean and flat surface, which is ion bombarded with Ar^+ at 3 keV at room temperature with doses up to 8×10^{16} ions cm^{-2}. Auger electron spectroscopy (AES) shows a clear chemical reduction: a decrease of the O/Ti ratio and a shift of the Ti_{LMM} and Ti_{LMV} transitions to higher kinetic energies. The incidence of the ion beam is normal, and so the modified surfaces show a rough topography, but with no recognizable pattern or symmetry as seen with atomic force microscopy (AFM). However, X-ray diffraction of the bombarded surfaces already shows the emergence of a new reflection (not present in the pristine sample) compatible with the cubic rock salt titanium monoxide phase with its (001) crystallographic direction oriented along the surface normal (**Figure 6a**). Low-energy electron diffraction (LEED) measurements performed before and after the modification show the transformation of the rectangular surface diffraction pattern corresponding to TiO_2(110) to a different diffuse LEED pattern displaying square symmetry, with its main directions rotated 45° with respect to the TiO_2(110) directions (**Figure 6b–d**).

Grazing incidence XRD (GIXRD) measurements help determine the crystalline orientations of both the dioxide and monoxide phases. HK scans in reciprocal space (those which explore the in-plane directions) show all the allowed reflections (not subject to extinction rules) of TiO(001) and TiO_2(110), confirming the 45° rotation of the square surface lattice of TiO(001) with respect to the rectangular surface lattice of TiO_2(110) (blue and black lattices, respectively, of **Figure 6e**). L scans (to explore the out-of-plane direction) determine that the periodicity of the TiO phase is indeed the corresponding one. These observations confirm the ion-induced transformation of the upper layers of TiO_2(110) into TiO(001), with the particularity that both lattices are in registry. Being both lattices rotated 45°, the matching is almost perfect along the [001] direction of TiO_2(110). Along the [1–10] the mismatch is large (about 10%), which clarifies the observations carried out with LEED, XRD, and scanning transmission electronic microscopy (STEM), all of them revealing the tilting of the lattice along that direction. This tilting, probably stabilized by the existence of misfit dislocations, helps relieve that large mismatch along that particular direction. STEM cross-sectional images of the modified layer show the homogeneity of the modified layer, revealing a constant thickness of 10 nm and its relatively good crystallinity.

Density functional theory (DFT) calculations confirm the high stability of the interface for a particular structural configuration, with an energy estimated to be $\gamma_{int} = 3.2$ J m^{-2}. The good structural and chemical matchings justify this low value. Also, the calculations suggest that a contraction of the TiO bonds at the interface (the out-of-plane TiO distance slightly increases with the interface distance) is due to the charge transfer from TiO to TiO_2, resulting in an interface with metallic character.

http://dx.doi.org/10.5772/66651

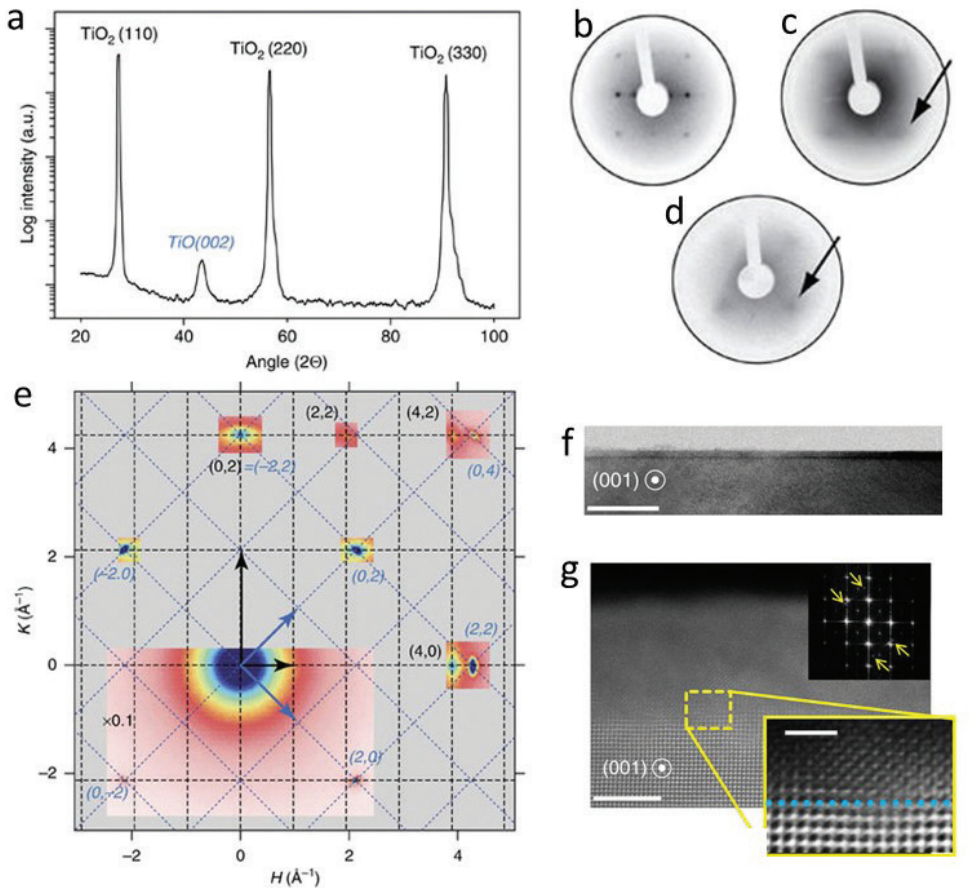

Figure 6. (a) θ–2θ scan of a TiO_2(110) single crystal after ion bombardment. A new reflection from TiO(002), not present before, emerges. (b) LEED image of the TiO_2(110) surface before LEIB, (c) during LEIB, and (d) after LEIB and a soft thermal annealing. New spots (marked with arrows), with a different symmetry, appear. They become sharper after the annealing. All diffractograms are taken at E = 63 eV. (e) X-ray diffraction HK map in reciprocal space of the ion-bombarded TiO_2(110) surface, where both sets of reflections are seen: black for TiO_2(110) and blue for TiO(001). The two surface lattices, with their corresponding lattice vectors, are marked. (f) Scanning transmission electron microscopy (STEM) image of the irradiated layer. The transformed surface is seen. (g) Higher magnification STEM image and fast Fourier transform (top right) of the image. The yellow rectangle is a detail of the interface. Adapted with permission from Ref. [38].

All results together indicate that the initial stages of ion bombardment induce the formation of a chemically reduced and defective version of the dioxide at the initial stages, which transforms into a very disordered (or even amorphous) phase for intermediate doses, as the rutile structure is not stable for a high density of defects. The absence of a LEED pattern after medium doses supports the existence of this disordered intermediate phase. At sufficiently high doses, while preferential oxygen sputtering continues operative, the TiO(001) phase emerges, favored by the good registry between both oxides at the interface.

An interesting fact is that the thickness of the modified layer (10 nm) is larger than the average depth where most of the ion damage is generated (around 4 nm, according to SRIM simulations). This implies that diffusion is active, probably assisted by radiation, and also enhanced by a locally higher temperature due to the dissipation of the energetic ions. Most probably, mass transport is governed by interstitial Ti cations [41, 42] generated by ion bombardment, which migrate to the interface transforming it locally into TiO. The interface thus advances toward the bulk. When the diffusion length of the species is not sufficiently long to compensate for the receding surface (atoms are being continuously sputtered by the ion beam), then a steady state is reached, and the thickness of the modified layer saturates.

Acknowledgements

I would like to thank all my former and present collaborators, especially those participating in the works reviewed in the last section of this chapter. Financial support from Projects MAT2012-38045-C04-03 and FIS2014-61839-EXP from the Spanish MINECO is also acknowledged.

Author details

Oscar Rodríguez de la Fuente

Address all correspondence to: oscar.rodriguez@fis.ucm.es

Materials Physics Department, Universidad Complutense de Madrid, Madrid, Spain

References

[1] Grove WR. On some anomalous cases of electrical decomposition. Philos. Mag. 1853;5:203.

[2] Goldstein E. Verh. Dtsch. Phys. Ges. 1902;4:228.

[3] Sigmund P. Sputtering by ion bombardment: theoretical concepts. In: Behrisch R, editor. Sputtering by Particle Bombardment I. Springer-Verlag. Berlin Heidelberg. 1981. pp. 9-71.

[4] Gnaser H. Low-Energy Ion Irradiation of Solid Surfaces. Springer-Verlag. Berlin Heidelberg. 1999. DOI: 10.1007/BFb0110693

[5] Betz G, Wehner GK. Sputtering in multicomponent materials. In: Behrisch R, editor. Sputtering by Particle Bombardment II. Springer-Verlag. Berlin Heidelberg. 1983. pp. 11-90.

[6] van der Heide P. Secondary Ion Mass Spectrometry: An Introduction to Principles and Practices. Wiley. Hoboken, New Jersey. 2014. DOI: 10.1002/9781118916780.

[7] Prieto P, de la Figuera J, Martín-García L, Prieto JE, Marco JF. Fourfold in-plane magnetic anisotropy of magnetite thin films grown on TiN buffered Si(001) by ion-assisted sputtering. J. Mater. Chem. C. 2016;4:7632. DOI: 10.1039/c6tc02152b.

[8] Taylor HS. R. Soc. London Ser. A. A theory of the catalytic surface 1925;108:105.

[9] Palacio I, Rojo JM, Rodríguez de la Fuente O. Surface defects activating new reaction paths: Formation of formate during methanol oxidation on Ru(0001). ChemPhysChem. 2012;13:2354. DOI: 10.1002/cphc.201200190.

[10] de la Fuente, OR, González MA, Rojo JM. Experimental evidence of two-dimensional dislocations in a reconstructed layer. Surf. Sci. 2000;454:16.

[11] de la Fuente OR, González MA, Rojo JM. Ion bombardment of reconstructed metal surfaces: From two-dimensional dislocation dipoles to vacancy pits. Phys. Rev. B. 2001;6:85420.

[12] Carrasco E, de la Fuente OR, González MA, Rojo J. Characterising and controlling surface defects. Eur. Phys. J. B. 2004;40:421. DOI: 10.1140/epjb/e2004-00231-9.

[13] Navarro V, Rodríguez de la Fuente O, Mascaraque A, Rojo JM. Plastic properties of gold surfaces nanopatterned by ion beam sputtering. J. Phys. Cond. Matter. 2009;21:224023. DOI: 10.1088/0953-8984/21/22/224023.

[14] Rodríguez de la Fuente O, Gonzalez-Barrio MA, Navarro V, Pabon BM, Palacio I, Mascaraque A. Surface defects and their influence on surface properties. J. Phys. Cond. Matter. 2013;25:484008. DOI: 10.1088/0953-8984/25/48/484008.

[15] Cai A, Piercy P. Morphology of the rutile (110) surface after low sputter dose and annealing. Phys. Rev. B. 2002;66:115414. DOI: 10.1103/PhysRevB.66.115414

[16] Navez M, Sella C, Chaperot D. C.R. Acad. Sci. Microscopie electronique-etude de lattaque du verre par bombardement ionique. 1962;254:240.

[17] Bradley RM, Harper JME. J. Vac. Sci. Technol. A Theory of ripple topography induced by ion bombardment 1988;6:2390.

[18] Sigmund P. Phys. Rev. Theory of sputtering I. Sputtering yield of amorphous and polycrystalline targets 1964;184:383.

[19] Norton DP. Synthesis and properties of epitaxial electronic oxide thin-film materials. Mater. Sci. Eng. R. 2004;43:139. DOI: 10.1016/j.mser.2003.12.002.

[20] Keller A, Facsko S, Möller W. The morphology of amorphous SiO_2 surfaces during low energy ion sputtering. J. Phys.: Condens. Matter. 2009;21:495305. DOI: 10.1088/0953-8984/21/495305.

[21] Romero-Gomez P, Palmero A, Ben T, Lozano JG, Molina SI, González-Elipe R. Surface nanostructuring of TiO_2 thin films by high energy ion irradiation. Phys. Rev. B. 2010;82:115420. DOI: 10.1103/PhysRevB.82.115420.

[22] Berkó A, Biró T, Kecskés T, Solymosi F. Self-organization of oxide nanodots generated by low energy Ar^+ bombardment on TiO_2(110)-(1x2). Vacuum .2001;61:317.

[23] Luttrell T, Batzill M. Nanoripple formation on TiO_2(110) by low-energy grazing incidence ion sputtering. Phys. Rev. B. 2010;82:035408. DOI: 10.1103/PhysRevB.82.035408.

[24] Kolmer M, Zebari AA, Goryl M, Buatier de Mongeot F, Zasada F, Piskorz F, Pietrzyk P, Sojka Z, Krok F, Szymonski M. Temperature-dependent orientation of self-organized nanopatterns on ion-irradiated TiO_2(110). Phys. Rev. B. 2013;88:195427. DOI: 10.1103/PhysRevB.88.195427.

[25] Luttrell T, Li WK, Gong XQ, Batzill M. New directions for atomic steps: step alignment by grazing incident ion beams on TiO_2(110). Phys. Rev. Lett. 2009;102:166103. DOI: 10.1103/PhysRevLett.102.166103.

[26] Lee SA, Jeong H, Woo S, Hwang JY, Choi SY, Kim SD, Choi M, Roh S, Yu H, Hwang J, Kim SW, Choi WS. Phase transitions via selective elemental vacancy engineering in complex oxide thin films. Sci. Rep.. 2016;6:23649. DOI: 10.1038/srep23649.

[27] Wang Q, Zhang W, Zhang W, Zeng H. In-situ monitor of insulator to metal transition in $SrTiO_3$ by Ar^+ irradiation. Appl. Surf. Sci. 2016;365:84.

[28] Reagor DW, Butko VY. Highly conductive nanolayers on strontium titanate produced by preferential ion-beam etching. Nat. Mater. 2005;4:593. DOI: 10.1038/nmat1402

[29] Cooper CM, Nayar PS, Hale EB, Gerson R. Conducting strontium titanate layers produced by boron-ion implantation. J. Appl. Phys. 1979;50:2826.

[30] Singh A, Hänisch J, Matias V, Ronning F, Mara N, Pohl D, Rellinghaus B, Reagor D. Transforming insulating rutile single crystal into a fully ordered nanometer-thick transparent semiconductor. Nanotechnology 2010;21:415303. DOI: 10.1088/0957-4484/21/41/415303.

[31] Kan D, Terashima T, Kanda R, Masuno A, Tanaka K, Chu S, Kan H, Ishizumi A, Kanemitsu Y, Shimakawa Y, Takano M. Blue-light emission at room temperature from Ar^+-irradiated $SrTiO_3$. Nat. Mater.. 2005;4:816. DOI: 10.1038/nmat1498.

[32] Majumder S, Paramanik D, Solanki V, Bag BP, Varma S. Bandgap tailoring of rutile TiO_2(110) via surface patterning with electron cyclotron resonance sputtering. Appl. Phys. Lett. 2011;98:053105. DOI: 10.10631/1.3549768.

[33] Rogala M, Klusek Z, Rodenbücher C, Waser R, Szot K. Quasi-two-dimensional conducting layer on TiO_2(110) introduced by sputtering as a template for resistive switching. Appl. Phys. Lett. 2013;102:131604.

[34] Gross H, Seongshik O. Efficient resistive memory effect on $SrTiO_3$ by ionic-bombardment. Appl. Phys. Lett. 2011;99:092105. DOI: 10.1063/1.3633114.

[35] Zheng C, Lan TC, Shueh C, Desautets RD, van Lierop J, Lin KW, Pong WT. Effect of ion bombardment on microstructural and magnetic properties of $Ni_{80}Fe_{20}/\alpha$-Fe_2O_3 thin films. Jap. J. Appl. Phys. 2014;53:06JB03. DOI: 10.7567/JJAP.53.06JB03

[36] Aurino PP, Kalabukhov A, Tuzla N, Klein A, Erhart P, Boikov YA, Serenkov IT, Sakharov VI, Claeson T, Winkler D. Reversible metal-insulator transition of Ar-irradiated $LaAlO_3$/$SrTiO_3$ interfaces. Phys. Rev. B. 2015;92:155130. DOI: 10.1103/PhysRevB.92155130.

[37] Bruno FY, Tornos J, Gutierrez del Olmo M, Sánchez-Santolino G, Nemes NM, Garcia-Hernandez M, Mendez B, Piqueras J, Antorrena G, Morellón L, de teresa JM, Clement M, Iborra E, León C, Santamaría J. Anisotropic magnetotransport in $SrTiO_3$ surface electron gases generated by Ar^+ irradiation. Phys. Rev. B. 2011;83:245120. DOI: 10.1103/PhysRevB.83.245120.

[38] Pabón BM, Beltrán JI, Sánchez-Santolino G, Palacio I, López-Sánchez J, Rubio-Zuazo J, Rojo JM, Ferrer P, Mascaraque A, Muñoz MC, Varela M, Castro GR, Rodríguez de la Fuente O. Formation of titanium monoxide (001) single-crystalline thin film induced by ion bombardment of titanium dioxide (110). Nat. Comm. 2014;6:6147. DOI: 10.1038/ncomms7147

[39] Diebold U. The surface science of titanium dioxide. Surf. Sci. Rep. 2003;48:53.

[40] Fujishima A, Zhang X, Tryk DA. TiO_2 photocatalysis and related surface phenomena. Surf. Sci. Rep. 2008;63:515. DOI: 10.1016/j.surfrep.2008.10.001.

[41] Henderson MA. A surface perspective on self-diffusion in rutile TiO_2. Surf. Sci. 1999;419:174.

[42] Jug K, Nair NN, Bredow T. Molecular dynamics investigation of oxygen vacancy diffusion in rutile. Phys. Chem. Chem. Phys. 2005;7:2616.

Chapter 3

Conventional and Un-Conventional Lithography for Fabricating Thin Film Functional Devices

Abdelhanin Aassime and Frederic Hamouda

Additional information is available at the end of the chapter

http://dx.doi.org/10.5772/66028

Abstract

Thin film devices are conquering many aspects of today's life, and continuous shrinking of building block dimensions of these structures enhances their performances and makes them economically attractive. This chapter is an overview of some conventional and unconventional lithography techniques used to fabricate thin film functional structures. Several aspects of pattern transfer were addressed with emphasis on the limits of these lithography techniques. We have thus highlighted the issue of pitch resolution for optical lithography and discussed some aspect of proximity effects for electron beam lithography. Pattern transfer from resist image to the wafer was also discussed. Considered as unconventional, we discussed several aspects linked to thin film fabrication using nanoimprint and nanosphere lithography techniques.

Keywords: optical lithography, electron beam lithography, nanoimprint lithography, nanosphere lithography, liftoff

1. Introduction

The continuous trend toward miniaturized and high-performance systems has been leading research and development in novel materials and devices with superior and new functionalities. In this regard, the high sensitivity of modern technologies at submicron scale opens prospects for realization of thin film functional devices such as capacitors for power components [1], sensing devices for biomedical applications [2] and magnetic thin films structures for data processing technology [3]. These devices were mostly fabricated following top-down view where deposition techniques were combined with lithography and eventually etching. In this chapter, we will mainly focus on depicting conventional and un-conventional lithog-

raphy (see **Figure 1**) used for fabricating thin film functional devices when combined with physical vapor deposition (PVD) technique.

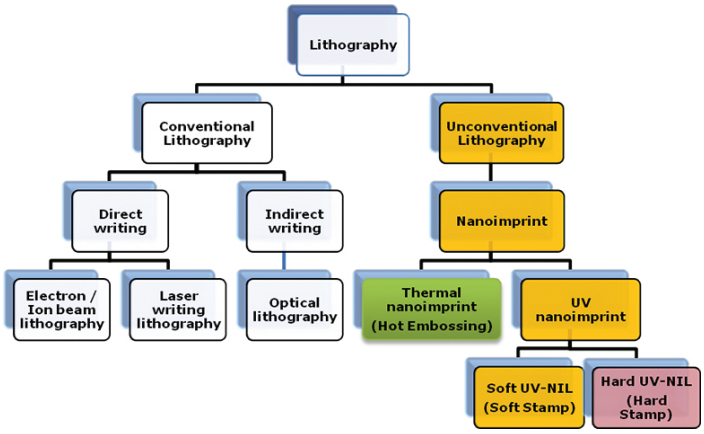

Figure 1. Scheme showing different lithography techniques.

The first part of this chapter reports on most known conventional lithography techniques. These techniques consist of transferring a given pattern to a thin resist by means of local interaction between the resist and the beam of particles like photons or electrons. Once the resist is structured, functional devices can be obtained by liftoff technique after PVD deposition of thin films [4] or by etching [5]. Existing conventional lithography can be divided in two categories depending on the way of writing (transferring) the pattern: parallel and series writing methods. For parallel method such as optical lithography with different wavelengths, transfer to resist is done at once by using a mask containing the pattern. This technique has the advantage of being fast but limited by the mask fabrication step and diffraction effects. For series writing (maskless), such as electron beam lithography (EBL) and laser lithography, pattern is transferred to the resist pixel-by-pixel which makes them more precise but unfortunately slower. In the industry, parallel lithography technique is commonly used for mass production and serial method is mostly used for mask making. The aim of this first part is to present the principle of these various fabrication techniques with the focus on pitch resolution for optical lithography and proximity effects for electron beam lithography (EBL). Pattern transfer to the wafer using both lithography techniques will also be addressed.

In this second part, we report alternative techniques considered as unconventional lithography. Among them, we find nanoimprint lithography (NIL). This method is based on the printing patterns in a polymer with a mold which can be rigid or flexible, and after separation, transfer the pattern in the substrate. The first results were achieved in 1995 with the thermal NIL and rigid molds, more commonly known as hot embossing [6]. It permits to carry out high-density nanostructures on large areas and at low cost. A second method based on UV has been developed in 1996 at Philips Research Labs, which offers the advantage to work at room

http://dx.doi.org/10.5772/66028

temperature and low pressure [7]. This technique uses the photon energy to crosslink the resist. Molds are transparent and can be flexible or rigid. Then, two ways have been developed: soft UV-NIL and hard UV-NIL. Each has advantages and will be addressed in this chapter with different steps to implement these techniques. Application examples will be also presented.

Among emerging methods, we find nanosphere lithography (NSL), also called as colloidal lithography. It is a low-cost simple technique to implement and permits to pattern well-ordered 2D nanoparticle arrays on large surface [8]. Another advantage of the NSL is to be a good candidate for the fabrication of diameter tunable nanoparticles in a wide range of 20–1000 nm. We will present the different technical steps to obtain a two-dimensional colloid mask.

2. Optical lithography

Optical lithography consists mainly on a light source illuminating, through an ensemble of optical lenses and apertures, a mask containing pattern aimed to be transferred to a given substrate. The mask can be set in the vicinity of the substrate (contact/proximity mode) or at a certain distance from it (projection mode). The mask is called "binary" in the sense that the light either passes through metal-free area (1) or being reflected in metal-covered surface of the mask (0). Pattern transfer is intermediated by a specific resist which covers the substrate. The interaction between light and resist results in local modification of molecules arrangement of the resist which can be revealed in a specific solution (development process). **Figure 2** depicts the mask replication in contact/proximity and projection modes. The contact mode is a configuration where the mask is directly touching the resist, whereas a gap of few microns separates them in the proximity mode.

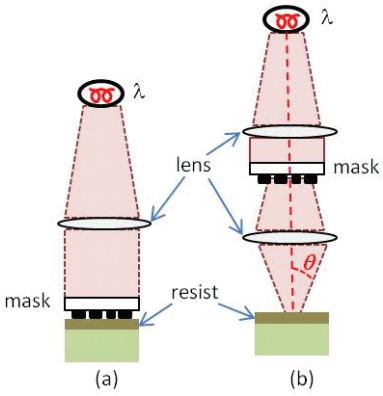

Figure 2. Mask replication in contact/proximity mode (a) and projection configuration (b). The condenser collects light from the source and illuminates the mask pattern. An additional imaging lens is needed to de-magnify the mask pattern (up to ~1:4).

The fundamental limit of optical lithography is not determined by the optical system alone but rather by an overall contribution from the optics, resist and subsequent process steps. As depicted in **Figure 3**, there exist in general two kinds of resolution, one which is linked to feature size and the other to pitch. While the feature size determines the critical dimension that can be obtained (e.g., size of the transistor), the pitch determines its density on the wafer (e.g., number of transistors per wafer).

Figure 3. Example of pattern to be exposed showing a hole diameter as smallest feature and related pitch.

For clarity, we will focus only on projection systems in this paragraph. The pitch resolution (R) of these systems is usually expressed in terms of source wavelength λ and numerical aperture ($NA = nsin(\theta)$) as

$$R = k1\frac{\lambda}{n\sin\theta} \tag{1}$$

where $k1$ a process-dependent constant with values in 0.5–1 range, n is the refractive index of the media between the mask and the wafer, and θ is half acceptance angle of the lens (see **Figure 2**).

To improve the pitch resolution, it is necessary to decrease (λ, $k1$) and to enhance the numerical aperture. Historically, this improvement was driven by decrease in wavelength λ of the source. From mercury lamps at 365nm–435nm wavelength, to excimer laser sources with Krypton Fluoride (248 nm), Argon Fluoride (193 nm), and molecular Fluorine (157 nm) [9]. Furthermore, optical resolution limit has been pushed toward sub-100 nm features using resolution enhancement techniques (RET) such as optical proximity correction, high numerical aperture, and phase-shift masks; 65 nm device geometry (nodes) was indeed achieved using wavelength as large as 193 nm [10, 11]. While numerical aperture higher than 1 is not possible in conventional air-media imaging, using water between the last imaging lens and the wafer has pushed down the limit to sub-45 nm [12]. This technique, known as immersion lithography, is a potential candidate to take over the actual 193 nm technology in the industry. To complete the picture, extreme UV (EUV) is another immerging technique on which relies the future of next generation of circuit components to push further resolution down to sub-20 nm [13].

http://dx.doi.org/10.5772/66028

3. Electron beam lithography

Electron beam lithography has been generally accepted as a valuable tool in research and technology development because of its high degree of flexibility and its outstanding resolution capability. There are many versions of electron lithography systems starting from modified scanning electron microscope (SEM) to mask-writers, shaped-spot systems, and electron-beam projection machines.

Converted SEM systems are best adapted for research where the throughput is not a critical issue. They are useful for applications involving small devices such as metallic junctions, few transistors, lines, dots, and small gratings. The pattern data are transferred to the controlling computer, which then directs a tiny focused electron beam (ebeam) to desired locations on the resist by deflecting and turning the beam on and off. The area of an individual chip is selected, and the beam draws out the features in that area pixel-by-pixel with a predefined dose. The scan rate is adjusted to deliver a "desired dose" of electrons to a selected area of the resist.

A crucial factor for electron beam lithography in the industry is the throughput performance. Scaling down features increases pattern density and hence exposure time. Throughput rate can be increased by projecting large complex patterns at one shot onto a resist-coated wafer. In this case, electron beam passes through apertures and masks on which shaped geometries like square or rectangle are fabricated. Electron projection lithography is one of the next-generation lithography techniques that could be used for printing sub-70 nm structures on a wafer. Well-known and promising projection systems are scattering with angular limitation projection electron-beam lithography (SCALPEL) developed at Lucent Technologies [14] and IBM prototype called projection reduction exposure with variable axis immersion lenses (PREVAIL) [15].

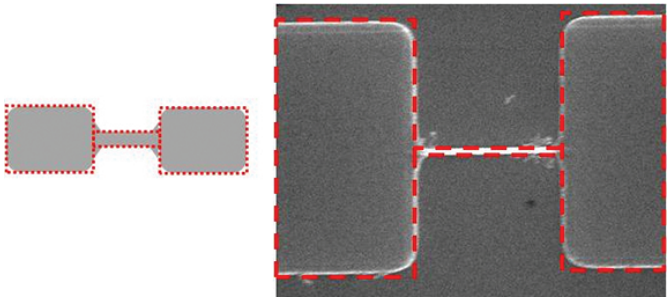

Figure 4. A schematic illustration of proximity effects where red rectangles represent original exposed area. The beam energy was 20 keV and the exposing current is 15 pA.

The resolution of ebeam lithography depends strongly on the interaction which occurs between the electron and the resist/substrate layer. Considerable efforts have been made to understand the resolution limits in ebeam lithography [16, 17]. The size of the beam is not the limiting factor because sizes of nearly 2 nm are routinely reached and the diffraction effects are negligible. As

the primary electrons hit the resist, part of their energy is dissipated in form of secondary electrons and backscattered electrons. Secondary electrons with energy lying between 2 and 50 eV and of few nanometer range contribute to the major resist exposure. Backscattered electrons experience instead a wide scattering angle into the resist and the substrate which dramatically broadens the exposure area [18, 19]. At 20 keV, for example, the range of backscattered electrons is about 5 μm meaning that patterns of less than that range will experience cumulative exposure. As a consequence, proximity effects, sample charging, and placement accuracy are major factors affecting electron beam lithography systems. **Figure 4** is an example showing proximity effects on 200-nm-thick HSQ negative resist on silicon substrate. As a result, the corners of the big rectangles are not developed to desired size and also overlap between the small rectangle and the big ones is over exposed.

Fortunately, correction techniques exist to circumvent and attenuate effects of these limiting factors. This topic will not be completely addressed in this chapter, but we will instead present few ways used to correct for proximity effects. On way to perform this correction is to change the initial pattern and assign a proper dose to each element as illustrated in **Figure 5**.

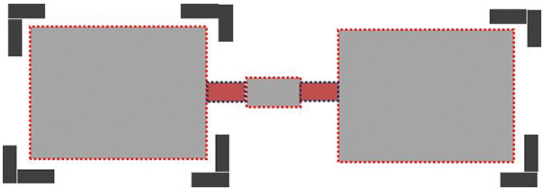

Figure 5. A schematic illustration of proximity effects correction made by changing the shape of the design and by assigning a dose to each element.

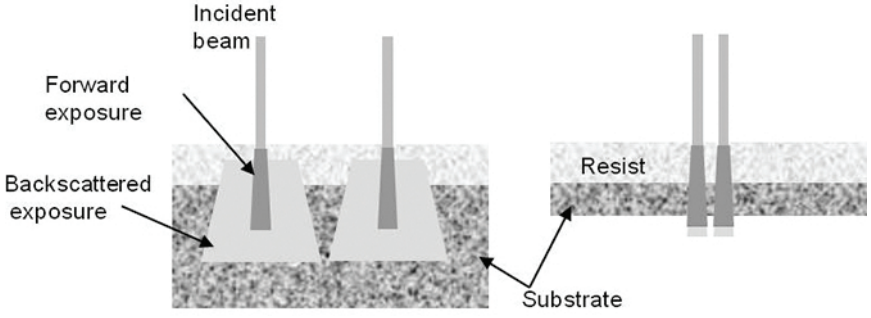

Figure 6. A schematic illustration showing the extent of exposed regions in thick (left) and thin (right) substrate for two subsequent point exposures.

From a practical point of view, using thin resist layer and substrates with low atomic mass helps to decrease proximity effects by lowering the backscattered coefficient. As sketched in **Figure 6**, an incident electron beam "forward-scatters" hits the resist. Consequently, strong

http://dx.doi.org/10.5772/66028

scattering in the thick substrate layer results in broadly distributed "back-scattered" electrons, which expose a wide region of the resist. This broadening is less pronounced for thin substrate. As demonstrated in Ref. [20], metallic nanogaps of sub-5 nm opening were successfully transferred to 100 nm thick using a thin silicon nitride substrate. In Ref. [20], the resist was 100-nm-thick PMMA exposed with 30 keV beam energy.

4. Pattern transfer

We had so far introduced lithography techniques widely used to expose appropriate resists. This lithography step is principally devoted to create a resist image and precisely define appropriate areas (pattern) on the substrate. After resist development, the pattern is transferred with micrometric or nanometric scale to the substrate after subsequent process steps such as liftoff or etching (see **Figure 7**).

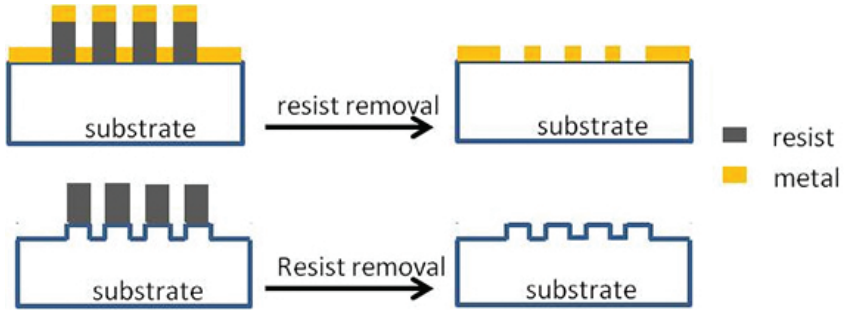

Figure 7. Exposed resist pattern transferred to the substrate by liftoff (top) and by etching (bottom).

Two major factors impact dramatically the fidelity of pattern transfer to the wafer, namely resist profile and overlay. Resist shape, that is, resist profile, requirement is generally dictated by post-lithography process steps. The profile is governed by exposure dose, the developer, as well as resist properties such as sensitivity and contrast. Let's consider the case of liftoff process which is a widely used technique for fabricating micro- and nanodevices that combines lithography and thin film deposition. The resist under the deposited film is removed with a solvent leaving only the film on required locations of the substrate. The main conditions for a proper liftoff are the formation of an undercut in the resist after development and the perpendicular incidence of the film particle beam onto the substrate (**Figure 8a**). The undercut ensures that the evaporated metal, deposited on the patterned resist, is discontinuous, thereby enabling the working metal liftoff. As illustrated in **Figure 8c**, a successful lift-off could be obtained with resist profile having an "undercut" shape. In fact, wings at the edges of structure appear when the profile is not favorable like in the bowel shape case (**Figure 8b**, **d**).

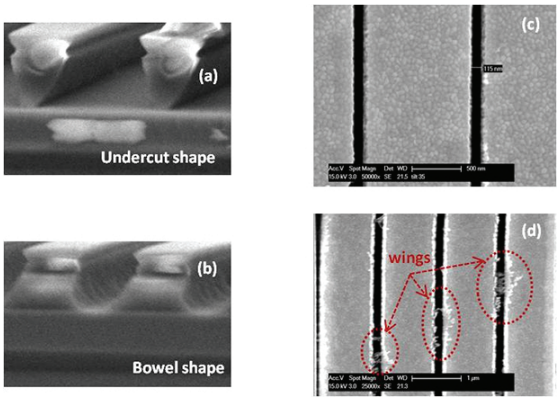

Figure 8. Scanning electron microscope images of resist profile (a,b) and line metallic structure (c,d). Images (a) and (b) were obtained using a trilayer of SML/ZEP520A/PMMA electron beam resists. Images (c) and (d) correspond to liftoff process of 100-nm-thick gold using SML electron beam resist. Raith 150 ebeam system was used to expose resists.

Overlay comes into play when several fabrication levels are needed to fabricate a given structure. Overlay error determines the precision at which a pattern is placed accurately in wanted position on the chip. Mostly, placement accuracies of sub-30 nm up to 1 μm are required to connect micrometric or nanometric scale elements to the pads or between other elements of the structure. Alignment marks are usually used to achieve such precisions, and the pattern-placement accuracy increases when the marks are as close as possible to the critical areas. Alignment system consists generally of a detector, which detects a given mark, and a software that analyzes and determines the center of the mark relatively to a reference. The accuracy depends not only on the detector signal but also on the quality of the marks. Depending on subsequent process requirements, these marks can be made from resist, metal or being etched. **Figure 9** illustrates transferred ellipsoidal on silicon waveguide gold obtained by liftoff of 30-nm-thick gold. An alignment of <30 nm was required to properly align gold nanostructure on the waveguide [21].

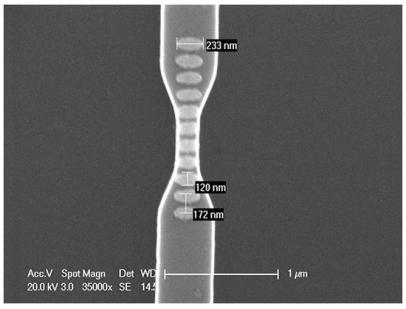

Figure 9. Scanning electron image of 11 ellipsoidal gold on Si waveguide for guided plasmonic applications.

http://dx.doi.org/10.5772/66028

5. Unconventional lithography techniques

As we have previously shown, lithography is a key step in the processes of micro and nano-technologies. The aim is to structure a pattern in a polymer that has been deposited on a substrate. The polymer is generally an organic or inorganic resist. The structure will allow to realize other steps such as etching or materials' deposit. Currently, this technology use conventional lithography techniques like optical lithography or electron beam lithography (EBL). Beyond these technologies, other methods are referenced as un-conventional to reduce the cost of production and permit large series. Among them, we have the nanoimprint lithography (NIL) (see **Figure 1**). This technique is based on printing in a polymer by using a mold which may be rigid or flexible. This method was developed in the 1990s because it allowed to obtain rapidly large area nanoscale patterns with low costs. The main steps are printing in the polymer with a mold, demolding, and transferring the pattern into the substrate. As shown in **Figure 10**, there are two main techniques of NIL. The first developed method is more commonly known as hot embossing thermal process. S.Y. Chou published the first results of this technique in 1995 [6].

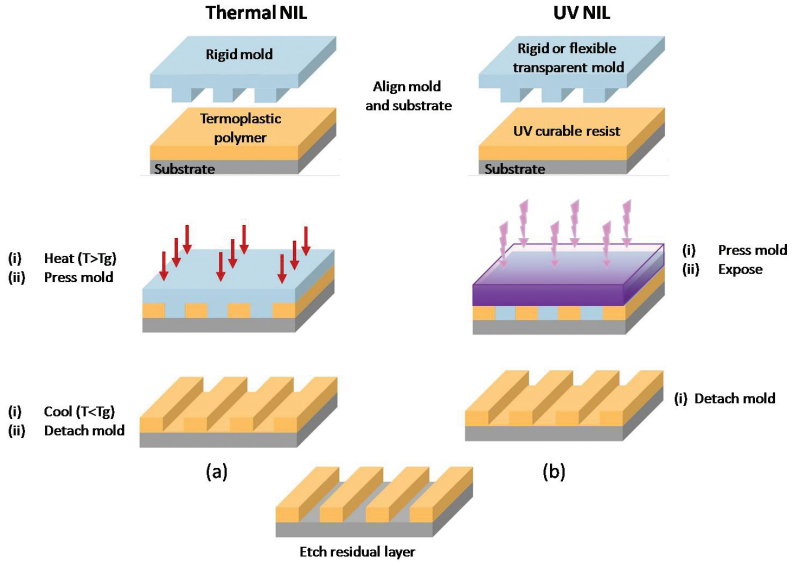

Figure 10. Principle of Thermal NIL (a) and UV-NIL (b).

A few years later, a second method called UV-NIL was developed in the Philips Research Labs [7]. In this case, the photon energy is used to cure the photosensitive resist. This process requires transparent mold and offers other advantages than thermal NIL. In the following paragraphs, we will present NIL techniques, mainly thermal and UV-NIL, how to design the mold, and we will also discuss about a new method called nanosphere lithography (NSL).

5.1. Thermal NIL

The principle of thermal NIL is to imprint in a thermoplastic polymer with a structured rigid mold [6]. The mold needs to have an antisticking treatment to avoid lifting printed patterns. This process uses a polymer heated at a temperature above its glass transition temperature (Tg) and a pressure between 10 and 200 bars during the imprint [22]. Thus, the mold is removed after cooling the substrate. **Figure 10a** shows the main steps of this method which provides resolution in the nanometer range. However, it has the drawbacks to operate with high temperatures and high pressures.

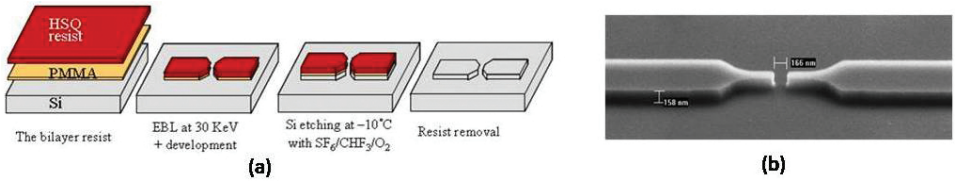

Figure 11. (a) Process scheme for Si mold developed by EBL and HSQ resist and (b) SEM image of a silicon mold for nanogap electrodes (150 nm).

The fundamental step is to design the rigid mold; the materials used are mainly Si, SiO_2, or quartz; and the pattern is realized by an electron beam lithography to achieve high resolution. **Figure 11a** shows an example scheme to process Si mold developed for nanogap electrodes with high-resolution HSQ negative-tone resist. **Figure 11b** is a SEM image of master mold (Si) obtained with this process for a gap of 150 nm and usable for thermal NIL. More complete details of the thermal NIL process are given in Ref. [23].

5.2. UV-NIL

The cross-linking of the resist with UV nanoimprint lithography is obtained by the photon energy. The mold can be flexible or rigid and necessarily transparent. **Figure 10b** summarizes this method used for both soft UV-NIL with a flexible mold and hard UV-NIL with a rigid mold in quartz. The UV transparent mold is imprint in a low-viscosity UV-curable resist UV at room temperature and low pressure between 0 and 1 bar [24]. The mold is firstly removed followed by etching of residual resist layer to permit a transfer of patterns in the substrate by liftoff technique or etching process.

For hard UV-NIL, the main goal is to design by ebeam lithography, the mold generally made in quartz. It is necessary to use a metallic or dielectric mask to control form factor of the pattern during the etch process [25, 26]. Before imprinting in UV-curable resist, a special treatment is applied to reduce surface energy of the mold. An antisticking is needed to avoid resist tear-off during "demold" step between mold and substrate [27]. The next step is to etch the residual layer and transfer in the substrate.

With soft UV-NIL, the flexible mold is generally in poly(dimethylsiloxane) PDMS [28] and obtained from a Si master mold. PDMS offers good chemical stability and high optical

http://dx.doi.org/10.5772/66028

transparency [29]. The method to get the master mold is the same as described in the thermal NIL process. The next step is an antisticking treatment of the master mold, deposits PDMS mixed with his curing agent on master mold and bakes at 60° during 2 h. A full description of the process is made in reference [30]. **Figure 12** shows an example of dots AFM image in PDMS stamp and stamp PDMS imprint in a UV-curable resist from AMO for gold nanoparticle applications. An example of 30-nm-thick gold array for plasmonic application is illustrated in **Figure 12c**.

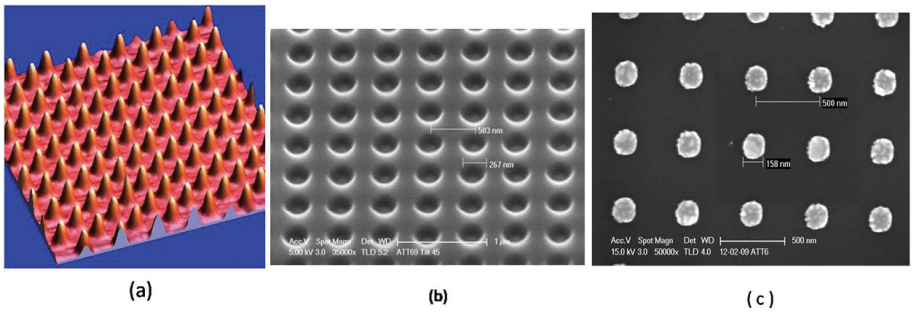

Figure 12. (a) AFM image of dots in PDMS stamp with a periodicity of 500 nm and height of 90 nm, (b) SEM image of an imprint in UV-curable resist (AMONIL from AMO GMBH) with PDMS flexible stamp obtained from the Si master mold and (c) 30-nm-thick gold nanoparticles array obtained by UV-NIL for plasmonic applications.

5.3. Nanosphere lithography

Nanosphere lithography (NSL) is a simple technique to implement and inexpensive. It is also called as colloidal lithography and allows well-ordered nanoparticles in a plane and on large surface. The structure obtained by NSL based on a self-assembling nanosphere achieves a colloidal mask in two dimensions (**Figure 13**). This technique has demonstrated to be well suited for the fabrication of size-tunable nanoparticles in the 20–1000 nm range [8]. This method can also be used to obtain silicon mold for NIL application. To file a nanosphere solution onto the substrate, several methods exist as spin coating, [31] drop coating file [32], and thermo-electrically cooled angle coating [33]. Nanospheres meet into 2D hexagonal mesh on the substrate due to capillary forces during the solvent evaporation. After the step of deposition of self-assembling nanospheres, a thickness material layer is evaporated by electron beam through the nanosphere mask. Then, nanosphere mask is removed with a solvent.

NSL mask fabrication may depend on the number of layers required to obtain nanostructure networks [34]. **Figure 14** shows an example with a single and a double NSL layers and nanostructure arrays obtained with theses configurations. When a gold layer is deposited through a single monolayer by self-assembled nanospheres onto the substrate and NSL mask is removed, an array of triangular nanoparticles is obtained (**Figure 14**, left). For a configuration with two monolayers of nanospheres deposited and assembled, this is obtained by an increasing of the nanosphere concentration. When the second layer is assembled on the first, in order

to obtain a significant part of a double layer of hexagonally assembled nanospheres, the free interstices where the material can be deposited on the substrate form an homogeneous pattern of hexagonal nanoparticles (**Figure 14**, right).

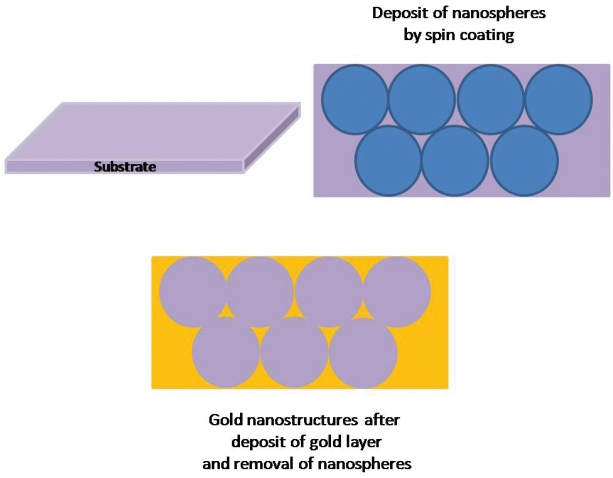

Figure 13. Principle of nanosphere lithography.

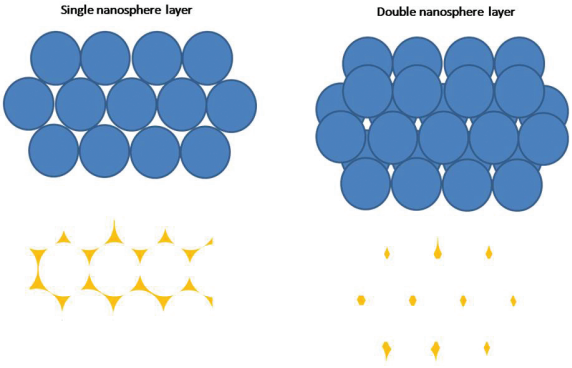

Figure 14. Schematic representation of gold nanostructures obtained with a single (left) and double layer (right).

6. Conclusion

Combined with deposition techniques, conventional lithography and un-conventional lithography are powerful tools to fabricate thin film functional devices. These tools offer

tremendous opportunities to enhance not only device performances and reduce effective cost, but also to discover and explore new functionalities. It provides, in particular, the possibility to better control of pattern transfer in terms of resolution, density, and resist profile.

Acknowledgements

This work was done within the Center for Nanoscience and Nanotechnology clean room and partly supported by the RENATECH network and the General Council of Essonne.

Author details

Abdelhanin Aassime* and Frederic Hamouda

*Address all correspondence to: abdelhanin.aassime@u-psud.fr

Centre de Nanosciences et de Nanotechnologies, C2N-Site d'Orsay, Université Paris-Sud, Orsay Cedex, France

References

[1] Reynolds GJ, Kratze M, Dubs M, Felzer H, Mamazza R. Electrical properties of thin film capacitors fabricated using high temperature sputtered modified barium. Materials. 2012;5(4):644–660. doi:10.3390/ma5040644

[2] Borges J, Costa D, Antunes E, Lopes C, Rodrigues MS, Apreutesei M, Alves E, et al. Biological behaviour of thin films consisting of Au nanoparticles dispersed in a TiO2 dielectric matrix. Vacuum. 2015;122(Part B):360–368. doi:10.1016/j.vacuum.2015.03.036

[3] Qiu WL, Chang L, Lee D, Dannangoda C, Martirosyan K, Litvinov D. Patterning of magnetic thin films and multilayers using nanostructured tantalum gettering templates. ACS Applied Materials and Interfaces. 2015;7(11):6014–6018. doi:10.1021/am5090463

[4] Le-Van Q, Le Roux X, Aassime A, Degiron A. Electrically driven optical metamaterials. Nature Communication. 2016;7(12017). doi:10.1038/ncomms12017

[5] Roland I, Zeng Y, Checoury X, El Kurdi M, Sauvage S, Brimont C, Guillet T, Gayral B, Gromovyi M, Duboz JY, Semond F, de Micheli MP, Boucaud P. Near-infrared III-nitride-on-silicon nanophotonic platform with microdisk resonators. Optics Express. 2016;24(9):9602–9610. doi:10.1364/OE.24.009602

[6] Chou SY, Krauss PR, Renstrom PJ. Imprint of sub-25 nm vias and trenches in polymers. Applied Physics Letters. 1995;67(21):3114–3116. doi:10.1063/1.114851

[7] Haisma J, Verheijen M, VandenHeuvel K, VandenBerg J. Mold-assisted nanolithography: a process for reliable pattern replication. Journal of Vacuum Science and Technology B. 1996;14(6):4124–4128. doi:10.1116/1.588604

[8] Haynes CL, Van Duyne RP. Nanosphere lithography: a versatile nanofabrication tool for studies of size-dependent nanoparticle optics. Journal of Physical Chemistry B. 2001;105(24):5599–5611. doi:10.1021/jp010657m

[9] Mizoguchi H, Saitoh T, Matsunaga T. Development of light sources for lithography at present and for the future. Komatsu Technical Report. 2013;59(166).

[10] Trouiller Y. From 120 to 32 nm CMOS technology: development of OPC and RET to rescue optical lithography. Comptes Rendus Physique. 2006;7(8):887–895. doi:10.1016/j.crhy.2006.10.001

[11] Pease RF, Chou SY. Lithography and other patterning techniques for future electronics. Proceedings of the IEEE. 2008;96(2):248–270. doi:10.1109/JPROC.2007.911853

[12] Bae WJ, Trikeriotis M, Rodrigues R, Zettel MF, Piscani E, Ober CK, Giannelis EP, Zimmerman P. High index nanocomposite photoresist for 193 nm lithography. Advances in Resist Materials and Processing Technology XXVI. 2009;7273:727326. doi:10.1117/12.814154

[13] Kulmala TS, Vockenhuber M, Buitrago E, Fallica R, Ekinci Y. Toward 10 nm half-pitch in extreme ultraviolet lithography: results on resist screening and pattern collapse mitigation techniques. Journal of Micro-Nanolithography MEMS and MOEMS. 2015;14(3):033507. doi:10.1117/1.JMM.14.3.033507

[14] Harriott LR, Berger SD, Biddick C, Blakey MI, Bowler SW, Brady K, Camarda RM, Connelly WF, et al. The SCALPEL proof of concept system. Microelectronic Engineering. 1997;35(1–4):477–480. doi:10.1016/S0167-9317(96)00189-X

[15] Dhaliwal RS, Enichen WA, Golladay SD, Gordon MS, Kendall RA, Lieberman JE, Pfeiffer HC, Pinckney DJ, Robinson CF, Rockrohr JD, Stickel W, Tressler EV. Prevail—electron projection technology approach for next-generation lithography. IBM Journal of Research and Development. 2001;45(5):615–638.

[16] Broers AN. Resolution limits for electron beam lithography. IBM Journal of Research and Development. 1988;32(4):502–513.

[17] Vieu C, Carcenac F, Pepin A, Chen Y, Mejias M, Lebib A, Manin-Ferlazzo L, Couraud L, Launois H. Electron beam lithography: resolution limits and applications. Applied Surface Science. 2000;164:111–117. doi:10.1016/S0169-4332(00)00352-4

[18] Dubonos SV, Gaifullin BN, Raith HF, Svintsov AA, Zaitsev SI. Evaluation, verification and error determination of proximity parameters alpha, beta and eta in electron beam

lithography. Microelectronic Engineering. 1993;21(1–4):293–296. doi:10.1016/0167-9317(93)90076-H

[19] Rooks M, Belic N, Kratschmer E, Viswanathan R. Experimental optimization of the electron-beam proximity effect forward scattering parameter. Journal of Vacuum Science and Technology B. 2005;23(6):2769–2774. doi:10.1116/1.2062431

[20] Fischbein MD, Drndic M. Nanogaps by direct lithography for high-resolution imaging and electronic characterization of nanostructures. Applied Physics Letters. 2006;88(6):063116. doi:10.1063/1.2172292

[21] Fevrier M, Gogol P, Aassime A, Megy R, Delacour C, Chelnokov A, Apuzzo A, Blaize S, Lourtioz JM, Dagens B. Giant coupling effect between metal nanoparticle chain and optical waveguide. Nano Letters. 2012;12(2):1032–1037. doi:10.1021/nl204265f

[22] Gourgon C, Perret C, Tallal J, Lazzarino F, Landis S, Joubert O, Pelzer R. Uniformity across 200 mm silicon wafers printed by nanoimprint lithography. Journal of Physics D: Applied Physics. 2005;38(1):3870–3873.

[23] Guo LJ. Nanoimprint lithography: methods and material requirements. Advanced Materials. 2007;19(1):495–513. doi:10.1002/adma.200600882

[24] Hamouda F, Barbillon G, Held S, Agnus G, Gogol P, Maroutian T, Scheuring S, Bartenlian B. Nanoholes by soft UV nanoimprint lithography applied to study of membrane proteins. Microelectronic Engineering. 2009;86(XX):583–585. doi:10.1016/j.mee.2008.11.086

[25] Bender M, Otto M, Hadam B, Spangenberg B, Kurz H. Fabrication of nanostructures using a UV-based imprint technique. Microelectronic Engineering. 2000;53(1–4):233–236. doi:10.1016/S0167-9317(00)00304-X

[26] Voisin P, Zelsmann M, Gourgon C, Boussey J. High resolution silica molds fabrication for UV-Nanoimprint. Microelectronic Engineering. 2007;84(5):916–920. doi:10.1016/j.mee.2007.01.087

[27] Truffier-Boutry D, Galand R, Beaurain A, Francone A, Pelissier B, Zelsmann M, Boussey J. Mold cleaning and fluorinated anti-sticking treatments in nanoimprint lithography. Microelectronic Engineering. 2009;86(4):669–672. doi:10.1016/j.mee.2009.01.065

[28] Hamouda F, Barbillon G, Gaucher F, Bartenlian B. Sub-200 nm gap electrodes by soft UV nanoimprint lithography using polydimethylsiloxane mold without external pressure. Journal of Vacuum Science and Technology B. 2010;28(1):82–85. doi:10.1116/1.3273535

[29] Schmid H, Biebuyck H, Michel B, Martin OJM. Light-coupling masks for lensless, sub-wavelength optical lithography. Applied Physics Letters. 1998;72(XX):2379–2381. doi:10.1063/1.121362

[30] Barbillon G, Hamouda F, Held S, Gogol P, Bartenlian B. Gold nanoparticles by soft UV nanoimprint lithography coupled to a lift-off process for plasmonic sensing of anti-

bodies. Microelectronic Engineering. 2010;87(5):1001–1004. doi:10.1016/j.mee.2009.11.114

[31] Hulteen JC, Van Duyne RP. Nanosphere lithography: a materials general fabrication process for periodic particle array surfaces. Journal of Vacuum Science and Technology A. 1995;13(XX):1553–1558. doi:10.1116/1.579726

[32] Hulteen JC, Treichel DA, Smith MT, Duval ML, Jensen TR, Van Duyne RP. Nanosphere lithography: size-tunable silver nanoparticle and surface cluster arrays. Journal of Physical Chemistry B. 1999;103(19):3854–3863. doi:10.1021/jp9904771

[33] Micheletto R, Fukuda H, Ohtsu M. A simple method for the production of a two-dimensional, ordered array of small latex particles. Langmuir. 1995;11(9):3333–3337. doi:10.1021/la00009a012

[34] Kadiri H, Kostcheev S, Turover D, Salas-Montiel R, Nomenyo K, Gokarna A, Lerondel G. Topology assisted self-organization of colloidal nanoparticles: application to 2D large-scale nanomastering. Beilstein Journal of Nanotechnology. 2014;5(XX):1203–1209. doi:10.3762/bjnano.5.132

Chapter 4

In Situ Engineering and Characterization of Correlated Materials with Integrated OMBE–ARPES

Dawei Shen, Haifeng Yang and Zhengtai Liu

Additional information is available at the end of the chapter

http://dx.doi.org/10.5772/65711

Abstract

Oxide molecular beam epitaxy has emerged as an effective technique to fabricate complex oxide thin films and novel superlattices with atomic-level precision. In this chapter, we first briefly introduce the oxide molecular beam epitaxy technique and then show how to use this technique to achieve high-quality thin films with good stoichiometry. Moreover, we exhibit that the combination of oxide molecular beam epitaxy and *in situ* angle-resolved photoemission spectroscopy is indeed a versatile toolkit to tailor and characterize properties of novel quantum materials.

Keywords: oxide molecular beam epitaxy (OMBE), correlated materials, angle-resolved photoemission spectroscopy (ARPES)

1. Introduction

In transition metal oxides, the subtle interplay among charge, orbital, lattice and spin degrees of freedom gives rise to a spectrum of fascinating physical phenomena, including high-temperature superconductivity [1], metal-insulator transition [2], colossal magnetoresistance [3], and so on. Remarkably, in thin film interfaces and ultrathin films of correlated oxides, emergent physics, which does not exist in bulk crystals, occurs [4, 5]. As a well-known example, two-dimensional electron gas with high mobility amazingly emerges at the interface of two-band insulators $LaAlO_3$ and $SrTiO_3$ [6]. This emergent electron gas was even found to be superconducting [7]. Another example is that strong ferroelectricity and ferromagnetism were found in $EuTiO_3/DyScO_3$ superlattices [8]. As Nobel laureate Herbert Kroemer said that 'the interface is the device' [9], these emergent physics may potentially revolutionize our modern technologies.

In order to access these thin film-based physics, the first and most important step is to grow these oxide thin film structures with high quality. This needs exquisite control of growth, and usually is very challenging. In the past several decades, fortunately, reactive oxide molecular beam epitaxy (OMBE) has been proved to be an effective technique in the growth of some oxides with high quality, though being not easy [10–12]. Recently, the *in situ* combined system of OMBE and angle-resolved photoemission spectroscopy (ARPES) [13–17] have shown great potential in exploring intricate many-body physics based on oxide film structures, which further intensifies the power of OMBE.

In this chapter, we first present basics of OMBE technique. Then, we show how to grow high-quality films with good stoichiometry, and the power of the integrated OMBE-ARPES in studying and designing many-body interactions in complex oxides.

2. Basics of OMBE technique

MBE is a vacuum deposition technique in which well-defined thermal beams of atoms or molecules react at a crystalline surface to produce an epitaxial film. Originally, it was developed to fabricate GaAs and (Al, Ga)As films [18], and soon successfully expanded to other semiconductors as well as metals and insulators. In addition to molecular beams coming from individual heated element source, gas molecular may also be introduced into MBE. Including gas oxidants (e.g., oxygen or ozone) can make an OMBE, which is now applied to grow oxides [11, 12].

In 1985, Betts and Pitt began to use this technique to grow $LiNbO_3$ films [19]. Later, motivated by the discovery of high-temperature superconductivity, OMBE was used to grow complex cuprate thin films. Up to now, it has been broadly employed to fabricate a pool of oxides, including oxide superconductors (e.g., (Ba, K)BiO_3, (La, Sr)$_2CuO_4$, $Bi_2Sr_2Ca_{n-1}Cu_nO_{2n+4}$, etc.), ferroelectrics (e.g., $LiTaO_3$, $PbTiO_3$, etc.), ferromagnets (e.g., (La, Ca)MnO_3, EuO, etc.), multiferroics (e.g., $BiFeO_3$, $YMnO_3$, etc.) and superlattices of these phases [11, 12].

While conventional MBE growth occurs in an ultra-high vacuum, in OMBE growth the induction of active gas oxidants can pose new challenges in the instrumentation as well as the film growth [11, 17]. The presence of oxidant species requires the hardware to be necessarily compatible with an oxidizing environment, thus high-temperature components (e.g., heater filaments, effusion cells and substrate holders, etc.) need to be made of highly oxidant-resistive materials. Moreover, adequate pumping is needed to deal with the oxidant gas load. Furthermore, oxygen acts as another variable which needs to be optimized in the growth, and oxygen inside films is tricky to study and manipulate. In addition, the oxidants can oxidize the cell materials such that one cannot get well-controlled fluxes as planned during growth. These challenges make the use of OMBE in the growth of oxides less mature than the use of MBE in semiconductor growth [11].

Figure 1 shows the schematic of a typical OMBE system. Single-element evaporators are used to generate atomic beams for OMBE growth. Knudsen cells and crucibles are chosen for

http://dx.doi.org/10.5772/65711

elements with desired fluxes below 2000°C, while electron beam evaporators are adopted for refractory elements (e.g., tungsten, ruthenium and iridium) which require higher temperature to provide the fluxes necessary for the growth. The atomic beams impinge upon the substrate unless they are blocked by shutters which are positioned at the output end of each cell and remotely controlled by a computer. The utilization of shutters enables the elemental fluxes to be supplied to in a continuous or a sequential way. The fluxes can be adjusted by changing the cell temperature, and are *in situ* measured by a quartz crystal microbalance (QCM). Reflective high-energy electron diffraction (RHEED) is used in OMBE for the *in situ* characterization of the growing surface. Due to the grazing angle diffraction, it can provide surface-sensitive information including thin film crystallinity, roughness, in-plane lattice constants, growth mechanism and phase purity. If intermediate products or impurity phases are formed, the growth conditions would be adjusted accordingly. Distilled ozone was used as the oxidant. Compared to oxygen, ozone has stronger oxidizing ability and thus needs lower pressure.

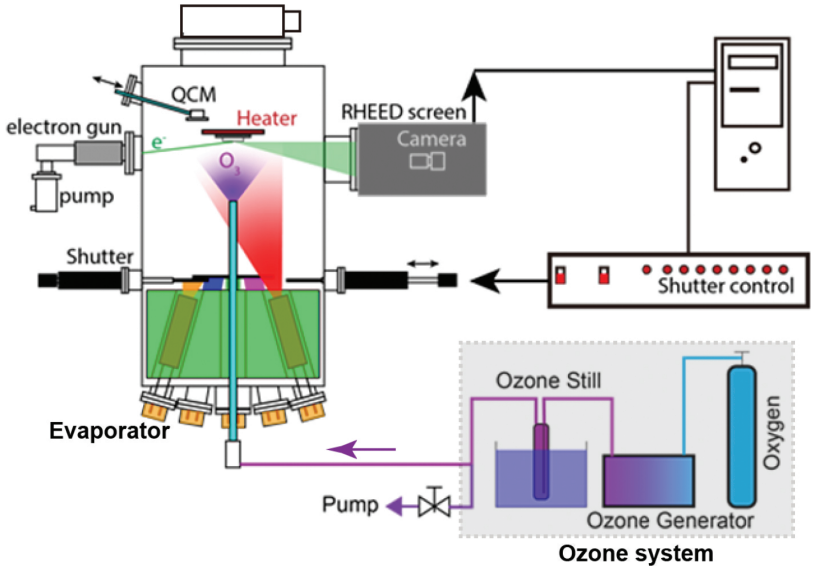

Figure 1. Schematic illustration of an OMBE system with an ozone-generating system. Reproduced with permission from Ref. [17].

Figure 2 displays the photo of DCA R450 OMBE system in Shanghai Institute of Microsystem and Information Technology (SIMIT). It is equipped with 10 changeable effusion cells, and one four-seat e-beam evaporator for at most four refractory elements, which can cover all transition metals of interests. It also has *in situ* QCM to measure the fluxes and real-time RHEED to directly monitor the growth. Ozone was obtained from self-made ozone-generating-and-distilling system. Ozone generator would generate a small amount of ozone out of oxygen gas, then silica gel cooled down with liquid nitrogen would absorb ozone. Warming up the silica gel would give out the ozone gas to be used in OMBE growth.

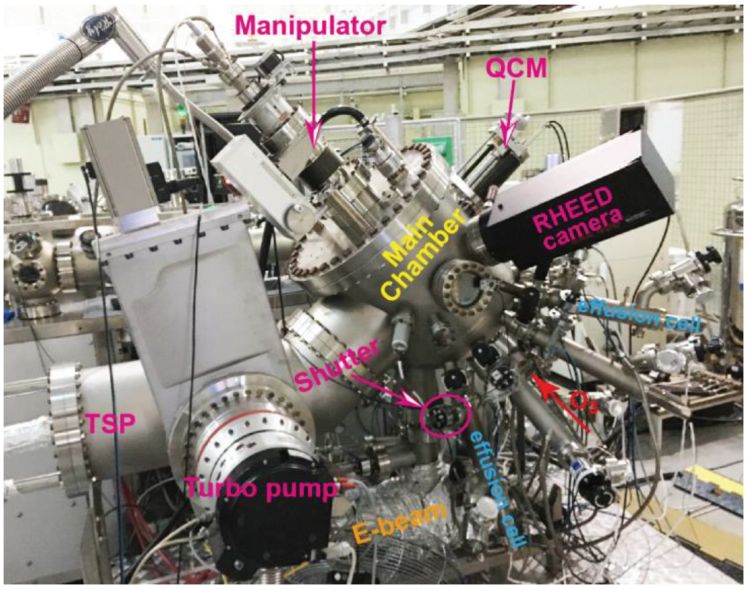

Figure 2. OMBE system in Shanghai Institute of Microsystem and Information Technology (SIMIT), Chinese Academy of Sciences.

3. Fabricating oxide thin films with good stoichiometry by OMBE

In this section, we show generally how to grow high-quality oxide thin film with good stoichiometry by OMBE. Starting with choosing the proper substrate, we mainly talk about two growth methods commonly used—absorption-controlled growth and shutter growth—to achieve high-quality films.

Epitaxial thin films cannot be obtained without using proper substrates. The substrate not only guides the growth of thin film with the right crystalline structure but also provides the knob of strain which can essentially tune the electronic structure of the material [20]. **Figure 3** displays lattice constants of single-crystalline perovskite substrates which are commercially available and commonly used to grow perovskite or layered perovskite oxide thin films. If growing $LaNiO_3$ films with a pseudo-cubic lattice constant of 3.84 Å on $LaAlO_3$ (3.75 Å) substrates, an in-plane compressive strain was applied; if using $SrTiO_3$ (3.905 Å) as the substrate, an in-plane tensile strain was applied. In addition to the strain, in some cases, the choice of the substrate is vital to obtain high-quality films. For example, Proffit et al. reported that (1 1 0) orthorhombic $CaRuO_3$ films grown on orthorhombic (1 1 0) $NdGaO_3$ substrates (symmetry matched) exhibit atomically smooth surfaces, whereas films on cubic lanthanum aluminate-strontium aluminium tantalate (LSAT) substrates (symmetry mismatched) show rather rough surfaces [21]. Another example is the film growth of $LaNiO_3$ with polar orientations. As polar discontinuity is suggested to induce surface reconstructions which further lead

http://dx.doi.org/10.5772/65711

to bad quality of films [22, 23], metallic Nb-doped $SrTiO_3$ and iso-polarity $LaAlO_3$ substrates were shown to be more suitable than the common $SrTiO_3$ in the growth of $LaNiO_3$ films [24].

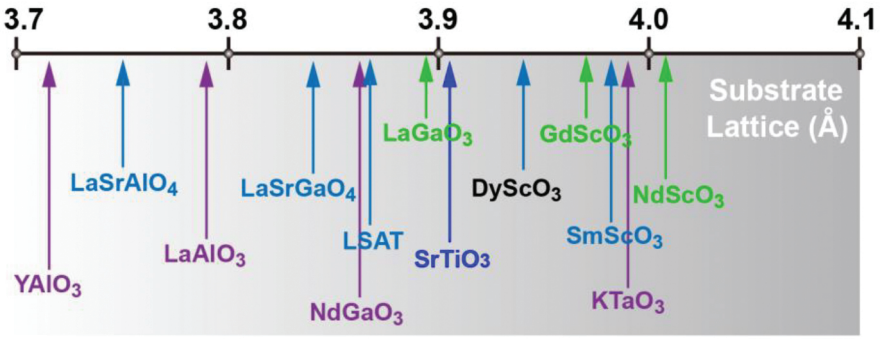

Figure 3. A number line showing the *a*-axis lattice constants in angstroms of the perovskite and perovskite-related substrates that are commercially available.

As illustrated above, the remotely controlled shutters in OMBE allow elemental fluxes to be supplied to in a continuous or a sequential way. Take the growth of perovskite ABO_3 (can be viewed as alternate stacking of AO and BO_2 layers along the (0 0 1) direction) as an example. As schematically shown in **Figure 4**, both shutters of A cell and B cell keeping open in the whole growth make a co-deposition growth. If the shutters of A cell and B cell alternately turn open (finishing the growth of one AO layer, and then starting the growth of one BO_2 layer), we can call this the shutter growth. In either growth, stoichiometry is the most important goal which needs to be achieved.

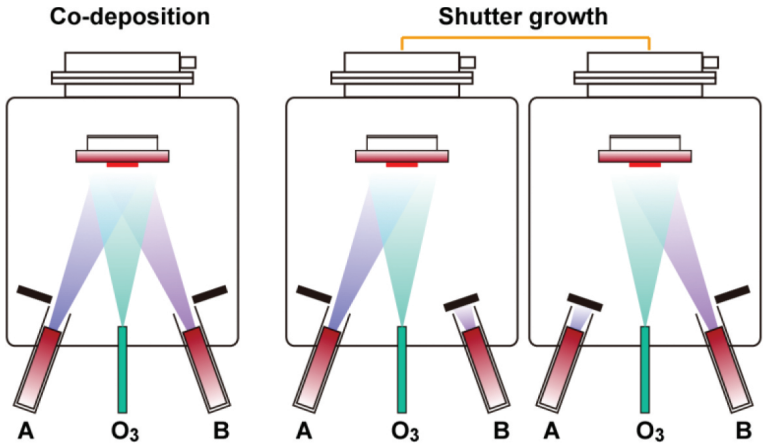

Figure 4. Schematics of co-deposition and shutter growth in OMBE growth.

A well-known growth method to achieve stoichiometric films is the adsorption-controlled growth, which was previously used to grow GaAs and recently has been used to fabricate several oxides such as $PbTiO_3$ [25], $BiFeO_3$ [26] and $BiMnO_3$ [27]. It is used in the growth of some compounds containing volatile species which can re-evaporate during growth while the others are less volatile. If always making this volatile species excess during the growth as well as optimizing the substrate temperature and oxygen partial pressure, stoichiometric growth can be conveniently achieved. Lee et al. reported the adsorption-controlled growth of $BiMnO_3$ in which the bismuth oxides are volatile [27]. **Figure 5** displays the calculated Ellingham diagram and obtained RHEED patterns [27]. The Bi:Mn flux ratio was fixed to be 3:1. Besides, the substrate temperature and oxygen partial pressure were fully explored to finally expose the growth window (see shadow region II in **Figure 5**) for phase-pure stoichiometric $BiMnO_3$ films which were verified by the shiny diffraction spots in the RHEED pattern.

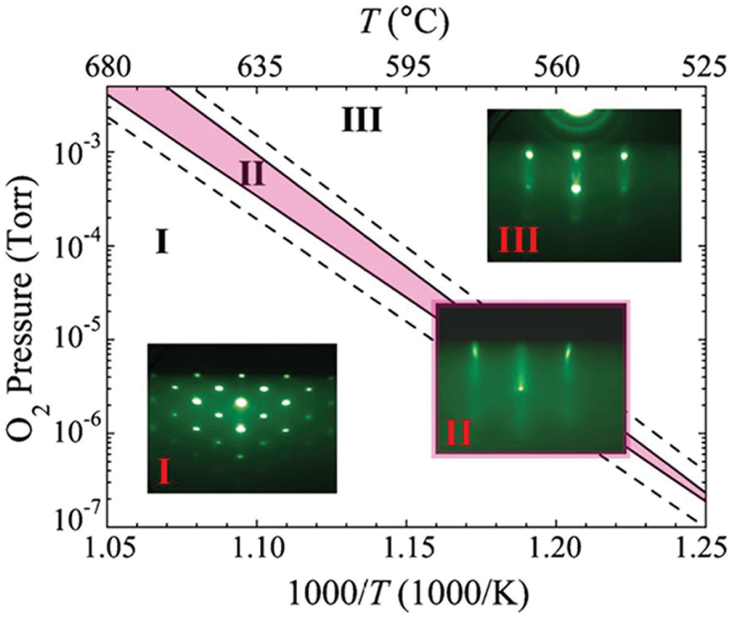

Figure 5. Calculated Ellingham diagram and RHEED patterns collected along the [1 1 0] azimuth of $SrTiO_3$ during the deposition of $BiMnO_3$ at different temperatures and oxygen partial pressures. Phase stability between Bi_xO_y gases and $BiMnO_3$ + Mn_3O_4, $BiMnO_3$ and $BiMnO_3$ + $Bi_2O_{2.5}$ condensed phases is represented by regions I, II and III, respectively. Reproduced with permission from Ref. [27].

For most oxides, adsorption-controlled growth unfortunately cannot be applied. To achieve good stoichiometry, generally, one has to adjust the deposition amount based on cycles of combined studies of QCM, RHEED patterns and oscillations, X-ray diffraction (XRD) pattern fitting, Rutherford backscattering spectroscopy, and so on. In the homo-epitaxial growth of $SrTiO_3$, Schlom's group reported the empirical method of optimizing shuttered RHEED oscillations to successfully achieve stoichiometric $SrTiO_3$ film within 1% composition deviation

http://dx.doi.org/10.5772/65711

[28, 29]. In the shutter growth of $SrTiO_3$, the intensity of diffraction spot would exhibit periodic oscillations at the pace of mechanically closing/opening shutters: in Ti doses, the intensity will decrease monotonically while in Sr doses the intensity will increase. It was shown that if oscillations exhibited smooth sinoidal shape with similar amplitude (**Figure 6(a)**), the resulted film was investigated to be stoichiometric [29]. If Sr is 10% excess, the combined feature of cusp and shoulder would show up (**Figure 6(b)**); if Sr is 10% deficient, the amplitude of individual oscillations would oscillate (**Figure 6(c)**). Thus, in growth, the real-time performance of RHEED oscillations would infer what to do next to achieve the stoichiometry [29].

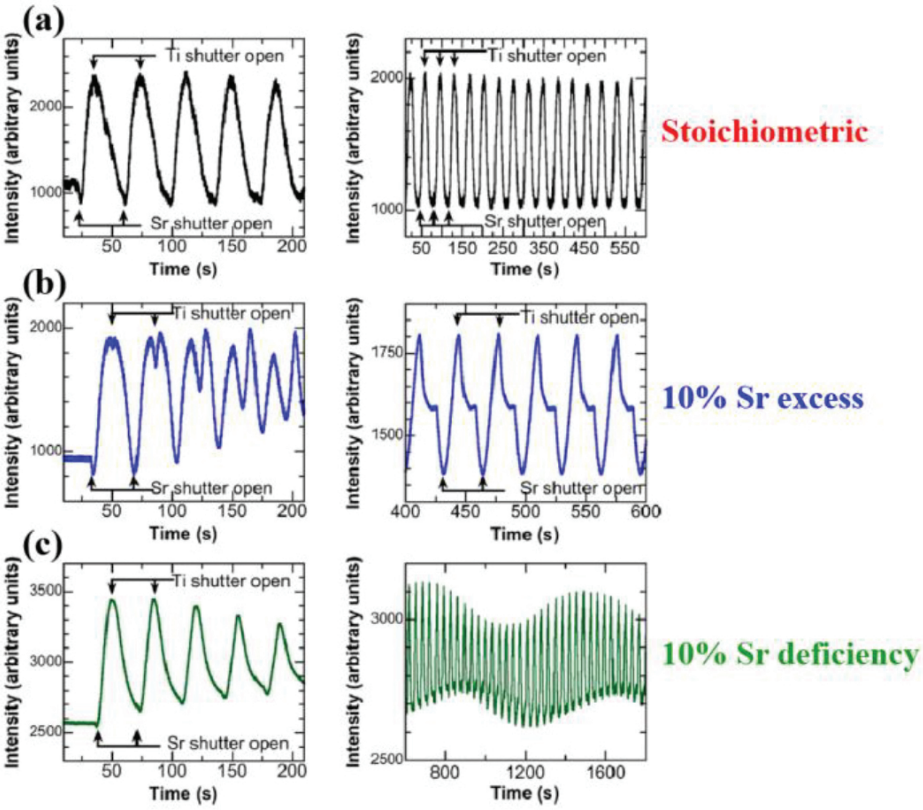

Figure 6. Shuttered RHEED oscillation behaviour of $Sr_{1+x}TiO_{3+\delta}$ films with stoichiometric (x = 0) (a), 10% strontium excess (x = 0.1) (b) and 10% strontium deficiency (x = -0.1) (c). Reproduced with permission from Ref. [29].

Compared to adsorption-controlled growth, shutter growth is a more straightforward way to control the film thickness and grow complex oxide structures such as Ruddlesden-Popper (RP) series $A_{n+1}B_nO_{3n+1}$ and various superlattices which display a wide range of physics. By conveniently changing the shuttering sequence of A and B ions to match the layering sequence of the desired RP phase, Haeni et al. and Tian et al. reported the OMBE growth of five RP members

of $Sr_{n+1}Ti_nO_{3n+1}$ [30] and $Sr_{n+1}Ru_nO_{3n+1}$ [31], respectively. Their structures with right-layering sequences were verified by high-resolution cross-sectional TEM measurements (**Figure 7**).

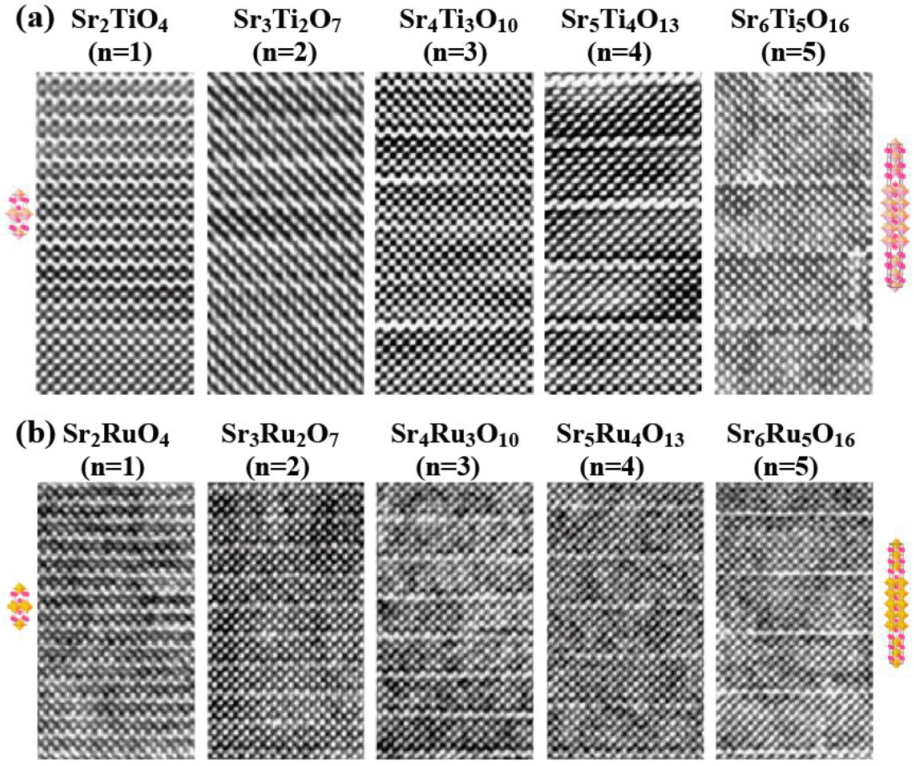

Figure 7. High-resolution cross-sectional TEM images of the same five members of the (a) $Sr_{n+1}Ti_nO_{3n+1}$ and (b) $Sr_{n+1}Ru_nO_{3n+1}$ Ruddlesden-Popper homologous series grown by OMBE. Reproduced with permission from Refs. [30] and [31].

4. The unique *in situ* combo of OMBE and ARPES

ARPES can directly visualize electronic band structures of solids, and therefore has emerged as an essential experimental technique to study various novel quantum materials such as superconductors and topological quantum materials [13, 14, 32]. It can be viewed as the 'k-space' microscope, and can provide the essential information about how electrons move inside the material. Based on the well-known photoelectric effect, an electron inside the solid can absorb an incident photon with a high enough energy and then emit out of the solid. If the kinetic and momentum of the photoelectrons are detected, the band structure of the material (as a function of binding energy and momentum) can be reconstructed in the context of

http://dx.doi.org/10.5772/65711

conversation laws and some reasonable assumptions, as shown in **Figure 8**. Generally being a surface-sensitive probe, ARPES demands clean and well-ordered sample surface, which is usually obtained by cleaving single crystals.

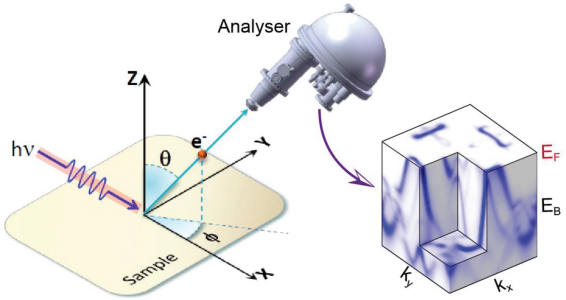

Figure 8. Schematic of ARPES measurement and the obtained band structure. Photoelectrons are emitted when shining the sample with light whose energy is larger than the sample work function. By using an electron analyser to pick up these electrons, we could obtain their energy and momentum information.

Recently, there has been increasing awareness that the *in situ* combo of OMBE and ARPES (ARPES is *in situ* connected to OMBE) could be a powerful approach in tailoring many-body interactions and uncovering the underlying physics of complex oxides. It is a win-win case: OMBE can provide high-quality thin films (especially those who cannot be cleaved properly in bulk form, e.g., perovskite oxides) and interesting superlattices, whose clean surfaces 'naturally' allow for the *in situ* ARPES studies; in return, ARPES can characterize the quality of these films which further give feedbacks to the growth, and moreover it can fully explore the band structures of films and study their intriguing physics [15–17, 33, 34].

Figure 9 shows the photo of such an *in situ* combo system located in Shanghai Institute of Microsystem and Information Technology (SIMIT), Chinese Academy of Sciences. A transfer chamber with high vacuum ($\sim 10 \times 10^{-10}$ Torr) is used to bridge the OMBE system and ARPES

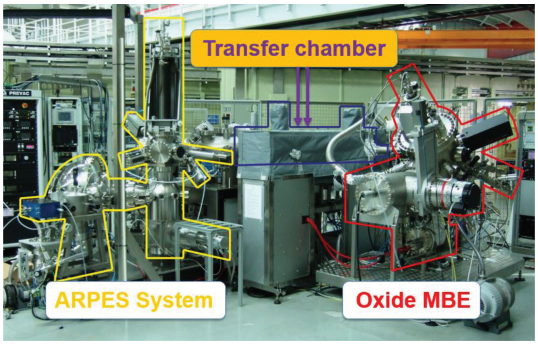

Figure 9. A photo of the *in situ* combo of OMBE and ARPES system in Shanghai Institute of Microsystem and Information Technology (SIMIT), Chinese Academy of Sciences.

system. Once the growth was finished, the film was immediately transferred to the ARPES chamber within 5 min through the transfer chamber. In so doing, the clean sample surface is expected to be preserved for ARPES studies.

Below, we first present studies on ultrathin perovskite $LaNiO_3$ films (*3d* system) [16], $SrRuO_3$ films (*4d* system) [35] and $SrIrO_3$ films (*5d* system) [36] of which the bulk form lacks natural cleaving planes, as examples to show the power of this *in situ* combo in studying the many-body interactions of complex oxides. Generally, when going from *3d* to *5d* elements, Coulomb interactions among electrons would increase as electrons are more and more delocalized, while the spin-orbital coupling (SOC) would become stronger due to the heavier elements. Then, we show the studies on $(LaMnO_3)_{2n}/(SrMnO_3)_n$ superlattices [17].

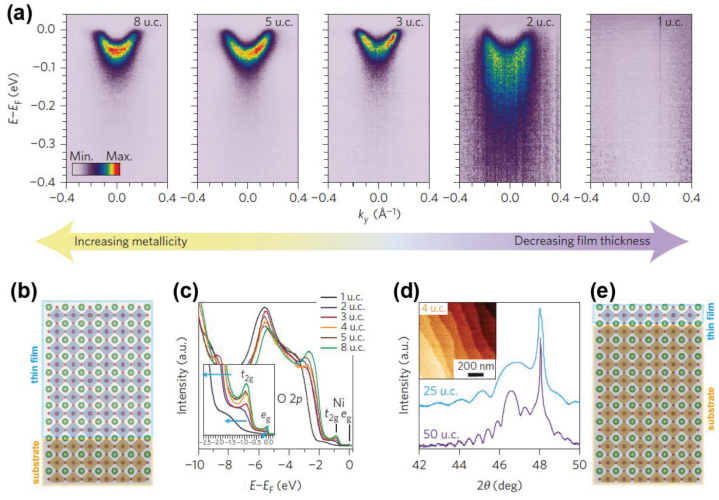

Figure 10. Metal-insulator transition in ultra-thin $LaNiO_3$ films. (a) The evolution of the electronic structure across the metal-insulator transition with decreasing the $LaNiO_3$ film thickness. (b) Schematic of 8-UC-thick $LaNiO_3$ film on $LaAlO_3$ substrate. (c) Angle-integrated photoemission spectroscopy along ($0.5\pi/a$, $0.7\pi/a$) of films varying from 8-UC-thick to 1-UC-thick. The inset shows the near-E_F angle-integrated spectra. (d) X-ray diffraction and atomic force microscopy results. (e) Schematic of 1-UC-thick $LaNiO_3$ film on $LaAlO_3$. Reproduced with permission from Ref. [16].

Bulk $LaNiO_3$, though being strongly correlated with $3d^7$ configuration of Ni^{3+}, remains a paramagnetic metal at low temperatures. By means of OMBE, King et al. synthesized atomically defined layers of $LaNiO_3$ films down to just one unit cell (UC) thickness, and observed an abrupt metal-insulator transition in 2-UC-thick film by transport studies [16]. The high quality of the films with atomically flat surfaces was revealed by the Kiessig fringes in XRD patterns and atomic force microscope image (**Figure 10(d)**). Then, *in situ* ARPES studies were carried out to investigate the competing electronic phases while crossing the transition, as shown in **Figure 10(a)** and **(c)**. The bulk-like electronic structure and Fermi liquid characteristics were found to remain almost unaffected by film thickness down to 3 UC (all exhibiting similar electron pocket), which is in contrast to the previous reports that an insulating state

http://dx.doi.org/10.5772/65711

emerged in 5-UC thickness or above and again reflects the high quality of the films. This makes 3-UC-thick LNO the thinnest metallic nickelate reported. Reducing the thickness by just one further UC (2 UC), however, causes the spectral weight near E_F to be suddenly suppressed. For 1-UC-thick $LaNiO_3$ film, no spectral weight was observed at E_F, indicative of a full-charge gap. This evolution was also observed in angle-integrated photoemission spectra. The authors claimed that the metal-insulator transition is driven by instability to an incipient order of the underlying quantum many-body interactions, and demonstrated the power of artificial confinement to harness control over competing phases in complex oxides with atomic-scale precision [16].

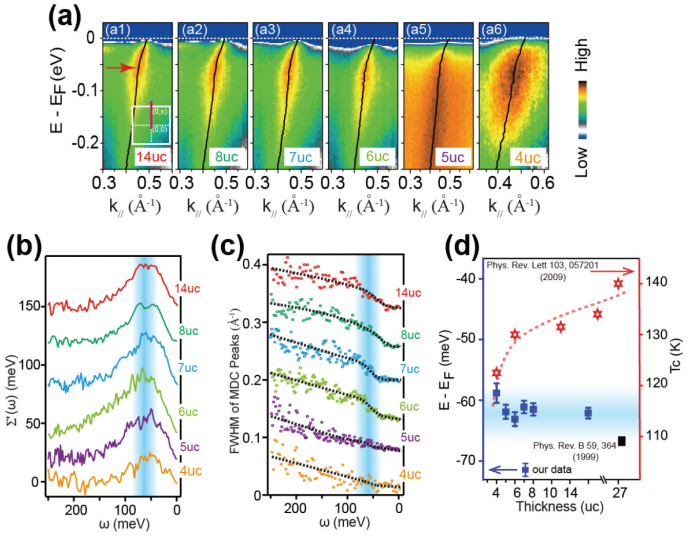

Figure 11. Electron-phonon coupling origin of the kink in the dispersion of $SrRuO_3$. (a) The evolution of the electronic structure of $SrRuO_3$ film with reducing the thickness. The kink persists in all films down to 4-UC thick. (b) and (c) Real part and imaginary part analyses of self-energies. All kinks occur at around 62 meV below E_F. (d) Electron-phonon coupling origin of the kink in $SrRuO_3$ films. Left axis: measured negligible thickness dependence of the kink energy. Right axis: reported thickness dependence of the Curie temperature. The black rectangular marker displays the energy scale of in-phase-stretching phonon mode proposed by the combined studies of Raman spectroscopy and calculation. Reproduced with permission from Ref. [35].

Perovskite $SrRuO_3$, a prototypical conductive ferromagnetic oxide, exhibits a kink in its band dispersion signalling the unusual electron dynamics therein [34]. The kink could originate from electron-magnon coupling or electron-phonon coupling. Uncovering the origin of this kink would hint on the studies of kinks' origins in many other intriguing systems [37–39] including the cuprate superconductor family [40]. Yang et al. reported the systematic thickness-dependent electronic structure studies on $SrRuO_3$ films with well-controlled thicknesses by using the OMBE and ARPES system [35]. **Figure 11(a)** shows the evolution of band dispersions of $SrRuO_3$ films with reducing the film thickness. Evidently, in all these spectra, the slope of the dispersion near E_F is markedly smaller than that of high-binding-energy region, namely

the kink persists even down to 4-UC-thick film. Empirical self energy analyses were carried out to determine the kink energy. As shown in **Figure 11(b)** and **(c)**, both real part and imaginary part analyses reveal that all films' kinks are around 62 meV below E_F. This is in sharp contrast to the report that reducing the thickness would decrease the Curie temperature [41], which implies that electron-magnon should not play a dominant role. On the other hand, the kink energy matches that of in-phase-stretching phonon mode proposed by the combined studies of Raman spectroscopy and calculation [42]. Thus, electron-phonon coupling should mainly contribute to this kink. This work can serve as an example to study the low-energy excitations of complex oxides.

Perovskite $SrIrO_3$, due to the heavy element of Ir, is expected to have strong SOC which is the key ingredient in building topological quantum materials [43, 44]. Therefore, novel topological phases were proposed in artificial $SrIrO_3$-based structures [45]. In particular, $SrIrO_3$ was proposed to be an exotic semimetal induced by the delicate interplay between SOC and electron correlations, in which a Dirac nodal ring near the *U* point would render a non-trivial topological semi-metallic state [46, 47]. Based on the OMBE-ARPES combo, Liu et al. synthesized high-quality $SrIrO_3$ films, and investigated its low-lying electronic structure [36]. **Figure 12** displays the measured band structure of $SrIrO_3$. In addition to the semimetal state (the Fermi level simultaneously crosses the hole and electron pockets), near the *U* point, a lifted Dirac node was directly observed, which agrees well with the authors' calculations. This Dirac node lifting could be due to the selectively breaking of *n*-glide symmetry in the hetero-epitaxial $SrIrO_3$ structure [36]. Iridates would continue acting as the profound platform to explore novel physics that may combine the SOC and electron correlations.

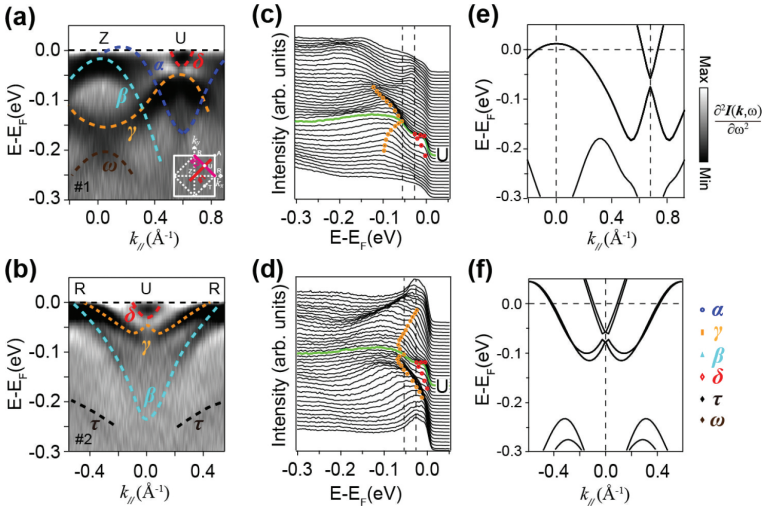

Figure 12. Dirac line node degeneracy lifting around the *U* point of $SrIO_3$. (a) and (b) The second derivative images along *Z*-*U* and *U*-*R* high-symmetry directions, respectively. (c) and (d) The corresponding energy-distribution curves for the photoemission data in (a, b). (e) and (f) The calculated band dispersions along *Z*-*U* and *U*-*R* high-symmetry directions, respectively. Reproduced with permission from Ref. [36].

http://dx.doi.org/10.5772/65711

With the powerful capability of the OMBE-ARPES combo, one can fabricate artificial superlattices which do not exist in nature and study their intriguing emergent physics. Monkman et al. reported the comprehensive investigations on the interfacial electronic structure of $(LaMnO_3)_{2n}/(SrMnO_3)_n$ superlattices as a function of dimensionality [17]. Bulk $LaMnO_3$ and $SrMnO_3$ are anti-ferromagnetic Mott and band insulators, respectively, and $La_{2/3}Sr_{1/3}MnO_3$ is a ferromagnetic metal that exhibits colossal magnetoresistance around its Curie temperature of 370 K. Monkman et al. synthesized high-quality $(LaMnO_3)_{2n}/(SrMnO_3)_n$ superlattices with $n = 1–3$. Transport studies show that $n = 1$ and $n = 2$ members show metallic behaviours at low temperatures, while the $n = 3$ member exhibits a metal-insulator crossover. **Figure 13** illustrates the evolution of the electronic structure and properties of superlattices upon different n. For $n = 1$ and 2 members, the Fermi surfaces are apparent and consist of two Mn e_g-derived states: a hole pocket around the Brillouin zone corner, and a smaller electron pocket around the zone centre. For the insulating $n = 3$ member, the spectral weight at E_F is highly suppressed, although clear states are still observed below E_F. The authors also investigated the near-E_F band dispersions. The $n = 1$ and 2 members exhibit well-defined and dispersive bands, whereas the $n = 3$ sample shows only pseudo-gapped intensity at E_F which is similar to polaronic systems with strong electron-phonon coupling. For the critical $n = 2$, there exists a dramatic difference in electronic states compared to that of $n = 1$. The states near E_F are substantially suppressed, and a broad incoherent feature appears below E_F, indicating the enhanced correlations. This work provides unique insight into how many-body interactions could be engineered at correlated oxide interfaces, which is an important prerequisite to exploiting such effects in novel electronics [17].

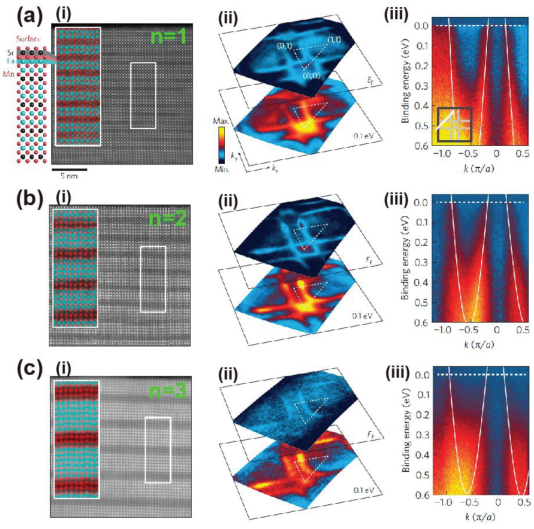

Figure 13. (a)–(c) High-angle annular dark-field scanning transmission electron micrograph (i), Fermi surface (ii) and band dispersion (iii) of $(LaMnO_3)_{2n}/(SrMnO_3)_n$ superlattices with $n = 1–3$, respectively. Reproduced with permission from Ref. [17].

These examples reflect the powerful capability of the integrated OMBE-ARPES system in studying many-body interactions and resulted novel physics in complex oxides.

5. Conclusion and outlook

In this chapter, we presented the brief inductions to OMBE technique, growth methods and the *in situ* combo integrating oxide MBE and APRES. We demonstrate that OMBE and the *in situ* combo formed with ARPES will continue playing a role in unveiling the intriguing many-body physics of correlated oxide thin films and superlattices as well as exploring novel topological materials in oxide structures.

Author details

Dawei Shen[1,2,3*], Haifeng Yang[1] and Zhengtai Liu[1]

*Address all correspondence to: dwshen@mail.sim.ac.cn

1 State Key Laboratory of Functional Materials for Informatics, Shanghai Institute of Microsystem and Information Technology (SIMIT), Chinese Academy of Sciences, Shanghai, China

2 CAS Centre for Excellence in Superconducting Electronics (CENSE), Shanghai, China

3 CAS-Shanghai Science Research Centre, Shanghai, China

References

[1] P. A. Lee, N. Nagaosa, X. -G. Wen. Doping a Mott insulator: Physics of high-temperature superconductivity. Rev. Mod. Phys. 2006; 78 (1): 17–85.

[2] M. Imada, A. Fujimori, Y. Tokura. Metal-insulator transitions. Rev. Mod. Phys. 1998; 70 (4): 1039–1263.

[3] M. B. Salamon, M. Jaime. The physics of manganites: Structure and transport. Rev. Mod. Phys. 2001; 73 (3): 583–628.

[4] H. Y. Hwang, Y. Iwasa, M. Kawasaki, B. Keimer, N. Nagaosa, Y. Tokura. Emergent phenomena at oxide interfaces. Nat. Mater. 2012; 11 (2): 103–113.

[5] J. Chakhalian, A. J. Millis, J. Rondinelli. Whither the oxide interface. Nat. Mater. 2012; 11 (2): 92–94.

[6] A. Ohtomo, H. Y. Hwang. A high-mobility electron gas at the $LaAlO_3/SrTiO_3$ heterointerface. Nature. 2004; 427 (6973): 423–426.

[7] N. Reyren, S. Thiel, A. D. Caviglia, L.F. Kourkoutis, G. Hammerl, C. Richter,C. W. Schneider, T. Kopp, A. -S. Rüetschi, D. Jaccard, M. Gabay, D.A. Muller, J. -M. Triscone, J. Mannhart. Superconducting interfaces between insulating oxides. Science. 2007; 317 (5842): 1196–1199.

[8] J. H. Lee, L. Fang, E. Vlahos, X. Ke, Y. W. Jung, L. F. Kourkoutis, J. -W. Kim, P. J. Ryan, T. Heeg, M. Roeckerath, V. Goian, M. Bernhagen, R. Uecker, P. C. Hammel, K. M. Rabe, S. Kamba, J. Schubert, J. W. Freeland, D. A. Muller, C. J. Fennie, P. Schiffer, V. Gopalan, E. Johnston-Halperin, D. G. Schlom. A strong ferroelectric ferromagnet created by means of spin-lattice coupling. Nature. 2010; 476 (7358): 954–958.

[9] H. Kroemer. Nobel Lecture: Quasielectric fields and band offsets: teaching electrons new tricks. Rev. Mod. Phys. 2001; 73 (3): 783–793.

[10] A. T. Bollinger, J. Wu, I. Bozovic. Perspective: Rapid synthesis of complex oxides by combinatorial molecular beam epitaxy. APL materials. 2016; 4 (5): 053205.

[11] D. G. Schlom, L. -Q. Chen, X. Q. Pan, A. Schmehl, M. A. Zurbuchen. A thin film approach to engineering functionality into oxides. J. Am. Ceram. Soc. 2008; 91 (8): 2429–2454.

[12] D. G. Schlom. Perspective: Oxide molecular-beam epitaxy rocks! APL materials. 2015; 3 (6): 062403.

[13] A. Damascelli, Z. Hussain, Z. -X. Shen. Angle-resolved photoemission studies of the cuprate superconductors. Rev. Mod. Phys. 2003; 75 (2): 473–541.

[14] A. Damascelli. Probing the electronic structure of complex systems by ARPES. Phys Scripta. 2004; T109: 61–74.

[15] E. J. Monkman, C. Adamo, J. A. Mundy, D. E. Shai, J. W. Harter, D. W. Shen, B. Burganov, D. A. Muller, D. G. Schlom, K. M. Shen. Quantum many-body interactions in digital oxide superlattice. Nat. Mater. 2012; 11 (10): 855–859.

[16] P. D. C. King, H. I. Wei, Y. F. Nie, M. Uchida, C. Adamo, S. Zhu, X. He, I. Bozovic, D. G. Schlom, K. M. Shen. Atomic-scale control of competing electronic phases in ultrathin $LaNiO_3$. Nat. Nanotechnol. 2014; 9 (6): 443–447.

[17] H. C. Xu, R. Peng, D. W. Shen, D. L. Feng. In situ engineering and characterization on the artificial heterostructures of correlated materials with integrated OMBE-ARPES. J. Electr. Spectr. Related Phenom. 2015; 200: 347–355.

[18] A. Y. Cho, J. R. Arthur. Molecular beam epitaxy. Prog. Solid State Chem. 1975; 10 (3): 157–191.

[19] R. A. Betts, C. W. Pitt. Growth of thin-film lithium niobate by molecular beam epitaxy. Electron. Lett. 1985; 21 (21): 960–962.

[20] B. Burganov, C. Adamo, A. Mulder, M. Uchida, P. D. C. King, J. W. Harter, D. E. Shai, A. S. Gibbs, A. P. Mackenzie, R. Uecker, M. Bruetzam, M. R. Beasley, C. J. Fennie, D. G. Schlom, K. M. Shen. Strain control of Fermiology and many-body interactions in two-dimensional Ruthenates. Phys. Rev. Lett. 2016; 116 (19): 197003.

[21] D. L. Proffit, H. W. Jang, S. Lee, C. T. Nelson, X. Q. Pan, M. S. Rzchowski, C. B. Eom. Influence of symmetry mismatch on heteroepitaxial growth of perovskite thin films. Appl. Phys. Letts. 2008; 93 (11): 111912.

[22] N. Nakagawa, H. Y. Hwang, D. A. Muller. Why some interfaces cannot be sharp. Nat. Mater. 2006; 5 (3): 204–209.

[23] J. L. Blok, X. Wan, G. Koster, D. H. A. Blank. Epitaxial oxide growth on polar (111) surfaces. Appl. Phys. Lett. 2011; 99 (15): 151917.

[24] H. F. Yang, Z. T. Liu, C. C. Fan, Q. Yao, P. Xiang, K. L. Zhang, M. Y. Li, J. S. Liu, D. W. Shen. Avoiding polar catastrophe in the growth of polarly orientated nickel perovskite thin films by reactive oxide molecular beam epitaxy. AIP Advs. 2016; 6: 085115.

[25] C. Theis, J. Yeh, D. Schlom, M. Hawley, G. Brown. Adsorption-controlled growth of $PbTiO_3$ by reactive molecular beam epitaxy. Thin Solid Films. 1998; 325 (1C2): 107–114.

[26] J. F. Ihlefeld, A. Kumar, V. Gopalan, D. G. Schlom, Y.B. Chen, X.Q. Pan, T. Heeg, J. Schubert, X. Ke, P. Schiffer, J. Orenstein, L. W. Martin, Y.H. Chu, R. Ramesh. Adsorption-controlled molecular-beam epitaxial growth of $BiFeO_3$. Appl. Phys. Lett. 2007; 91 (7): 071922.

[27] J. H. Lee, X. Ke, R. Misra, J. F. Ihlefeld, X. S. Xu, Z. G. Mei, T. Heeg, M. Roeckerath, J. Schubert, Z. K. Liu, J. L. Musfeldt, P. Schiffer, D. G. Schlom. Adsorption-controlled growth of $BiMnO_3$ by molecular-beam epitaxial. Appl. Phys. Lett. 2010; 96 (26): 262905.

[28] J. Haeni, C. Theis, D. Schlom. RHEED intensity oscillations for the stoichiometric growth of $SrTiO_3$ thin films by reactive molecular beam epitaxy. J. Electroceram. 2000; 4 (2–3): 385–391.

[29] C. M. Brooks, L. F. Kourkoutis, T. Heeg, J. Schubert, D. A. Muller, D. G. Schlom. Growth of homoepitaxial $SrTiO_3$ thin films by molecular-beam epitaxy. Appl. Phys. Lett. 2009; 94 (16): 162905.

[30] J. H. Haeni, C. D. Theis, D. G. Schlom, W. Tian, X. Q. Pan, H. Chang, I. Takeuchi, X. -D. Xiang. Epitaxial growth of the first five members of the $Sr_{n+1}Ti_nO_{3n+1}$ Ruddlesden-Popper homologous series. Appl. Phys. Lett. 2001; 78 (21): 3292–3294.

[31] W. Tian, J. H. Haeni, D. G. Schlom, E. Hutchinson, B. L. Sheu, M. M. Rosario, P. Schiffer, Y. Liu, M. A. Zurbuchen, X. Q. Pan. Epitaxial growth and magnetic properties of the first five members of the layered $Sr_{n+1}Ru_nO_{3n+1}$ oxide series. Appl. Phys. Lett. 2007; 90 (2): 022507.

[32] Y. L. Chen. Studies on the electronic structures of three-dimensional topological insulators by angle resolved photoemission spectroscopy. Front Phys-Beijing. 2012; 7 (2): 175–192.

[33] M. Y. Li, Z. T. Liu, H. F. Yang, J. L. Zhao, Q. Yao, C. C. Fan, J. S. Liu, B. Gao, D. W. Shen, X. M. Xie. Tuning the electronic structure of Sr_2IrO_4 thin films by bulk electronic doping using molecular beam epitaxy. Chin. Phys. Lett. 2015; 32 (5): 057402.

[34] D. E. Shai, C. Adamo, D. W. Shen, C. M. Brooks, J. W. Harter, E. J. Monkman, B. Burganov, D. G. Schlom, K. M. Shen. Quasiparticle mass enhancement and temperature dependence of the electronic structure of ferromagnetic $SrRuO_3$ thin films. Phys. Rev. Lett. 2013; 110 (8): 087004.

[35] H. F. Yang, Z. T. Liu, C. C. Fan, Q. Yao, P. Xiang, K. L. Zhang, M. Y. Li, H. Li, J. S. Liu, D. W. Shen, M. H. Jiang. Origin of the kink in the band dispersion of the ferromagnetic perovskite $SrRuO_3$: electron-phonon coupling. Phys. Rev. B. 2016; 93 (4): 121102(R).

[36] Z. T. Liu, M. Y. Li, Q. F. Li, J. S. Liu, W. Li, H. F. Yang, Q. Yao, C. C. Fan, X. G. Wan, Z. Wang, D. W. Shen. Direct observation of the Dirac node lifting in semimetallic perovskite $SrIrO_3$ thin films. Sci. Rep. 2016; 6: 30309.

[37] Y. Aiura, Y. Yoshida, I. Hase, S. I. Ikeda, M. Higashiguchi, X. Y. Cui, K. Shimada, H. Namatame, M. Taniguchi, H. Bando. Kink in the dispersion of layered strontium ruthenates. Phys. Rev. Lett. 2004; 93 (11): 117005.

[38] Z. Sun, Y. -D. Chuang, A. V. Fedorov, J. F. Douglas, D. Reznik, F. Weber, N. Aliouane, D. N. Argyriou, H. Zheng, J. F. Mitchell, T. Kimura, Y. Tokura, A. Revcolevschi, D. S. Dessau. Quasiparticlelike peaks, kinks, and electron-phonon coupling at the $(\pi,0)$ regions in the CMR oxide $La_{2-2x}Sr_{1+2x}Mn_2O_7$. Phys. Rev. Lett. 2006; 97 (5): 056401.

[39] S. Aizaki, T. Yoshida, K. Yoshimatsu, M. Takizawa, M. Minohara, S. Ideta, A. Fujimori, K. Gupta, P. Mahadevan, K. Horiba, H. Kumigashira, M. Oshima. Self-energy on the low- and high-energy electronic structure of correlated metal $SrVO_3$. Phys. Rev. Lett. 2012; 109 (5): 056401.

[40] A. Lanzara, P. V. Bogdanov, X. J. Zhou, S. A. Kellar, D. L. Feng, E. D. Lu, T. Yoshida, H. Eisaki, A. Fujimori, K. Kishio, J. -I. Shimoyama, T. Noda, S. Uchida, Z. Hussain, Z. -X. Shen. Evidence for ubiquitous strong electron-phonon coupling in high-temperature superconductors. Nature. 2001; 412 (6846): 510–514.

[41] Y. J. Chang, C. H. Kim, S. -H. Phark, Y. S. Kim, J. Yu, T. W. Noh. Fundamental thickness limit of itinerant ferromagnetic $SrRuO_3$ thin films. Phys. Rev. Lett. 2009; 103 (5): 057201.

[42] M. N. IIiev, A. P. Litvinchuk, H. -G. Lee, C. L. Chen, M. L. Dezaneti, C. W. Chu, V. G. Ivanov, M. V. Abrashev, V. N. Popov. Raman spectroscopy of $SrRuO_3$ near the paramagnetic-to-ferromagnetic phase transition. Phys. Rev. B. 1999; 59 (1): 364.

[43] X. L. Qi, S. C. Zhang. Topological insulators and superconductors. Rev. Mod. Phys. 2011; 83 (4): 1057–1110.

[44] Z. Hasan, C. L. Kane. Colloquium: Topological insulators. Rev. Mod. Phys. 2010; 82 (4): 3045–3067.

[45] D. Xiao, W. Zhu, Y. Ran, N. Nagaosa, S. Okamoto. Interface engineering of quantum Hall effects in digital transition-metal oxide heterostructures. Nat. Commun. 2011; 2 (6): 596.

[46] J. -M. Carter, V. V. Shankar, M. A. Zeb, H. -Y. Kee. Semimetal and topological insulator in perovskite iridates. Phys. Rev. B. 2012; 85 (11): 115105.

[47] M. A. Zeb, H. -Y. Kee. Interplay between spin-orbit coupling and Hubbard interactions in $SrIrO_3$ and related Pbnm perovskite oxides. Phys. Rev. B. 2012; 86 (86): 085149.

Chapter 5

Anomalous Rashba Effect of Bi Thin Film Studied by Spin-Resolved ARPES

Akari Takayama

Additional information is available at the end of the chapter

http://dx.doi.org/10.5772/66278

Abstract

The Rashba effect is a momentum-dependent splitting of spin bands in two-dimensional systems such as surface, interface and heterostructure. The effect is caused by broken space-inversion symmetry and spin-orbit coupling and allows to manipulate and generate the spin by the electric fields, that is, without the magnetic field. It means that the devices applied to the Rashba effect have many advantages. Bismuth is known as a promising candidate to investigate the surface Rashba effect, and the spin structure of Bi surface has also been intensively discussed. However, it is unclear to what extent the so far believed simple vortical spin structure is adequate. To understand the surface properties of the Rashba system is particularly important when utilizing the Rashba effect to the spintronic devices, since it is desirable to control the spin polarization when developing new types of devices. In this chapter, we report that the surface spin states of the Bi thin film exhibit unusual characteristics unlike the conventional Rashba splitting by using a spin- and angle-resolved photoemission spectroscopy measurement.

Keywords: Rashba effect, spin-resolved ARPES, thin film, bismuth

1. Introduction

As we know and use, spintronic devices to use a spin-polarized electrons have actualized. The magnetic storage technology uses giant magneto-resistance [1]. A more advanced approach is to control spin-polarized electrons without the aid of a ferromagnetism nor to apply the magnetic field [2]. Spin-orbit coupling (SOC) makes it possible to generate and manipulate spin-polarized electrons only by the electric field, since the electric field acts on a moving charge carrier as an effective magnetic field. Thus, it is regarded as an

essential ingredient for further development of next-generation spintronic devices such as the spin-field-effect transistor [3]. In nonmagnetic solids, the electronic states with opposite spin have the same energy (Kramers degeneracy) because of the time-reversal and the space-inversion symmetries (TRS and SIS). In the strong SOC environment with the broken space-inversion symmetry (typically at the surface or interface), the energy band splits in the momentum (k) space (Rashba effect [4]), leading to a spin helical structure of surface bands. This Rashba effect leads to the vortical spin structure of surface bands where the spin vector points parallel to the surface and perpendicular to the measured momentum. To be more specific, here we postulate the model of two-dimensional free electron gas at the surface. In the surface, as shown in **Figure 1a**, there is asymmetry of the potential in the direction perpendicular to the two-dimensional plane [$\nabla V = (0, 0, E_z)$]. When an electron moves with momentum (p), the $\nabla V \times p$ term acts as an effective magnetic field B_{eff}, which is orthogonal to p (=$\hbar k$) and ∇V. As a result, the electron spin is quantized along the direction perpendicular to k in the surface plane. The energy of free electron gives the following,

$$E(k) = \frac{\hbar^2}{2m} k^2 \pm \alpha_R k \tag{1}$$

which is well known as the Rashba effect, where α_R is a so-called Rashba parameter. **Figure 1b** shows the band dispersion of this model. As described above, two-dimensional (2D) system with strong SOC has provided a useful platform for realizing novel quantum phenomena

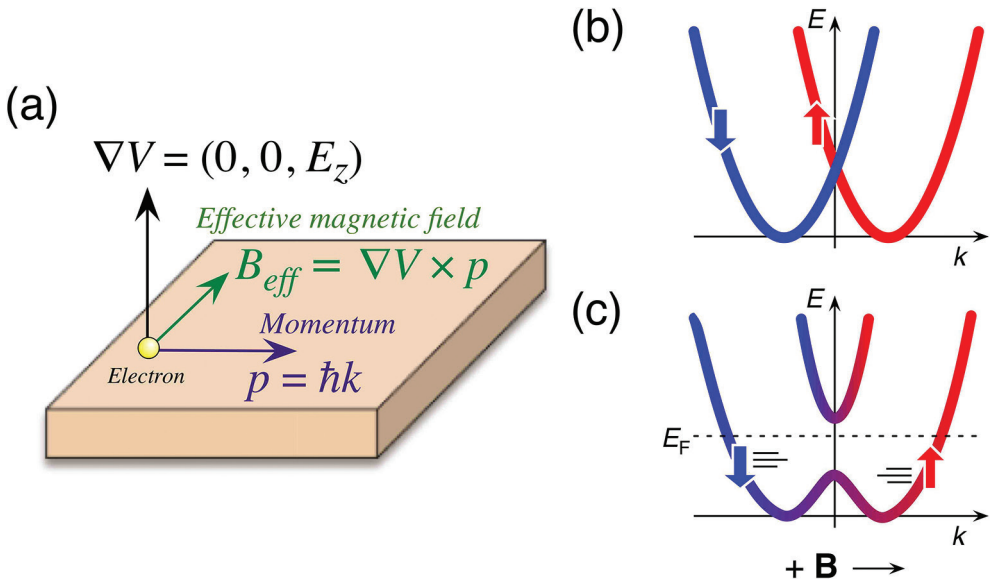

Figure 1. (a) Relationship between momentum (p) and surface potential (∇V) at surface. (b) Rashba-type spin-splitting band structure in 2D free electron gas model. (c) A band structure breaking the time-reversal symmetry by applying a magnetic field.

http://dx.doi.org/10.5772/66278

applicable to advanced spintronic devices [2, 5, 6]. To discuss and understand Rashba effect, spin- and angle-resolved photoemission spectroscopy (spin-resolved ARPES) is a powerful experimental technique, which can simultaneously determine all key quantum parameters of electrons in solids, that is, momentum, energy and spin. Furthermore, by high-resolution measurements, we will be able to discuss the spin-related physical phenomena not only qualitatively but also quantitatively, which would certainly lead to the deeper understanding of the condensed matter physics. Elucidation of the electron spin is very important to understand physical property in solid state and its surface as well as the possible applications to spintronic devices.

The first observation of the surface Rashba effect by ARPES is the Au(1 1 1) surface [7]. After that, various materials such as group-V semimetals and their alloy surfaces [8–16], as well as heavy-atom adsorbed semiconductor surfaces [17–22] and so on, are studied. Among them, the group-V semimetal bismuth (Bi) is a prime candidate to investigate the surface Rashba effect and many experiments and theoretical calculations studied in order to clarify the fundamental properties of the Rashba effect [8, 10–14]. However, in previous researches, although the band structure and Fermi surfaces of Bi distinctly show strong anisotropy, the spin structure of Bi was argued by assuming an isotropic two-circular Fermi-surface model like Au(1 1 1) [7, 20–22]. The reason is because the energy and momentum resolutions of the previous spin-resolved ARPES machine are insufficient. To understand whole aspect of the Rashba effect, it is necessary to clarify that the spin structure of Bi consists with the conventional Rashba model or not. Moreover, in the film, electronic states originating from the bulk Bi are quantized, and they are connected to the surface bands continuously. So it would be necessary to take into account the relationship between bulk and surface states. On the other hand, intensive attempts have been made to extend the investigations on 2D Rashba systems to quasi one-dimensional (1D) system like artificially grown nanowires and quantum wires, because of the merits in downsizing of devices.1D Rashba effect in utilization of vicinal surfaces such as in Au chains on vicinal Si [23] and the vicinal Bi surface is also reported [24]. In such a case, breaking the TRS by applying magnetic field or adding magnetic impurities would create an energy gap at the Kramers point, and when the chemical potential is tuned to be located in the spin-orbit gap, the dissipation-less spin transport and the quantized conductance [25, 26] may be realized (**Figure 1c**). However, the Rashba effect in edge state is not known because the signal from the edge is extremely faint. To understand the proposed novel properties of a true 1D system, we may be able to apply them to advanced spintronic devices.

In this chapter, we introduce the electronic structure of Bi thin film to elucidate the details of the Rashba effect by utilizing the high-resolution spin-resolved ARPES spectrometer equipped with a highly efficient mini-Mott detector. We show three novel Rashba effects of Bi thin film: (i) anisotropic Rashba effect from momentum-dependent measurement [27], (ii) the interface Rashba effect between metal-semiconductor from thickness-dependent [28] and (iii) 1D Rashba effect of edge state [29]. The present finding provides a useful platform to study the Rashba effect and at the same time opens a pathway to utilize the novel properties to advanced spintronic devices.

2. Experimental technique and sample fabrication

2.1. Spin- and angle-resolved photoemission spectromete

Figure 2 shows a schematic diagram of the ultra-high-resolution spin-resolved ARPES spectrometer with a highly efficient mini-Mott detector [30]. This spectrometer consists of mainly four parts: (i) a photoemission measurement system including a hemispherical electron energy analyzer and an ultra-high-vacuum measurement chamber, (ii) a spin-detection system based on a mini-Mott detector, (iii) an intense xenon/helium plasma discharge lamp and (iv) a surface chamber to prepare the thin-film samples. We explain the detail of each part. We have improved a MBS-A1 electron energy analyzer to achieve both spin-resolved and regular (non-spin-resolved) ARPES measurement. The spectrometer has two detectors: one is a multichannel plate for ARPES measurement, and the other is mini-Mott detector for spin-resolved ARPES. To determine the three-dimensional spin polarization, an electron deflector has been placed between the analyzer and the Mott detector. The Mott detector observes the spin polarization of essentially two independent axes by using four channeltrons, enabling us to determine the in-plane and out-of-plane spin component. The scattering efficiency of the Mott detector is as high as 2.3×10^{-2}. The optical system consists of helium (He) and xenon (Xe) plasma discharge lamps and a monochromator with the gratings, in which we can select

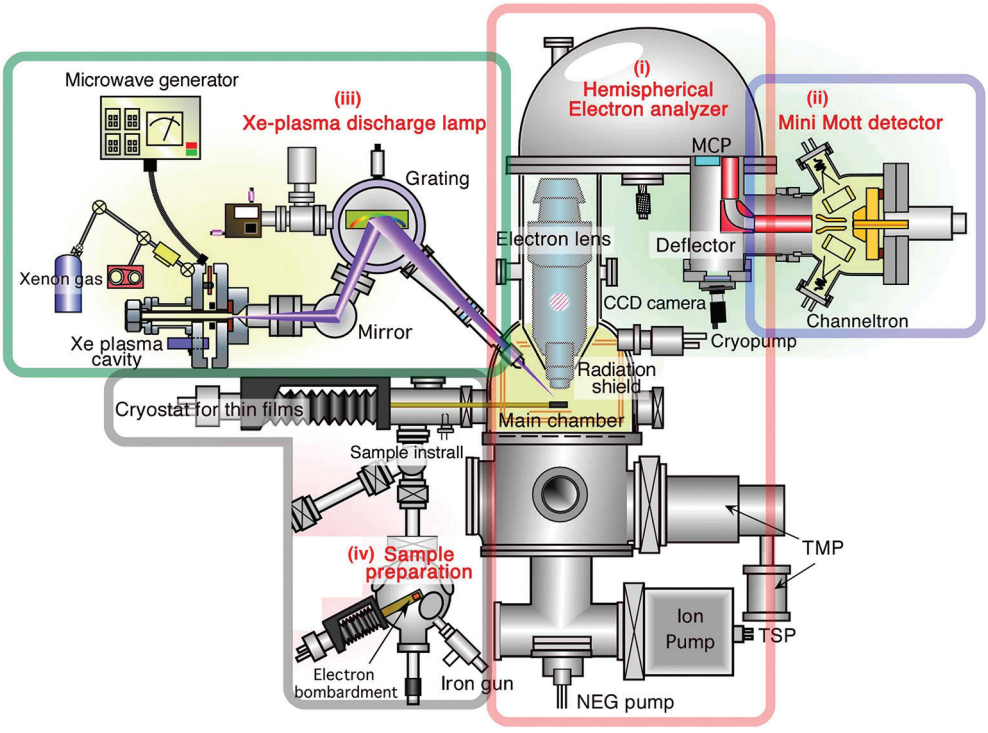

Figure 2. Schematic view of high-resolution spin-resolved photoemission spectrometer.

http://dx.doi.org/10.5772/66278

photon energy if necessary. In this study, we used one of the Xe I lines ($h\nu = 8.437$ eV) to excite photoelectrons. In order to fabricate high-quality samples, a surface chamber has been constructed and is connected to the spin-resolved ARPRS spectrometer. The spectrometer achieves the energy resolutions of 0.9 and 8 meV for non–spin-resolved and spin-resolved modes, respectively. **Figure 3** shows a schematic view of the surface chamber. A surface chamber contains heating systems for a semiconductor sample, a few kinds of dispensers, a quartz crystal microbalance and a low-energy electron diffraction (LEED) system for checking the quality of the sample surface. The vacuum of the surface chamber is basically kept 1×10^{-10} Torr to prepare a high-quality sample surface. It allows the in situ preparation of the sample and its transfer to the spin-resolved spectrometer. It is particularly useful for elucidating the electronic states of the samples containing a clean well-ordered surfaces required for the accurate ARPES measurements. Thus, we can prepare the Bi thin-film samples by the evaporation of Bi on semiconducting substrate. We expect that the performance of the spectrometer is demonstrated by the observation of a clear Rashba splitting of the surface states in Bi. The energy and momentum resolutions for the regular (spin-integrated) ARPES were 5–20 meV and 0.3°, and for spin-resolved ARPES measurements were 40 meV and 3°, respectively. The Sherman function value was set at 0.07. The measurement temperature was 300 and 30 K.

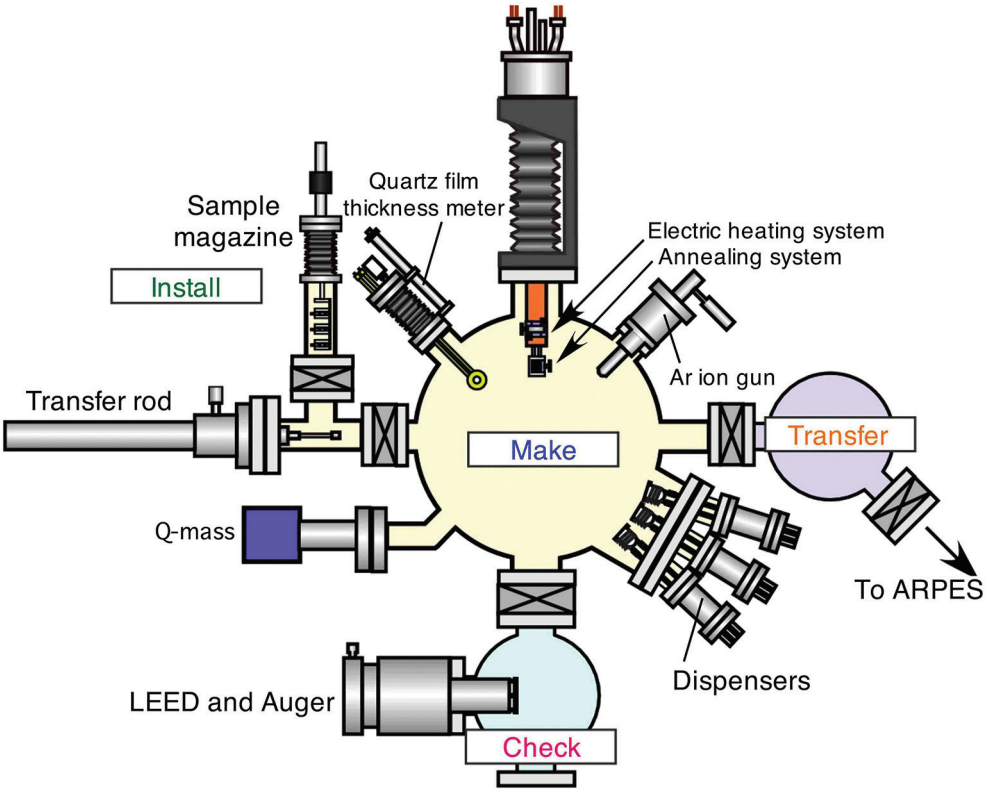

Figure 3. Schematic view of the sample preparation chamber.

2.2. Sample fabrication

To get a high-quality Bi(1 1 1) thin film, we prepare a clean surface of the Si(1 1 1) substrate. We use a commercially available Si wafer (n-type, As-doped: 0.001–0.005 Ω cm, Sb-doped: 0.01–0.02 Ω cm), and the surface of Si forms native SiO_2 in the air. So we must remove it by electrical heating in high vacuum. **Figure 4** displays the design of a holder for the electrical heating system (**Figure 4**). The holder is made of molybdenum, and a main holder is insulated from a subholder by the alumina. We can control a current and temperature with 5 mA and 1°C, respectively. The sample size is 13 × 3 mm, and we have selected four different kinds of crystal orientations on the basis of orientation flat as shown in **Figure 5**. The sample geometry has been confirmed by the brightness symmetry of the LEED spots. The most stable structure of the Si(1 1 1) surface is the 7 × 7 reconstructed surface, as shown in **Figure 6a** [31, 32]. Now, we describe the method to pre-

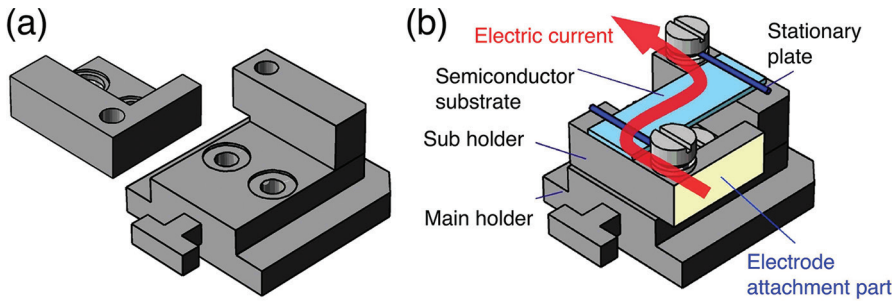

Figure 4. (a) A main and subparts of sample holder. (b) A constructed holder.

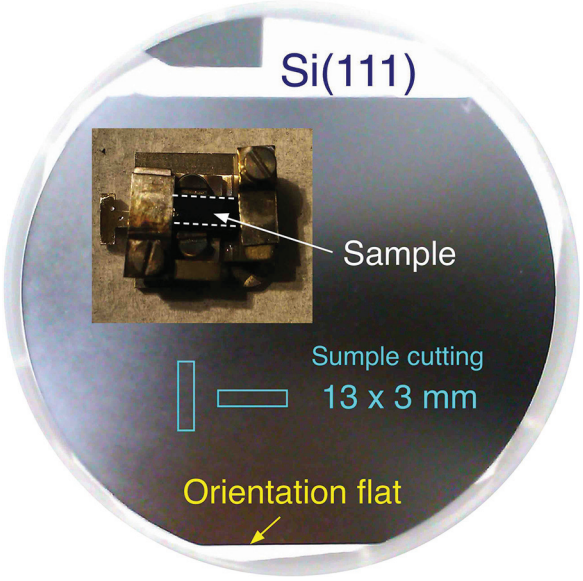

Figure 5. Cutting the sample from the Si(1 1 1) wafer. Inset shows the picture of a sample holder compared to the sample size. The geometry of the sample was determined by the direction of "orientation flat."

http://dx.doi.org/10.5772/66278

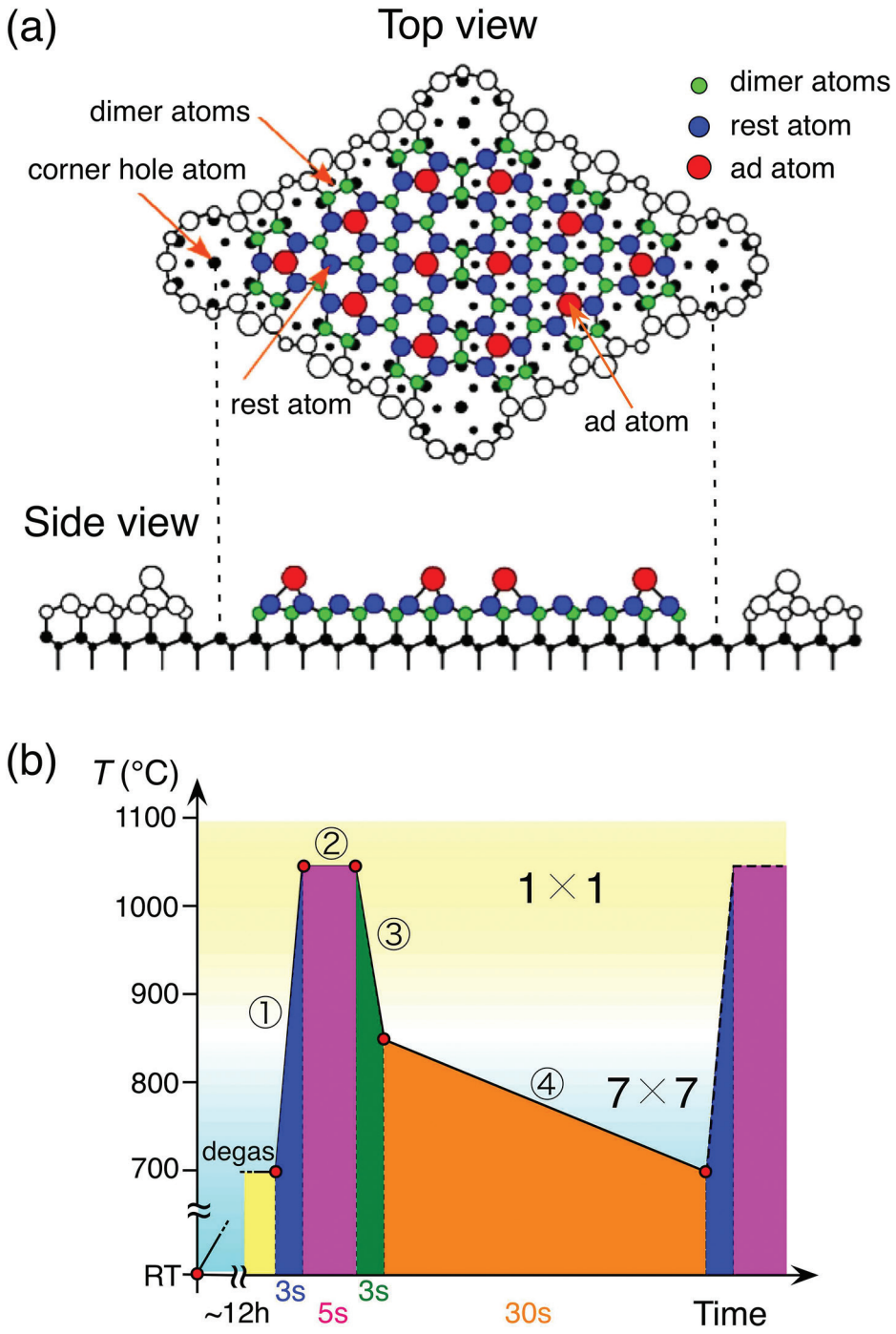

Figure 6. (a) Atomic-structure model (Das model) of Si(1 1 1)-7 × 7. (b) Detailed annealing process to prepare the Si(1 1 1)-7 × 7 clean surface.

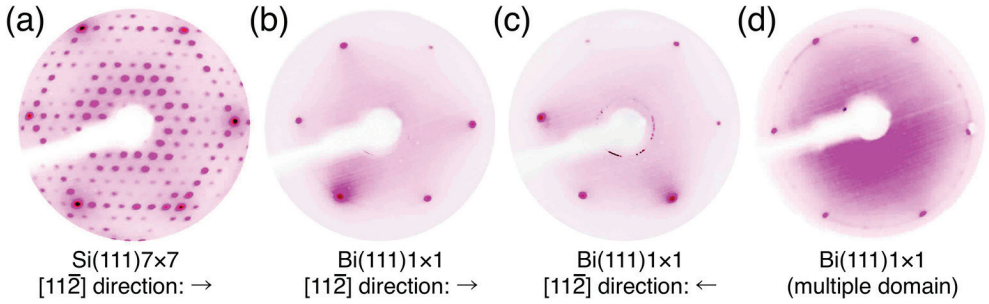

Figure 7. Comparison of the LEED pattern. (a) Si(1 1 1)-7 × 7. (b) and (c) Bi(1 1 1)-1 × 1. These two samples have a different cutting directions from Si wafer [sample direction in (c) is rotated in 180° from (b)]. (d) A multiple-domain sample of Bi(1 1 1)-1 × 1.

pare a Si(1 1 1)-7 × 7 reconstructed surface. First, the Si wafers were outgassed for more than 12 h below 750°C. After the outgassing enough, we have carried out flash annealing. **Figure 6b** shows a flash-annealing process to get a Si(1 11)-7 × 7 reconstructed surface; sample was (i) heated at 750°C to 1050–1200°C for a few seconds, (ii) keep temperature to maximum for 5 s, (iii) cooled down to 850°C for a few seconds and (iv) cooled to 750°C in 30 s [33]. We have repeated this cycle, and all of the above processes should be performed under the ultra-high vacuum of ~1×10^{-10} Torr. As shown in **Figure 7a**, we have obtained the LEED pattern of the well-ordered 7 × 7 surface.

Next, Bi atoms are evaporated on Si substrate, which is called as a molecular beam epitaxy (MBE). Bi atoms are deposited at room temperature on Si(1 1 1)-7 × 7 reconstructed surface. Then, the Bi thin film was annealed at 150°C. The deposition rate is estimated by the quartz oscillator thickness monitor, and the film thickness was controlled by varying the deposition time with keeping the constant deposition rate. We can also estimate the film thickness from the energy position of the quantum well states (QWSs) in the ARPES spectra [28]. It is noted that 1 bilayer (BL) Bi is defined as 1.14×10^{15} atoms/cm^2, and the thickness is 0.39 nm [13]. In this study, we prepared several thickness sample (8–40 BL). After the deposition of Bi atoms, the LEED pattern shows the 1 × 1 surface structure as shown in **Figure 7b** and **c**, and the intensity of the LEED spot has threefold symmetry. When the sample has a multi-domain structure, the LEED pattern shows circular features surrounding the 1 × 1 spots (**Figure 7d**). We could repeatedly use one Si substrate by a flashing. Here we describe a structure of Bi thin film on Si substrate. Details of the thin-film growth process are shown in **Figure 8a**, which is reported in previous works such as STM and LEED [34]. Although the lattice constant of Bi (4.538 Å) is very different from Si (5.43 Å), it is possible to fabricate the Bi/Si thin film due to the existence of disordered layer called "wetting layer" between Bi and Si substrate. As shown in **Figure 8b**, the structural transition from {0 1 2} direction to (1 1 1) direction more than 8.4 ML suddenly takes place upon Bi deposition.

http://dx.doi.org/10.5772/66278

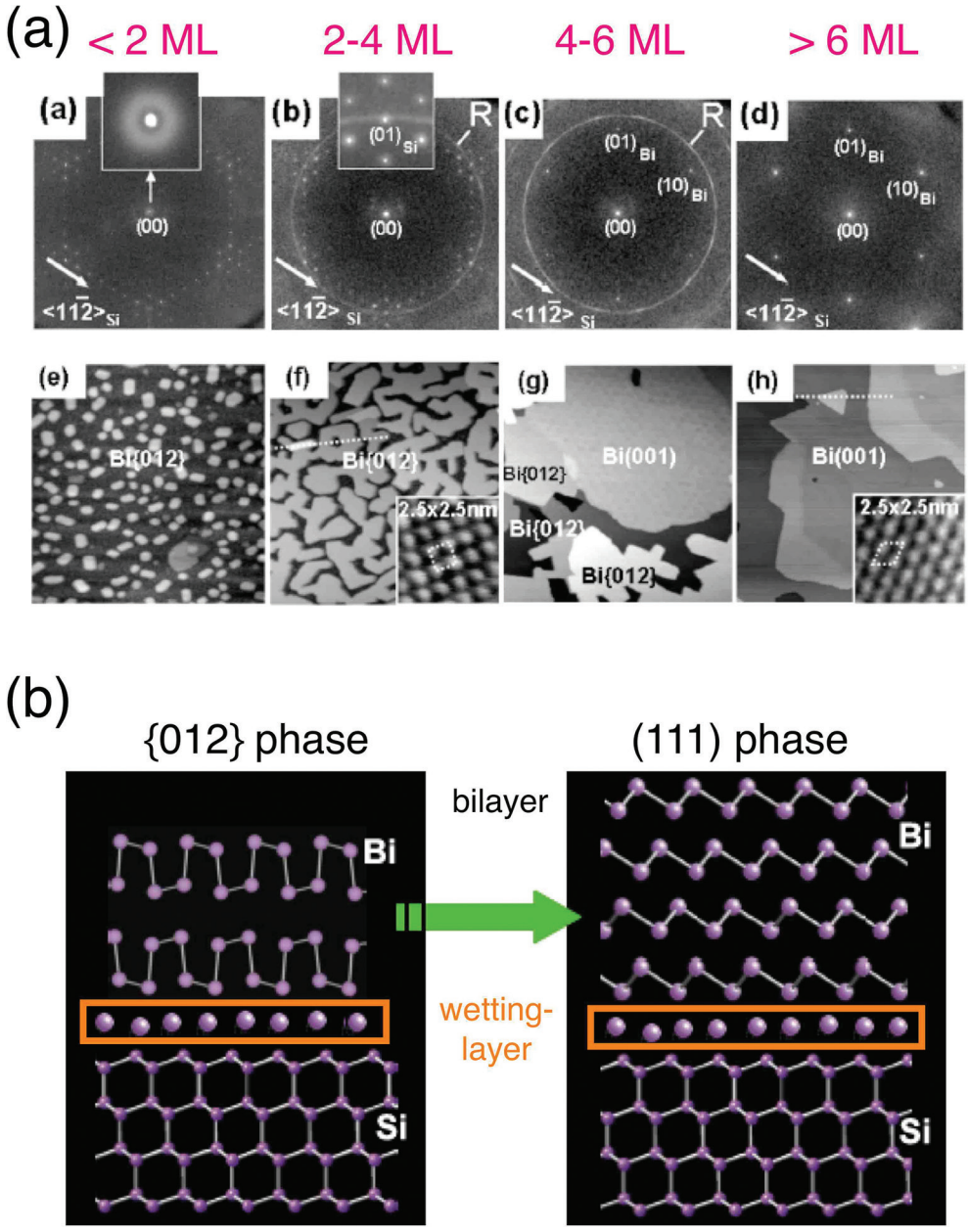

Figure 8. (a) Thickness dependence of spot-profile-analyzing-LEED pattern (top) and STM image (bottom) [34]. (b) Schematic illustration of the transformed structure in growth process of Bi thin film [34].

3. Results and discussion

3.1. Anisotropic Rashba effect of Bi thin film

At first, we have performed normal (non–spin-resolved) ARPES measurement of the Bi thin film in order to check the sample quality and geometry, since even a subtle misalignment of the sample orientation would cause a significant error in determining the spin polarization. **Figure 9a** and **b** shows the band dispersion along the $\bar{\Gamma}\,\overline{\mathrm{M}}$ line and Fermi surface of Bi/Si(1 1 1). Areas with hatched lines in **Figure 9a** are bulk band projection. We distinctly see that several bands cross E_F and three kinds Fermi surfaces exist; a hexagonal Fermi surface centered at the $\bar{\Gamma}$ point (S_1), surrounding elongated pockets (S_2) and the ellipsoidal pocket (S_3) near the $\overline{\mathrm{M}}$ point. Judged from the band dispersion in **Figure 9a**, the S_1 and S_3 are attributed to the electron pockets, while the S_2 to a hole pocket, all of which arise from the spin-split surface states [8, 10–14].

This section focuses on the spin structure of the S_2 band. In a conventional 2D Rashba model, the in-plane spin has a vortical structure and isotropic magnitude as denoted by black arrows in **Figure 10a**. In **Figure 10b** and **e**, we display the near-E_F spin-resolved energy distribution curves (EDCs) for the in-plane (y/x) and out-of-plane (z) spin components measured in various k regions, A–J as shown in **Figure 10a**. As displayed in **Figure 10b** and **e**, the spin-resolved

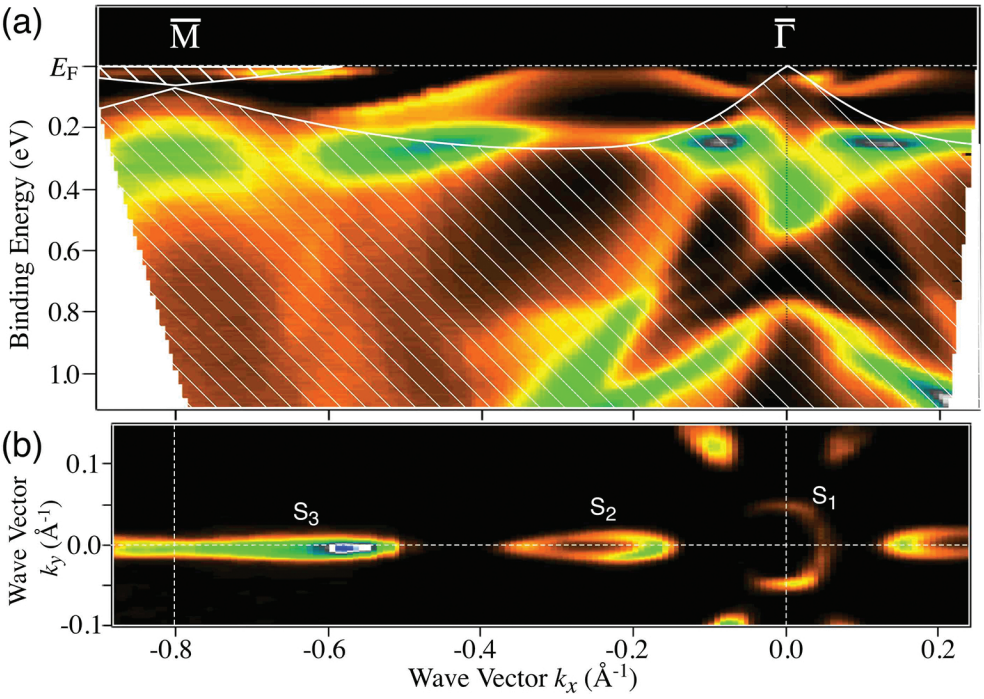

Figure 9. (a) Band dispersion of the ARPES spectra of Bi/Si(1 1 1) along the $\bar{\Gamma}\overline{\mathrm{M}}$ line at $T = 30$ K. Shaded areas indicate the bulk band projection. (b) 2D ARPES intensity plot at E_F as a function of kx and ky around the $\bar{\Gamma}\,\overline{\mathrm{M}}$ line.

http://dx.doi.org/10.5772/66278

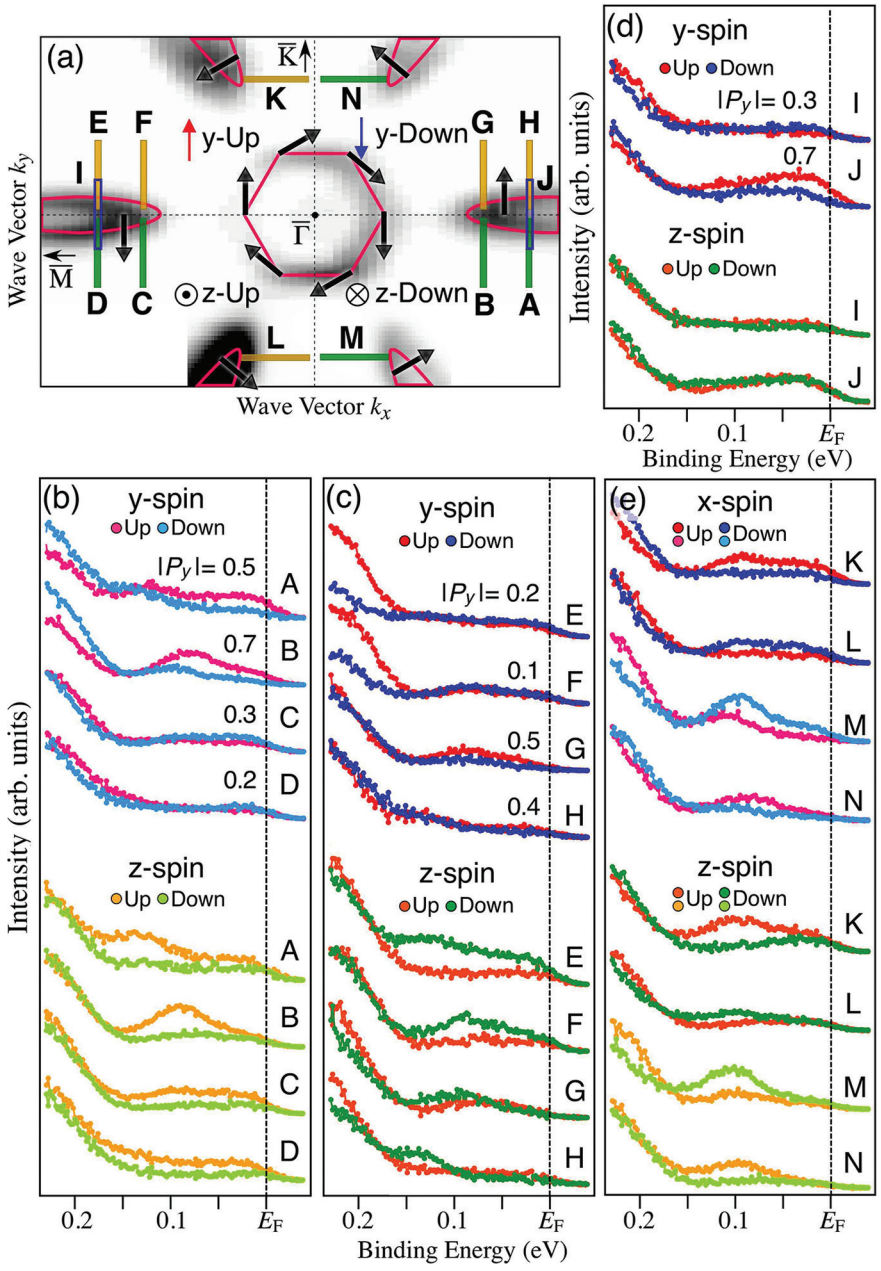

Figure 10. (a) Fermi surface of Bi/Si(1 1 1) around the $\bar{\Gamma}$ point. Red lines are guides for the Fermi surface of the surface bands. Lines A–N represent the *k* region where the spin-resolved EDCs in (b) and (e) were obtained. Expected spin configuration from the normal Rashba spin-obit coupling is indicated by black arrows. Spin-resolved EDCs in regions (b) A–D, (c) E–H, (d) I, J and (e) K–N, respectively.

EDC mainly consists of two components: a slope-like feature, which rapidly increases its intensity at the binding energy (E_B) higher than 0.15 eV corresponding to the tail of the QWS, and a weaker broad feature at E_F-0.1 eV assigned as the S_2 band.

First, we take a closer look at the spin polarization in regions A–D. In regions A and B, as seen in **Figure 10b**, the in-plane spin polarization of the S_2 band is dominated by the up spin. On the other hand, the down spin is barely superior in regions C and D. It means that the in-plane spin structure is qualitatively consistent with the Rashba picture [13–14]. However, it seems that the spin polarization is markedly suppressed in C and D. In fact, the magnitude of the spin polarization along the *y* direction $|P_y|$ is 0.5–0.7 in regions A and B, while it is 0.2–0.3 in regions C and D. This is unexpected since $|P_y|$ should keep the same value across the $\bar{\Gamma}$ point in the normal Rashba picture. Then, we focus on the out-of-plane (*z*) spin component. We immediately notice that there exists a sizable up-spin polarization, while theoretically predicted out-of-plane spin polarization for simple isotropic Rashba system is zero. More surprisingly, the magnitude of the z-axis spin polarization $|P_z|$ (0.4–0.7) is as large as that of $|P_y|$.

We have also observed a finite in-plane and out-of-plane spin polarization in regions E–H. As shown in **Figure 10c**, the estimated maximum $|P_y|$ of the S_2 band in regions E and F (0.1–0.2) is much smaller than that in regions G and H (0.4–0.5), and it is similar to the result of regions A–D. But then, the down-spin component dominates for out-of-plane spin polarization in regions E–H. This result suggests that P_z has opposite spin direction across the $\bar{\Gamma}\,\overline{M}$ line: the up-spin component is superior in the negative k_y (regions A–D), while the down-spin component is superior in the positive k_y (regions E–H).

The data in regions I and J are also the same trend as shown in **Figure 10d**. The difference in $|P_y|$ across the $\bar{\Gamma}$ point is also recognized by comparing the EDCs between regions I and J. In addition, the value of $|P_z|$(~zero) is a good agreement in regions I and J where the up- and down-spin components almost overlap with each other because of the cancellation of two opposite spins. To see if a similar trend is observed along another high-symmetry line $\bar{\Gamma}\,\overline{K}$, we demonstrate in **Figure 10e** the spin-resolved EDCs measured in regions K–N. It is apparent that the sign of P_z (also P_x) in region K (L) is the same as that in the region N (M), indicating that P_z (P_x) does not switch the sign across the $\bar{\Gamma}\,\overline{K}$ line.

Figure 11 shows a schematical view of the spin polarization vectors of the S_2 band from **Figure 10**. We symmetrized the data by taking into account the threefold crystal symmetry due to the presence of a second bismuth layer. The in-plane spin component has a vortical structure, but the magnitude of the spin polarization is perpendicular to *k*, called here P_θ. P_z has a large component and switches the sign by every 60° step. These features would lead to the periodic oscillation of P_θ and P_z, unlike the general Rashba SOC where P_θ = const and $P_z = 0$. Now, we discuss the origin of anomalous Rashba effect of Bi thin film. In the conventional Rashba effect, the in-plane spin polarization of S_2 is symmetry with respect to the $\bar{\Gamma}$ point. In this study, the TRS is not broken by some magnetic impurities because the Bi and Si are nonmagnetic materials. Another possibility of causing the broken TRS is the local surface conditions or the final-state effect [35, 36]. However, this possibility might be also unlikely by the reproducibility of data and comparing with previous studies. Here it is noted that the LEED pattern of Bi/Si(1 1 1) in **Figure 7** shows the threefold symmetry due to the bilayer-Bi

http://dx.doi.org/10.5772/66278

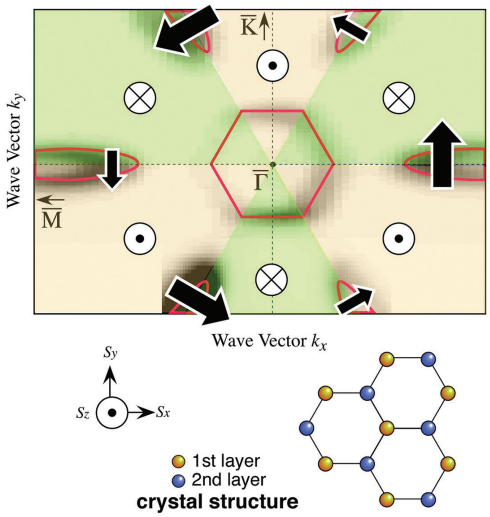

Figure 11. Schematic view of the spin structure of the S_2 hole pocket in Bi/Si(1 1 1). Size of arrows roughly scales with the observed spin polarization. Data are folded by taking into account the threefold symmetric variation of the bilayer-crystal structure.

crystal structure, and we conjecture that the origin of the in-plane spin asymmetry would be related to the crystal symmetry at present. Next, we discuss the out-of-plane spin polarization. Unlike in-plane spin polarization, the threefold symmetry in the out-of-plane spin component is reported, and sign-switching behavior is in good agreement with the previous studies in Bi/Ag(1 1 1) and $Bi_{1-x}Sb_x$ [15, 37]. The spin structure of Bi surface state is also similar to the spin-resolved ARPES experiments on the hexagonally warped Dirac-cone Fermi surface of the topological insulator as well as the prediction of the $k\hat{A}\cdot p$ theory [38, 39]. On the other hand, the absolute value of the out-of-plane spin polarization obtained by our experiment is 40–70%, while the theoretical value of previous studies is a few percent. In order to clarify the spin structure of Bi Rashba effect, we need to evolve theoretical and experimental studies.

3.2. Rashba effect at interface of a Bi Thin film on Si(1 1 1)

In this section, we focus on the spin structure around the $\overline{M}$ point of the Bi/Si(1 1 1) thin film. As shown in **Figure 12a**, the band dispersion of the QWSs dramatically alters around the $\overline{M}$ point as a function of the film thickness d, and we prepared five different thickness film for $d = 8$, 10, 15, 20 and 40 BL. All of the samples, the bottom energy of an electron-like dispersion is located at ~30 meV below E_F. This band is well separated from the hole-like band at higher E_B arising from the QWSs that originate from the confinement of the wave function in the direction perpendicular to the surface (z direction). There is no evidence for the Kramers degeneracy of the S_3 band or the QWSs at the $\overline{M}$ point ($k_y = 0$). The absence of the Kramers degeneracy at the $\overline{M}$ point has also been observed in the previous research of the Bi, and it is explained by the

hybridization of the surface states and the QWS [9, 12]. As clearly visible, we identify the QWSs at $E_B = 0.1–0.25$ eV for $d = 40$ BL. Upon decreasing d, the top of the highest QWS shifts downward, and the energy separation of each QWS becomes wider, enabling us to unambiguously identify the overall energy dispersion of the individual QWS in the band dispersion plots.

In conventional Rashba picture, the in-plane spin polarization of the S_3 band is dominated by the up spin independently of a thickness at the cut 1 shown in **Figure 12b**. **Figure 12c** shows the spin-resolved EDCs and spin polarization of P_y for various d values of 8–40 BL. All of the spin-resolved EDCs consist of the tail of the QWSs at $E_B > 0.1$ eV and the S_3 electron band at ~50 meV. As seen in **Figure 12c**, the in-plane spin-resolved EDCs of the S_3 band for 10–40 BL are dominated by the up spin, and this indicates that the in-plane spin direction is qualitatively consistent with the normal Rashba picture. However, our result clearly demonstrates that the observed P_y value strongly depends on d. The obtained P_y value at $d = 40$ BL has a maximum at ~0.7, then gradually reduces at $d = 15$ BL (P_y ~0.3) and finally reaches ~0 at $d = 8$ BL. It is noted that the much smaller spin polarization in the above-E_F region for $d = 15$ BL as compared to that for $d = 40$ BL might be due to much weaker peak weight in the original EDC and an intrinsic suppression of the spin polarization, which would lead to a relative enhancement of the background weight and less statistical reliability of the states above E_F.

We discuss the physical mechanism behind the unusual thickness dependence of P. The coupling between the Bi film and the Si(1 1 1) substrate is fairly weak due to the presence of a disordered wetting layer at the interface, suggesting that the Bi film is nearly freestanding [34]. Namely, the Bi/Si interface is also broken SIS, and it can be thought of as another (bottom) surface as with vacuum-side (top) surface. These Rashba states of top and bottom surface should have opposite spin directions as illustrated in **Figure 13**. In case of bulk Bi, which is thick enough, the top and bottom Rashba states do not interfere with each other. On reducing

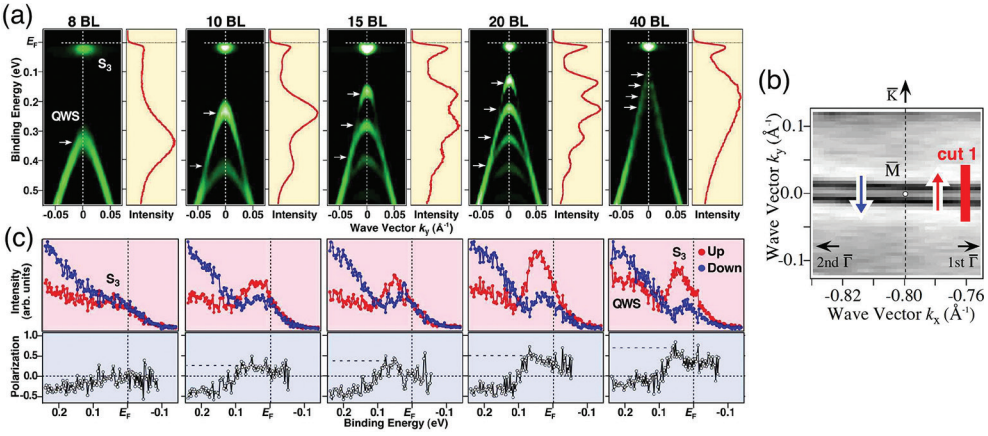

Figure 12. (a) Thickness dependence of the band dispersion near E_F along the $\overline{KM}$ $\overline{K}$ line, obtained by taking the second derivative of the EDCs at 30 K. EDC at the $\overline{M}$ point is also shown for each thickness. (b) The Fermi surface around the $\overline{M}$ point. Blue and red arrows indicate expected spin configuration of the normal Rashba effect. (c) Corresponding spin-resolved EDCs and their spin polarizations for cut 1 in (b).

http://dx.doi.org/10.5772/66278

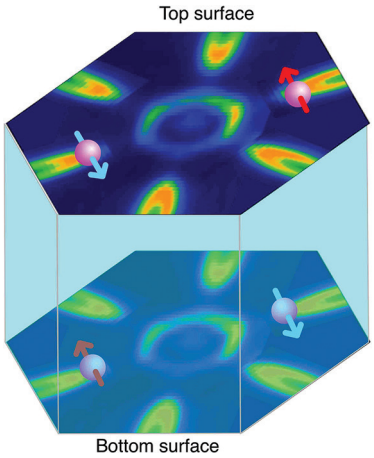

Figure 13. Schematic view of the spin vectors for the Fermi surface at the top and bottom surfaces.

thickness, the wave functions of the two Rashba states overlap and hybridize, which means that the up- and down-spin states merge and the *P* observed by spin-resolved ARPES would become small. This picture is a very simple model but explains in a nice way the thickness dependence of *P*. We also found that the decay length of the surface-state wave function is around at least 20 BL (~80 Å) since the reduction in experimental *P* is already started in 20 BL (**Figure 12**). A thin film of Bi_2Se_3 topological insulator also exhibits a similar decay length, as inferred from the experimental fact that the hybridization gap starts to open at six quintuple layers (~60 Å) [40]. Our result also suggests that the Rashba effect of Bi/Si interface is useful for the spintronic devices because the interface is generally more stable than the surface.

3.3. 1D edge state with Rashba effect in Bi thin film

As observed by the atomic force microscopy of our Bi thin film (**Figure 14**), triangular-shaped Bi BL islands with typically ~0.1 μm edge length are formed on the top surface of the Bi thin film as reported previously [34], and the edge of each island is perpendicular to the $\bar{\Gamma}\,\overline{M}$ direction considering sample geometry; namely, the edge runs along the $\bar{\Gamma}\overline{K}$ direction in the *k* space. According to previous experimental and theoretical studies, there are no bulk and surface states near the $\overline{K}$ point, and we might observe some electronic state if edge state exists along the $\bar{\Gamma}\overline{K}$ line.

We demonstrate the band dispersion of Bi thin film along the $\bar{\Gamma}\overline{K}$ line for $d = 15$ BL in **Figure 15**. With a careful look at the region between $\bar{\Gamma}\overline{K}$ line (yellow rectangle in **Figure 15a**), one finds unexpected faint intensity displaying a finite energy dispersion, as better illustrated with enhanced color contrast in the inset. To establish the energy dispersion of this unexpected feature, we have measured the ARPES data along several cuts in the surface Brillouin zone (**Figure 15b**). A careful band searching with the enhanced intensity scale (**Figure 15c**) shows the band dispersion with a characteristic *x*-shape along cuts 1–3. The intersection of

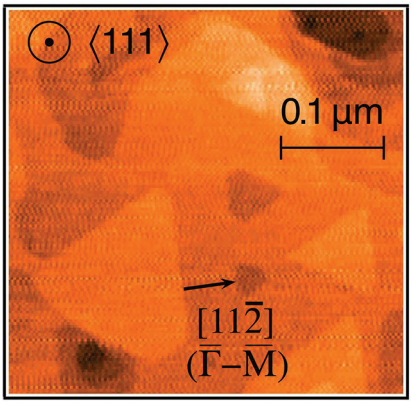

Figure 14. The atomic force microscopy image of a Bi thin film (d = 15 BL) at T = 300 K.

the x-shaped band is at $k_y \sim 0.7$ Å^{-1} not at the high-symmetry points of the surface and bulk Brillouin zone. Intriguingly, this band is robust against the change in the k_x location of cut (cuts 1–3). This demonstrates that the x-shaped dispersion has a 1D character along the k_y direction. Indeed, the observed band structure along cut 4 (perpendicular to cuts 1–3) shows no obvious dispersion, confirming the 1D nature. To experimentally clarify the spin-split nature of the edge band, we have performed a spin-resolved ARPES experiment. As shown in **Figure 15d** which plots the spin-resolved EDCs at a representative k_y point (marked by a pink line in **Figure 15c**), we clearly find a difference between the up- and down-spin spectra in both the in-plane and out-of-plane components.

As for the origin of the unexpected 1D state, we have taken into account various possibilities such as the mixture of domains with different film thickness, surface reconstruction, slight isolation of the topmost Bi bilayer and surface stacking faults. A most natural and convincing explanation is that it originates from the edge states of Bi bilayer. To further strengthen our conclusion, we have carried out first-principles electronic band structure calculations for a specific crystal structure (**Figure 16**). Electronic band structure calculations were carried out by means of a first-principles density functional theory approach with the all-electron full-potential linearized augmented-plane-wave method in the scalar relativistic scheme. The spin-orbit coupling was included as the second variation in the self-consistent-field iterations. Thin-film systems were simulated by adopting periodic slab models with sufficiently thick vacuum layer. In this model, Bi atoms in 1D allay are removed from the topmost Bi 1BL (**Figure 16a**) so as to reproduce the infinitely long edge structure along the y direction. Assumption of such an idealized model crystal is turned out to be sufficient for reasonably simulating the edge band structure. As shown in **Figure 16c**, the Brillouin zone for this model crystal structure has a rectangular shape. The vertical length of Brillouin zone is the same as the $\bar{\text{M}}\,\bar{\text{M}}$ interval since the size of unit cell along y-axis is the same for the edge structure and the Bi thin film. On the other hand, the horizontal Brillouin zone length has no important physical role because the unit-cell length for x-axis was simply chosen for the sake of calculations. Thus,

http://dx.doi.org/10.5772/66278

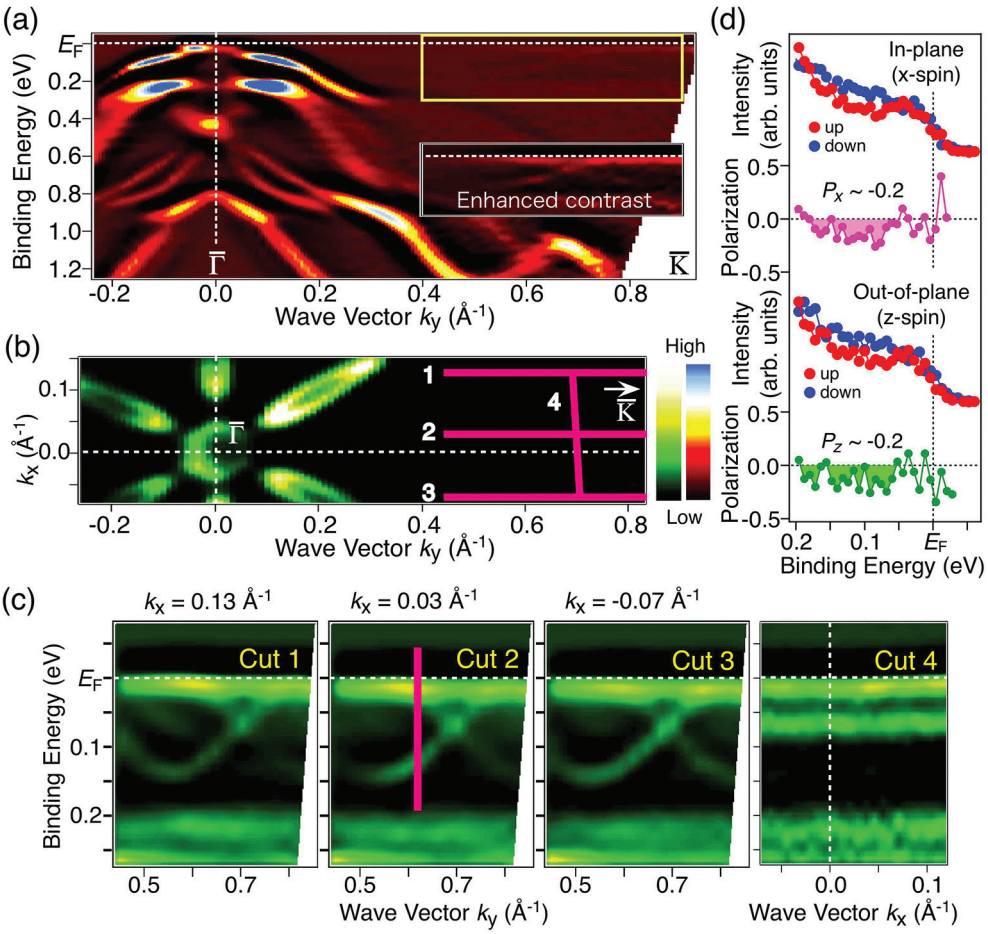

Figure 15. (a) Band structure of a Bi thin film along the $\bar{\Gamma}$ $\bar{K}$ high-symmetry lines. To better trace the weak signal around the $\bar{K}$ points, an enhanced color scale image is shown in the inset. (b) ARPES intensity plot at E_F around the $\bar{\Gamma}$ $\bar{K}$ line. (c) Band dispersion near EF along cuts 1–4 in (b), respectively. (d) Spin-resolved EDCs for the in-plane and out-of-plane spin components at the k point indicated by the pink line in (c), together with the corresponding energy dependence of the spin polarization.

the high-symmetry point $\bar{Y}$ now becomes the time-reversal-invariant momentum and is located exactly at the horizontal projection of the $\bar{M}$ point (k_y = 0.69 Å^{-1}), which actually coincides with the intersection of the x-shaped band. **Figure 16c** displays the calculated band dispersion along the $\bar{\Gamma}$ - $\bar{Y}$ direction of Bi thin film for d = 10 BL. We identify two prominent dispersive bands, which cross E_F and have the edge-state origin. Moreover, the edge bands show the Rashba spin splitting due to the strong spin-orbit coupling at the edge, as evidenced by the degeneracy at the $\bar{Y}$ point. We found that the overall spin-vector direction in the experiment, that is, sign of spin polarization for each component, is also consistent with the

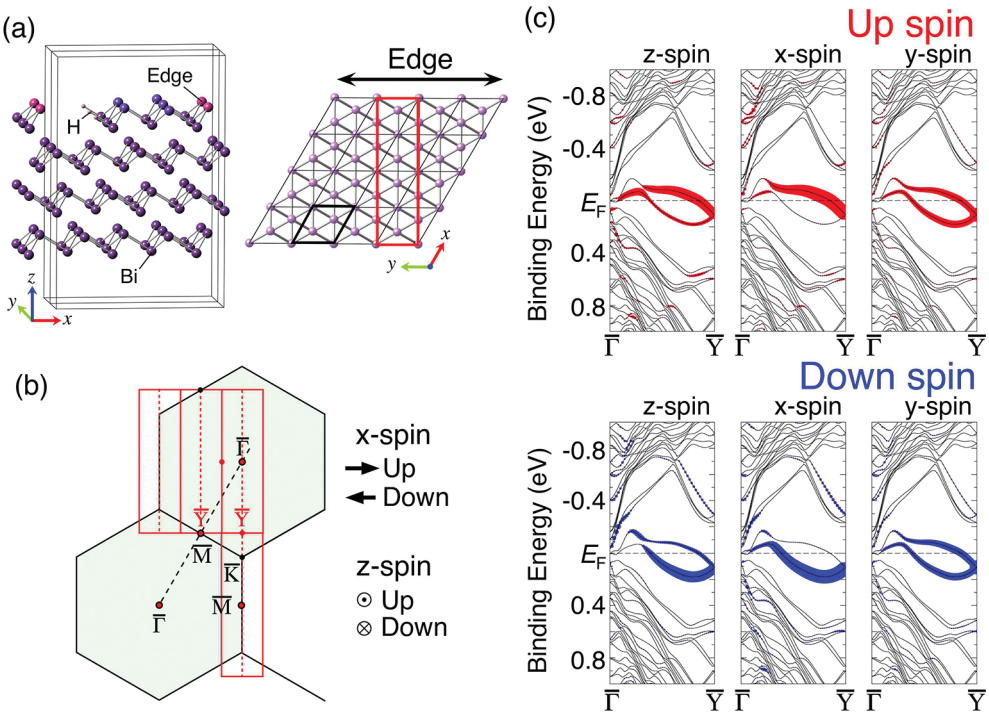

Figure 16. (a) Side and top views of the artificially constructed model crystal structure used to calculate the energy band structure of the edge state. Area enclosed by gray and red solid lines shows the unit cell. Crystal structure in the unit cell contains 1 BL Bi ribbon on 3 BL Bi where hydrogen atoms terminate one side of the edge in Bi ribbon. (b) The 1D Brillouin zone (red line) of the model crystal structure shown in (a), compared to the 2D hexagonal surface Brillouin zone (black line). (c) Band calculations for the model crystal structure along the $\bar{\Gamma}$ $\bar{Y}$ line. The wide of red or blue curves indicates the concentration of the up- and down-spin electrons along the axis specified in the figure.

calculation, while the absolute magnitude of the spin polarization in the experiment (~0.2) is much smaller than that of the calculation (~0.26 to 0.64) in both the in-plane and out-of-plane components, likely due to a finite contribution from the angle-integrated-type background in the ARPES spectra and the spin-orbit entanglement effect [41]. Finally, we have estimated the Rashba parameter α_R by numerical simulation for the 1D parabolic band with the SOC and obtained $\alpha_R = 0.80 \pm 0.05$ eVÅ (**Figure 17**). This value is much larger than that for the 2D surface state (0.56 eVÅ) [11, 15], and the difference could be explained in terms of the presence of an in-plane potential gradient [15, 42] at the edge in addition to the out-of-plane component, which already exists in the 2D film, as supported by observation of the out-of-plane spin polarization as large as the in-plane counterpart. Recently, STM study on the edge states of Bi crystal and thin film [43, 44]. The STM study reported that one of two types of edges, where Bi atoms are terminated at close to vacuum, which corresponds to our calculation, has a 1D character. The band dispersion of the edge state observed in ARPES shows a good agreement with the calculated bands, suggesting that both ARPES and STM observe the same edge state. It is true that 1D electronic state that observed our ARPES measurement is localized at edge.

http://dx.doi.org/10.5772/66278

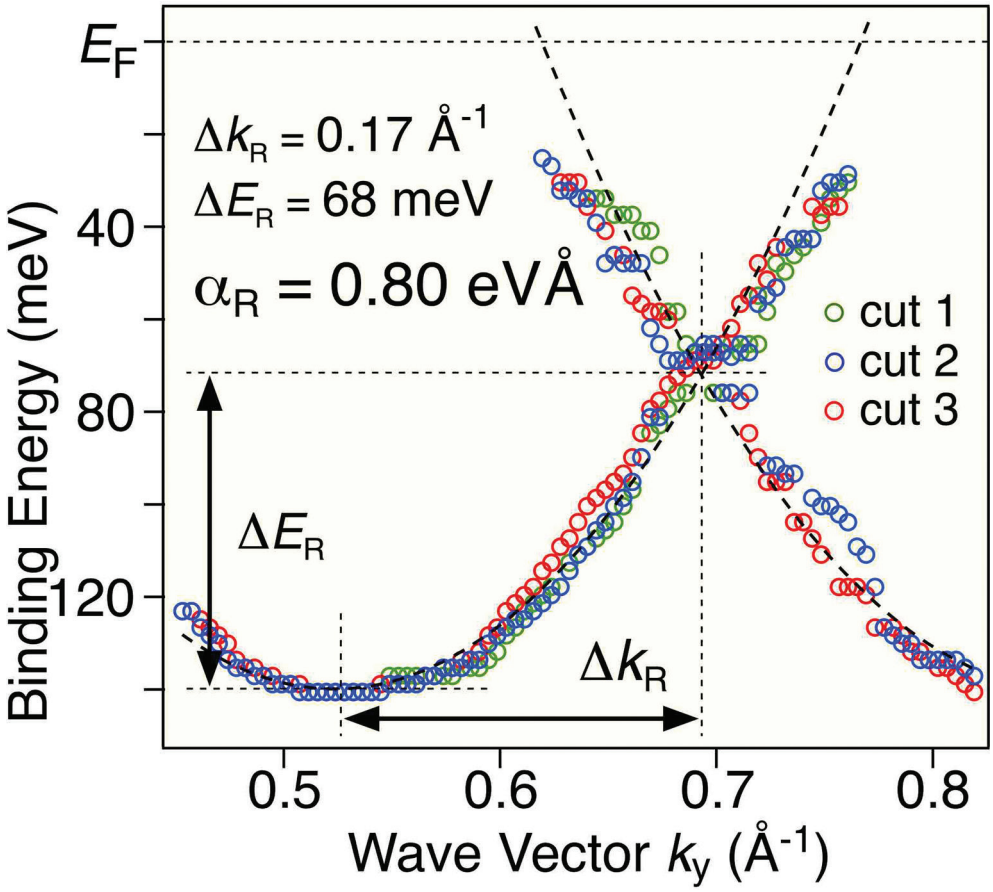

Figure 17. Experimental band dispersion for cuts 1–3 extracted from the peak position of the EDCs in Figure 15c, compared with the numerical simulation for a simple 1D Rashba splitting (dashed black curve).

The edge state in Bi would be also useful in realizing novel physical properties and new spintronic devices.

4. Conclusions

We have demonstrated anomalous Rashba effect of Bi thin film on Si(1 1 1) by using spin-resolved ARPES. Major findings of the present work are the following three features: (i) the surface Rashba states of Bi exhibit the asymmetric in-plane spin polarization and the giant out-of-plane spin polarization, (ii) the spin polarization of the surface states is reduced on decreasing thickness and (iii) 1D band dispersion from the edge state of Bi islands on Si(1 1 1) exhibits large Rashba effect. These observed peculiar spin states are not explained in terms of

the conventional Rashba effect, and these results open a pathway for realizing exotic physical properties at the strong SOC systems.

Acknowledgements

This study is a collaborative research with Prof. Takahashi, Associate Prof. Sato and Associate Prof. Souma in Tohoku University and Prof. Oguchi in Osaka University. We thank K. Sugawara and K. Kosaka for his assistance in the ARPES experiment. This work was supported by JSPS, MEXT of Japan and the Mitsubishi foundation.

Author details

Akari Takayama

Address all correspondence to: a.takayama@surface.phys.s.u-tokyo.ac.jp

The University of Tokyo, Tokyo, Japan

References

[1] Baibich MN, Broto JM, Fert A, Nguyen Van Dau F, Petroff F, Eitenne P, Creuzet G, Friedrich A, and Chazelas J. Giant magnetoresistance of (001)Fe/(001)Cr magnetic superlattices. Phys. Rev. Lett. 1988;**61**:2472. doi:10.1103/PhysRevLett.61.2472

[2] Awschalom D and Samarth N. Trend: Spintronics without magnetism. Phyics 2009;**2**:50. doi:10.1103/Physics.2.50

[3] Datta S and Das B. Electronic analog of the electro-optic modulator. Appl. Phys. Lett. 1990;**56**:665–667. DOI:10.1063/1.102730

[4] Bychkov YA and Rashba EI. Properties of a 2D electron gas with lifted spectral degeneracy. JETP Lett. 1984;**39**:78–81.

[5] Hasan MZ and Kane CL. Colloquium: topological insulators. Rev. Mod. Phys. 2010;**82**:3045. doi:10.1103/RevModPhys.82.3045

[6] Qi XL and Zhang SC. Topological insulators and superconductors. Rev. Mod. Phys. 2011;**83**:1057. doi:10.1103/RevModPhys.83.1057

[7] LaShell S, McDougall BA, and Jensen E. Spin splitting of an Au(1 1 1) surface state band observed with angle resolved photoelectron spectroscopy. Phys. Rev. Lett. 1996;**77**:3419. doi:10.1103/PhysRevLett.77.3419

[8] Hofmann P. The surfaces of bismuth: structural and electronic properties. Prog. Surf. Sci. 2006;**81**:191. doi:10.1016/j.progsurf.2006.03.001

[9] Sugawara K, Sato T, Souma S, Takahashi T, Arai M, and Sasaki T. Fermi surface and anisotropic spin-orbit coupling of Sb(1 1 1) studied by angle-resolved photoemission spectroscopy. Phys. Rev. Lett. 2006;**96**:046411. doi:10.1103/PhysRevLett.96.046411

[10] Ast CR and Höchst H. Fermi surface of Bi(1 1 1) measured by photoemission spectroscopy. Phys. Rev. Lett. 2001;**87**:177602. doi:10.1103/PhysRevLett.87.177602

[11] Koroteev YM, Bihlmayer G, Gayone JE, Chulkov EV, Blügel S, Echenique PM, and Hofmann PH. Strong spin-orbit splitting on Bi surfaces. Phys. Rev. Lett. 2004;**93**:046403. doi:10.1103/PhysRevLett.93.046403

[12] Hirahara T, Nagao T, Matsuda I, Bihlmayer G, Chulkov EV, Koroteev YM, Echenique PM, Saito M, and Hasegawa S. Role of spin-orbit coupling and hybridization effects in the electronic structure of ultrathin Bi films. Phys. Rev. Lett. 2006;**97**:146803. doi:10.1103/PhysRevLett.97.146803

[13] Hirahara T, Miyamoto K, Matsuda I, Kadono T, Kimura A, Nagao T, Bihlmayer G, Chulkov EV, Qiao S, Shimada K, Namatame H, Taniguchi M, and Hasegawa S. Direct observation of spin splitting in bismuth surface states. Phys. Rev. B 2007;**76**:153305. doi:10.1103/PhysRevB.76.153305

[14] Kimura A, Krasovskii EE, Nishimura R, Miyamoto K, Kadono T, Kanomaru K, Chulkov EV, Bihlmayer G, Shimada K, Namatame H, and Taniguchi M. Strong Rashba-type spin polarization of the photocurrent from bulk continuum states: experiment and theory for Bi(1 1 1). Phys. Rev. Lett. 2010;**105**:076804. doi:10.1103/PhysRevLett.105.076804

[15] Ast CR, Henk J, Ernst A, Moreschini L, Falub MC, Pacilé D, Bruno P, Kern K, and Grioni M. Giant spin splitting through surface alloying. Phys. Rev. Lett. 2007;**98**:186807. doi:10.1103/PhysRevLett.98.186807

[16] Meier F, Dil H, Checa JL, Patthey L, and Osterwalder J. Quantitative vectorial spin analysis in angle-resolved photoemission: Bi/Ag(1 1 1) and Pb/Ag(1 1 1). Phys. Rev. B. 2008;**77**:165431. doi:10.1103/PhysRevB.77.165431

[17] Gierz I, Suzuki T, Frantzeskakis E, Pons S, Ostanin S, Ernst A, Henk J, Grioni M, Kern K, and Ast CR. Silicon surface with giant spin splitting. Phys. Rev. Lett. 2009;**103**:046803. doi:10.1103/PhysRevLett.103.046803

[18] Sakamoto K, Kakuta H, Sugawara K, Miyamoto K, Kimura A, Kuzumaki T, Ueno N, Annese E, Fujii J, Kodama A, Shishidou T, Namatame H, Taniguchi M, Sato T, Takahashi T, and Oguchi T. Peculiar Rashba splitting originating from the two-dimensional symmetry of the surface. Phys. Rev. Lett. 2009;**103**:156801. doi:10.1103/PhysRevLett.103.156801

[19] Frantzeskakis E, Pons S, and Grioni M. Band structure scenario for the giant spin-orbit splitting observed at the Bi/Si(1 1 1) interface Emmanouil. Phys. Rev. B 2010;**82**:085440. doi:10.1103/PhysRevB.82.085440

[20] Sakamoto K, Oda T, Kimura A, Miyamoto K, Tsujikawa M, Imai A, Ueno N, Namatame H, Taniguchi M, Eriksson PEJ, and Uhrberg RIG. Abrupt rotation of the Rashba spin to

the direction perpendicular to the surface. Phys. Rev. Lett. 2009;**102**:096805. doi:10.1103/PhysRevLett.102.096805

[21] Yaji K, Ohtsubo Y, Hatta S, Okuyama H, Miyamoto K, Okuda T, Kimura A, Namatame T, Taniguchi M, and Aruga T. Large Rashba spin splitting of a metallic surface-state band on a semiconductor surface. Nature Commun. 2010;**1**:17. doi:10.1038/ncomms1016

[22] Matetskiy AV, Ichinokura S, Bondarenko LV, Tupchaya AY, Gruznev DV, Zotov AV, Saranin AA, Hobara R, Takayama A, and Hasegawa S. Two-dimensional superconductor with a giant Rashba Effect: one-atom-layer Tl-Pb compound on Si(1 1 1). Phys. Rev. Lett. 2015;**115**:147003. doi:10.1103/PhysRevLett.115.147003

[23] Barke I, Zheng F, Rughheimer TK, and Himpsel FJ. Experimental evidence for spin-split bands in a one-dimensional chain structure. Phys. Rev. Lett. 2006;**97**:226405. doi:10.1103/PhysRevLett.97.226405.

[24] Wells JW, Dil JH, Meier F, Lobo-Checa J, Petrov VN, Osterwalder J, Ugeda MM, Fernandez-Torrente I, Pascual JI, Rienks EDL, Jensen MF, and Hofmann Ph. Nondegenerate metallic states on Bi(1 1 4): a one-dimensional topological metal. Phys. Rev. Lett. 2009;**102**:096802. doi:10.1103/PhysRevLett.102.096802

[25] Quay CHL, Hughes TL, Sulpizio JL, Pfeiffer LN, Baldwin KW, West KW, Goldhaber-Gordon D, and de Picciotto R. Observation of a one-dimensional spin–orbit gap in a quantum wire. Nat. Phys. 2010;**6**:336. doi:10.1038/nphys1626

[26] Pershin YV, Nesteroff JA, and Privman V. Effect of spin-orbit interaction and in-plane magnetic field on the conductance of a quasi-one-dimensional system. Phys. Rev. B. 2004;**69**:121306(R). doi:10.1103/PhysRevB.69.121306

[27] Takayama A, Sato T, Souma S, and Takahashi T. Giant out-of-plane spin component and the asymmetry of spin polarization in surface Rashba States of Bismuth thin film. Phys. Rev. Lett. 2011;**106**:166401. doi:10.1103/PhysRevLett.106.166401

[28] Takayama A, Sato T, Souma S, Oguchi T, and Takahashi T. Tunable spin polarization in bismuth ultrathin film on Si(1 1 1). Nano Lett. 2012;**12**:1776. doi:10.1021/nl2035018

[29] Takayama A, Sato T, Souma S, Oguchi T, and Takahashi T. One-dimensional edge states with giant spin splitting in a bismuth thin film. Phys. Rev. Lett. 2015;**114**:066402. doi:10.1103/PhysRevLett.114.066402

[30] Souma S, Takayama A, Sugawara K, Sato T, and Takahashi T. Ultrahigh-resolution spin-resolved photoemission spectrometer with a mini Mott detector. Rev. Sci. Instrum. 2010;**81**:095101. doi:10.1063/1.3480542

[31] Schlier E and Farnsworth HE. Structure and adsorption characteristics of clean surfaces of germanium and silicon. J. Chem. Phys. 1959;**30**:917. doi:10.1063/1.1730126

[32] Takayanagi K, Tanishiro Y, Takahashi M, and Takahashi S. Structural analysis of Si(1 1 1)-7×7 by UHV-transmission electron diffraction and microscopy. J. Vac. Sci. Technol. A. 1985;**3**:1502. doi:10.1116/1.573160

[33] Viernow J, Lin JL, Petrovykh DY, Leibsle FM, Men FK, and Himpsel FJ. Regular step arrays on silicon. Appl. Phys. Lett. 1998;**72**:948. doi:10.1063/1.120882

[34] Nagao T, Sadowski JT, Saito M, Yaginuma S, Fujikawa Y, Kogure T, Ohno T, Hasegawa Y, Hasegawa S, and Sakurai T. Nanofilm allotrope and phase transformation of ultrathin Bi film on Si(1 1 1)-7×7. Phys. Rev. Lett. 2004;**93**:105501. doi:10.1103/PhysRevLett.93.105501

[35] Kirschner J, Feder R, and Wendelken JF. Electron spin polarization in energy- and angle-resolved photoemission from W(0 0 1): experiment and theory. Phys. Rev. Lett. 1981;**47**:614. doi:10.1103/PhysRevLett.47.614

[36] Oepen HP, Hunlich K, and Kirschner J. Spin-dependent photoemission intensities from solids. Phys. Rev. Lett. 1986;**56**:496. doi:10.1103/PhysRevLett.56.496

[37] Zhang HJ, Liu CX, Qi XL, Deng XY, Dai X, Zhang SC, and Fang Z. Electronic structures and surface states of the topological insulator $Bi_{1-x}Sb_x$. Phys. Rev. B. 2009;**80**:085307. doi:10.1103/PhysRevB.80.085307

[38] Fu L. Hexagonal warping effects in the surface states of the topological insulator Bi_2Te_3. Phys. Rev. Lett. 2009;**103**:266801. doi:10.1103/PhysRevLett.103.266801

[39] Souma S, Kosaka K, Sato T, Komatsu M, Takayama A, Takahashi T, Kriener M, Segawa K, and Ando Y. Direct measurement of the out-of-plane spin texture in the dirac-cone surface state of a topological insulator. Phys. Rev. Lett. 2011;**106**:216803. doi:10.1103/PhysRevLett.106.216803

[40] Zhang Y, He K, Chang CZ, Song CL, Wang LL, Chen X, Jia JF, Fang Z, Dai X, Shan WY, Shen SQ, Niu Q, Qi XL, Zhang SC, Ma XC, and Xue QK. Crossover of the three-dimensional topological insulator Bi2Se3 to the two-dimensional limit. Nat. Phys. 2010;**6**:584. doi:10.1038/nphys1689

[41] Yazyev OV, Moore JE, and Louie SG. Spin polarization and transport of surface states in the topological insulators Bi_2Se_3 and Bi_2Te_3 from first principles. Phys. Rev. Lett. 2010;**105**:266806. doi:10.1103/PhysRevLett.105.266806

[42] Park J, Jung S, Jung MC, Yamane H, Kosugi N, and Yeom H. Self-assembled nanowires with giant Rashba split bands. Phys. Rev. Lett. 2013;**110**:036801. doi:10.1103/PhysRevLett.110.036801

[43] Drozdov IK, Alexandradinata A, Jeon S, Nadj-Perge S, Ji H, Cava RJ, Andrei Bernevig B, and Yazdani A. One-dimensional topological edge states of bismuth bilayers. Nat. Phys. 2014;**10**:664. doi:10.1038/nphys3048

[44] Kawakami N, Lin CL, Kawai M, Arafune R, and Takagi N. One-dimensional edge state of Bi thin film grown on Si(1 1 1). Appl. Phys. Lett. 2015;**107**:031602. doi:10.1063/1.4927206

Chapter 6

Electrochemical Deposition of P3AT Films Used as a Probe of Optical Properties in Polymeric System

Sankler Soares de Sá, Fernando Costa Basílio, Henrique de Santana, Alexandre Marletta and Eralci Moreira Therézio

Additional information is available at the end of the chapter

http://dx.doi.org/10.5772/66921

Abstract

Poly(3-alkylthiophene) (P3ATs) have been extensively used in photovoltaic devices such as a p-type organic Semiconductors. However, several electronic properties of P3ATs present energy transfer inter- and intra-chains that have direct consequences on the performance of optoelectronic devices. Traditionally electrochemical techniques, such as cyclic voltammetry, chronoamperometry and chronocoulometry, have been applied to process polymer thin films and unconventional spectroscopy techniques are used to characterize the electronic properties. In the present work, we used an innovative technique called ellipsometry emission to investigate the optical properties of P3AT films. We propose a new approach to study the electrochemical synthesize and unintentional doping processes of polymeric systems. We showed a strong correlation between the electrochemical synthesis and the optical properties controlling the film growth conditions for P3ATs. The results obtained in the present study can be potentially utilized for applications in organic devices, mainly in photovoltaic cells when the film deposition and the optical properties control are relevant.

Keywords: poly(3-alkylthiophene), electrochemical synthesis, optical properties, energy transfer, emission ellipsometry

1. Introduction

Over the last decades, semiconductor polymers have attracted considerable interest, particularly for the production of organic electroluminescent diodes (OLEDs) and organic photovoltaic cells (OPVs), in which they present high emission efficiency in the visible region and UV-Vis absorption in the broad spectral window [1, 2]. Devices using conductive polymers

exhibit some advantages over inorganic semiconductors. They are easily deposited on thin solid films by low-cost techniques such as spin coating, casting or electrochemical [2, 3]. Among the wide variety of conductive polymers, poly(3-*alkylthiophene*) (P3AT) has been studied due to its various physical-chemistry characteristics, e.g., good chemical stability, solubility (making it an easy deposition material on substrates) and has electrochromic and thermochromic characteristics [4]. Besides these properties, the luminescence efficiency of this polymer has increased significantly in the function of the *alkyl* chain length [5, 6]. Basically, P3ATs are the derivatives of polythiophene (PT) which are obtained from the polymerization of thiophene (monomer), a sulfur heterocyclic ring [7]. The precursor monomer of P3ATs, 3-*alkylthiophene* is also composed of thiophene ring and alkyl groups, in compliance with the following combination [5]:

$$C_n H_{2n+1} \tag{1}$$

where C is the carbon chemical element, H is the hydrogen chemical element and n is the number of carbons that compose the molecule.

The P3ATs chemically synthesized presented an energy *gap* of around 1.93 eV (640 nm) [5, 6, 8–12]. Interestingly, this *energy gap* independent of the size of the *alkyl* lateral chain because it is not conjugated. Therefore, the recombination of excited carriers occurs only in the main conjugated polymer chain. However, the intensity of the emission band is directly related to the alkyl chain [6]. Another important observation about the emission band intensity is the anomalous temperature dependence [5].

Ohmori et al. [6] have observed luminescence intensity dependence in function of the length of the *alkyl* chain. They used three P3ATs with different sizes of the *alkyl* chain. The P3ATs have traditionally been prepared by chemical synthesis from 3-AT monomers with $FeCl_3$ as a catalyst. Chemical synthesis of P3AT polymer, using a standard way in the literature, was first obtained by Yoshino et al. in 1984 [13]. In addition, Yoshino et al. [5] noted that the photoluminescence intensity (PL) of P3AT films increases in the function of the sample temperature and decreases after the melting point. This result has been discussed in terms of the effective conjugation length, since the dynamics of the excited species are influenced by the occurrence of a twist between the vicinity of the thiophene rings together with the interchain interaction. In the last decade, the interest in the organic electronic devices has increased significantly; however, some effects on their operation are not fully understood, in particular the interface effects of the substrate/polymer and energy transfer of excited carriers [9, 14–16]. Since the physical-chemistry properties and investigation of organic active layers, such as P3ATs thin solid films, can elucidate the development of new optoelectronic devices [16–18]. Interface effects cause significant quenching of excited carriers and it is commonly investigated by conventional spectroscopic techniques [15, 19], such as ultraviolet-visible absorption (UV-Vis), photoluminescence (PL), photoluminescence excitation (PLE), vibrational spectroscopy (FT-IR and RAMAN) [8, 12, 20, 21] and the morphological technique of atomic force microscopy (AFM) [22–24]. In the case of energy transfer processes of excited carriers, the analysis of polarization of emitted light can be directly correlated with polymeric chain position parallel to the direction of the transition dipole moment [25–27]. Moreover, we need to consider the effects of the deposition method.

In present work, we used the electrochemical synthesis for deposition of P3AT thin solid film correlating with optical properties. We demonstrated an easy and efficient alternative method

http://dx.doi.org/10.5772/66921

to control the processing of organic optoelectronic devices. In that context, Therézio et al. in [8] show two distinct structures of the polymer chain morphology shifting the band gap to higher energies, using an optical analysis of P3ATs films electrochemically prepared. Moreover, reference [9] also indicated that it is possible to analyze the polarization of the emitted light by the supporting electrolyte effects on the emission properties of P3ATs films. The results conclude quantitatively that the best-supporting electrolyte concentration for the P3ATs film's production is 0.100 mol L^{-1}. It is in absolute agreement of the electrolyte concentration used in the literature to P3ATs synthesis. Recently, Santana and coworkers [10, 12, 28, 29] have shown that the P3ATs synthesis is possible using different supporting electrolytes, solvents and thicknesses. Therefore, it was possible to correlate the growth conditions of the electrochemical synthesis and optical properties to produce polymer films with possible application in optoelectronic devices. We present the systematic study of two sets of poly(3-dodecylthiophene) (P3DDT) films grown electrochemically with two different electrolytes. All thin films were deposited on a transparent electrode FTO (fluorine-doped tin oxide) and cycles ranging from 1 to 10 cycles. In addition, it was possible to obtain the emission optical characteristics in the function of the amount of polymer deposited or the polymeric film thickness. We used, in the present investigation, UV-Vis absorption, photoluminescence and ellipsometry emission. As a result, we assign the use of an alternative optical characterization to probe the organic semiconductors obtained via electrochemical techniques [20, 23].

2. Electrochemical deposition in poly(3-alkylthiophenes) films

P3DDT samples were deposited on the FTO substrate by the electrochemical synthesis of 3-dodecylthiophene ($C_{16}H_{28}S$) monomer in an electrolyte solution containing a solvent, salt and monomer. In stoke solution, we used acetonitrile (CH_3CN), monomer 3-dodecylthiophene and lithium perchlorate ($LiClO_4$) or tetraethylammonium tetrafluoroborate ($((C_2H_5)_4NBF_4$ or Et_4NBF_4) salts [9]. The concentrations used are 0.100 mol L^{-1} for the support electrolyte (SE), 0.050 mol L^{-1} for the monomer and 0.040 mol L^{-1} for Et_4NBF_4 or $LiClO_4$ electrolyte. The options for the previous concentrations is based on the literature for poly(3-methylthiophene) and poly(3-octylthiophene) [9, 10, 30–32]. The films grown in the present study are labeled in **Table 1**.

2.1. Cyclic voltammetry

The P3DDT films were electropolymerized and deposited on FTO substrates by cycles of the voltammetry method (CV) using the IVIUM COMPACTSTAT potentiostat/galvanostat. Alternatively, reference [9] presented additional deposition techniques of chronoamperometry and chronocoulometry used to synthesize P3AT films [9]. Polymerization was accomplished by continuous cycling the potential of the FTO electrode between +2.200 and -0.000 V for Et_4NBF_4 and +2.900 and -1.000 V for $LiClO_4$. Electropolymerization scan rate was determined at 0.050 V/s. Different sample thicknesses were obtained by increasing the number of cycles in CV ranging from 1 to 10 for each electrolyte. In the electropolymerization CV technique, we used standard-three-electrodes-cells: platinum auxiliary electrode, reference electrode containing saturated demonized water solution of potassium chloride (KCl) and FTO-working electrode. Electrodes were immersed in an electrolyte solution containing acetonitrile, monomer 3-dodecylthiophene and inert salt under a controlled atmosphere using argon gas.

Electrolyte	Number of cycles	Nomenclature used
Et_4NBF_4	1	EtNBF01
	2	EtNBF02
	4	EtNBF04
	6	EtNBF06
	8	EtNBF08
	10	EtNBF10
$LiClO_4$	1	LiClO01
	2	LiClO02
	4	LiClO04
	6	LiClO06
	8	LiClO08
	10	LiClO10

Table 1. Label of P3DDT film in function of the cycles number and electrolyte.

Initially, the voltammetry cyclic synthesis, oxidate or reducte the polymer monomers bonding its covalently increasing the main chain length and deposit the polymer via physical-chemistry interaction with the working electrode. The polymer chain length formed in this process occurs until the saturation limit of the chain is achieved. Then, in each CV cycle new polymer chains are deposited on the previously deposited polymer layer. **Figure 1** shows the cyclic voltammogram for EtNBF10 (**Figure 1a**) and LiClO10 (**Figure 1b**) films. We observe that between the first and the last cycles, there are different maximum of reduction potentials 0.56 and 0.32 V for EtNBF10 and 0.36 and 0.48 V for LiClO10, respectively. These ddp differences indicate the film thickness and material deposited amount is increasing between consecutive CV cycles [33].

The increase in number of electropolymerization cycles leads to the formation of various layers until the saturation point of the film. Assuming that in each cycle, the maximum voltage of oxidation or reduction represents the cathode and anodic ionizing potential, respectively, the difference in ionization potentials allows us to infer the *energy gap* (E_g) of the material. It is important to observe that the CV curves need to display only one oxidation or reduction process, as in the case of P3DDT films, see **Figure 1**. This method was first introduced by Eckhardt et al. [34] for organic semiconductor materials. **Table 2** shows the oxidation and reduction maximum values for all P3DDT films. Calculated E_g values increase from the first to the last cycle regardless of the electrolyte since the resistance of the carriers is greater for the additional P3DDT layer after each cycle, thus increasing film thickness [30, 33].

By comparing the values, shown in **Table 2** for the *energy gap*, it can be observed that the films with the Et_4NBF_4 electrolyte require less energy for their formation. The increase in voltage required for the formation of films and of energy is due to the presence of BF_4^- and ClO_4^- anions in the electropolymerization, which has great influence on the morphology, structure and

http://dx.doi.org/10.5772/66921

electrochemical polymer properties [7–9, 19, 20, 31]. In addition, great E_g can be correlated with the high doping of P3DDT chains producing higher polymer quinone form. It was showed by Therézio et al. [8, 19] studied that the energy gap in doped P3AT films increases. Therefore, in our study, we also recommend the P3DDT films with lesser deposition cycles and lesser doped or lower *gap energy* which displays major polymer chains in the pristine form.

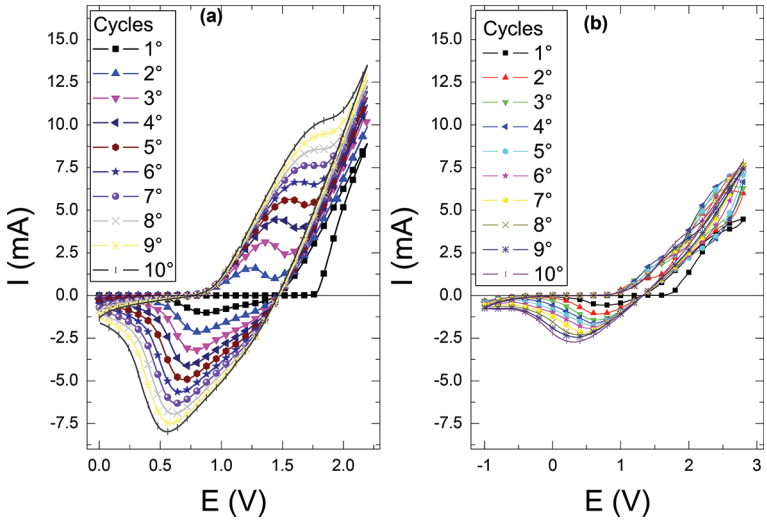

Figure 1. Cyclic voltammetry of (a) EtNBF10 and (b) LiClO10 films.

Film	Cathodic maximum (V)	Anodic maximum (V)	E_g (V)
EtNBF01	–	0.84	–
EtNBF02	1.25	0.80	0.45
EtNBF04	1.44	0.70	0.74
EtNBF06	1.62	0.68	0.94
EtNBF08	1.76	0.55	1.21
EtNBF10	1.82	0.55	1.27
LiClO01	2.40	0.84	1.56
LiClO02	2.55	0.68	1.87
LiClO04	2.61	0.64	1.97
LiClO06	2.80	0.59	2.21
LiClO08	2.80	0.45	2.35
LiClO10	2.80	0.30	2.50

Table 2. Cathodic and anodic ionization potential for P3DDT films.

3. Optical characterizations

3.1. UV-Vis absorption[1]

In the UV-Vis spectral range with maximum absorption centered at ~450 nm. For the EtNBF02 film, a well-resolved absorbance band at ~775 nm is also observed. This band is the result of the interaction between the BF_4^- anion and P3DDT polymer chains [8, 9, 20]. Similar results are observed in different P3AT polymers [35–37]. To higher electropolymerization cycle number, the band at ~775 nm is further evident (not shown), in which it is possible to correlate the cycle number and UV-Vis absorption intensity to follow the polymer-grown deposition. **Figure 2b** shows the absorption spectra for the LiClO01 and LiClO02 films in the UV-Vis spectral range. It observes in **Figure 2b** that the maximum absorption is approximated at ~400 nm for the LiClO02 film, but it cannot be confirmed by the exact spectral position because of the absorption of the FTO substrate. The blue shift of the absorption maximum position in comparison of absorbance spectra of the Et_4NBF_4 films should be considered due to the presence of two different P3DDT molecules morphologies or the diminish of the length of the polymer chains. As a result, the decrease of the conjugation and the increase of the gap energy of the material occur. That effect was recently reported by Therézio et al. [8, 12] to the P3AT derivative where the maximum position and intensity of absorption change in function of the electrolyte. Other castellation is the exposition of the film on the atmosphere environment that induces relatively quick (days) polymer films degradation. Lower intensity and poorly resolved absorbance band at ~650 nm is observed in **Figure 2b** for LiClO02 and thick films (not shown) due to the interaction between the ClO_4^-anions and the P3DDT molecules [8, 9, 12, 20, 31].

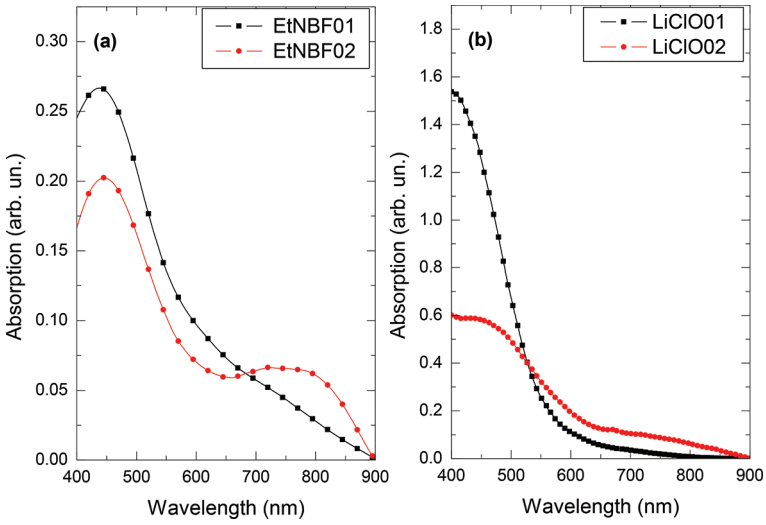

Figure 2. UV-Vis spectra for P3DDT films with one and two electropolymerization cycles: (a) EtNBF01 and EtNBF02 films and (b) LiClO01 and LiClO02 films.

[1]UV-Vis measurements were conducted using a spectrophotometer FEMTO XI 800, operating in the 190-900 nm range.

http://dx.doi.org/10.5772/66921

3.2. Photoluminescence (PL)[2]

We consider several radiative contributions associated with different interactions to simulate the emission spectra due to the presence of the anion in the electrolyte solution and polymer chain [8, 9, 12, 31]. Basically, for P3ATs emission spectra we may approximate the line shape considering quinone or oligomer structures (high energy) and pristine (low energy) structures. The main structures present in these polymers such as the quinone and pristine structures are shown in **Figure 3**. The result is the maximum shift or relative intensity change due to the interaction of electron-vibrational modes of quinone or pristine structures [8, 19] or different lengths of polymer chains [38].

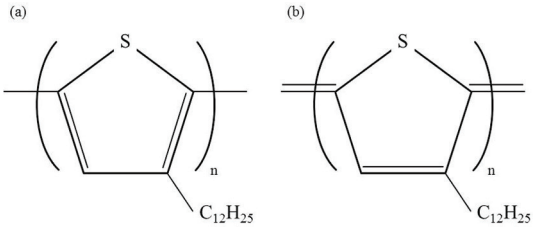

Figure 3. Scheme for P3DDT (a) pristine and (b) quinone structure.

Figure 4a and **b** shows the PL spectra of P3DDT film synthesized using both Et_4NBF_4 or $LiClO_4$ electrolytes, respectively. Note that the spectra are broad in the UV-Vis spectral range. **Figure 4a** shows normalized PL spectra for P3DDT films grown using the Et_4NBF_4 electrolyte, where the maximum of the emission redshift increased the number of cycles. This is due to the presence of oligomers with smaller conjugation lengths [38] and quinone chains [8, 19]. In addition for EtNBF01–EtNBF04 films, it is possible the occurrence of polymer chains with lower molecular weight and interface substrate/polymer, polymer/polymer and polymer/electrolyte effects [14, 22]. By increasing the film thickness (>4 cycles), PL spectra shifted to high wavelengths (*redshift*), it according the rise of in residence time in the electropolymerization process in the presence of higher conjugated polymer chains and pristine structures [8, 9, 12]. **Figure 4b** shows the PL spectra of P3DDT films synthesized with $LiClO_4$, presenting the similar line shape characteristics observed in **Figure 4(a)**. Film emission spectra utilizing that electrolyte also display different radiative processes. In this case, we consider two different configurations of P3DDT molecules, i.e., pristine or quinone structures [8, 9, 12]. The emission line shape is practically identical to LiClO01–LiClO08 films. However, the PL spectra for the thicker LiClO10 film is red shifted due to the new polymer structures created by the interaction ClO_4^- ion present in the solution [8, 12]. It is possible in the synthesis the presence of high

[2]PL measurements were obtained by exciting the samples with the 405 nm line of a diode laser at 4.0 mW (Laser Line-iZi), vertically polarized in relation to the laboratory reference. The emission was detected and analyzed by a USB 2000 ocean optics spectrophotometer.

polymer conjugation length or pristine structures [8, 9, 12]. Results are coherent with recent observation of P3ATs when different electrolytes tend to influence the molecular polymer structure [7, 33].

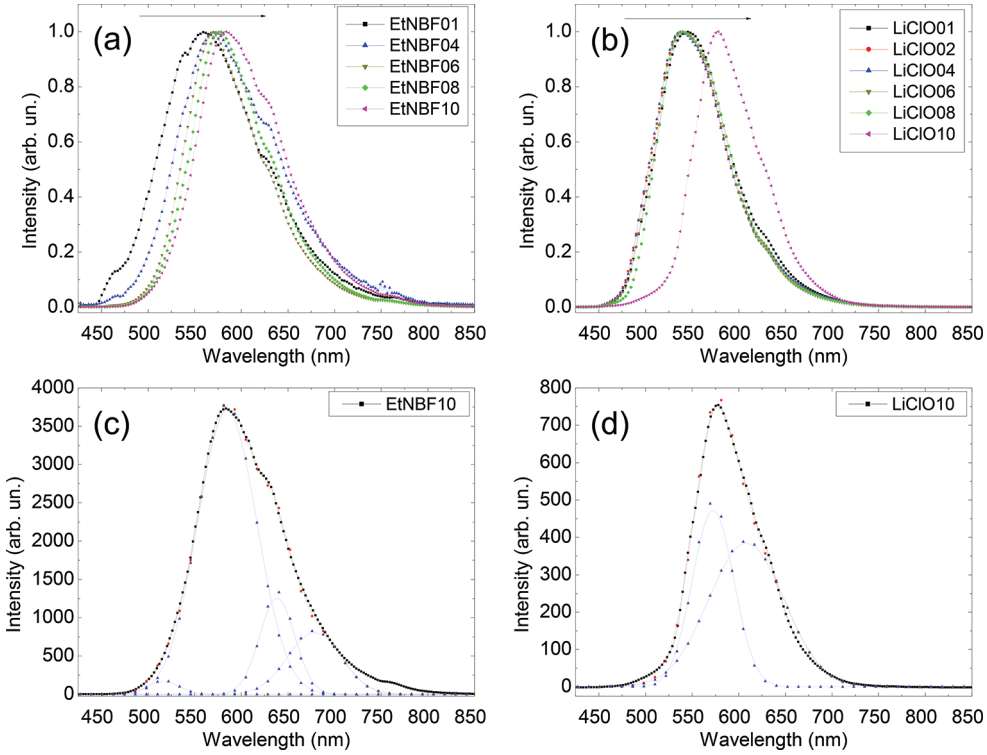

Figure 4. PL spectra for P3DDT films formed with electrolyte (a) Et4NBF4 and (b) LiClO4. PL simulation for (c) EtNBF10 and (d) LiClO10 films.

Figure 4(c) and **(d)** shows the spectra simulation for EtNBF10 and LiClO10 films, respectively, using the multi-Gaussian function, following the procedure utilized for P3AT polymers [8, 9, 12, 13]. First, we consider the polymer chains without the presence of dopants and without structural changes. Second, we introduce the contribution to the emission line shape of dopants and possible new structural changes (**Figure 3**) [8], as established by the P3AT family [35–37] in the energy range of polymeric chains or oligomers [38, 39]. Moreover, it was also added bands due to the interaction of the electron-vibrational modes. The typical optically active vibration mode is 1450 cm^{-1} for the C=C group [37]. In **Figure 4(c)**, the PL spectra centered at ~516 nm can be assigned to high conjugation polymer chains. The second band at ~584 nm is due to quinone structures, which is the result of interaction between the salt and the polymer chains. The band at ~638 nm is attributed to pristine without the salt-polymer interaction.

Finally, the last one at ~678 nm is normally reported as the vibrational replica [35–37]. We perform a similar procedure to simulate the spectra of P3DDT films processed with $LiClO_4$ and the results are presented in **Figure 4(d)**. Note in this case, the spectrum may be simulated with only Gaussians curves [8, 12]. The emission band at ~572 nm is assigned to the interaction between the electrolyte and the polymer chain forming mainly quinone structures and a band at ~610 nm is due to the pristine structure. That result is agreement with the reports on the P3ATs family [8, 9, 12, 19]. A similar simulation was performed for all samples analyzed and the results are shown in **Table 3**. And it observed that the films synthesized with Et_4NBF_4 have vibrational replicas at 680 nm. The presence of the bands assigned to the quinone and pristine structures is also evident for both electrolytes. As a result, it is possible to correlate the maximum emission spectral position to the amount of these structures in the polymeric film.

Table 2 shows that the P3DDT *band gap* should change, increasing the number of the deposition cycles. However, data in **Table 3** demonstrate that the emission of quinone or pristine chains does not change the spectral position, respectively, at 569 ± 7 and 631 ± 8 nm for films grown in Et_4NBF_4 and 538 ± 9 and 588 ± 7 nm for the films grown in $LiClO_4$. The redshift in the emission spectra is due to the emission bands of the pristine or quinone species. In addition, the present result shows how the use of electropolymerization is able to synthesize regular polymer chains, in which it is an important point when the reproducibility of polymeric layers is important, mainly to applied in an organic device area.

Films	1st oligomers band nm (eV)	2nd oligomers band nm (eV)	Quinone band nm (eV)	Pristine band nm (eV)	Vibrational replica nm (eV)
EtNBF01	465 (2.66)	520 (2.38)	568 (2.18)	630 (1.96)	684 (1.81)
EtNBF02	461 (2.68)	515 (2.40)	556 (2.22)	610 (2.03)	674 (1.83)
EtNBF04	–	500 (2.47)	569 (2.17)	638 (1.94)	691 (1.79)
EtNBF06	–	499 (2.48)	566 (2.19)	625 (1.98)	683 (1.81)
EtNBF08	–	512 (2.42)	575 (2.15)	632 (1.96)	675 (1.83)
EtNBF10	–	516 (2.40)	584 (2.12)	638 (1.94)	678 (1.82)
LiClO01	–	–	540 (2.29)	589 (2.10)	–
LiClO02	–	–	539 (2.30)	588 (2.10)	–
LiClO04	–	–	537 (2.30)	587 (2.11)	–
LiClO06	–	–	535 (2.31)	579 (2.14)	–
LiClO08	–	–	534 (2.32)	576 (2.15)	–
LiClO10	–	–	572 (2.16)	608 (2.03)	–

Table 3. Maximum of curves of the deconvolution in the PL spectra for EtNBFxx and LiClOxx films.

3.3. Emission ellipsometry (EE)[3]

Recently, we demonstrated the correlation between polarized emission light and P3DDT films grown using the electrochemical using emission ellipsometry technique [25, 26, 40]. Photoluminescence polarization reveal important properties of the material structure, e.g., anisotropy, which has immediate application in industry [41]. By using the ellipsometry technique, the polarization state of the emitted light can be determined by calculating the S_0, S_1, S_2 and S_3 Stokes parameters. S_0 is associated with the total light emitted amount, S_1 describes the linearly polarized amount of light in the vertical or horizontal direction, S_2 describes the linear polarization amount rotated by +45° or -45° and S_3 describes the circularly polarized light to the right or left. These parameters are obtained by adjusting the intensity I of the equation [25, 40]:

$$I(\theta) = \frac{1}{2}[A + B \,.\, \sin(2\theta) + C \,.\, \cos(4\theta) + D \,.\, \sin(4\theta)] \tag{2}$$

where I is the electric field intensity, θ is the angle between the axes of the quarter-wave plate and of the polarizer, $A = S_0 - \frac{S_1}{2}$, $B = S_3$, $C = -\frac{S_1}{2}$ and $D = -\frac{S_2}{2}$, where S_0, S_1, S_2 and S_3 are the Stokes parameters. In practice, the quarter-wave plate is rotated by discrete angles θ_j such that:

$$\begin{aligned} A &= \frac{2}{N}\sum_{n=1}^{N} I\left(n\,\theta_j\right) \\ B &= \frac{4}{N}\sum_{n=1}^{N} I\left(n\,\theta_j\right)\sin\left(2n\,\theta_j\right) \\ C &= \frac{4}{N}\sum_{n=1}^{N} I\left(n\,\theta_j\right)\cos\left(4n\,\theta_j\right) \\ D &= \frac{4}{N}\sum_{n=1}^{N} I\left(n\,\theta_j\right)\sin\left(4n\,\theta_j\right) \end{aligned} \tag{3}$$

where N is the number of steps of the quarter-wave plate. Eq. [2] can be solved considering the eight possible combinations of the harmonic functions (sine and cosine) and the total intensity (parameter S_0). In other words, the minimum number of points for solving Eq. (2) is $N = 9$ or $\Delta\theta = 40°$ and, from the experimental point of view, the symmetry $I(\theta) = I(\theta + 2\pi)$. The new method to solve Eq. (2) was introduced by Basílio [42]. Stokes parameters are associated with the degree of polarization (P) of the emitted light by [25, 40]:.

$$P = \frac{\left(S_1^2 + S_2^2 + S_3^2\right)^{\frac{1}{2}}}{S_0}. \tag{4}$$

Moreover, it is also possible to obtain the dissymmetry factor g the circularly polarized light emission degree and the anisotropy factor r, it is associated with molecular ordering of the

[3]The emission ellipsometry experiment was performed using the setup described by Alliprandini et al. [25–27]. The samples were excited by a laser in 405 nm, and the emitted light was collected by a set of lenses and directed through an achromatic quarter-wave-plate (Newport 10RP54-1), as a compensator and an achromatic polarizer (Newport 10LP-VIS-B). The emission was detected and analyzed by an USB 2000 Ocean Optics spectrophotometer. The experiment was performed by rotating the compensator in its own plane from 0 rad (0°) to ~6.28 rad (360°), with steps of ~0.17 rad (10°). All measurements were performed at room temperature (~20°C) and under 10-4 Torr vacuum.

http://dx.doi.org/10.5772/66921

polymer chains [22, 43]. These factors are obtained from the Stokes parameters in Eqs. (5) and (6). The use of the dissymmetry factor g equation is conditioned to the referential adopted: the vertical direction (y-axis) as a positive sign and the horizontal direction (x-axis) as a negative sign.

$$g = \pm 2\frac{S_3}{S_0} \tag{5}$$

$$r = \frac{-2\frac{S_1}{S_0}}{3+\frac{S_1}{S_0}} \tag{6}$$

3.3.1. Emission ellipsometry in P3DDT

The results presented in this section are dedicated to study the photophysical effects of P3AT films. In addition, it is possible to correlate the energy transfer mechanisms [44, 45] and polarization light states [22, 25–27]. Note that, in general, they are intrinsic characteristics semiconductor polymers. Stokes parameters are directly related to the light polarization states and, consequently, with factors related to orientation of the polymer chains in the films [25, 26], in which it provides information about the samples molecular ordering along the polymer films. In principle, the electrochemically synthesis by cyclic voltammetry does not show a molecular order [9].

Figure 5 shows the parameters S_1/S_0, S_2/S_0 and S_3/S_0 in the spectral range of P3DDT emission obtained from the EE data for EtNBF01 and EtNBF10 films. The Stokes parameter values are virtually null in **Figure 5a**. It indicates that the light emitted by EtNBF01 films has random polarizing directions, i.e., depolarized with high probability of energy transfer from the photoexcited carriers in all directions of the polymeric film plane. It is important to remember that the excitation polarization is linear in the vertical direction (laboratory referential) and only chronophers with transition dipole in the parallel direction are excited. However, for EtNBF10 film thickness, we observe, in **Figure 4b** significant variation for the S_1/S_0 and S_2/S_0 parameters. In principle, the films grown using electrochemical techniques have not molecular order [40], but they may have partially polarized emission when the excitation light is linearly polarized [9, 24, 40, 43]. Another important observation is that the inversion signal of the S_1/S_0 curve occurs simultaneously with the reversal of S_2/S_0 curve. This may be explained, according to Foster's energy transfer process mechanism [44] by the excitation low molecular weight chains or oligomers that have their transition electric dipole or part thereof aligned with the excitation source, energy absorbing (405 nm). Thus, part of the absorbed light is transferred via Förster processes to another polymer with larger conjugation length, pristine and quinone structures, in a random direction, depolarized and decreasing the values of the S_1/S_0 factor close to zero above 525 nm. However, some excited oligomers and low molecular weight chains may not energy transfer increasing the emission in the parallel direction of excitation polarized light [9, 26]. It is observed in the S_1/S_0 factor from 475 to 525 nm spectral range due to the effects of the substrate-polymer or polymer-polymer interface [14, 22]. Finally, the S_3/S_0 parameter indicates that the light emitted does not have significant right or left circular polarization.

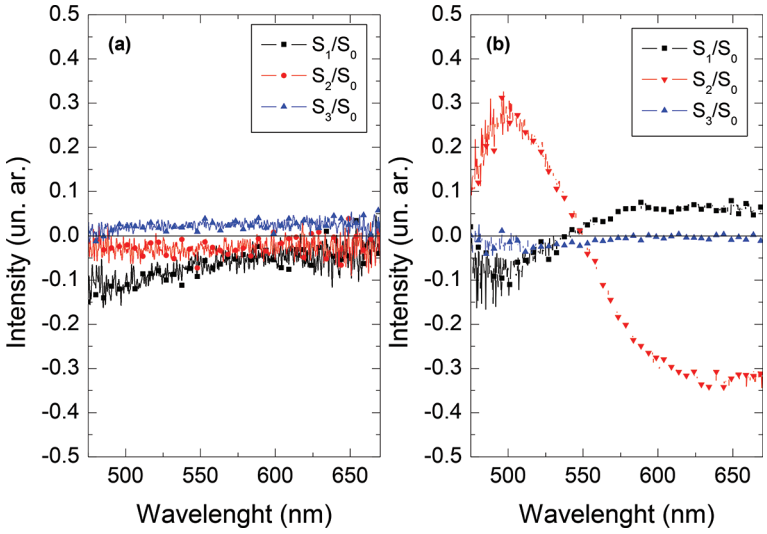

Figure 5. EE curves for films (a) EtNBF01 and (b) EtNBF10.

Förster energy transfer occurs when two conditions are met [44, 45]. First (i), the distance between the donor and the acceptor chromophores is up to ~ 10 nm, and (ii) second, parallelism condition, i. e, the electric dipole moment of the donor and the acceptor is parallel (aligned) or component of electric dipole moment of the acceptor is in the parallel direction of electric dipole moment of the donor [44]. Thus, when conjugated polymer segments absorb energy partially or totally is transferred to another, generally, higher conjugation polymer degree due to the electronic-vibrational relaxation mechanism. During the transfer process, the energy undergoes depolarization or rotational changes due to the misalignment of the dipoles in the same direction of the polymer main chains. As a result, when there is an emission in another part of the polymer or different polymer chains, a different polarization compared to the initial direction of the excitation polarization is obtained. Thus, the molecules, whose dipole or parts of its components are aligned with the excitation source, transfer energy to the polymers with greater conjugation lengths, causing an emission at lower energies. For the thick film in **Figure 5b**, the oligomers show great probability to transfer energy to other chains with greater conjugation lengths (quinone and pristine chains), parameter S_1/S_0 ~0, see spectral range assigned to oligomers between 475 and 525 nm. Similarly, **Figure 6** shows the EE curves for LiClO01 (**Figure 6a**) and LiClO10 (**Figure 6b**) films. Note that the emission of these films has horizontal and linear polarization, $S_1/S_0 > 0$ and polarization rotation to + 45° in relation to the polarization of the excitation light $S_2/S_0 < 0$. Circular polarization emission is not observed at S_3/S_0~0 to 500–675 nm. All samples processed using $LiClO_4$ have the same EE curves characteristics (**Figure 6**). An explanation for the absence of reverse bias directions and rotation observed for the films processed using the Et_4NBF_4 electrolyte is the preferential

http://dx.doi.org/10.5772/66921

formation of polymer chains with smaller conjugation lengths. It is compatible with the lower energy transfer at a higher spectral range <550 nm.

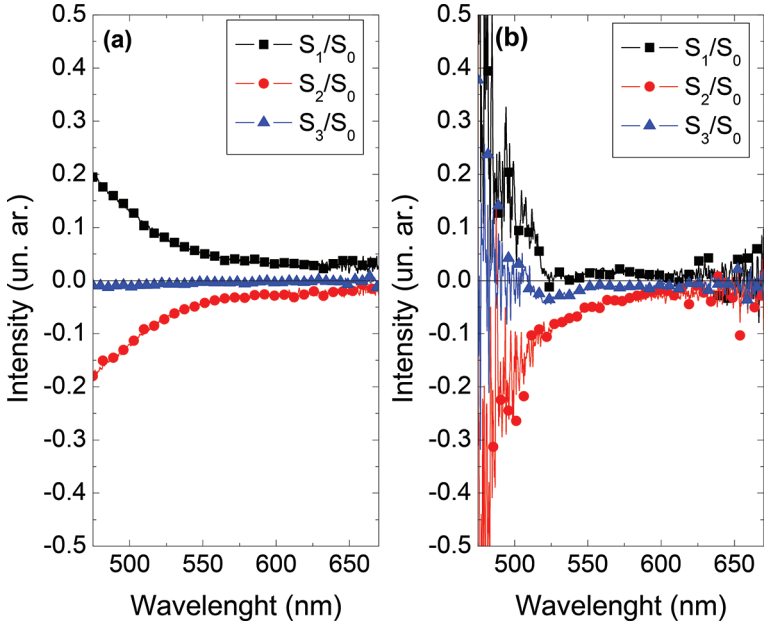

Figure 6. EE curves for films (a) LiClO01 and (b) LiClO10.

The polarization degree P (Eq. (4)) indicates the amount of light that is polarized, without differentiating between linearly or circularly polarized lights [25, 27, 40]. There are other two important parameter to quantify the polarization: the anisotropy factor r (Eq. (6)) that may be correlated with the direction of the polymer chains and the dissymmetry factor g (Eq. (5)) associated with the emission of the circularly polarized light [22, 40, 43]. The parameters P, r and g are obtained directly from Stokes parameter values [22, 43]. **Figures 5a** and **7a** show the polarization degree parameters for the EtNBF10 film in the function of the emission wavelength, presenting maximum at 495 and 630 nm. At 495 nm, we observe the signal inversion of S_2/S_0 coinciding with the minimal value for S_1/S_0 curves. The dissymmetry factor g in the emission spectral region is around ~5% or below, indicating that there is no emission of circularly polarized light [44]. **Figure 5b** shows the polarization degree P, anisotropy factors r and dissymmetry factor g for the LiClO10 film. We can observe that the polarization of the emitted light is high (~28%) at a low wavelength region (<550 nm) addressed with oligomers decreasing monotonic above 550 nm. The parameters r and g followed the spectral dependence of p. However, the parameter g does not display significant values. On the other hand, r values in the spectral range of oligomers emission are related to the decrease of energy transfer between adjacent polymer chain, according to reference [26]. The dissymmetry factor g has no significant intensity.

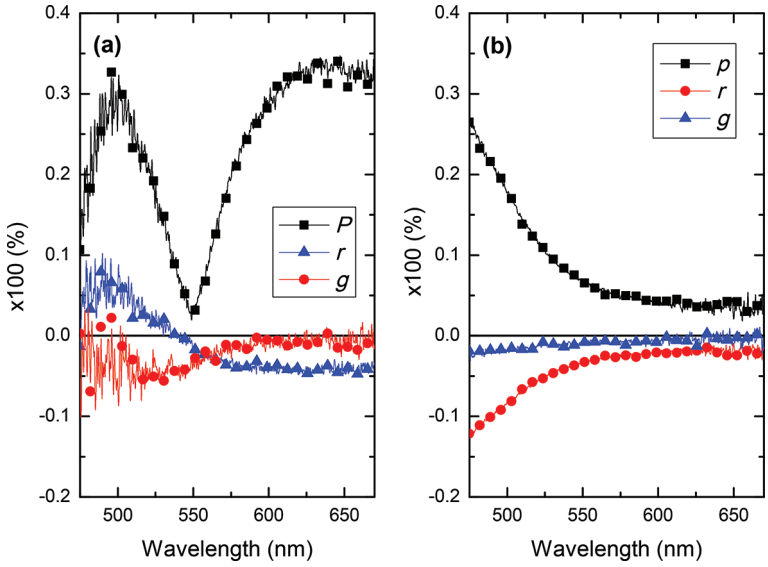

Figure 7. Polarization degree *P*, anisotropy factor *r* and dissymmetry factor *g* obtained from the Stokes parameters for the (a) EtNBF10 film and (b) LiClO10 film.

4. Conclusions

We showed the strong correlation between the optical properties of a P3AT polymer and the conditions of the polymer electrochemical growth, demonstrating that it is possible to control the optical properties of polymeric films by controlling the growth conditions. For this, we use different electrolytes during the synthesis of polymeric films, which were linked to the number of growing cycles, according to the cyclic voltammetry electrochemical technique. Electrochemical synthesis is shown in efficient growth polymeric films when the concentrations of the reagents are equilibrated, e.g., the concentration for electropolymerization of the P3DDT occurs homogeneously with 0.050 mol L^{-1} monomer and 0.100 mol L^{-1} of $LiClO_4$. Furthermore, it is possible to measure the energy gap E_g for organic semiconductor directly from the cyclic voltammogram.

Through the UV-Vis results, it is possible to conclude that the electrolytes reacted differently in this material, shifting the spectrum to other regions of absorption as occurs to electrolyte change. PL results showed the existence of several contributions in each spectrum, in which the highest intensity contributions, quinone and pristine are the result of two structures that the polymer chains can take through the interactions between each electrolyte/polymer. These contributions are able to shift the maximum emission in each spectrum when the film thickness increases, and more effectively for the films containing Et_4NBF_4. There are also contributions resulting from the oligomers emission and the electron-phonon interactions. The EE demonstrated energy transfer processes by the Förster mechanism, where the emission polarization is observed and this has gradually changed with increasing emission wavelength. However, it is an isotropic material when obtained for CV, shown by the anisotropy factor, *r*. These

analyses show that the Förster *energy transfer process* occurs in this material and is responsible for the emission throughout the spectral window. Furthermore, more accentuated emissions polarization can be related to the oligomer emission.

Results show that the P3ATs deposited electrochemically has great potential for application in optoelectronic organic devices since P3ATs optical properties can be easily adjusted by controlling the deposition. In addition, results also showed the great light absorption capacity and a broad spectral window for the P3DDT emission. Moreover, it is also observed the presence of electron-phonon combination, which can contribute to the occurrence of energy transfer or charge transfer significantly, enhancing the use of P3DDT in optoelectronic devices, which makes this promising material to form the active layer of multiple devices, such as organic light emitting diodes (OLEDs), photovoltaics, photodetectors and mobile devices screens (displays), among others.

Acknowledgements

The authors are grateful to the following Brazilian Agencies: FAPEMIG, CAPES, CNPQ and FUFMT.

Author details

Sankler Soares de Sá[1], Fernando Costa Basílio[2], Henrique de Santana[3], Alexandre Marletta[2] and Eralci Moreira Therézio[4]*

*Address all correspondence to: therezio@ufmt.br

1 Institute of Agricultural and Technology Science, Federal University of Mato Grosso, Rondonópolis, Brazil

2 Physics Institute, Federal University of Uberlândia, Uberlândia, Brazil

3 Chemistry Department, State University of Londrina, Londrina, Brazil

4 Institute of Exact and Natural Sciences, Federal University of Mato Grosso, Rondonópolis, Brazil

References

[1] Bundgaard E, Krebs FC. Low band gap polymers for organic photovoltaics. Solar Energy Materials and Solar Cells. 2007;**91**(11):954–985. DOI: 10.1016/j.solmat.2007.01.015

[2] Fujii A, Kawahara H, Yoshida M, Ohmori Y, Yoshino K. Emission enhancement in electroluminescent diode utilizing poly(3-alkylthiophene) doped with oxadiazole derivative. Journal of Physics D: Applied Physics. 1995;**28**(10):2135.

[3] Valaski R, Moreira LM, Micaroni L, Hümmelgen IA. The electronic behavior of poly(3-octylthiophene) electrochemically synthesized onto Au substrate. Brazilian Journal of Physics. 2003;**33**:392–397. DOI: 10.1590/S0103-97332003000200043

[4] Wang G, Yuan C, Lu Z, Wei Y. Enhancement of organic electroluminescent intensity by charge transfer from guest to host. Journal of Luminescence. 1996;**68**(1):49–54. DOI: 10.1016/0022-2313(95)00092-5

[5] Yoshino K, Manda Y, Sawada K, Onoda M, Sugimoto Ri. Anomalous dependences of luminescence of poly(3-alkylthiophene) on temperature and alkyl chain length. Solid State Communications. 1989;**69**(2):143–146. DOI: 10.1016/0038-1098(89)90379-7

[6] Ohmori Y, Uchida M, Muro K, Yoshino K. Visible-light electroluminescent diodes utilizing poly(3-alkylthiophene). Japanese Journal of Applied Physics. 1991;**30**(11B):L1938. DOI: 10.1143/JJAP.30.L1938

[7] Roncali J. Conjugated poly(thiophenes): synthesis, functionalization and applications. Chemical Reviews. 1992;**92**(4):711–738. DOI: 10.1021/cr00012a009

[8] Therézio EM, Duarte JL, Laureto E, Di Mauro E, Dias IL, Marletta A, et al. Analysis of the optical properties of poly(3-octylthiophene) partially dedoped. Journal of Physical Organic Chemistry. 2011;**24**(8):640–645. DOI: 10.1002/poc.1802

[9] Therézio EM, Franchello F, Dias IFL, Laureto E, Foschini M, Bottecchia OL, et al. Emission ellipsometry as a tool for optimizing the electrosynthesis of conjugated polymers thin films. Thin Solid Films. 2013;**527**:255–260. DOI:10.1016/j.tsf.2012.11.093

[10] Cervantes TNM, Bento DC, Maia ECR, Fernandes RV, Laureto E, Moore GJ, et al. The influence of different electrolytes on the electrical and optical properties of polymer films electrochemically synthesized from 3-alkylthiophenes. Journal of Materials Science: Materials in Electronics. 2014;**25**(4):1703–1715. DOI: 10.1007/s10854-014-1787-4

[11] Cervantes TNM, Bento DC, Maia ECR, Zaia DAM, Laureto E, da Silva MAT, et al. In situ and ex situ spectroscopic study of poly(3-hexylthiophene) electrochemically synthesized. Journal of Materials Science: Materials in Electronics. 2012;**23**(10):1916–1921. DOI: 10.1007/s10854-012-0880-9

[12] Maia ECR, Bento DC, Laureto E, Zaia DAM, Therézio EM, Moore JG, et al. Spectroscopic analysis of the structure and stability of two electrochemically synthesized poly(3-alkylthiophene)s. Journal of the Serbian Chemical Society. 2013;**78**(4):507–521. DOI: 10.2298/JSC120327111R

[13] Yoshino K, Hayashi S, Sugimoto R. Preparation and properties of conducting heterocyclic polymer films by chemical method. Japanese Journal of Applied Physics. 1984;**23**(12A):L899. DOI: 10.1143/JJAP.23.L899

[14] Therézio EM, Piovesan E, Anni M, Silva RA, Oliveira ON, Marletta A. Substrate/semiconductor interface effects on the emission efficiency of luminescent polymers. Journal of Applied Physics. 2011;**110**(4):044504. DOI: 10.1063/1.3622143

[15] Marletta A. Optical properties of organic semiconductors based on Light Emitting Polymers [thesis]. São Carlos: Universidade de São Paulo; 2001. DOI:10.11606/T.76.2001.tde-10022002-091803

[16] Therézio EM, Rodrigues PC, Tozoni JR, Marletta A, Akcelrud L. Energy-transfer processes in donor–acceptor poly(fluorenevinylene-alt-4,7-dithienyl-2,1,3-benzothiadiazole. Journal of Physical Chemistry C.2013;**117(**25):13173–13180. DOI: 10.1021/jp400823d

[17] Beaujuge PM, Amb CM, Reynolds JR. Spectral engineering in π-conjugated polymers with intramolecular donor-acceptor interactions. Accounts of Chemical Research. 2010; **43**(11):1396–1407. DOI: 10.1021/ar100043u

[18] van Mullekom HAM, Vekemans JAJM, Havinga EE, Meijer EW. Developments in the chemistry and band gap engineering of donor–acceptor substituted conjugated polymers. Materials Science and Engineering: R: Reports. 2001;**32**(1):1-40. DOI: 10.1016/S0927-796X(00)00029-2

[19] Therézio EM. Electrochemical synthesis, characterization and optical properties analysis of the poly (3-octylthiophene) (P3OT) [dissertation]. Londrina: Universidade Estadual de Londrina; 2009.

[20] Bento DC, Maia ECR, Cervantes TNM, Fernandes RV, Di Mauro E, Laureto E, et al. Optical and electrical characteristics of poly(3-alkylthiophene) and polydiphenylamine copolymers: applications in light-emitting devices. Synthetic Metals. 2012;**162**(24):2433–2442. DOI: 10.1016/j.synthmet.2012.12.006

[21] Kaur M, Gopal A, Davis RM, Heflin JR. Concentration gradient P3OT/PCBM photovoltaic devices fabricated by thermal interdiffusion of separately spin-cast organic layers. Solar Energy Materials and Solar Cells. 2009;**93**(10): 1779–1784. DOI: 10.1016/j.solmat.2009.06.009

[22] Therézio EM, Piovesan E, Vega ML, Silva RA, Oliveira ON, Marletta A. Thickness and annealing temperature effects on the optical properties and surface morphology of layer-by-layer poly(p-phenyline vinylene)+dodecylbenzenesulfonate films. Journal of Polymer Science Part B: Polymer Physics. 2011;**49**(3):206–213. DOI: 10.1002/polb.22180

[23] Therézio EM, Vega ML, Faria RM, Marletta A. Statistical Analysis in Homopolymeric Surfaces. In: Dr. Vijay Nalladega, editor. Scanning Probe Microscopy-Physical Property Characterization at Nanoscale. Rijeka: InTech; 2012. pp. 59–80. DOI: 10.5772/36461

[24] Marletta A, Vega ML, Rodrigues CA, Gobato YG, Costa LF, Faria RM. Photo-irradiation effects on the surface morphology of poly(p-phenylene vinylene) films. Applied Surface Science. 2010;**256**(10):3018-3023. DOI: 10.1016/j.apsusc.2009.11.066

[25] Alliprandini-Filho P, da Silva GB, Barbosa Neto NM, Silva RA, Marletta A. Induced secondary structure in nanostructured films of poly(p-phenylene vinylene). Journal of Nanoscience and Nanotechnology. 2009;**9**(10):5981–5989. DOI: 10.1166/jnn.2009.1293

[26] Alliprandini-Filho P, da Silva RA, Barbosa Neto NM, Marletta A. Partially polarized fluorescence emitted by MEHPPV in solution. Chemical Physics Letters. 2009;**469** (1–3):94–98. DOI: 10.1016/j.cplett.2008.12.057

[27] Alliprandini-Filho P, Silva RA, Silva GB, Barbosa Neto NM, Cury LA, Moreira RL, et al. Measurement of the emitted light polarization state in oriented and non-oriented PPV films. Macromolecular Symposia. 2006;**245–246**(1):406–409. DOI: 10.1002/masy.200651357

[28] Bento DC, Louarn G, de Santana H. Structural stability and improved properties of poly(3-alkylthiophenes) synthesized in an acid medium. Journal of Materials Science: Materials in Electronics. 2016;**27**(5):5371–5382. DOI: 10.1007/s10854-016-4437-1

[29] de Santana H, Maia ECR, Bento DC, Cervantes TNM, Moore GJ. Spectroscopic study of poly(3-alkylthiophenes) electrochemically synthesized in different conditions. Journal of Materials Science: Materials in Electronics. 2013;**24**(9):3352–3358. DOI: 10.1007/s10854-013-1254-7

[30] Silva TH, Barreira SVP, Moura C, Silva F. Electrochemical characterization of a self-assembled polyelectrolyte film. Portugaliae Electrochimica Acta. 2003;**21**(3):281–292.

[31] Bento DC, Maia ECR, Cervantes TNM, Olivati CA, Louarn G, de Santana H. C. Complementary study on the electrical and structural properties of poly(3-alkylthiophene) and its copolymers synthesized on ITO by electrochemical impedance and Raman spectroscopy. Journal of Materials Science: Materials in Electronics. 2015;**26**(1):149–161. DOI: 10.1007/s10854-014-2377-1

[32] Skompska M, Szkurłat A. The influence of the structural defects and microscopic aggregation of poly(3-alkylthiophenes) on electrochemical and optical properties of the polymer films: discussion of an origin of redox peaks in the cyclic voltammograms. Electrochimica Acta. 2001;**46**(26–27):4007–4015. DOI: 10.1016/S0013-4686(01)00710-1

[33] Obaid AY, El-Mossalamy EH, Al-Thabaiti SA, El-Hallag IS, Hermas AA, Asiri AM. Electrodeposition and characterization of polyaniline on stainless steel surface via cyclic, convolutive voltammetry and SEM in aqueous acidic solutions. International Journal of Electrochemical Science. 2014;**9**(2):1003–1015.

[34] Eckhardt H, Shacklette LW, Jen KY, Elsenbaumer RL. The electronic and electrochemical properties of poly(phenylene vinylenes) and poly(thienylene vinylenes): an experimental and theoretical study. The Journal of Chemical Physics. 1989;**91**(2):1303–1315. DOI: 10.1063/1.457153

[35] Österbacka R, An CP, Jiang XM, Vardeny ZV. Two-dimensional electronic excitations in self-assembled conjugated polymer nanocrystals. Science. 2000;**287**(5454):839. DOI: 10.1126/science.287.5454.839

[36] Kobayashi T, Hamazaki J-i, Kunugita H, Ema K, Endo T, Rikukawa M, et al. Coexistence of photoluminescence from two intrachain states in polythiophene films. Physical Review B. 2003;**67**(20):205214. DOI: 10.1103/PhysRevB.67.205214

[37] Kanemoto K, Sudo T, Akai I, Hashimoto H, Karasawa T, Aso Y, et al. Intrachain photoluminescence properties of conjugated polymers as revealed by long oligothiophenes and polythiophenes diluted in an inactive solid matrix. Physical Review B. 2006;**73**(23):235203. DOI: 10.1103/PhysRevB.73.235203

[38] Alves MRA, Calado HDR, Matencio T, Donnici CL. Thiophene-based oligomers and polymers: syntheses and applications. Química Nova. 2010;**33**(10):2165–2175. DOI: 10.1590/S0100-40422010001000029

[39] Chan HSO, Ng SC. Synthesis characterization and applications of thiophene-based functional polymers. Progress in Polymer Science. 1998;**23**(7):1167–1231. DOI: 10.1016/S0079-6700(97)00032-4

[40] Collet E. Polarized Light: Fundamentals and Applications. New York: Marcel Dekker; 1993. 581 p.

[41] Cimrová V, Remmers M, Neher D, Wegner G. Polarized light emission from LEDs prepared by the Langmuir-Blodgett technique. Advanced Materials. 1996;**8**(2):146–149. DOI: 10.1002/adma.19960080209

[42] Basílio FC. Implementation of the New Technique Raman Spectroscopy by Elipsometry no Chiral Molecules Study [dissertation]. Uberlândia: Universidade Federal de Uberlândia; 2014.

[43] Therézio EM, da Silva SFC, Dalkiranis GG, Alliprandini Filho P, Santos GC, Ely F, et al. Light polarization states of a cholesteric liquid crystal probed with optical ellipsometry. Optical Materials. 2015;**48**:7–11. DOI: 10.1016/j.optmat.2015.07.010

[44] Förster T. Intermolecular energy migration and fluorescence. Annalen der Physik. 1948;**437**(1–2):55–75.

[45] Dexter DL. Cooperative optical absorption in solids. Physical Review. 1962;**126**(6):1962–7.

Chapter 7

Magnetic Properties of Hausmannite Thin Films

Petya Petkova

Additional information is available at the end of the chapter

http://dx.doi.org/10.5772/66533

Abstract

The magnetic properties of hausmannite thin films are investigated in this chapter. The Verdet constant and angle of Faraday rotation are determined. The magnetic anisotropy of Mn_3O_4 is explained by the measurement of the zero-field cooled (ZFC) and field cooled (FC) curves. This experiment is connected with the presentation of the ferromagnetic to superparamagnetic transition of the hausmannite.

Keywords: hausmannite Mn_3O_4, Faraday effect, verdet constant, ferromagnet, superparamagnet

1. Introduction

The hausmannite Mn_3O_4 can be fabricated by many methods, but the spray pyrolysis method can give it the highest quality. This material is very interesting because it is a transition metal oxide and has application in semiconductor devices [1]. This oxide has two valance states on manganese—Mn^{2+} and Mn^{3+}. Thus, spinel Mn_3O_4 occurs in nature as the mineral hausmannite [$Mn^{2+}Mn_2{}^{3+}O^4$]. The Mn^{2+} cations occupy the tetrahedral sites and Mn^{3+}cations occupy the octahedral sites [2]. The nanoparticles of Mn_3O_4 thin film behave as single-domain ferromagnets. However, above the blocking temperature, the particles behave as paramagnets due to the dominance of thermal fluctuations over the magnetocrystalline anisotropy energy. These nanoparticles have much higher magnetic moments than other paramagnets and are called superparamagnet.

The detailed investigation of magnetic properties of hausmannite thin film is presented in this chapter.

2. Method of preparation and characterization techniques

Several techniques have been used to prepare thin films of these types of transparent and conductive materials to meet the requirements of search and industries such as MOCVD (organometallic chemical vapor deposition) [3], chemical vapor transport (CVT) [4], sputtering [5] and laser ablation [6, 7], which are generally either sophisticated or expensive and hence the need for a simple, easy to meter out and less expensive technique. In addition to these techniques, spray pyrolysis [8–11] has received a little bit of extra attention because of its simplicity and cost-effectiveness as it does not require sophisticated vacuum apparatus. Furthermore, this method can be selected for film production of large area with size grain controllable by controlling the doping concentration. Also, this technique leads to a large production area and it permits also the formation of thin films with possible control of oxygen vacancy by means of the use of both appropriate precursors and postannealing treatments in air [12–15].

Thin films of Mn_3O_4 were grown at 350°C on 1 × 2 cm^2 glass substrate using the spray pyrolysis technique. The substrate temperature was fixed using a digital temperature controller with a k-type thermocouple. The aqueous solution with a flow of about 4 ml/min contains magnesium chloride ($MnCl_2.6H_2O$) 0.1 M as precursor. The distance between the nozzle and the substrate was about 27 cm. Spray solutions quantity (75 ml) was kept fixed during the growth. The filtered compressed nitrogen air was used as gas carrier at a flow of 4 l/min. The total deposition time was maintained at 20 min. After deposition, the coated substrates were allowed to cool down naturally to room temperature (**Figure 1**).

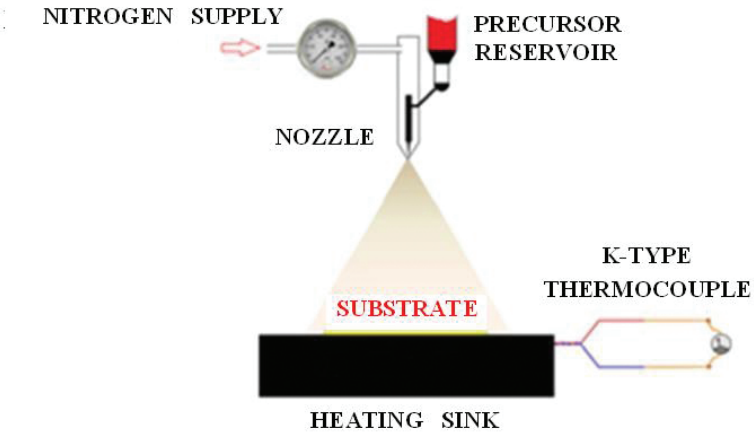

Figure 1. The experimental set up for the spray pyrolysis technique.

The crystalline structure was analyzed by X-ray diffraction, using a Siemens D500 diffractometer with monochromatic CuKα radiation (λ = 1.54 Å) [16]. The surface morphology of the Mn_3O_4 thin film is further analyzed using atomic force microscope (AFM) using a Veeco digital

http://dx.doi.org/10.5772/66533

instrument 3 A microscope. The sample was probed in a tapping mode with a nanometer scale.

3. Magnetic study

The magneto-optic Faraday effect presents the connection between optics, magnetism and atomic physics. Faraday rotation manifests itself as a rotation of the polarization plane of the light passing through the sample in the presence of a magnetic field and is characterized by the Verdet constant (V) of the investigated sample (**Figure 2**). The rotation angle φ can be expressed by the formula [17]:

$$\varphi(\lambda) = A/(\lambda^2 - \lambda_0{}^2), \tag{1}$$

where A is a constant determined from the matrix elements of the interband transitions, λ is the wavelength and λ_0 is the wavelength related to the interband transitions and corresponding to the natural frequency $\omega_0 = 2\pi/\lambda_0$ of an effective harmonic oscillator. The relationship between the rotation angle and the Verdet constant is $\varphi = VBl$, where B is the magnetic induction of the field and l is the sample thickness (**Figure 3**). The magneto-optic anomaly factor γ (**Figure 4**) can be taken as a measure of the degree of covalency that exists in the bonds connecting the ions and atoms [18]:

$$\gamma = \frac{\varphi}{\frac{e}{2mc^2}\lambda D} \tag{2}$$

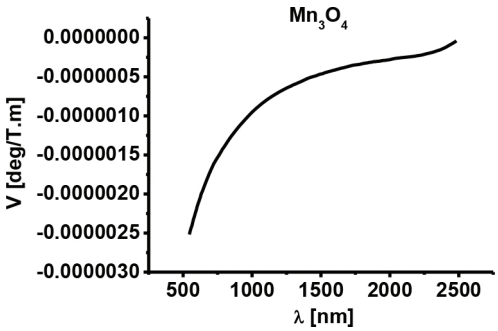

Figure 2. The Verdet constant for Mn_3O_4 in the spectral region 500–2500 nm.

In the paramagnetic materials, the anomaly factors γ can vary with the wavelength of the incident light, even if there is only one absorption frequency contributing to dispersion. The dispersivity of the investigated crystal can be presented by the following equation:

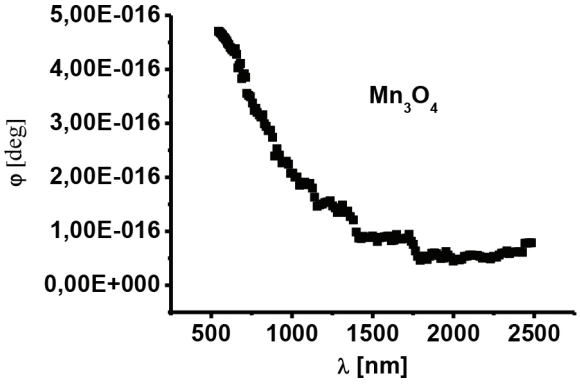

Figure 3. The Faraday rotation angle as a function of the wave length (500–2500 nm) for Mn_3O_4 thin film.

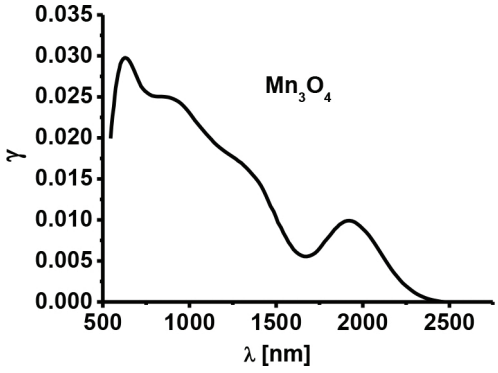

Figure 4. The magneto-optic anomaly factor γ for hausmannite in the spectral region 500–2500 nm.

$$D = -\frac{\gamma}{c}\frac{d^2n}{d\lambda^2}. \tag{3}$$

$$\gamma = -\frac{VBl}{\frac{e\lambda^2}{2mc^2}\frac{d^2n}{d\lambda^2}}. \tag{4}$$

The spectral dependence of the spin-spin exchange interaction constant K in the case of Mn_3O_4 thin film is presented in **Figure 5**. It can be calculated by the following formula [19]:

$$K(\lambda) = \frac{V\left[\left(\left(\frac{\lambda}{\lambda_g}\right)^2 - 1\right)\right]^{3/2}}{\chi^{\lambda}}, \tag{5}$$

where V is the Verdet constant, χ is the magnetic susceptibility of the sample (**Figure 6**) and λ_g represents the band gap of the material. For the investigated vanadium doped crystal

http://dx.doi.org/10.5772/66533

λ_g = 556 nm [16]. When the spin-spin exchange interaction constant has negative values, the spins align antiparallel to each other so that the net magnetization is zero. Therefore, the material is antiferromagnet and it is modeled to be made up of two sublattices [20].

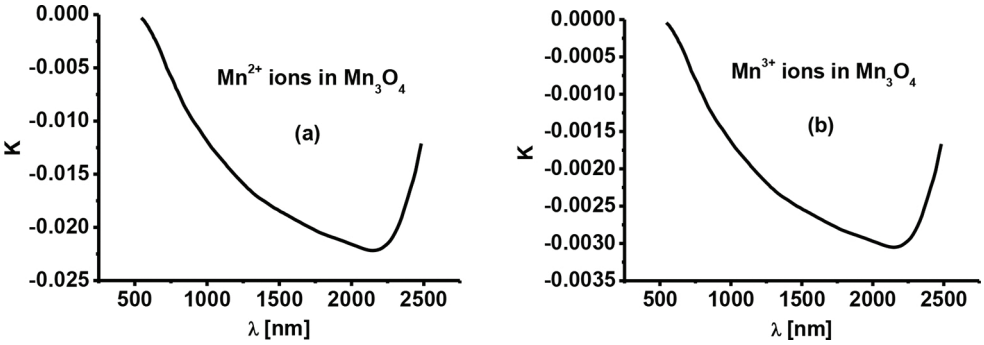

Figure 5. The constant of spin-spin exchange interaction $K(\lambda)$ for Mn^{2+} (a) and Mn^{3+} (b) in Mn_3O_4 thin film (500–2500 nm).

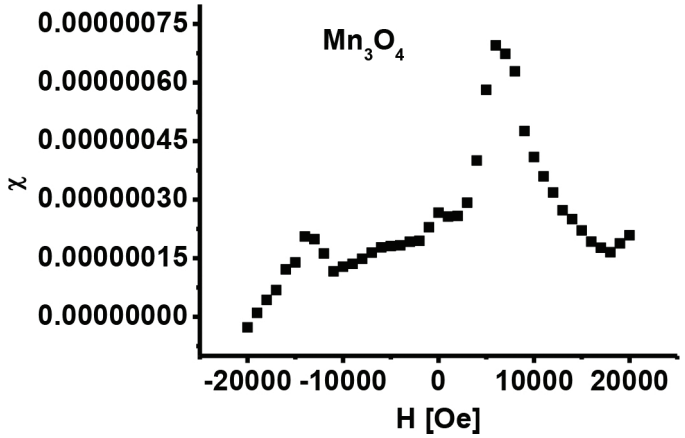

Figure 6. The dependence $\chi(H) = dM/dH$ for Mn_3O_4 in the magnetic field from −20,000 to 20,000 Oe.

The exchange interaction energy leads to the alignment of neighboring atomic moments and this forms magnetic domains. The magnetostatic interaction energy tries to break them into smaller domains oriented antiparallel to each other. The domain size depends on the relative counterbalance between both energies. The system is composed of a single domain, when the magnetostatic energy does not allow the breaking of domains into smaller parts. This condition is connected with the critical value r_c of the radius of a spherical particle. If the rotation of the atomic magnetic moments is coherent (the structure is a single-domain one), then the particle can be characterized by its total magnetic supermoment $|\vec{\mu}_p| = M_S V$, where V is the particle volume and M_S is saturation magnetization. The ferromagnetism and super paramagnetism are observed, respectively, below and above the blocking temperature T_B. Its origin is

connected with magnetic anisotropy within particles. This anisotropy tends to orientate the particle supermoment along some preferential direction.

The spin-orbit coupling and dipolar interaction dictate preferential orientation directions of the magnetic moments because of the finite size of the particles. The magnetic anisotropy energy E_A of the particles can be described by a simple model. This model includes two main contributions: crystalline and shape, which are connected with the core and surface atoms, respectively. When the particles are spherical and the anisotropy is uniaxial crystalline, the considered situation is the simplest [21]. If the magnetic anisotropy is proportional to the particle volume, then $\vec{K}_{\text{eff}} = KV\hat{n}$, where K is the effective uniaxial anisotropy constant (per unit volume) and $\hat{n}$ is the unitary vector describing the easy-magnetization anisotropy. The energy term for the i particle can be written as:

$$E_A^{(i)} = -K_i V_i \left(\frac{\vec{\mu}_i \cdot \hat{n}_i}{|\vec{\mu}_i|} \right)^2 = -K_i V_i \cos^2\theta, \tag{6}$$

where θ_i is the angle between the magnetic supermoment of the particle and the easy anisotropy axis (**Figure 7**). The moment of the particle has therefore two preferred orientations, energetically equivalent, along the easy-magnetization anisotropy axis direction. Both directions are separated by an energy barrier E_B of height K_iV_i.

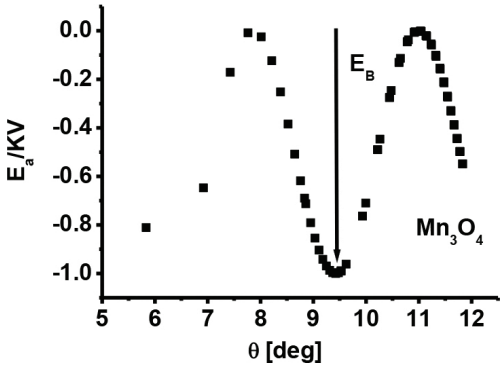

Figure 7. Schematic drawing of the ideal simplest model of noninteracting and parallel aligned easy axes along the applied field.

If the particles are magneto anisotropic, the calculation of equilibrium magnetization is complicated. The special role for nanoparticles having superficial anisotropy is the violation of local symmetry surroundings and crystal field change that acts on the magnetic ions from the surface. The simplest type of magnetic anisotropy is the easy anisotropy axis.

When external magnetic field is applied over the nanoparticles, it tries to orientate their magnetic moments in the direction of its action. Therefore, if the magnetic field is applied perpendicular of anisotropy axis and the orientation of magnetic moment of the particle is labeled with i, the next equation is fulfilled:

http://dx.doi.org/10.5772/66533

$$E^i = E_A^{(i)} + E_Z^{(i)} = -K_i V_i \left(\frac{\vec{\mu}_i \hat{n}_i}{|\vec{\mu}_i|} \right)^2 - \vec{\mu}_i . \vec{H}, \tag{7}$$

where E_A and E_Z are Zeeman energies.

The influence of external magnetic field in the orientation of magnetic supermoments is known as Stoner-Wohlfart model [22]. They assume that the coherent rotation of atomic magnetic moments exists and the magnetic field is applied at a certain angle θ_0 with respect to the easy anisotropy axis. When the temperature effects are ignored the problem can be solved with minimal number of energetic arguments. The situation is very interesting, when we can describe the change of magnetic moments in dependence of anisotropic energy barrier and the temperature T_B. This is the reason for the study of a simple case when the field is applied parallel to the easy anisotropy axis. It should also be noted that the particles are identical and do not interact with each other. The application of the field leads only to their arrangement in the direction of the easy anisotropy axis. Thus, the following equation can be written (**Figure 8**):

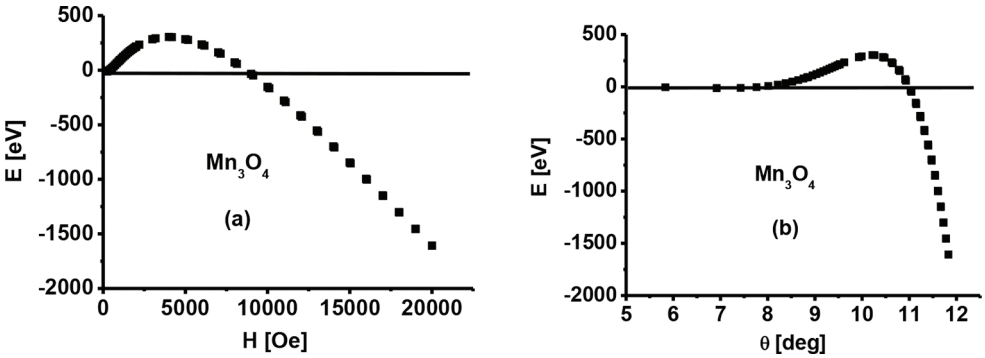

Figure 8. The dependence of anisotropic energy barrier from the external magnetic field (a) and the angle between the applied field and easy anisotropy axis (b).

$$E = -KV\cos^2\theta - M_S VH\cos\theta \tag{8}$$

when $H < 2K/M_S$, Eq. (8) gives two local minima (the directions of easy magnetization) at $\theta = 0$, π with values $E_{\min} = -KV \pm M_S VH$ (**Figure 9**) and one maximum (the direction of hard magnetization) at $\theta = \arccos(HM_S/2K)$, with value $E_{\max} = KV(HM_S/2K)^2$. The direction of hard magnetization is perpendicular of the anisotropy axis in the case, when $H = 0$. The value $\theta = 0$ is valid, when the moment of particles is oriented parallel to the magnetic field (↑↑). The equation $\theta = \pi$ is fulfilled when the orientation of the moment of the particles is antiparallel to the magnetic field (↑↓). The difference between the shapes of the energy wells is connected with the different energy barriers. These barriers depend on the orientation of the moments of particles to the applied field which can be written as $E_B^{\uparrow\downarrow}$ and $E_B^{\uparrow\uparrow}$ for the cases of antiparallelism and parallelism, respectively.

The anisotropy field of the particles is introduced as $H_A = 2K/M_S$. The energy barriers can be calculated as the difference between the minimal and maximal energies: $E_B^{\uparrow\downarrow} = \frac{KV}{H_A^2}(H-H_A)^2$ and $E_B^{\uparrow\uparrow} = \frac{KV}{H_A^2}(H+H_A)^2$ (**Figure 10**). The difference between the heights of energy barriers also shows a change in the characteristic time for relaxation of the particles, since it depends on the relative orientation of the magnetic dipoles to the field: antiparallel oriented particles have smaller energy barrier in comparison with the particles which are oriented along the easy anisotropy axis. They have also small heat energy sufficient to overcome the barrier. The parallel oriented particles are limited by deeper anisotropy well and the jump of their magnetic moments requires higher heat energy. When the particle has to rotate its magnetic moment, the energy of jump beyond the energy barrier is $E_B \approx KV$. The characteristic time of heat fluctuations of the magnetic moments can be presented by the formula [23]:

$$\tau = \tau_0 \exp(E_B/k_B T), \tag{9}$$

where $E_B/k_B T \geq 1$.

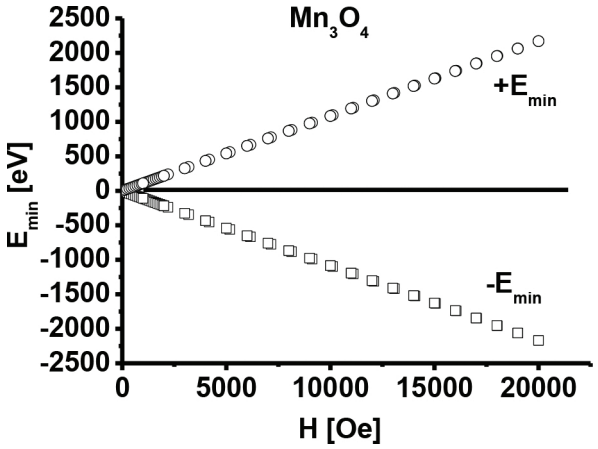

Figure 9. The local minimal energy $\pm E_{\min}(H)$ in the directions of easy magnetization for the hausmannite Mn_3O_4.

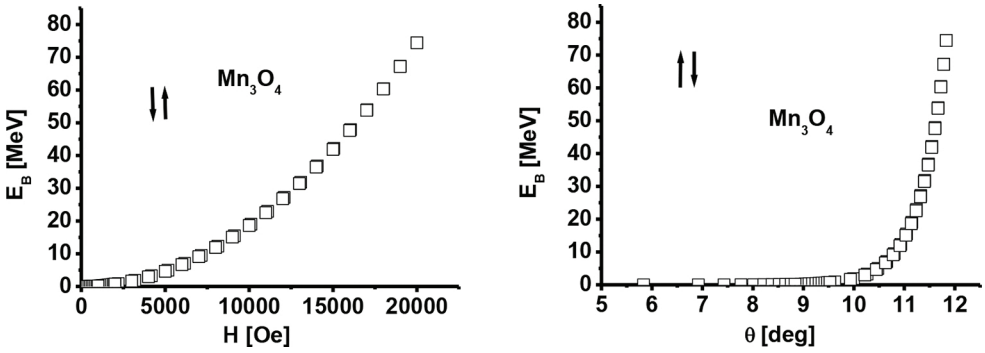

Figure 10. The dependence of the energy barriers E_B of: applied magnetic field and angle θ in the case of antiparallelism.

http://dx.doi.org/10.5772/66533

The multiplier τ_0 depends on many parameters such as temperature, gyromagnetic ratio, saturation magnetization, anisotropy constant and the size of the energy barrier. It is of the order of $10^{-9} - 10^{-13}$ s [24]. The formula (9) determines the characteristic time of establishing heat equilibrium in the system of noninteracting single-domain magnetic particles. At high temperatures, the following inequality is fulfilled: $E_B/k_BT \ll 1$. Therefore, the time of transition of the system in the state with minimal energy is small in comparison with the characteristic time of measurement τ_m. In this case, the system should not appear magnetic hysteresis. When $E_B/k_BT \gg 1$, the time of transition of a system in the equilibrium state depends on the size of the particles. If $\tau_m > \tau$, the system is in the super paramagnetic state and it quickly reaches equilibrium magnetization, when the temperature or the external field change. In the opposite case, when the external magnetic field changes, the system does not fail to relax in the new equilibrium state for the time τ_m and its magnetization does not change. The case when $\tau_m = \tau$ is connected with the blocking temperature:

$$T_B = \frac{KV}{25k_B}. \tag{10}$$

Formula (10) presents the temperature T_B, when the magnetic field is zero. This temperature decreases with the increasing of the external magnetic field by the law:

$$T_B(H) = T_B(0)\left(1 - \frac{H}{H_c}\right)^k, \tag{11}$$

where $k = 2$ for small fields and $k = 2/3$ for big fields and $H_c = \frac{2k}{M_S}$.

The magnetization curve increasing to reaching saturation magnetization is measured in the study of the magnetic properties of the hausmannite Mn_3O_4 which containing nano-objects. To determine the temperature dependence of the magnetic moment Mare carried out two types of measurements—cooling in zero magnetic field (zero-field-cooling, ZFC) and cooling in a nonzero field (field-cooling, FC). The sample is cooled (to liquid helium temperature) during the method of ZFC in the absence of a magnetic field and then a small field (2–5 kOe) is included. The temperature values begin slowly to increase and the magnetic moment (M_{ZFC}) values can be registered. The technique FC differs from ZFC only by the fact that a sample is cooled in a nonzero magnetic field. The curves $M_{ZFC}(T)$ and $M_{FC}(T)$ for the magnetic nano-objects coincide at sufficiently high temperatures, but they begin to vary below a temperature T_H (irreversibility temperature). The curve $M_{ZFC}(T)$ has a maximum at a certain temperature T_{max} and it increases monotonically down to very low temperatures (**Figure 11**). The dependence of the magnetization from the applied field at two various temperatures is shown in **Figure 12(a)** and **(b)**. For an idealized system containing similar nanoparticles with uniaxial anisotropy and random orientation of easy magnetization axis, the difference of the temperature dependence $M_{ZFC}(T)$ and $M_{FC}(T)$ at a qualitative level follows from Eq. (8). In the case of zero field during the cooling below the blocking temperature, the magnetic moments of the particles are oriented along their axes of easy magnetization ($\theta = 0$ in Eq. (8)). The total magnetic moment of the system is zero in the beginning and in the end of the cooling process. The magnetic moments for which $\theta < 90°$ (see Eq. (8)) it is not necessary to overcome the

energy barrier, when the external field H is included. Therefore, they turn to a position with minimum energy, creating a nonzero magnetization of the system. In contrast, the magnetic moments for which the external field is included ($\theta > 90°$) are separated from the minimum energy of the potential barrier. They can overcome only this barrier for a very long time (see Eq. (9)). Therefore, in the case of ZFC measurements ($T < T_B$), the system is in a metastable state with a small total magnetic moment $\frac{M_S^2 H}{3k_V}$, which does not depend on the temperature.

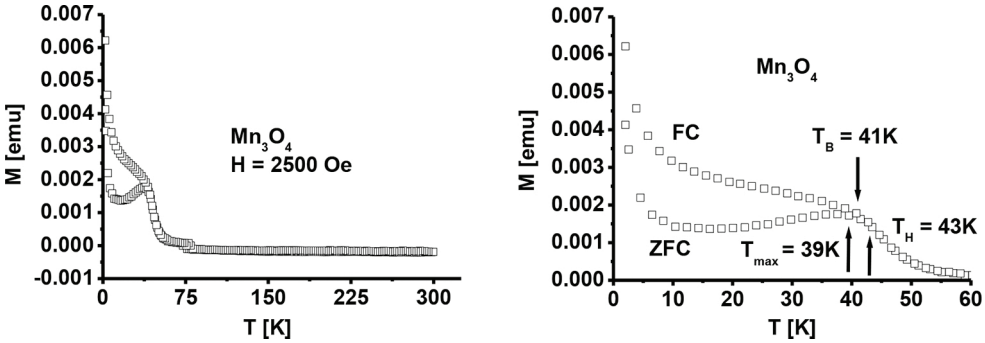

Figure 11. FC and ZFC induced magnetization as a function of temperature measured in a 2500 Oe field.

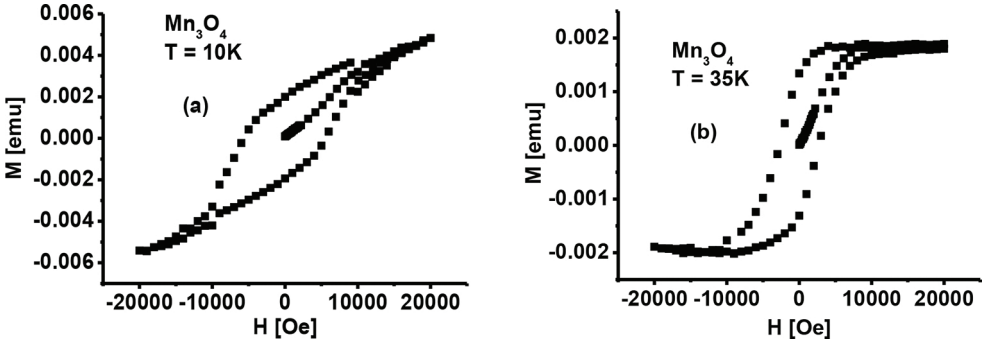

Figure 12. The magnetization $M(H)$ of hausmannite thin film for two temperatures $T = 10$ K (a) and $T = 35$ K (b).

At $T = T_B$, the system jumps into a stable superparamagnetic state with magnetic moment

$$M_{ZFC} \approx \frac{M_S^2 VH}{3k_B T} \tag{12}$$

When $M_S VH \ll k_B T$ and random orientation of the easy magnetization axes of particles, formula (12) is also valid for $T > T_B$. The sample is cooled in a nonzero magnetic field during FC

http://dx.doi.org/10.5772/66533

measurement and the magnetization at temperatures above T_B is determined by formula (12). At $T < T_B$, the system cannot change its magnetization during the measurement. Therefore, the magnetic moment which is determined by the FS method for $T < T_B$ is

$$M_{\mathrm{ZFC}} \approx \frac{M_S^2 VH}{3k_B T} = \text{const.} \tag{13}$$

The curves $M_{\mathrm{ZFC}}(T)$ and $M_{\mathrm{FC}}(T)$ are not separated at $T = T_B$ for a system consisting of a single-domain nanoparticles with dispersion of the size, the shape, etc. Their separation realizes at a higher temperature $T_H > T_B$, where T_H is called the irreversibility point. Another characteristic point on the curve $M_{\mathrm{ZFC}}(T)$ is the temperature $T_{\max}$ which is often equated with the average blocking temperature of the system $<T_B>$. At temperatures below $<T_B>$ we can observe the increase of $M_{\mathrm{FC}}(T)$ that replaced section "saturation" and sometimes we can observe a maximum [25]. The value of T_H can be identified with the blocking temperature for the particles with a maximum size and the temperature $T_{\max}$ corresponds to a blocking temperature for particles with minimum size. However, all of these characteristic temperatures (as well as their relationship with the particle size distribution by volume) may depend on the cooling rate and the subsequent heating of the sample. The intensity of the interaction between the particles also influences on the characteristics temperatures. If the heating rate of the sample is much smaller than its cooling rate, a maximum may be formed on the curve $M_{\mathrm{FC}}(T)$ at $T << T_B>$ [26].

Note that the difference between the curves $M_{\mathrm{ZFC}}(T)$ and $M_{\mathrm{FC}}(T)$ is not observed only in systems of magnetic nano-objects, but also in macroscopic magnets with disorder elements (frustration of exchange bonds, topological disorder, structural defects) and even in ordered ferromagnets with a large magnetic anisotropy. The difficulties of theoretical research of the magnetic hysteresis in nano-objects consist in the fact that the phenomenon is nonlinear, nonequilibrium and nonlocal and it is caused by the existence of energy minima (due to the magnetic anisotropy) and separated barriers which have complicated dependence of the external magnetic field. The results of theoretical studies of simple models rarely give an acceptable description for real magnetic nanomaterials since their microstructure do not account, in particular, the influence of boundaries and defects on the local magnetization is not taken into account. The ferromagnetic-to-superparamagnetic transition of the hausmannite particles in the zero-field cooled (ZFC) and field cooled (FC) curves is presented in **Figure 8**.

The orientation of electron spin in the manganese ions is very interesting for study. One of the electrons of the inner shell is responsible for the magnetism and its spin is oriented upwards. If the conductivity electrons move in the same region, where there is the motion of "magnetic" electrons than their spins rotate in the opposite direction. Thus, the conductivity electrons can rotate the electron spins of the other ions. This double interaction is equivalent of the interaction between two "magnetic" electrons which are oriented in one direction. This means that the neighboring spins have to be parallel, which is a result from the action of intermediate environment. This mechanism does not require all electrons to be oriented upwards. It is sufficient that conductivity electrons can be slightly oriented downwards. Thus, the possibility for the rotation of "magnetic" electrons upwards increases.

The energy of electron spin can be presented as (**Figure 13**):

$$x = |\mu|\left(H + \frac{\lambda M}{\varepsilon_0 c^2}\right), \tag{14}$$

where $\mu = 2.8363*10^{-4}$ eVT^{-1}, $\lambda = 5700$ m^{-1}, $\varepsilon_0 = 8.8542*10^{-12}$ Fm^{-1} and $c = 8*10^8$ m/s (**Figure 13**).

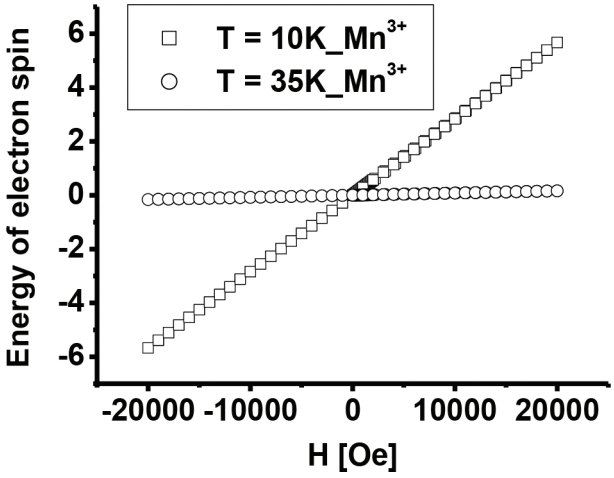

Figure 13. The energy of electron spin x as a function of the intensity of magnetic field H for Mn^{3+} ions at temperatures T = 10 K and T = 35 K.

On the other hand, we can write that

$$x = |m|(H + dM/\varepsilon_0 c^2)/kT, \tag{15}$$

where $d = 2.2971 \times 10^{-10}$ m.

The magnetic moment of the electron is

$$|m| = \frac{|\mu|\left(H + \frac{\lambda M}{\varepsilon_0 c^2}\right)}{(H + dM/\varepsilon_0 c^2)/kT} = 2.444110^{-7}, \tag{16}$$

where $k = 8.6173 \times 10^{-5}$ eVK^{-1}:

$$thx = th[|m|(H + dM/\varepsilon_0 c^2)/kT] \tag{17}$$

The energy of interaction between two electrons is expressed by the next equation (**Figure 14**):

http://dx.doi.org/10.5772/66533

$$\langle U \rangle = -N|\mu|\left(H + \frac{M}{2\varepsilon_0 c^2}\right) thx \tag{18}$$

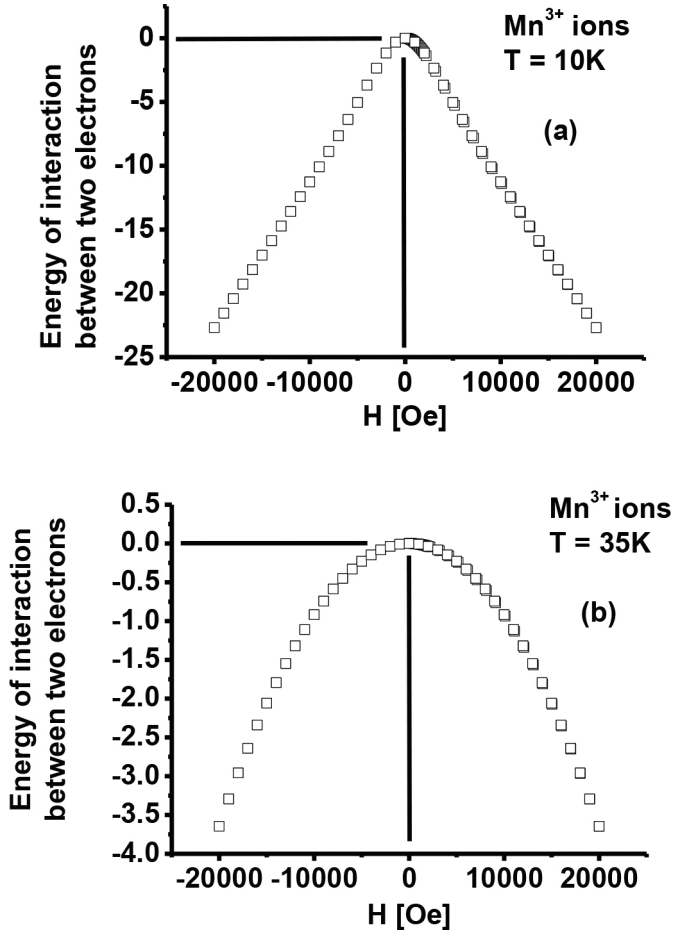

Figure 14. The average value of the energy of interaction between two electrons in Mn^{3+} ions as a function of the intensity of magnetic field *H*: (a) *T* = 10 K and (b) *T* = 35 K.

4. Conclusions

The magneto-optic anomaly factor γ for the hausmannite thin films decreases with the increasing of the wave length. The spin-spin exchange interaction constant *K* decreases to λ_1 = 2172 nm (for Mn^{2+} ions) and λ_2 = 2180 nm (for Mn^{3+} ions) and after that it begins to increase. The magnetic susceptibility of Mn_3O_4 has maximal value, when the intensity of applied magnetic

field is 5868 Oe. The anisotropic energy barrier decreases with the increasing of H and θ. The energy barrier increases quadratic with the increasing of H and θ. The energy of electron spin x has bigger values for Mn^{3+} ions in the case when T = 10 K. The values of energy of interaction between two electrons are bigger when T = 35 K.

Acknowledgements

The author would like to express here gratefulness to Pr. Dr. Ing. Karem Boubaker, Unité de physique des dispositifs à semi-conducteurs, Tunis EL MANAR University, Tunisia, for providing hausmannite thin films for investigation. The author would like to thank for the financial support of the project RD-08-109/08.02.2016 from Shumen University "Konstantin Preslavsky."

Author details

Petya Petkova

Address all correspondence to: petya232@abv.bg

Department of Experimental Physics, Faculty of Natural Sciences, Konstantin Preslavsky University of Shumen, Shumen, Bulgaria

References

[1] Xiao J, Yang S, Wan I, Xiao F, Wang S, J. Power Sources 245 (2014) 1027

[2] Chen W Z, Jiao Z, Wu H M, Shek H C, Wu L M C, Lai L K J, Progr. Mater. Sci. 56 (2011) 901

[3] Sanga B, Nagoyab Y, Kushiyab K, Yamase O, Sol. Energ. Mat. Sol. Cells 75 (2003) 179

[4] Fu Q, Hu L, Yu D, Sun J, Zhang H, Huo B, Zhao Z, Mater. Lett. 63 (2009) 316

[5] Shimomura T, Kim D, Nakayama M, J. Lumin. 112 (2005) 191

[6] Henley J S, Ashfold R N M, Cherns D, Surf. Coat. Technol. 177–178 (2004) 271

[7] Sasi B, Gopchandran G K, Sol. Energ. Mat. Sol. Cells 91 (2007) 1505

[8] Boukhachem A, Boughalmi R, Karyaoui M, Mhamdi A, Chtourou R, Boubaker K, Amlouk M, Mater. Sci. Eng. B 188 (2014) 72

[9] Krunks M, Soon J, Unt T, Mere A, Mikli V, Vacuum 107 (2014) 242

[10] Sharmaa R, Acharya D A, Shrivastava B S, Shripathi T, Ganesan V, Optik 125 (2014) 6751

[11] Kerli S, Alver U, Yaykaşlı H, Appl. Surf. Sci. 318 (2014) 164

[12] Boukhachem A, Kamoun O, Mrabet C, Mannai C, Zouaghi N, Yumakc A, Boubaker K, Amlouk M, Mater. Res. Bull. 72 (2015) 252

[13] Boukhachem A, Bouzidi C, Boughalmi R, Ouerteni R, Kahlaoui M, Ouni B, Elhouichet H, Amlouk M, Ceram. Int. 40 (2014) 13427

[14] Boukhachem A, Ziouche A, Ben Amor M, Kamoun O, Zergoug M, Maghraoui-Meherzi H, Yumak A, Boubaker K, Amlouk M, Mater. Res. Bull. 74 (2016) 202

[15] Arifa H, Boukhachem A, Askri B, Boubaker K, Yumak A, Raouadi K, Ceram. Int. 42 (2016) 2147

[16] Larbi T, Ouni B, Boukhachem A, Boubaker K, Amlouk M, Mater. Res. Bull. 60 (2014) 457–466

[17] Kizel A V, Krassilov I J, Burkov I V, Uspehi fizicheskih nauk 114 (1974) 295

[18] Sivaramakrishnan V, Magneto-optic study of some inorganic acids and their salts, Journal of the Indian Institute of Science. 1954

[19] Syed M, Siahmakoun A, Optical Mat. 27 (2005) 1629–1636

[20] Alwyn Scott, Encyclopedia of Nonlinear Science, Edited by Scott A, Taylor & Francis Group, New York, 2005

[21] Jönsson E P, Super paramagnetism and spin glass dynamics of interacting magnetic nanoparticle systems, Edited by Rice SA, Advances in chemical physics, Hoboken, JN: John Wiley & Sons, Inc, 2004, vol. 128, pp. 191–248

[22] Stoner C E, Wohlfarth P E, Proc. R Soc. Lond. A. 240 (1948) 599–642

[23] Speliotis E D, J. Magn. Magn. Mater. 193 (1999) 29

[24] Suzdalev P I, Suzdalev I P, Russian Chem. Rev. 70(3) (2001) 177–210

[25] Chantrell W R, Grady O K, Magnetism, Boston: Dordrecht, 1992

[26] Veynger I A, Zabrodskii G A, Tisnek V T, Phys. Technol. Semiconduct. 34 (2000) 1

Chapter 8

Advance Deposition Techniques for Thin Film and Coating

Asim Jilani , Mohamed Shaaban Abdel-wahab and
Ahmed Hosny Hammad

Additional information is available at the end of the chapter

http://dx.doi.org/10.5772/65702

Abstract

Thin films have a great impact on the modern era of technology. Thin films are considered as backbone for advanced applications in the various fields such as optical devices, environmental applications, telecommunications devices, energy storage devices, and so on . The crucial issue for all applications of thin films depends on their morphology and the stability. The morphology of the thin films strongly hinges on deposition techniques. Thin films can be deposited by the physical and chemical routes. In this chapter, we discuss some advance techniques and principles of thin-film depositions. The vacuum thermal evaporation technique, electron beam evaporation, pulsed-layer deposition, direct current/radio frequency magnetron sputtering, and chemical route deposition systems will be discussed in detail.

Keywords: thin films, coatings, physical deposition, sol-gel, chemical bath deposition, chemical route

1. Introduction

Nowadays, most of the technologies are used for minimizing the materials into nano-size as well as nano-thickness leading to the emergence of new and unique behaviors of such materials in optical, electrical, optoelectronic, dielectric applications, and so on. Hence, a new branch of science/materials science is called thin films or coatings. Thin film can be defined as a thin layer of material, where the thickness is varied from several nanometers to few micrometers. Like all materials, the structure of thin films is divided into amorphous and polycrystalline structure depending on the preparation conditions as well as the material nature. Thin films comprise

two parts: the layer and the substrate where the films are deposited on it. Also, thin films can be composed of different layers such as thin-film solar cells, electrochromic cells, and so on.

In order to obtain thin films with good quality, there are two common deposition techniques: physical and chemical depositions. It can be summarized as shown in **Table 1**.

Physical deposition	Chemical deposition
1. Evaporation techniques	**1. Sol-gel technique**
a. Vacuum thermal evaporation.	**2. Chemical bath deposition**
b. Electron beam evaporation.	**3. Spray pyrolysis technique**
c. Laser beam evaporation.	**4. Plating**
d. Arc evaporation.	**a.** Electroplating technique.
e. Molecular beam epitaxy.	**b.** Electroless deposition.
f. Ion plating evaporation.	**5. Chemical vapor deposition (CVD)**
2. Sputtering techniques	**a.** Low pressure (LPCVD)
a. Direct current sputtering (DC sputtering).	**b.** Plasma enhanced (PECVD)
b. Radio frequency sputtering (RF sputtering).	**c.** Atomic layer deposition (ALD)

Table 1. Methods of thin films deposition.

This chapter describes some common deposition techniques for thin films in detail to give some confidential and important points of view for readers on how thin films can be formed.

2. Physical deposition techniques

2.1. Evaporation techniques

Evaporation methods are considered as the common deposition of materials in the form of thin-layer films. The general mechanism of these methods is obtained by changing the phase of the material from solid phase to vapor phase and converting again to solid phase on the specific substrate. It takes place under vacuum or controlled atmospheric condition.

2.1.1. Vacuum thermal evaporation technique

Vacuum evaporation technique is the simplest technique used to prepare amorphous thin films especially chalcogenide films such as CdSSe [1], MnS [2], Ge-Te-Ga [3], and so on. In general, chalcogenide materials can be used for memory-switching applications [4, 5], phase-change materials [6, 7], and solar applications [8].

http://dx.doi.org/10.5772/65702

The technique of thermal evaporation is strongly dependent on two parameters: thermally vaporized material and applying a potential difference to the substrate under medium- or higher-vacuum level ranging from 10^{-5} to 10^{-9} mbar. The schematic diagram for thermal evaporation is shown in **Figure 1** taken from elsewhere [9].

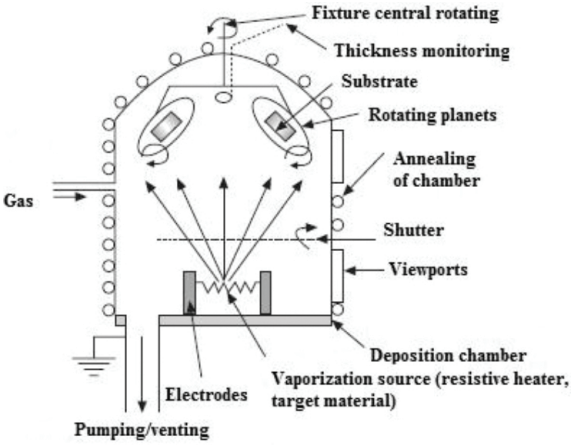

Figure 1. Schematic of thermal evaporation system with substrate holder on a planetary rotation system and directly above the evaporating source.

2.1.2. Electron beam evaporation

This type of evaporation is another method of physical deposition where the intensive beam of electrons is generated from a filament and steered through both electric and magnetic fields to hit the target and vaporize it under vacuum environment as shown in **Figure 2**. Thin films prepared by electron beam evaporation are of good quality and purity [10].

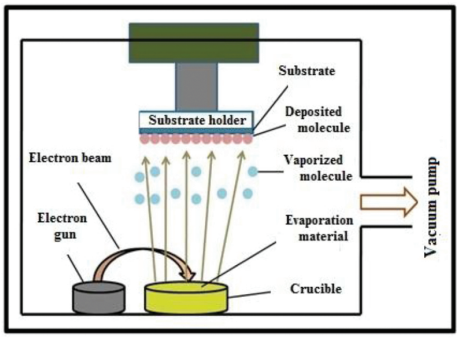

Figure 2. Schematic diagram of electron beam evaporation.

Large categories of materials can be prepared by electron beam evaporation technique [11] such as amorphous and crystalline semiconductors [12], metals [13], oxides [14], and molecular materials [15].

2.1.3. Laser beam evaporation (pulsed-laser deposition)

Pulsed-laser deposition (PLD) is another physical deposition technique to deposit the thin-film-coating system [16]. During the thin-film deposition process, the laser beam is used to ablate the material for depositing the thin films inside a vacuum chamber as shown in **Figure 3**.

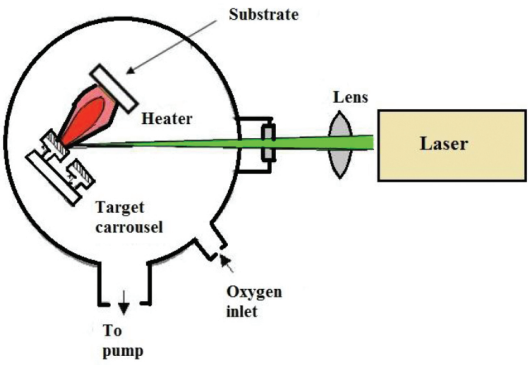

Figure 3. Schematic of pulsed-laser deposition taken from Ref. [17].

Different kinds of laser sources are being used to ablate the target. The most common sources are Nd-YAG laser, KrF (248 nm), and XeCl (308 nm). When the laser beam strikes the target material, it produces the plume which could deposit on the various substrates. The created plume may contain neural- and ground-state atoms and ionized species. In the case of metal oxide thin films, oxygen is used to deposit the oxides of metals [18]. The thin-film quality from the PLD depends on the various parameters such as wavelength of the laser, energy, ambient gas pressure, pulsed duration, and the distance of the target to the substrate [19]. The ablation process during the deposition may control and monitor by using laser-induced fluorescence [20], laser ablation molecular isotopic spectroscopy [21], and optical emission spectroscopy [22]. The morphology of the deposited thin films is also affected by the substrate temperature. The coating of thin films through PLD follows three modes: Frank–-van der Merwe, Stranski–-Krastanov, and Volmer–-Weber [23, 24]. PLD has some advantages over other physical deposition systems because of its fast deposition time and its compatibility to oxygen and other inert gases.

2.2. Sputtering technique

Sputtering technique is mostly used for depositing metal and oxide films by controlling the crystalline structure and surface roughness [11, 25]. The simple form of the sputtering system

http://dx.doi.org/10.5772/65702

consists of an evacuated chamber containing metallic anode and cathode [25] in order to obtain a glow discharge in the residual gas in the chamber. Also, an applied voltage in the order of several KeV with pressure more than 0.01 mbar is sufficient for film deposition. The sputtering process depends on the bombardment of the ions released from the discharge to the molecules in the cathode leading to the liberation of the molecules from the cathode with higher kinetic energy. The atomic weight of the bombarding ions should be nearly to that of the target material in order to maximize the momentum transfer. These molecules move in straight lines and strike on the anode or on the substrate to form a dense thin film [25]. The diagram of the sputtering system is shown in **Figure 4**.

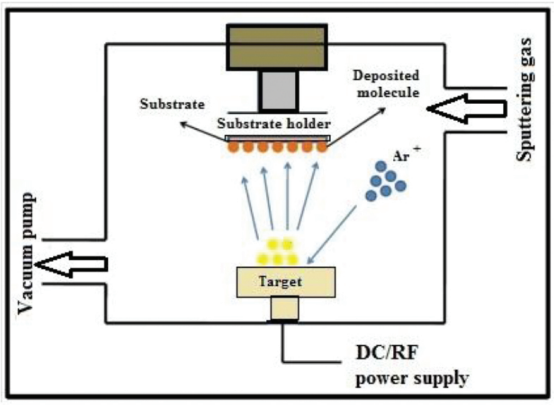

Figure 4. Sputtering system diagram.

The process of sputtering has several advantages. High-melting point materials can be easily formed by sputtering. The deposited films have composition similar to the composition of the starting materials. Sputtering technique is available to use for ultrahigh vacuum applications. The sputtering sources are compatible with reactive gases such as oxygen. Contrarily,' thick coatings cannot be obtained and there is a difficulty to deposit uniformly on complex shapes.

There are two common types of sputtering process: direct current (DC) and radio frequency (RF) sputtering. The first one depends on DC power, which is generally used with electrically conductive target materials. It is easy to control with low-cost option. The RF sputtering uses RF power for most dielectric materials. A common example for sputtered films is aluminum nitride films. These films were prepared by both DC- and RF-sputtering technique, and their structure and optical properties were compared [26, 27].

3. Chemical deposition techniques

Although the production of thin films via physical methods as previously described gives good quality and functionalizes properties, it is highly expensive and perhaps requires a large

amount of material target. Since the need to produce good-quality thin films with low economical cost is necessary, chemical deposition techniques are widely used globally. These techniques are cheap producing good-quality films. Most of them do not require expensive equipment. The chemical deposition is strongly dependent on the chemistry of solutions, pH value, viscosity, and so on. The most common chemical deposition has been obtained via sol-gel route, chemical bath deposition, electrodeposition, chemical vapor deposition (CVD), and spray pyrolysis technique. This section is concerned only on sol-gel and chemical bath deposition techniques because they can form good film quality with low equipment requirement.

3.1. Sol-gel technique

The sol-gel technique is broadly used for the synthesis of oxide materials [28]. Sol-gel process is one of the famous wet-chemical methods. It works under lower-temperature processing and gives better homogeneity for multicomponent materials. The word "'sol"' means the formation of a colloidal suspension and 'gel' means the conversion of 'sol' to viscous gels or solid materials. Two routes are used to prepare transition metal oxides (TMOs) as follows:

a. Preparing of inorganic precursors via inorganic salts in aqueous solution.

b. Preparing of metal alkoxide precursors via metal alkoxides in nonaqueous solvents.

In this section, we are concerned on the famous route "the metal alkoxide precursor solution by an alcoholic solution."

3.1.1. Alkoxide precursors in organic solvents

The sol-gel technique is based on the polycondensation of metal alkoxides **M (OR)**$_z$ in which **R** represents an alkyl group (R = CH_3, C_2H_5, …) and **z** is the oxidation state of the metal atom $\mathbf{M}^{z+}$ [29]. It can be synthesized via the reaction of metal salt (chloride, acetate, nitrate, etc.) with alcohol as follows:

$$\left(CH_3COO\right)_z M + zROH \rightarrow M\left(OR\right)_z + zCH_3COOH \quad (1)$$

After this process, two important steps should be involved:

1. *Hydrolysis:* this step is aimed to form reactive **M-OH** groups [30]:

$$M — OR + H_2O \rightarrow M — OH + ROH \quad (2)$$

2. *Condensation*: condensation is the second step after hydrolysis leading to the departure of a water molecule. The process of condensation can be either olation process or oxolation process.

- *Olation:* a hydroxyl bridge ("ol" bridge) is formed between two metal centers as shown in **Figure 5**.

http://dx.doi.org/10.5772/65702

- *Oxolation:* oxolation is a reaction in which an oxo bridge (—O—) is created between two metal centers. When the metal is coordinately unsaturated, oxolation with rapid kinetics leads to edge- or face-shared polyhedral as shown in **Figure 6**.

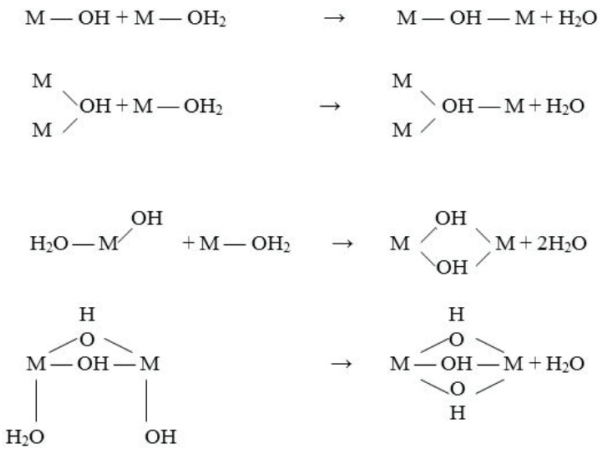

Figure 5. Several types of OH bridges can be formed by olation condensation process.

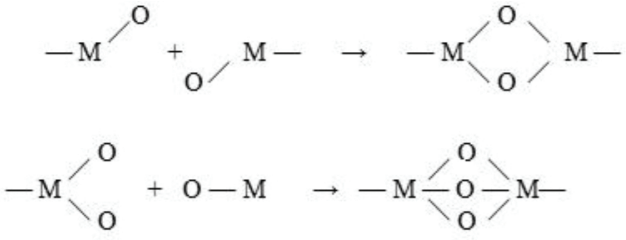

Figure 6. Formation of oxo-bridging links between two metal centers.

Hence, olation process occurs mainly for lower oxidation states of cations **($z < 4$),** whereas oxolation is mainly observed with cations of high oxidation state **($z > 4$)** [29, 31].

The previous description provides the preparation of the precursor solution. In order to make thin film from the precursor solution, there are two processes for the production of the films, that is, dip-coating and spin-coating techniques.

3.1.2. Dip-coating technique

Dip-coating technique is almost used to fabricate transparent layers of oxides on a transparent substrate with a high degree of planarity and surface quality [32]. Other substrates are also

possible to use. Well-defined film thicknesses up to 1 μm can be deposited. Several additive layers can be superimposed.

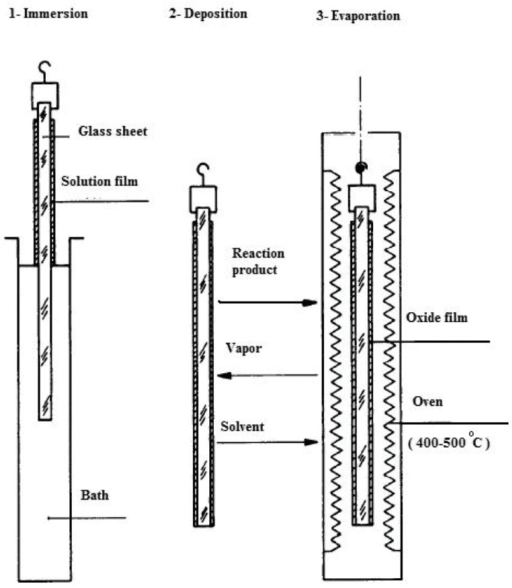

Figure 7. Dip-coating process levels.

Scriven [33] described the dip-coating process in five stages: immersion, start-up, deposition, drainage, and evaporation. Hence, the evaporation normally accompanies the start-up, deposition, and drainage steps as shown in **Figure 7**.

3.1.3. Spin-coating technique

Another technique is also available for usage after the precursor solution is prepared known as spin coating or spinning. The solution is dripped onto a spinning substrate and spreads evenly. The spinning process is most suitable for the coating of small disks or lenses but is not very economical. The process of spinning film can be described as shown in **Figure 8**.

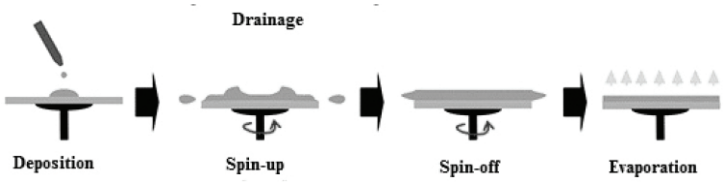

Figure 8. Spin-coating process.

http://dx.doi.org/10.5772/65702

3.2. Chemical bath deposition technique

Chemical bath deposition method is also known as solution growth technique or controlled precipitations [34]. It is the oldest method to deposit films on a substrate. Solution growth technique is mostly used to prepare chalcogenide films as well as metal oxide films. Also, the deposition can be performed at lower temperatures. In the solution growth method, the precursor solution of metal ions must be complexed by ligands. The complex solution is almost obtained with ammonia solution, triethanol amine, ethylene-diamine-tetraacetic acid (EDTA), citric acid, and so on. When the complexation is completed, the addition of the anions should take place. These anions come from the thiourea, thioacetamide, thiosulfate, and sodium Sulfide solutions [34] as sources of sulfur anions or selenourea and sodium selenosalfate for selenium anions to deposit the chalcogenides. Substrates are put in vertical, horizontal, or specific position inside the solution and left until the desired film thickness is obtained. The deposition of oxide films is quite different than chalcogenides. After making the complexation by controlling the pH value, the substrate is immersed in the solution under the desired temperature varied in the range 60°–100 °C to deposit in most cases the metal hydroxide films. The hydroxide film can then be transferred to oxide by the annealing process. **Figure 9** represents the simple chemical bath deposition method taken from Ref. [34]. Indeed, much

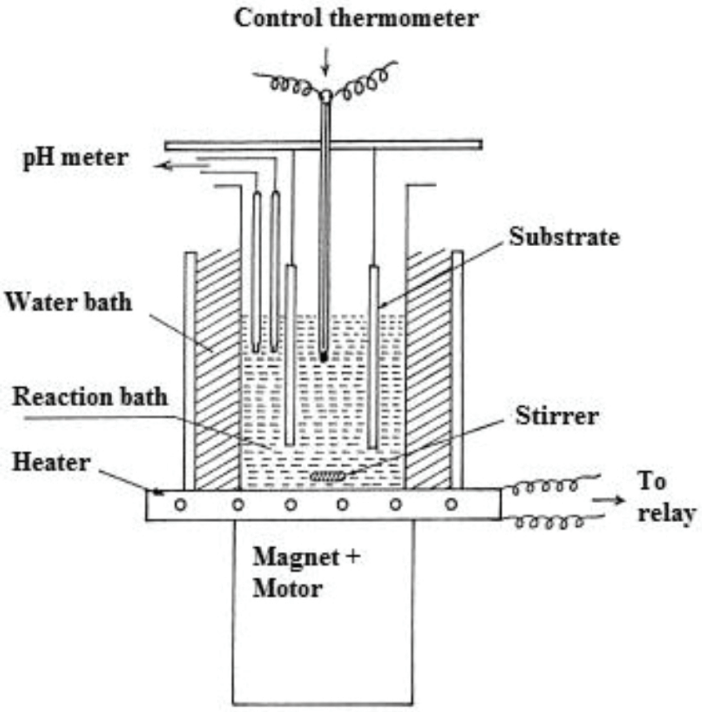

Figure 9. Home-made chemical bath deposition technique.

reviews and literature, which describes the chemical bath deposition for both chalcogenide and oxide films, are found elsewhere [34–36].

Author details

Asim Jilani[1*], Mohamed Shaaban Abdel-wahab[1] and Ahmed Hosny Hammad[1,2]

*Address all correspondence to: asim.jilane@gmail.com

1 Center of Nanotechnology, King Abdulaziz University, Jeddah, Saudi Arabia

2 Electron Microscope and Thin Films Department, Physics Division, National Research Centre, Dokki, Giza, Egypt

References

[1] Hassanien AS, Akl AA. Effect of Se addition on optical and electrical properties of chalcogenide CdSSe thin films. Superlattices Microstruct. 2016;89:153–169. DOI: 10.1016/j.spmi.2015.10.044

[2] Hannachi A, Segura A, Meherzi HM. Growth of manganese sulfide (α-MnS) thin films by thermal vacuum evaporation: Structural, morphological, optical properties. Mater. Chem. Phys. 2016;181:326–332. DOI: 10.1016/j.matchemphys.2016.06.066

[3] Wang G, Nie Q, Shen X, Chen F, Li J, Zhang W, Xu T, Dai S. Phase change and optical band gap behaviour of Ge-Te-Ga thin films prepared by thermal evaporation. Vacuum. 2012;86(10):1572–1575. DOI: 10.1016/j.vacuum.2012.03.036

[4] Malligavathy M, Kumar RTA, Das C, Asokan S, Padiyan DP. Growth and characteristics of amorphous Sb_2Se_3 thin films of various thicknesses for memory switching applications. J. Non-Cryst. Solids. 2015;429:93–97. DOI: 10.1016/j.jnoncrysol.2015.08.038

[5] Kumar RTA, Das C, Lekha PC, Asokan S, Sanjeeviraja C, Padiyan DP. Enhancement in threshold voltage with thickness in memory switch fabricated using $GeSe_{1.5}S_{0.5}$ thin films. J. Alloys Compd. 2014;615:629–635. DOI: 10.1016/j.jallcom.2014.07.068

[6] Rafea MA, Farid H. Phase change and optical band gap behaviour of $Se_{0.8}S_{0.2}$ chalcogenide glass films. Mater. Chem. Phys. 2009;113(2–3):868–872. DOI: 10.1016/j.matchemphys.2008.08.045

[7] Sangeetha BG, Joseph CM, Suresh K. Preparation and characterization of $Ge_1Sb_2Te_4$ thin films for phase change memory applications. Microelect. Eng. 2014;127:77–80. DOI: 10.1016/j.mee.2014.04.032

[8] Salomé PMP, Alvarez HR, Sadewasser S. Incorporation of alkali metals in chalcogenide solar cells. Sol. Ener. Mater. Sol. Cells. 2015;143:9–20. DOI: 10.1016/j.solmat.2015.06.011

[9] Orava J, Kohoutek T, Wagner T. Deposition techniques for chalcogenide thin films. In: Adam JL, Zhang X, editors. Chalcogenide Glasses Preparations, Properties and Applications. Oxford: Woodhead Publishing Series; 2014. DOI: 10.1533/9780857093561.1.265

[10] Lokhande AC, Chalapathy RBV, He M, Jo E, Gang M, Pawar SA, Lokhande CD, Kim JH. Development of Cu_2SnS_3 (CTS) thin film solar cells by physical techniques: A status review. Sol. Ener. Mater. Sol. Cells. 2016;153:84–107. DOI: 10.1016/j.solmat.2016.04.003

[11] Barranco A, Borras A, Elipe ARG, Palmero A. Perspectives on oblique angle deposition of thin films: From fundamentals to devices. Progress Mater. Sci. 2016;76:59–153. DOI: 10.1016/j.pmatsci.2015.06.003

[12] Merkel JJ, Sontheimer T, Rech B, Becker C. Directional growth and crystallization of silicon thin films prepared by electron-beam evaporation on oblique and textured surfaces. J. Cryst. Growth. 2013;367:126–130. DOI: 10.1016/j.jcrysgro.2012.12.037

[13] Mukherjee S, Gall D. Structure zone model for extreme shadowing conditions. Thin Solid Films. 2013;527:158–163. DOI: 10.1016/j.tsf.2012.11.007

[14] Schulz U, Terry SG, Levi CG. Microstructure and texture of EB-PVD TBCs grown under different rotation modes. Mater. Sci. Eng. A. 2003;360(1–2):319–329. DOI: 10.1016/S0921-5093(03)00470-2

[15] Yang B, Duan H, Zhou C, Gao Y, Yang J. Ordered nanocolumn- array organic semiconductor thin films with controllable molecular orientation. Appl. Surf. Sci. 2013;286:104–108. DOI: 10.1016/j.apsusc.2013.09.028

[16] Lorenz M, Rao MSR. 25 years of pulsed laser deposition. J. Phys. D. Appl. Phys. 2014;47:030301–030303. DOI: 10.1088/0022-3727/47/3/030301

[17] Rainer W. Electronic Materials Research Laboratory [Internet]. Available fromml: http://www.emrl.de/r_m_1.html

[18] Lowndes DH, Geohegan DB, Puretzky AA, Rouleau CM. Synthesis of novel thin film materials by pulsed laser deposition. Science. 1996; 273(5277):898–903. DOI: 10.1126/science.273.5277.898.

[19] Ashfold MNR, Claeyssens F, Fuge GM, Henley SJ. Pulsed laser ablation and deposition of thin films. Chem. Soc. Rev. 2004;33(1):23–31. DOI: 10.1039/B207644F

[20] Lynds L, Weinberger BR, Potrepka DM, Peterson GG, Lindsay MP. High temperature superconducting thin films: The physics of pulsed laser ablation. Physica C. 1989;159(1–2):61–69. DOI: 10.1016/0921-4534(89)90104-4

[21] Russo RE, Mao X, Gonzalez JJ, Zorba V, Yoo J . Laser ablation in analytical chemistry. Anal. Chem. 2013;85(13):6162–6177. DOI: 10.1021/ac4005327

[22] Geyer TJ, Weimer WA. Parametric effects on plasma emission produced during excimer laser ablation of $YBa_2Cu_3O_{7-x}$. Appl. Spectros. 1990;44(10):1659–1664. DOI: 10.1366/0003702904417454

[23] Karl H, Stritzker B. Reflection high-energy electron diffraction oscillations modulated by laser pulse deposition $YBa_2Cu_3O_{7-x}$. Phys. Rev. Lett. 1992;69(20):2939–2942. DOI: 10.1103/PhysRevLett.69.2939

[24] Lippmaa M, Nakagawa N, Kawasaki M, Ohashi S, Inaguma, Itoh M, Koinuma H. Step-flow growth of SrTiO3 thin films with a dielectric constant exceeding 104. Appl. Phys. Lett. 1999; 74(23):3543–3545. DOI: 10.1063/1.124155

[25] Angusmacleod H. Recent developments in deposition techniques for optical thin films and coatings. In: Piegari A, Flory F, editors. Optical Thin Films and Coatings from Materials to Applications. Oxford: Woodhead Publishing Series; 2013. p. 3–-25. DOI: 10.1533/9780857097316.1.3

[26] Morosanu C, Dumitru V, Cimpoiasu E, Nenu C. Comparison between DC and RF magnetron sputtered aluminum nitride films. In: Prelas MA, Benedictus A, Lin LTS, Popovici G, Gielisse P, editors. Diamond Based Composites and Related Materials. 1st ed. Petersburg, Russia: Springer Science+Business Media Dardrecht; 1997. p. 127–132. DOI: 10.1007/978-94-011-5592-2_9

[27] Dumitru V, Morosanu C, Sandu V, Stoica A. Optical and structural differences between RF and DC Al_xN_y magnetron sputtered films. Thin Solid Films. 2000;359:17–20. DOI: 10.1016/S0040-6090(99)00726-9

[28] Livage J, Sanchez C, Henry M, Doeuff S. The chemistry of sol-gel process. Solid State Ionics. 1989;32–33(2):633–638. DOI: 10.1016/0167-2738(89)90338-X

[29] Livage J, Ganguli D. Sol-gel electrochromic coatings and devices: A review. Sol. Ener. Mater. Sol. Cells. 2001;68:365–381. DOI: 10.1016/S0927-0248(00)00369-X

[30] Tjong SC, Chen H. Nanocrystalline materials and coatings. Mater. Sci. Eng. R. 2004;45(1–2):1–88. DOI: 10.1016/j.mser.2004.07.001

[31] Brinker CJ, Scherer GW. Sol-Gel Science. San Diego: Academic Press; 1990.

[32] Klein LC. Sol-Gel Technology for Thin Films, Fiber, Preform, Electronics and Specialty Shapes. Park Ridge, NJ, USA: Noyes Publications; 1987. DOI: 10.1002/pi.4980210420

[33] Scriven LE. Physics and applications of dip coating and spin coating. In: Brinker CJ, Clark DE, Ulrich DR, editors. Better Ceramics Through Chemistry. 3rd ed. Pittsburgh, PA: Materials Research Society; 1988. p. 712–729.

[34] Mane RS, Lokhande CD. Chemical deposition method for metal chalcogenide thin films. Mater. Chem. Phys. 2000;(1):1–31. DOI: 10.1016/S0254-0584(00)00217-0

[35] Pawar SM, Pawar BS, Kim JH, Joo OS, Lokhande CD. Recent status of chemical bath deposited metal chalcogenide and metal oxide thin films. Curr. Appl. Phys. 2011;11(2): 117–161. DOI: 10.1016/S0254-0584(00)00217-0

[36] Hammad AH, Elmandouh ZS, Elmeleegi HA. Structure and some physical properties of chemically deposited nickel sulfide thin films. In: Proceedings of the 4th International Congress APMAS 2014; 24–27 April 2014; Fethiye, Turkey. Acta Phys. Polonica A: Polish Academy of Sciences Institute of Physics; 2015. p. 901–903. DOI: 10.12693/APhysPolA.127.901

Chapter 9

Vanadium Oxide Thin Films Obtained by Thermal Annealing of Layers Deposited by RF Magnetron Sputtering at Room Temperature

Hernan M. R. Giannetta, Carlos Calaza,
Liliana Fraigi and Luis Fonseca

Additional information is available at the end of the chapter

http://dx.doi.org/10.5772/67054

Abstract

This chapter describes a new deposition method proposed to achieve Vanadium Oxide VO_x/V_2O_5 thin films with high temperature coefficient of resistance (TCR), intended to be used as functional material in IR microsensors (bolometers). The main aim of the work is to attain a deposition method compatible with the lift-off microstructuring technique in order to avoid the use of a reactive-ion etching (RIE) process step to selectively remove the VO_x/V_2O_5 deposited layer in the course of the definition of the bolometer geometry, preventing the harmful effects linked to the spatial variability and the lack of selectivity of the RIE process. The proposed technique makes use of a two-stage process to produce the well-controlled VO_x or V_2O_5 thin films by applying a suitable thermal annealing to a previously deposited layer, which was obtained before at room temperature by RF magnetron sputtering and patterned by lift-off. A set of measurements has been carried out with thin films attained in order to check the quality and properties of the materials achieved with this method. The results reached with V_2O_5 pure phase films are consistent with a charge transport model based on the small polarons hopping derived from Mott's model under the Schnakenberg form.

Keywords: VO_x thin film, V_2O_5 thin film, lift-off compatible, RF magnetron sputtering, thermal annealing, Meyer-Neldel rule, small polaron hopping

1. Introduction

Thin films of materials with high temperature coefficient of resistance (TCR) values are widely used as thermoresistive transducers in uncooled infrared imaging sensors. Mixed Vanadium

Oxide (VO_x) thin films were among the first functional materials chosen for this application due to its simple integration with MEMS technology, which led to the development of the first IR image sensors based on focal plane arrays (FPAs) with thermoresistive transducers in the 1970s–1980s [1]. The main reasons leading to the election of the VO_x thin films as bolometer functional material were its high TCR value (for most commercial devices TCRs are in the range of −2 to –3%/K [2]) and its low 1/*f* noise. First microbolometers were achieved using polycrystalline VO_x mixed oxide thin films, formed by a blend of VO_2, V_2O_3, and V_2O_5 oxide phases, with a thickness of 500–1000 Å, a resistivity of 20kΩ/sq. and a TCR (measured at room temperature) of −2%/K [3]. Since then, numerous works have been published presenting methods to improve the performance of these films and the associated devices. The best balance between the resistivity and the TCR reported for a commercial device was achieved using VO_x thin films with a mixing V−O proportion equal to (x = 1.8) [4]. The TCR value of a specific material can be obtained experimentally by measuring the slope of the variation of the film resistivity with the temperature, which is described by the expression TCR = 1/R(dR/dT) [1]. But, as will be shown later, it can be also linked to a material parameter known as the material activation energy ΔW, given by $TCR = -\Delta W/kT^2$ [5], where k is the Boltzmann constant and T the temperature.

Two main methodologies able to control the mixing ratio x of the oxide phases present in the sample have been described in the literature for the experimental synthesis of VO_x thin films. The first one achieves the control of the mixing proportion by using multilayers of pure phase materials. Among the published works based on this method, we can highlight Ref. [6] in which authors were able to control the mixing proportion with a sequence of successive depositions of two known phases, VO_2 and V_2O_5, or Ref. [7] in which authors controlled this ratio with a multilayer of $V_2O_5/V/V_2O_5$. However, the most extended method in literature controls the film-mixing ratio by managing the oxidation rate of the material taken from a pure metallic precursor target (pure vanadium material, 99.9%) used for thin film growth. The deposition process parameters are tuned during the growth cycle to adjust the oxidation rate and, consequently, the ratio of the existing oxide phases that will determine the final thin film properties.

This chapter presents a novel technique to obtain vanadium oxide thin films (VO_x or V_2O_5) using different annealing conditions with starting materials previously deposited and patterned at room temperature. The key objective of the method is to offer compatibility with the lift-off microstructuring technique in order to allow the definition of the bolometer active material geometry without need of a dry etching process. The bolometer functional materials are usually deposited on top of thin dielectric membranes (Si_3N_4/SiO_2) required to accomplish an adequate thermal isolation with respect to the silicon substrate. The thickness and stress level of materials used in this membrane can be crucial for bolometer mechanical stability and a partial etch of these layers during a reactive-ion etching (RIE) step used to conform the active layer (due to an over-etch linked to a spatial variability or a lack of selectivity of the RIE process) can compromise future structure reliability. For that reason, the solution proposed splits the thin film formation into two stages: a first deposition of a precursor thin film on samples with a photoresist layer ready for the lift-off process, obtained from a VO_2 or a metallic V target using RF magnetron sputtering at room temperature; and a second annealing step at a high temperature after the photoresist removal, to promote the oxidation and obtain the desired oxide phase mix required for the application.

http://dx.doi.org/10.5772/67054

The morphological, structural, and optical characterization of the thin films obtained with this method under different annealing conditions were performed using field emission scanning electron microscopy (FE-SEM), X-ray diffraction (XRD), and Raman spectroscopy. The electrical conductivity of the samples was measured as a function of the temperature using a probe station attached to a heated chuck. The DC-conduction data measured for pure phase V_2O_5 thin films was fitted using the Mott's small polaron hopping transport model, taking into account the Schnakenberg phonon distribution model equation. The consistency between the different parameters measured for the V_2O_5 samples processed with the optimal conditions and the assumptions of strong electron-phonon interaction, existence of small polarons, and the nonadiabatic regime for the hopping of charge carriers has been checked, suggesting that small polarons hopping is the main conduction mechanism in pure phase V_2O_5 thin films obtained with this method.

2. Vanadium oxides

Vanadium is a transition metal with a [Ar] $3d^3 4s^2$ electron configuration for the ground state and a centered cubic crystal structure [8]. As a consequence of its multivalent character, it has a number of possible oxidation states (V^{+2}, V^{+3}, V^{+4}, V^{+5}), which form an extensive list of binary V−O systems. Some of them are grouped in the so-called "Magneli phases," with stoichiometric formula V_nO_{2n-1}, and others in the Wadsley phases, with stoichiometric formula V_nO_{2n+1}.

The most commonly used phases, found in various applications due to their particular properties, are the VO, VO_2, V_2O_3, and V_2O_5 oxide phases. Their main characteristics are the following:

VO is one of the many vanadium oxide phases with crystalline cubic structure and good electrical conductivity due to the partially filled conduction band and the delocalization of electrons in the 2 g orbital [9].

VO_2 is an amphoteric compound with the unique property of changing from a semiconductor monoclinic phase to a (semi)metal tetragonal rutile phase at a temperature around 340 K and, therefore, its electrical resistivity together with the optical properties also change up to several orders of magnitude between these two states [10].

V_2O_3 phase, like VO_2 compound, presents an abrupt conductivity change at a temperature around 160 K, evidenced of a metal-insulator transition. In addition, it presents a thermochromic behavior in the infrared band [9].

V_2O_5 is the most stable of all vanadium oxide phases, and the preferred one to be used as thermoresistive material in microbolometer arrays for thermal imaging due to its high TCR value. Vanadium pentoxide is a semiconductor with a bandgap of 2.1–2.4 eV, which presents the following polymorphs: α-V_2O_5 (orthorhombic), β-V_2O_5 (monoclinic or tetragonal), and γ-V_2O_5 (orthorhombic), being the α-polymorph the most stable one [11].

There are many other V−O binary compounds with unique properties beyond the most used ones. A complete guide to the various V=O phases can be found in Ref. [9], including a diagram

that represents the different V−O oxide phases as a function of their oxygen atomic fraction, obtained by thermodynamic calculations.

3. Synthesis of VO_x films

A number of deposition techniques can be highlighted among the different synthesis methods reported in the literature for the synthesis of a multiplicity of Vanadium oxide compounds: sputtering [12], sol-gel process [13], chemical vapor deposition (CVD) [14], pulse laser deposition (PLD) [15], atomic layer deposition (ALD) [9], molecular beam epitaxy (MBE) [16], aqueous solution process [17], and the reactive vacuum evaporation [6].

Nevertheless, to obtain a specific oxide phase, it is necessary to complement one of these deposition methods with a thermal annealing process in order to enhance the crystallinity of the film, as well as to modify its stoichiometry [18]. Two illustrative cases can be found in Refs. [19, 20], where VO_x samples were subjected to a thermal annealing process in air at different temperatures (up to 300°C) and a film recrystallization was detected. Furthermore, it was observed that an increase of the substrate temperature after film deposition promotes the loss of oxygen atoms, which results in a modification of the VO_x film stoichiometry [12].

The temperature conditions required to achieve a particular oxide phase will depend on the enthalpy of formation of the various vanadium oxide compounds [19]. On the basis of the change in the Gibbs free energy associated with each stable Vanadium oxide phase, it can be established that V_2O_5 formation requires temperatures above 434°C, and the stable oxide phases formation sequence will be given in the order: $VO_2 \rightarrow V_2O_3 \rightarrow VO \rightarrow V_2O_5$ [21].

Consequently, it has been necessary to explore the influence of the temperature and the annealing time conditions used in the second step of the proposed thin film growth method in order to establish the optimal set of parameters that lead to attain the desired vanadium oxide phase combination.

3.1. Preparation and synthesis of VO_x films

The sputtering technique, one of the most common physical vapor deposition methods [22], has been the process selected for the growth of vanadium oxide thin films. The key advantages of the sputtering technique over other alternative methods include the resultant film uniformity, the easy scalability to larger substrates, and the high deposition efficiency [23]. There are three main sputtering deposition modes available: DC, RF, and magnetron. The first reported growth of a VO_2 thin film deposited with a reactive sputtering method is typically attributed to Fuls and collaborators, from Bell Telephone Labs in 1967 [24].

A wide range of sputtering process conditions have been reported in the literature for the growth of VO_x thin films with different compositions. The main process parameters that can be customized to control the final composition of the resultant material include the selection of a starting target with a virtually pure precursor material, such as metallic-V [25], VO_2 [12], V_2O_5 [11]; the choice of a specific sputtering deposition method, RF [25] or DC [26];

http://dx.doi.org/10.5772/67054

the alteration of the substrate temperature during the deposition process [27]; the subsequent annealing in vacuum or in an oxidizing atmosphere with a controlled O_2/N_2 ratio [28]; or the application of a varying voltage to the substrate during the deposition [29].

In this work, the conditions explored to achieve the desired vanadium oxide thin films include the use of two different sputtering target materials: VO_2 and metallic-V. The thin films obtained with the sputtering process have been patterned using the lift-off technique, and finally, the samples have gone through a thermal annealing step to obtain the desired film composition. The experimental conditions used for this final annealing step in the case of the metallic-V target have been investigated in order to establish the set of parameters that are required to obtain VO_x and V_2O_5 thin films.

The first step in sample preparation has been the arrangement of a base substrate on which the different layers of vanadium oxide compounds have been deposited. The substrate used has been a Si wafer (100) single-side polished, with a precoating of SiO_2 and Si_3N_4, which has acted as an electrical insulator and as a mechanical buffer layer for subsequent thermal annealing. The surface was subjected to a standard cleanroom cleaning process previously to the deposition.

In order to confirm the compatibility of the proposed growth method with the lift-off microstructuring technique, the vanadium oxide thin films have been deposited on top of substrates partially covered with a photoresist layer. The preparation of the samples starts with the deposition of a layer of TI35E image reversal photoresist (MicroChemicals GmbH) on top of the Si substrates, which is selectively exposed using a photolithographic mask taking advantage of the image reversal feature of the photoresist to obtain negative sidewall profiles adequate for the lift-off process. The photoresist has been finally removed in exposed areas using an AZ developer.

The deposition of the Vanadium oxide thin films has been accomplished by using a BOC Edwards auto 500 Sputtering system, which was equipped with both RF and DC sources, using a maximum substrate temperature of 80°C to avoid damaging the photoresist. A set of vanadium oxide thin film depositions has been conducted under two different conditions.

A first set of samples (labelled as type A) has been obtained from a VO_2 target (brand MCSE, 99.9% purity, 3″ diameter, and 6 mm thick) with the RF source, using a 20 sccm argon flow, a 200 W RF power, and 30 min of deposition time. During deposition, the partial pressure on the chamber was 3.31×10^{-3} mBar, and sample holder was maintained at room temperature.

A second set of samples (labelled as type B) has been obtained from a metallic-V target (brand Kurt J. Lesker, 99.5% purity, 3″ diameter, and 6 mm thick) with the DC source, using a 30 sccm argon and 10 sccm oxygen flow, a 400 W DC power, and 30 min deposition time. During deposition, the partial pressure on the chamber was 6.61×10^{-3} mBar, and sample holder was maintained at 80°C.

Sample preparation was concluded with the lift-off process, which removes the photoresist and the material deposited on top of it with an acetone solvent. At this point, films are ready to endure the thermal treatment required to modify the crystallography and stoichiometry.

Type A samples were subjected to annealing processes using different temperatures: 80, 280, 400, and 475°C and times 8, 6, 4, and 3 h, respectively, in an air atmosphere making use of

an electrical oven with a temperature control. In contrast, with type B samples, it was essential to promote the additional oxidation of the metallic-V and, therefore, all samples were subjected to an annealing process at a higher temperature of 500°C for 30 min, making use of a vacuum oven with a controlled argon/oxygen environment (1 sccm oxygen and 3 sccm argon flow).

After the thermal annealing of the samples, the electrical contacts with the vanadium oxide films were obtained making use of an aluminium metallization in a subsequent process step. The samples resulting from this process sequence are illustrated in **Figure 1**.

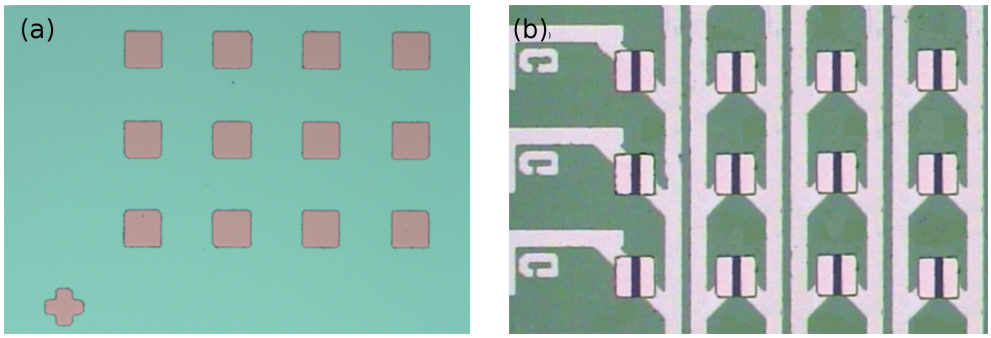

Figure 1. VO_x film conformation by lift-off and metal interconnections: (a) VO_x after lift-off, (b) VO_x with Al metal connections.

4. Characterization of VO_x films

The morphological characterization of the samples has been performed using a field emission scanning electron microscope (FE-SEM, FEI Helios Nanolab 650) with a low acceleration potential, 3 kV. The morphology of the VO_x thin films that result from the proposed growth method is shown in **Figure 2**, with FE-SEM images corresponding to the samples A and B annealed at the highest temperatures, 475 and 500°C, respectively. A good film uniformity can be observed in both the cases as well as in an enhancement of the crystal grain size and shape due to the effect of the thermal annealing [30]. The measured grain sizes are between 100 and 250 nm in both the cases, values that are similar to those reported in the literature for similar materials [31].

The structural characterization was performed by X-ray diffraction (XRD), using a CuKa cathode = 1.5406 Å (XRD-Philips PW 1730/10) configured in a standard Bragg-Brentano powder diffraction geometry. The analysis of the peak coincidences for each sample was performed using the PDF2 database with license from the International Center for Diffraction Data (ICDD). The crystalline phases present in the different samples were determined after the identification of the peak coincidences in the XRD patterns. The most significant results have been obtained for samples annealed at highest temperatures, A@475 and B@500, due to the presence of the dominant V_2O_5 phase, as shown in **Figure 3**.

http://dx.doi.org/10.5772/67054

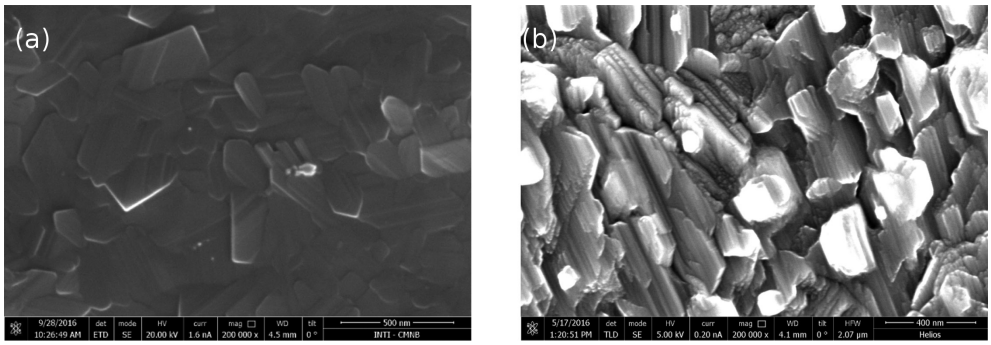

Figure 2. Microscopy Image performed by FE-SEM: (a) sample A@475°C, (b) sample B@500°C.

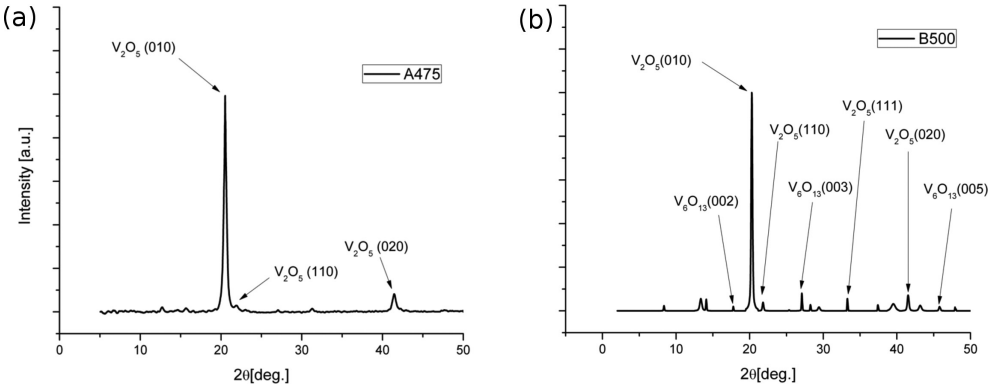

Figure 3. XDR peak matching analysis: (a) sample A@475°C, (b) sample B@500°C.

The analysis of the diffractogram corresponding to A@475 sample shows the presence of a practically pure V_2O_5 oxide phase. Peaks identified correspond to V_2O_5 reflection planes V_2O_5 (010) = 20.25°, V_2O_5 (110) = 21.72°, and V_2O_5 (020) = 41.22°.

In contrast, the presence of a mixed oxide phase can be observed on the diffractogram corresponding to B@500 sample, where main peaks can be attributed to a V_2O_5 phase and secondary ones to a V_6O_{13} phase. The reflection planes identified are V_2O_5 (010) = 20.25°, V_2O_5 (110) = 21.72°, V_2O_5 (111) = 33.27°, V_2O_5 (020) = 41.42°, and V_6O_{13} (002) = 17.77°, V_6O_{13} (003) = 27.08°, V_6O_{13} (005) = 45.78,° and V_6O_{13} (006) = 55.53° for the secondary V_6O_{13} phase.

Optical vibrational modes have been analyzed by means of Raman spectroscopy using a LabRAM HR Raman system (Horiba Jobin Yvon) equipped with a confocal microscope and a charge coupled device (CCD) detector. The 514.5 nm emission line of an Ar + laser has been used as an excitation source. The material databases for peak identification were included in the instrument. The prevailing V_2O_5 phase is once more clearly identified in Raman spectrums obtained for A@475 and B@500 samples due to the perfect matching of the spectrum peaks

with data extracted from the database. **Figure 4** displays the clear correspondence between the measured spectrum for both the samples and the one relative to the V_2O_5 reference material in the database.

The presence of two main emission peaks can be clearly spotted in the Raman spectrum of both samples; a first one in 141.6 cm^{-1}, which corresponds to the V–O–V Raman vibration mode and a second one in 993 cm^{-1}, associated with the V=O double-bond vibration mode [32]. In contrast, the strong emission peak observed in the Raman spectrum of A@475 sample (**Figure 4a**), in 520 cm^{-1}, cannot be assigned to any V–O vibration mode and has been related to the silicon crystalline substrate used as a support for the samples.

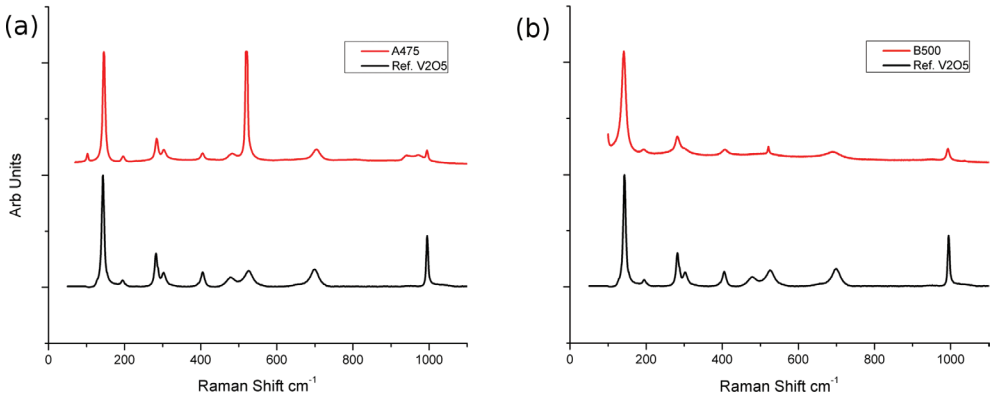

Figure 4. Raman characterization: (a) sample A@475°C, (b) sample B@500°C.

Finally, the electrical conductivity of the Vanadium oxide films has been measured as a function of the sample temperature, using a semiconductor parameter analyser Keithley 4200 CSC connected to a probe station and a thermal chuck equipped with an electronic temperature controller. Resistance measurements were performed using four collinear probes to implement a four-wire measurement scheme. A temperature swept, from room temperature up to 100°C, was applied to the chuck, and the actual temperature achieved by samples was recorded with the help of an additional thermocouple in contact with sample surface.

The measurement of the electrical conductivity as a function of the sample temperature has been used to establish the activation energy corresponding to the different materials by fitting the experimental data with Eq. (1):

$$\sigma_{(T)} = \sigma_0 \exp\left(\frac{-\Delta W}{\kappa T}\right), \tag{1}$$

where σ_0 is a constant, ΔW is the activation energy, k is the Boltzmann constant expressed in eV/k, and T is the temperature in Kelvin. The activation energy was obtained by fitting the experimental data obtained for the electrical conductivity vs. temperature (log(σ) vs. 1000/T) to

http://dx.doi.org/10.5772/67054

a linear expression derived from Eq. (1) using the least squares method (**Figure 5**). Such linear fits over the experimental measurements provide activation energy values of $\Delta W = 0.267$ eV for the A@475 sample, and $\Delta W = 0.056$ eV for the B@500 sample.

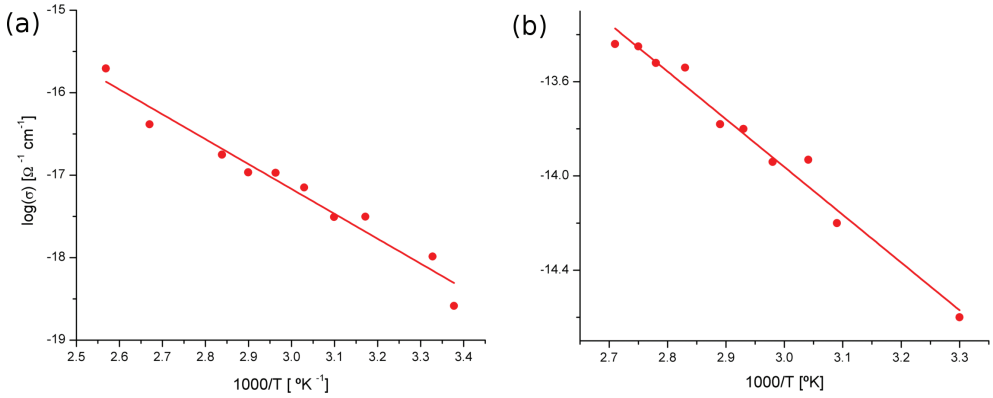

Figure 5. Electrical characterization of samples: (a) sample A@475°C, (b) sample B@500°C.

These activation energy values corroborate that A@475 sample presents a single V_2O_5 phase, as it presents an activation energy similar to that reported by Ioffe [33] for the V_2O_5 single-crystal material with a purity of 99%, $\Delta W = 0.27$ eV. In contrast, the activation energy that has been measured for the B@500 sample is much lower due to the presence of other mixed vanadium oxide phases. Consequently, the TCR value will be higher for the A@475 sample than for the B@500 sample, but the higher value of electrical conductivity in B type samples can represent a benefit in terms of the $1/f$ noise. The TCR estimated for each sample from the measured activation energy using the formerly stated equality $TCR = -\Delta W/kT^2$ [5] is $TCR_{A@475} = 3.44\%/K$ and $TCR_{B@500} = 0.72\%/K$, respectively.

5. Electrical charge transport

The different morphological and structural analysis performed with samples A@475 and B@500 has shown that V_2O_5 is the prevailing vanadium oxide phase formed in all samples due to the use of an annealing temperature well above 434°C, but a slightly different behavior has been perceived in electrical conductivity measurements. The morphological tests determine that A@475 sample presents an almost pure V_2O_5 phase, while a set of mixed vanadium oxide phases VO_x has been obtained for all B type samples, even those that have been processed at the highest temperature, 500°C. Nevertheless, even for these B type samples, the clear preponderance of the V_2O_5 phase when compared with other identified oxide phases, as can be seen on the Raman spectrums in **Figure 4**, should be noted.

The electrical behavior measured for the different vanadium oxide samples, illustrated in **Figure 6a**, shows that electrical conductivity (σ) has an Arrhenius behavior as a function of

temperature (T), indicating that electrical conduction in this material is the result of a thermally activated process. A Meyer-Neldel rule (MNR) relationship is found to hold in a wide variety of such activated processes as the electron conduction in extended states, the ionic conduction, or the thermally activated hopping [34–36]. According to the MNR, the prefactor in Eq. (1) (σ_0) and the activation energy (ΔW) are related by Eq. (2), where σ_{00} is a constant and ΔW_{MNR} is the Meyer-Neldel activation energy

$$\log(\sigma_0) = \log(\sigma_{00}) + \frac{\Delta W}{\Delta W_{MNR}}. \quad (2)$$

The activation energies for the processed samples range from 0.093 to 0.217 eV, according to the experimental data obtained for the electrical conductivity, measured in a temperature range between 25 and 100°C. As can be seen in **Figure 6b**, all of them obey the MNR, with a value of $\sigma_{00} = 4.2 \times 10^{-3}\ \Omega^{-1}\ cm^{-1}$ and $\Delta W_{MNR} = 0.9374$ eV, with a goodness of fit $R^2 = 0.8944$.

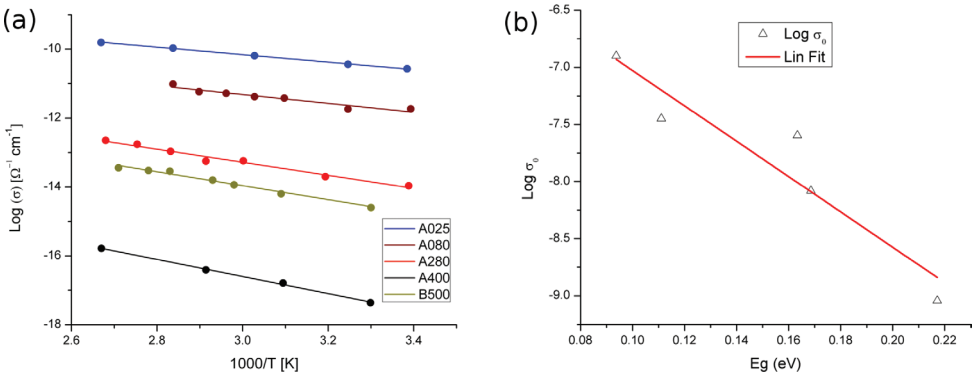

Figure 6. Compliance of activation energy for different processing temperatures with Meyer-Neldel rule: (a) log(σ) vs. 1000/T for samples A and B, (b) fit of ΔW to Meyer-Neldel rule.

The good correspondence observed between the activation energies derived from the electrical conductivity measurements carried out with the different samples and the conventional Meyer-Neldel rule can be attributed to a modification of the location of the Fermi energy level ε_F with respect to the conduction band ε_C with the different annealing conditions applied, similar to the behavior noted in amorphous semiconductors [37].

5.1. Electrical transport in V_2O_5

It is well known that the presence of the V_2O_5 oxide phase is responsible for the high TCR value observed at room temperature in mixed VO_x samples. Small polaron hopping between localized states is the prevailing mechanism that handles the electrical charge transport in the V_2O_5 phase. Mott's works [34, 38] established the basis for the study of this transport mechanisms in transition metals [39], and the proposed models were successively used to experimentally identify this behavior in both single crystal [33] and amorphous V_2O_5 [40] materials. In this section, Mott's models are used to confirm that experimental measurements obtained

http://dx.doi.org/10.5772/67054

with sample A@475, with an almost pure V_2O_5 phase, are consistent with the small polaron hopping charge transport mechanism.

Charge transport through polarons is a well-known effect observed under conditions of strong electron-phonon interaction. One evident effect of strong electron-phonon interaction in a material is the dependence of the electrical conductivity with temperature as seen in analyzed samples. However, other less obvious effect is revealed under this condition, an increase in the effective mass of the electrons due to the interaction with heavy ion nuclei [41]. The assembly formed by the electron and its associated field deformation is known as polaron.

Polarons can be classified taking into account the size of the field deformation radius with respect to the lattice constant, which gives rise to large or small polarons. Charge transport mechanism depends on polaron size; while for large polarons, charges are moved in a unique band, with small polarons, the charge remains trapped on a single ion most of the time. The interaction between the lattice vibration and the localized electron induces charges to jump from one atom to a neighboring one. This process is called conduction by hopping charge carriers and takes place through thermal activation at high temperature [42].

Based on Mott's model, the DC conductivity for the hopping of polarons in a nonadiabatic approximation, above the Debye temperature θ_D is given by Eq. (3) [34, 38]:

$$\sigma = \nu_0 N e^2 R^2 \frac{C(1-C)}{\kappa T} \exp(-2\alpha R) \exp\left(\frac{-\Delta W}{kT}\right), \tag{3}$$

where ν_0 is the optical phonon frequency, N is the number of transition metal ion sites per unit volume, e is the electron charge, α is the wave function decay constant, C is the ratio of ion concentration (V^{+4} vs. V^{+5}), R is the hopping distance, and θ_D is the Debye temperature given by $\theta_D = h\nu_0/k$, where h and k are the Plank and Boltzmann constants. Schnakenberg proposed a simplified model formulation taking into account the phonon distribution [43] in which the dependence of the electrical conductivity with the temperature can be expressed with Eq. (4) [44],

$$\ln(\sigma T) = \ln(\sigma T)_0 - \frac{W_D}{2kT} - \frac{W_H}{kT} \frac{\tanh(h\upsilon_0/4kT)}{h\upsilon_0/4kT}, \tag{4}$$

where σ_0 is a constant, W_D is the activation energy for hopping due to disorder, W_H is the polaron hopping energy, and T the temperature in K. Eq. (4) is valid for the hopping of polarons in the nonadiabatic approximation, above $\theta_D/2$ temperature, where θ_D is the Debye temperature. Total activation energy ΔW can be derived from previous parameters using an expression proposed by Austin-Mott in Eq. (5) [34, 38],

$$\begin{cases} \Delta W = W_H + \frac{W_D}{2} & for\ T > \theta_D/2, \\ \Delta W = W_D & for\ T < \theta_D/4. \end{cases} \tag{5}$$

In order to verify the nature of the electronic transport mechanism in sample A@475, with an almost pure V_2O_5 phase, the experimental data obtained for the electrical conductivity was fitted by using the Mott-Schnakenberg model, as shown in our previous work [45].

The fitting parameters derived by least squares for σ_0, W_H, $W_{D,}$ and $h\nu_0$ have been used to check the condition for polaron existence and to identify the particular type of polaron that is responsible of charge transport. The parameters obtained from the best linear fit, with a 95% confidence interval limits, were W_H = 0.1682 ± 0.0121 eV, W_D = 0.2241 ± 0.0139 eV, and $h\nu_0$ = 0.02755 ± 0.00994 eV; with a goodness of fit R^2 = 0.9827 [45]. The Debye temperature $\theta_D = h\nu_0/k$ that corresponds to these values is θ_D = 319 K.

5.2. Verification of the polaron charge transport in V_2O_5

The values extracted for Mott's model parameters with the fit of the electrical conductivity data have been used to check the consistency of the results with the several hypotheses used by Schnakenberg in Mott's model simplified formulation, which involve significant assumptions regarding the transport mechanism. Specifically, we have certified that the strong electron-phonon interaction condition proposed by Austin-Mott, the small polaron formation condition established by Emin-Holstein, the minimum mobility condition for conduction by hopping formulated by Cohen, and the condition proposed by Holstein to set the limit between the adiabatic and nonadiabatic regimes are verified for the temperature range used in measurements.

The strong electron-phonon interaction condition was verified by calculating the ratio of the polaron effective mass m_p to the rigid-lattice effective mass m^*. The higher this ratio, the greater the electron-phonon coupling. The ratio between these two parameters was obtained using Eq. (6) [34, 38],

$$m_p = (\hbar^2/2J R^2)\exp(\gamma) = m^* \exp(\gamma), \tag{6}$$

where J is the polaron bandwidth, R is the mean separation between the transition metal ions, and γ is the electron-phonon interaction parameter, which is given by Eq. (7) [34, 38],

$$\gamma = 2\left(\frac{W_H}{h\upsilon_0}\right). \tag{7}$$

The condition of small polaron formation was verified using the expression proposed by Emin-Holstein in Ref. [46], an inequality that relates the polaron hopping energy W_H with the bandwidth of the polaron J, as expressed in Eq. (8),

$$J < \frac{W_H}{3}. \tag{8}$$

The bandwidth of the polaron J was estimated from the fitting parameters using the approximate expression proposed by Holstein [47], as shown in the relationship in Eq. (9),

$$J \approx 0.67\, h\upsilon_0 \left(T/\theta_D\right)^{1/4}. \tag{9}$$

The type of conduction mechanisms followed by the charge carriers was established using the condition proposed by Holstein [47] to set the limit between the adiabatic and nonadiabatic regimes [34], given by Eq. (10),

http://dx.doi.org/10.5772/67054

$$H = \left(2kT\,W_H/\pi\right)^{1/4}\left(h\upsilon_0/\pi\right)^{1/2}. \tag{10}$$

The polaron conduction regime is determined by the inequality,

$$\begin{cases} J > H & \textit{for} \text{ adiabatic hopping,} \\ J < H & \textit{for non} \text{ - adiabatic hopping.} \end{cases} \tag{11}$$

Finally, for the case of the nonadiabatic regime, the mobility μ has been evaluated using Eq. (11) based on the model proposed by Murawsky [48],

$$\mu = \left(\frac{e\,R^2 J^2}{\hbar kT}\right)\left(\frac{\pi}{4\,W_H\,kT}\right)^{1/2}\exp\left(-\frac{\Delta W}{kT}\right). \tag{12}$$

Table 1 condenses the values obtained for Mott's model parameters from the fit of the electrical conductivity experimental data achieved with A@475 sample [45], together with the values derived for other parameters using the proposed equations. It can be seen that for temperatures in the range used for measurements (from 25 to 100°C), these values are consistent with the simultaneous verification of the four implicit hypotheses used by Schnakenberg in Mott's model simplified formulation and, therefore, allows us to deduce that the small polarons hopping is the conduction mechanism in V_2O_5 thin films obtained for A@475 samples.

Parameter	Value	Parameter	Value
ΔW	0.2670 eV	J	0.0182 eV
W_H	0.1682 eV	γ	12.2
W_D	0.2241 eV	θ_D	319.7 K
$h\upsilon_0$	0.0275 eV	μ	1.5×10^{-5} cm²/Vs

Table 1. Mott's model parameters obtained for V_2O_5 thin films [45].

As a final remark, it is noteworthy that the low value of mobility has been achieved with A type samples, $\mu = 1.5 \times 10^{-5}$ cm²/Vs. Cohen condition [49] establishes that mobility μ has to be much lower than 10^{-2} cm²/Vs in the case of a hopping conduction process. This condition was completely met in our V_2O_5 thin film type A samples, with a mobility of $\mu = 1.5 \times 10^{-5}$ cm²/Vs, while for V_2O_5, monocrystal mobility value of $\mu = 0.15–0.5 \times 10^{-2}$ cm²/Vs [33] is the limit of Cohen condition.

6. Summary and conclusion

A new method for the preparation of vanadium oxide thin films has been proposed with the aim of providing compatibility with the lift-off microstructuring technique. The thin film

formation has been separated into two phases: a first deposition at low temperature using RF magnetron sputtering and an additional thermal annealing at high temperature to adjust film structure after patterning with the lift-off technique. Different starting materials (sputtering targets) and annealing conditions have been analyzed in order to obtain films with high TCR values for application as infrared microsensors (bolometers).

Samples were analyzed using a variety of characterization techniques comprising SEM, XRD, and Raman. I-V curves were measured in a probe station to establish the dependence of electrical conductivity with the temperature for the different samples.

Structural and optical characterization by XRD and Raman shows that V_2O_5 is the predominant oxide phase identified in all samples, even if mixed phases are observed in samples obtained from the metallic-V target (type B samples).

The electrical characterization showed a negative exponential behavior with temperature for all samples, with an activation energy of 0.267 eV in the case of the pure V_2O_5 phase observed in sample A@475, which corresponds to a TCR value of 3.44%/K.

Regarding the electron transport mechanism in processed samples, it has been found that the electrical conductivity measurements performed with the B type VO_x samples annealed at different temperatures found correlation with a conventional Meyer-Neldel rule, suggesting a thermally activated conduction mechanism.

Finally, it has been found that electrical measurements performed with type A samples, with a pure V_2O_5 phase, are consistent with the electron transport model proposed by Mott for the small polarons hopping. The experimental data was fitted using the Schnakenberg simplified formulation obtaining a polaron hopping energy W_H = 0.1682 eV and an activation energy for hopping due to disorder W_D = 0.2241 eV. The type of charge transport in type A samples was verified by checking the consistency of the resulting fitting parameters with the implicit hypothesis in Schnakenberg formulation: the conditions for the strong electron-phonon interaction, for the existence of small polarons, for the nonadiabatic regime of the hopping of charge carriers, and for the maximum mobility limit. Overall, results suggest that small polarons hopping is the prevalent mechanism driving the electron transport in V_2O_5 thin films obtained with the proposed method.

Acknowledgments

This research leading to these results and chapter edition has been partially funded by the Spanish Ministerio de Economía y Competitividad, through project TEC2013-48147-C6-6-R (TEMINAIR) and supported by grant PRH 2007 No. 203 (PAE 37079), funded by National Institute of Industrial Technology (INTI) and the National Agency for Promotion of Science, Ministry of Science and Technology of Argentina. The authors also wish to thank B. Halac and E. Di Liscia for the Raman spectroscopy, S. Amore for the XRD diffractograms measurements, and L. Patrone for the SEM images performed on samples.

http://dx.doi.org/10.5772/67054

Author details

Hernan M. R. Giannetta[1, 2], Carlos Calaza[3], Liliana Fraigi[1, 2] and Luis Fonseca[3]

*Address all correspondence to: hgiannetta@frba.utn.edu.ar

1 Centro de Micro y Nano Electrónica del Bicentenario (CMNB), Instituto Nacional de Tecnología Industrial (INTI), San Martín, Buenos Aires, Argentina

2 Universidad Tecnológica Nacional (UTN) - Facultad Regional Buenos Aires (FRBA), Argentina

3 Institute of Microelectronics of Barcelona (IMB-CNM, CSIC), Campus UAB, Bellaterra, Barcelona, Spain

References

[1] Kruse P.W., Uncooled Thermal Imaging Arrays, Systems, and Applications. 1st ed. Bellingham, Washington, USA: SPIE; 2001. 90pp. DOI: 10.1117/3.415351

[2] Wang B., Lai J., Li H., Hu H., Chen S., Nanostructured vanadium oxide thin film with high TCR at room temperature for microbolometer. Infrared Physics & Technology, Elsevier. 2013;**57**(03):8–13. DOI: 10.1016/j.infrared.2012.10.006

[3] Wood R.A., Chapter 3. Monolithic silicon microbolometer arrays. In: Kruse P.W. and Skatrud D.D., editors. Infrared Imaging Arrays and Systems. 1st ed. San Diego, CA, USA: Academic Press; 1997. pp. 43–121. DOI: 10.1016/S0080-8784(08)62689-7

[4] Fieldhouse N., Pursel S.M., Horn M.W. and Bharadwaja S.S.N., Electrical properties of vanadium oxide thin films for bolometer applications: processed by pulse dc sputtering. Journal of Physics D: Applied Physics. 2009;**42**(5):055408. DOI: 10.1088/0022-3727/42/5/055408

[5] Jerominek H., Picard F., Vincent D., Vanadium oxide films for optical switching and detection. Optical Engineering. 1993; **32**(9):2092–2099. DOI: 10.1117/12.143951

[6] Subramanyam A., Bharat Kumar Reddy Y. and Nagendra C.L., Nano-vanadium oxide thin films in mixed phase for microbolometer applications. Journal of Physics D: Applied Physics. 2008;**41**(19):195108. DOI: 10.1088/0022-3727/41/19/195108

[7] Han Y.H., Choi I.H., Kang H.K., Park J.Y., Kim K.T., Shin H.J., Moon S., Fabrication of vanadium oxide thin film with high-temperature coefficient of resistance using V_2O_5/V/V_2O_5 multi-layers for uncooled microbolometers. Thin Solid Films, Elsevier. 2003; **425**(1-2):260–264. DOI: 10.1016/S0040-6090(02)01263-4

[8] Shackelford J.F., Han Y.H., Kim S., Kwon S.H., editors. CRC Materials Science and Engineering Handbook. Boca Raton, FL, USA. 4th ed. CRC Publisher; 2015. 634pp.

[9] Bahlawane N., Lenoble D., Vanadium oxide compounds: structure, properties, and growth from the gas phase. Chemical Vapor Deposition, Wiley. 2014;**20**(7–9):299–311. DOI: 10.1002/cvde.201400057

[10] Cardarelli F., editor. Materials Handbook: A Concise Desktop Reference. Springer, London-UK. 2008. ISBN 978-1-4471-3648-4

[11] Zou C.W., Yan X.D., Han J., Chen R.Q. and Gao W., Microstructures and optical properties of β-V_2O_5 nanorods prepared by magnetron sputtering. Journal of Physics D: Applied Physics. 2009;**42**(14):145402. DOI: 10.1088/0022-3727/42/14/145402

[12] Ruzmetov D., Zawilski K.T., Narayanamurti V. and Ramanathan S., Structure-functional property relationships in rf-sputtered vanadium dioxide thin films. Journal of Applied Physics. 2007;**102**(11):113715. DOI: 10.1063/1.2817818

[13] Chae B.G., Kim H.T., Yun S.J., Kim B.J., Lee Y.W. and Kang K.Y., Comparative analysis of VO_2 thin films prepared on sapphire and SiO_2/Si substrates by the sol–gel process. Japanese Journal of Applied Physics. 2007;**46**(2R):738. DOI: 10.1143/JJAP.46.738

[14] Piccirillo C., Synthesis and functional properties of vanadium oxides: V_2O_3, VO_2, and V_2O_5 deposited on glass by aerosol-assisted CVD. Chemical Vapor Deposition. 2007;**13**(4):145–151. DOI: 10.1002/cvde.200606540

[15] Pauli, S.A. and Herger, R. and Willmott, P.R. and Donev, E.U. and Suh, J.Y. and Haglund, R.F., X-ray diffraction studies of the growth of vanadium dioxide nanoparticles. Journal of Applied Physics. 2007;**102**(7):073527. DOI: 10.1063/1.2786917

[16] Rata A.D., Chezan A.R., Haverkort M.W., Hsieh H.H., Lin H.J., Chen C.T., Tjeng L.H. and Hibma T., Growth and properties of strained VO_x thin films with controlled stoichiometry. Physical Review B. 2004;**69**(7):075404. DOI: 10.1103/PhysRevB.69.075404

[17] Takahashi I., Hibino M. and Kudo T., Thermochromic $V_{1-x}W_xO_2$ thin films prepared by wet coating using polyvanadate solutions. Japanese Journal of Applied Physics. 1996;**35**(4A):L438. DOI: 10.1143/jjap.35.l438

[18] Suh J.Y., Lopez R., Feldman L.C. and Haglund R.F., Semiconductor to metal phase transition in the nucleation and growth of VO_2 nanoparticles and thin films. Journal of Applied Physics. 2004;**96**(2):1209–1213. DOI: 10.1063/1.1762995

[19] Melnik V., Khatsevych I., Kladko V., Kuchuk A., Nikirin V., Romanyuk B., Low-temperature method for thermochromic high ordered VO_2 phase formation. Materials Letters. 2012;**68**(1):215–217. DOI: 10.1016/j.matlet.2011.10.075

[20] Fu G., Polity A., Volbers N., and Meyer B., Annealing effects on VO_2 thin films deposited by reactive sputtering. Thin Solid Films. 2006;**515**(4): 2519–2522. DOI: 10.1016/j.tsf.2006.04.025

[21] Xu X., He X., Wang G., Yuan X., Liu X., Huang H., Yao S., Xing H., Chen X. and Chu J., The study of optimal oxidation time and different temperatures for high quality {VO_2} thin film based on the sputtering oxidation coupling method. Applied Surface Science. 2011;**257**(21):8824–8827. DOI: 10.1016/j.apsusc.2011.04.068

[22] Thornton J.A., Plasma-assisted deposition processes: theory, mechanisms and applications. Thin Solid Films. 1983;**107**(1):3–19. DOI: 10.1016/0040-6090(83)90003-2

[23] Nag J. and Haglund Jr R.F., Synthesis of vanadium dioxide thin films and nanoparticles. Journal of Physics: Condensed Matter. 2008;**20**(26):264016. DOI: 10.1088/0953-8984/20/26/264016

[24] Fuls E.N., Hensler D.H., Ross A.R., Reactively sputtered vanadium dioxide thin films. Applied Physics Letters. 1967;**10**(7):199–201. DOI: 10.1063/1.1754909

[25] Schneider K., Lubecka M., Czapla A., VO_x thin films for gas sensor applications. Procedia Engineering. 2015;**120**:1153–1157. DOI: 10.1016/j.proeng.2015.08.1009

[26] Zhang H., Wu Z., Yan D., Xu X., Jiang Y., Tunable hysteresis in metal-insulator transition of nanostructured vanadium oxide thin films deposited by reactive direct current magnetron sputtering. Thin Solid Films. 2014;**552**:218–224. DOI: 10.1016/j.tsf.2013.12.007

[27] Raj, P.D., Gupta S. and Sridharan M., Studies on VO_x thin films deposited over Si_3N_4 coated Si substrates. AIP Conference Proceedings. 2015;**1665**(1):080007. DOI: 10.1063/1.4917911

[28] Tao W., He Y., Xiang D., Ya-Dong J., Chao C. and Ro-Land W., Modeling for VO_2 reactive sputtering process using a pulsed power supply. Chinese Physics B. 2014;**23**(8):088113. DOI: 10.1088/1674-1056/23/8/088113

[29] Kürüm U, Yaglioglu H.G., Küçüköz B., Oksuzoglu R.M., Yıldırım M., Yağcı A.M., Yavru C., Özgün S., Tıraş T. and Elmali A., Modifying ultrafast optical response of sputtered VO_X nanostructures in a broad spectral range by altering post annealing atmosphere. Journal of Optics. 2015;**17**(1):015503. DOI: 10.1088/2040-8978/17/1/015503

[30] Luo Z., Wu Z., Xu X., Du M., Wang T., and Jiang Y., Impact of substrate temperature on the microstructure, electrical and optical properties of sputtered nanoparticle V_2O_5 thin films. Vacuum. 2010;**85**(2):145–150. DOI: 10.1016/j.vacuum.2010.05.001

[31] Chen S., Jianjun L., Jun D., Hong M., Hongchen W., and Xinjian Y., Characterization of nanostructured VO_2 thin films grown by magnetron controlled sputtering deposition and post annealing method. Optics Express. 2009;**17**(26):24153–24161. DOI: 10.1364/oe.17.024153

[32] Benmoussa M., Structural, electrical and optical properties of sputtered vanadium pentoxide thin films. Thin Solid Films. 1995;**265**(1–2):22–28. DOI: 10.1016/0040-6090(95)06617-9

[33] Ioffe V.A. and Patrina I.B., Comparison of the small-polaron theory with the experimental data of current transport in V_2O_5. Physica Status Solidi (b). 1970;**40**(1):389–395. DOI: 10.1002/pssb.19700400140

[34] Austin I.G. and Mott N.F., Polarons in crystalline and non-crystalline materials. Advances in Physics. 1969;**18**(71):41–102. DOI: 10.1080/00018736900101267

[35] Meyer W, Neldel H. Über die Beziehungen zwischen der Energiekonstanten ε under der Mengenkonstantenα in der Leitwerts-Temperaturformel bei oxydischen Halbleitern. [On the relations between the energy constant ε and the quantity constant α in temperature dependent conductivity of oxide semiconductors] Zeitschrift für Technische Physik [J Techn Physics]. 1937;18:588–593.

[36] Yelon A., Movaghar B. and Crandall R.S., Multi-excitation entropy: its role in thermodynamics and kinetics. Reports on Progress in Physics. 2006;**69**:1145. DOI: 10.1088/0034-4885/69/4/R04

[37] Spear W.E., Allan D., Comber P.L., Ghaith A., A new approach to the interpretation of transport results in a-Si. Philosophical Magazine Part B. 1980;**41**(4):419–438. DOI: 10.1080/13642818008245397

[38] Mott N., Conduction in glasses containing transition metal ions. Journal of Non-Crystalline Solids. 1968;**1**(1):1–17. DOI: 10.1016/0022-3093(68)90002-1

[39] Davis E.A. and Mott N.F., Conduction in non-crystalline systems V. Conductivity, optical absorption and photoconductivity in amorphous semiconductors. Philosophical Magazine. 1970;**22**(179):903–922. DOI: 10.1080/14786437008221061

[40] Sanchez C., Morineau R., Livage J. Electrical conductivity of amorphous V_2O_5. Physica Status Solidi (a). 1983;**76**(2):661–666. DOI: 10.1002/pssa.2210760232

[41] Kittel C., editor. Introduction to Solid State Physics. 8th ed. USA: Wiley; 2004. 704pp. ISBN: 978-0-471-41526-8

[42] Devreese J. T., "Polarons" in Encyclopedia of Applied Physics, Vol. 14, pp. 383 – 409. Ed. by G.L. Trigg (VCH, Weinheim, 1996).

[43] Schnakenberg J., Polaronic impurity hopping conduction. Physica Status Solidi (b). 1968;**28**(2):623–633. DOI: 10.1002/pssb.19680280220

[44] Culea E., Gheorghiu, C. and Nicula A., Electrical conductivity of vitreous 75%V_2O_5 − 25%(As_2O_3·B_2O_3), Physica Status Solidi (a). 1986;**96**(1):K85–K88. DOI: 10.1002/pssa.2210960163

[45] Giannetta H.M.R., Calaza C., Lamas D., Fonseca L., Fraigi L., Electrical transport properties of V_2O_5 thin films obtained by thermal annealing of layers grown by RF magnetron sputtering at room temperature. Thin Solid Films. 2015;**589**:730–734. DOI: 10.1016/j.tsf.2015.06.048

[46] Emin D., David E., Holstein T., Studies of small-polaron motion IV. Adiabatic theory of the Hall effect. Annals of Physics. 1969;**53**(3):439–520. DOI: 10.1016/0003-4916(69)90034-7

[47] Holstein T., Studies of polaron motion: Part I. The molecular-crystal model. Annals of Physics. 1959;**8**(3):325–342. DOI: 10.1016/0003-4916(59)90002-8

[48] Murawski L., Chung C.H. and Mackenzie J.D., Electrical properties of semiconducting oxide glasses. Journal of Non-Crystalline Solids. 1979;**32**(1):91–104. DOI: 10.1016/0022-3093(79)90066-8

[49] Cohen M., Review of the theory of amorphous semiconductors. Journal of Non-Crystalline Solids. 1970;**4**:391–409. DOI: 10.1016/0022-3093(70)90068-2

Chapter 10

Smart Thermoresponsive Surfaces Based on pNIPAm Coatings and Laser Method for Biological Applications

Laurentiu Rusen, Valentina Dinca,
Cosmin Mustaciosu, Madalina Icriverzi,
Livia Elena Sima, Anca Bonciu, Simona Brajnicov,
Natalia Mihailescu, Nicoleta Dumitrescu,
Alexandru I. Popovici, Anca Roseanu and
Maria Dinescu

Additional information is available at the end of the chapter

http://dx.doi.org/10.5772/66280

Abstract

Various applications within last decades such as bacterially resistant surfaces, soft robotics, drug delivery systems, sensors and tissue engineering are poised to feature the importance of the ability to control bio-interfacial interactions. An enhanced attention is dedicated to designing smart stimuli-responsive interfaces for DNA, drug delivery, protein and cell based applications. Within this context, the thermoresponsive materials, especially poly(N-isopropylacrylamide) (pNIPAm) have been intensively used in tissue engineering applications for a controlled detachment of proteins and cells with a minimum of invasive effect on protein and cell structural conformation. The properties of smart bio-interfaces can be controlled by its composition and polymer architecture. Therefore, appropriate methods for obtaining controlled coatings are necessary. Laser methods were successfully used in the last decades for obtaining controlled organic and inorganic coatings for various types of applications, from electronics to tissue engineering. Among these, Matrix-Assisted Pulsed Laser Evaporation (MAPLE) technique bring us a step forward to other laser methods by avoiding damage and photochemical decomposition of materials. In this chapter we describe materials and approaches used for design of smart bio-interfaces aimed at controlling protein and cells behavior *in vitro*, focusing MAPLE method for tuning coatings characteristics in relation with biological response.

Keywords: bio-smart interfaces, temperature responsive, laser processing, mammalian cells

1. Introduction to poly(N-isopropylacrylamide) (pNIPAm) characteristics, its thermoresponsive mechanism and its applicability in bioengineering

The design of smart bio-interfaces for a wide variety of applications is based nowadays on stimuli-responsive surfaces. Depending on the type of bioengineering applications implying bio-adhesion, manipulation of microorganisms or mammalian cell, bio-adsorption of proteins, various surfaces that can respond to different stimulus (e.g., temperature, pH, light and magnetic field) [1–3] could be obtained by tuning not only the nature of material or its characteristics and chemistry but also the obtaining method. Among these types of smart- or stimuli-responsive materials, thermoresponsive group of smart polymers consists of the polymers which exhibit rapid, reversible phase transition/phase separation phenomena in response to changes in temperature. The thermosensitive behavior is based on the reversible solubility of the smart polymers caused by increasing temperature above a critical transition temperature (lower critical solution temperature (LCST) or "cloud point") [1–5].

There are several groups of thermosensitive polymers with different transition temperatures such as poly(ethylene glycol) with a transition temperature of 100°C, poly(N-alkyl-substituted acrylamides) and poly(N-vinylalkylamides) with a transition temperature ranging from 32 to 39°C depending on polymer molecular weight as well as other polymers such as poly (N-vinyl piperidine) with low-transition temperature of 4–5°C.

Particularly, poly(N-isopropylacrylamide) (pNIPAm) coatings are of great promise in both basic developmental biology studies and regenerative medicine, as thermoresponsive smart bio-interfaces responding within the physiological temperature range [1–9]. Its chemical formula is $(C6H11NO)_{n}$, having a white solid form. Starting from 1968, from the first report on the phase-transition temperature as a function of pNIPAm concentration, there are various studies implying the use of reversible behavior phase transition of swelling/shrinking cycles that can be performed by a gel at around 32°C, with no sign of material fatigue [9]. For example, one of the first studies on the deswelling mechanism [6] demonstrated that bound water molecules are freed at LCST (38.5°C) which lead to a collapse phenomenon, followed by trapping water with a layer/skin. Moreover, depending on how dense the polymeric layer is, this process could have biphasic kinetics (slow for dense-packed surfaces, fast for less dense-packed surfaces) [6].

The abovementioned process implies a phase separation by changing the hydrophobic-hydrophilic moieties balance of the uncharged polymer. Solubility in water is based on the hydrogen bonding with water molecules which, however, is dependent/reduced with temperature increase, leading eventually to separation phase. Therefore, there are two phases formed: an aqueous phase containing practically no polymer and a polymer-enriched phase that could be easily separated by centrifugation, decanting, or even filtration. Moreover, the temperature of phase transitions also depends on the polymer concentration and its molecular weight and it can be further modified by incorporating various hydrophilic co-monomers or coupling other active compounds. For example, as phase transition at increased temperature of thermosensitive polymers is the result of hydrophobic interactions between polymer molecules, by increasing salt concentrations, a shift of cloud

http://dx.doi.org/10.5772/66280

point to lower temperatures can be achieved. The opposite effect can be obtained by deteriorating the hydrophobic interactions by the simple addition of organic solvents, detergents and other active agents [7–10].

Besides modifying or adjusting the cloud point of pNIPAm with salts or surfactants, interesting results were achieved by copolymerization with other hydrophilic or hydrophobic co-monomers, nanoparticles, bioactive agents such as peptides and enzymes [10–15]. The resulted block copolymers based on the pNIPAm thermosensitive part and on hydrophilic monomers conducted to an elevating LCST while those based on the hydrophobic monomers lead to a decrease of the LCST. Additionally, these modifications imply also the stimuli response, as being able to respond not only to temperature variations but also to pH variations. For example, studies have been reported on the increase in the LCST of pNIPAm from 32 to 38°C, as well as adding a pH response after carrying out its copolymerization with hydrophilic methacrylic acid and PEG (polyethylene glycol). Depending on the followed application, it is essential to control the characteristics of the smart polymeric systems, especially for applications envisaging bioengineering area.

As previously mentioned, due to its response within the physiological temperature range, pNIPAm coatings are of great promise not only in basic developmental biology studies but also in drug delivery and regenerative medicine. There are several directions in which pNIPAm in the form of coatings could be applied within these areas [16–22].

For example, by obtaining a responsive polymer surface consisting of a densely packed monolayer of copolymer molecules onto a solid substrate, the switching of the surface properties upon changing solvent selectivity or pH of the aqueous environment facilitated the patterned cell seeding and coculture [18, 19]. Polymer brushes, which consist of an assembly of polymer chains that are attached by one end to the surface, were obtained for tuning physicochemical surface characteristics such as wettability, surface charge and morphology, for further even more complex environments such as for fabrication and manipulation of tissue-like architectures with multiple cell types [19, 20]. Another important direction is the use of the smart polymer networks in the delivery of therapeutic drugs at body temperatures as well as structures for tissue engineering [21, 22].

2. Approaches for obtaining pNIPAm surfaces

Nevertheless, nowadays, there are various approaches for obtaining pNIPAm surfaces, in different forms such as membranes, thin films and nanoparticles. Within the context of cell culture substrates or drug-delivery platforms, the ideal use of pNIPAm bio-interfaces is as controlled coating. Based on the fact that the coating response toward and within the biological medium is closely related to its structural and architectural characteristics, a variety of methods are envisaged and developed to comply the specific requirements. However, there are cases when some surfaces based on pNIPAm do not support cell adhesion even above the LCST, making them unsuitable as culture substrates. That is why the choice of surface fabrication methods is directly correlated to the ability to use the smart coating within the desired

application. Some of the most used techniques [5, 16–33] for obtaining smart bio-interfaces based on stimuli-responsive polymers within a large area of applications are listed below:

- Radiation cross-linking. By using this method, the polymer molecular mass is increased by linking the polymer chains under irradiation initialization. The irradiation produces free radicals which recombine forming the cross-links (depending on the polymer type and radiation dose). Graft polymerization can be initiated by high-energy irradiation such as γ-ray, swift heavy ions and electron beam (e-beam) [23].
- Atom transfer radical polymerization (ATRP) is another simple method to obtain well-defined and high functionalized (co)polymers. It allows a good control of polymers functionalities, topologies and compositions. pNIPAm surfaces obtained using surface-initiated atom transfer radical polymerization (ATRP) technique show strong adhesive properties and can be used for cell sheets for tissue engineering applications [24]. By combining the self-assembled monolayer of initiator and atom transfer radical polymerization (ATRP), relatively homogeneous polymer brush can be obtained [25].
- Electron-beam (e-beam) processing of polymers is also widely used for cross-linking of polymer chains in order to improve chemical properties [26–31]. The method implies two steps: first uniformly coating a surface with NIPAm monomer solution and irradiating it using 0.3-MGy EB [30] and second washing the non-grafted NIPAm monomers with deionized (DI) water. It was observed that cell adhesion depends on the grafting density of the pNIPAm layers obtained by e-beam (cell attachment/detachment significantly decreased for high grafting densities). Surfaces with optimized thicknesses of around 15–20 nm were used for temperature-controlled adhesion and detachment studies implying various cell lines. Meanwhile, it was observed that if the thickness is increase around 30 nm, grafted pNIPAm surfaces do not support cell adhesion at any temperature anymore.
- Plasma polymerization or plasma-deposited pNIPAm coatings provide a thermoresponsive surface that is covalently attached to a solid substrate with a good retention of the monomer integrity [30–32]. This method is based on gradually decreasing the plasma glow discharge for the deposition of the pNIPAm coating in the outer surface. The polymer retained its monomeric structure, with the preservation of the phase transition. Fourier transform infrared spectroscopy (FTIR) measurements revealed that the functional groups remained the same after plasma discharge. Cell culture studies as well as thermal detachment of the cell performed on pNIPAm surfaces proved successful, but no influence of the thickness of the films on cell was observed. The atmospheric plasma treatment followed by free radical graft copolymerization was used also for obtaining pNIPAm surfaces onto nylon. The atmospheric plasma exhibits the activation capability to initiate graft copolymerization [30–32].
- Other methods for the modification of large surface area with thin polymer films include solvent casting, dip, spin, or spray coating [30, 33, 34]. These methods have been employed to create bulk pNIPAm films which are not grafted to a substrate, but conjugated with some bioactive agents and deposited on a solid support such as tissue culture-grade polystyrene (TCPS) or glass.

http://dx.doi.org/10.5772/66280

- Another method of producing thermoresponsive surfaces involves using UV light irradiation to produce cross-linked surface layer. Moreover, this method can be used for engineering micropatterned surfaces with thermoresponsive regions. The first step involves using photolithography followed by the solvent washing from the shadowed regions [30, 35–37]. By using this approach, cells can be selectively detached from the grafted regions providing a good spatial control over detachment of adhered cells and therefore with high potential in the spatial distribution of different cell types in coculture systems.

2.1. The limitation of the current approaches and laser method perspectives

Most of the methods previously described use the hydrophobic-to-hydrophilic switch to recover cell sheets, instead of disintegration of the coating, present just in the case of solvent casting or spin coating. Although most of the methods ensure that the coating is not harvested with the cell sheet, keeping the cell construct free of unwanted soluble polymer after detachment, there are still several disadvantages such as high cost, the lack of flexibility in controlling the surface density, morphology or thickness of the films, adhesion onto substrate and even the abnormal cellular activity due to physiological alteration within cell microenvironment. Especially for applications such as cell sheets engineering or drug delivery, the efficiency of attachment/detachment of certain cell types or drugs is varied to the thickness and density of grafted pNIPAm. Thus, developing of simple strategy, allowing a rapid recovery of cell sheet transfer with the cell-extracellular matrix (ECM) intact but also which would allow a controlled release of active compounds, is desirable.

Nevertheless, laser methods proved to be viable solutions in the last decades, for processing various and multiple material surfaces. Due to the laser unique ability for surface heating, providing that the applied energy to be placed precisely on the needed area, laser can be used as a unique tool for surface engineering not only in research but also in industry and medicine [38, 39]. The distinct advantages compared to alternative methods of processing the materials can be summarized as follows:

- Versatility, as it can be applied to a wide range of organic and inorganic materials/biomaterials.
- Controlled thermal penetration allowing features high-resolution characteristics, up to tens of nanometers in size, speed, adaptability and scalability through parallel processing.
- Controlled thermal profile, shape and location of heat, therefore providing flexibility in making topographical features defined on a wide variety of biomaterials with no affected region in a noncontact way.
- Flexibility in the selection of parameters that can allow handling sensitive biological and living cells without losing their activity.

The most commonly used techniques for thin films or coatings at this moment are the laser-based methods of laser-assisted chemical vapor deposition (LCVD) and pulsed-laser deposition (PLD) [39]. LCVD is characterized by localized heating produced by a laser beam on a substrate. This technique is traditionally used to directly deposit complex geometries of

different materials, including metals and ceramics. PLD has been applied to a wide range of materials such as semiconductors, metals and alloys, presenting numerous advantages: the ability to control the thickness of the monolayer, good adhesion of film-substrate material consumption low and low temperature substrate.

These methods, however, are not suitable for the deposition of large and sensitive molecules, such as polymers and biomaterials as molecular bonds in the polymers can be destroyed by the laser energy pulse. There are few exceptions, the polymer, such as Teflon (PTFE), polymethylmethacrylate (PMMA), polypernaphthalene (PPN), or polyisobutylene (PIB) which were successfully deposited as coatings by using PLD [40, 41]. However, as most of the organic materials are damaged by the direct interaction of the laser beam, that is why, in order to avoid damage and photochemical decomposition of materials caused by PLD method, a new technique based on laser evaporation (matrix-assisted pulsed-laser evaporation—MAPLE) was introduced in the end of the 1990s at the Naval Research Laboratory. It provides multiple advantages for the area of biosensors, active multifunctional bio-coatings and multilayered coatings where the organic and sensitive materials are required to maintain their structure and functionality. By providing a much "softer" transfer by pulsed-laser evaporation, the degradation or the thermal decomposition of the materials is avoided.

An extension of MAPLE is resonant infrared matrix-assisted pulsed-laser evaporation (RIR-MAPLE) using free electron lasers or Er:YAG lasers, aiming to control and reduce the degradation of the materials during deposition process. The advantage of RIR-MAPLE method is based on using infrared radiation in order to excite specific molecular vibrational bond stretches in the host material.

MAPLE technique [41–52] brings us a step forward to laser method by avoiding damage and photochemical decomposition of materials and it is now used for obtaining different types of thin films such as follows:

- Fibronectin thin films were transferred stable and functional onto silica substrate for studies on human osteoprogenitor cells [49];
- Complex polymer or organic molecules (functionalized polysiloxanes and carbohydrates) were deposited on different substrates chemical sensor applications [40, 42];
- Light proteins thin films (such as lysozyme and myoglobin) with possible applications in drugs industry [50];
- Collagen thin films deposited on Si substrates with high structural fidelity as well as good uniformity and surface smoothness [51];
- Biodegradable hybrid polymeric thin films without or with embedded antitumoral agents (lactoferrin, cisplatin, or their combination with a biodegradable polycaprolactone) which can act as a hybrid platform with increased antitumor efficiency [43, 44];
- Polymer-inorganic nano-composite films with fluorescence properties with a potential for applications such as light emitters and chemical sensors [45];

http://dx.doi.org/10.5772/66280

- Composite thin films of calcium alendronate monohydrate, octacalcium phosphate as well as CaAl-H_2O/OCP on different titanium substrates with applications in implant coatings [46];
- Lipase enzyme for applications in enzymatic production and biosensors [47].

3. MAPLE techniques for smart pNIPAm thin-film engineering

Within the above discussed context, as most of the implied or required applications within bioengineering field require controlled bio-coating and sterile condition, laser-based techniques (i.e., matrix-assisted pulsed-laser evaporation—MAPLE) are contact-free technique and also easy to be integrated with required sterile processes.

Moreover, by controlling laser and target parameters in MAPLE process, an overall control over the thickness, porosity and architecture of mono- or multilayer can be easily achieved with no limitations in the use of materials to be deposited or structured, the ability to deposit multilayers without interlayer blending, as well as flexibility in engineering a wide range of simple or hybrid materials (nanoparticles, polymers, ceramics and biological compounds).

Although MAPLE technique was successfully used for a variety of biomaterials, there are only two groups that used recently the laser evaporation for engineering either simple pNIPAm coatings for mammalian cells attachment and detachment studies [5] or a mixed antimicrobial oligo (p-phenylene-ethynylene) (OPE)-PNIPAAm) coatings with biocidal activity, which provides also on-demand bacteria-releasing functionality [39]. In the last example, the multifunctional films of OPE-PNIPAAm with tailored chemical composition were deposited on substrates by using a sequential co-deposition mode, namely resonant infrared matrix-assisted pulsed laser evaporation (RIR-MAPLE) [39].

3.1. MAPLE system description for pNIPAm coatings deposition

The MAPLE process takes place in a vacuum chamber and it implies the use of an external laser source (UV, excimer, IR), a solid cryogenic target and a receiving substrate. In an ideal system for the MAPLE process, the material to be deposited (guest material) is mixed or suspended into a solvent (host matrix), rapidly frozen in a copper holder using liquid nitrogen and placed inside the vacuum chamber. During the deposition procedure, in order to avoid target melting problem during laser irradiation, the copper holder has to be continuously kept at low temperature by using a cooling system specifically designed for the transfer and circulation of liquid nitrogen inside the deposition chamber. Another step taken in order to avoid the melting was the rotation of the target holder, which avoids local overheating of the target as well as drilling of the copper holder due to multiple laser pulses. The material is ejected from the solid cryogenic target due to the laser energy absorbed into the target, followed by the evaporation of the host matrix solvent which transport and deposit the guest material on the substrate positioned above the target. The substrates are placed at a fixed distance of 3–4 cm from the target matrix. The background pressure ($1–4 \times 10^{-3}$ Pa) in the vacuum chamber

is maintained by using a turbomolecular pump (i.e., Pfeiffer-Balzers TPU 170). A simplified MAPLE setup is presented in **Figure 1**.

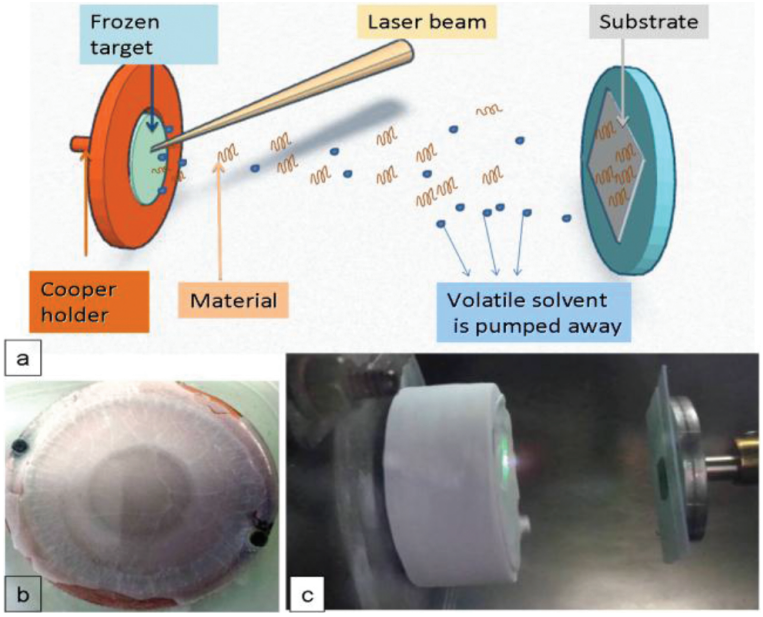

Figure 1. Schematic representation of MAPLE setup (a), image of the target system containing the frozen pNIPAm solutions and (b) inside chamber view during the deposition process (c).

3.2. Structural and morphological characteristics of the smart bio-interfaces engineered by laser methods

3.2.1. The structural characteristics of the pNIPAm coatings deposited by MAPLE

The characteristic vibrations of functional groups in the deposited pNIPAm thin films were subsequently analyzed and compared with a reference, that is, those obtained by drop-cast method by using Fourier transform infrared spectroscopy (FTIR). Fourier transform infrared spectroscopy is a technique for nondestructive chemical analysis used for characterizing thin films, allowing the identification of organic and inorganic chemical compounds. This technique is based on the chemical properties of the different groups to have specific resonance frequencies in the IR range of the electromagnetic spectrum (absorption bands presented/transmission). By comparing the film spectrum subjected to the action of the laser radiation to the spectrum of the control film, obtained by evaporation in air of a drop of solution from which was made the target, it can be determined whether the transfer was carried out with keeping its chemical composition.

http://dx.doi.org/10.5772/66280

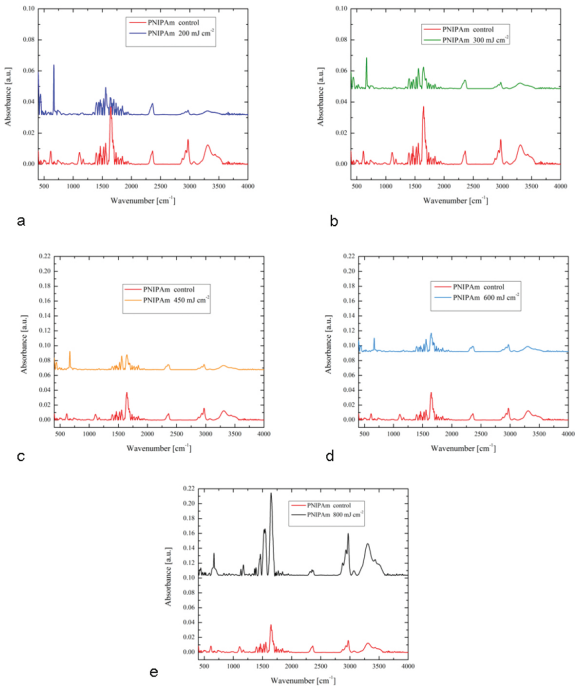

Figure 2. FTIR spectra for the coatings obtained with the following laser fluences: (a) 200, (b) 300, (c) 450, (d) 600 and (e) 800 mJcm^{-2}. A Jasco FT/IR-6300 spectrometer was used in transmission mode by accumulation of 1024 scans in the spectral range from 400 to 4000 cm^{-1}, with a resolution of 4 cm^{-1} [5]. The characteristic vibrations of functional groups in the deposited pNIPAm thin films obtained at different laser fluences were subsequently analyzed and compared with control thin films obtained by drop cast revealing the structural integrity of our samples.

As seen in **Figure 2a–e**, FTIR spectra confirmed the functionality of the polymer thin films obtained by MAPLE. At all laser fluences used, specific bonds corresponding to secondary amide C=O stretching of amide I bond at 1650 cm^{-1} and, respectively, to N–H stretching of amide II bond at 1550 cm^{-1} were observed on the thin films when compared with the control films [5]. The differences in FTIR spectral between these two bonds are correlated with the laser fluence used during MAPLE experiments. The absorption bands, which can be observed at 1368 and 1388cm^{-1}, correspond to the presence of isopropyl methyl (–CH(CH_3)$_2$)) deformation bands in the thin films. It can be observed also, in the high wave-number region, the presence of secondary amide N–H stretching around 3308 and 3437 cm^{-1} which are associated to free N–H stretching [5]. Specific vibrations of CH_2 and CH_3 radicals in the polymeric thin films are evidenced through the superposition of CH_2-scissoring and CH_3-rocking vibrations around 1465 cm^{-1}, as well as the symmetric- and asymmetric-stretching modes of CH_3 at 2873 and 2971 cm^{-1}, respectively and to the asymmetric-stretching vibration of CH_2 at 2934 cm^{-1} [5]. The appearance of a sharp positioned at 3067 cm^{-1}, especially at 600 and 800 mJ cm^{-2}, was observed, which corresponds to the solvent chemical composition. A possible explanation is that the pNIPAm thin films obtained by MAPLE contain chloroform due to the fact that the

solvent could not be totally evaporated and absorbed outside the vacuum chamber because of the rapid transfer of the target material to the substrates. For possible biomedical applications, the presence of the chloroform could impede the cell development/adhesion.

3.2.2. The morphologic characteristics of the MAPLE-deposited coatings

The coating characteristics in the case of MAPLE are related to wavelength, pulse duration, repetition rate, solvent absorption, target composition and percentage (preferably under 5–10% in mass). For example, using same number of pulses (Nd: YAG, 266 nm, 72-k pulses) but different laser fluences, pNIPAm coating with different arrangement of pNIPAm nanoparticles within the deposited coatings were obtained: uniform and low roughness (below 20 nm) coatings obtained for fluence value of 250 mJcm^{-2}, (**Figure 3a**), and highly rough coatings obtained for fluence value of 600 mJ cm^{-2} (**Figure 3b**). The obtained features and the film's surface roughness were determined by atomic force microscopy (AFM) measurements performed in air in noncontact mode.

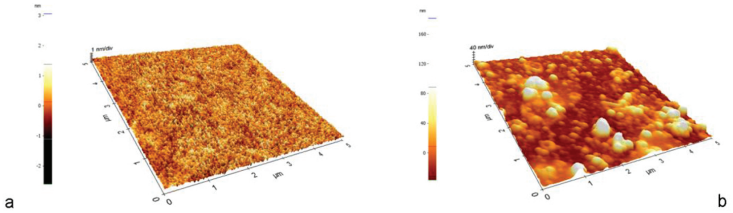

Figure 3. AFM images of pNIPAm thin films morphological characteristics obtained with 250 and 600 mJcm^{-2}. Scanning of the sample was carried out with a sharp tip with a diameter of about 100 Å and a length of the order of microns, positioned at the end of a cantilever having a length of 200 μm. The device used was the type XE100 AFM Park Systems, with maximum vertical movement of 8 μm, lateral resolution of tens of nanometers and optical resolution of 1 μm.

The surface of the samples can be tuned to exhibit special topography features on the surface from smooth, with roughness below 25 nm, to grain-like structures or porous surfaces, with roughness in the range of 110–150 nm [5] by changing either the fluences used or the target composition. It was shown that the surface roughness can impact both protein adsorption and desorption but also cell detachment process and time [5].

3.2.3. Thermoresponsive character of pNIPAm coatings obtained by MAPLE

In order to assess the behavior of the deposited materials upon hydration and heating, the step height was observed at 37°C water and in room temperature (RT) water (**Figure 4**). The decrease in temperature in water leads to an increase in coating thickness of 28 nm. The change in step height confirmed the stimuli-responsive character of the MAPLE-deposited pNIPAm coatings due to the change in temperature.

http://dx.doi.org/10.5772/66280

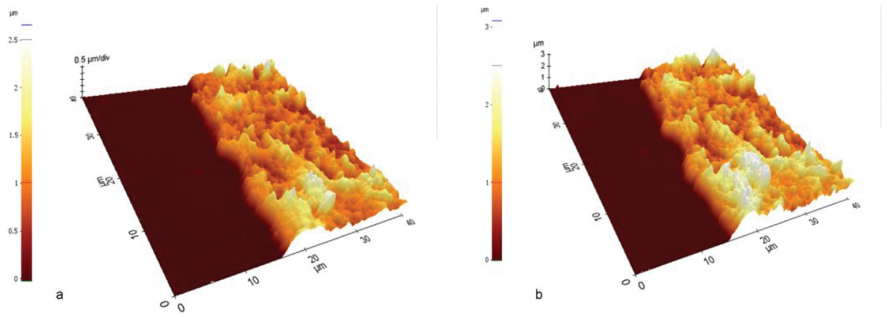

Figure 4. AFM images of pNIPAm samples measured in liquid at room temperature (RT) (a) and 37°C (b). Each sample was hydrated for ~60 min before measuring the step-height variation due to temperature change.

A change in the contact angle value from 47° (measured at 37°C) to 30° (measured at 21°C) by applying temperature as external stimuli confirmed the thermoresponsive character of the pNIPAm coatings (obtained with Nd:YAG laser, 266 nm, 72-k pulses, 10 Hz, 250 mJcm^{-2}).

An explanation for the above observations could be given by the fact that in a dehydrated state, the hydrophobic groups from the polymer surface are oriented outward to maximize hydrogen bonding underneath the surface [53], while in the aqueous environment at room temperature, the hydrophobic isopropyl groups appear to bend inward. In this way, the hydrogen bonding of the polar amide groups with water is facilitated to lower surface energy. Moreover, increasing temperature, there takes place a rearrangement of the surface based on tuning the intramolecular hydrogen bonds under the surface and freeing the bound water molecules [53].

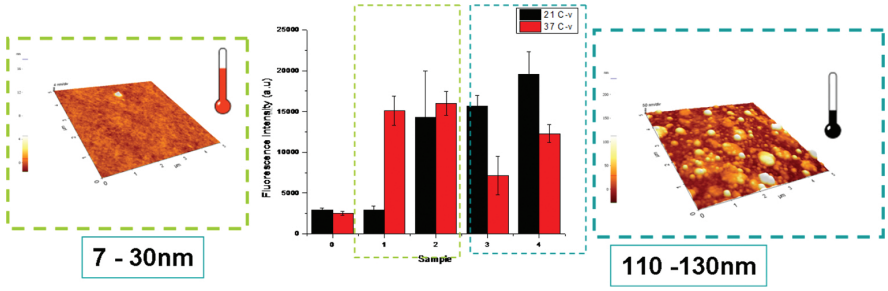

Figure 5. Protein adsorption studies on the coatings obtained by MAPLE using fluorescein isothiocyanate (FITC)-labeled BSA in PBS. The total fluorescence was determined using the built-in FITC filter of the microscope, with a constant exposure time, magnification and image area for all the surfaces. Duplicate images of each coating before and after incubation with BSA were recorded using a CCD camera (ANDOR iXon DU897 E-CSO-UVB) and Olympus IX71 microscope. The total fluorescence from BSA was calculated by extracting the background fluorescence for each coating type (zero, one and two samples with roughness in the range of 7–30 nm and three and four samples with roughness in the range of 110–130 nm). The left side of the image represents an example of AFM image of low roughness surface (7–30 nm) while the right side presents an example of AFM image of pNIPAm coatings with higher roughness (110–130 nm).

However, both protein adsorption and cell reversible attachment are correlated to pNIPAm density, grafting, or conformation onto a substrate [54]. In the case of pNIPAm coatings obtained by MAPLE, a model protein (bovine serum albumin (BSA)) was used to probe the changes in the interfacial properties coatings and two trends depending on roughness surfaces were observed. Negligible protein adsorption at 21°C was noticed for low roughness surfaces (samples 0–7 nm, 1–20 nm and 2 with roughness up to 30 nm) and increase of protein on denser and rougher pNIPAm coatings (samples 2–110 nm and 3 with roughness up to 130 nm) (**Figure 5**).

However, the changes in the pNIPAm surface properties (roughness) affected protein adsorption, with lower protein adsorption on dense and rough coatings at 37°C and higher adsorption on low roughness surfaces, which is in contradiction with the measurements reported on pNIPAm obtained by other methods [54]. This discrepancy could be explained by the swelling ratio which decreases with increasing material density, as the chains in more densely packed coatings swell less upon full hydration. When compared to the modification of the heights of the coatings under temperature influence (about 24 nm) to the protein dimensions (length 14 nm, height and width 4 nm), it can be assumed that the lowest density is insufficient for exceeding primary adsorption and the proteins are able to penetrate the rough coatings and they would adsorb to the underlying surface. Nevertheless, the thin-film irregularities or roughnesses were shown to be important factors in influencing the mobility of adsorbed proteins [5].

4. Cell interaction and answer to pNIPAm-based interfaces obtained by MAPLE

Cell interaction and answer to pNIPAm substrates/surfaces are determined, besides the chemical characteristics, also by the thickness and surface morphology. The porosity and uniformity of the thin films as well as low roughness plays an important role in the cell adhesion/detachment behavior. The thickness of the films has an important role in the temperature-induced alterations of the films (changing from hydrophilic to hydrophobic properties [5–7, 28–34]. The cell culture-based studies (phase-contrast microscopy, fluorescence microscopy and MTT assays) have proved a good biocompatibility and a cell behavior correlated with the chemical composition of biomaterial substrates in the case of pNIPAm coatings obtained by MAPLE.

4.1. Mammalian cells adhesion and morphology on pNIPAm coatings obtained by MAPLE

A first observation of the effect of pNIPAm coatings onto the behavior of L929 and human mesenchymal stem cells (hMSC) is given in **Figure 6**, where cells adhesion and morphology were analyzed by phase-contrast microscopy, showing that cells spread on the coatings surfaces without shape alteration.

http://dx.doi.org/10.5772/66280

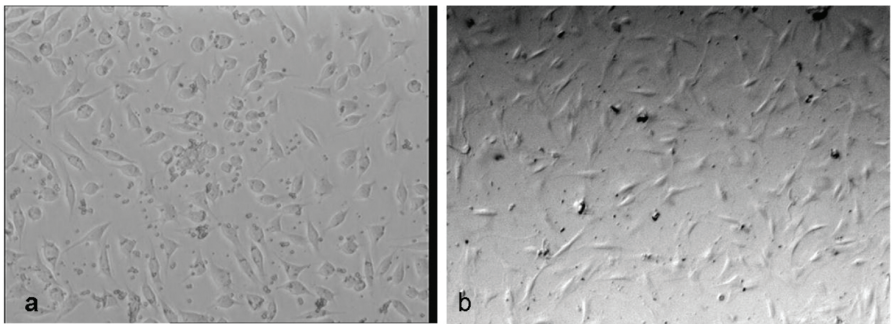

Figure 6. The attachment and morphology of the L929 cells (a) and hMSC cells (b) on pNIPAm coatings observed after 72 h of culture (using SteREO DiscoveryV20 microscope, with PlanApo S 1.0× objective, 32.5× magnification with an AxioCamICm1 camera attached to the microscope setup). L929 (mouse fibroblast) cells and human mesenchymal stem cells (hMSC) were cultured in Dulbecco's minimal essential medium (DMEM) containing 4-mM L-glutamine (Gibco) and supplemented with 10% fatal calf serum (FBS) and 50-U/ml penicillin/streptomycin (50 mg/ml) and maintained at 37°C with 5% CO_2.

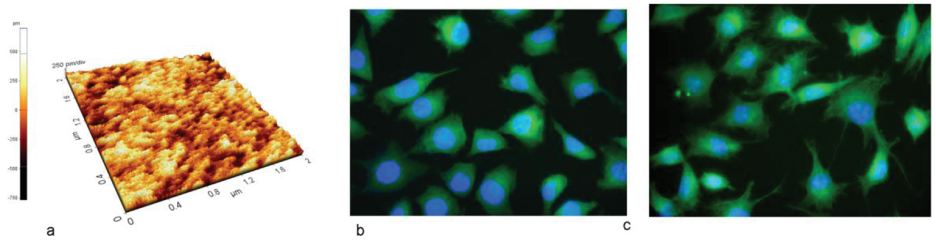

Figure 7. AFM image of pNIPAm coating obtained for a fluence of 400 mJcm^{-2} (a) and (b) fluorescence microscopy image of L929 cells stained with Hoechst (Sigma) nucleus—blue and fluorescein phalloidin (ThermoFisher) green-actin fibers on pNIPAm samples and on controls (c).

The above observations were confirmed by the fluorescence microscopy analysis. The initial cell attachment, spreading and morphological features of fibroblasts cells were assessed and correlated to surface characteristics.

As fibroblasts are ubiquitous in the body and are the first to populate prostheses surface (implants), the morphology of the cells (seeded at a density of 5000 cells/100 μl) for 24 h can give a first information on how and if pNIPAm coating obtained by MAPLE can support cell adherence and if the confluence on highly dense coatings is possible.

As shown by florescence images in **Figure 7**, L929 cells adhere and spread uniformly onto the laser-engineered pNIPAm surfaces and start projecting long dendrites along the surface area. These results are confirmed by scanning electron microscopy (SEM) analysis of cells cultured onto the pNIPAm coatings for 24 h (**Figure 8**).

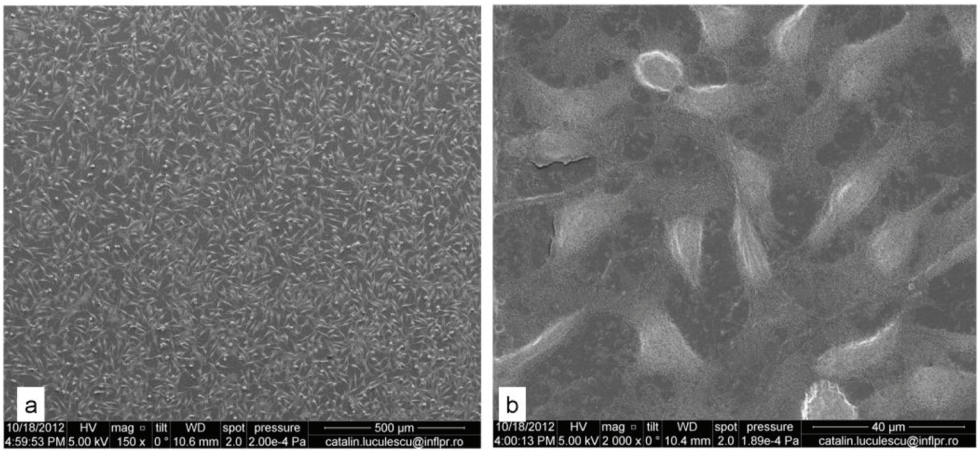

Figure 8. SEM images of the cells seeded on pNIPAm materials for 24 h: overview on the cells distributions over large area (a) and a close-up on the shape of the adhered L929 cells (b). For preparation of the samples for SEM analysis, the samples were washed with PBS and fixed with 2.5% glutaraldehyde in PBS for 20 min and subjected for ethanol gradient dehydration.

Nevertheless, the spreading of the cells and adherence can be inhibited by either surface chemistry or surface morphology [5]. The viability of the fibroblast cells after 3 days of culture on the pNIPAM coatings was calculated showing similar proliferation rate for the coatings obtained in the range of 200–600 mJcm^{-2}. A cytotoxic effect and a decrease in proliferation rate in the case of the coatings obtained for higher fluences [5] were observed.

4.2. Cell harvesting based on temperature change

A recent study by Rusen et al. [5] on the cell detachment upon temperature reduction showed that the roughness of the thin films represents a significant parameter in tuning the detachment time. The quantitative analysis on the fibroblast cell harvesting upon temperature reduction showed that if cells detached from rougher films within 10–20 min, the detachment time on smooth surfaces increased with more than 25%.

The sequence of images presenting an example of the cell detachment from a pNIPAm thin film obtained by MAPLE is shown in **Figure 9**. The cells presented flat, spread, normal morphology at the beginning of the observations (**Figure 9a**), when the temperature was 37°C. However, by lowering the temperature the cells morphology started to change, becoming less spread and rounder (**Figure 9b–d**). When compared with previously reported data on cell detachment from pNIPAm coatings obtained by MAPLE [5], the detachment time is increased due to the low roughness (20 nm) pNIPAm surfaces used in this study. Moreover, the cells collected from pNIPAm coating obtained by MAPLE did not change their shape or viability. This represent a strong indication that a nondestructive reversible cell detachment takes place when using pNIPAm bio-interfaces obtained by MAPLE [5].

http://dx.doi.org/10.5772/66280

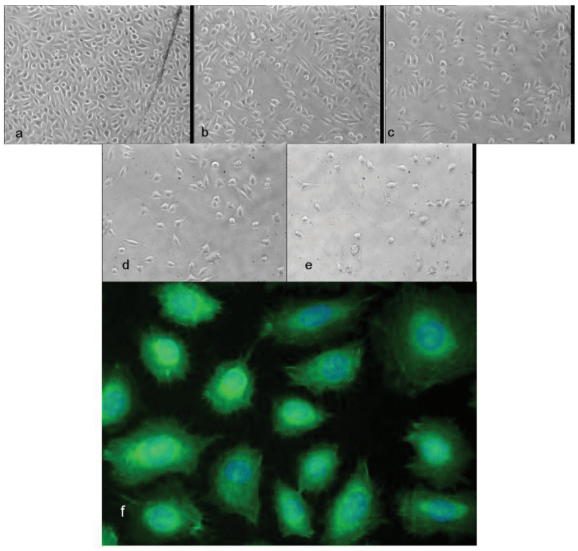

Figure 9. Cell detachment sequence images at 0 min (a), 5 min (b), 10 min (c), 15 min (d), 20 min (e) from pNIPAm coatings obtained by MAPLE at 250 mJ cm^{-2}. (f) Fluorescence microscopy image of L929 cells grew on other pNIPAm surfaces, indicating no damage to either the structural or functional aspects of the cells recovered from pNIPAm samples.

4.3. Multifunctional pNIPAm-based surfaces with biocidal and releasing properties obtained by MAPLE

Based on the same principle, resonant infrared matrix-assisted pulsed-laser evaporation (RIR-MAPLE) was used to co-deposit two components OPE/pNIPAm films with precise ratio control [39]. The sequential co-deposition mode allows depositions of a multifunctional coating comprising OPE and PNIPAm, used to kill bacteria and then release the accumulated dead bacteria from the film surface [39]. If laser fluence was previously used to change surface morphology [5], in this case, both surface morphology and wettability were adjusted by changing the OPE/PNIPAAm volume ratio in emulsion target used in the sequential deposition mode in RIR-MAPLE.

The biocidal activity and bacterial-releasing ability of the multifunctional films implied the use of both Gram-negative and Gram-positive bacteria strains such as *Escherichia coli* K12, respectively, *Staphylococcus epidermidis*. An inverse relationship between the biocidal activity and capability for bacterial release based on OPE content was observed. In this way, by increasing the quantity of OPE within the coatings, the resultant films showed increased biocidal activity but lower bacterial release capability. By optimizing the OPE/PNIPAAm ratio, coatings with enhanced biocidal activity against attached bacteria as well as good-removal capacity for the debris and bacteria when rinsing the films at a temperature below the LCST [39] were observed.

5. Conclusions and future prospects

In this chapter, the new and rapidly emerging importance of smart-coating engineering was introduced, with focused attention on smart thermoresponsive pNIPAm interfaces obtained by matrix-assisted laser evaporation-based method. In this chapter, the thermoresponsive-coatings characteristics obtained by MAPLE-based method were emphasized along with some of the deposition parameters and used for biological assays *in vitro* implying BSA model proteins, mammalian cells and microorganisms.

MAPLE as technique for obtaining smart polymeric coatings with specific characteristics envisaging biological application provides the advantage of tailoring not only the thickness of the pNIPAm layer, which is an important parameter in the cell attachment, but also the morphology of the deposited thin films for influencing protein and cells detachment and its increased stability in the fluid medium. Although significant progress has been achieved in the field of smart coatings based on stimuli-responsive materials, the materials and methods discussed within this chapter still have limitations in practical applications that need to be overcome in the future.

Although the majority of the previous works in this field have used insoluble pNIPAm-based coatings, future research should be more directed toward biomimetic bio-interfaces, with integrated analysis platforms able to address the complexity of bio-environments accordingly to the desired application.

Considering the abovementioned advantages of the MAPLE method on tuning not only the surface characteristics and properties but also the chemical composition and film functionality, this approach could provide a new strategy to engineer multifunctional films for biological studies, regenerative medicine, tissue engineering and industrial applications.

Conflict of interest

The authors declare no competing interests.

Acknowledgements

The research leading to these results has received funding from the Romanian National Authority for Scientific Research (CNCS – UEFISCDI), under the projects PN-II-PT-PCCA-2013-4-1643, PNII- PT-PCCA-2013-4-199, PN-II-RU-TE-2014-4-2434, Romanian Academy Project 1/2015-2016 of the Institute of Biochemistry, University of Bucharest-Biology Doctoral School and Nucleus program—contract 4N/2016.

http://dx.doi.org/10.5772/66280

Author details

Laurentiu Rusen[1], Valentina Dinca[1*], Cosmin Mustaciosu[2,3], Madalina Icriverzi[4,5], Livia Elena Sima[4], Anca Bonciu[1,6], Simona Brajnicov[1,7], Natalia Mihailescu[1], Nicoleta Dumitrescu[1,7], Alexandru I. Popovici[8], Anca Roseanu[4] and Maria Dinescu[1]

*Address all correspondence to: valentina.dinca@inflpr.ro

1 National Institute for Lasers, Plasma and Radiation Physics, Măgurele, Romania

2 Horia Hulubei National Institute for R&D in Physics and Nuclear Engineering (IFIN-HH), Măgurele, Romania

3 Department of Science and Engineering of Oxide Materials and Nanomaterials, Faculty of Applied Chemistry and Materials Science, Politehnica University of Bucharest, Bucharest, Romania

4 Institute of Biochemistry of the Romanian Academy, Bucharest, Romania

5 Department of Biochemistry and Molecular Biology, Faculty of Biology, University of Bucharest, Bucharest, Romania

6 Faculty of Physics, University of Bucharest, Bucharest-Măgurele, Romania

7 Faculty of Mathematics and Natural Sciences, University of Craiova, Craiova, Romania

8 University of Medicine and Pharmacy Carol Davila, Bucharest, Romania

References

[1] Cole M A,' Voelcker N H, Thissen H, Griesser H J. 2009. Stimuli-responsive interfaces and systems for the control of protein–surface and cell–surface interactions Biomaterials 30(9), 1827–1850.

[2] Cooperstein M A, Canavan H E. 2010. Biological cell detachment from poly(*N*-isopropyl acrylamide) and its applications Langmuir 6(11), 7695–7707.

[3] Yamato M, Akiyama Y, Kobayashi J, Yang J, Kikuchi A, Okano T. 2007. Temperature-responsive cell culture surfaces for regenerative medicine with cell sheet engineering Progress in Polymer Science 32(8–9), 1123–1133.

[4] Ohashi K, Yokoyama T, Yamato M, Kuge H, Kanehiro H, et al. 2007. Engineering functional two- and three-dimensional liver systems in vivo using hepatic tissue sheets Nature Medicine 13, 880–885.

[5] Rusen L, Dinca V, Mitu B, Mustaciosu C, Dinescu M. 2014. Temperature responsive functional polymeric thin films obtained by matrix assisted pulsed laser evaporation for cells attachment-detachment study Applied Surface Science 302, 134–140.

[6] Aguilar M R, Elvira C, Gallardo A, Vázquez B, Román J S. 2007. Smart Polymers and Their Applications as Biomaterials, Topics in Tissue Engineering, Vol. 3, Chapter 6 Eds. N Ashammakhi, R Reis & E Chiellini.

[7] Nakayama M, Okano T, Winnik F M. 2010. Poly(N-isopropylacrylamide)-based smart surfaces for cell sheet tissue engineering Material Matters 53, 56–62.

[8] Ding Z, Chen G, Hoffman A. 1996. Synthesis and purification of thermally sensitive oligomer−enzyme conjugates of poly(N-isopropylacrylamide)−trypsin Bioconjugate Chemistry 7, 121–125.

[9] Heskins M, Guillet E. 1968. Solution properties of poly(N-isopropylacrylamide) Journal of Macromolecular Science: Part A - Chemistry 2, 8 1441–1455.

[10] Chen G, Hoffman A S. 1995. Graft-copolymers that exhibit temperature-induced phase-transitions over a wide-range of pH Nature 373, 49.

[11] Schmaljohann D, Oswald J, Jorgensen B, et al. 2003. Thermo-responsive PNiPAAm-g-PEG films for controlled cell detachment. Biomacromolecules 4, 1733–1739.

[12] Brazel C S, Peppas N A. 1996. Pulsatile local delivery f thrombolytic and antithrombotic agents using poly(N-isopropylacrylamide- co-methacrylic acid) hydrogels. Journal of Controlled Release 39, 57–64.

[13] Singh N, Lyon L A. 2007. Au nanoparticle templated synthesis of pNIPAm nanogels. Chemistry of Materials 19, 719–726.

[14] Ramanan R M K, Chellamuthu P, Tang L, et al. 2006. Development of a temperature-sensitive composite hydrogel for drug delivery applications. Biotechnology Progress 22, 118–2511.

[15] Kim M R, Jeong J H, Park T G. 2002. Swelling induced detachment of chondrocytes using RGD-modified poly(N-isopropylacrylamide) hydrogel beads. Biotechnology Progress 18, 495–500.

[16] Arijit G, Abhijit P, Suma Oommen S, Kalyan Kumar S. 2015. Studies on thermoresponsive polymers: phase behaviour, drug delivery and biomedical applications. Asian Journal of Pharmaceutical Sciences 10, 99–107.

[17] Aghabegi M A, Khoshnevis D, Zarrabi A. 2016. A concise review on smart polymers for controlled drug release. Drug Delivery and Translational Research 6, 333–340.

[18] Mark A. Ward, Theoni K. Georgiou 2011. Thermoresponsive polymers for biomedical applications, Polymers 3, 1215–1242.

http://dx.doi.org/10.5772/66280

[19] Lupitskyy R, Roiter Y, Minko S, Tsitsilianis C. 2005. From smart polymer molecules to responsive nanostructured surfaces, Langmuir 21, 8591–8593.

[20] Yamato M, Konno C, Utsumi M, Kikuchi A, Okano T. 2002. Thermally responsive polymer-grafted surfaces facilitate patterned cell seeding and co-culture, Biomaterials 23, 561–567.

[21] Uhlmann P, Houbenov N, Stamm M, Minko S. 2005. Surface functionalization by smart binary polymer brushes to tune physico-chemical characteristics at biointerfaces, EPolymers 075, 1–10.

[22] Mizutani A, Kikuchi A, Yamato M, Kanazawa H, Okano T. 2008. Preparation of thermoresponsive polymer brush surfaces and their interaction with cells, Biomaterials 29(13), 2073–2081.

[23] Ramirez- Fuentes Y S, Bucio E, Burillo G. 2007. Radiation-induced grafting of N - isopropylacrylamide and acrylic acid onto polypropylene films by two step method, Nuclear Instruments & Methods in Physics Research, Section B, Beam Interactions with Materials and Atoms, 265(1), 183–186.

[24] Turana E, Demirci W, Caykara T. 2010. Synthesis of thermoresponsive poly (Nisopropylacrylamide) brush on silicon wafer surface via atom transfer radical – Polymerization, Thin Solid Films, 518(21), 5950–5954.

[25] Wang X, McCord M G. 2007. Grafting of poly(N-isopropylacrylamide) onto nylon and polystyrene surfaces by atmospheric plasma treatment followed with free radical graft copolymerization, Journal of Applied Polymer Science, 104(6), 3614–3621.

[26] Akiyama Y, Kikuchi A, Yamato M, Okano T. 2004. Ultrathin poly(N-isopropylacrylamide) grafted layer on polystyrene surfaces for cell adhesion/detachment control, Langmuir 20, 5506–5511.

[27] Ide T, Nishida K, Yamato M, Sumide T, Utsumi M, Nozaki T, et al. 2006. Structural characterization of bioengineered human corneal endothelial cell sheets fabricated on temperature-responsive culture dishes, Biomaterials 27, 607–614.

[28] Yamada N, Okano T, Sakai H, Karikusa F, Sawasaki Y, Sakurai Y. 1990. Thermoresponsive polymeric surfaces; control of attachment and detachment of cultured cells, Makromol Chem-Rapid 11, 571–576.

[29] Tamura A, Kobayashi J, Yamato M, Okano T. 2012. Temperature-responsive poly(Nisopropylacrylamide)-grafted microcarriers for large-scale non-invasive harvest of anchorage-dependent cells, Biomaterials 33(15), 3803–3812.

[30] Patel N G, Zhang G E. 2013. Responsive systems for cell sheet detachment, Organogenesis 9(2), 93–100.

[31] Tang Z, Okano T. 2014. Recent development of temperature-responsive surfaces and their application for cell sheet engineering, Regenerative Biomaterials 1(1), 91–102.

[32] Moran M T, Carroll W M, Selezneva I, Gorelov A, Rochev Y. 2007. Cell growth and detachment from protein coated PNIPAAm-based copolymers, Journal of Biomedical Materials Research Part A 81, 870–876.

[33] Reed J A, Lucero A E, Hu S, Ista L K, Bore M T, López G P, et al. 2010. A low-cost, rapid deposition method for "smart" films: applications in mammalian cell release, ACS Applied Materials & Interfaces 2, 1048–1051.

[34] Patel N G, Cavicchia J P, Zhang G, Zhang N B M. 2012. Rapid cell sheet detachment using spin-coated pNIPAAm films retained on surfaces by an aminopropyltriethoxysilane network, Acta Biomaterialia 8, 2559–2567.

[35] Nash M E, Carroll WM, Nikoloskya N, Yang R, O'Connell C, et al. 2011. Straightforward, one-step fabrication of ultrathin thermoresponsive films from commercially available pNIPAm for cell culture and recovery, ACS Applied Materials & Interfaces 3, 1980–1990.

[36] Morra M, Cassinelli C. 1997. Thermal recovery of cells cultured on poly(N-Isopropylacrylamide) surface-grafted polystyrene dishes. in BD Ratner, DG Castner (eds). Surface Modification of Polymeric Biomaterials. New York, NY: Springer, 175–181.

[37] Ito Y, Chen G, Guan Y, et al. 1997. Patterned immobilization of thermoresponsive polymer, Langmuir 13, 2756–2759.

[38] Steen W M. 2009. Laser Surface Treatment in Laser Material Processing, Springer, London, 172–219.

[39] Basting D, 2005. Overview, chapter 10 in Excimer Laser Technology, Springer Science & Business Media, ISBN3540200568, 9783540200567

[40] Chrisey D B, Piqué A, McGill R A, et al. 2003. Laser deposition of polymer and biomaterial films, Chemical Reviews 103(2), 553–576.

[41] Smausz T, Hopp B, Kresz N. 2002. Pulsed laser deposition of compact high adhesion polytetrafluoroethylene thin films, Journal of Physics D: Applied Physics, 35(15).

[42] Piqué A, McGill R A, Chrisey D B, Leonhardt D, Mslna T E, et al. 1999. Growth of organic thin films by the matrix assisted pulsed laser evaporation (MAPLE) technique, Thin Solid Films 355–356(1), 536–541.

[43] Dinca V, Florian P E, Sima L E, Rusen L, Constantinescu C, et al. 2014. MAPLE-based method to obtain biodegradable hybrid polymeric thin films with embedded antitumoral agents, Biomedical Microdevices 16(1), 11–21.

[44] Rusen L, Mustaciosu C, Mitu B, Filipescu M, Dinescu M, Dinca V. 2013. Protein-resistant polymer coatings obtained by matrix assisted pulsed laser evaporation, Applied Surfaces Science 278, 198–202.

[45] Darwish A M, Burkett A, Blackwell A, Taylor K, Sarkisov S, et al. 2015. Polymer-inorganic nano-composites thin films upconversion light emitters prepared by double-

beam matrix assisted pulsed laser evaporation (DB-MAPLE) method, Composites Part B: Engineering 68, 355–364.

[46] Boanini E, Torricelli P, Forte L, Pagani S, Mihailescu N, et al. 2015. Antiresorption implant coatings based on alendronate and octacalcium phosphate deposited my matrix assisted pulsed laser evaporation, Colloids and Surfaces B: Biointerfaces 136, 449–456.

[47] Aronne A, Bloisi F, Calabria R, Califano V, Depeso L E, et al. 2015. Lipase biofilm deposited by matrix Assisted Pulse Laser evaporation technique, Applied Surfaces Science 336, 196–199.

[48] Yu Q, Ge W, Atewologun A, Stiff-Roberts A D, López G P. 2015. Antimicrobial and bacteria-releasing multifunctional surfaces: oligo (p-phenylene-ethynylene)/poly (N-isopropylacrylamide) films deposited by RIR-MAPLE, Colloids Surface B Biointerfaces 126, 328–334.

[49] Sima F, Davidson P, Pauthe E, Sima L E, Gallet O, Mihailescu I N, Anselme K. 2011. Fibronectin layers by matrix-assisted pulsed laser evaporation from saline buffer-based cryogenic targets, Acta Biomaterialia 7(10), 3780–3788.

[50] Matei A, Schou J, Constantinescu C, Kingshott P, Dinescu M. 2011. Growth of thin films of low molecular weight proteins by matrix assisted pulsed laser evaporation (MAPLE), Applied Physics A 105, 629–633.

[51] Cristescu R, Mihaiescu D, Stamatin I, Socol G, Mihailescu I N, Chrisey D B. 2004. Deposition of biopolymer thin films by matrix assisted pulsed laser evaporation, Applied Physics A – Material Science & Processing, 79(4–6), 1023–1026.

[52] Darwish A M, Burkett A, Blackwell A, Taylor K, Sarkisov S, et al. 2015. Polymer-inorganic nano-composites thin films upconversion light emitters prepared by double-beam matrix assisted pulsed laser evaporation (DB-MAPLE) method, Composites Part B: Engineering, 68, 355–364.

[53] Cheng X, Canavan H E, Stein M J, Hull J R, Kweskin S J, et al. 2005. Surface chemical and mechanical properties of plasma-polymerized N-isopropylacrylamide, Langmuir 21, 7833–7841.

[54] Xue C, Choi B -C, Choi S, Braun P V and Leckband D E. 2012. Protein adsorption modes determine reversible cell attachment on poly(N- isopropyl acrylamide) brushes, Advanced Functional Materials 22, 2394–2401.

Chapter 11

Controlled Rate Thermal Analysis (CRTA) as New Method to Control the Specific Surface in Hydroxyapatite Thin Coatings

E. Peón, A. El hadad, F.R. García-Galván,
A. Jiménez-Morales and J.C. Galván

Additional information is available at the end of the chapter

http://dx.doi.org/10.5772/66468

Abstract

The control of the texture in synthetic hydroxyapatite ceramics had limited their application in the field of the materials for bone implantation, even more when it is used as a filling in cements and other formulations in orthopedic surgery. The present article shows preliminary results demonstrating the effectiveness of a modification of the controlled rate thermal analysis (CRTA), developed by J. Rouquerol, used for the preparation of ceramic materials with controlled textural characteristics, during the formation of ceramic powders of synthetic hydroxyapatite at low temperatures. The thermal treatments of the hydroxyapatite were carried out in a device connected to a computer, to control temperature and pressure system, keeping the decomposition speed constant. Results, reported when preparing ceramic powders of hydroxyapatite at 300 and 850°C under controlled pressure, using synthetic hydroxyapatite with a Ca/P molar ratio equal to 1.64, were checked using IR spectroscopy and X-ray diffraction, showed that the formed phase corresponds to that of crystalline hydroxyapatite, even at 300°C of maximum temperature. Values of specific surface (BET) between 17 and 66 m^2/g, with pore size in the range of 50–300 Å in both cases are obtained by N_2 absorption isotherms, when analyzing the isotherms of nitrogen absorption.

Keywords: hydroxyapatite, formation, thermal analysis to controlled speed, specific surface, pore size

1. Introduction

It is known the diversity of materials in use today as bone substitutes. Among them the hydroxyapatite (HA) has deserved special attention because of its excellent biocompatibility, almost the same of that of natural bone. Most of commercial HA used in clinical and research applications are in solid and granulated forms with pore sizes between 100 and 150 μm. It has been demonstrated that such a range of pore dimension is appropriate to cause tissue growth in direct applications as bone substitutes [1–5]. HA ceramics and thin films can be synthesized by many methods [3, 4]. The conventional chemical precipitation method is the more extended method [6]. Following chemical precipitation, combination methods and the hydrothermal process are the next most well-known methods of preparing HA [6–10]. Nevertheless, the scientific community is devoting great efforts looking for new alternative methods in order to obtain hydroxyapatite ceramics with improved microstructural and corrosion properties. In this way, laser-assisted bioprinting and pulsed laser deposition techniques are very promising methods to obtain this kind of hydroxyapatite ceramics and thin films [11–14]. Also, alternating current electric field modified synthesis [15] and magnetron sputtering techniques (MST) [16, 17].

In this context, several methods of synthesis of HA with appropriately controlled textural characteristics as well as its use as a filler in formulations for systems in orthopedic surgery have been reported, however, the uniformity of the pore size is a problem unsolved up to now [18–20]. The sol-gel synthesis of HA thin films and ceramics has attracted much attention because it offers a molecular-level mixing of the calcium and phosphorus precursors, which is capable of improving chemical homogeneity of the resulting HA to a significant extent, in comparison with conventional methods [18–20]. Fortunately, Vila et al. have obtained significant progress in recent years using the sol-gel process [22]. In the context of the present work, they have obtained a bimodal porous process for nanocrystalline hydroxyapatite (HA) coatings with pore sizes in the range of meso/macrometer scale deposited onto Ti6Al4V substrates by the sol-gel method using nonionic surfactants as the porous former agent [22].

When phosphates are treated at several temperatures important changes occur in their properties, in particular, in their chemical contents and physicochemical characteristics, which permit an assessment of admixtures in the phosphates and the effects of substitution of the fundamental elements with others. But, on the other hand, the thermal treatment of the material poses a serious problem, due to difficulties to effectively control the gradients of pressure and temperature originated in different parts of the sample in most experiments [23–25].

The method for the thermal analysis developed by Rouquerol [26, 27], known as “control rate thermal analysis” (CRTA), has been tested in formulations for the control of textures in solids [28–30]. This method is very useful in cases of complex thermolysis usually lapses through superimposed, parallel or serial reactions. Thermal treatment at a controlled speed can allow the formation of homogeneous porosity and a homogeneous surface in its chemical composition and distribution of defects.

http://dx.doi.org/10.5772/66468

In previous studies, we have prepared organic-inorganic hybrid sol-gel films with nanocrystalline hydroxyapatite as a filler and triethylphosphite (TEP)as a network forming agent to enhance the *in vitro* biocompatibility and corrosion protection of these coatings deposited on Ti6Al4V alloys [31, 32]. Now, the purpose of this new study is to apply the CRTA technique to crystallize synthetic HA with a controlled specific surface and homogeneous distribution of pores, appropriate to be used in bone implantation and other formulations for orthopedic surgery. These parameters may be very important in different situations. For example, when HA is used as a filler in cement-based composites, the superficial specific area must be small because a frail material may be obtained due to the presence of microfracture centers when are too big. Taking into account thermogravimetric analysis results, several pressures and temperatures of control were tested in the preparation of ceramic powders.

2. Experimental

2.1. Preparation of hydroxyapatite

Hydroxyapatite used in this study was obtained by hydrolysis and condensation of suitable precursors following a water-based sol-gel process in accordance with the preparation method of Dean Mo Liu et al. [33–35]. Triethylphosphite (TEP), $C_6H_{15}O_3P$ (Aldrich, 98%) and calcium nitrate tetrahydrate, $Ca(NO_3)_2{\cdot}4H_2O$ (Aldrich) were used as precursors of phosphorus and calcium, respectively.

The preparation process includes the following stages: the first stage is the hydrolysis of the precursor of phosphorus. TEP is mixed with ultrapure distilled water under vigorous agitation. Given the immiscibility between TEP and water, the mixture initially becomes opaque. However, after 24 hours of agitation the emulsion is transformed into a clear dissolution indicating that the TEP is hydrolyzed completely. In the second stage, the saline precursor of calcium is added to the medium in a stoichiometric quantity (Ca/P molar ratio = 1.64) using a 4 M aqueous solution of nitrate of calcium. In this step, the agitation is continued for 30 min and then the mixture is left to stand for 24 hours at room temperature. The gelation is guaranteed by the evaporation of the solvent at 80°C, until a viscous liquid is obtained whose volume is about 40% of the initial solution.

2.2. Preparation of HA sol-gel coatings on Ti6Al4V substrates

Ti6Al4V disks of 2 cm of diameter and 0.4 cm of thickness were polished using different silicon carbide grit up to 1200 grade. The substrates were ultrasonically degreased with acetone for 10 min and washed with distilled water. Finally, the substrates were dried at 200°C for one hour in an air oven to form a titanium oxide layer. The formation of TiO_2 layer might decrease the stress concentration and thermal expansion coefficient mismatch between the coatings and the titanium substrate.

These substrates were dip coated in the HA sol solution, with a dipping and withdraw speed of 12 cm/min. The sol-coated substrates were then immediately transferred into an air oven and held at 80°C for 30 min to stabilize the deposited layer. To increase the coating thick-

ness, the above process was repeated three times and finally it was thermally treated under conventional and controlled rate thermal treatments (CRTA). Cross section SEM micrographs revealed that the estimated thickness of all the HA crystalline sol-gel derived coatings was about 1–2 μm. Nevertheless, these thicknesses were nonuniform due to roughness of the Ti6Al4V substrate.

2.3. Crystallization of hydroxyapatite under conventional and controlled rate thermal treatment

The conventional thermal treatment was carried out in a furnace, burning the precipitate at various temperatures (600, 800°C) for 2 h, at a heating speed of 2°C/min. For the controlled rate thermal analysis (CRTA), samples of 1 g were placed in a quartz sample holder, which was introduced in a programmable tubular oven with Eurotherm control of ±1°C error temperature and connected to a vacuum group, where a Pirani for measuring pressure and a diaphragm with an aperture of 0.1 mm are already present. A home-made software allows the regulation of the temperature and the measurement of generated pressure. This last parameter is the one that regulates the transformation rate. The basis of this thermal treatment is to control the temperature and the pressure system, keeping the decomposition rate constant. **Figure 1** shows a photograph of the CRTA equipment and a simplified schematic diagram of the device.

In parallel studies a set of HA sol-gel coatings previously deposited on Ti6Al4V substrates was densified at the optimal pressure and temperature, which is determined by CRTA. The adequate pressure was accomplished with the use of a vacuum pump connected to the muffle furnace.

2.4. Characterization of the powders of hydroxyapatite

The relation Ca/P was calculated starting from the percentage of Ca, determined by absorption spectroscopy in Philips Pye Unicam SP9 at a λ = 422.7 nm and the percentage of P obtained by emission spectrometry in a Perkin Elmer Capture 40 at a λ = 213.6 nm. On the other hand, powders were characterized by infrared spectroscopy (IR) in a PHILIPS FTIR PU 9800, using the method of pills of KBr and X-ray diffraction (XRD), in a Philips Pye Unicam PW1710, by the method of powders. The thermogravimetric analysis (TGA) was carried out

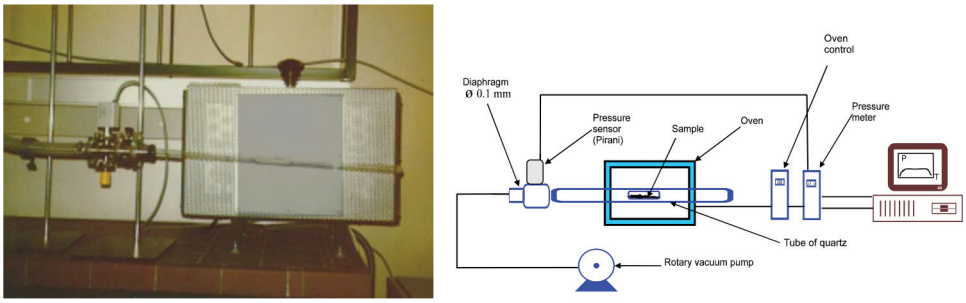

Figure 1. Equipment for controlled rate thermal treatment (CRTA).

http://dx.doi.org/10.5772/66468

with 30 mg of the sample in a SHIMATZU at a speed of 10°C/min, up to 1200°C. The morphology of powders was examined by scanning electron microscopy (SEM) in a SEM Tescan Vega TS 5130SB. The specific surface (BET) and porosity of the material were determined in Coulter equipment; model Omnisorp TM 100, starting from isotherms of adsorption for N_2 at a temperature of 77 K.

2.5. Cytotoxicity/osteoblasts adhesion

The cytocompatibility of coated samples was analyzed by indirect contact as described in ISO 10993-5 (ISO Standards 1999). Briefly, HA coated Ti6Al4V alloy were placed in culture plates and incubated in 15 ml of culture medium (DMEM, Dulbecco's Modified Eagle Medium, Gibco) without fetal bovine serum (FBS) for 24 hours at 37°C. The supernatant of this mixture is called pure extract (100%) which then subjected to dilutions of 0, 10, and 50%.

Fibroblast cells (BALB/c, 3T3, ATCC clone A31) were purchased from American Type Culture Collection (ATCC; MD, USA) and seeded in 24-well plates and cultured in DMEM. 1% antibiotic was added, supplemented with 10% FBS and kept in incubator at 37°C in 5% CO_2 atmosphere. The culture medium was then replaced by extracts of the material to which 10% FBS was added and after 24 hours, the cells were counted using a Neubauer camera. The number of cells cultured in DMEM containing 10% FBS alone was considered the negative control (corresponding to 0% of the extract dilution).

The experiment was carried out six times, means and standard deviations were subjected to a variance analysis, considering significant differences if $p < 0.05$. Additionally, were seeded, 30.000 cells of pre osteoblasts of femur of Balb/c 3T3 (FOST) in plates with Ti6Al4V coated samples, these were maintained in culture supplement DMEM with 10% FBS at 37°C and atmosphere of 5% CO2 for 24 hours. At the end of this period, the plates were moved and the cells were fixed in 2.5% of glutaraldehyde solution, then subjected to treatment with 0.1 M of cacodylate buffer solution at pH 7.3 for 24 hours.

After the cells were washed twice with buffer solution 0.1 M cacodylate, dehydrated with increasing concentrations of alcohol (50–100%), they were immersed in ethanol-hexamethyldisilazane absolute solution (50:50 v/v) and then in hexamethyldisilazane (100%) and dried for 24 hours. Finally, metallization of samples with palladium-gold allowed them to be observed using a scanning electron microscope (SEM).

2.6. Corrosion behavior

The corrosion behavior of the HA film/Ti6Al4V system was evaluated by applying electrochemical impedance spectroscopy (EIS) [21, 31, 32]. These electrochemical measurements were performed using an AutoLab potentiostat/galvanostat PGSTAT30 equipped with a FRA2 frequency response analyzer module (EcoChemie, The Netherlands). A standard three-electrode cell was used for this purpose. The working electrode was the investigated sample with an area of 3.14 cm^2. The reference and the counter-electrode were a saturated calomel electrode (SCE) and a large size graphite sheet, respectively. The electrochemical cell was filled with Kokubo's solution. (SBF; pH = 7.4) [36, 37]. The EIS measurements were made at the open

circuit potential (OCP). Logarithmic frequency scans were carried out by applying sinusoidal wave perturbations of ±10 mV in amplitude, in the range of 10^{5}–10^{-3}Hz. Five impedance sampling points were registered per frequency decade. The impedance data were analyzed by using the ZView software, version 3.5a (Scribner Associates Inc, Southern Pines, NC, USA).

3. Results and discussion

3.1. Characterization of the powders of hydroxyapatite

The Ca/P rate was determined by chemical analyses (absorption spectroscopy for the Ca and emission spectrometry for the P) of the powder preparations and was 1.64. This rate is appropriate to keep the apatite structure after the thermal treatment.

It has been found reports are scarce in the literature of application of controlled rate thermal treatment (CRTA) technique, for treatments of HA. Consequently, a thermogravimetric analysis (TGA) of as-prepared HA green powders (without a previous thermal treatment) was carried out (**Figure 2**) for determining the characteristic temperatures of HA decomposition. The TGA showed different stages in the thermolysis of HA, the first one is associated with the dehydration. The second one and last one are associated with dehydration-crystallization. These processes have been studied by other authors [38–40]. However, practically no effort has been dedicated to study the influence of the experimental conditions used for the thermal decomposition on the morphology of the final products.

The results obtained for TGA, were verified by CRTA (**Figure 3**) to obtain characteristic temperatures and partial pressure for each step of crystallization of the HA. **Table 1** shows the

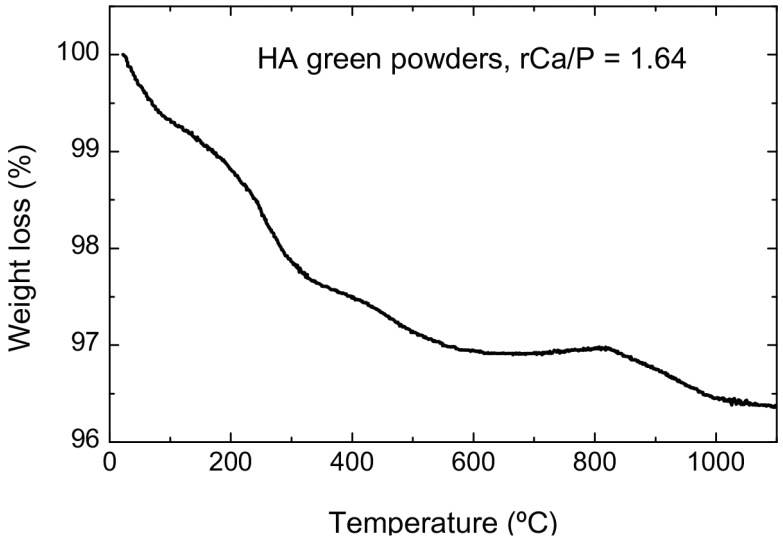

Figure 2. TGA of as-prepared HA green powders.

http://dx.doi.org/10.5772/66468

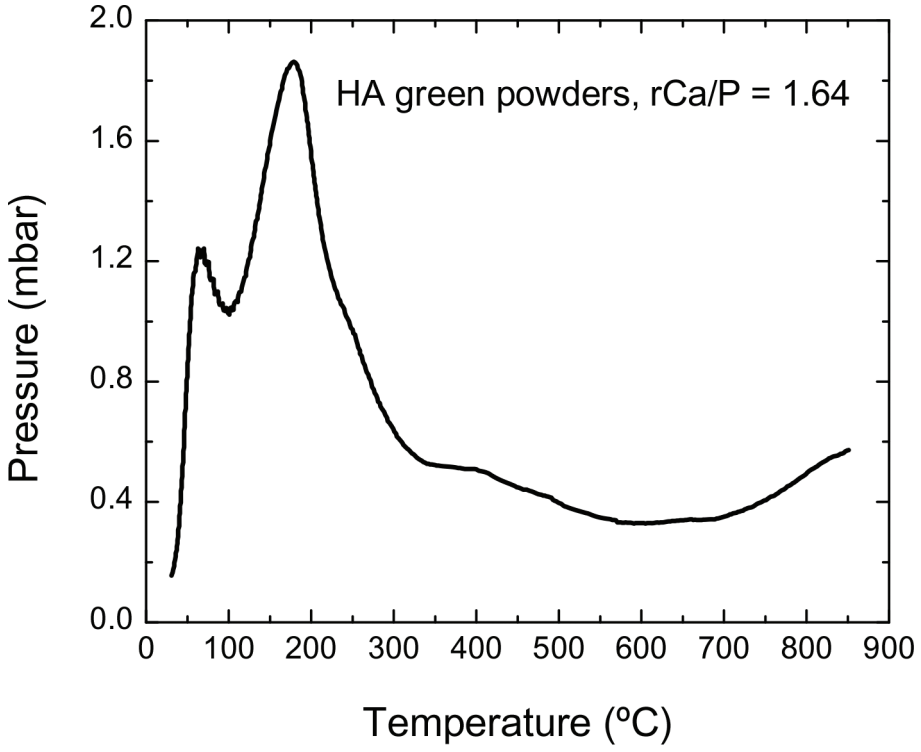

Figure 3. CRTA of as-prepared HA green powders.

Sample	r_c (°C/min)	T_{cp} (°C)	p_c (mbar)	T_m (°C)
HA-1	2	100	2.65	300
HA-2	2	100	0.50	300
HA-3	2	300	1.00	850
HA-4	2	300	0.33	850

Table 1. Experimental conditions for the CRTA.

experimental parameters used in the different CRTA, which seeks to determine the optimal parameters of crystallization of HA at the lower temperature; where r_c is the controlled rate, T_{cp} is the temperature of control of the pressure, p_c is the pressure of control and T_m is the maximum temperature used to achieve such pressure control.

Analyses by IR and XRD demonstrated that both types of the sample, conventional treated and treated with CRTA, were pure crystalline phases of HA.

In **Figure 4** are shown the IR spectra typical of HA without thermal treatment (HA-green), conventional thermal treatment (HA-CTT) and after CRTA (HA-1 to HA-4), where the characteristic bands observed are reported for this material type, corresponding to the fundamental vibrations 3571.46 and 631.73 cm^{-1} of the OH^- and ν_3 1092.75 and 1045.49 cm^{-1}, ν_1 963.51 cm^{-1}, ν_4 602.80 and 568.08 cm^{-1} of the PO_4^{3-} [41].

The bands are very similar in all the IR spectra (**Figure 4**). The wide band from OH^- vibration only could be observed in the green-HA and in HA-CTT and was due to hydrate water

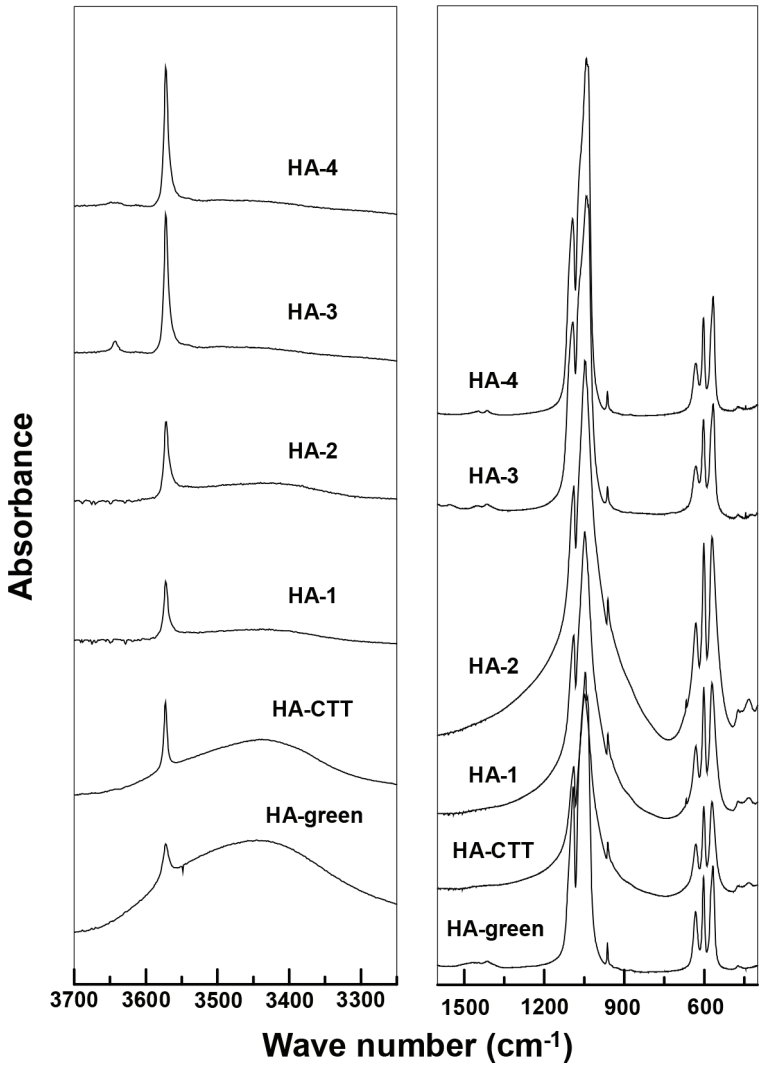

Figure 4. FTIR spectrum characteristic of an as-prepared HA-green sample and HA samples after the thermal treatments.

http://dx.doi.org/10.5772/66468

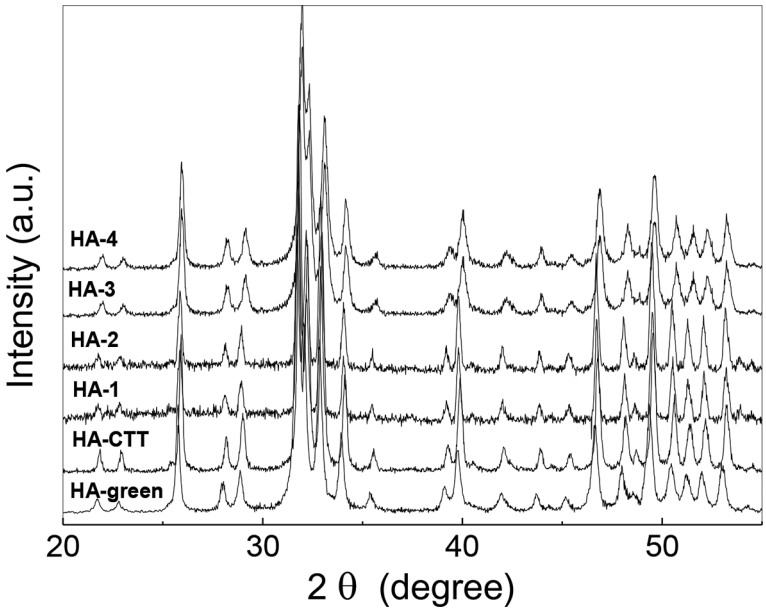

Figure 5. X-ray diffraction pattern of as-prepared HA green powders and HA samples obtained by applying different thermal treatments.

(3442.22 cm^{-1}). All bands become narrower and more symmetrical for HA-3 and HA-4, indicating an increase in the crystallinity of the material according to results obtained by other authors [42, 43].

Figure 5 shows X-ray diffraction, where typical lines for this material appear. In all cases, the signs appeared in X-ray diffraction corresponds to those reported in Chart No. 9-432 of ASTM [44, 45].

By applying conventional thermal treatments, HA was typically calcined above 900°C in order to obtain a stoichiometric, apatitic structure. However, it is interesting to note that applying CRTA the degree of crystallization of HA in this study at temperatures as low as 300°C it can be observed in **Figure 6a** and **6b**. The HA here obtained was composed of white tiny crystals, where the particles are fused together and, consequently, they are forming a cluster. This phenomenon might be attributed to a high surface area to volume ratio of ultrafine crystals related to thermal treatments. It should be also pointed out that the shape of HA grains is quite different from the biological apatite, which mostly exhibits a needle-like structure. However, we expect that it may be possible to obtain a grain shape similar to biological apatite by optimizing CRTA conditions.

Results for surface measures by BET method are described in **Table 2**. In the table, the range of specific surface areas achieved after CRTA can be observed. Samples HA-1 and HA-2 showed remarkable dependence on pressure for the surface area, increasing almost to double when

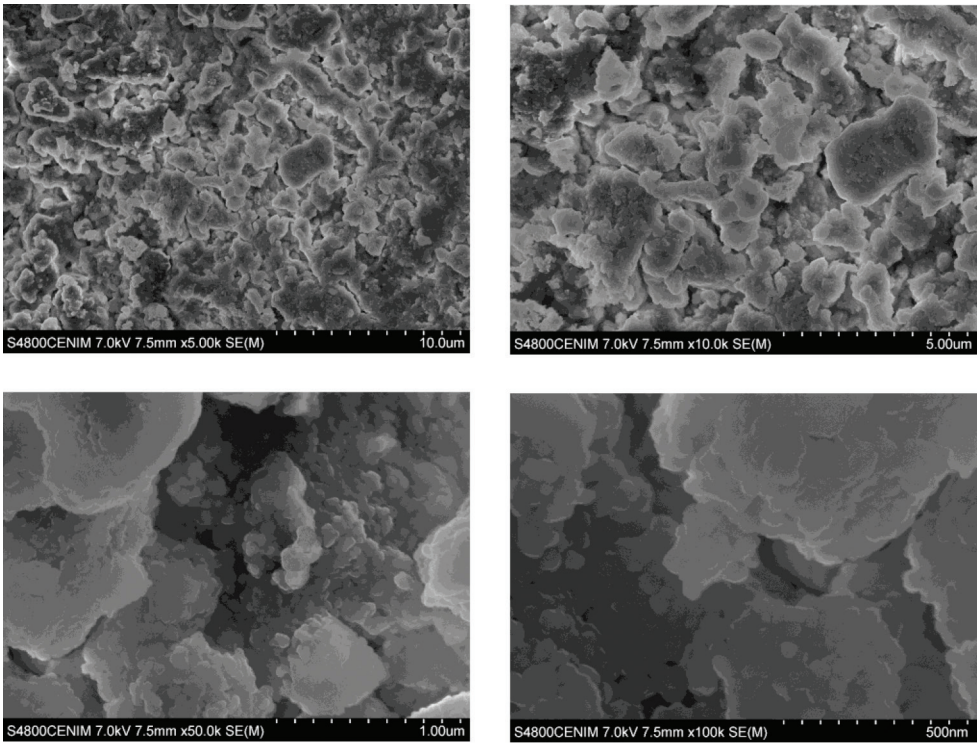

Figure 6. SEM micrographs under different magnifications of HA-2 powders prepared using CRTA (T_m = 300°C).

Sample	S (BET) (m^2/g)
HA-CTT	14.0
HA-1	34.9
HA-2	66.7
HA-3	17.2
HA-4	26.0

Table 2. Determinations of the surface area obtained by the BET method for HA-CTT and for different CRTA experimental conditions.

this parameter diminishes, at equal temperature of control and final. It is standing out that both samples, in spite of having been treated at 100°C as the temperature of control for pressure, and at 300°C as the final temperature, crystallized in a pure phase of hydroxyapatite.

In samples HA-3 and HA-4, also the same behavior is also observed, that is to say, an increase of the surface area when diminishing the control pressure, in this case it is four times less.

http://dx.doi.org/10.5772/66468

Although for both samples, the surface area notably diminishes when increasing the temperature of control and the final temperature of the process.

In summary, CRTA technology offers a better resolution and a more detailed interpretation of the decomposition processes of hydroxyapatite via approaching equilibrium conditions of decomposition through the elimination of the slow transfer of heat to the sample as a controlling parameter on the process of decomposition.

3.2. Cytotoxicity and adhesion of osteoblasts

The cytotoxicity assay allows toxicological risk assessment of a material by using cell cultures. Taking into account that migrating substances from biomaterials interact at the cellular level with cell membranes, the cellular organelles (mitochondria and Liposomes), the synthesis of proteins and DNA, cell division and the sequence of DNA, this essay covers from the cell

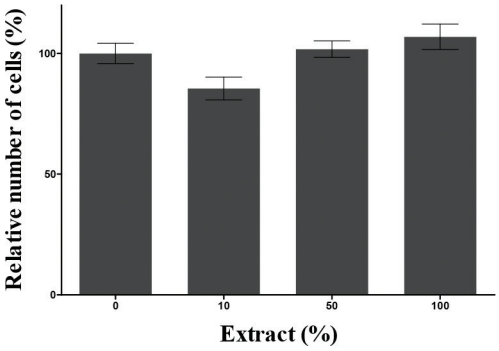

Figure 7. Relative number of cells as a function of exposure to different concentrations of extract for a Ti-6Al-4V alloy coated by sol-gel with HA-2 film.

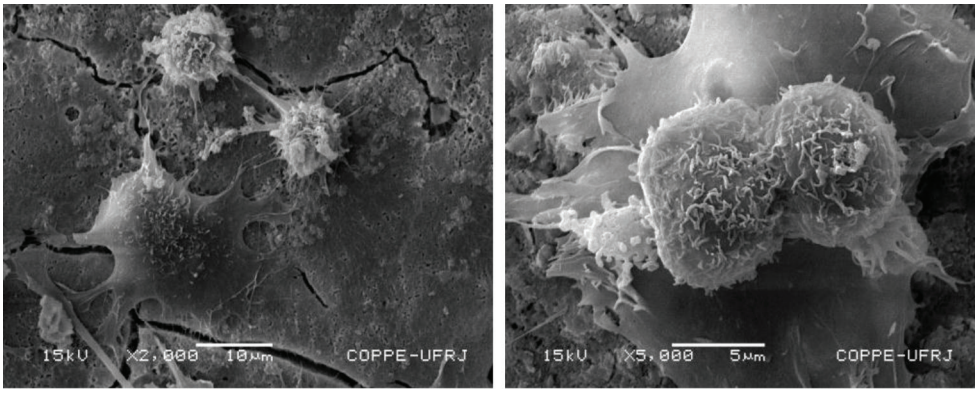

Figure 8. SEM images of cells morphology cultured on Ti-6Al-4V sheets coated by sol-gel with HA-2 film.

viability and death to more sophisticated forms that have to do with the cell functionality and genotoxicity.

Figure 7 shows, the percent (%) of living cells in each one of the tested extracts. The concentration of 0 corresponds to the negative control, or cells without being subjected to any concentration of the extracts.

It can be observed that there is no significant difference ($p > 0.05$) in the number of living cells exposed to different concentrations of the extracts of cultures with alloys coated by HA sol-gel, with respect to the control group. This indicates that HA coatings on Ti6Al4V does not affect the viability of the cells evaluated, which demonstrating its cytocompatibility.

SEM (micrographs) of preosteoblast cells femur seeded in Ti6Al4V alloy coated by sol-gel are shown in **Figure 8**. It is observed that cells were emitting cytoplasmic extensions (filopodia and pseudopodia) that indicate adhesion to the substrate. In addition, mitotic phases were observed (large cells) which suggested that the cells were divided. Apparently, all layers of HA indicate a good biocompatibility because the living cells of osteoblasts hold and spread (propagated) well over all the coating. The observed biocompatibility of HA could be due to roughness and surface porosity that provides sites for attachment and growth of cells.

3.3. Corrosion behavior

The corrosion protection behavior of the HA films deposited on Ti6Al4V samples was evaluated by applying electrochemical impedance spectroscopy (EIS). **Figure 9** shows the Bode impedance spectra for the tested samples the in Kokubo's solution at variable immersion time (1 hour and 1, 3, 7, 15 and 30 days).

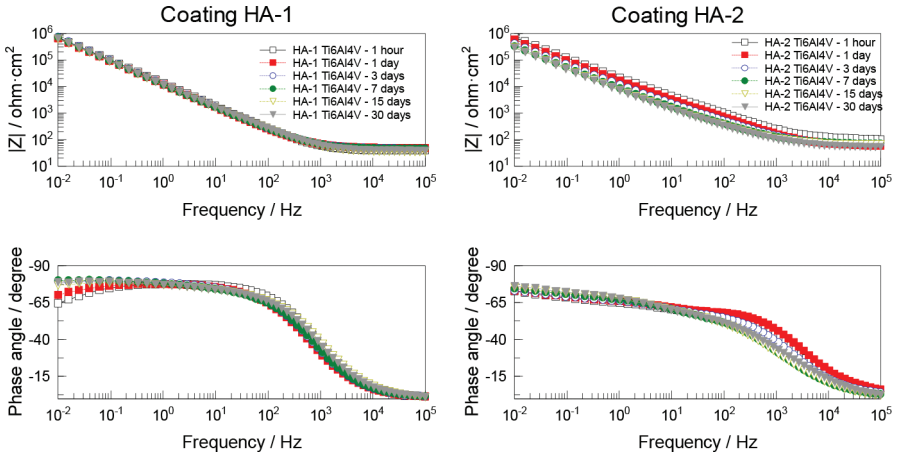

Figure 9. Bode impedance spectra representing the evolution of the impedance modulus (|Z|) in a double-logarithmic scale and the phase angle in a semi-logarithmic scale versus frequency for Ti6Al4V/HA coating systems at different immersion time in Kokubo's solution. Coatings: HA-1 and HA-2.

http://dx.doi.org/10.5772/66468

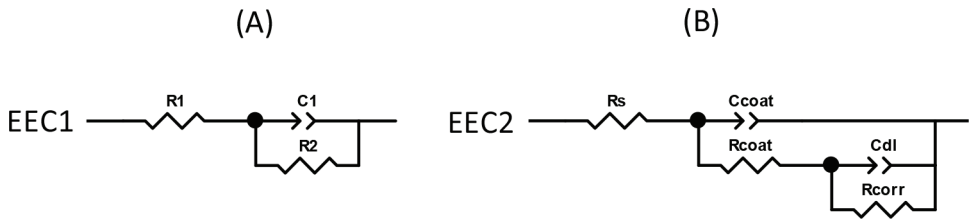

Figure 10. Electrical equivalent circuits used for studying the corrosion behaviour of the Ti6Al4V/hydroxyapatite coating system in contact with Kokubo's solution. One time-constant circuit (A) and two time-constant circuit (B).

In these Bode plots, the modulus of the impedance |Z| and the phase angle are represented versus the frequency, the first one in double-logarithmic scale and the second in semi-logarithmic scale.

These impedance spectra can be ascribed to the typical behavior of porous thin films deposited on metal substrates with high corrosion resistance [21, 31, 32, 46, 47]. In the first approach, the single electrical equivalent circuit EEC1 shown in **Figure 10a** can be used to describe the electrochemical behavior of these systems. R_s is associated with the resistance of the electrolyte sited between the working electrode and the reference electrode. The problem is to assign a correct physical meaning to the elements *C*1 and *R*2. Respectively, *C*1 could be associated with the coating capacitance or to the double layer capacitance at the base of the pores filled with electrolyte into the thin film. *R*2 could be ascribed the ionic resistance of the coating pores impregnated with electrolyte or to charge transfer of the metal/electrolyte interface at the base of the pores. In some cases, the electrical equivalent circuit EEC2 shown in **Figure 10b** could be more convenient to describe the impedance plots of these metal/coating systems [48, 49]. Following the notation of the ZView software [49], R_s is the solution resistance of the bulk electrolyte. C_{coat} is the capacitance of the coating. In this case C_{coat} is implemented as a constant phase element (CPE). R_{coat} is the resistance of the coating and C_{dl} represents the double layer capacitance of the electrolyte/metal surface interface. This capacitance is also implemented as a CPE.

As a representative example, **Figure 11** shows fit results obtained by using these two electrical equivalent circuits and complex nonlinear least-squares (CNLS) analysis methods. Three types of impedance plots are given in **Figure 11**, i.e.; Nyquist plot (for real and imaginary values of IZI), Bode plot (for IZI versus applied frequency) and the other Bode plot (for the phase angle versus frequency). This example corresponds to the Ti6Al4V/hydroxyapatite system based on the HA-1 coating after 1 hour in contact with Kokubo's solution. The fit plots generated by the EEC1 and EEC2 electrical equivalent circuits proposed are good. Physical meaning of the values of the electrical elements of the corresponding equivalent circuit and relative errors in % are also good. Finally, the chi-squared values (χ^2) are also very acceptable (9.9×10^{-4} for EEC1 and 3.9×10^{-4} for EEC2). It is known that low values of χ^2 are related to a better quality of the fitting results [31, 32].

However due to the uncertainty associated with the difficult interpretation of the results generated by these adjustments and simulations, has been more useful to follow the variations of

the impedance modulus |Z| at the lowest frequency as a function of exposure time of coatings to the Kokubo's solution. This parameter has allowed to reevaluate systematically the results obtained with the impedance measurement.

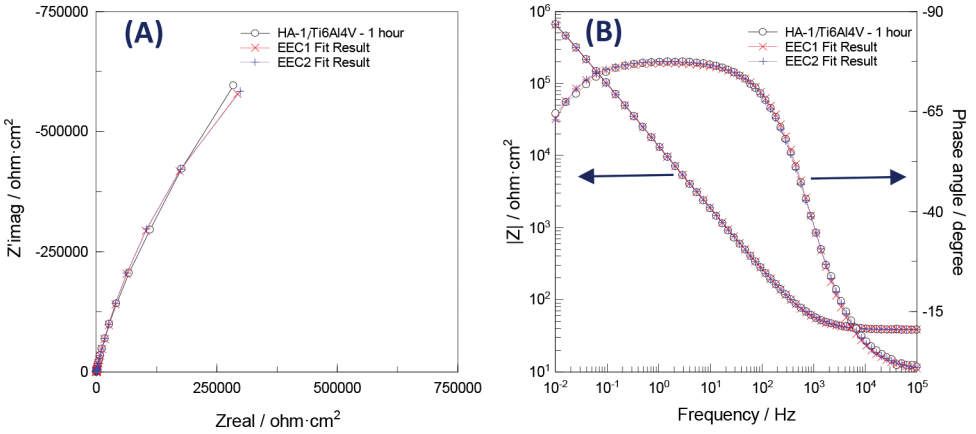

Figure 11. Nyquist plots (A), Bode Impedance spectra (B) and fit results obtained by applying the EEC1 and EEC2 electrical equivalent circuits to a Ti6Al4V/hydroxyapatite system based on the HA-1 coating after 1 hour in contact with Kokubo's solution.

Table 3 shows the variations of the impedance modulus |Z| at a frequency of 10 mHz with the immersion time for Ti6Al4V/hydroxyapatite systems based on the coatings HA-1 and HA-2, respectively. It can observe from the evolution of the values of the parameter $|Z|_{10mHz}$ that both systems show a satisfactory stability when they are tested in a saline solution. Particularly attractive was the protective behavior of the HA-1 coating whose $|Z|_{10mHz}$ values remained almost constant during the 30 days of the immersion test. However, for the system based on the HA-2 coating, although very slowly the values of this parameter decrease, down

Immersion time	**$|Z|_{10mHz}$ (ohm/cm²)**	
	Coating HA-1	**Coating HA-2**
1 hour	6.60×10^5	7.14×10^5
1 day	$6.23\ 10^5$	5.74×10^5
3 days	7.31×10^5	4.10×10^5
7 days	7.00×10^5	3.26×10^5
15 days	6.07×10^5	2.97×10^5
30 days	6.54×10^5	2.88×10^5

Table 3. Variations of the impedance modulus |Z| for 10 MHz frequency with the immersion time for coatings based on the samples HA-1 and HA-2, respectively.

http://dx.doi.org/10.5772/66468

from 7.14 × 10^5 ohm/cm^2 at the start to 2.88 × 10^5 ohm/cm^2 at the end of the immersion test (30 days). This behavior can be ascribed to a slow loss of the protection properties of the coating HA-2 due to the ingress of electrolyte in the coating pores. These results are indicating that the increase of the control pressure of the CRTA associated with the decrease in specific surface (BET) produces an enhancment of the corrosion protection behavior of the hydroxyapatite coatings. This means that a high specific surface is good for enhancing the adhesion of the preosteoblast cells but provokes a decrease in the corrosion protection of the HA coatings. It is necessary to reach a compromise to balance both properties.

4. Conclusion

In the present work, it was demonstrated the effectiveness and usefulness of the CRTA technique, for the preparation of crystallization of powders of synthetic hydroxyapatite and thin films with different specific surface areas, making this technique attractive for medical purposes. The purity of the phase of the samples obtained by CRTA was proved by IR spectroscopy and XRD. Several temperatures of control for pressure and watchword pressures were tested, observing the dependence of the specific surface area to these parameters, making possible to obtain surface areas from 14 up to 66 m^2/g. It was possible to crystallize pure hydroxyapatite at temperature of 100°C of control of the pressure and 300°C as maximum temperature. Moreover, the results of this study have also indicated that it was also possible to cover commercial Ti6Al4V alloy with these sol-gel-derived hydroxyapatite thin films. Cytotoxicity tests and corrosion studies showed an improvement for coated surfaces compared to the base Ti6Al4V alloy. Biocompatibility expressed in terms of adhesion of living cells and their spread on coating was also adequate. According to the ISO 10993-5 standard, the system was considered nontoxic. The cytocompatibility test shows that the sol-gel coating did not provoke the cell death significantly higher than the control ($p > 0.05$). In addition, the electrochemical impedance spectra confirm that these sol-gel coatings show promising corrosion protection properties. It can conclude that the sol-gel process in conjunction with the CRTA method can be a viable alternative for the production of crystallized synthetic hydroxyapatite thin films and ceramics with controlled specific surface and homogeneous distribution of pores, appropriate to be used in bone implantation and other formulations for orthopedic surgery.

Acknowledgements

This work has been supported by the National Program for Materials, Spanish Ministry of Science and Innovation (Project MAT2012-38541-C02-02) and by the Spanish Agency for International Development Cooperation (AECI) under the expert fund project entitled "Development of calcium phosphate ceramics for medical use". SEM images of cells were carried out in COPPE UFRJ.

Author details

E. Peón[1, 2], A. El hadad[1, 3], F.R. García-Galván[1], A. Jiménez-Morales[4] and J.C. Galván[1]*

*Address all correspondence to: jcgalvan@cenim.csic.es

1 National Center for Metallurgical Research (CENIM), CSIC, Madrid, Spain

2 Center for Biomaterials, Havana University, Havana, Cuba

3 Department of Physics, Al-Azhar University, Cairo, Egypt

4 Universidad Carlos III de Madrid, Avda, Leganés, Madrid, Spain

References

[1] M. Jarcho, "Calcium phosphate ceramics as hard tissue prosthetics", *Clinical Orthopaedic*, Vol. 157, pp. 259–278, 1981.

[2] K. De Groot, *Bioceramics of Calcium Phosphate*, CDC Press, Inc. Boca Raton, FL, 1983.

[3] J. Black, *Orthopaedic Biomaterials in Research and Practice*, Churchill Livingstone Ed., New York, 1988.

[4] J. B. Park, D. Joseph (Eds.), *Biomaterials*: *Principles and Applications*, CRC Press, Bronzino, 2003.

[5] K. I. Humear, A. D. Séller, R. G. Slighter, S. S. Rothstein, H. P. Drobeck, "Tissue response in dogs to dense HA implantation in the femur", *Journal Oral Maxillofacial Surgery,* Vol. 44, pp. 618–627, 1986.

[6] M. Sadat-Shojai, M. T Khorasani, E. Dinpanah-Khoshdargi, A. Jamshidi, "Synthesis methods for nanosized hydroxyapatite with diverse structures", *Acta Biomaterialia*, Vol. 9, Iss. 8, pp. 7591–7621, 2013.

[7] A. Kumar Nayak, "Hydroxyapatite synthesis methodologies: An overview", *Journal of ChemTech Research*, Vol. 2, Iss. 2, pp. 903–907, 2010.

[8] F. Sun, H. Zhou, J. Lee, "Various preparation methods of highly porous hydroxyapatite/polymer nanoscale biocomposites for bone regeneration", *Acta Biomaterialia*, Vol. 7, Iss. 11, pp. 3813–3828, 2011.

[9] N. Farahiyah Mohammad, R. Othman Fei Yee-Yeoh, "Nanoporous hydroxyapatite preparation methods for drug delivery applications", *Reviews on Advanced Materials Science*, Vol. 38, pp. 138–147, 2014.

[10] A. Shavandi, A. El-Din, A. Bekhit, Z. Fa Sun, A. Ali, "A review of synthesis methods, properties and use of hydroxyapatite as a substitute of bone", *Journal of Biomimetics, Biomaterials and Biomedical Engineering*, Vol. 25, pp. 98–117, 2015.

http://dx.doi.org/10.5772/66468

[11] S. Catros, J. C. Fricain, B. Guillotin, B. Pippenger, R. Bareille, M. Remy, E. Lebraud, B. Desbat, J. Amédée, F Guillemot, "Laser-assisted bioprinting for creating on-demand patterns of human osteoprogenitor cells and nano-hydroxyapatite" *Biofabrication*, Vol. 3, Iss 2, p. 025001, 2011.

[12] K. Mensah-Darkwa, R. K. Gupta, D. Kumar, "Fabrication and characterization of hydroxyapatite-magnesium composite thin films on magnesium plates for implant applications", *ASME International Mechanical Engineering Congress and Exposition, Proceedings (IMECE)*, Vol. 3, Iss. Parts A, B, and C, pp. 717–722, 2012.

[13] K. Mensah-Darkwa, R.K. Gupta, D. Kumar, "Mechanical and corrosion properties of magnesium-hydroxyapatite (Mg-HA) composite thin films", *Journal of Materials Science & Technology*, Vol. 29, Iss. 9, pp. 788–794, 2013.

[14] M. A. Surmeneva, E. A. Chudinova, I. Y. Grubova, O. S. Korneva, I. A. Shulepov, A.D. Teresov, N. N. Koval, J. D. Mayer, C. Oehr, R. A. Surmenev, "Effect of pulsed electron beam treatment on the physico-mechanical properties of hydroxyapatite-coated titanium", *Ceramics International*, Vol. 42, Iss. 1, pp. 1470–1475, 2016.

[15] Z. Janićijević, M. J. Lukić, L. Veselinović, "Alternating current electric field modified synthesis of hydroxyapatite bioceramics", *Materials & Design*, Vol. 109, pp. 511–519, 2016.

[16] V. Nelea, C. Morosanu, M. Iliescu, I. N. Mihailescu, "Hydroxyapatite thin films grown by pulsed laser deposition and radio-frequency magnetron sputtering: Comparative study", *Applied Surface Science*, Vol. 228, Iss. 1–4, pp. 346–356, 2014.

[17] T. Mukhametkaliyev, M. Surmeneva, R. Surmenev, B. K. Mathan, "Hydroxyapatite coating on biodegradable AZ31 and Mg-Ca alloys prepared by RF-magnetron sputtering", *AIP Conference Proceeding*, Vol. 1688, p. 030006, 2015.

[18] S. W. K. Kweha, K. A. Khora, P. Cheang, "The production and characterization of hydroxyapatite (HA) powders", *Journal of Materials Processing Technology*, Vol. 89–90, pp. 373–377, 1999.

[19] S. Madhavi, C. Ferraris, T. J. White, "Synthesis and crystallization of macroporous hydroxyapatite", *Journal of Solid State Chemistry*, Vol. 178, pp. 2838–2845, 2005.

[20] C. Balazsi, F. Weber, Z. Kover, E. Horvath, C. Nemeth, "Preparation of calcium-phosphate bioceramics from natural resources", *Journal of the European Ceramic Society*, Vol. 27, pp. 1601–1606, 2007.

[21] A. A. El Hadad, V. Barranco, A. Jiménez-Morales, E. Peon, J. C. Galván, "Multifunctional sol-gel derived thin film based on nanocrystaline hydroxyapatite powders", *Journal of Physics: Conference Series*, Vol. 252 (1), Art. No. 012007, 2010.

[22] M. Vila, I. Izquierdo-Barba, A. Bourgeois, M. Vallet-Regí, "Bimodal meso/macro porous hydroxyapatite coatings", *Journal of Sol-Gel Science and Technology*, Vol. 57, pp. 109–113, 2011.

[23] C. Balazsi, F. Weber, Z. Kover, E. Horvath, C. Nemeth, "Preparation of calcium-phosphate bioceramics from natural resources", *Journal of the European Ceramic Society*, Vol. 27, pp. 1601–1606, 2007.

[24] D. K. Pattanayak, R. Dash, R. C. Prasad, B. T. Rao, T. R. Rama Mohan, "Synthesis and sintered properties evaluation of calcium phosphate ceramics", *Materials Science and Engineering C*, Vol. 27, pp. 684–690, 2007.

[25] F. Z. Mezahi, H. Oudadesse, A. Harabi, A. Lucas-Girot, Y. Le Gal, H. Chaair, G. Cathelineau, "Dissolution kinetic and structural behaviour of natural hydroxyapatite vs. thermal treatment: Comparison to synthetic hydroxyapatite", *Journal of Thermal Analysis and Calorimetry*, Vol. 95, Iss. 1, pp. 21–29, 2009.

[26] J. Rouquerol, "L'analyse thermique a vitesse de decomposition constant", *Journal of Thermal Analysis*, Vol. 2, Iss. 2, pp. 123–140, 1970.

[27] J. Rouquerol, O. Toft Sørensen, General Introduction to Sample-Controlled Thermal Analysis (SCTA). In: O. Toft Sørensen and J. Rouquerol editors. *Hot Topics in Thermal Analysis and Calorimetry - Sample Controlled Thermal Analysis. Origin, Goals, Multiple Forms, Applications and Future*. Dordrecht: Kluwer Academic Publishers, Vol. 3, pp 1–7, 2003.

[28] K. Nahdi, F. Rouquerol, M. T. Ayadi, $Mg(OH)_2$ dehydroxylation: A kinetic study by controlled rate thermal analysis (CRTA), *Solid State Sciences*, Vol. 11, pp. 1028–1034, 2009.

[29] J. Rouquerol, K.S.W. Sing, P. Llewellyn, Adsorption by Metal Oxides. In F. Rouquerol, J. Rouquerol, K.S.W. Sing, P.L. Llewellyn and G. Maurin editors. *Adsorption by Powders and Porous Solids*, 2nd ed. Amsterdam: Elsevier/AP, pp. 393-465, 2014.

[30] M. D. Alcalá, F. J. Gotor, L. A. Pérez-Maqueda, C. Real, M. J. Dianez, J. M. Criado, "Constant rate thermal analysis (CRTA) as a tool for the synthesis of materials with controlled texture and structure", *Journal of Thermal Analysis and Calorimetry*, Vol. 56, pp. 1447–1452, 1999.

[31] A. A. El hadad, V. Barranco, A. Jiménez-Morales, E. Peón, G. J. Hickman, C. C. Perry, J. C. Galván, "Enhancing in vitro biocompatibility and corrosion protection of organic-inorganic hybrid sol-gel films with nanocrystalline hydroxyapatite", *Journal of Materials Chemistry B*, Vol. 2, pp. 3886–3896, 2014.

[32] A. A. El hadad, V. Barranco, A. Jiménez-Morales, G. J. Hickman, J. C. Galván, C. C. Perry, "Triethylphosphite as a network forming agent enhances in-vitro biocompatibility and corrosion protection of hybrid organic-inorganic sol-gel coatings for Ti6Al4V alloys", *Journal of Materials Chemistry B*, Vol. 2, pp. 7955–7963, 2014.

[33] D. Mo Liu, T. Troczynski, W. J. Tseng, "Water-based sol-gel synthesis of hydroxyapatite: process development", *Biomaterials*, Vol. 22, Iss. 13, pp. 1721–1730, 2001.

[34] D. Mo Liu, Q. Yang, T. Troczynski, "Sol-gel hydroxyapatite coatings on stainless steel substrates", *Biomaterials*, Vol. 23, Iss. 3, pp. 691–698, 2002.

[35] D. Mo Liu, Q. Yang, T. Troczynski, W. J. Tseng, "Structural evolution of sol-gel-derived hydroxyapatite", *Biomaterials*, Vol. 23, Iss. 7, pp. 1679–1687, 2002.

[36] T. Kokubo, H. Kushitani, S. Sakka, T. Kitsugi, T. Yamamuro, "Solutions able to reproduce in vivo surface-structure changes in bioactive glass-ceramic A-W^3", *Journal of Biomedical Materials Research*, Vol. 24, pp. 721–734, 1990.

[37] T. Kizuki, T. Matsushita, T. Kokubo, "Antibacterial and bioactive calcium titanate layers formed on Ti metal and its alloys", *Journal of Materials Science: Materials in Medicine*, Vol. 25, Iss. 7, pp. 1737–1746, 2014.

[38] A. I. Mitsionis, T. C. Vaimakis, "A calorimetric study of the temperature effect on calcium phosphate precipitation", *Journal of Thermal Analysis and Calorimetry*, Vol. 99, pp. 785–789, 2010.

[39] K. Tõnsuaadu, K. A. Gross, L. Pluduma, M. Veiderma, "A review on the thermal stability of calcium apatites", *Journal of Thermal Analysis and Calorimetry*, Vol. 110, Iss. 2, pp. 647–659, 2012.

[40] K. Tõnsuaadu, M. Peld, V. Bender, "Thermal analysis of apatite structure", *Journal of Thermal Analysis and Calorimetry*, Vol. 72, pp. 363–371, 2003.

[41] B. O. Fowler, "Infrared studies of apatites I", *Inorganic Chemistry*, Vol. 13, pp. 194–206, 1974.

[42] N. Pleshko, A. Boskey, R. Mendelsohn, "Novel infrared spectroscopic method for the determination of crystallinity of hydroxyapatyte minerals", *Biophysical Journal*, Vol. 60, pp. 786–793, 1991.

[43] A. Antonakos, E. Liarokapis, T. Leventouri, "Micro-Raman and FTIR studies of synthetic and natural apatites", *Biomaterials*, Vol. 28, pp. 3043–3054, 2007.

[44] S. Mazumder, B. Mukberjee, "Quantitative determination of amorphous content in bioceramic hydroxyapatite (HA) using x-ray powder diffraction data", *Materials Research Bulletin*, Vol. 30, Iss. 11, pp. 1439–1445, 1995.

[45] E. Landi, A. Tampieri, G. Celotti, S. Sprio, "Densification behavior and mechanisms of synthetic hydroxyapatites", Journal European Ceramic Society, Vol. 20, pp. 2377–2387, 2000.

[46] A. A. El hadad, "An approach to the design new coatings for biomedical applications" [thesis]. Universidad Carlos III de Madrid, Leganés. 2012. Available from: http://e-archivo.uc3m.es/handle/10016/16374 [accessed: 2016-09-19].

[47] E. Peón, "Recubrimientos bioactivos de base hidroxiapatita sobre Ti6Al4V para aplicaciones biomédicas" [thesis]. Universidad de La Habana, Cuba. 2013.

[48] B. Chico, J. C. Galván, D. de la Fuente, M. Morcillo, "Electrochemical impedance spectroscopy study of the effect of curing time on the early barrier properties of silane systems applied on steel substrates", *Progress in Organic Coatings*, Vol. 60, Iss. 1, pp. 45–53, 2007.

[49] ZView 3.5a Software, Scribner Association Inc., D. Johnson. Available from: http://www.scribner.com/ [accessed: 2016-09-19].

Chapter 12

Radio Frequency Magnetron Sputter Deposition as a Tool for Surface Modification of Medical Implants

Roman Surmenev, Alina Vladescu,
Maria Surmeneva, Anna Ivanova, Mariana Braic,
Irina Grubova and Cosmin Mihai Cotrut

Additional information is available at the end of the chapter

http://dx.doi.org/10.5772/66396

Abstract

The resent advances in radio frequency (RF)-magnetron sputtering of hydroxyapatite films are reviewed and challenges posed. The principles underlying RF-magnetron sputtering used to prepare calcium phosphate-based, mainly hydroxyapatite coatings, are discussed in this chapter. The fundamental characteristic of the RF-magnetron sputtering is an energy input into the growing film. In order to tailor the film properties, one has to adjust the energy input into the substrate depending on the desired film properties. The effect of different deposition control parameters, such as deposition time, substrate temperature, and substrate biasing on the hydroxyapatite (HA) film properties is discussed.

Keywords: Hydroxyapatite, magnetron sputtering, corrosion resistance, cell viability

1. Introduction

It is well known that the long-term success of the dental and orthopedic implants is determined by a good osseointegration, which can be guaranteed by a good connection between the bone cell and implant. This connection is dependent on the phenomena which can take place immediately after insertion of the implant in human body. The first process after implantation is the interface between implant and the proteins, by formatting a thin layer which will act as a mediator of a good proliferation of the cells. Thus, protein adsorption determines the nature of the interface between the bone and implant, which will stimulate a fast cell growth, leading to a rapid osseointegration of the implant. In the past few years, it was demonstrated that the osseointegration of the metallic implants could be increased by coating the implant surface

with bioactive coatings, which proved to accelerate the bone bonding rate. It was certified by World Biomaterial Congress in 2008 and 2012 and 2016 that this topic is one of the major topics in biomaterials.

Various different techniques are currently available for deposition of calcium phosphate (CaP), in particular hydroxyapatite (HA) coating, to metallic materials, including plasma spraying, pulsed laser deposition, biomimetic crystallization methods, electrophoretic deposition, sol-gel deposition, magnetron sputtering, etc. [1].

Among the listed methods, plasma spraying is the only approach which is commercially approved for HA coatings deposition on metal implants by the food and drug administration (FDA) [1]. The method is based on the formation of a condensed layer of individual particles deposited on a metal substrate. The particles originating from a powder material are carried by a gas stream and passed through electrical plasma produced by a low voltage, high current electrical discharge. During this process, the heated particles crystallize and agglomerate during film formation. The coating features are determined by the chemical and mechanical properties of the used powder material, by the distance between a source and a substrate, the current of the electric arc, the deposition rate, and the work gas composition. Plasma spraying allows to produce coatings up to 300 μm in thickness. This technique has some significant limitations: poor uniformity in coating thickness and adherence to substrate, low crystallinity, poor mechanical properties on tensile strength, wear resistance, hardness, toughness, and fatigue [2]. Furthermore, plasma spraying does not allow to produce an uniform HA coating on substrates with complex geometry. Meanwhile, the most important disadvantages of this method are considered to be the presence of impurity phases. A higher temperature (6,000–10,000°C) is used during plasma spraying, the crystal structure of the HA powder can be easily destabilized and decomposition into mixture of HA, CaO, tricalcium phosphate, and tetracalcium phosphate, and a considerable amount of amorphous phases is occurs [3]. Structural inhomogeneity can lead to differences in coating resorption [3] and a reduction in coating-substrate interfacial strength [4, 5]. The alternative coating approaches have been extensively developed and tested to overcome the weaknesses of plasma spraying, namely sol-gel deposition and RF-magnetron sputtering. An overview of these three techniques is given in **Table 1.**

Sol-gel deposition is a widespread method to produce CaP coatings [6, 7]. This method is based on the preparation of a suspension (sol) in the dispersion phase with its subsequent transition into a gel and the treatment of a metal surface with the resulting colloid. Thermal treatment at the coating material's crystallization temperature is required as the final step. The method makes it possible to produce a dense CaP coating with the thickness of 0.5–30 μm. Sol-gel deposition is a relatively inexpensive technique compared to others. The method has the potential to coat implant with complex shape by using simple setup [8]. Furthermore, it has the benefits of phase and structural uniformity [9, 10]. However, too low processing temperature leads to an amorphous or a nanocrystalline coating structure and requires, therefore, additional annealing of the coating to increase the degree of crystallinity. The major advantages of sol-gel method are good mechanical properties, corrosion resistance, and adhesion strength due to their nanocrystalline structure [11, 12]. However, the sol-gel deposition has disadvantages such as high permeability, low wear-resistance, and difficult porosity control, which hinders its commercial

http://dx.doi.org/10.5772/66396

Technique	Thickness (μm)	Advantages	Disadvantages	Ref.
Plasma spraying	~30–300	High deposition rate; sufficiently low cost; coatings usually have microrough surface and porosity	Poor adhesion; low crystallinity, poor mechanical properties on tensile strength, wear resistance, hardness, toughness and fatigue; high temperatures induce structural inhomogeneity and HA decomposition; rapid cooling produces cracks in coatings	[2–5]
Sol-gel coating	~0.5–30	Inexpensive; low processing temperatures; high purity; fairly good adhesion (40 MPa); can coat complex substrates; high phase and structural uniformity	Requires high sintering temperatures; poor control of chemical and phase composition; high permeability; low wear-resistance; difficult porosity control	[6–14]
RF-magnetron sputtering	~0.04–3.5	Uniform coating thickness; dense pore-free coating; ability to coat heat-sensitive substrates and with complex structure; high-purity films; ability to control the coating structure and the Ca/P ratio; good adhesion (30 MPa)	Line-of-sight method; low deposition rate; expensive	[2, 3, 6–9, 15, 16]

Table 1. The advantages and disadvantages of the most applied methods for HA coating deposition.

application [13]. Meanwhile, annealing can lead to a deterioration of the coating's adhesion. Furthermore, adsorbed organics within the sol-gel process can also cause coating failure.

Despite all the advantages of the above-described methods, their most essential limitation is the difficulty to control the phase and chemical composition of a CaP coating. In its turn, RF-magnetron sputtering allows to control the properties of CaP films within a rather wide range and to form a dense, uniform coating to devices with complex configurations with high adhesion and with uniformity in thickness and composition [17–24].

This high flexibility makes RF-magnetron sputtering, however, a rather complex method, especially for the deposition of multicomponent materials such as calcium phosphates. There are many process parameters that can have a direct effect on the coating's characteristics. For example, the coating composition can be influenced by the target composition and sputtering parameters such as gas pressure, substrate bias, and the deposition temperature. During

RF-magnetron sputtering, the dense plasma interacts strongly with the substrate [25], which causes an intense ion bombardment of the growing coating. The energetic particle bombardment may determine the growth film. During the RF discharge, the positive ions are accelerated and bombard the substrate with high energies, which are dependent on the discharge excitation frequency. It is plausible that the plasma density is higher in front of the substrate opposite to the plasma torus above the erosion racetrack. Under target erosion zone, the bombardment of the substrate surface by high energetic oxygen species (O^-) occurs, which was confirmed by a number of authors [26–30]. These ions are generated at the target surface, accelerated in the cathode dark space and move with a high energy perpendicular from the target toward the substrate surface [31–33]. Cai et al. [34] described the effect of a local change in the growth rate of ZnO coating in the region of the target erosion zone which is connected with the sputtering of the coating with negatively charged ions. So, the Ar^+ and O^- bombardment is the major part of the energetic particle bombardment occurring in RF discharges. It plays an important role during the film deposition in RF sputtering, because the temperature of the substrate may increase with increasing discharge power. The properties of the RF-magnetron sputter-deposited films are highly influenced by the bombardment of the growing film with species from the sputtering target and from the plasma. The latter is determined by the deposition parameters such as the working gas pressure and composition, target-substrate distance, and substrate bias voltage. Different energetic and thermal circumstances may result in a different final quality and structure of the applied coating. Control of these parameters is essential to modify the HA coating structural properties, its composition, and mechanical characteristics.

This chapter reports on the influence of discharge RF-power, substrate temperature, and spatial sample arrangement regarding the target erosion zone on the properties of the CaP films, its mechanical properties, and behavior *in vitro*.

2. Literature overview of RF-magnetron sputtering of CaP coating and its comparison with chemical method

2.1. Principles of RF-magnetron sputtering

A magnetron sputtering system is a technological equipment which allows depositing thin films by sputtering of a target material in a magnetron discharge plasma. This type of system is based on the formation of electric and magnetic fields perpendicular to each other in the near-cathode region. By supplying a voltage between the cathode and the anode, a glow discharge is ignited. When the voltage is applied, the free electrons are repelled from the cathode or target and collide with the atoms of the working gas, creating ions, and new electrons. The positive ions are accelerated toward the target. The collision of the positive, energetic ions with the target leads to its sputtering. Particles removed from the target surface are transported to the substrate and the chamber walls. Not only atoms but also emission of electrons occurs due to the interaction of the ion flux with the target surface. The amount of emitted electrons to each approaching ion is known as the secondary electron emission yield and depends on the properties of the target material, the energy, and the type of bombard-

http://dx.doi.org/10.5772/66396

ing particles. Secondary electrons are necessary for the ionization of the working gas and the maintenance of the discharge.

The magnetic field holds electrons in immediate proximity to the target in a so-called electron "trap" that is created by the intersecting electric and magnetic fields. The electrons oscillate in this trap until several ionizing collisions with atoms of the working gas occur. The plasma is localized above the target surface, due to the presence of the magnetic field. Hence, the target surface is sputtered in areas located between the magnets of the magnetic system. As a result, an erosion zone (racetrack) is created in the form of a closed-loop path with a shape determined by the magnetic system.

The RF plasma is conducted by electron ionization, which exhibited an oscillating movement at the RF-magnetron frequency of 13.56 MHz. At this frequency, the ions could not pursue these oscillations due to their mechanical inertia. This excitation is much more effective than the ionization by nonoscillating secondary electrons, leading to decrease of the voltage of the RF discharge. During the positive half-cycle, the target acts not as a cathode but as an anode. Therefore, the plasma density in front of the substrate is significantly higher for RF. **Figure 1** shows the potential distributions, in which the positive ions (Ar^+, O^+, and Ca^+) are accelerated in the cathode fall V_p-V_{dc} and the target sputtering will take place. At the same time, the electrons and negative ions (O^-) were moved from the target to the substrate, which along to the reflected neutral argon atoms will arrive at the substrate and perform the growth of the coating. In **Figure 2**, the effects of energetic particles on a solid surface during ion-assisted growth during the RF discharge are shown. The secondary and back-scattered electrons, as well as the reflected ions and neutrals, cause a higher plasma density in front of the substrate for RF excitation and hence a higher ion saturation current to the growing film.

It can be seen that the electrons are kept out of the substrate and only those, which have a sufficiently high energy, will be able to pass through the potential barrier and arrive to the substrate, even if they have a low current. Both neutral species and high-energy negative ions (i.e., O^-) are capable of striking the substrate.

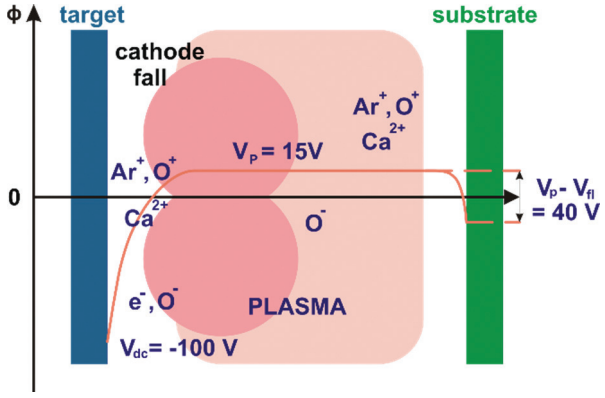

Figure 1. Potential distribution in a magnetron sputtering discharge, excited by RF.

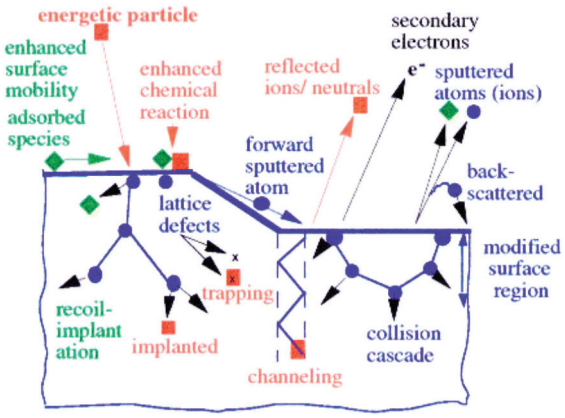

Figure 2. The effects of energetic particles on a solid surface during ion assisted growth [35].

The properties of the RF-magnetron sputter-deposited films are highly influenced by the bombardment of the growing film with species from the sputtering target and from the plasma. The latter is determined by the deposition parameters such as the working gas pressure and composition, target-substrate distance, and substrate bias voltage. Control of these parameters is essential to modify the HA coating structural properties, its composition and mechanical characteristics. The thermal and energetic conditions at the substrate surface influenced by the different plasma species determine the elementary processes (adsorption, diffusion, and chemical reactions) as well as the microstructure and stoichiometry of the film growth. The energy available per incoming particle and ion-to-atom ratio is, therefore, essential in plasma processing of solid surfaces in the case of thin film growth. Functional properties of the thin films are largely determined by the intrinsic coating features, which defined not only by the material properties but, to a large extend, also by the thin film growth mechanism. Passing through several stages, adsorption, nucleation growth, and increase film thickness, a defined coating structure is formed. The extended structure zone model identifies the evolution of a polycrystalline thin film and its relation with the deposition conditions.

2.2. Morphology of RF-magnetron sputtering of CaP coating

The surface morphology of the HA coatings appears to play a significant role in implant-tissue interaction and osseointegration [1]. RF-magnetron sputtering allows to deposit dense, uniform coating, without apparent defects (cracks, gas bubbles, and others) keeping the initial substrate topography [1, 36]. The latter is beneficial in case of porous scaffolds and other substrates with the complex structure. Meanwhile, it is well known that the coating surface morphology is connected to their growth mechanisms. In this way, it varies according to the deposition process conditions. Most often CaP coatings produced by RF-magnetron sputtering at room temperature possess a low crystalline or amorphous structure. It occurs due to the energy flux arriving the substrate at the applied process conditions that is not high enough to ensure crystalline coating formation on the unheated substrate holder. To induce the crystal-

http://dx.doi.org/10.5772/66396

linity of the coatings and transform the amorphous calcium phosphate into HA, the thermal treatment at $T > 500°C$ (*in situ* and *ex situ*) is applied [37–42].

The surface morphology of the coatings to be shown strongly depends on the substrate temperature. Bramowicz et al. [43] performed the deposition on silicon substrates with the temperature varied in the range of 400–800°C (**Figure 3**). The sample deposited at 400°C was observed to exhibit some circular cavities. At the increase of the deposition temperature, the cavities started to overlap, leading to the formation of uniform grains with comparable size. At 500°C, a threshold in the growth mode was observed, as the predominant morphology (cavities in otherwise flat surface) turned into a series of convex grains with well-developed grain boundaries. The authors concluded that the deposited HA coatings exhibit bifractal behavior, their surface topography can be thought of as two interpenetrating spatial structures with different characteristic length scales (cavities and clusters of cavities), which independently evolve with the deposition temperature.

The change of the routine of the coating preparation by adjusting the process parameters, such as substrate-target distance, working gas pressure, bias potential on substrate holder, ensuring higher energy flux arriving at the substrate allow to obtain crystalline coating at room temperature [44–47]. López et al. [44] published a study on the control of the thermodynamic properties of the plasma to form a coating with higher crystallinity. The authors modified the sputtering geometry by positioning two magnetrons face-to-face with a substrate holder kept in a floating electric potential positioned at a right angle to the magnetrons (off-axis). It was shown that at an RF-power density of 24 W/cm^2 after 180 min of sputtering, the transformation of amorphous phase in the coating to the crystalline one occurred. Surmeneva et al. [48] in their work deposited higher crystalline coatings by sputtering a Si-containing HA target using a setup with an RF-magnetron source (5.28 MHz) at an RF-power density of 0.5 W/cm^2 and a target-substrate distance of 40 mm. The experiments were performed with a grounded substrate holder (bias 0 V) and a bias voltage of -50 or -100 V. The temperature of the substrate

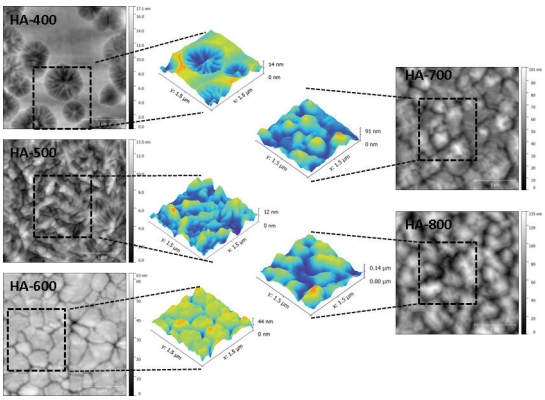

Figure 3. 10 × 10 μm, 2 planar AFM images of residual surfaces of the HA substrate on Si substrate deposited at: (A) 400°C, (B) 500°C, (C) 600°C, (D) 700°C, and (E) 800°C. Insets: 3D projections of marked areas to show changes in surface morphology [43].

during deposition reached 200°C due to heating by plasma. The effect of ion bombardment on the morphology and microstructure modification of Si-HA coatings is shown in **Figure 4**. The typical surface morphology of the HA coatings deposited on a flat silicon grounded substrate consisted of mound-shape grains (**Figure 4a**). By applying a substrate bias a distinct decrease in the morphological features dimension was observed. The coating cross-section structure was studied by SEM. The samples were prepared by the chemical etching of one half of the coating in 1 M aqueous HCl. The etched regions of the coating are shown in **Figure 4** (right side). The SEM study showed that the coatings deposited on the grounded substrate consisted of dense columnar grains grown perpendicular to the substrate surface. The columnar structure is the typical characteristic of films deposited by means of magnetron sputtering. The physical reason for the phenomenon of this structure is explained by Krug [49] and Bales and Zangwill [50] as a shadowing effect which can occur if adatoms impinge on the substrate under an angle which deviates from the substrate normal. With negative bias, the columnar structure was completely replaced by a very fine equiaxed grain structure which is reflected in the surface morphology. Therefore, it is considered that due to applying the negative bias, the particles arriving on the growing film have higher enough energy to disrupt column growth and force renucleation. Moreover, an increased ion bombardment may induce coating resputtering effect resulting in flat surface morphology. Thereby, the HA coatings can be deposited by RF-magnetron sputtering in such a way to control the coating morphology.

2.3. Composition of RF-magnetron sputtering of CaP coating

The thermodynamic stability, reactivity, solubility, and mechanical properties of CaPs were reported to strongly depend on the Ca/P ratio [4]. The calcium phosphate with low Ca/P ratio proves to have high dissolution rate. When the Ca/P ratio is equal to 1.67, the stoichiometric compound is obtained, which is referred as hydroxyapatite (HA). In biomedical applications,

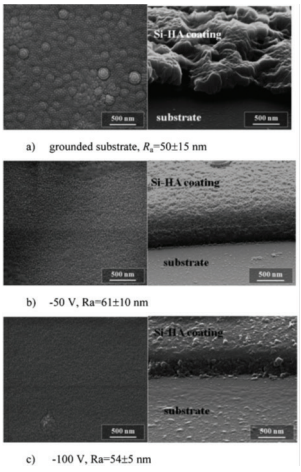

Figure 4. SEM images of the Si substrate coated with HA coating at the grounded substrate holder (a) 0 V, (b) −50 and (c) −100 V. Left: top view; right: side view after etching. The R_a was measured before etching [48].

http://dx.doi.org/10.5772/66396

this compound is the most desired to obtain because the Ca/P ratio is close to that of natural bone. Thus, the Ca/P ratio is one of the main characteristics of a biocompatible film and it depends on the applied deposition control parameters such as RF-power, substrate bias, working gas pressure, and configuration of the samples in the vacuum chamber [51]. It is shown that the ratio of elements in the deposited coating may differ substantially from their ratio in the target [24, 28, 52]. It was reported that when sputtering from multicomponent ceramic targets, such as superconducting oxides, HA, and other CaP materials, the alteration in coating composition may occur due to the preferential sputtering, which can initially cause the stoichiometry of the film to deviate from that of the target. However, at steady state, the composition of the sputtered flux must be the same as the target composition unless extensive diffusion occurs in the target [53]. It was also reported that at least 1000 Å (or more of the multicomponent target) need to be removed before the coating would reflect the stoichiometry of the bulk target [54]. Thus, the composition of the coating may be quite different from that of the target material, depending on the type of sputtering system, and parameters used for deposition.

Figure 5 shows the typical spectra for the fitted high resolution XPS obtained for O1s, Ca2p, and P2p regions of CaP films deposited by RF-magnetron sputtering onto titanium substrates. For the studied CaP coating, the O1s envelope (**Figure 5a**) was fitted with energy O1s = 531.9 eV of the calcium in the structure of HA. The energy of $Ca2p_{3/2}$ = 347.1 eV (**Figure 5b**) was established for all Ca-O bindings. Finally, the P2p was fitted with two binding energies for the $P2p_{3/2}$ peak (**Figure 5c**): (i) the $P2p_{3/2}$ = 132.9 eV was established to the phosphorous bonded to the oxygen in the $(PO_4)^{3-}$—groups in the hydroxyapatite structure and (ii) the $P2p_{3/2}$ = 133.8 eV was attributed to the P-O bindings in the calcium phosphate phase. For nanocrystalline HA coatings deposited via the RF-magnetron sputtering the ratio of Ca/P was reported in the range between 1.6 and 2.9 [47, 55]. The optimum Ca/P ratio was reported to be in the range of 1.67–1.76 [4].

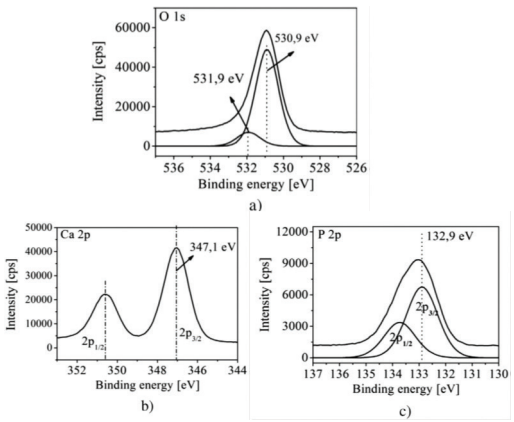

Figure 5. XPS: (a) O 1s, (b) Ca 2p, and (c) P 2p spectra of the CaP coating deposited via RF magnetron sputtering onto a titanium substrate [56].

At the low deposition temperature an amorphous coating structure was obtained; the increase of the deposition temperature leads to the Ca/P ratio change in the range of 1.41–1.69 [43]. It was demonstrated that the Ca/P ratio achieved the value of 1.63–1.69 for samples prepared at temperatures between 600 and 800°C. It was found that the Ca/P ratio of the coating is different than that of the target, due to specific target sputtering mechanisms. Moreover, it was reported that P ions are pumped away before reaching the substrate [17]. In the present case, at relatively low deposition temperature, the deposition conditions yielded Ca-deficient films, whereas temperature increase resulted in stoichiometric HA films. Possible phenomena causing these results include differences in sticking and removal rates of atoms on the growth surface and gas scattering phenomena [53]. Film growth at relatively high temperatures implies that the sticking probability of the incoming species can be less than unity, which in the case of compound growth can result in modified film composition.

An increase of the negative bias applied to the substrate led to the increase of the coating crystallinity and of Ca/P ratio from 1.53 to 3.88 [52, 55, 56]. Feddes et al. [57] explained this phenomenon by assuming that phosphorus was resputtered from the growing film surface by ion bombardment with the energy determined by the potential drop in the cathode dark sheath. The authors of the study reported that calcium was carried by positively charged radicals (e.g., CaO^+) and ions (e.g., Ca^+ and Ca^{2+}) generated in the plasma [57]. Moreover, it is explained that higher negative substrate biasing resulted in higher fluxes of CaO^+ cations onto the surface and it became more difficult for $(PO_4)^{3-}$ anions to reach the surface, which explained the higher Ca/P ratios at higher negative biases [48].

The composition of the CaP coatings may be controlled by the RF-magnetron sputtering and may be changed by deposition temperature. The increase of the deposition temperature leads

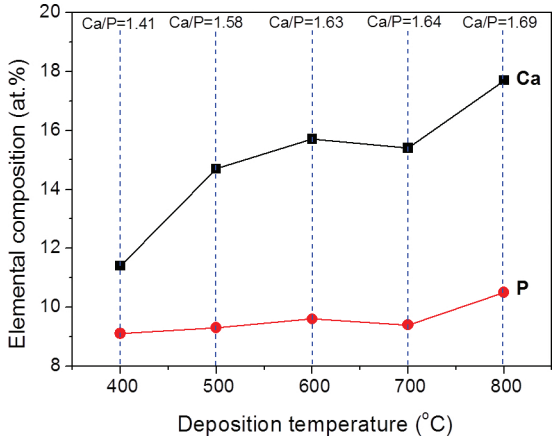

Figure 6. Elemental composition determined by XPS of the CaP coating deposited via RF magnetron sputtering at different deposition temperature onto a silicon substrate [43].

http://dx.doi.org/10.5772/66396

to the Ca/P ratio change in the range 1.41–1.69 [43]. The deposition temperatures influence the Ca/P ratio, which achieves 1.63–1.69, that is very close to the stoichiometric HA (Ca/P = 1.67), for samples prepared at temperatures between 600 and 800°C (**Figure 6**).

2.4. Water addition into an working gas atmosphere effect of RF-magnetron sputtering of CaP coating

A similar trend was observed for the coatings deposited in H_2O-containing atmosphere by Ivanova et al. [28] (see **Figure 7**). The Ca/P ratio varied within the range of 1.53–1.70, and first increased with the distance from the center of the substrate holder. The highest Ca/P ratio was obtained for the samples exposed above the racetrack. Feddes et al. [57] reported that the P ions can be resputtered by negatively charged oxygen ions, leading to the variation of the Ca/P. Also Takayangi et al. [58] found that the high-energy negative ions appear in the erosion area of the oxidized cathode due to a large amount of electrons which are trapped by magnetic field within this zone. So, the negative oxygen ions formed as well as Ar ion bombardment of the growing HA film caused its stoichiometric deviation from the target composition. So, the RF-magnetron sputtering is well-suited method to prepare coatings with different Ca/P molar ratios by variation of the substrate temperature, substrate bias, and position of the sample with regard to the target erosion zone [48].

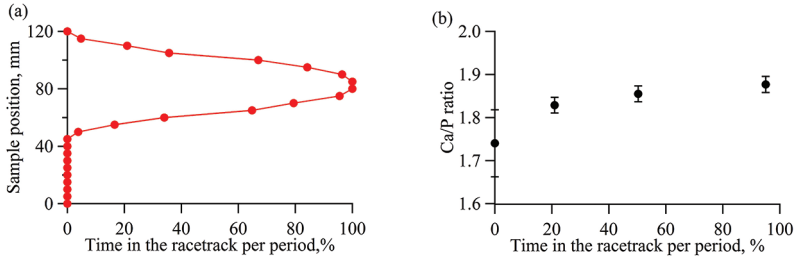

Figure 7. The relation between the sample positions on the substrate holder: (a) and a Ca/P ratio, (b) as function of the time in the race track per period [28].

2.5. Microstructure of RF-magnetron sputtering of CaP coating

At the low energy flux into the substrate, the amorphous HA coating is growing [59]. Thus, the deposition temperature of the HA coating plays an important role to the formation of the crystalline structure, which influence many other properties of the coatings. **Figure 8** shows the evolution of the crystallinity on the deposition temperature. At low temperature, the CaP coating shows only two peaks: (002) and (202). As the deposition temperature increased, more peaks are seen, the (200), (222), (213), and (004) planes) indicating the formation of the crystalline structure. The grain sizes, calculated by the Scherrer formula, increase with the deposition temperature, resulting in crystallites aggregation due to the higher adatoms mobility.

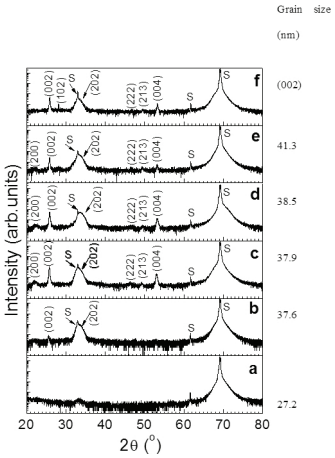

Figure 8. XRD spectra of the CaP coatings deposited at different deposition temperature [59].

The phase composition and structure of the CaP coating depend on the process conditions as it was mentioned above. RF-magnetron sputtering allows to deposit the CaP coatings of either amorphous or crystalline structure of a certain phase composition that along with the Ca/P ratio influences the coating behavior *in vitro* and *in vivo* [60]. The high dissolution rates of the amorphous lead to long-term stability reduction of the implanted devises. With the aim to maintain the HA coating integrity the researchers apply the postdeposition or *in situ* annealing of the films. Several authors reported that the transition from amorphous to crystalline coatings can be controlled by the heat-treatment temperatures and heating environment (air

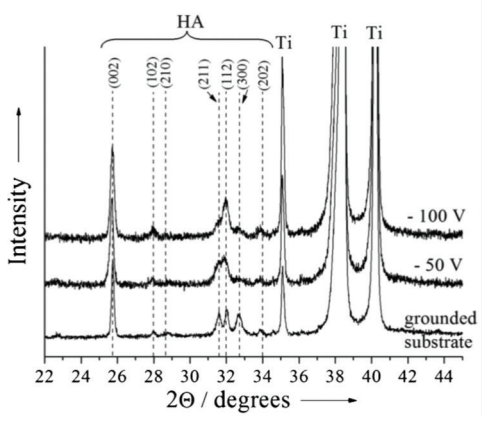

Figure 9. XRD spectra show variations of the intensity distributions, revealing that the studied samples have a different texture [48].

http://dx.doi.org/10.5772/66396

and water vapor) [61–63]. Meanwhile, crystalline coating can be obtained by turning the energy of the bombarding ions or ion to atom ratio arriving the substrate through manipulation with the substrate bias, working gas composition, pressure, and target-substrate distance.

The influence of the substrate bias voltage on the structure of the Si-containing HA coating was studied by Surmeneva et al. [48]. The X-ray diffractograms of the deposited coatings consisted of the reflexes corresponding well to the expected Bragg peaks for hydroxyapatite (ICDD PDF No. 9-432) (**Figure 9**). With a grounded substrate, the strongest peak of the Si-HA coating was the reflection from the (002) plan resolved at 25.9°. Thus, crystallites of Si-HA preferentially grew in the (002) crystallographic orientation perpendicular to the substrate surface. With an increase in the substrate bias voltage to −100 V, the intensity of the (002) peak relative to the other peaks was observed to decrease. The XRD pattern of the coating at negative bias showed broad overlapping peaks around 32°, which indicates the decrease of the crystallite size or/and the presence of the microstress in the film. The average crystallite size as determined by the Scherrer formula was 70 nm for the coating obtained on a grounded substrate (0 V) and 45 nm for the coatings deposited at negative bias (−50 and −100 V). Thus, the enhancement of the energy of the bombarding ions reduces the texture of the film and the crystallite dimension.

The crystalline HA coatings were obtained by RF-magnetron sputter deposition in water containing atmosphere [28]. It was shown that the HA coatings exhibited considerable change on preferential orientation while the samples approach the target erosion zone. According to XRD analysis with shifting the sample radially from the center of the substrate holder the texture coefficient of (002) peak decreases while the (300) peak grows up. **Figure 10** shows detailed highlights from the two ultimate cases of the deposited HA coatings preferentially oriented in the (002) and (300) directions. The structural features of

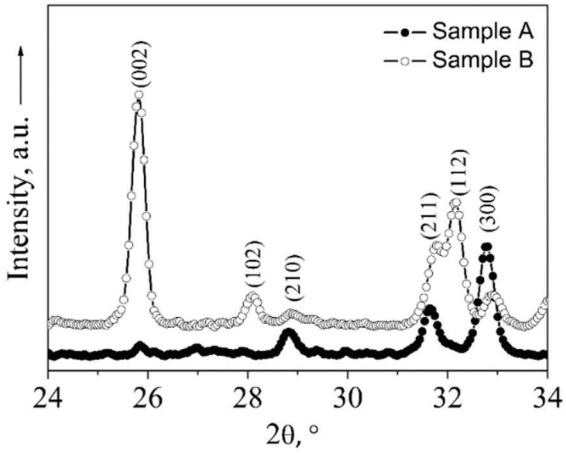

Figure 10. Highlights from X-ray diffractograms of HA films deposited under racetrack (Sample A) and in the centre of the substrate holder (Sample B).

the films were quantitatively studied. The lattice parameters (*a*, *b*, and *c*) of the measured samples were revealed to be higher than that of the bulk HA. The (002) textured coating (Sample B) is characterized by *a* = 9.410 Å and *c* = 6.934 Å; the (300) textured film (Sample A) is with a = 9.490 Å and *c* = 6.925 Å. This behavior is commonly observed in physical vapor deposited thin films and is attributed to the compressive stress arising in the film within growth and the stoichiometric imbalance of the film composition. In this way, the deposition conditions which were realized under the racetrack lead to the transformation of the HA film orientation. It is considered that the texture change is resulted by high energy ion bombardment of the growing film deposited under the target erosion zone. This not only affects the deposition rate but also influences the structure and functional properties of the film.

The development of microstructure in the trend of the coating growth was also studied with the help of TEM cross-section images. **Figure 11** shows the cross-sectional bright and dark fields of a 250-nm thick CaP layer prepared by FIB. Note that the coatings had a gradient structure with a nanocrystalline layer at the interface. This result is in good agreement with the results published in reference [48]. The first columnar structure nucleated perpendicular to the interface, within the range of 30–50 nm from the interface between the coating and substrate. The CaP film is well defined, dense, and homogenous. In the dark-field images, the columns have a lateral size of about 40 nm. In **Figure 11a**, the clear structure of HA, with reflections from (100), (002), (211), and (200) planes, was seen. Based on TEM, the average crystal size of the top CaP layer was 30 ± 20 nm. The crystals showed a perfect crystalline structure, being in concordance with the value obtained from the XRD spectra (40 nm).

Also in **Figure 11**, the polycrystalline structure of the HA coating can be observed. Both ED patterns and d-spacing values (1.90, 2.12, 2.25, 2.82, 3.19, 3.43, 4.10, and 8.20 Å) confirmed that the deposited coatings possess the structure of HA and the absence of other crystalline phases. The physical reason for the phenomenon of this structure is explained by the authors of the study [64] as a shadowing effect which can occur if adatoms impinge on the substrate under an angle which deviates from the substrate normal. The microstructure evolution of the thin film can be described with the structure, zone model (SZM), which characterizes the

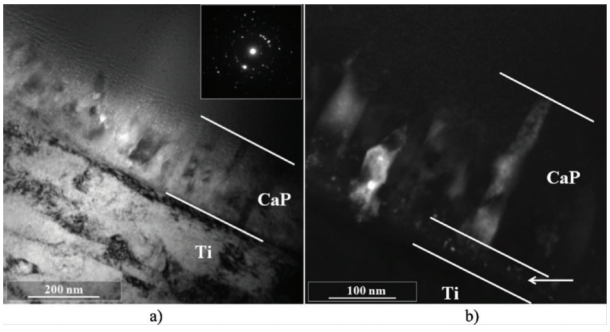

Figure 11. Cross-sectional bright field: (a) and dark field, (b) TEM images of a 250 nm thick CaP layer were prepared by FIB. The electron diffraction pattern (insert left image) reveals the presence of a polycrystalline phase [52].

http://dx.doi.org/10.5772/66396

microstructure and texture as a function of the deposition parameters. A good overview of an SZM is given by Mahieu et al. [65–67] developed the extended structure zone model (ESZM) that explains the transformation of the texture and microstructure of thin films as a function of adatom mobility.

The texture change occurred in thin films during their growth is a fundamental issue. It can be determined with the help of several factors, such as precursor adatoms sticking probability, adatom diffusion on the surface, and interaction of high-energy particles with the surface of the growing film. In the HA structure, the (002) plane has the lowest surface energy [68]. For this reason, to minimize the surface energy, the HA coatings grow on (002) orientation. In the literature, it was reported that the preferred (002) orientation can be thermodynamically changed by increasing oxygen ions bombardment in the deposition process [66]. For example, Van Steenberge et al. [69] demonstrated that the preferential orientation of the CeO_2 films prepared using the reactive magnetron sputtering method can be controlled by increasing oxygen flow. The influence of different crystalline planes during the collision anisotropy can also be treated as an explanation of the obtained results. The (002) plane of hexagonal structure is the most closely packed and it can be easily damaged by severe bombardment of ions accelerated in the cathode racetrack giving rise to loosely packed (100) plane [70, 71]. This finding is important, because crystallographic texture of polycrystalline thin film is one of the essential microstructural features, which is responsible for its properties. In hexagonal HA, a, b, and c planes exhibit anisotropy in mechanical properties, resolvability, biocompatibility, and absorption ability [72–75]. Naturally occurring apatite crystals frequently exhibit preferred orientations resulting from highly specific biological processes and these preferred orientations are believed to affect the biological and biomechanical performance of hard tissue [73, 76, 77]. Moreover, recent investigations suggest that HA with textured in a tailored manner surfaces may enable a new level of control over cellular behavior due to of protein adsorption anisotropy on the different faces of hexagonal HA crystals. Molecular modeling and *in vitro* analysis have shown that acidic bone proteins and other proteins exhibited high affinity to the (100) plane of HA [55]. Moreover, adsorption-desorption of the protein on nanosurface plays an important role in cell adhesion and mineralization of biomaterials. Thus, by controlling the preferential orientation of sputtered HA coatings, the behavior of the coatings in human body can be tailored, assuring their successful for biomedical applications.

2.6. Electrochemical *in vitro* tests of RF-magnetron sputtering of CaP coating

After implantation in human body, any metallic biomaterials are affected by the action of the body fluids [60]. The metallic biomaterials are degraded by corrosion processes, which disturb the normal body system, leading in the end at the rejection of the implant. For this reason, before the preparation of new biomaterial, it is important to know the effect of the corrosive solutions on its characteristics. In the case of the coatings, the corrosion resistance can be controlled by the adjustment of deposition parameters. The corrosion behavior of the biomaterials at the contact with simulated body solutions (saliva, SBF, PBS, and 0.9% NaCl, etc.) can be evaluated by various techniques; the most used being the potentiodynamic polarization method. The corrosion behavior of hydroxyapatite is influenced by the many factors such as composition, crystallinity, compactness, and porosity,

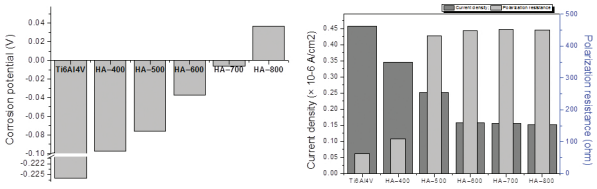

Figure 12. Evolution of corrosion potential, corrosion current density, and polarization resistance on the deposition temperature of the sputtered hydroxyapatite coatings in Fusayama artificial saliva solution (pH = 5) at 37°C [59].

which are depended on the deposition parameters. For example, Ducheyne et al. found that the stoichiometric hydroxyapatite coatings (Ca/P = 1.67) exhibited low dissolution rate than other types of calcium phosphates [78].

In a previous paper, we demonstrated that the deposition temperature is one of the factors which can affect the corrosion resistance of sputtered hydroxyapatite coatings as following [59]. The increase of the deposition temperature from 400 to 600°C leads to the decrease of the corrosion current density and increase of the polarization resistance (**Figure 12**), indicating an improvement of the corrosion resistance. For further increase of deposition temperature from 600 to 800°C, the corrosion current density and polarization resistance were not affected (**Figure 12**). Comparing the values of corrosion potentials, all the coatings presented more electropositive values than the uncoated Ti alloy (**Figure 12**), demonstrating that the coatings are a good solution for improving corrosion resistance of the Ti6Al4V alloy. The increase of the deposition temperature tends toward more electropositive values for hydroxyapatite, indicating also an enhancement of the corrosion resistance. In the literature, it is commonly admitted that a material is resistant to the corrosion when exhibited more electropositive values for corrosion potential, low values for corrosion current density and high ones for polarization resistance [79, 80]. If we take into account these criteria, it can be observed that the hydroxyapatite prepared between the 600 and 800°C has the best resistance in Fusayama artificial saliva solution (pH = 5) at 37°C, being proper for the dental applications. This results was accounted to the differences in the composition of the samples, the EDS measurements showing that HA-400 is nonstoichiometric (Ca/P = 1.80) while the HA-600, HA-700, and HA-800 exhibited Ca/P ratio closed to 1.67 [59].

2.7. Mechanical properties of RF-magnetron sputtering of CaP coating

To assure the success on long term of the metallic implants coated with HA, the coated surface should exhibit a high hardness, low friction performance and superior bonding strength to the metallic surfaces in order to support potential fatigue stress at the time of surgical procedure or after implantation. Altering the metallic surface texture, namely, the implant roughness, via different pretreatment techniques or/and their combination is the most common used and relatively inexpensive way that can help in tackling above mentioned challenges as the substrate properties play an important role in obtaining the effective implant-tissue interaction and osseointegration.

http://dx.doi.org/10.5772/66396

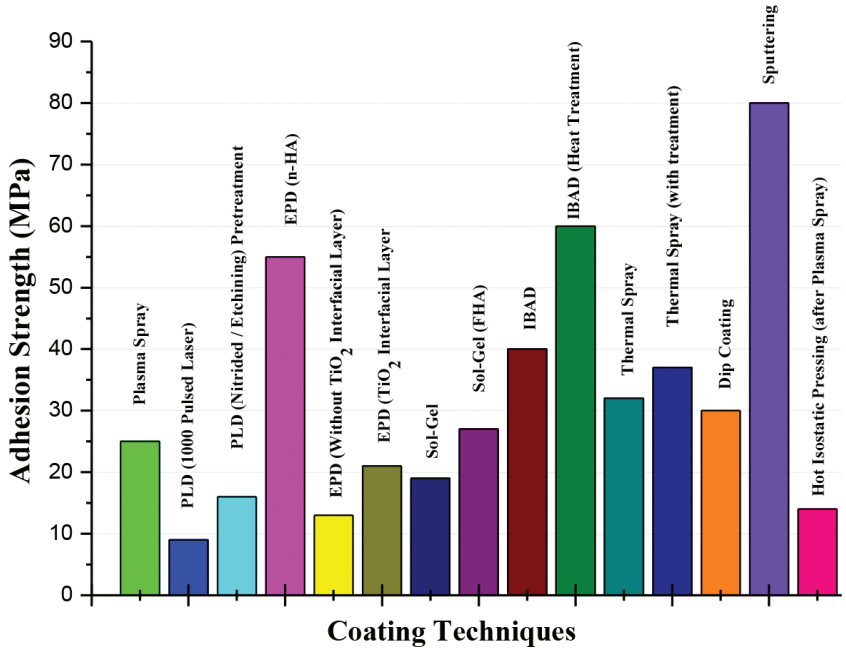

Figure 13. The quantitative comparison of different coating techniques. Reprinted from Mohseni et al. [81].

Substrate topography can be varied via different surface treatment procedures: exposition to abrasive paper (grinding and GR); sand, glass, or ceramic microspheres accelerated toward the surface (sandblasting and SB); exposition to acid chemicals (wet etching and AE); exposition to electron beams (EB). It is known that the mechanical properties of biomaterials are strongly governed by the film fabrication method and substrate characteristics. According to Mohseni et al. [81], the sputtering technique provides the highest adhesion of coating to the substrate compared to other methods which can be attributed to the sputter cleaning and ion bombardment processes (**Figure 13**). However, a simple and direct comparison of the effect of different pretreatment methods for enhancing the adhesion strength of magnetron sputtered HA coating is difficult because the deposition parameters are different and the authors use different techniques and experimental equipment to determine the mechanical properties. Nevertheless, the main tasks in the pretreatments of a metal surface prior to coating deposition may be defined as follows: to remove all foreign matter, to render surface suitable (suitable roughness) for the coating, to impart uniformity throughout all treated work piece surfaces.

Nowadays, the most common pretreatment methods of metallic substrate surface used prior to RF-magnetron coating deposition procedure are GR, SB, AE, and EB treatments [24, 56, 79, 81–84]. A number of studies reported that the combination of these pretreatment techniques

Sample	Substrate	*Thickness* (nm)	R_a (μm)	S_a, (nm)	h_c (nm)	*H* (GPa)	*E* (GPa)	*H/E*	H^3/E^2 (GPa)	Ref.
SB + AE + HA	Pure Ti (Grade 4)	500–800	0.8 ± 0.1		71.1 ± 2.9	15.2 ± 0.7	147 ± 16	0.101	164×10^{-3}	[85]
SB + AE + Ag - HA	Pure Ti (Grade 4)	450 ± 60	1.2 ± 0.1			2.8 ± 0.5	94 ± 24	0.030	2.4×10^{-3}	[87]
SB + AE + Ag - HA	Pure Ti (Grade 4)	450 ± 60	1.2 ± 0.1			5.3 ± 1.2	136 ± 28	0.039	7.8×10^{-3}	
HA	AZ31 magnesium alloy	700 ± 60			100	3.1 ± 2.0	79 ± 11	0.039	4.7×10^{-3}	[121]
					50	4.9 ± 2.5	78 ± 16	0.063	19.3×10^{-3}	
EB + HA	AZ31 magnesium alloy	700 ± 60			100	4.6 ± 0.8	63 ± 5	0.072	23.9×10^{-3}	
					50	8.5 ± 1.4	86 ± 5	0.099	82.9×10^{-3}	
AE + HA	Pure Ti (Grade 4)	500			100	3.8 ± 0.3	90 ± 8	0.047	6.6×10^{-3}	[83]
					50	3.6 ± 0.1	82 ± 10	0.047	6.9×10^{-3}	
AE + Ag - HA	Pure Ti (Grade 4)	500			100	7.2 ± 0.2	122 ± 4	0.060	25.1×10^{-3}	
					50	6.0 ± 0.5	96 ± 8	0.062	23.4×10^{-3}	
AE + HA	Pure Ti (Grade 4)	690 ± 125		50 ± 28	150 ± 10	3.7 ± 0.2	85 ± 10	0.043	7×10^{-3}	[56]
EB + HA	Pure Ti (Grade 4)	690 ± 125		21 ± 7	81 ± 4	7.0 ± 0.3	124 ± 3	0.056	22.3×10^{-3}	
GR + HA	NiTi and commercially pure Ti (Grade 4) i	90	<0.10		55 ± 15	11 ± 4	100 ± 20	0.110	133.1×10^{-3}	[24]
		270			165 ± 10	5 ± 1	100 ± 10	0.050	12.5×10^{-3}	
		450			202 ± 10	7 ± 2	100 ± 20	0.070	34.5×10^{-3}	
		720			150 ± 10	12 ± 2	130 ± 20	0.090	97.2×10^{-3}	
		1080			152 ± 20	13 ± 1	140 ± 10	0.090	112.1×10^{-3}	
		1600			130 ± 30	9 ± 1	111 ± 1	0.080	63.2×10^{-3}	
		2700			162 ± 10	9 ± 2	120 ± 20	0.080	50.6×10^{-3}	

Table 2. The most frequently applied pretreatment techniques prior the RF-magnetron sputtering and their influence on the mechanical characteristics of deposited HA-based coatings.

http://dx.doi.org/10.5772/66396

could be more effective for the improvement of hardness, Young's modulus and adhesion of the HA coatings to substrate [56, 85]. **Table 2** summarizes the use of different pretreatment methods prior the deposition of HA-based RF-magnetron coating on metallic substrate with comparison on their mechanical properties.

For instance, the increased surface roughness and enhanced mechanical properties of implants by SB and AE, so-called SLA process [86], were demonstrated by Grubova et al. [85]. Nanohardness H and Young's modulus E of the coatings prepared on Ti after SB with Al_2O_3 microspheres of 50 μm diameter followed the etching with a mixture of 1 ml HF + 2 ml HNO_3 + 2.5 ml H_2O at the penetration depth of hc = 71.11 ± 2.87 nm were 15.2 ± 0.7 and 147 ± 16 GPa, respectively. The values of H/E and H^3/E^2 for the HA coating (0.101 and 0.164 GPa, respectively) were significantly higher than that of the uncoated substrate (0.038 and 0.005 GPa). Scratch test results revealed that the deposited HA coatings exhibited improved wear resistance and lower friction coefficient. Eventually, the coating was delaminated from the substrate along the scratch path when the load increased up to 3.14 N.

Based on the data obtained in study [24] for pure HA coatings with a thickness of 0.09–2.7 μm prepared by RF-magnetron sputtering deposition on mechanically polished (GR) NiTi and Ti substrates at a substrate temperature of 500°C in argon atmosphere, we can assume that substrate surface microstructure affected the mechanical properties of HA films, if the film is thinner than about 1 μm. Their hardness and Young's modulus were of about 10 and 110 GPa, respectively. The bond strength of the HA coating to the metallic substrates is affected by its thickness. For example, upon increasing the thickness more than 1.6 μm, the bond strength decreased. The coating with a thickness of less than 1.6 μm was not damaged during the scratch test experiment even at a maximal load of 2 N. No difference was observed between NiTi and Ti substrates [24].

Control of the formation of the surface nanopatterns on Ti via pretreatments can allow varying the grain size of the HA coating. For instance, Grubova et al. [87] investigated the influence of the grain size on the mechanical properties of the nanostructured RF-magnetron sputter-deposited Ag-HA coatings with a concentration of silver in the range of 0.13–0.36 wt% prepared on the Ti substrates treated through SB with Al_2O_3 particles (250–320 μm) for 10 s at 0.45 and 0.61 MPa and AE using a 1:2:2.5 mixture of HF (40%), HNO_3 (66%), and distilled water. Larger nanostructure sizes were found on the surface of Ti prepared at a lower SB pressure. From the nanoindentation results, it is possible to conclude that smaller grains of the Ag-HA coatings resulted in significantly higher values of nanohardness and Young's modulus.

The treatment of Ti surfaces by EB has also been used prior the deposition of magnetron HA coatings [56]. EB irradiation of Ti samples has been found to reduce the roughness and to improve the nanohardness of the material [88], allowing for the deposition of smoother HA coatings [56]. For example, Surmeneva et al. [56] studied the nanoindentation hardness and the Young's modulus of the HA coating deposited onto Ti modified by the pulse EB treatment with an electron energy density of 15 J cm^{-2} were determined to be 7.0 ± 0.3 and 124 ± 3 GPa, respectively, which were significantly higher than those of the HA coating on AE Ti in a mixture of HF (48% concentration) and HNO_3 (65% concentration) acids; H_2O was set to 1:4:5 in volume. **Figure 14** shows the load-deformation curves of the tested in [56] surfaces.

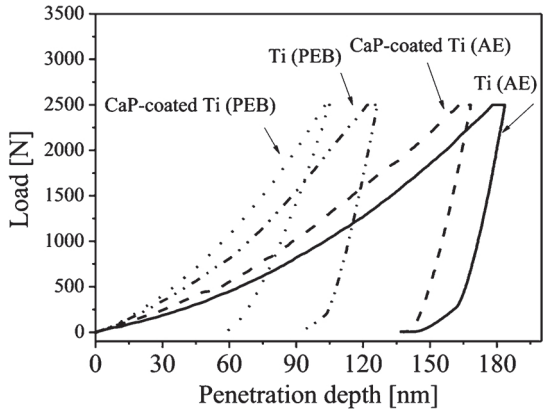

Figure 14. Representative load-displacement curves for uncoated and CaP—coated Ti prepared by AE and pulse EB treatment at a maximum load of 2.5 mN [56].

The CaP coating deposited onto the nanocrystalline EB treated Ti surface is more resistant to plastic deformation than the same coating on the AE Ti substrate. Moreover, Surmeneva et al. [89] also have evaluated the application of negative electrical bias to the Ti substrates preheated to $T = 200°C$ during the Si-HA coating deposition; the substrate surface was chemically etched and then treated with a low energy EB prior to deposition. It was found that for the case of the grounded substrate, the adhesion coefficient is the highest (HSC = 1). With increasing negative bias, the adhesion coefficient HSC lowers to 0.98, indicating a decrease in adhesion. Decreasing adhesion may be associated with an increasing level of microstrains because of a finer grained structure, an increasing volume fraction of defects, and incoherent interfaces, as evidenced by XRD and IR studies of the coating structures. Surmeneva et al.

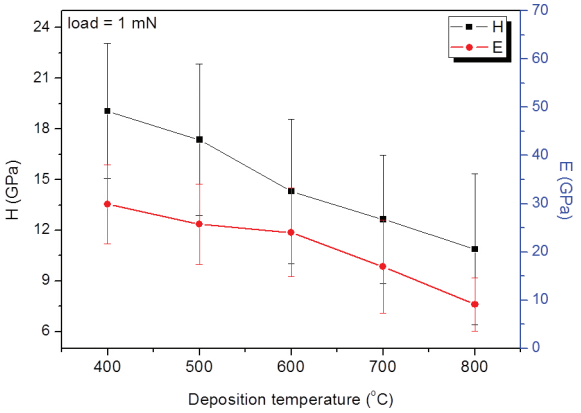

Figure 15. Hardness and elastic modulus of the sputtered CaP coatings prepared at different deposition temperatures; the measurements were performed on the coating deposited on the Si wafers in order to avoid the influence of other factors (e.g., roughness or cast defects occur during the deposition of the coatings on metallic substrates) [59].

http://dx.doi.org/10.5772/66396

found that the HA coating prepared on EB-treated magnesium AZ31 alloy exhibited higher hardness and the Young's modulus values compared to those of HA coated on untreated AZ 31 alloy. Furthermore, HA coating prepared on treated AZ31 alloy substrate showed the best resistance to plastic deformation than HA coated prepared on treated AZ31 alloy substrate. Although we cannot do the right comparison of the pretreatment methods usually used prior RF-magnetron coating deposition due to the differences in techniques and experimental equipment for the determination of the mechanical properties, we assume that pretreatments such as AE, SB, GR, and EB treatments and their combinations enhance the bonding strength and hardness of the coating. However, the pretreatments are not the only one way to guarantee a stable (high hardness and low friction) HA coating on metallic substrate. Using an interfacial layer (such as TiO_2, TiN, SiC, etc.) as the initial coating layer on the substrate followed by HA coating layer also can enhance the bonding strength and mechanical properties as well as post-treatments [84, 90–93].

In biomedical applications, the mechanical properties of the CaP coatings are important parameters. For success of dental or orthopedic implants, it is important to use a material with high hardness and elastic modulus close to the bone. In the case of CaP, both parameters are influenced by deposition temperature (**Figure 15**). Due to the plastic deformation, we presented the results of the hardness and elastic modulus measured at low load (1 mN). The elastic modulus and hardness values decreased with increasing deposition temperature (**Figure 15**). For both parameters, high values were obtained for the coatings with amorphous structure (sample deposited at 400°C). Note that the crystallinity plays an important role also in the case of mechanical properties. Despite that the high hardness is desired, the elastic modulus should be low, for the biomedical applications. Moreover, the CaP coatings exhibited a high dissolution rate in contact with human body fluids and it is not desired. Thus, the CaP coatings prepared at high deposition temperature (700 or 800°C) is more proper for coating the surface of dental or orthopedic implants.

2.8. Behavior *in vitro* of RF-magnetron sputtering of CaP coating

Cellular responses to an implanted biomaterial are highly complicated biological and chemical processes related to several surface properties [82]. In the literature, it was reported that the Ca and P content affected cell response such as attachment, spreading, and differentiation [61, 94–96]. Moreover, it was demonstrated that the biological properties of Ti or Mg alloys, ceramics, and polymers could be significantly enhanced by substrate coating with CaP thin film [61, 94–96].

In vitro cell viability tests studied after 5 days of culture with human osteosarcoma cell line (MG-63) showed that all of the cells have a good adhesion, spreading, and growth on the surface of all of the coatings, whatever deposition temperature was (**Figure 16**). Comparing all of the coatings, one may observe that there are no differences between the cell growths after increasing the deposition temperature. On all of the coated surfaces, the cells showed a dense cytoskeletal F-actin (stained green) and proliferated well, being situated close to each other. For the CaP coatings prepared at 700 and 800°C, more cell nuclei numbers (blue color) were found, indicating that these two coatings have better promoted the cell proliferation. The SEM micrograph of cell growth on the coating prepared at 800°C is presented in **Figure 17**. There

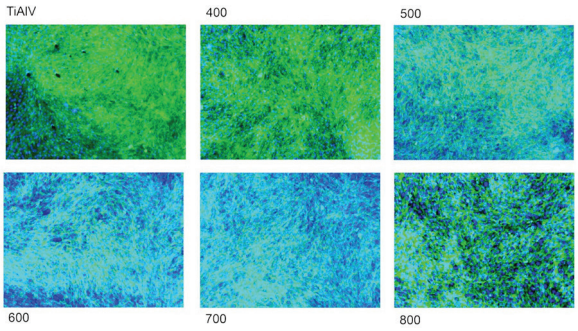

Figure 16. Fluorescence micrograph of the osteosarcoma cell growth after 5 days of culture on the uncoated Ti6Al4V substrate and coated at different deposition temperatures. Blue fluorescence represents the nuclei due to Hoechst 33342; green fluorescence is F-actin fibres due to FITC conjugated phalloidin [59].

are observed many cells well attached and spreading over the whole coated surface, with spindle-shaped, indicating good biocompatibility. In our previous paper, we demonstrated that this behavior was due to the increase of surface roughness which was increased due to the deposition temperature [59]. Immediately after the implantation, the first contact of the implant surface is with proteins, which are known as a promotor of attachments, spreading and proliferation of osteoblasts, leading to a successful implantation [97]. The proteins adhere better to the porous or rough surface due to larger contact areas which assure a bigger surface-cell interface [98, 99].

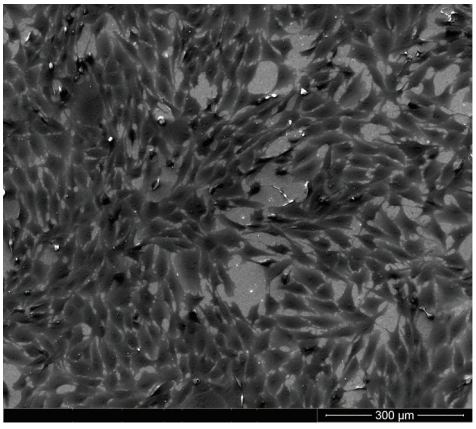

Figure 17. SEM image of the osteosarcoma cell growth after 5 days of culture on the coating prepared at 800°C.

Recent studies have shown that the cell-substrate interactions depend on the material type and are associated with the surface topography [100, 101], chemical and elemental composition [101, 102], dissolution behavior [101, 103], and surface macro and microstructure [101,

http://dx.doi.org/10.5772/66396

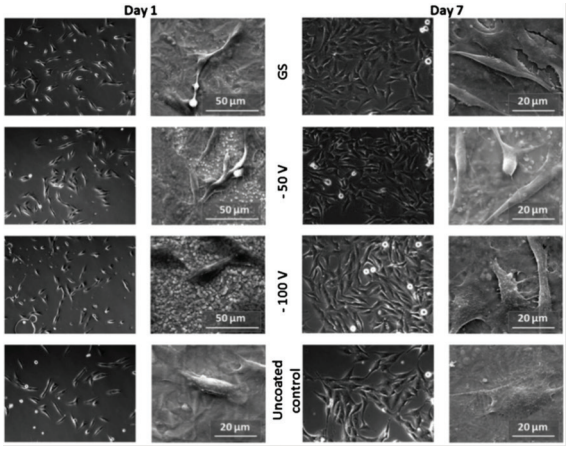

Figure 18. Morphology of MG-63 cells growth for 1 and 7 days on glass and Ti substrates coated with HA prepared by different methods [48].

104]. These physicochemical characteristics can be manipulated during RF-magnetron sputtering to promote the clinical integration of implants with the surrounding cells and tissue [100, 105]. The response of a human osteoblast-like cell line (MG-63) to titanium coated with silicon-containing calcium phosphate was investigated by Surmeneva et al [48]. *In vitro* cell culture studies showed that cells maintained their natural spindle-like morphology, are well spread out and adherent to the substrate (**Figure 18**). After 7 days, the cells covered the whole surface coated with HA. All the tested coatings revealed a low toxicity and a very good adhesion of cells on the surface.

By conducting the biological *in vitro* assay of the HA coatings with DPS cells the surface mineralization of the tested samples was revealed. The mineralized nodules typical for amorphous calcium phosphate (ACP) deposited from solutions were found in the extra-cellular region during the 3-day culture (**Figure 19a**) on the poor crystalline HA coating deposited at 200 W and 0.1 Pa on the titanium substrates. The calcification degree in the matrix of fibrous col-

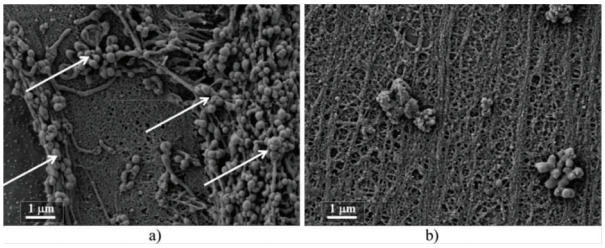

Figure 19. SEM image of the mineralized matrix synthesized by DPS cells cultured on the 440-nm thick CaP coating. The signs of mineralization are marked by arrows in (a). (b) Reveals the signs of mineralization in the case of uncoated titanium [52].

lagen was significantly lower in the case of the uncoated titanium (**Figure 19b**). It is reported that nodule formation in multilayers of cells is an important factor for *in vitro* mineralization [61, 62]. These results are consistence with those published in Ref. [63]. In the literature, it has been shown that the mineralization process is initiated by controlling the Ca and P concentrations in the medium [66, 68]. Nodule formation of mineralized is correlated with most of the biological events more or less with a spontaneous precipitation of CaP minerals, depending on the behavior of cellular osteogenic [69, 70]. In other words, poor crystalline HA coatings accelerated the attachment, proliferation, and formation of mineralized nodules by the cells grow on the surface than those grown on uncoated titanium surface.

The geometric and physical characteristics of the CaP film are important for regulation of the cells attachment and migration, such as crystallinity, composition, and thickness. Many scientific papers reported on the effect of crystalline and amorphous CaP coatings prepared by different techniques based on the adhesion, proliferation, and growth of bone-related cells [106–109]. Anyhow, most of the published papers acknowledged various effects of the CaP coating crystallinity on cell behavior. For example, a low dissolution rate of the coating was found for the coatings with low crystallinity or amorphous ones. On the other hand, the amorphous CaP coatings induce faster bone formation, even though its faster release of calcium ions [110]. Based on some *in vitro* analysis, it was found that the surface chemistry and topography of amorphous HA coatings stimulate the cell attachment, but result in a cytotoxic effect that inhibits proliferation of the cells attached to the coating surfaces [106, 110]. Simultaneously, highly crystalline HA coatings revealed nodule formation [106] and higher rates of osteogenic cell proliferation than the less crystalline or amorphous HA coatings deposited on Ti substrates [106, 110]. It is also reported in reference [107] that the amorphous sputtered CaP coatings constrain the growth and differentiation of rat bone marrow cells and osteoblast-like cells. On the other hand, crystalline HA coating prove to have better adhesion and accelerates proliferation of bone marrow mesenchymal stem cells compared with an amorphous ACP coating with the same topography and roughness [108].

It is difficult to highlight the most significant properties of the CaP coating that lead to a better cellular response. Furthermore, it is impossible to compare the results of *in vitro* experiments that have been conducted using different methodologies. For instance, the cell types influenced the Ca^{2+} and PO_4^{3-} and by varying the Ca/P ratio, the proliferation and differentiation could be controlled [111]. For this reason, the standardization to establish the effects of CaP on the biological assay is required. Up to date, there are some methodologies, but the published studies on the biological assay of the magnetron sputter-deposited coating demonstrate that this method can potentially be used for the development of future biomaterials.

3. Solutions for improving the properties of RF-magnetron sputtering of CaP coating

As it was underlined in the introduction, hydroxyapatite is one of the most extensively used materials in medicine for hard tissues repairment or for enhancing the osseointegration of

http://dx.doi.org/10.5772/66396

the metallic implants or their components. It is commonly used due to its chemical similarities to the component of bones and teeth. However, the high dissolution rate in contact with human fluids, the low mechanical strength and the relatively low bone bonding rate restrict its use as biomaterial. Therefore, the actual challenge in the biomedical field is to find a solution to improve the mentioned properties, but the difficulties are redoubtable, as these surface, characteristics deteriorate in time. A novel approach to obtain these surfaces is to modify HA properties by doping with small amounts of beneficial elements for human bones, as discuss below.

3.1. Si or SiC addition

In the present, the addition of Si into the HA matrix has successful clinic practice as bone graft material in spinal fusion (www.orthoaospl.com). However, this solution is not sufficient for the hard tissue, because they exhibited low hydrophobicity involves a decrease of the proteins adsorption and low mechanical and tribological properties. Thian et al. showed that sputtered Si-HA coatings could be a good candidate for hard tissue replacement, owing to their ability to form a carbonate-containing apatite layer rapidly [112]. Azem et al. showed that by SiC addition to the pure HA matrix, their corrosion resistance in artificial saliva and mechanical properties were enhanced, without affect the bioactive abilities of HA [91, 113]. Also, Vladescu et al. reported that the SiC consisting of hydroxyapatite coatings exhibited high adhesion strength to the Ti6Al4V substrates, better corrosion resistance to the SBF attack, better cells proliferation and viability compared with the undoped HA coatings. However, the elastic modulus is still higher than that of the bone [91].

3.2. Mg addition

Some researchers have also proposed the incorporation of Mg in the HA lattice, in order to accelerate the osseointegration process of dental or orthopedic implants. The Mg was selected as dopant because Mg is found in the natural dentin (1.23 wt%) and bone (0.73 wt%). However, a major drawback of the Mg-HA coatings is their high dissolution rate in physiological solutions, leading to a high pH value in the surrounding environment, which is detrimental to cell survival [114]. This effect appeared because Mg inhibits the apatite crystallization, leading to a destabilization of the apatite structure, by formation of the β-tricalcium phosphate, known as a phase with high dissolution rate in human body environment [113]. The 1.8 wt% Mg content decreased the compressive strength and hardness of the HA, but these are still higher than the values for bone [115].

3.3. Ti addition

A recent study reported that some of the properties of sputtered HA, such as mechanical properties, *in vitro* and *in vivo* bioactivity, could be enhanced by the incorporation of Ti in the HA lattice. Ribeiro et al. showed that the hydroxyapatite doped with Ti enhanced the protein adsorption, especially the activity of the enzyme GCR, indicating that this coatings may be used as a delivery matrix for biologically active molecules [116].

3.4. Ta addition

Ligot et al. identified that Ta could also be a promising doping element, proving that for Ta content less 4.5 at%, Ta substituted the Ca in the HA cell, and the (Ca + Ta)/P ratio is close to 1.67 (ratio of stoichiometric HA) and exhibited an elastic modulus of 120 GPa, which is comparable to the value of some conventional materials used for load-bearing implants (stainless steel, Co-Cr alloys or Ti alloys) for which the elastic modulus ranges between 110 and 232 GPa [117]. Unfortunately, up to date, no information about the effect of Ta addition on the osseointegration ability, bioactivity, or dissolution rate of sputtered HA coatings are available. Future work need to be done in this area.

3.5. Ag addition

In the present, in the biomedical applications, especially for dental and orthopedic implants, there is necessary to use surfaces with bioactive and antibacterial surfaces, which helps also the implant osseointegration. The bioactive surface could be achieved by using HA coatings, but the antibacterial or antifungal properties of HA coatings are under development. For example, Park et al. doped HA coatings with different Ag content and found that some of the Ca^{2+} ions in the hydroxyapatite were replaced with Ag^{+} ions [118]. The drawback of this solution is that the hardness and modulus of the Ag doped HA coatings decreased with an increasing Ag content [118], which is not desired for load bearing implants. Ciuca et al. found that the addition of 2.1 at.% Ag is enough for assuring of antifungal activity of the HA coating, without affecting the formation of the stoichiometric HA phase [119]. Also, it was demonstrated that the addition of a small Ag content (0.7 at.%) into HA structure could improve the resistance to the *Staphylococcus aureus*, *Streptococcus pyogenes*, *Salmonella typhimurium* attack of hydroxyapatite without any change of the other characteristics such as microchemical, microstructural, or anticorrosive ones of the sputtered hydroxyapatite [120].

4. Conclusions

The fabrication of a controlled crystallinity, chemistry, and stoichiometry of HA nanocoatings is shown to be possible based on the knowledge gained up to now, which will have a high efficiency in orthopedic implant applications. The HA coatings can be deposited on the surfaces of diverse metallic permanent and biodegradable implants. The complex geometries of implants can be coated by RF-magnetron sputter, even if this technique is a line-of-sight technique. An overall control of the coating properties keeping the adhesion strength to the substrate high makes RF-magnetron sputtering technique prospective for future commercial applications in the case of biocompatible coating fabrication.

Acknowledgements

This research was supported by the Federal Target Program #14.587.21.0013 (unique application number 2015-14-588-0002-5599), the Russian President grants MK-7907.2016.8, MK-6459.2016.8 and the State order NAUKA #11.1359.2014/K. The work was also supported by the grants of

the Romanian National Authority for Scientific Research and Innovation—UEFISCDI, Project numbers PN-II-PT-PCCA-2014-212, 44/2016 and 43/2016— INTELBIOCOMP, within PNCDI III and by the Core Program, under the support of ANCSI, project no. PN16.40.01.02.

Author details

Roman Surmenev[1], Alina Vladescu[1,2]*, Maria Surmeneva[1], Anna Ivanova[1], Mariana Braic[2], Irina Grubova[1] and Cosmin Mihai Cotrut[1,3]

*Address all correspondence to: alinava@inoe.ro

1 Tomsk Polytechnic University, Tomsk, Russia

2 National Institute for Research and Development in Optoelectronics, Bucharest, Romania

3 University Politehnica of Bucharest, Bucharest, Romania

References

[1] Surmenev RA, Surmeneva MA, Ivanova AA. Significance of calcium phosphate coatings for the enhancement of new bone osteogenesis—A review. Acta Biomater. 2014;10(2):557–579.

[2] Sobieszczyk S, Zieliński A. Coatings in arthroplasty: review paper. Adv Mater Sci. 2008;9:35–54.

[3] Liu D, Chou H, Wu J. Plasma-sprayed hydroxyapatite coating: effect of different calcium phosphate ceramics. J Mater Sci Mater [Internet]. 1994;147–153. Available from: http://link.springer.com/article/10.1007/BF00053335

[4] Yang Y, Kim KH, Ong JL. A review on calcium phosphate coatings produced using a sputtering process an alternative to plasma spraying. Biomaterials. 2005;26(3):327–337.

[5] Chu P. Plasma-surface modification of biomaterials. Mater Sci Eng R Reports. 2002;36(5–6):143–206.

[6] Zhang JX, Guan RF, Zhang XP. Synthesis and characterization of sol-gel hydroxyapatite coatings deposited on porous NiTi alloys. J Alloys Compd. 2011;509(13):4643–4648.

[7] Azem FA, Eroglu EO, Cakir A. Synthesis and structural properties of sol-gel derived Si-substituted hydroxyapatite coatings. J Biomech. 2011;44:13.

[8] Choi AH, Ben-Nissan B. Sol-gel production of bioactive nanocoatings for medical applications. Part II: current research and development. Nanomedicine (Lond). 2007;2(1):51–61.

[9] Eshtiagh-Hosseini H, Housaindokht MR, Chahkandi M. Effects of parameters of sol-gel process on the phase evolution of sol-gel derived hydroxyapatite. Mater Chem Phys. 2007;106:310–316.

[10] Liu DM, Troczynski T, Tseng WJ. Water-based sol-gel synthesis of hydroxyapatite: process development. Biomaterials. 2001;22(13):1721–30.

[11] Qu H, Wei M. Improvement of bonding strength between biomimetic apatite coating and substrate. J Biomed Mater Res - Part B Appl Biomater. 2008;84(2):436–443.

[12] Ballarre J, Seltzer R, Mendoza E, Orellano JC, Mai YW, García C, et al. Morphologic and nanomechanical characterization of bone tissue growth around bioactive sol-gel coatings containing wollastonite particles applied on stainless steel implants. Mater Sci Eng C. 2011;31(3):545–552.

[13] Rojaee R, Fathi M, Raeissi K, Sharifnabi A. Biodegradation assessment of nanostructured fluoridated hydroxyapatite coatings on biomedical grade magnesium alloy. Ceram Int. 2014;40(9):15149–15158.

[14] Olding T, Sayer M, Barrow D. Ceramic sol-gel composite coatings for electrical insulation. Thin Solid Films. 2001; 398–399:581–586.

[15] Cheang P, Khor KA. Addressing processing problems associated with plasma spraying of hydroxyapatite coatings. Biomaterials. 1996;17(5):537–544.

[16] Overgaard S, Soballe K, Josephsen K, Hansen ES, Bunger C. Role of different loading conditions on resorption of hydroxyapatite coating evaluated by histomorphometric and stereological methods. J Orthop Res. 1996;14(6):888–894.

[17] Vandijk K, Schaeken H, Wolke J, Jansen J. Influence of annealing temperature on RF magnetron sputtered calcium phosphate coatings. Biomaterials. 1996;17(4):405–410.

[18] Van Dijk K, Schaeken HG, Wolke JCG, Maree CHM, Habraken FHPM, Verhoeven J, et al. Influence of discharge power level on the properties of hydroxyapatite films deposited on Ti6A14V with RF magnetron sputtering. J Biomed Mater Res. 1995;29(2):269–276.

[19] Wolke JG, van Dijk K, Schaeken HG, de Groot K, Jansen JA. Study of the surface characteristics of magnetron-sputter calcium phosphate coatings. J Biomed Mater Res. 1994;28(12):1477–1484.

[20] Jansen JA, Wolke JG, Swann S, Van der Waerden JP, de Groot K. Application of magnetron sputtering for producing ceramic coatings on implant materials. Clin Oral Implants Res. 1993;4(1):28–34.

[21] Peter MM. Handbook of deposition technologies for films and coatings: Science, applications and technology. 3rd Edition. Andrew W, editor. Elsevier Inc, USA 2009. pp. 1–936.

[22] Yang J, Cui F, Lee IS, Wang X. Plasma surface modification of magnesium alloy for biomedical application. Surf Coat Technol. 2010;205:S182–S187.

[23] Paital SR, Dahotre NB. Calcium phosphate coatings for bio-implant applications: materials, performance factors, and methodologies. Mater Sci Eng R Reports. 2009.66: pp. 1–70.

[24] Pichugina VF, Surmeneva RA, Shesterikova EV, Ryabtsevaa MA, Eshenkoa EV, Tverdokhlebova SI, et al. The preparation of calcium phosphate coatings on titanium and nickel-titanium by rf-magnetron-sputtered deposition: composition, structure and micromechanical properties. Surf Coat Technol. 2008;202(16):3913–3920.

[25] Yeom GY, Thornton JA, Kushner MJ. Cylindrical magnetron discharges. II. The formation of dc bias in rf-driven discharge sources. J Appl Phys. 1989;65(10):3825–3832.

[26] Bikowski A, Welzel T, Ellmer K. The impact of negative oxygen ion bombardment on electronic and structural properties of magnetron sputtered ZnO: Al films. Appl Phys Lett. 2013;102(24):242106.

[27] Ellmer K, Welzel T. Reactive magnetron sputtering of transparent conductive oxide thin films: Role of energetic particle (ion) bombardment. J Mater Res. 2012;27(5):765–779.

[28] Ivanova AA, Surmeneva MA, Surmenev RA, Depla D. Influence of deposition conditions on the composition, texture and microstructure of rf-magnetron sputter-deposited hydroxyapatite thin films. In: Thin Solid Films. 2015. pp. 368–374.

[29] Tominaga K, Yuasa T, Kume M, Tada O. Influence of energetic oxygen bombardment on conductive ZnO films. Jpn J Appl Phys. 1985;24(8 R):944–949.

[30] Van Steenberge S, Leroy WP, Hubin A, Depla D. Momentum transfer driven textural changes of CeO_2 thin films. Appl Phys Lett. 2014;105(11):111602.

[31] Xu S, Long J, Sim L, Diong CH, Ostrikov K. RF plasma sputtering deposition of hydroxyapatite bioceramics: Synthesis, performance, and biocompatibility. Plasma Process Polym. 2005;2(5):373–390.

[32] Kester DJ, Messier R, Daniel J, Kestera. Macro-effects of resputtering due to negative ion bombardment of growing thin films. J Mater Res. 1993;8(8):1928–1937.

[33] Cuomo JJ, Gambino RJ, Harper JME, Kuptsis JD, Webber JC. Significance of negative ion formation in sputtering and SIMS analysis. J Vac Sci Technol. 1978;15(2):281.

[34] Cai Y, Liu W, He Q, Zhang Y, Yu T, Sun Y. Influence of negative ion resputtering on Al-doped ZnO thin films prepared by mid-frequency magnetron sputtering. Appl Surf Sci. 2010;256(6):1694–1697.

[35] Mattox DM. Particle bombardment effects on thin-film deposition: A review. J Vac Sci Technol A Vac Surf Film. 1989;7(3):1105–1114.

[36] Surmenev RA. A review of plasma-assisted methods for calcium phosphate-based coatings fabrication. Surf Coat Technol. 2012;206:2035–2056.

[37] Snyders R, Bousser E, Music D, Jensen J, Hocquet S, Schneider JM. Influence of the chemical composition on the phase constitution and the elastic properties of RF sputtered hydroxyapatite coatings. Plasma Process Polym. 2008;5(2):168–174.

[38] Snyders R, Music D, Sigumonrong D, Schelnberger B, Jensen J, Schneider JM. Experimental and ab initio study of the mechanical properties of hydroxyapatite. Appl Phys Lett. 2007;90(19):193902.

[39] Shi JZ, Chen CZ, Yu HJ, Zhang SJ. The effect of process conditions on the properties of bioactive films prepared by magnetron sputtering. Vacuum. 2008;83(2):249–256.

[40] Boyd AR, Meenan BJ, Leyland NS. Surface characterisation of the evolving nature of radio frequency (RF) magnetron sputter deposited calcium phosphate thin films after exposure to physiological solution. Surf Coat Technol. 2006;200(20–21):6002–6013.

[41] Boyd AR, Duffy H, McCann R, Cairns ML, Meenan BJ. The Influence of argon gas pressure on co-sputtered calcium phosphate thin films. Nucl Instrum Methods Phys Res Sect B Beam Interact Mater Atoms. 2007;258(2):421–428.

[42] Ozeki K, Goto T, Aoki H, Masuzawa T. Influence of the crystallinity of a sputtered hydroxyapatite film on its osteocompatibility. Biomed Mater Eng. 2015;26(3–4):139–147.

[43] Bramowicz M, Braic L, Azem FA, Kulesza S, Birlik I, Vladescu A. Mechanical properties and fractal analysis of the surface texture of sputtered hydroxyapatite coatings. Appl Surf Sci. 2016;379:338–346.

[44] López EO, Mello A, Farina M, Rossi AM, Rossi AL. Nanoscale analysis of calcium phosphate films obtained by RF magnetron sputtering during the initial stages of deposition. Surf Coat Technol. 2015;279:16–24.

[45] Surmeneva MA, Surmenev RA, Chaikina MV, Kachaev AA, Pichugin VF, Epple M. Phase and elemental composition of silicon-containing hydroxyapatite-based coatings fabricated by rf-magnetron sputtering for medical implants. Inorg Mater Appl Res. 2013;4(3):227–235.

[46] Surmenev RA, Ryabtseva MA, Shesterikov EV, Pichugin VF, Peitsch T, Epple M. The release of nickel from nickel-titanium (NiTi) is strongly reduced by a sub-micrometer thin layer of calcium phosphate deposited by rf-magnetron sputtering. J Mater Sci Mater Med. 2010;21(4):1233–1239.

[47] Surmeneva MA, Chaikina MV, Zaikovskiy VI, Pichugin VF, Buck V, Prymak O, et al. The structure of an rf-magnetron sputter-deposited silicate-containinghydroxyapatite-based coating investigated by high-resolution techniques. Surf Coat Technol. 2013;218(1):39–46.

[48] Surmeneva MA, Kovtun A, Peetsch A, Goroja SN, Sharonova AA, Pichugin VF, et al. Preparation of a silicate-containing hydroxyapatite-based coating by magnetron sputtering: structure and osteoblast-like MG63 cells in vitro study. RSC Adv. 2013;3:11240–112406.

[49] Krug J. Origins of scale invariance in growth processes. Adv Phys. 1997;46:139-282.

[50] Bales G, Zangwill A. Macroscopic model for columnar growth of amorphous films by sputter deposition. J Vac Sci Technol A. 1991;9(1):145–149.

[51] Ong JL, Harris LA, Lucas LC, Lacefield WR, Rigney D. X ray photoelectron spectroscopy characterization of ion beam sputter deposited calcium phosphate coatings. J Am Ceram Soc. 1991;74(9):2301–2304.

[52] Surmeneva MA, Surmenev RA, Nikonova YA, Selezneva II, Ivanova AA, Putlyaev VI, et al. Fabrication, ultra-structure characterization and in vitro studies of RF magnetron sputter deposited nano-hydroxyapatite thin films for biomedical applications. Appl Surf Sci. 2014;317:172–180.

[53] Wang X, Helmersson U, Madsen LD, Ivanov IP, Munger P, Rudner S, et al. Composition, structure, and dielectric tunability of epitaxial SrTiO3 thin films grown by radio frequency magnetron sputtering. J Vac Sci Technol VacSurf Film. 1999;17(2):564–570.

[54] Cuomo JJ, Rossnagel SM, Haufman HR, Komanduri R. Handbook of ion beam processing technology: principles, deposition, film modification, and synthesis. J Eng Mater Technol. 1990;112(2):253.

[55] Surmenev RA, Surmeneva MA, Evdokimov KE, Pichugin VF, Peitsch T, Epple M. The influence of the deposition parameters on the properties of an rf-magnetron-deposited nanostructured calcium phosphate coating and a possible growth mechanism. Surf Coat Technol. 2011;205(12):3600–3606.

[56] Surmeneva MA, Surmenev RA, Tyurin AI, Mukhametkaliyev TM, Teresov AD, Koval NN, et al. Comparative study of the radio-frequency magnetron sputter deposited CaP films fabricated onto acid-etched or pulsed electron beam-treated titanium. Thin Solid Films. 2014;571(P1):218–224.

[57] Feddes B, Wolke JGC, Jansen JA, Vredenberg AM. Radio frequency magnetron sputtering deposition of calcium phosphate coatings: The effect of resputtering on the coating composition. J Appl Phys. 2003;93:9503.

[58] Takayanagi S, Yanagitani T, Matsukawa M, Watanabe Y. Quantitative analysis of the effect of energetic particle bombardment during deposition on (1120) texture formation in ZnO films. In: IEEE International Ultrasonics Symposium. 2011. pp. 2317–2320.

[59] Vladescu A, Braic M, Azem FA, Titorencu I, Braic V, Pruna V, et al. Effect of the deposition temperature on corrosion resistance and biocompatibility of the hydroxyapatite coatings. Applied Surface Science. 2015;354:373–379.

[60] Xu L, Pan F, Yu G, Yang L, Zhang E, Yang K. In vitro and in vivo evaluation of the surface bioactivity of a calcium phosphate coated magnesium alloy. Biomaterials. 2009;30(8):1512–1523.

[61] Ueda K, Narushima T, Goto T, Taira M, Katsube T. Fabrication of calcium phosphate films for coating on titanium substrates heated up to 773 K by RF magnetron sputtering and their evaluations. Biomed Mater. 2007;2(3):S160–S166.

[62] Khor K, Dong Z, Quek C, Cheang P. Microstructure investigation of plasma sprayed HA/Ti6Al4V composites by TEM. Mater Sci Eng A. 2000;281(1–2):221–228.

[63] Dong Z, Khor K, Quek C, White T, Cheang P. TEM and STEM analysis on heat-treated and in vitro plasma-sprayed hydroxyapatite/Ti-6Al-4V composite coatings. Biomaterials. 2003;24(1):97–105.

[64] Karunasiri RPU, Bruinsma R, Rudnick J. Thin-film growth and the shadow instability. Phys Rev Lett. 1989;62(7):788–791.

[65] Mahieu S, Ghekiere P, Depla D, De Gryse R. Biaxial alignment in sputter deposited thin films.Thin Solid Films. 2006;515:1229–1249.

[66] Mahieu S, Depla D. Reactive sputter deposition of TiN layers: modelling the growth by characterization of particle fluxes towards the substrate. J Phys D Appl Phys. 2009;42(5):53002.

[67] Mahieu S, Leroy WP, Van Aeken K, Depla D. Modeling the flux of high energy negative ions during reactive magnetron sputtering. J Appl Phys. 2009;106(9):093302.

[68] Filgueiras MRT, Mkhonto D, Leeuw NH. Computer simulations of the adsorption of citric acid at hydroxyapatite surfaces. J Cryst Growth. 2006;294(1):60–68.

[69] Van Steenberge S, Leroy WP, Depla D. Influence of oxygen flow and film thickness on the texture and microstructure of sputtered ceria thin films. Thin Solid Films. 2014;553:2–6.

[70] Hong RJ, Helming K, Jiang X, Szyszka B. Texture analysis of Al-doped ZnO thin films prepared by in-line reactive MF magnetron sputtering. Appl Surf Sci. 2004;226(4):378–86.

[71] Lee YE, Lee J Bin, Kim YJ, Yang HK, Park JC, Kim HJ. Microstructural evolution and preferred orientation change of radio-frequency-magnetron sputtered ZnO thin films. J Vac Sci Technol A. 1996;14(3):1943–1998.

[72] Dong XL, Zhou HL, Wu T, Wang Q. Behavior regulation of adsorbed proteins via hydroxyapatite surface texture control. J Phys Chem B. 2008;112(15):4751–4759.

[73] Kim H, Camata RP, Chowdhury S, Vohra YK. In vitro dissolution and mechanical behavior of c-axis preferentially oriented hydroxyapatite thin films fabricated by pulsed laser deposition. Acta Biomater. 2010;6(8):3234–3241.

[74] Oonishi H. Orthopaedic applications of hydroxyapatite. Biomaterials. 1991;12(2):171–178.

[75] Zhuang Z, Fujimi TJ, Nakamura M, Konishi T, Yoshimura H, Aizawa M. Development of a,b-plane-oriented hydroxyapatite ceramics as models for living bones and their cell adhesion behavior. Acta Biomater. 2013;9(5):6732–6740.

[76] Wenk HR, Heidelbach F. Crystal alignment of carbonated apatite in bone and calcified tend on: results from quantitative texture analysis. Bone. 1999;24(4):361–369.

[77] Nakano T, Kaibara K, Tabata Y, Nagata N, Enomoto S, Marukawa E, et al. Unique alignment and texture of biological apatite crystallites in typical calcified tissues analyzed by microbeam x-ray diffractometer system. Bone. 2002;31(4):479–487.

[78] Radin SR, Ducheyne P. The effect of calcium phosphate ceramic composition and structure on in vitro behavior. II. Precipitation. J Biomed Mater Res. 1993;27(1):35–45.

[79] Baboian R. Corrosion tests and standards: application and interpretation. 2nd Edition. ASTM International, Philadelphia, USA; 2005. 867 p.

[80] Mansfeld F. The Polarization Resistance Technique for Measuring Corrosion Currents. In: Fontana, Mars G., Staehle RW, editor. Advances in Corrosion Science and Technology Springer US, New York. 1976;6:pp. 163–262.

[81] Mohseni E, Zalnezhad E, Bushroa AR. Comparative investigation on the adhesion of hydroxyapatite coating on Ti–6Al–4V implant: a review paper. Int J Adhes Adhes. 2014;48:238–257.

[82] Ozeki K, Fukui Y, Aoki H. Hydroxyapatite coated dental implants by sputtering technique. Biocybern Biomed Eng. 2006;26(1):95–101.

[83] Ivanova AA, Surmeneva MA, Tyurin AI, Pirozhkova TS, Shuvarin IA, Prymak O, et al. Fabrication and physico-mechanical properties of thin magnetron sputter deposited silver-containing hydroxyapatite films. Appl Surf Sci. 2016;360:929–935.

[84] Nelea V, Morosanu C, Iliescu M, Mihailescu IN. Microstructure and mechanical properties of hydroxyapatite thin films grown by RF magnetron sputtering. Surf Coat Technol. 2003;173(2–3):315–322.

[85] Grubova I, Priamushko T, Chudinova E, Surmeneva M, Korneva O, Epple M, et al. Formation and characterization of crystalline hydroxyapatite coating with the (002) texture. In: IOP Conf Ser Mater Sci Eng. 2016. p. 12016.

[86] Buser D, Schenk RK, Steinemann S, Fiorellini JP, Fox CH, Stich H. Influence of surface characteristics on bone integration of titanium implants. A histomorphometric study in miniature pigs. J Biomed Mater Res. 1991;25(7):889–902.

[87] Grubova IY, Surmeneva MA, Ivanova AA, Kravchuk K, Prymak O, Epple M, et al. The effect of patterned titanium substrates on the properties of silver-doped hydroxyapatite coatings. Surf Coat Technol. 2015;276:595–601.

[88] Gao Y. Surface modification of TA2 pure titanium by low energy high current pulsed electron beam treatments. Appl Surf Sci. 2011;257(17):7455–7460.

[89] Surmeneva MA, Surmenev RA, Pichugin VF, Koval' NN, Teresov AD, Ivanova AA, et al. Adhesion properties of a silicon-containing calcium phosphate coating deposited by RF magnetron sputtering on a heated substrate. J Surf Invest X-ray, Synchrotron Neutron Tech. 2013;7(5):944–951.

[90] Brossa F, Cigada A, Chiesa R, Paracchini L, Consonni C. Post-deposition treatment effects on hydroxyapatite vacuum plasma spray coatings. J Mater Sci Mater Med. 1994;5(12):855–857.

[91] Vladescu A, Birlik I, Braic V, Toparli M, Celik E, Ak Azem F. Enhancement of the mechanical properties of hydroxyapatite by SiC addition. J Mech Behav Biomed Mater. 2014;40:362–368.

[92] Azem FA, Birlik I, Braic V, Toparli M, Celik E, Parau A, et al. Effect of SiC interlayer between Ti6Al4V alloy and hydroxyapatite films. Proc Inst Mech Eng Part H J Eng Med. 2015;229(4):307–318.

[93] Nelea V, Morosanu C, Iliescu M, Mihailescu IN. Hydroxyapatite thin films grown by pulsed laser deposition and radio-frequency magnetron sputtering: comparative study. Appl Surf Sci. 2004;228(1–4):346–536.

[94] Feng B, Weng J, Yang BC, Qu SX, Zhang XD. Characterization of titanium surfaces with calcium and phosphate and osteoblast adhesion. Biomaterials. 2004;25(17):3421–3428.

[95] Pisarek M, Roguska A, Andrzejczuk M, Marcon L, Szunerits S, Lewandowska M, et al. Effect of two-step functionalization of Ti by chemical processes on protein adsorption. Appl Surf Sci. 2011;257(19):8196–8204.

[96] Schade R, Sikiri MD, Lamolle S, Ronold HJ, Lyngstadass SP, Liefeith K, et al. Biomimetic organic-inorganic nanocomposite coatings for titanium implants. in vitro and in vivo biological testing. J Biomed Mater Res - Part A. 2010;95(3 A):691–700.

[97] Andrade J, Hlady V, Feng L, Tingey K. Proteins at interfaces: principles, problems, and potential. In: Bioprocess Technology. Dekker, New York 1996. pp. 19–55.

[98] Woo KM, Chen VJ, Ma PX. Nano-fibrous scaffolding architecture selectively enhances protein adsorption contributing to cell attachment. J Biomed Mater Res A. 2003;67:531–537.

[99] Webster TJ, Ergun C, Doremus RH, Siegel RW, Bizios R. Specific proteins mediate enhanced osteoblast adhesion on nanophase ceramics. J Biomed Mater Res. 2000;51(3):475–483.

[100] Yang SP, Yang CY, Lee TM, Lui TS. Effects of calcium-phosphate topography on osteoblast mechanobiology determined using a cytodetacher. Mater Sci Eng C. 2012;32(2):254–262.

[101] Chai YC, Truscello S, Bael S Van, Luyten FP, Vleugels J, Schrooten J. Perfusion electrodeposition of calcium phosphate on additive manufactured titanium scaffolds for bone engineering. Acta Biomater. 2011;7(5):2310–2319.

[102] Habibovic P, Kruyt MC, Juhl MV, Clyens S, Martinetti R, Dolcini L, et al. Comparative in vivo study of six hydroxyapatite-based bone graft substitutes. J Orthop Res. 2008;26(10):1363–1370.

[103] Becker P, Neumann HG, Nebe B, Lüthen F, Rychly J. Cellular investigations on electrochemically deposited calcium phosphate composites.J Mater Sci Mater in Med. 2004;15: 437–440.

[104] Yuan H, Kurashina K, De Bruijn JD, Li Y, De Groot K, Zhang X. A preliminary study on osteoinduction of two kinds of calcium phosphate ceramics. Biomaterials. 1999;20(19):1799–1806.

[105] Yu S, Yu Z, Wang G, Han J, Ma X, Dargusch MS. Biocompatibility and osteoconduction of active porous calcium-phosphate films on a novel Ti-3Zr-2Sn-3Mo-25Nb biomedical alloy. Colloids and Surf B Biointerfaces. 2011; 85:103–115.

[106] Berube P, Yang Y, Carnes DL, Stover RE, Boland EJ, Ong JL. The effect of sputtered calcium phosphate coatings of different crystallinity on osteoblast differentiation. J Periodontol. 2005;76(10):1697–1709.

[107] Brugge, Ter PJ, Wolke JG, Jansen JA. Effect of calcium phosphate coating composition and crystallinity on the response of osteogenic cells in vitro. Clin Oral Implants Res. 2003;14(4):472–480.

[108] Hu Q, Tan Z, Liu Y, Tao J, Cai Y, Zhang M, et al. Effect of crystallinity of calcium phosphate nanoparticles on adhesion, proliferation, and differentiation of bone marrow mesenchymal stem cells. J Mater Chem. 2007;17(44):4690.

[109] Siebers MC, Walboomers XF, Leeuwenburgh SCG, Wolke JGC, Jansen JA. The influence of the crystallinity of electrostatic spray deposition-derived coatings on osteoblast-like cell behavior, in vitro. J Biomed Mater Res—Part A. 2006;78(2):258–267.

[110] Chou L, Marek B, Wagner WR. Effects of hydroxylapatite coating crystallinity on biosolubility, cell attachment efficiency and proliferation in vitro. Biomaterials. 1999;20(10):977–985.

[111] Barrère F, van Blitterswijk CA, de Groot K. Bone regeneration: molecular and cellular interactions with calcium phosphate ceramics. IntJ Nanomed. 2006;1:317–332.

[112] Thian ES, Huang J, Best SM, Barber ZH, Bonfield W. Novel silicon-doped hydroxyapatite (Si-HA) for biomedical coatings: An in vitro study using a cellular simulated body fluid. J Biomed Mater Res - Part B Appl Biomater. 2006;76(2):326–333.

[113] Azem FA, Kiss A, Birlik I, Braic V, Luculescu C, Vladescu A. The corrosion and bioactivity behavior of SiC doped hydroxyapatite for dental applications. Ceram Int. 2014;40(10):15881–15887.

[114] Šupová M. Substituted hydroxyapatites for biomedical applications: a review. Ceram Int. 2015;41(8):9203–9231.

[115] Zyman Z, Tkachenko M, Epple M, Polyakov M, Naboka M. Magnesium-substituted hydroxyapatite ceramics. Materwiss Werksttech. 2006;37(6):474–477.

[116] Ribeiro AR, Piedade AP, Ribeiro CC, Vieira MT, Barbosa MA. Characterization of hydroxyapatite sputtered films doped with titanium. Key Eng Mater. 2007;330–332:649–652.

[117] Ligot S, Godfroid T, Music D, Bousser E, Schneider JM, Snyders R. Tantalum-doped hydroxyapatite thin films: Synthesis and characterization. Acta Mater. 2012;60(8):3435–3443.

[118] Park SS, Lee HJ, Oh IH, Lee BT. Effects of Ag-doping on microstructure and mechanical properties of hydroxyapatite films. Key Eng Mater. 2005;277–279:113–8.

[119] Ciuca S, Badea M, Pozna E, Pana I, Kiss A, Floroian L, et al. Evaluation of Ag containing hydroxyapatite coatings to the *Candida albicans* infection. J Microbiol Methods. 2016;125:12–18.

[120] Badea M, Braic M, Kiss A, Moga M, Pozna E, Pana I, et al. Influence of Ag content on the antibacterial properties of SiC doped hydroxyapatite coatings. Ceram Int. 2016;42(1):1801–1811.

[121] Surmeneva MA, Tyurin AI, Teresov AD, Koval NN, Pirozhkova TS, Shuvarin IA, et al. Combined effect of pulse electron beam treatment and thin hydroxyapatite film on mechanical features of biodegradable AZ31 magnesium alloy. IOP Conf Ser Mater Sci Eng. 2015;98:12030.

Chapter 13

Thin Films for Immobilization of Complexes with Optical Properties

Joana Zaharieva and Maria Milanova

Additional information is available at the end of the chapter

http://dx.doi.org/10.5772/66512

Abstract

Thin film deposition techniques, such as dip coating, spin coating, and spray pyrolysis, are applied for the production of SiO_2-, poly-(methylmethacrylate) (PMMA)-, and SiO_2-/polyester-based "hybrid" matrices. The factors influencing the film properties are briefly discussed. The morphology of the films presented is studied by different microscopy techniques such as atomic force microscopy, electron (scanning and transmission) microscopy, and fluorescence microscopy. The composites based on SiO_2-, PMMA-, and SiO_2/polyster "hybrid" matrices possess the optical properties of the immobilized complexes of Ru(II) and Eu(III) with different organic ligands. The preparation of the PMMA matrix by the monomer methylmethacrylate polymerization (instead of using of PMMA solution) caused partial destruction of the less stable complexes and thereby a decrease in the fluorescence intensity.

Keywords: dip coating, spin coating, spray pyrolysis, SiO_2-based films, poly-(methylmethacrylate)-based films, SiO_2/polyester "hybrid" matrix, morphology, immobilization, composites, optical properties

1. Introduction

The methods applied for thin film production by deposition have been divided into two groups, physical and chemical, based on the nature of the deposition process [1]. Among them, the chemical methods include gas-phase deposition and solution techniques. The sol-gel process can produce glassy materials by reactions of precursors at room temperature. This process is suitable for thin film fabrication because the sol can easily be deposited on different substrates. It is very easily combined with deposition methods such as dip coating, spin coating, or spray pyrolysis. The convenience of such a combination will be shown in the chapter below along with the characterization of the films by different microscopy techniques such as

atomic force microscopy, AFM, and electron microscopy, transmission, TEM and scanning, SEM. The morphology of the sol-gel produced films coated on different substrates as well as their roughness, surface formations, and thickness are crucial parameters for the application of the films. One of the applications of such films is as a support matrix for the immobilization of complexes. The immobilization of complexes with optical properties in films and matrices is among the approaches applied to obtain new materials with interesting optical properties. Besides the fact that the new materials can possess the properties of both the complex and the matrix, the immobilization itself can improve the stability of the complex immobilized and can protect its properties, for instance, the quenching of fluorescence by the environment molecules. Three different types of composites with immobilized complexes were produced: SiO_2- and poly-(methylmethacrylate) (PMMA)-based composites as well as composites based on a SiO_2/polyester "hybrid" matrix. Complexes with different organic ligands of Ru(II) and Eu(III) were used because of their fluorescence in the visible region of the spectrum. The optical properties of the composites as well as the deposition techniques influencing them are presented.

2. Dip-coating technique

2.1. Advantages of dip-coating technique

Dip-coating is a low-cost, waste-free process that is easy to scale up and offers a good control on thickness of the films made by it, so it is popular in research and in industrial production as well. It has been demonstrated that the method is good enough to fill porosity, to make nanocomposites, as well as to perform nanocasting [2]. In spite of the ways of deposition proposed, involving a capillary induced convective coating [2], usually dip coating is combined with a sol-gel process and a substrate is immersed and withdrawn from a sol of the precursor at a certain rate, followed by evaporation of the solvent. Different substrates such as glass, polycarbonate and polymethylmethacrylate have been tested for production of transparent films of SiO_2, ZnO, indium tin oxide [3] as well as substrates such as Si, Si_3N_4 and SiO_2 for layers of γ-Fe_2O_3 nanoparticles [4].

The factors determining the structure of the films produced via dip coating such as structure of the precursors, relative rates of condensation and evaporation, capillary pressure, and substrate withdrawal speed are presented in [5–7]. An essential factor for the film quality is the film thickness, which is determined by the hydrolysis and condensation behavior characteristics of the precursors and depends on their concentration in the starting solution [8–12], the pH of the sol [13–15], the aging time [8, 12–14], the withdrawal speed [16, 17], the number of immersions, and the ratio of water and precursor [8, 13, 14, 16]. By careful control of hydrolysis and condensation reactions of selected precursors, various surface roughnesses and morphologies can be been achieved [18].

Information about the surface morphology including surface area and roughness is provided by an atomic force microscopy, AFM [18–20]. The united power of the SEM, TEM, and AFM methods contributes to the examination of the surface morphology of thin films prepared by the sol-gel technique using different types of precursors and different parameters of the dip-coating deposition procedure [19].

http://dx.doi.org/10.5772/66512

2.2. Films, matrices and composites produced by dip coating

2.2.1. Sol-gel produced SiO_2-based films and composites by dip coating

The process conditions as well as the solution properties are factors influencing the thickness and uniformity of thin films. The SiO_2-based films were made using Si-containing precursors such as the alkoxysilanes TEOS (tetraethoxysilane), OtEOS (octyltriethoxysilane), and MtEOS (methyl triethoxysilane). The latter two are also called organic modified silanes or ormosils because of the C-Si bond in the structure of these hybrid materials. On the surface, the silanol groups are replaced by alkyl groups that have a poor affinity for water so by that they are keeping the sol-gel surface hydrophobic [13]. Films deposited at a withdrawal speed of 0.4 mm/s with variations of the number of the immersions (from 1 to 7) on microscope glass using gels produced from TEOS, OtEOS, or mixtures of TEOS/OtEOS (mole ratio 1:1) as well as TEOS/MtEOS (mole ratio 1:3) were obtained, showing the influence of the alkoxysilane used [19]. It can be seen that the films obtained from pure TEOS sol have smooth, glassy surface (**Figure 1**). By using organic modified silanes (OtEOS, MtEOS), structuring of the surface is observed **(Figures 1–7),** and the appearance of formations with raindrop or ellipsoid shape with a widely varying size is observed; both the size and the concentration of the shapes depend on the film deposition conditions.

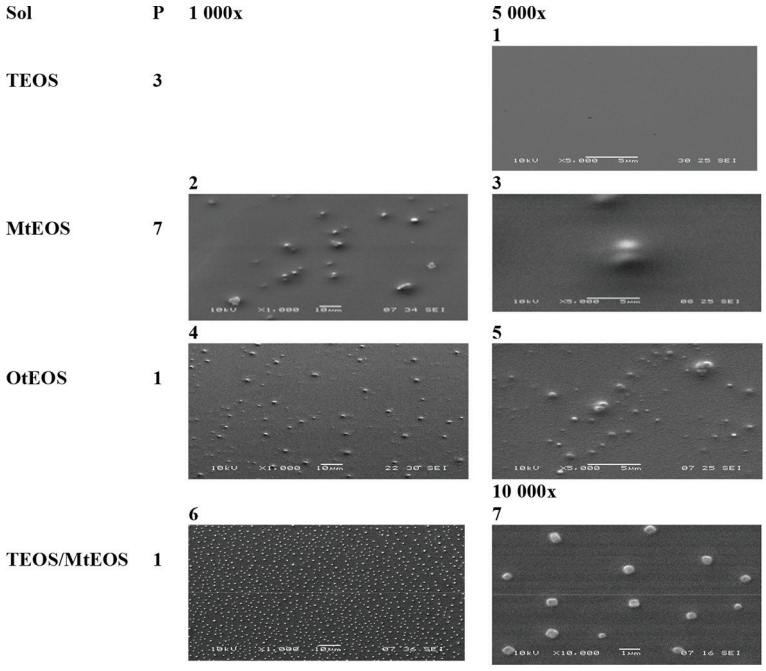

Figure 1. SEM images of films, obtained from different sols, at a withdrawing speed of 0.4 mm/s and different number of immersions, P [19].

SEM images of layers, prepared from TEOS, TEOS+MtEOS, MtEOS, and OtEOS containing sols with different numbers of immersions and different speeds (**Figure 2**), show the influence of these factors on the film morphology.

Films, 10 000 x	P	Dip speed, mm/s	Main grain size, nm
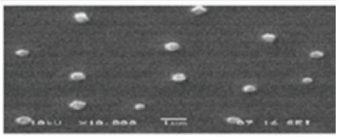 1	1	0.4	550 x 300
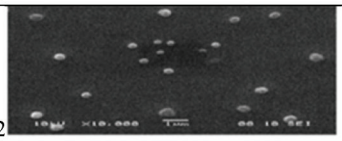 2	3	0.4	400 x 200
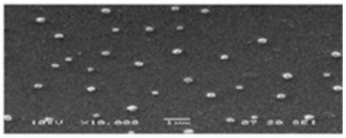 3	5	0.4	300 x 180
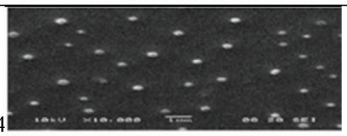 4	3	0.3	400 x 150 up to 1200 x 540
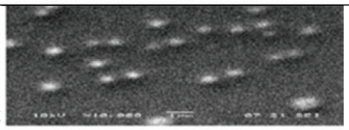 5	1	0.2	600 x 300
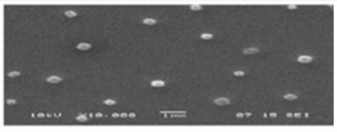 6	3	0.2	500 x 350
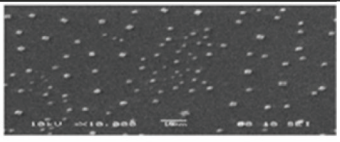 7	5	0.2	300 x 200

Figure 2. SEM images (10,000×) of the matrices, produced by dip coating from TEOS/MtEOS sol at different withdrawal speed and number of immersions, P [19].

The ellipsoid or rhombohedral grains observed (approximately 200 nm in size, **Figure 3**) showed a decreasing size and an increasing number per unit surface area with increasing number of immersions (**Figure 2**).

http://dx.doi.org/10.5772/66512

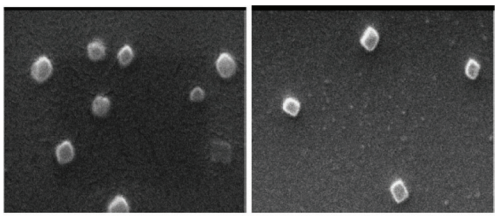

a b

Figure 3. SEM image (30,000×) of the films obtained after (a) 3 and (b) 5 immersions with withdrawing speed (a) 0.3 and (b) 0.4 mm/s, produced from sol TEOS/MtEOS (ellipsoid or rhombohedral grains are approximately 200 nm in size) [19].

The dot distribution can be ascribed to and connected with the randomly formed macroscopic "pores" or hollows observed in the AFM images (**Figure 4**), with a higher concentration and better appearance in samples prepared with larger numbers of immersions.

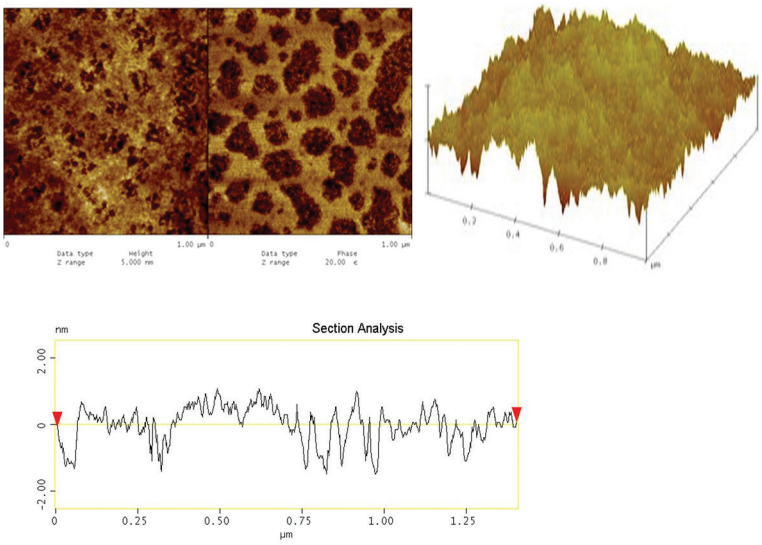

Figure 4. AFM images of films produced by dip coating (withdrawing speed 0.4 mm/s) from TEOS/OtEOS sol (1 immersion), bearing area 0.8 μm^2. The section analysis is performed along the diagonal of the bearing area [19].

Sol-gel produced SiO_2-based composites were made by orthosilanes with immobilization of the complex Rudpp, (Ru(II)-tris(4,7-diphenyl-1,10-phenanthroline) dichloride, $[Ru(dpp)_3]Cl_2$). The films produced (10–15 mm) from TEOS/OtEOS and Rudpp sols at withdrawal speed of 0.4 mm/s and up to 5 immersions have a good uniformity and thickness of about 500 nm. Smoothness of the films, combined with the good linkage between the layers, is ensured by these conditions [19]. The presence of Rudpp in the films produced from TEOS leads to the

appearance (due to microcrystallization of the Rudpp) of dots (**Figure 5b–d**) on the otherwise smooth surface of the Rudpp-free dip-produced film (**Figure 5a**).

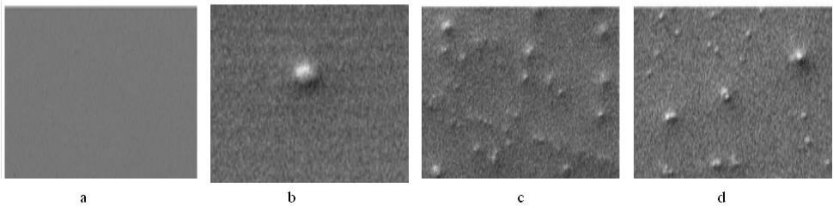

Figure 5. SEM images of layers without and with Ru(dpp), produced from TEOS-containing sols (a) TEOS (1), (b) TEOS-Rudpp (1), (c) TEOS-Rudpp (5), and (d) TEOS-Rudpp (7) (in brackets the number of the immersions) [19].

The synthetic conditions were improved by applying an ultrasound treatment to the sol after its magnetic stirring. It was found that this improves the surface of the films. Uniform, smooth films were obtained, and no microcrystallization of the complex was observed in the SEM or TEM images. Apparently, the ultrasound treatment of the sol is a powerful tool to avoid microcrystallization of the complex, leading to production of high-quality films. Films from non-sonicated sol show some heterogeneity due to microcrystallization of the Rudpp [21] (**Figure 6**), whereas films produced from sonicated sol are entirely homogeneous [19].

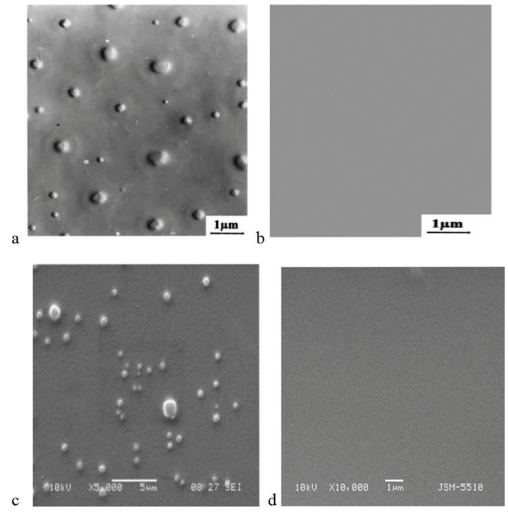

Figure 6. TEM (a, b) and SEM (c, d) images of TEOS/OtEOS/Rudpp dip-coated films without (a, c) and with (b, d) gel sonication [21].

http://dx.doi.org/10.5772/66512

The presence of OtEOS causes roughness of the films with sharply expressed hills and valleys as observed with AFM (**Figure 7b**). The chain-like surface structure in the OtEOS Rudpp film may be due to the presence of the long CH_3-$(CH_2)_7$ radicals that are likely difficult to fit into the SiO_2 network.

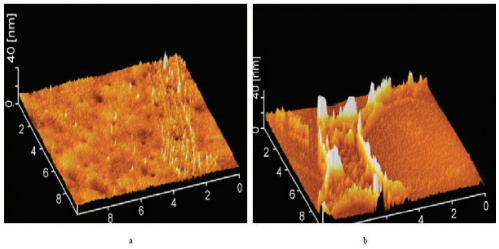

Figure 7. AFM images of films produced by dip coating (withdrawing speed 0.4 mm/s) from sols TEOS/OtEOS/Rudpp (a), and OtEOS-Rudpp (b); 1 immersion [19].

2.2.2. Sol-gel produced SiO_2-based matrix made from TEOS with immobilized $Eu(DBM)_3$ and $Eu(DBM)_3$·dpp complexes

A sol-gel produced SiO_2-based matrix was used for immobilization of the europium (III) complex with dibenzoylmethane (DBM), $Eu(DBM)_3$, and the mixed-ligand complex $Eu(DBM)_3$·dpp (dpp is 4,7-diphenyl-1,10-phenanthroline). The synthetic procedure for obtaining the composites is presented in [22]. To a magnetically stirred ethanol-dimethylformamide (DMF) solution (volume ratio 1:4) of the complex (2.5 g/dm^3), TEOS was added dropwise until an ethanol:TEOS mole ratio of 4 was obtained. After that water (with pH 8, adjusted by aqueous ammonia solution) was added in the same way, by this reaching mole ratio ethanol:TEOS:water = 4:1:4. Experiments with ratios 8:1:4 were also performed. After 2 h stirring, the sol obtained was aged at 50–70°C for different times. In some experiments, the fresh sol was sonicated for 30 min in an ice-water ultrasound bath. From the prepared gels, films with a typical thickness of ~300 nm were produced from one immersion with a withdrawing speed of 0.2 mm/s. Membranes (1–2 mm in thickness) were prepared by casting of a gel in a Teflon® mould. The influence of the temperature (ambient to 70°C) and time (3 h to 4 weeks) of ageing of the sol before film/membrane preparation and of their drying on the photoluminescence properties was investigated. When adding distilled water to the sol instead of water with pH = 8, a sol with pH of ~5 was obtained. Films produced from such sols showed no photoluminescence; it was concluded that the complex suffered destruction at this pH, by this the importance of pH control is shown [22]. Despite the positive effect of the sonication on the uniform distribution of the complex in the immobilization matrix [19], it caused quenching of the photoluminescence. This was probably due to some destruction of the complexes, and sonication is thus not recommended when these complexes are used. Emission spectra of the pure powdered complexes $Eu(DBM)_3$ and $Eu(DBM)_3$·dpp along with the SiO_2-based composites containing these complexes are shown in **Figure 8**. The characteristic emission band for Eu^{3+} is preserved in the spectra after immobilization.

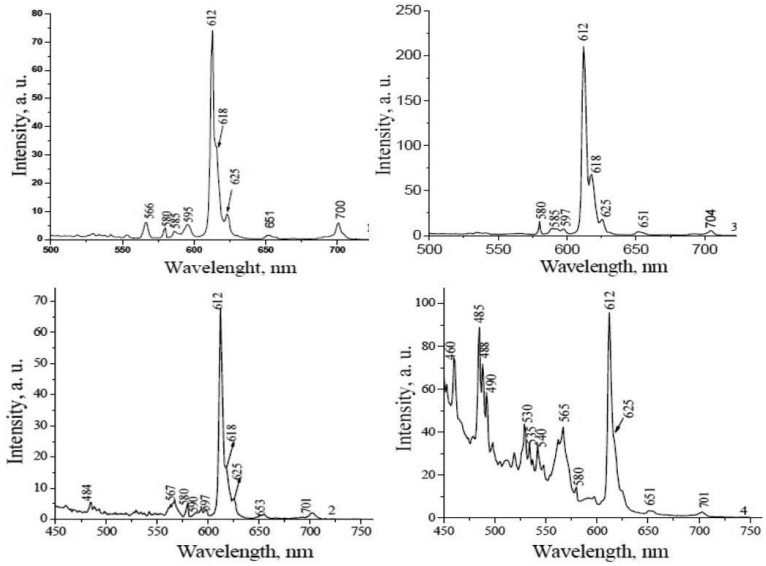

Figure 8. Emission spectra of $Eu(DBM)_3$ (1) and $Eu(DBM)_3$·dpp (3) and of the composites containing $Eu(DBM)_3$ (2) and $Eu(DBM)_3$·dpp (4) [22].

When larger amounts of DMF solvent were used than described above, it was found that after 6 weeks storage of the composites, they became opalescent and their optical properties changed. A possible explanation could be the disturbance of the Eu^{3+} coordination shell caused by the strong donor ability of the DMF. The presence of contaminant ions (using NaOH instead of NH_4OH for adjustment of the pH for alkoxide hydrolysis) strongly decreases the lifetime of the excitation states to 31 μs for $Eu(DBM)_3$ and to 19 μs for $Eu(DBM)_3$·dpp containing composites, compared with 82 and 318 μs for the pure complexes, respectively.

2.2.3. SiO_2/polyester hybrid (inorganic/organic) matrix with immobilized Rudpp

Inorganic–organic hybrids combine the functional variety of organic compounds with the benefits of thermally stable and strong inorganic substrates and they can be promising precursors for immobilization matrices [23]. In the review quoted [23] different ways of making such "hybrid" materials are mentioned and among them is the simultaneous condensation of silica and organosilica precursors ("cocondensation"). A similar possibility is given by the application of the polymerized complex method [24], where a formation of polymeric resin is a result of condensation and polyesterification between a hydroxopolycarboxilic acid (preferably citric acid, CA) and a polyvalent alcohol (most often ethylene glycol, EG). If simultaneous hydrolysis of tetraethoxysilane (TEOS), esterification of the hydrolyzed product with CA, and esterification between CA and EG can happen, then it can be expected a formation more complicated structure in comparison with the relatively regular one obtained from pure TEOS. The formed polymer net may ensure suitable places for entrapping a complex and its uniform distribution (which may be very important, for example for gas sensor). Mole ratios

of TEOS:CA:EG = 4:1:1, 4:2:2, 2:1:1, and 1:1:1 were used, and an ultrasound treatment time was 40 min was applied. Substrates such as microscope glass were used. Before deposition, the slides were cleaned by 15 min treatment in an ultrasound bath consecutively with distilled water, methanol, acetone, and finally with distilled water. The factors influencing the properties of the composites synthesized based on SiO_2/polyester "hybrid" are (i) the mole ratio TEOS:CA:EG, (ii) the sol production method, (iii) the sol sonication, and (iv) the film thickness, determined itself by the sol composition, aging time, and withdrawing speed.

Microcrystallization of Rudpp complex was found to occur in a SiO_2 matrix produced from acid-catalyzed non-sonicated sol [21]; no indications for such a separation were found in the SiO_2/polyester "hybrid" films. Immobilization in the SiO_2/polyester films does not significantly change the fluorescent properties of the Rudpp complex, as shown in the fluorescence microscopy images (**Figure 9**).

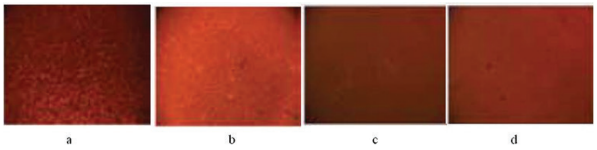

Figure 9. Images from fluorescence microscopy (×160) of films produced on microscope glass by dip coating at mole ratios TEOS:CA:EG = 4:1:1 (a), 4:2:2 (b), 2:1:1 (c), and 1:1:1 (d), respectively [25].

The fluorescence intensity from different regions of a "hybrid" film were followed in time. It can be seen that after a 150 s stabilization period, the fluorescence emission intensity from different regions stays constant within about 1.8% (**Figure 10**) [25].

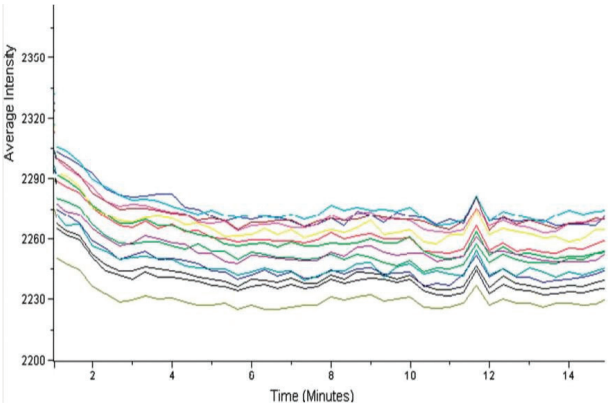

Figure 10. Fluorescence intensity from different regions of a "hybrid" film as a function of time [25].

The matrix composition (ratio TEOS:CA:EG) does not influence the excitation (**Figure 11a**) and emission (**Figure 11b**) spectra of the films and the position of the maxima (310 and 619 nm, respectively).

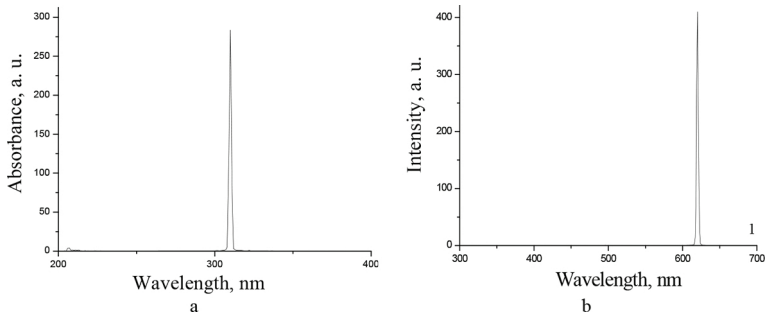

Figure 11. Excitation (a) and emission (b) spectra of Rudpp in hybrid matrix (TEOS:CA:EG = 4:1:1) [25].

The results obtained gives the opportunity to conclude that by formation of SiO_2/polyester "hybrid" matrix the films can be produced with a good stability, density and homogeneity, as well as with a good adhesion to different substrates such as glass, silica, and ceramics. An additional advantage of that matrix is the uniform distribution of the optically active complex immobilized, especially the fact that it preserves its optical properties. The film morphology strongly depends on the sol composition and deposition mode. Films prepared by dip coating at a withdrawing speed of 0.4 mm s^{-1} from sonicated sol with molar ratio TEOS:CA:EG = 4:1:1 produced by acid catalysed hydrolysis were found promising as an active component of optical sensors [25].

2.2.4. Composites based on poly-(methylmethacrylate), PMMA, with immobilized complexes

2.2.4.1. Immobilization of Rudpp in PMMA-based composites

A PMMA matrix was prepared by a catalytically induced polymerization of the monomer methylmethacrylate (MMA), following a procedure described in [26]. It was found that poly(methylmethacrylate) films produced from monomer, containing 1.5% Rudpp, are dense with a smooth surface and uniform distribution of the complex (**Figure 12a, b**) and fluorescent properties (**Figure 12c**). The fluorescence emission intensity from films produced by polymerization of the monomer MMA was significantly (2.5-fold) weaker in comparison with those prepared from PMMA solution, probably due to partial destruction of the complex.

Using a chloroform solution of PMMA, membranes and thin films of good quality can be obtained. Membranes (0.4–1.5 mm in thickness) were prepared by casting of the PMMA solution or partially polymerized MMA into a Teflon® mould. Both types of samples were dried at 50°C for 24 h. The use of PMMA as an immobilization matrix for Rudpp is a cheap and easy to be applied composite preparation method, ensuring the production of dense and smooth

http://dx.doi.org/10.5772/66512

specimens with uniformly distributed optically active complex with the possibility to prepare membranes up to 1 mm thick. No significant interaction of the complex with the matrices takes place, and the emission spectra of the complexes are practically unchanged as a result of immobilization in both types of studied matrices (**Figure 13a, b**). The reported results show the preparation of PMMA by the polymerization of the monomer MMA in the presence of benzoyl peroxide as a polymerization initiator is not a suitable method for the production of Rudpp-PMMA composites due to a partial destruction of the complex.

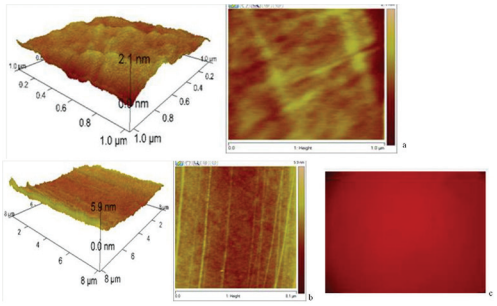

Figure 12. AFM (at different scanning area) (a, b) and fluorescence (x160) (c) images of dip-coated films from Rudpp-containing composite prepared from catalyst-induced polymerization of MMA [26].

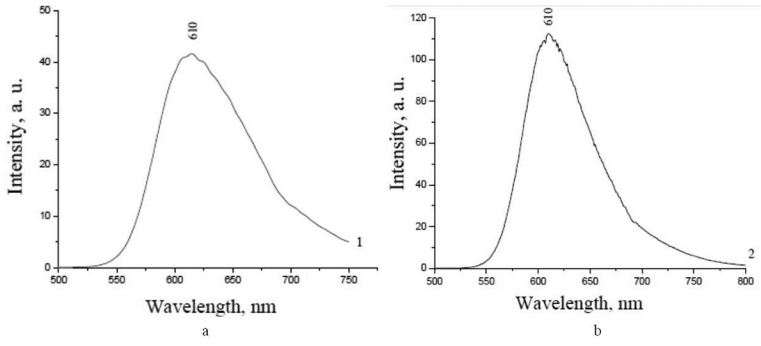

Figure 13. Emission spectra of a PMMA/Rudpp-containing membrane (excitation at 450 nm) prepared from catalyst-induced polymerization of MMA (a) and from PMMA solution (b) [26].

2.2.4.2. Immobilization of Eu(III) beta-diketonates in PMMA

The optically active complexes ($Eu(DBM)_3$, $Eu(DBM)_3$·phen, $Eu(DBM)_3$·dpp, $Eu(TTA)_3$·phen, and $Eu(TTA)_3$·dpp) are well-known fluorescent dyes with high fluorescent emission intensity (phen is phenanthroline, and TTA is thenoyltrifluoroacetone). The complexes of the type $Eu(DBM)_3$·Q (Q is phen or dpp) are of special interest due to their higher stability (compared to $Eu(DBM)_3$) and increased luminescence intensity [27].

A PMMA matrix was prepared by a catalytically induced polymerization of the monomer MMA [28]. The deposited films were aged at 50°C for 4–6 h. The experiments showed that thicker membranes can be prepared by applying 24 h of aging time at the temperature mentioned. The content of the complex in the final product after evaporation of the solvent was determined to be 1.5%. Using a solution of PMMA, films were deposited and membranes were prepared with a complex concentration in the final matrix of 1.0%. Films were deposited by dip coating at a withdrawal speed of 0.4 mm/s, using the device described in [29]. The films were uniform with a typical thickness of 200 nm. By varying the withdrawal speed, films with thickness of 0.1–1 μm were prepared. Membranes 0.1–1 mm in thickness can be easily obtained by placing the initial complex-binder mixture in a mould or by pouring along glass slides. SEM (**Figure 14**) or AFM (**Figure 15**) showed that no microcrystallization or aggregation (observed for example in [30], reaching 10 nm in size) of the complexes in the matrix took place and that cracks in films and membranes were absent. Qualitative tests with adhesive tape and brass edge showed that films thicker than 400–500 nm have poorer adhesion to the microscope glass.

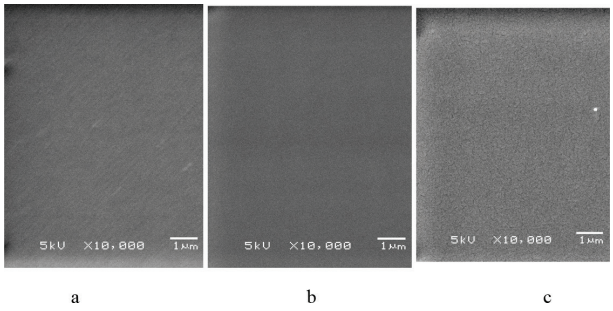

Figure 14. SEM images of dip -coated films of $Eu(DBM)_3$ (a) and $Eu(TTA)_3$phen (b, c,) in MMA (b) and PMMA (a, c) [28].

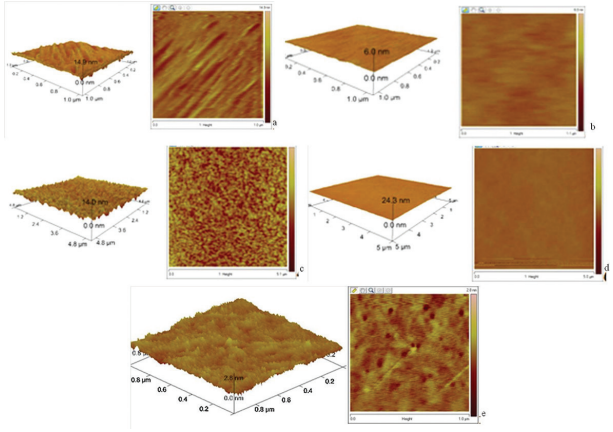

Figure 15. AFM images of dip-coated thin films of immobilized Eu complexes: $Eu(DBM)_3$ (a), $Eu(DBM)_3$phen (b), $Eu(DBM)_3$dpp (c), $Eu(TTA)_3$dpp (d) in PMMA, produced from the monomer, and $Eu(DBM)_3$ (e) in PMMA produced from polymer solution [28].

http://dx.doi.org/10.5772/66512

Embedding of the complexes causes some changes in the excitation spectra but does not influence the emission spectra significantly. The uniform distribution of the complex in the matrix and lack of aggregates, obtained by the applied deposition methods, also have a positive effect on the preservation of the lifetime of the excited states of the embedded complexes (**Figure 16**).

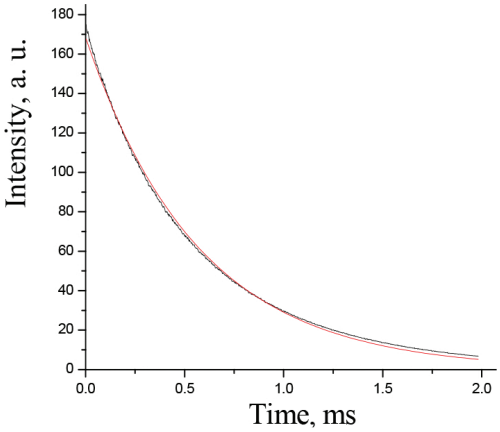

Figure 16. Lifetime of the excited state of composite $Eu(TTA)_3$phen in MMA [28].

The preparation of the matrix by the monomer polymerization leads to partial destruction of the less stable complexes and thereby a decrease in the fluorescence intensity. It was shown that the films produced by dip coating from europium-diketonates–PMMA chloroform solution can be used both as components of luminescent devices and for temperature sensing [28].

3. Spin-coating technique for film production

The basic principles of the spin-coating technique and the parameters controlling the process are presented, for example in Ref. [31], including the spin speed, spin time, acceleration, etc. The process generally involves four stages, namely a dispense stage (or deposition), substrate acceleration (spin-up) stage, a stage of substrate spinning at a constant rate, and evaporation [31, 32]. Evaporation may accompany the other stages [32, 33]. In order to understand the mechanism of thin-film formation by spin coating, the relationship between the thickness and the solvent evaporation rate of spin-coated thin films has been studied [34]. Spin coating combined with the sol-gel process offers a simple, low cost, and highly controlled way of film deposition [35]. In recent years, the method has been used for coating in microelectronics [36] and studied for deposition of transparent conducting oxides [37], for ferroelectric thin films [38], for indium oxide thin films [39], for doped and undoped hematite films [40], for ZnO thin films [35, 41–44], for titanium oxide films [45], for yttria-stabilized zirconia thin films [46], for mesoporous silica thin films on a silicon substrate [47], and so on.

3.1. SiO_2 films and composites produced by spin coating

The spin-coating technique was applied for sol-gel produced SiO_2-based films. The deposition was done by means of a KW-4A (USA) spin coater at 2000–6000 rpm, spinning time 20–60 s, and 1–3 spinning procedures (0.5 cm^3 sol per procedure) [19]. Different orthosilanes were used for SiO_2 precursors, such as TEOS, OtEOS, or their mixture. The morphology of the films prepared from TEOS and TEOS/OtEOS is shown in the SEM images (**Figure 17**).

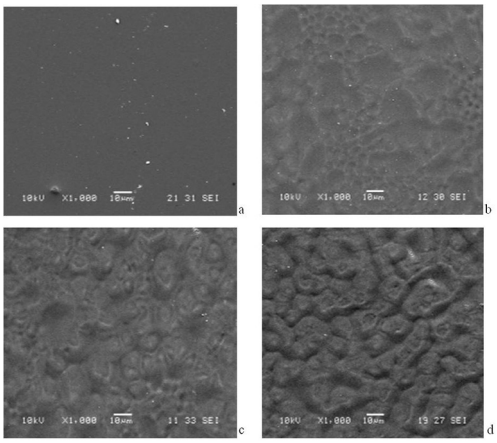

Figure 17. SEM images of films produced by spin coating at a spinning speed of 3000 min-1 from sols: TEOS (a); TEOS/OtEOS (b) (spinning time 30 s); TEOS/OtEOS (60 s), at an image angle of 90° (c) or 45°(d) [19].

The alkoxysilane used has an influence on the morphology of the spin-coated films. Films prepared using TEOS are similar to the dip-coated films (part 2.2.1.), that is, the films are dense and uniform (**Figure 17a**). The use of an ormosil-type precursor (TEOS/OtEOS mixture) leads to the production of "structured" films (**Figure 17b**) whose SEM images are different from those of dip-deposited films. The ''structuring'' improves with increasing of the spinning time from 30 to 60 s (**Figure 17b–d**), that is, with decreasing film thickness, which is opposite to the effect of the same parameter for dip coating.

A well expressed chain-like surface structure is seen in the AFM image (**Figure 18a**, without Rudpp) where the above mentioned hills and valleys are very regular. The section analysis (**Figure 18b**, with Rudpp) reveals hollows with diameters of 25–60 nm and depths of 1–1.6 nm and differences between the lowest and highest points in the scanned region of 2.8 nm. There is an influence of the spinning time: chains are observed at a spinning time of 60 s that are not noticed at 30 s spinning time (**Figure 17c, d**).

The thickness of the spin-produced films can be controlled by the gel spinning rate and the time. The thickness decreases with increasing spinning rate (2000–4000 min^{-1}) and time (20–40 s). The effect is significant (a factor two) when the spinning time was increased from

http://dx.doi.org/10.5772/66512

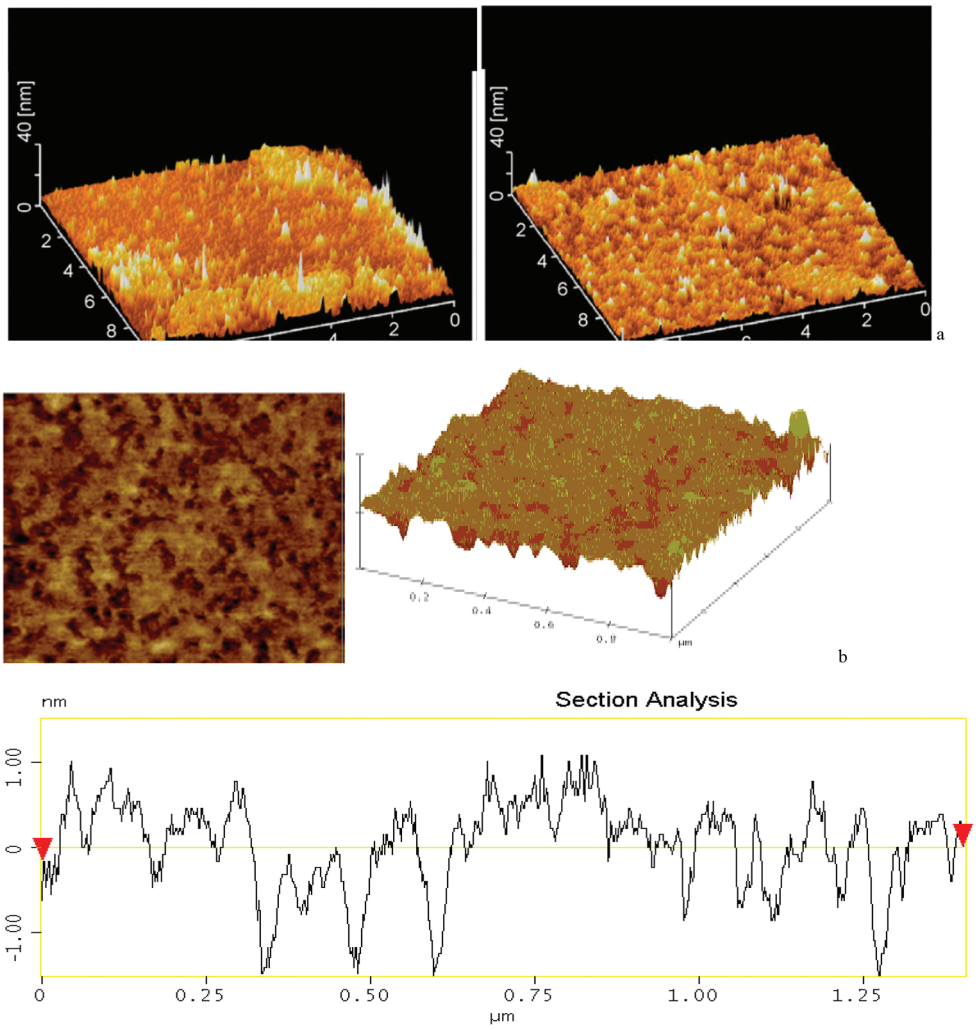

Figure 18. AFM images of films produced by spin coating (60 s, 3000 min^{-1}) from TEOS/OtEOS (a) and TEOS/OtEOS-Rudpp sol (b). The section analysis is performed along the diagonal of the bearing area [19].

20 to 30 s. No significant differences were found between films produced from TEOS/OtEOS and pure TEOS at spinning times of 30 and 40 s [21]. The thickness of the produced films (1 × 1 cm), measured by a Talystep profilomer, depends on the deposition conditions and is typically around 300 nm for dip-coated films. The thickness of the spin-deposited films is much larger: from 7 µm (at 0.5 cm^3 gel, 3000 rpm, 30 s) to 19 µm (1.5 cm^3 gel, 2000 rpm, 20 s) [19]. Their morphology depends mainly on the nature of the precursor and somewhat on the deposition method [19].

The ruthenium complex Rudpp was immobilized in a SiO_2 matrix by following a commonly used sol preparation procedure (with 1.25–2.5 g Rudpp/dm^3 sol). It was found that microcrystallization of the complex occurs with formation of randomly distributed crystals of 100–400 nm in size. An ultrasound treatment of the sol by means of an ultrasound disintegrator leads to homogeneous distribution of the complex without observable crystallization (**Figure 18b**).

3.2. Rudpp complex immobilized in a SiO_2/polyester "hybrid" composite

A SiO_2/polyester "hybrid" with immobilized Rudpp complex was prepared, using a polished fused silica substrate spinning at 2000 min^{-1} and a precursor solution with mole ratio TEOS:CA:EG = 1:2:2. The sol aging time was 2 h, the spraying/spinning time was 30 s, and ultrasound treatment time was 40 min [21]. It was found that the spin-produced specimens obtained from sols enriched in CA and EG were not uniform.

4. Spray pyrolysis method for film production

Spray pyrolysis is a simple and inexpensive technique, which does not require high-quality substrates or chemicals for the production of various materials. It is easy for preparing films of any composition, such as thin films with large surface area, ceramic coatings, dense films, porous films at relatively low temperatures, and multilayered films [1].

It has been used for decades in the glass industry and in solar cell production [1], for powder production [48] and for electrodes and counter electrodes for dye-sensitized solar cells [49]. The method is used for deposition of thin ferrite films [50], thin films of the perovskite $LaFeO_3$ [51], thin films of TiO_2 (pure or modified) [52–55], films of poly-(methyl)methacrylate [28], and thin films of cerium-doped yttrium-iron garnet [56], each of them with potential applications in water purification, oxygen sensing, thermosensors, for deposition of thin yttria-stabilized zirconia films [1, 57, 58], for crystalline and non-crystalline iron oxide (α-Fe_2O_3) thin films onto glass substrates at different temperatures [59, 60], highly structured ZnO layers [61], transparent conducting zinc oxide thin films [62], lead(II) oxide thin films [63], nanoporous aluminum oxide [64], europium doped lanthanum oxide films [65], and UV excited green emitting Eu(II) activated $BaAl_2O_4$ and $SrAl_2O_4$ [66] and etc. Typical spray pyrolysis equipment consists of an atomizer, precursor solution, substrate heater, and temperature controller. The atomizers usually used in spray pyrolysis technique are mentioned and explained in [1], namely air blast (the liquid is exposed to a stream of air), ultrasonic (ultrasonic frequencies produce the short wavelengths necessary for fine atomization), and electrostatic atomizer (the liquid is exposed to a high electric field).

4.1. Factors influencing the properties of the films produced by spray pyrolysis

The processes involved in the spray pyrolysis technique as well as the effects of spray pyrolysis parameters on film quality such as the influence of the substrate surface temperature on the film roughness, cracking, and crystallinity are discussed in Ref. [1]. The substrate surface temperature is a parameter that determines the film morphology and properties so that by increasing the temperature, the film morphology can be changed from a cracked to a porous microstructure [1]. The influence of different parameters on the thickness, morphology, crystal

http://dx.doi.org/10.5772/66512

structure, and adhesion of the films is discussed in [5, 67], and optimal values are given (in brackets) for the nature of the carrier gas (oxygen or nitrogen) and its flow rate (0.5–1.2 dm^3/min), the substrate temperature during the spraying (350°C or 400°C), the spraying angle (varied in the interval 20°–90°), the distance between the substrate and the nozzle (15–25 cm), the duration of spraying (10–20 s), the interval between the consecutive sprayings (1–5 min), the number of sprayings (1–20 cycles), the postdeposition annealing temperature (350–480°C), and the type of substrate. A comprehensive model for spray pyrolysis using solutions is presented in [67]. Different solutions or suspensions have been used such as ethylene glycol solution of mixed metal citrate complexes [67, 68] and aqueous or methanol suspensions containing TiO_2 and EG or PEG [54]. In some of the experiments, sonication for 20 min by means of ultrasonic disintegrator, UD, 20 (Technopan, Poland) was applied before spraying [54]. The device used [69] is suitable for film deposition. The suspension was passed through a pneumatic nebulizer with a 1 mm nozzle diameter using pressurized O_2 [5, 54] or N_2 [50] as a carrier gas. A nebulizer with nozzle of 0.7 mm in diameter was also used [50]. Microscope slides and optical grade glass of various shapes and sizes were used [51]. The substrate was situated at 20 cm from the nozzle at an angle of 45° and heated at temperatures, depending on the nature of the substrate and of the spraying material and kept within the limits of ±5°C. The suspension was sprayed for 30 s periods, separated by intervals of 5 min. The deposited films were heated at 300–500°C for 1 h [54] or 480–750°C for 0.5–3 h [50] in static air. The prepared films had a very good adhesion to the substrate as demonstrated by the standard tests with scotch tape and brass edge. The film thickness was controlled by the number of spraying cycles [50]. Typically, 10 cycles can be applied to produce 0.5 mg/cm^2 layers of TiO_2 that were approximately 1.5 μm thick [54]. With O_2 as a carrier gas, more uniform films were formed compared with those prepared using N_2 at the same conditions. This is probably due to a more even and complete burning of the organic components in the initial solution, when citric complexes were applied as precursors (**Figure 19**) [51].

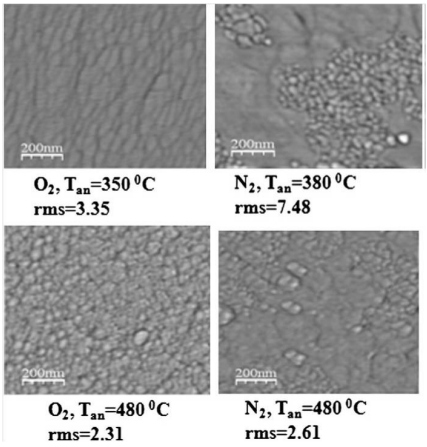

Figure 19. AFM images of films deposited on microscope glass slides at a substrate temperature of 350°C; as carrier gas are used O_2 or N_2, at a flow rate of 1 dm^3/min; annealing of the films in air for 3 h at 350°C (O_2-produced films) or 380°C (N_2-produced films) and at 480°C (rms: root mean square roughness) [51].

The method is suitable for the production of films up to ~700 nm thickness. The film thickness above 700 nm can cause cracking during the thermal treatment, following the deposition [51]. Thin films of $La_2Ti_2O_7$ were deposited by spray pyrolysis using as starting material the ethylene glycol solutions of La–Ti citric . The films produced on silica glass and Si substrates after 2 h postdeposition annealing at 750°C were with good stoichimetry, homogeneous and with highly crystallinity. It was found that the size of the crystallites was between 25 and 45 nm and it depended on the nature of the substrate and slightly on the conditions for deposition and postdeposition. Using the number of the spraying cycles, the thickness of the films can be controlled (up to 1.2 mm). The size of the grains may also be controlled by the diluents used and by the conditions for annealing [68]. Highly crystalline uniform Y_2O_3 films (0.2 1 μm) were obtained using EG solutions of yttrium citric complexes, demonstrating that thin films can be deposited using spray pyrolysis of nonaqueous solutions of citric complexes as a starting material and using O_2 as a carrier gas. The substrate was heated at 350°C during the deposition, and a postdeposition annealing at 850°C for 2 h was applied [70].

The optimal coating conditions were similar to the ones used in [53]. The suspension was passed through a pneumatic nebulizer with a 1 mm nozzle diameter using pressurized O_2 as a carrier gas. The substrate was situated 20 cm from the nozzle at an angle of 45° and heated at temperatures that depended on the nature of the substrate and of the spraying material. The suspension was sprayed for 30 s periods, separated by intervals of 5 min. The deposited films were heated at 300–500°C for 1 h in static air. The prepared films had a very good adhesion to the substrate as demonstrated by the standard tests with scotch tape and brass edge. The film thickness was controlled by the number of spraying cycles. Typically, 10 cycles can be applied to produce 0.5 mg/cm^2 layers that were approximately 1.5 μm thick [54].

4.2. Spray pyrolysis for immobilization of complexes and synthesis of composites with optical properties

4.2.1. PMMA-based composites

The composite $Eu(DBM)_3$/PMMA was obtained by two methods. The first one includes the dissolving of the complex into the MMA monomer solution followed by polymerization, and the second one includes the dissolving of the polymer and the complex in a solvent, followed by the evaporation of the latter. After the solution was prepared, the spray pyrolysis device, described in details in Ref. [69], was applied. The spraying conditions for $Eu(DBM)_3$-containing solution of MMA are as follows: a nebulizer with a nozzle diameter of 0.8 mm, under an angle of 45° and at a distance of 20 cm from the substrate surface was used. As a carrier gas, air was applied with a flow rate of 0.7–0.9 dm^3/min. The substrates used were heated at temperature varied between 50 and 70°C. The spraying time was 15 s, and the interval between different layer depositions was about 30 min. [28]. An example of the morphology of the films can be seen in **Figure 20**.

A tendency for decreasing film roughness when the monomer MMA polymerization was applied can be seen. This is explained by the relatively fast polymerization inside the very

http://dx.doi.org/10.5772/66512

small droplets as well as by the sharp temperature decrease in the solution containing oligomerized monomer during deposition. This limits the possibility of formation of long chains and disturbs the structure obtained when PMMA polymer solution is used.

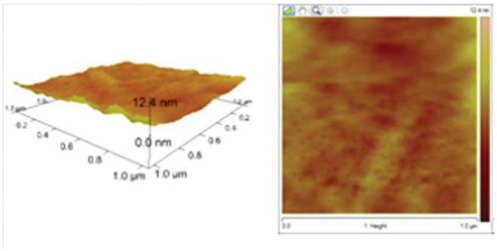

Figure 20. AFM-image of $Eu(DBM)_3$/PMMA film produced by spray coating [28].

The optical properties of the $Eu(DBM)_3$ complex and its derivatives as well as of $Eu(TTA)_3$·phen after their immobilization both in films and in membranes produced from MMA or PMMA solutions were followed. For both types of matrices, the excitation spectra of the complexes showed some changes (with general pattern preserved), whereas the emission spectra were not disturbed (**Figure 21**) [28].

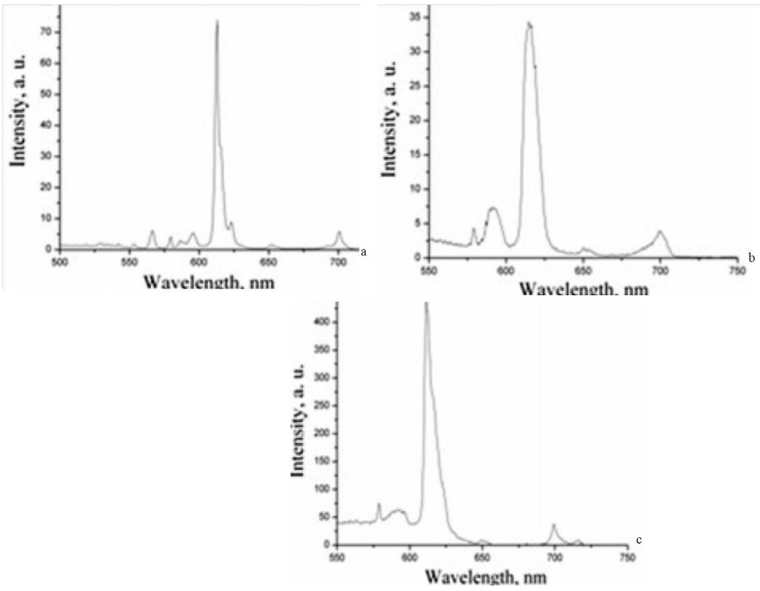

Figure 21. Emission spectra of (a) complex in solid state, (b) immobilized in a matrix from MMA solution, and (c) immobilized in a matrix from PMMA solution [28].

The lifetime is 75, 214, and 265 μs for the pure $Eu(DBM)_3$ and the complex immobilized in MMA and in PMMA, respectively. The preparation of the matrix by monomer polymerization leads to partial destruction of the less stable complexes and thereby a decrease in the fluorescence intensity.

4.2.2. Spray pyrolysis produced composites based on SiO_2/polyester "hybrid" matrix

The synthetic procedure for composited preparation consists of citric acid (a measured amount) dissolved in ethanol under stirring, and of EG added in small portions to the solution obtained. Stirring for 15 min was applied in order to obtain a homogeneous final solution. To the latter one, TEOS was added dropwise in an amount that the desired mole ratio of TEOS:CA:EG:EtOH to be reached. By adding HCl (0.1 M), the pH value was adjusted equal to 2. To obtain a complex concentration of 2.5 g dm^{-3} sol, an ethanol solution of Rudpp (0.014 g mL^{-1}) was added. The variation of the complex concentration was experimented, but it did not show an effect on the main functional parameters of the films produced.The films produced by spray pyrolysis were uniform, without cracks and with a satisfactory adhesion, and contained pores that were about 100 nm in diameter (**Figure 22**).

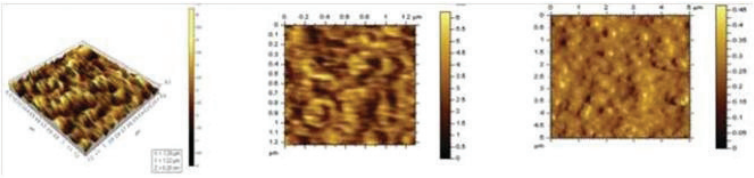

Figure 22. AFM images of based on SiO_2 polyester hybrid film made by spray pyrolysis [25].

The pores are probably due to the faster evaporation of the excess of EG in the course of spraying on the heated surface. It is concluded that the chain structure is common for spray-produced films based on SiO_2/polyester "hybrid" [25].

Author details

Joana Zaharieva* and Maria Milanova

*Address all correspondence to: jzaharieva@abv.bg

University of Sofia "St. Kliment Ohridski," Faculty of Chemistry and Pharmacy, Department of Inorganic Chemistry, Sofia, Bulgaria

References

[1] Perednis D, Gauckler LJ. Thin film deposition using spray pyrolysis. J Electroceram. 2005;**14**:103–111.

[2] Grosso D. How to exploit the full potential of the dip-coating process to better control film formation. J Mater Chem. 2011;**21**:17033-17038. doi: 10.1039/C1JM12837J

[3] Ebert D, Bhushan B. Transparent, superhydrophobic, and wear-resistant coatings on glass and polymer substrates using SiO_2, ZnO, and ITO nanoparticles. Langmuir. 2012;**28:**11391–11399. doi: 10.1021/la301479c

[4] Yoon T-S, Oh J, Park S-H, Kim V, Jung BG, Min S-H, Park J, Hyeon T, Kim K-B. Single and multiple-step dip-coating of colloidal maghemite nanoparticles onto Si, Si_3N_4, and SiO_2 substrates. Advanced Functional Materials, 2004;**14**:1062-1068.

[5] Todorovsky D, Todorovska R, Petrova N, Uzunova-Bujnova M, Milanova M, Anastasova S, Kashchieva E, Groudeva-Zotova S. Spray-pyrolysis and deep- or spin-coating deposition of thin films and their characterization. J Univ Chem Technol Metallurgy. 2006;**41**:93–96.

[6] Brinker CJ, Frye GC, Hurd AJ, Ashley CS. Fundamentals of sol-gel dip coating. Thin Solid Films. 1991;**201**(1):97–108. doi:10.1016/0040-6090(91)90158-T

[7] Brinker CJ, Hurd AJ. Fundamentals of sol-gel dip-coating. J Phys III. 1994;**4**:1231–1242. doi:10.1051/jp3:1994198

[8] MacCraith B, McDonagh C. Enhanced fluorescence sensing using sol-gel materials. J Fluorescence. 2002;**12**:333–342. doi:10.1023/A:1021301723885

[9] McDonagh C, MacCraith BD, McEvoy AK. Tailoring of sol−gel films for optical sensing of oxygen in gas and aqueous phase. Analyt Chem. 1998;**70**:45–50. doi:10.1021/ac970461b

[10] Ahmad M, Mohammad N, Abdullah J. Sensing material for oxygen gas prepared by doping sol–gel film with tris (2,2-bipyridyl)dichlororuthenium complex. J Non-Cryst Solids. 2001;**290**:86–91. doi:10.1016/S0022-3093(01)00719-0

[11] Mills A, Williams F. Chemical influences on the luminescence of ruthenium diimine complexes and its response to oxygen. Thin Solid Films. 1997;**306**:163–170. doi:10.1016/S0040-6090(97)00246-0

[12] Lobnik A, Wolfbeis OJ. Probing the polarity of sol-gels and ormosils via the absorption of nile red. Sol–Gel Sci Technol. 2001;**20**:303–311. doi:10.1023/A:1008734320809

[13] McDonagh C, Bowe P, Mongey K, MacCraith BD. Characterisation of porosity and sensor response times of sol–gel-derived thin films for oxygen sensor applications. J Non-Cryst Solids. 2002;**306**:138–148. doi:10.1016/S0022-3093(02)01154-7

[14] McDonagh C, Shields AM, McEvoy AK, MacCraith BD, Gouin JF. Optical sol-gel-based dissolved oxygen sensor: progress towards a commercial instrument. J Sol–Gel Sci Technol. 1998;**13**:207–211. doi:10.1023/A:1008608901645

[15] McEvoy AK, McDonagh CM, MacCraith BD. Dissolved oxygen sensor based on fluorescence quenching of oxygen-sensitive ruthenium complexes immobilized in sol–gel-derived porous silica coatings. Analyst. 1996;**121**:785–788. doi:10.1039/AN9962100785

[16] McDonagh C, Sheridan F, Butler T, MacCraith BD. Characterisation of sol-gel-derived silica films. J Non-Cryst Solids. 1996;**194**:72–77. doi:10.1016/0022-3093(95)00488-2

[17] Tang Y, Tehan EC, Tao Z, Bright FV. Sol–gel-derived sensor materials that yield linear calibration plots, high sensitivity, and long-term stability. Analyt Chem. 2003;**75**:2407–2413. doi:10.1021/ac030087h

[18] Shang HM, Wang Y, Limmer SJ, Chou TP, Takahashi K, Cao GZ. Optically transparent superhydrophobic silica-based films. Thin Solid Films. 2005;**472**:37–43. doi:10.1016/j.tsf.2004.06.087

[19] Anastasova S, Milanova M, Kashchieva E, Funakubo H, Kamo T, Grozev N, Stefanov P, Todorovsky D. Morphology of sol-gel produced composite films for optical oxygen sensors. Appl Surf Sci. 2008;**254**:1545–1558. doi:10.1016/j.apsusc.2007.07.090

[20] Preininger C, Ludwig M, Mohr GJ. Effect of the sol-gel matrix on the performance of ammonia fluorosensors based on energy transfer. J Fluorescence. 1998;**8**:199–205. doi:10.1023/A:1022549531746

[21] Anastasova S, Milanova M, Rangelov S, Todorovsky D. Influence of the precursor nature and deposition mode on the oxygen sensing properties of Ru(II) complex immobilized in SiO_2-based matrix. J Non-Cryst Solids. 2008;**354**:4909–4916.DOI: 10.1016/j.jnoncrysol.2008.07.006

[22] Zaharieva J, Milanova M, Todorovsky D. Europium dibenzoylmethane complexes in SiO_2-based matrix. J Optoelectron Adv Mater. 2010;**12**:1247–1254.

[23] Hoffmann F, Cornelius M, Morell J, Froba M. Silica-based mesoporous organic–inorganic "hybrid" materials. Angew. Chem. Int. Ed. 2006;**45**:3216–3251

[24] Todorovsky DS, Getsova MM, Milanova MM, Kakihana M, Petrova NL, Arnaudov MG, Enchev VG. The chemistry of the processes involved in the production of lanthanide titanates by the polymerized complex method. Can J Chem. 2007;**85**:547–559. DOI: 10.1139/v07-067

[25] Zaharieva J, Milanova M, Todorovsky D. SiO2/polyester hybrid for immobilization of Ru(II) complex as optical gas-phase oxygen sensor. J Mater Chem. 2011;**21**:4893–4903. doi:10.1039/C0JM03169K

[26] Zaharieva J, Milanova M, Todorovsky D. Poly(methylmethacrylate) as immobilization matrix for Ru(II)-complex, a potential optical oxygen sensor. J Optoelectron Adv Mater. 2011;**13**:727–732.

[27] Zaharieva J, Milanova M, Todorovsky D. Synthesis conditions impact on the composition, structure, and fluorescence properties of the europium dibenzoylmethane complexes. Synth React Inorg Met Org Nano Met Chem. 2010;**40**:651–661.

[28] Zaharieva J, Milanova M, Todorovsky D. Poly-(methylmethacrylate) as immobilization matrix for europium-diketonates. Morphology and fluorescent properties. Appl Surf Sci. 2011;**257**:6858–6866.

[29] Dushkin C, Stoyanov S, Bojinova A, Rusev S. Dip coating apparatus for deposition of TiO_2 films. Ann Univ Sofia Fac Chim. 2006;**98–99**:73–82.

[30] Mitsuishi M, Kikuchi S, Miyashita T, Amao Y. Characterization of an ultrathin polymer optode and its application to temperature sensors based on luminescent europium complexes. J Mater Chem. 2003;**13**:2875–2879.

[31] Tyona MD. A theoretical study on spin coating technique. Adv Mater Res. 2013;**2**:195–208. doi: 10.12989/amr.2013.2.4.195

[32] Brinker CJ, Scherer GW, editors. Sol–gel Science, the Physics and Chemistry of Sol–Gel Processing. Boston: Academic Press; 1990.

[33] Hall DB, Underhill P, Torkelson JM. Spin coating of thin and ultrathin polymer films. Polym Eng Sci. 1998;**38**:2039. doi:10.1002/pen.10373

[34] Chen BT. Investigation of the solvent-evaporation effect on spin coating of thin films. Polym Eng Sci. 1983;**23**:399–403. doi:10.1002/pen.760230706

[35] Znaidi L, Illia GJAAS, Benyahi S, Sanchez C, Kanaev AV. Oriented ZnO thin films synthesis by sol–gel process for laser application. Thin Solid Films. 2003;**428**:257–262. DOI: 10.1016/S0040-6090(02)01219-1

[36] Scriven LE. Physics and applications of dip coating and spin coating. MRS Proc. 1988;**121**:717 DOI: 10.1557/PROC-121-71

[37] Chang YJ, Lee DH, Herman GS, Chang CH. High-performance spin-coated zinc tin oxide thin-film transistors. Electrochem Solid State Lett. 2007;**10**:H135–H138. doi:10.1149/1.2666588

[38] Amanuma K, Hase T, Miyasaka Y. Preparation and ferroelectric properties of SrBi2Ta2O9 thin films. Appl Phys Lett. 1995;**66**:221. DOI: 10.1063/1.113140

[39] Chung W, Sakai G, Shimanoe K, Miura N, Lee D, Yamazoe N. Preparation of indium oxide thin film by spin-coating method and its gas-sensing properties. Sens Actuat B: Chem. 1998;**46**:139–145. DOI: 10.1016/S0925-4005(98)00100-2

[40] Souza FL, Lopes KP, Nascente PAP, Leite ER. Nanostructured hematite thin films produced by spin-coating deposition solution: Application in water splitting. Solar Energy Mater Solar Cells. 2009;**93**:362–368. DOI: 10.1016/j.solmat.2008.11.049

[41] Natsume Y, Sakata H. Zinc oxide films prepared by sol-gel spin-coating. Thin Solid Films. 2000;**372**:30–36. DOI: 10.1016/S0040-6090(00)01056-7

[42] Ilican S, Caglar Y, Caglar M. Preparation and characterization of ZnO thin films deposited by sol-gel spin coating method. JOAM. 2008;**10**:2578–2583.

[43] Habibi MH, Sardashti MK. Structure and morphology of nanostructured zinc oxide thin films prepared by dip-vs. spin-coating methods. J Iran Chem Soc. 2008;**5**:603–609.

[44] Srinivasan G, Gopalakrishnan N, Yud Y, Kesavamoorthy R, Kumar J. Influence of post-deposition annealing on the structural and optical properties of ZnO thin films prepared

by sol–gel and spin-coating method. Superlattices Microstruct. 2008;**43**:112–119. DOI: 10.1016/j.spmi.2007.07.032

[45] Wang MC, Lin H, Yang TS. Characteristics and optical properties of iron ion (Fe3+)-doped titanium oxide thin films prepared by a sol–gel spin coating. J Alloys Compd. 2009; **473**:394–400. DOI: 10.1016/j.jallcom.2008.05.105

[46] Chen K, Lu Z, Ai N, Huang X, Zhang Y, Xin X, Zhu R, Su W. Development of yttria-stabilized zirconia thin films via slurry spin coating for intermediate-to-low temperature solid oxide fuel cells. J Power Sources. 2006;**160**:436–438. DOI: 10.1016/j.jpowsour.2006.01.079

[47] Nishiyama N, Tanaka S, Egashira Y, Oku Y, Ueyama K. Enhancement of structural stability of mesoporous silica thin films prepared by spin-coating. Chem Mater. 2002;**14**:4229–4234. doi:10.1021/cm0201246

[48] Messing GL, Zhang SC, Jayanthi GV. Ceramic powder synthesis by spray pyrolysis. J Am Ceram Soc. 1993;**76**:2707–2726. doi:10.1111/j.1151-2916.1993.tb04007.x

[49] Senthilnathan V, Ganesan S. Novel spray pyrolysis for dye-sensitized solar cell. J Renew Sust Energy. 2010;**2**:063102. doi:10.1063/1.3517228

[50] Milanova M, Koleva I, Todorovska R, Zaharieva J, Kostadinov M, Todorovsky D. Polymetallic citric complexes as precursors for spray-pyrolysis deposition of thin ferrite films. Appl Surf Sci. 2011:**257**:7821–7826.

[51] Milanova M, Zaharieva J, Todorovska R, Todorovsky D. Polymetallic citric complexes as precursors for spray-pyrolysis deposition of thin LaFeO3 films. Thin Solid Films. 2014;**562**:43–48.

[52] Uzunova-Bujnova M, Kralchevska R, Milanova M, Todorovska R, Hristov D, Todorovsky D. Crystal structure, morphology and photocatalytic activity of modified TiO2 and of spray-deposited TiO_2 films. Catal Today. 2010;**151**:14–20.

[53] Uzunova-Bujnova M, Todorovska R, Milanova M, Kralchevska R, Todorovsky D. On the spray-drying deposition of TiO_2 photocatalytic films. Appl Surf Sci. 2009;**256**:830–837.

[54] Todorovska R, Uzunova-Bujnova M, Milanova M, Todorovsky D. Spray-deposited TiO2 films for phenol destruction in water. Ann de l'Univ de Sofia "St. Kliment Ohridski", Faculte de Chimie. 2011:102/103:129–143.

[55] Nakaruk A, Reece PJ, Ragazzon D, Sorrell CC. TiO_2 films prepared by ultrasonic spray pyrolysis. Mater Sci Technol. 2010;**26**:469–472.

[56] Petrova N, Todorovska R, Milanova M, Todorovsky D. Spray-pyrolysis deposition of cerium-doped yttrium-iron garnet thin films. Asian Chem Lett. 2010;**14**:41–46.

[57] Perednis D, Wilhelm O, Pratsinis SE, Gauckler LJ. Morphology and deposition of thin yttria-stabilized zirconia films using spray pyrolysis. Thin Solid Films. 2005;**474**:84–95.

[58] Wilhelm O, Pratsinis SE, Perednis D, Gauckler LJ. Electrospray and pressurized spray deposition of yttria-stabilized zirconia films. Thin Solid Films. 2005;**479**:121–129.

[59] Akl Alaa A. Optical properties of crystalline and non-crystalline iron oxide thin films deposited by spray pyrolysis. Appl Surf Sci. 2004;**233**:307–319. DOI:10.1016/j.apsusc.2004.03.263

[60] Garcıa-Lobato MA, Hernandez VA, Garcıa HMH, Martınez AI, Pech-Canul MI. Fe2O3 thin films prepared by ultrasonic spray pyrolysis. Mater Sci Forum. 2010;**644**:105–108.

[61] Krunks M, Dedova T, Açik IO. Spray pyrolysis deposition of zinc oxide nanostructured layers. Thin Solid Films. 2006;**515**:1157–1160.

[62] Prasada Rao T, Santhoshkumar MC. Effect of thickness on structural, optical and electrical properties of nanostructured ZnO thin films by spray pyrolysis. Appl Surf Sci. 2009;**255**:4579–4584. doi:10.1016/j.apsusc.2008.11.079

[63] Martos M, Morales J, Sánchez L, Ayouchi R, Leinen D, F Martin, Barrado JRR. Electrochemical properties of lead oxide films obtained by spray pyrolysis as negative electrodes for lithium secondary batteries. Electrochim Acta. 2001;**46**:2939–2948. DOI:10.1016/S0013-4686(01)00512-6

[64] Kim SH, Liu BYH, Zachariah MR. Synthesis of nanoporous metal oxide particles by a new inorganic matrix spray pyrolysis method. Chem. Mater. 2002;**14**:2889–2899. doi:10.1021/cm010957g

[65] Medina DY, Orozco S, Hernandez I, Hernandez RT, Falcony C. Characterization of europium doped lanthanum oxide films prepared by spray pyrolysis. J Non-Crystal Solids. 2011;**357**:3740–3743. DOI: 10.1016/j.jnoncrysol.2011.07.021

[66] Chung W, Hong JY, Sun HP, Chun BH, Kim J, Sung HK. Spray pyrolysis synthesis of MAl2O4:Eu2+ (M = Ba, Sr) phosphor for UV LED excitation . J Cryst Growth. 2011;**326**:73–76. DOI: 10.1016/j.jcrysgro.2011.01.055

[67] Nakaruk A, Sorrell CC. Conceptual model for spray pyrolysis mechanism: fabrication and annealing of titania thin films. J Coat Technol Res. 2010;**7**: 665–676. doi:10.1007/s11998-010-9245-6

[68] Todorovsky DS, Todorovska RV, Milanova MM, Kovacheva D. Deposition and characterization of La2Ti2O7 thin films via spray pyrolysis process. Appl Surf Sci. 2007;**253**:4560–4565. DOI: 10.1016/j.apsusc.2006.10.016

[69] Todorovska, R V, Groudeva-Zotova S, Todorovsky DS. Spray pyrolysis deposition of α-Fe_2O_3 thin films using iron (III) citric complexes. Mat. Lett. 2002; **56**: 770-774. DOI: 10.1016/S0167-577X(02)00611-0

[70] Todorovska R, Petrova N, Todorovsky D. Spray-pyrolysis deposition of Y2O3 thin films using citric complexes as a starting material, Comptes Rendus de l'Academie Bulgare des Sciences. 2003;**56**:41–44.

Chapter 14

Silicon Oxycarbide Thin films and Nanostructures: Synthesis, Properties and Applications

Spyros Gallis, Vasileios Nikas and Alain E. Kaloyeros

Additional information is available at the end of the chapter

http://dx.doi.org/10.5772/66992

Abstract

Silicon oxycarbide (SiC_xO_y) has been extensively investigated due to its wide use in the Si semiconductor industry in applications that include low-k dielectrics, passivation layers, and etch-stop layers. Furthermore, SiC_xO_y research has been exploring its prospective use in numerous other technological usages, such as lighting, energy, and biological applications. The latter include white light-emitting materials, hydrogen storage materials, gas sensors, anode materials for lithium batteries, and biomedical devices. SiC_xO_y materials can intensively luminescence in a broad emission spectral range that spans the ultraviolet, the visible, and even the near-infrared spectrum, when doped with erbium. Herein, we present pertinent results on the material behaviors from chemically synthesized SiC_xO_y thin films and nanowires. Moreover, their light-emitting properties and underlying mechanisms for light emission are explored in conjunction with data from their thin film counterparts, which are also employed as baseline comparison metric. We further highlight major challenges and promises of such materials.

Keywords: silicon oxycarbide, SiC_xO_y, Si-O-C, Si-C-O, nanowires, thin films, luminescence, CVD, e-beam lithography, structural properties, optical properties, band tails, disorder

1. Introduction

In silicon (Si) complementary metal-oxide-semiconductor (CMOS) chip technology, silicon oxycarbide (SiC_xO_y) materials have been extensively employed to serve multiple purposes. For example, SiC_xO_y materials have been the focus of extensive study due to their applicability

as low-k dielectrics, passivation layers, and etch-stop layers to name a few [1, 2]. SiC_xO_y materials have also been the focus of studies due to their potential application in a plethora of other technological applications (e.g. light emission, energy, and bioapplications). In particular, they have been proposed as candidates for white light-emitting materials [3–5], filters, porous adsorbents, and catalytic supports [6, 7], as hydrogen storage materials [8], gas sensors [9], negative electrode materials for lithium batteries [10, 11], and in biomedical devices [12]. Additionally, it has been also shown that SiC_xO_y can be utilized as a host material to optically active impurities (rare earth ions). To this end, europium (Eu^{2+})-doped SiC_xO_y thin films synthetized by RF magnetron sputtering [13] as well as erbium (Er^{3+})-doped SiC_xO_y thin films for near-infrared (IR) emission at the commercially useful telecommunication wavelength of 1540 nm have been recently reported [14–16].

The fabrication of luminescent Si-based nanostructured materials for light emission applications is highly desirable, similarly to how Si-based nanophotonics has undergone great advancements in recent years [17, 18]. Due to the seamless integration of Si-based materials with process protocols and technologies developed for semiconductor CMOS technology, manufacturing costs and process complexity could be also reduced. Furthermore, the extreme down-scaling methods achieved by CMOS technology offer the opportunity to study new compelling properties owing to possible confinement effects in one (1D) or two (2D) dimensions (e.g., the reduction of exciton-phonon interactions, the increase of extraction efficiency of spontaneous emission, and suppression of Auger recombination) [19, 20]. Therefore, the functionality of such nanostructured materials and their devices can be employed in a ubiquitous way in light emission applications [21]. To this extent, SiC_xO_y nanowires (NWs) have been recently shown to exhibit strong room-temperature visible luminescence [22–24].

In parallel, the identification and elimination of potential obstacles that could deteriorate the luminescence efficiency of such materials (e.g., temperature and excitation power density) needs to be taken into consideration. Indeed, the luminescence efficiency is known to be influenced by environmental fluctuations in temperature and pump-power-density changes [25, 26]. These fluctuations can become critical in luminescence applications such as light-emitting diodes (LEDs). In these applications, the operating temperature and power density can reach respectively ~150°C and ~200 W/cm^2, thus greatly influencing the light output and color chromaticity.

Silicon oxycarbide films have been grown predominantly through low-temperature plasma-enhanced chemical vapor deposition (PECVD) using an array of silane-based precursors for the needs of semiconductor industry [27–30]. However, the incorporation of source precursor fragments and decomposition byproducts in the resulting films has led to the observation of enhanced stress levels and increased defect density, both of which have detrimental effects on the optical performance of resulting materials and device structures. Recently, Lin et al. prepared amorphous SiC_xO_y using a very high-frequency plasma-enhanced chemical vapor deposition (VHF-PECVD) technique [31]. The resulting films exhibited intense room-temperature blue luminescence, characteristic of Si-related neutral oxygen vacancy defect centers. Ryan et al. and Vasin et al. showed that a wide variety of SiC_xO_y with a continuous range of compositions could be produced by reactive RF-magnetron sputtering [32, 33]. Karakuscu et al. and Abbass et al. have reported sol-gel-prepared SiC_xO_y thin films [34, 35], while Vasin

et al. have reported a-SiC_xO_y:H thin films growth by low-temperature oxidation of carbon-rich a-Si_xC_y:H thin films [36].

Nevertheless, it is desirable to identify alternative deposition methods, which can inhibit or minimize processing induced structural and/or compositional damage to SiC_xO_y materials due to phase separation owing to the non-stoichiometric composition. Herein, key findings are summarized pertaining to the development of a thermal chemical vapor deposition (TCVD) strategy for the growth of SiC_xO_y thin films approximating the $SiC_xO_{2(1-x)}$ ($0 < x < 1$) stoichiometry for light emission applications [37, 38]. These studies led to the identification of a deposition process window for the growth of SiC_xO_y thin films with strong room-temperature light emission [3]. Additionally, we present the findings pertaining to room-temperature visible photoluminescence (PL) from SiC_xO_y sub-100-nm nanowire materials fabricated by electron beam lithography (EBL) and reactive ion etching (RIE). These metal-free non-toxic Si-based nanostructured materials may offer an alternative and environmentally friendly pathway toward efficient visible light-emitting materials and devices.

2. Synthesis and fabrication of silicon oxycarbide thin films and nanostructures

2.1. SiC_xO_y materials grown by thermal chemical vapor deposition: composition control

SiC_xO_y thin films and their nanostructures are deposited on Si(100) or SiO_2 substrates in a hot-wall quartz tube reactor by thermal CVD at 800°C. A single source oligomer (2,4,6-trimethyl-2,4,6-trisila-heptane ($C_7H_{22}Si_3$)) is utilized as the source precursor for silicon and carbon atoms and ultra-high purity oxygen (O_2) and argon (Ar)/nitrogen (N_2) are also employed as co-reactant and dilution gases. The composition of the resulting amorphous $SiC_xO_{y\leq1.73}$ ($0.11 < x < 0.65$) thin films is regulated by modifying the oxygen flow rate and, hence, the oxygen partial pressure in the reaction zone. The films are deposited onto three types of substrates: single-crystal silicon (c-Si) (100), for composition, structural and optical analysis; double-polished intrinsic Si and high-quality UV transparent fused silica, for infrared and optical studies. A subset of the as-deposited SiC_xO_y films was annealed for 1 h in different ambient (e.g., O_2, Ar, N_2, or forming gas (FG, 5% H_2 and 95% N_2)) at temperatures in the range from 500 to 1100°C. Detailed description of the deposition and annealing processes can be found elsewhere [37, 38]. The resulting samples were subsequently employed in a comparative analysis of as-deposited and post-annealed films to determine the effects of thermal treatment on film structural and optical properties as well as their photoluminescence performance.

Rutherford backscattering spectroscopy (RBS) and X-ray photoelectron spectroscopy (XPS) were employed to determine the Si, C, and O content in the SiC_xO_y materials and they were separated in three different classes, defined by their composition: SiC-like ([O] < 5 at.%), Si-C-O, and SiO_2-like ([C] < 5 at.%). The compositional evolution of the SiC_xO_y thin films was plotted in the Si-C-O ternary diagram of **Figure 1a** along with the $SiC_xO_{2(1-x)}$ ($0 < x < 1$) line, with the latter representing stoichiometric silicon oxycarbide without any excess of carbon. The upper and lower limits in $SiC_xO_{2(1-x)}$ correspond to SiC and SiO_2, for, respectively, $x = 1$ and 0 [39, 40].

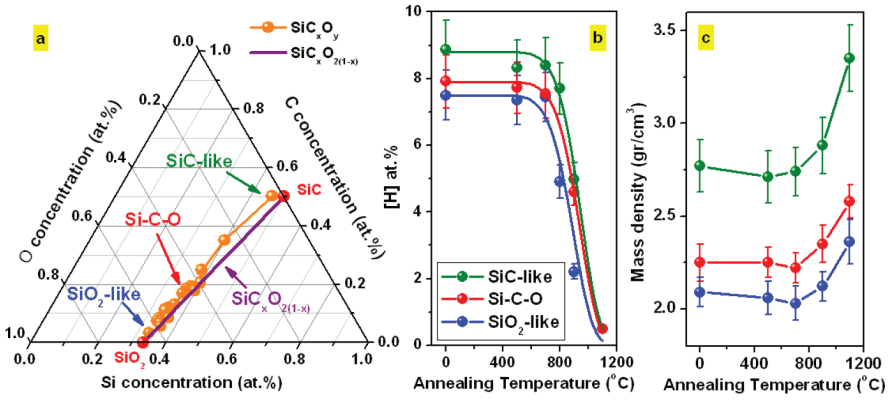

Figure 1. (a) Si-C-O ternary diagram with the compositions of as-deposited (AD) silicon oxycarbide (SiC_xO_y) materials, (b) NRA hydrogen depth profiles of the as-deposited SiC_xO_y and (c) mass density of $SiC_xO_yH_z$ films [22, 37].

As is shown in **Figure 1a**, the composition of the thermal CVD-grown SiC_xO_y was properly tailored to closely follow the pure stoichiometric oxycarbide formula over the whole range of the synthesis process parameters. The $SiC_xO_{2(1-x)}$ behavior observed in the samples produced herein suggests the substitution of two divalent oxygen atoms by one tetravalent carbon atom as the C concentration in the SiC_xO_y materials increases. The latter will be further discussed in Section 3.1. Furthermore, the observed small deviation from the stoichiometric $SiC_xO_{2(1-x)}$ trend suggests that there is much less excess of C compared to non-stoichiometric compositions reported for SiC_xO_y with SiC/SiO_2 phases and free carbon, as it is shown in **Figure 1** of reference [39].

Due to the presence of methyl groups in the CVD reactants, it is expected to have hydrogen atoms in the grown silicon oxycarbide thin films whose concentration cannot be quantified by the RBS or XPS techniques. Instead, the nuclear reaction analysis (NRA) was conducted by using the $^{15}N + {}^{1}H \rightarrow {}^{12}C + {}^{4}He + \gamma$-ray resonant nuclear reaction at 6.835 MeV [41]. **Figure 1b** shows the NRA-derived hydrogen concentration measurements of the silicon oxycarbide films as a function of post-deposition annealing temperature T_a [37]. After the 900°C annealing step, the hydrogen content is significantly reduced to 5, 2.2, and 4.5 at.%, respectively, for the SiC-like, Si-C-O, and SiO_2-like samples. For annealing temperatures above 1000°C, the hydrogen content was not detectable (>1 at.%) in all three different types of samples.

The mass density ρ (g/cm^3) of thin films was calculated using the elemental compositions determined by RBS and XPS and the thicknesses measured by scanning electron microscope (SEM) by employing the following equation:

$$\rho = \frac{D \times 10^{15}}{d} \times 1.66 \times 10^{-24} \frac{(A_{Si} + xA_C + yA_O + zA_H)}{(1 + x + y + z)} \quad (\mathrm{gr/cm^3}) \tag{1}$$

where D is the thickness in rump units, which is related to the planar density, d is the film thickness, A_{Si}, A_C, A_O, and A_H are the atomic weights of Si, C, O, and H, respectively, and x, y, and z are the normalized fractional contents, respectively, of C, O, and H.

http://dx.doi.org/10.5772/66992

The density of the silicon oxycarbide films was observed to increase with higher annealing temperature, due at least partly to the reduction in hydrogen concentration, as shown in **Figure 1c**. More specifically, the densities of the as-deposited films are 2.8, 2.2, and 2.1 for, respectively, SiC-like, Si-C-O, and SiO_2-like films. After annealing at 1100°C, the densities were measured to be significantly higher, with values of 3.3, 2.6, and 2.4 g/cm^3 for, respectively, SiC-like, Si-C-O, and SiO_2-like films.

2.2. Nanofabrication of silicon oxycarbide nanostructures

SiC_xO_y nanostructured systems were fabricated by electron beam lithography and reactive ion etching, namely periodically ordered sub-100-nm nanowire arrays. A representation of the baseline nanofabrication scheme of the SiC_xO_y NW arrays is schematically depicted in **Figure 2**. Following the synthesis of SiC_xO_y thin films, negative hydrogen silsesquioxane (HSQ) (6% HSQ in methyl-isobutyl-ketone solvent) resist is spun onto SiC_xO_y wafer pieces—deposited on Si (100)—at 1000 rpm, followed by a bake procedure for 4 min at 80°C. Line patterns are exposed using electron beam lithography and then the resulting wafer piece is developed in a chemical solution bath (low concentration (2.38%) of tetramethylammonium hydroxide (TMAH) developer), yielding 2D-nanowire HSQ patterns. The HSQ patterns then underwent a hardening annealing process in Ar/N_2 ambient at 500°C, followed by a fluorine-based (e.g., combination of CHF_3 and CF_4 gases) anisotropic RIE to transfer the pattern into the SiC_xO_y thin films. The HSQ residue is then removed by wet etching in buffered hydrofluoric (BHF) acid, resulting in periodically well-defined NWs [22].

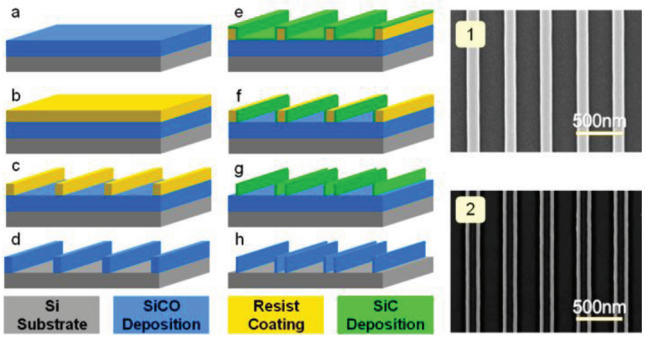

Figure 2. (a–d) Fabrication steps of the SiC_xO_y nanowires (NW) using lithography and RIE. The final NW arrays are shown in SEM image 1 and (e–h) fabrication steps of the SiC_xO_y nanowire (NW) arrays using the SIT method by SiC conformal deposition on the resist followed by RIE to open the SiC top layer, wet etch to remove the resist, and RIE. The final NW arrays made by SIT are shown in SEM image 2.

Pertaining to the NW fabrication, certain samples underwent a sidewall image transfer (SIT) process which was performed by conformal deposition of a thin silicon carbide (SiC) hard mask (sidewall layer) on the patterned photoresist followed by anisotropic RIE [23]. This allowed for a significant reduction of the critical dimensions as, during the SIT process, the NW width is defined by the thickness of the SiC layer rather than the resolution of the

lithography step. The SiC_xO_y NWs underwent different post-fabrication thermal treatments for up to 2 h at annealing temperatures in the range of 50–700°C in Ar, O_2, or forming gas (5% H_2 and 95% N_2) atmospheres.

3. Bonding configuration of silicon oxycarbide materials and nanowires

3.1. Fourier transform infrared spectroscopy (FTIR) characterization of silicon oxycarbide thin films

Figure 3a shows the Fourier transform infrared spectroscopy (FTIR) data of SiC_xO_y thin films in the 400–1700-cm^{-1} range. The spectra are characterized by three absorption bands and a shoulder assigned to the Si-O-C rocking, Si-C stretching, and Si-O transverse and longitudinal-stretching vibration modes, centered at, respectively, ~440, ~800, ~1000, and ~1150 cm^{-1} [22, 37, 38].

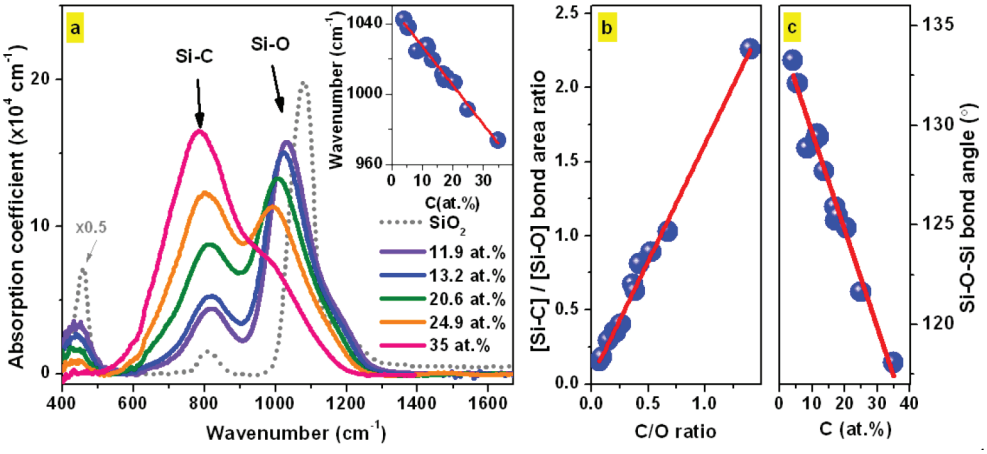

Figure 3. (a) The FTIR absorption spectra of the AD SiC_xO_y and SiO_2 control in the 400–1700 cm^{-1} range. The peak positions of the AD SiC_xO_y appear red-shifted compared to the SiO_2 control, due to the incorporation of less electronegative C, (b) the [Si-C]/[Si-O] bond-area ratio plotted as a function of the C/O content ratio showing a linear increase with increasing C/O and (c) the Si-O-Si bond angle of the bridging O atom in the SiC_xO_y [22].

More specifically, the Si-O-C vibration mode (~440 cm^{-1}) is caused by the ≡Si-O-Si≡ rocking mode due to out-of-plane motion of O in $O_{(3-x)}C_x$≡Si-O-Si≡$C_yO_{(3-y)}$ and is unaffected by the Si-O-Si-bridging bond-angle variation [42–45]. For samples with C content higher than 20 at.%, the density of ≡Si-O-Si≡-bonding groups decreased significantly, as dictated by the $SiC_xO_{2(1-x)}$ stoichiometry, suggesting that the backbone-bonding network related to the SiO_4 tetrahedral in SiC_xO_y changed toward SiC-like structures with significant presence of SiC_4 tetrahedral. The replacement of O atoms by C atoms with increasing C content in films is reflected in the monotonic increase of the bond area ratio of [Si-C] and [Si-O] as clearly depicted in **Figure 3b**.

http://dx.doi.org/10.5772/66992

Additionally, incorporation of the less electronegative C atoms leads to a reduced Si-O-Si bond angle between tetrahedral (see **Figure 3c**) [30, 44]. As a result, the density of the as-grown films is expected to increase with increasing C content, which is in agreement with the density values shown in Section 2.

Figure 4 displays the FTIR spectra collected in the range from 400 to 2300 cm^{-1} for the three classes of as-deposited silicon oxycarbide materials and for their annealed counterparts at 900 and 1100°C [37].

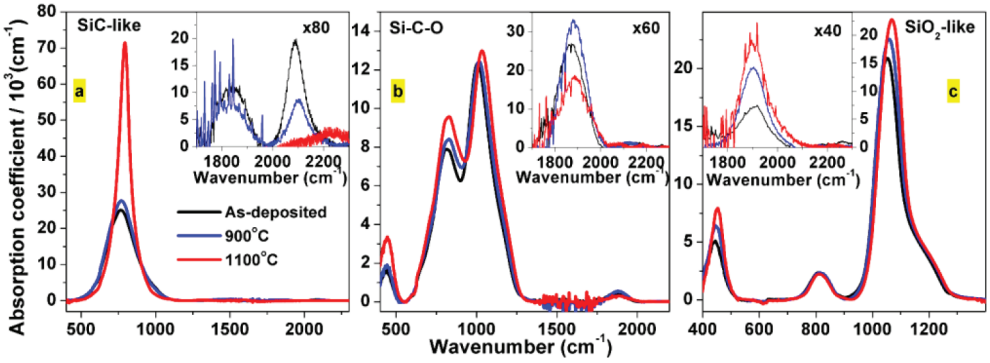

Figure 4. IR absorption spectra for the as-deposited, 900°C-, and 1100°C- annealed (a) SiC-like, (b) Si-C-O, and (c) SiO_2-like samples [37].

Deconvolution of the FTIR spectra reveals several bonding components in the as-deposited SiC_xO_y material systems [30, 37, 45, 46]. In particular, the deconvolution of the absorption bands in the range of 400–1400 cm^{-1} for the SiC-like film indicates the presence of a weak C-H mode at ~530 cm^{-1}, a major Si-C-stretching absorption mode at ~764 cm^{-1}, and a shoulder assigned to the Si-O-stretching mode at ~960 cm^{-1}. The hydrogen-related absorption bands (Si-H and C-H) are located at ~2100 and 2900 cm^{-1}, respectively. Finally, the absorption observed at ~1846 cm^{-1} is attributed to a C-O-stretching mode.

As seen in **Figure 4b**, the IR spectrum of Si-C-O film has three characteristic absorption band regions, originating from the Si-C and Si-O functional groups [37]. In comparison to the SiC-like matrix films, a new absorption peak is seen at ~440 cm^{-1}, attributed to the Si-O-C vibration mode discussed above. The IR region from 600 to 1300 cm^{-1} is broader compared to that in the SiC-like films, and its deconvolution shows the presence of four peaks centered at 663, 816, 1002, and 1114 cm^{-1} attributed to Si-C-H, Si-C stretching, and to the transverse optical (TO) and longitudinal optical (LO) asymmetric Si-O-stretching modes, respectively. Compared to the SiC-like films, the position of the Si-C absorption peak shifted from 764 to 816 cm^{-1}, owing to the addition of more electronegative O atoms in the network [47].

The FTIR absorption spectrum of the SiO_2-like film is characterized by an intense Si-O-Si mode (rocking), centered at ~440 cm^{-1}: a Si-O mode (bending) located at ~815 cm^{-1}, and an intense Si-O vibration mode (stretching) at ~1100 cm^{-1}. The hydrogen-related vibration modes for C-H and O-H are observed at, respectively, ~2900 cm^{-1} and in the 3100–3700-cm^{-1} range.

The findings outlined above describe the evolution of the as-deposited films from silicon carbide-like to silicon dioxide-like films as the amount of C decreases. Regarding the annealed samples up to 700°C, the IR absorption behavior remains similar to the case of their as-deposited counterparts, and it is worth mentioning that changes took place at annealing temperatures beyond 900°C [44–46].

In the case of the SiC-like sample annealed at 900°C (**Figure 4a**), the Si-C- and Si-O-stretching modes show minor changes. However, both hydrogen-related modes appear with reduced intensities, as expected from the NRA results shown in **Figure 1b**. After the 1100°C annealing, the Si-C absorption band increased drastically in intensity and its line shape changed from Gaussian to mix of Gaussian and Lorentzian, suggesting the presence of longer-range order (Lorentzian). Additionally, all hydrogen-related vibration modes are no longer present in the films owing to hydrogen desorption.

Similarly, for the 900°C-annealed Si-C-O a small intensity increase of the Si-C-stretching mode was observed, while further annealing at 1100°C led to an overall absorption intensity increase accompanied with a blue shift of the Si-O stretching (**Figure 4b**). Finally, the annealing studies on the SiO_2-like material (**Figure 4c**) revealed a significant intensity increase of the Si-O-Si-rocking and the Si-O-stretching modes.

The bond density is directly proportional to the area of the IR band absorption, and can be estimated as in reference [37] using the inverse absorption cross section found in literature (3×10^{19} cm^{-2} for Si-C [48], 1.4×10^{20} cm^{-2} for Si-H [49], and 1.35×10^{21} cm^{-2} for C-H [50, 51]). The Si-C bond density for the as-deposited SiC-like sample is ~2.2×10^{23} cm^{-3} while for the as-deposited Si-C-O sample is ~5.5×10^{22} cm^{-3}. The dependence of Si-C bond density with annealing temperature for both SiC-like and Si-C-O is presented in **Figure 5a**. It shows a constant concentration up to 700°C annealing temperature. At higher temperatures, the Si-C bond concentration increases owing to the densification of the materials and hydrogen desorption, which contributes to the increased availability of Si and C atoms formerly bonded to hydrogen. Indeed, as seen in **Figure 5b**, the bond density of the Si-H and C-H bonds decreases with annealing temperature $T_a \geq 900$°C for both classes of materials.

As shown in **Figure 5c**, the total concentration of hydrogen atoms as determined by the NRA measurements is greater than the total content of hydrogen as calculated by FTIR. Each H-related bond corresponds to one H atom; therefore, the H-related bond density corresponds to the H atomic density. The total atomic density is determined by RBS measurements. This finding suggests that some H atoms are incorporated during CVD growth and are not chemically bound to other elements. These non-bonded H atoms may be present in the form of molecular hydrogen formed during the decomposition of the precursor [37].

3.2. FTIR characterization of silicon oxycarbide nanowires

Large SiC_xO_y NW structures were fabricated on intrinsic Si substrates in order to perform bonding configuration analysis [22]. The normalized absorbance FTIR spectra of both the as-deposited $SiC_{0.34}O_{1.52}$ thin film and the as-fabricated NWs are shown in **Figure 6**. It was found that the bonding configuration of the $SiC_{0.34}O_{1.52}$ NW system was maintained after nanofabrication as the relative intensities of Si-C and Si-O absorption bands remained the

http://dx.doi.org/10.5772/66992

same with respect to the as-deposited thin film. A slight absorption increase of the Si-O shoulder at ~1200 cm^{-1} may be due to surface oxidation induced on the as-synthesized NWs.

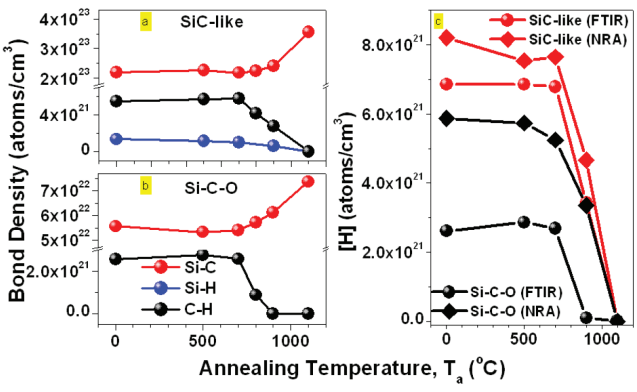

Figure 5. (a) Bond density of Si-C, Si-H, and C-H bonds as a function of annealing temperature for the SiC-like films, (b) bond density of Si-C and C-H bonds as a function of annealing temperature for the Si-C-O films and (c) total atomic concentration of H, as obtained by means of NRA and FTIR for the SiC-like and Si-C-O samples [37].

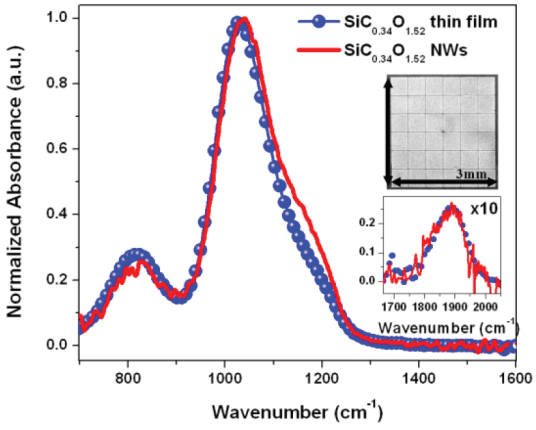

Figure 6. FTIR absorbance spectra of $SiC_{0.34}O_{1.52}$ thin film and its 70-nm-width NW array counterpart. Upper inset: SEM image of the NW array used for FTIR measurements (36 blocks of 490 × 490 μm^2 NW arrays). Lower inset: The conservation of the structural characteristics is also observed in the C=O vibration mode at ~1900 cm^{-1}, which remained unchanged [22].

3.3. XPS characterization of silicon oxycarbide thin films

The information about the bonding configuration in silicon oxycarbide thin films extracted by the means of FTIR analysis was also independently assessed by XPS studies [37]. The XPS analysis focused on examining the electronic environment (chemical bonding) of the Si 2p, C 1s, and O 1s core energy.

In the case of the as-deposited samples, the Si 2p spectrum of the SiC-like matrix (**Figure 7**) is composed of a center peak at 100.3 eV assigned to Si-C bonds and two shoulders centered at 99.2 and 101.2 eV assigned to Si-H- and Si-C-O-type bonding [37, 52]. In the case of the Si-C-O material, the Si 2p peak broadened and shifted to higher binding energies. The peak deconvolution showed the presence of three components centered at 100.8, 102.1, and 103.2 eV which are attributed to the Si-C, Si-C-O, and Si-O bonds, respectively [37, 46, 52]. This result agrees with the FTIR findings where, for both Si-C- and Si-O-stretching modes, the vibration frequencies increased with increasing O content (incorporation of more electronegative atom).

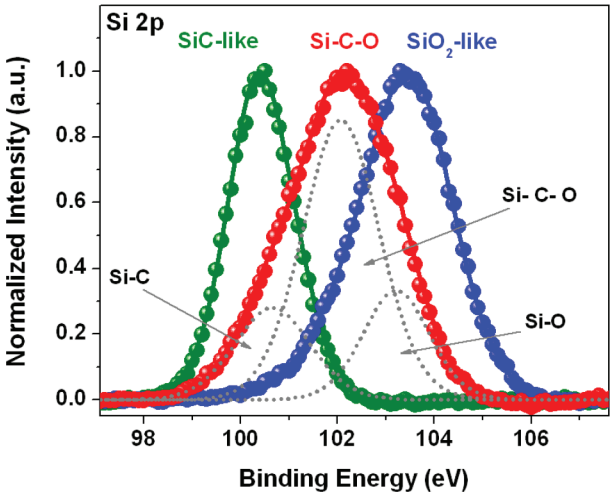

Figure 7. XPS spectra of the Si 2p peaks for the as-deposited SiC-like, Si-C-O and SiO_2-like samples [37].

In the case of the as-deposited SiO_2-like material, the Si 2p spectrum shifted to even higher binding energy and yielded two peaks centered at 102.3 and 103.5 eV which are related to two different Si-O electronic configurations [37, 53, 54].

4. Optical properties of silicon oxycarbide materials

The structural evolution of the as-deposited silicon oxycarbide materials along the $SiC_xO_{2(1-x)}$ stoichiometry was also reflected in their optical properties. The evolution of the index of refraction and the optical gap as a function of the C content of the materials and upon annealing treatments will be addressed in the following subsections.

4.1. Refractive index

The refractive index (n) of SiC_xO_y is found to exhibit a linear relationship with increasing the [Si-C]/[Si-O] bond area ratio (**Figure 8a**). The linear increase of n versus [Si-C]/[Si-O] over the

http://dx.doi.org/10.5772/66992

range analyzed is found to be partly associated with an increase of mass density in SiC_xO_y with increasing [Si-C]/[Si-O] [37]. To understand this behavior, someone can correlate the refractive index (n) or the dielectric constant ($\varepsilon = n^2$) with the structural parameters through the Lorentz-Lorenz (L-L) equation [55].

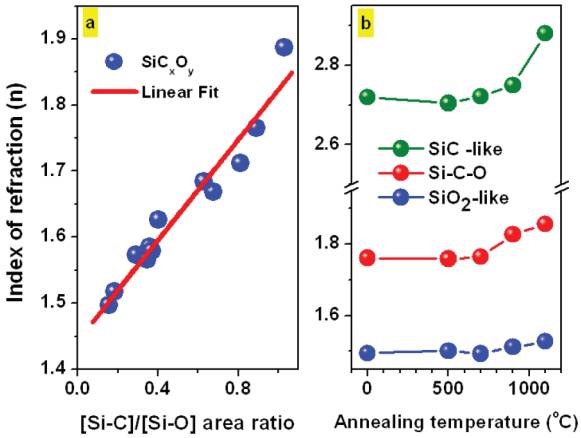

Figure 8. (a) The index of refraction at 800 nm of different SiC_xO_y given as a function of the [Si-C]/[Si-O] bond-area ratio. The solid line is the linear fit of the displayed data and (b) plot of index of refraction (n) at 800 nm as a function of annealing temperature [22, 37].

The FTIR measurements in **Figure 3** show a decrease in the Si-O-Si bond angle with C addition, which is expected considering the difference in the electronegativity between C and O. The mass density and Si atomic content (Si atoms possess higher electronic polarizability than O) of samples with higher carbon concentration is larger as opposed to SiO_2-like samples [56]. It is therefore suggested that the increased index of refraction with increasing [Si-C]/[Si-O] ratio is due to the variations in bond angles, larger mass density, and higher Si content. Further increase of the refractive index of all three classes of silicon oxycarbide materials is also observed upon post-deposition annealing beyond 900°C (**Figure 8b**). This behavior is expected considering the densification of SiC_xO_y materials upon annealing as shown in **Figure 1c** [22, 37].

4.2. Optical gap

The observed increase in the refractive index n, as C concentration increases along the $SiC_xO_{2(1-x)}$ stoichiometry, correlates well with the decrease in the optical gap of the films. For example, the E_{04} gap, which corresponds to the energy where the absorption coefficient (α) is equal to 10^4 cm^{-1} ($\alpha(E_{04})= 10^4$ cm^{-1}), is found to decrease with increasing [Si-C]/[Si-O] ratio (**Figure 9a**). The Tauc optical gaps, E_g, were also calculated from the optical absorption measurements using Tauc's law, $(\alpha h\nu)^{1/2} = B^{1/2}(h\nu\text{-}E_g)$, where α is the absorption coefficient and $h\nu$ is the photon energy [38].

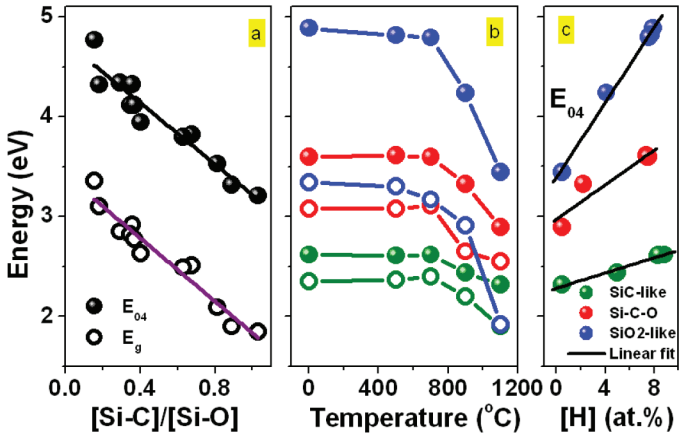

Figure 9. (a) E_{04} and E_g energy values for different SiC_xO_y materials versus the [Si-C]/[Si-O] bond-area ratio, (b) E_{04} (spheres) and E_g (circles) values with annealing temperature and (c) E_{04} values as a function of H content in the films [22, 37].

Similar to E_{04}, the E_g values decrease with increasing [Si-C]/[Si-O]. This behavior can be explained by considering the larger splitting energy difference between the bonding and anti-bonding electronic states in Si-O bonds in comparison to Si-C bonds [22, 38, 57].

In addition, as seen in **Figure 9a**, E_{04} values are generally higher than their E_g counterparts, similar to other hydrogenated disordered systems [58]. This could be explained by taking into account that Tauc's optical gap refers to the optical transitions between extended states close to the band edge, while E_{04} is related to transitions of the extended states away from the band edge [38, 58].

As seen in **Figure 9b**, both the E_{04} and E_g gaps decrease with increasing annealing temperature. It is worth mentioning that the decrease in the optical gap is more pronounced in the films with higher O concentration. For example, the decrease of the Tauc gap values between the as-deposited and post-1100°C annealed films are ~0.5, ~0.6, and ~1.4 eV for, respectively, the SiC-like, Si-C-O, and SiO_2-like classes of SiC_xO_y. It is suspected that the possible precipitation of carbon in the high O-containing systems could be responsible for this phenomenon at high annealing temperatures. The Si-C bond length (~1.88 Å) is longer than the Si-O bond length (~1.63 Å). Consequently, a high degree of strain may accumulate in the Si-C sites within the SiO_2 network (e.g., in the SiO_2-like sample with <5 at.% C). Thermal annealing may result in strain relaxation, with the subsequent structural rearrangements perhaps favoring the formation of carbon clusters, as reported in a previous study [59]. Their optical gap values may vary between ~0.6 and 3 eV, depending on the cluster size [58, 60]. Consequently, it would be expected that the precipitation of carbon in O-rich samples (e.g., SiO_2-like) could be relatively facile, with the optical gap in these samples decreasing more rapidly with increased annealing temperatures.

Furthermore, the decrease in optical gap with increased annealing temperatures seems to correlate well with the loss of hydrogen. As seen in **Figure 9c**, hydrogen reduction is accompanied by

http://dx.doi.org/10.5772/66992

a decrease in the energy band gap in the annealed SiC_xO_y films. The presence of Si-H bonds (~2000 cm^{-1}) can be an indication of dangling-bond passivation in the material, while the presence of other hydrogen-bonding configurations may be responsible for forming recombination centers and increasing the degree of structural disorder [61, 62].

In the as-deposited high C content samples, the Si-H_n stretching mode is found at ~2100 cm^{-1} (insets of **Figure 4**(**a**–**c**)). These peaks are attributed to Si-H-related bonds [63, 64]. Considering the absence of any Si-H_n bonding (2000–2200 cm^{-1}) in the Si-C-O- and SiO_2-like samples, it is suggested that any dangling bonds in the films remained unsaturated, resulting in enhanced structural disorder. Furthermore, hydrogen desorption upon annealing would likely contribute to the formation of additional dangling bonds and defect states, which lead to the increased density of localized states below the mobility edge, thereby decreasing the optical gap. This mechanism seems to be taking place in all thermally grown CVD SiC_xO_y films in this study.

4.3. Structural disorder and dangling bonds

Regarding the electronic structure of amorphous materials, it is common to expect the presence of band-tail states and localized defect states. These states exist due to the structural disorder in materials and may have a significant effect on the material's performance even at low concentrations. Therefore, it is important to elaborate on the degree and impact of structural disorder in the CVD-grown SiC_xO_y systems.

As it was discussed earlier, thermal annealing causes lowering of the optical gap owing to the increased optical absorption observed in the SiC_xO_y materials grown by CVD. The latter is true even at photon energies well below the optical gaps. The enhanced sub-band-gap absorption is a result of an increased density of band-tail states and localized defect states [31]. One of the proposed mechanisms responsible for the increased density of band-tail states upon annealing is the annealing-induced enhanced bond-angle disorder due to structural reconfiguration and/or strain relaxation [65]. In this context, the FTIR full-width half maximum (FWHM) values for both the Si-O- and Si-C-stretching modes in the TCVD SiC_xO_y films, with the exception of the 1100°C-annealed SiC-like sample, increased after annealing, suggesting that thermal treatments indeed enhance bond-angle distortion (see **Figure 4**(**b** and **c**)).

In the case of SiC-like material annealed at 1100°C, the FTIR spectrum shown in **Figure 4a** suggests that a significant amount of crystallization takes place resulting in the Lorentzian line shape of the infrared absorption band. This suggests that the bond-angle disorder is dramatically reduced. However, the optical absorption for the SiC-like films annealed at 1100°C is further increased compared to its as-deposited counterparts [38]. This suggests that, in addition to bond-angle variation, a different type of disorder is also present. Such behavior is known for amorphous covalent materials where both topological and compositional disorders are present simultaneously [66].

Furthermore, the deviation of the CVD-grown SiC_xO_y films from the purely stoichiometric $SiC_xO_{2(1-x)}$ shown in the ternary diagram of **Figure 1** suggests that there is a small excess of carbon that can form homonuclear bonds upon annealing. Also, this deviation increases for

high C concentration materials, toward the SiC-like class regime. The electronic states associated with the homonuclear bonds would exist as localized states within the gap due to their relatively weak bond strength [67, 68].

In this context, electron paramagnetic resonance (EPR) studies on SiC_xO_y materials, grown by CVD, showed the presence of unpaired electrons (dangling bonds) [5]. The same study proposed that one of the major EPR signals may be originated from $(\equiv Si\text{-})_3C^{\bullet}$ radicals or associated defects with different backbone atoms bonded to C atom, such as in C-Si-O configuration [69]. The $SiC_xO_{2(1-x)}$ stoichiometry trend of SiC_xO_y ($SiC_xO_{2(1-x)}$) suggests that two divalent oxygen atoms are replaced by one tetravalent C, further supporting the presence of $(\equiv Si\text{-})_3C^{\bullet}$ radicals in our films, originating from oxygen incorporation into $(\equiv Si\text{-})_4C$ structures. Consequently, the density of such radicals is expected to increase following thermal oxidation of $(\equiv Si\text{-})_{4-n}CH_n$ groups, as it was observed, which have not been completely dehydrated during the film deposition [70]. Similarly, the oxidation of $(\equiv Si\text{-})_{4-n}CH_n$ groups with one or two back-bonded C atoms to Si may also lead to an increased density of Si-dangling bonds in SiC_xO_y. Such dangling bonds may also contribute to the formation of band-tail states in SiC_xO_y [5].

5. Photoluminescence properties of silicon oxycarbide thin films and nanowires

5.1. Visible luminescence emission from SiC_xO_y thin films

The room-temperature photoluminescence spectra for SiC_xO_y samples with different C concentrations under excitation at 300 nm are shown in **Figure 10a**. The spectra are characterized by a broad emission in the whole visible range (350–800 nm). The photoluminescence excitation (PLE) intensity (**Figure 10b**) shows the presence of a shoulder at low excitation energies (<3.5 eV) and a steep increase at high excitation energies (>~3.7 eV). This was fit linearly and the intercept of the fitted line at the photon energy abscissa was taken as the *PLE edge*. As shown in **Figure 10c**, a strong correlation was observed between the values of E_{04} and the PLE edge, suggesting that the PL emission energy in the SiC_xO_y samples may be related to their optical gap [5].

Based on optical, FTIR characterizations, passivation experiments and electron paramagnetic resonance measurements, defect-related mechanisms and small sp^2-carbon clusters that could be attributed to white luminescence from SiC_xO_y thin films were excluded [3, 5]. For example, structural defects typical seen with EPR measurements in silicon oxides, which cannot be explicitly controlled by material processing and are not directly related to the stoichiometry and material characteristics, such as Si-related neutral oxygen vacancies or non-bridging oxygen-hole centers, were ruled out. Instead, the observed intense white luminescence originates from the recombination of photogenerated carriers between the energy bands and at their tail states associated with the Si-O-C/Si-C bonds, as indicated by the direct correlation between the integrated luminescence intensity and the Si-O-C bond density (see **Figure 11**) [3].

http://dx.doi.org/10.5772/66992

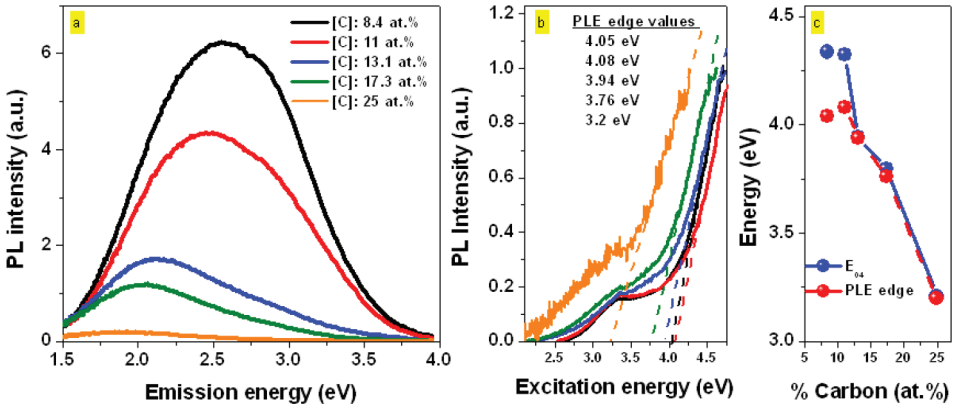

Figure 10. (a) PL emission spectra from as-deposited (AD) SiC_xO_y thin films (4.13 eV excitation, ~300 μW), (b) normalized PLE spectra of the AD SiC_xO_y samples at the PL maxima. The linear fits (dashed lines) of the steep increase of the PLE intensities are shown along with the intercept of these straight lines at the excitation energy (PLE-edge values), and (c) E_{04} and PLE-edge energy values of SiC_xO_y thin films versus C [5].

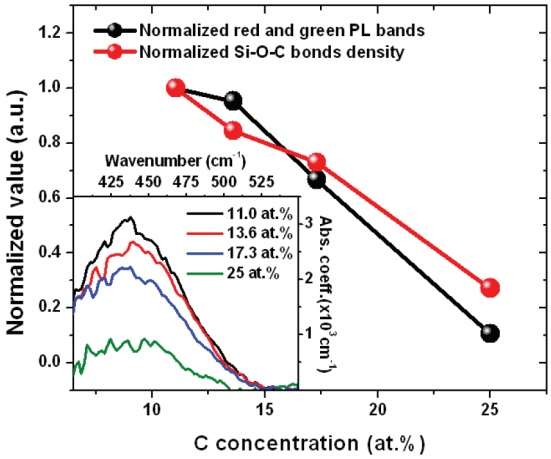

Figure 11. Normalized integrated red and green PL emission bands and the integrated FTIR absorption of Si-O-C functional group at ~440 cm^{-1}. Inset: FTIR absorptions of the Si-O-C-rocking mode in film [5].

On this, the integrated red and green PL emission bands were added and their normalized integrated values were plotted along with the intensity of the red-shifted Si-O-rocking (related to Si-O-C bond density) mode as a function of C content (**Figure 11**) [3]. A strong correlation between the emitted luminescence and the Si-O-C bond density in SiC_xO_y was revealed. This suggests that the emitted luminescence can be directly associated with the Si-O-C structure in the materials [5]. Additionally, the PL/PLE analysis revealed a strong similarity in the PLE behavior for the green/blue band emissions between the SiC control and SiC_xO_y, suggesting

that C-Si/C-Si-O bonding may be also responsible for the excitation path of the observed luminescence in SiC_xO_y.

5.2. Band-tail recombination model

Representative forming gas-annealed SiC_xO_y samples were additionally studied with means of PL and PLE analyses as presented in **Figure 12** [22].

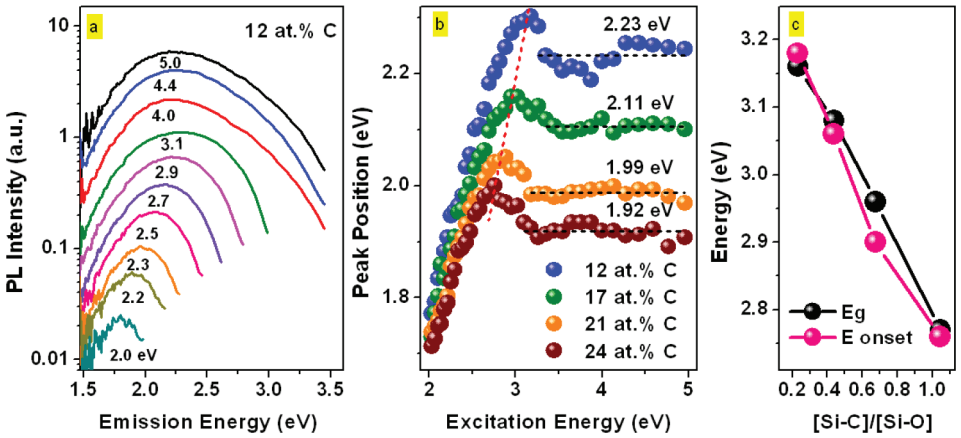

Figure 12. (a) Steady-state PL of the FG-annealed SiC_xO_y with 12 at.% *C* content ($SiC_{0.34}O_{1.52}$) under varying excitation photon energies (E_{exc}). The PL intensity increased monotonically by two orders of magnitude with E_{exc}, suggesting that the efficiency of photo-carrier generation increases with E_{exc}, (b) room-temperature steady-state PL peak position dependence on excitation energy of SiC_xO_y thin films of varying carbon concentrations. With increase in excitation energy, the PL peak-emission-position blue-shifts until ~$E_{exc,on}$ (red-dotted line is used as a guide to the eye). Hopping edges are indicated by horizontal black dotted lines and (c) E_g calculated from Tauc's law and $E_{exc,on}$ values as a function of [Si-C]/[Si-O] bond ratio [23].

The evolution of the PL peak position in SiC_xO_y was supported by the band-tail states recombination model, typical of amorphous materials [71]. Upon excitation, the photogenerated carriers thermalized to lower energies associated with band edges (hopping edge) before they recombined radiatively (energy plateau in **Figure 12b**). The PL peak position increased with the excitation energy up to the $E_{exc,on}$ value, as the electron population at high-lying band-tail levels of the conduction band increasing with higher excitation energy. The red shift of $E_{exc,on}$ seen with increasing C content in SiC_xO_y can be ascribed to the observed linear decrease of the optical gap (E_g) with increasing [Si-C]/[Si-O] and their values almost coincide with the E_g values of the films [22].

PL dynamics experiments showed a fast decrease of the PL intensity, suggesting the existence of fast recombination mechanisms in SiC_xO_y, and the PL decay spectra followed a stretched exponential law [23]. These findings further support a band-tail states recombination model, in which carriers recombine by tunneling between spatially separated conduction and valence band-tail states. Due to the diffusivity/tunneling of the photogenerated carriers during thermalization in the band-tail states before they recombine and the inhomogeneous

http://dx.doi.org/10.5772/66992

constitution of the band-tail states related to C-Si/Si-O-C bonding, where each state contributes with a slightly different PL lifetime, a distribution of lifetimes is expected, hence the stretched exponential behavior. This is inherent in disordered semiconductors, such as amorphous Si:H, C:H, SiC_x, and SiN_x, due to the broad and variable spatial density of these states [72–74].

To further elucidate on the band-tail states recombination model in SiC_xO_y, the PL luminescence decay at different emission energies was additionally investigated. The time evolution of the PL line shape is presented in **Figure 13a**. It can be seen that during the first 1 ns of the luminescence decay, the integrated intensity substantially decreased and a red shift, equal to $\Delta E = 0.31$ eV, in the PL emission peaks occurs for the SiC_xO_y thin film with 12 at.% C. This red shift is found to be less for samples with higher C concentration [23].

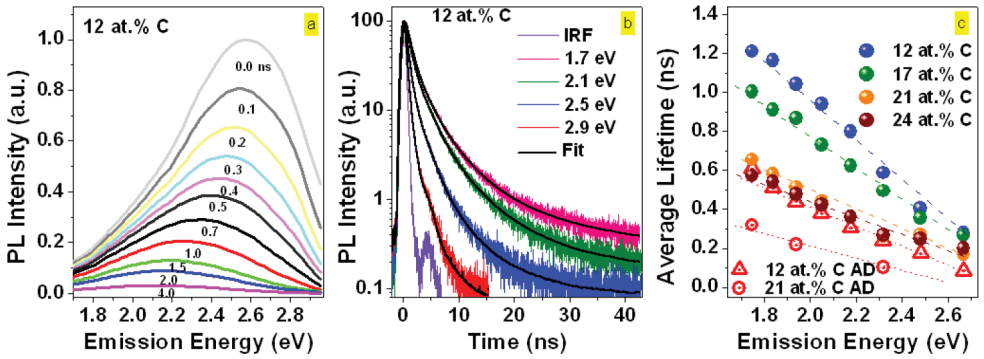

Figure 13. (a) Time evolution of PL spectrum of $SiC_{0.34}O_{1.52}$ ($E_{exc} = 3.06$ eV). The number associated with each spectrum indicates the elapsed time (in nanoseconds) after excitation. (b) Raw data of PL decay transients of $SiC_{0.34}O_{1.52}$ film at different emission energies (IRF in black). (c) Average lifetimes of FG-annealed SiC_xO_y films with different *C* contents at different emission energies. The average lifetimes of the as-deposited (AD) SiC_xO_y films with 12 at.% C and 21 at.% C are also shown (gray symbols) [23].

Furthermore, the PL lifetimes increased as the emission energy was decreased, in agreement with electron-hole (e-h) hopping within lower-energy tail states, as the rate of thermalization decreases significantly due to the rapidly decreasing density of band-tail states [75]. Similar behavior was observed in amorphous semiconductors where the luminescence lifetime increase is attributed to e-h hopping [74]. Upon FG annealing, the average lifetimes exhibited higher values compared to their as-deposited counterparts (**Figure 13c**). Furthermore, the integrated PL intensity of the FG-annealed films increased significantly along with a blue shift in peak position (e.g., six times for the sample with 21 at.% C with 0.2 eV blue shift). This change in lifetimes and PL intensity can be attributed primarily to the passivation of non-radiative recombination centers present in lower-energy portion of the band-tail states of the as-deposited films.

The increase in the luminescence lifetime in SiC_xO_y with low *C* content can be attributed to the decrease of non-radiative recombination paths compared to their high *C* content counterparts. As the SiC_xO_y composition evolves from SiC-like to SiO_2-like, a decrease of the local disorder is

expected. As presented above herein FTIR measurements suggest that the degree of bond-angle disorder decreases with decreasing *C* content in the chemically grown SiC_xO_y films.

Additionally, it is expected that in the case of high *C* content samples, the density of band-tail states should increase as indicated by their increased sub-bandgap absorption [15, 76]. Therefore, for SiC_xO_y films with higher *C* content (*C* >14 at.%), a higher density of band-tail states and enhanced disorder is expected, which results in faster thermalization of the photogenerated carriers yielding higher decay rates and a tighter lifetime distribution (**Figure 13b**) [23].

5.3. Visible luminescence from SiC_xO_y nanowires

Figure 14a and **b** shows the normalized room-temperature PLE and PL emission spectra of $SiC_{0.34}O_{1.52}$ nanowire arrays. To better understand the visible light emission in SiC_xO_y NWs, their PL and PLE properties were explored in conjunction with data from the thin film of the same composition. The PL emission spectrum of $SiC_{0.34}O_{1.52}$ NWs exhibits broadband characteristics ranging from blue to deep red, while the PLE spectrum monitored at the peak luminescence emission (~550-nm) spans from near-UV to blue/green regions of the spectrum.

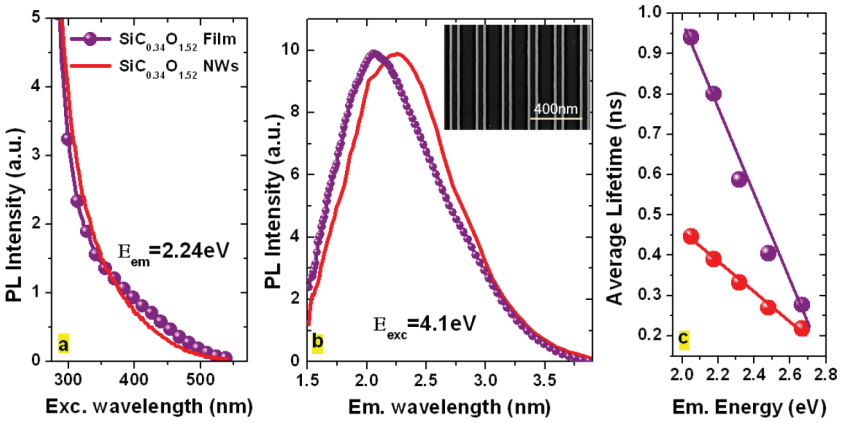

Figure 14. (a) Room-temperature PLE spectra of 120-nm-thick $SiC_{0.34}O_{1.52}$ thin film and its corresponding NWs measured at its emission peak. Almost identical PLE emission spectra between NWs and thin films were observed, suggesting that there is no change in the excitation path and emission origin of the observed luminescence in $SiC_{0.34}O_{1.52}$ nanowires, (b) ensemble steady-state normalized PL spectrum of the SiC_xO_y NWs array along with the normalized PL spectrum of its thin film analog (E_{exc} = 4.1 eV) and (c) average lifetimes of the SiC_xO_y NW array with 12 at.% C and its thin film analog at different PL emission energies [22, 23].

PLE analysis suggested that the observed luminescence from SiC_xO_y NWs is related to radiative recombination of photo-excited carriers in band-tail states associated with C-Si/Si-O-C-bonding groups [5, 22]. Furthermore, a supplementary mechanism, in addition to the proposed band-tail states recombination process, may be needed in order to take into account the reduced dimensionality of SiC_xO_y NW. In the case of the NW structure with spatially confined volume, the statistics of the lowest energy states due to Si-C bonds may be excluded [77]. Furthermore, by nanostructuring the recombination volume is reduced, thus, the tunneling

http://dx.doi.org/10.5772/66992

probability of a carrier between adjacent states at similar energy is expected to decrease. Consequently, the carriers will be exposed to a smaller number of non-radiative sites [23, 77, 78], resulting in enhanced PL efficiency, PL blue shift, and faster lifetimes with a tighter distribution as observed in $SiC_{0.34}O_{1.52}$ (12 at.% C) (**Figure 14c**). However, it is important to emphasize that the effects of NW-related surface recombination and optical scattering may not be ruled out.

5.4. Photo-stability upon thermal oxidation and excitation power density

In addition to PL and PLE studies, the luminescence performance of the $SiC_{0.34}O_{1.52}$ NW arrays was investigated as a function of oxidation temperature and excitation power density [22].

The oxidation treatments up to 250°C (**Figure 15a**) did not cause any change in the composition and bonding configuration of the $SiC_{0.34}O_{1.52}$ material. Consequently, the emission intensity and line shape, from $SiC_{0.34}O_{1.52}$ nanostructured arrays, did not reveal any changes, suggesting the absence of luminescence degradation due to thermal oxidation. This stability can be attributed to the similarity of the oxidation rates and activation energies of SiC_xO_y materials to those of SiC [79]. Hence, SiC_xO_y materials (with higher carbon content) appear to be significantly more resistant to oxidation annealing, compared to its SiO_2-like counterparts (with very low carbon content) [3].

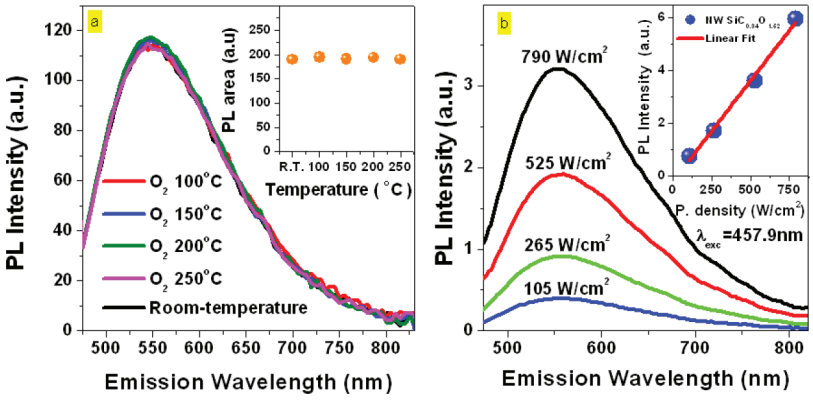

Figure 15. (a) PL spectra of the AD and 2-h-oxygen-annealed $SiC_{0.34}O_{1.52}$ NW at various temperatures (excitation wavelength λ_{exc} = 457 nm). The inset shows the integrated PL intensity versus annealing temperature and (b) room-temperature PL spectra of the 70-nm-width $SiC_{0.34}O_{1.52}$ NWs for different CW excitation probing power densities (excited at the λ_{exc} = 457.9 nm of an Ar ion laser). The inset shows the linear behavior of the integrated PL intensity as a function of the excitation power density [22].

The excitation power dependence study (**Figure 15b**) showed a linear behavior in the integrated PL with respect to the power density (up to ~800 W/cm^2). Similar to the thermal-oxidation study, the peak position and the line shape of the PL in the nanowires remained unchanged, suggesting good emission stability at high excitation intensity [22]. The latter is more supporting evidence suggesting the absence of defect-related localized emission in the proposed origin of the visible luminescence from SiC_xO_y nanowires, as no PL saturation at high powers was observed (e.g., due to state filling of the localized states) [80, 81].

6. Concluding remarks

The optical and luminescence properties of silicon oxycarbide thin films and nanostructured (e.g., NW) arrays are correlated to their synthesis routes, structural properties, and bonding configuration. The composition of the chemically CVD-grown SiC_xO_y thin films approximate the $SiC_xO_{2(1-x)}$ ($0 < x < 1$) stoichiometry. The index of refraction increases linearly as the [Si–C]/[Si–O] bond-area ratio increases, accompanied by a linear decrease of the optical gap. The white (red, green, and blue) emission can be achieved simultaneously from the same SiC_xO_y film following a single-deposition process, without the complications encountered in the case of using nanocrystals (e.g., Si, SiC). In particular, it was determined that the white PL emission of SiC_xO_y thin films is strong enough to be seen with the naked eye under bright room conditions. Based on the PL, FTIR, and EPR analyses, typical structural defects in oxides were ruled out as the mechanism for white luminescence from SiC_xO_y. Instead, the observed intense visible luminescence originates from the recombination of photo-generated carriers between the energy bands and at their tail states associated with Si-O-C/Si-C bonds. In this regard, the potential advantages offered by our proposed approach of SiC_xO_y thin films and NWs range from color tunability, thermal/photo-stability to enhanced light extraction efficiency and from cost reduction to environmental considerations. To this end, these compelling behaviors may provide a pathway for further controlling and enhancing the thermal stability and PL yield of white light emission from such films and nanostructured materials through optimal engineering of Si-O-C/Si-C bonds in the matrix.

Acknowledgements

The authors would like to thank Dr. Mengbing Huang, of the Colleges of Nanoscale Sciences and Engineering at SUNY POLY, for his contribution to the work presented herein.

Author details

Spyros Gallis*, Vasileios Nikas and Alain E. Kaloyeros

*Address all correspondence to: sgalis@sunypoly.edu

Colleges of Nanoscale Sciences and Engineering, SUNY Polytechnic Institute, Albany, NY, USA

References

[1] Grill A., Gates S. M., Ryan T. E., Nguyen S. V., and Priyadarshini D. Progress in the development and understanding of advanced low k and ultralow k dielectrics for very large-scale integrated interconnects-State of the art. Applied Physics Review 2014;1:011306.

[2] King S. W. Dielectric barrier, etch stop, and metal capping materials for state of the art and beyond metal interconnects. ECS Journal of Solid State Science and Technology 2015;4:N3029.

[3] Gallis S., Nikas V., Suhag H., Huang M., and Kaloyeros A. E. White light emission from amorphous silicon oxycarbide (a-SiC_xO_y) thin films: Role of composition and post-deposition annealing. Applied Physics Letters 2010;97:081905.

[4] Vasin A. V. Structural and luminescent properties of carbonized silicon oxide thin layers. In Nazarov A., Balestra F, Valeriya K, Flandre D. (ed) Functional Nanomaterials and Devices for Electronics, Sensors and Energy Harvesting Engineering Materials. Springer, Cham, Heidelberg, New York, Dordrecht, London; Switzerland, Germany, United States of America, The Netherlands, United Kingdom; 2014, p. 297.

[5] Nikas V., Gallis S., Nguyen A. P. D., Stesmans A., Afanas'ev V. V. and Kaloyeros A. E. The origin of white luminescence from silicon oxycarbide thin films. Appled Physics Letters 2014;104: 061906.

[6] Tamayo A., Rubio J., Rubio F., Oteo J. L., and Riedel R. Texture and micro-nanostructure of porous silicon oxycarbide glasses prepared from hybrid materials aged in different solvents. Journal of European Ceramics Society 2011;31: 1791.

[7] Kim Y. W., Kim S. H., and Park C. B. Processing of closed-cell silicon oxycarbide foams from a preceramic polymer. Journal of Materials Science 2004;39:5647.

[8] Nghiem Q. D., Cho S. J., and Kim D. P. Synthesis of heat-resistant mesoporous SiOC ceramic and its hydrogen adsorption. Journal of Materials Chemistry 2006;16:558.

[9] Karakuscu A., Ponzoni A., Aravind P. R., Sberveglieri G., and Soraru G. D. Gas sensing behavior of mesoporous SiOC glasses. Journal of American Ceramics Society 2013;96:2366.

[10] Liu X., Xie K., Zheng C.M, Wang J., and Jing Z. Q. Si-O-C materials prepared with a sol–gel method for negative electrode of lithium battery. Power Sources 2012;214:119.

[11] Bhandavat R., and Singh G. Stable and efficient Li-ion battery anodes prepared from polymer-derived silicon oxycarbide–carbon nanotube shell/core composites. Journal of Physical Chemistry C 2013;117:11899.

[12] Zhuo R., Colombo P, Pantano C, and Vogler E. A. Silicon oxycarbide glasses for blood-contact applications. Acta Biomaterialia 2005;1:583.

[13] Bellocchi G. Franzò G. Boninelli S., Miritello M., Cesca T., Iacona F. and F Priolo. Structural and luminescence properties of undoped and Eu-doped SiOC thin films. Materials Science and Engineering 2014;56:012009.

[14] Gallis S., Huang M., Efstathiadis H., Eisenbraun E., Nyein E., Hommerich U., and Kaloyeros A. E. Photoluminescence in erbium doped silicon oxycarbide thin films. Applied Physics Letters 2005;87:091901.

[15] Gallis S., Huang M., and Kaloyeros A. E. Efficient energy transfer from silicon oxycarbide matrix to Er ions via indirect excitation mechanisms. Applied Physics Letters 2007;90: 161914.

[16] Nikas V., Gallis S., Huang M., and Kaloyeros A. E. Thermal annealing effects on photoluminescence properties of carbon-doped silicon-rich oxide thin films implanted with erbium. Journal of Applied Physics 2011;109:093521.

[17] Liang D., and Bowers J. E.. Recent progress in lasers on silicon. Nature Photonics 2010;4:511.

[18] Fang Z., Chen Q. Y., and Zhao C. Z. A review of recent progress in lasers on silicon. Optics and Laser Technology 2013;46:103.

[19] Fan S., Villeneuve P.R, Joannopoulos J. D., and Schubert E. F. High Extraction efficiency of spontaneous emission from slabs of photonic crystals. Physical Review Letters 1997;78: 3294.

[20] Guichard A. R., Kekatpure R. D., Brongersma M. L., and Kamins T. I. Temperature-dependent Auger recombination dynamics in luminescent silicon nanowires. Physical Review B 2008;78:235422.

[21] He Y., Fan C., and Lee S. T. Silicon nanostructures for bioapplications. Nano Today 2010;5:282.

[22] Nikas V, Tabassum N., Ford B., Smith L., Kaloyeros A. E., and Gallis S., Strong visible light emission from silicon oxycarbide nanowire arrays prepared by electron beam lithography and reactive ion etching. Journal of Materials Research 2015;30:3692.

[23] Tabassum N., Nikas V., Ford B., Huang M., Kaloyeros A. E., and Gallis S. Time resolved analysis of the white photoluminescence from chemically synthesized SiC_xO_y thin films and nanowires. Applied Physics Letters 2016;109:043104.

[24] Wang Q., Zhang W., Zhong M., Ma J., Wu Z., and Wang G. Synthesis and Photoluminescence of Amorphous Silicon Oxycarbide Nanowires. Chinese Journal of Chemical Physics 2015;28:184.

[25] Zhao Y., Riemersma C., Pietra F., Koole R., Donegá C. M., and Meijerink A. High-temperature luminescence quenching of colloidal quantum dots. ACS Nano 2012;6:9058.

[26] Tayagaki T., Fukatsu S., and Kanemitsu Y. Photoluminescence dynamics and reduced Auger recombination in $Si_{1-x}Ge_x$/Si superlattices under high-density photoexcitation. Physical Review B 2009;79:041301.

[27] Grill A. Plasma enhanced chemical vapor deposited SiCOH dielectrics: from low-k to extreme low-k interconnect materials. Journal of Applied Physics 2003;93:1785.

[28] Chiang C. C., Chen M. C., Li L. J., Wu Z. C., Jang S. M., and Liang M. S. Physical and barrier properties of amorphous silicon-oxycarbide deposited by PECVD from octamethylcyclotetrasiloxane. Journal of the Electrochemical Society 2004;151(9):G612.

[29] Wang M. R., Rusli, Xie J. L., Babu N., Li C. Y., and Rakesh K. Study of oxygen influences on carbon doped silicon oxide low-k thin films deposited by plasma enhanced chemical vapor deposition. Journal of Applied Physics 2004;96:829.

[30] Kim Y. H., Hwang M. S., Kim H. J., Kim J. Y., and Lee Y. Infrared spectroscopy study of low dielectric-constant fluorine-incorporated and carbon-incorporated silicon oxide films. Journal of Applied Physics 2001;90:3367.

[31] Lin Z., Guo Y, Song J., Zhang Y., Song C, Wang X., Huang R. Effect of thermal annealing on the blue luminescence of amorphous silicon oxycarbide films. Journal of Non-Crystalline Solids 2015;428:184.

[32] Ryan J. V. and Pantano C. G. Synthesis and characterization of inorganic silicon oxycarbide glass thin films by reactive rf-magnetron sputtering. Journal of Vacuum Science & Technology A 2007;25:153.

[33] Vasin A. V., Rusavsky A. V., Kysil D. V., Prucna S., Piryatinsky Y. P., Starik S. P., Nasieka I., Strelchuk V. V., Lysenko V. S., Nazarov A. N. The effect of deposition processing on structural and luminescent properties of a-SiOC:H thin films fabricated by RF-magnetron sputtering. Journal of Luminescence 2016; in press. http://www.sciencedirect.com/science/article/pii/S0022231316314247. http://dx.doi.org/10.1016/j.jlumin.2016.10.029

[34] Karakuscu, A., Guider, R., Pavesi, L., Soraru, G.D.: Broad-band tunable visible emission of sol–gel derived SiBOC ceramic thin films. Thin Solid Films 2011;519:3822.

[35] Abbass A. E., Swart H. C., Kroon R. E. White luminescence from sol–gel silica doped with silver. Journal of Sol–gel Science Technology 2015;76:708.

[36] Vasin A.V., Ishikawa Y., Kolesnik S.P., Konchits A.A., Lysenko V.S., Nazarov A.N., Rudko G. Y. Light-emitting properties of amorphous Si:C:O: H layers fabricated by oxidation of carbon-rich a-Si:C: H films. Solid State Science. 2009;11:1833.

[37] Gallis S., Nikas V., Eisenbraun E., Huang M., and Kaloyeros A. E. On the effects of thermal treatment on the composition, structure, morphology, and optical properties of hydrogenated amorphous silicon-oxycarbide. Journal of Materials Research 2009;24: 2561.

[38] Gallis S., Nikas V., Huang M., Eisenbraun E., and Kaloyeros: A. E. Comparative study of the effects of thermal treatment on the optical properties of hydrogenated amorphous silicon-oxycarbide. Journal of Applied Physics 2007;102:024302.

[39] Bréquel H., Parmentier J., Walter S., Badheka R., Trimmel G., Masse S., Latournerie J., Dempsey P., Turquat C., Chomel A. D., Neindre-Prum L. L., Jayasooriya U. A., Hourlier D., Kleebe H. J, Soraru G. D., Enzo S., and Babonneau F. Systematic structural characterization of the high-temperature behavior of nearly stoichiometric silicon oxycarbide glasses. Chemistry of Materials 2004;16:2585.

[40] Kroll P. Searching insight into the atomistic structure of SiCO ceramics. Journal of Materials Chemistry 2010;20:10528.

[41] Lanford W. A., Trautvetter H. P., Ziegler J. F. and Keller J. New precision technique for measuring the concentration versus depth of hydrogen in solids. Applied Physics Letters 1976;28:566.

[42] Lehmann A., Schumann L., and Hubner K. Optical phonons in amorphous silicon oxides. I. Calculation of the density of states and interpretation of Lo-To splittings of amorphous SiO_2. Physical Status Solidi (b) 1983;117:689.

[43] Wolfe D. M., Hinds B. J., Wang F., Lucovsky G., Ward B. L., Xu M., Nemanich R. J., and Maher D. M. Thermochemical stability of silicon–oxygen–carbon alloy thin films: a model system for chemical and structural relaxation at SiC–SiO_2 interfaces. Journal of Vacuum Science and Technology A 1999;17:2170.

[44] Tolstoy V. P., Chernyshova I. V., and Skryshevsky V. A. Handbook of Infrared Spectroscopy of Ultrathin Films. Wiley; New York; 2003.

[45] Socrates G. Infrared Characteristic Group Frequencies. Wiley: Chichester; 2001.

[46] Besling W. F. A., Goossens A., Meester B., Schoonman J. Laser-induced chemical vapor deposition of nanostructured silicon carbonitride thin films. Journal of Applied Physics 1998;83:544.

[47] Demichellis F., Pirri C. F., and Tresso E. F. Influence of doping on the structural and optoelectronic properties of amorphous and microcrystalline silicon carbide. Journal of Applied Physics 1992;72:1327.

[48] Fang C. F., Gruntz K. J., Ley L., Cardona M., Demond F. J, Müller G., and Kalbitzer S. The hydrogen content of a-Ge:H and a-Si:H as determined by IR spectroscopy, gas evolution and nuclear reaction techniques. Journal of Non-Crystalline Solids 1980;35–36:255.

[49] Basa D. K. and Smith F. W. Annealing and crystallization processes in a hydrogenated amorphous Si-C alloy film. Thin Solid Films 1990;192:121.

[50] Fujimoto F., Ootuka A., Komaki K. I., Iwata Y., Yamane I., Yamashita H., Hashimoto Y., Tawada Y., Nishimura K., Okamoto H. and Hamakawa Y. Hydrogen content in a-SiC:H films prepared by plasma decomposition of silane and methane or ethylene. Japanese Journal of Applied Physics Part 1 1984;23:810.

[51] Nakazawa K., Ueda S., Kumeda M., Morimoto A., and Shimizu T. NMR and IR studies on hydrogenated amorphous $Si_{1-x}C_x$ Films. Japanese Journal of Applied Physics Part 1 1982;21:L176.

[52] Smith K. L., and Black K. M. Characterization of the treated surfaces of silicon alloyed pyrolytic carbon and SiC. Journal of Vacuum Science and Technology A 1984;2:744.

[53] Choi W. K., Ong T. Y., Tan L. S., Loh F. C., Tan K. L. Infrared and x-ray photolectron spectroscopy studies of as-prepared and furnace-annealed radio-frequency sputtered amorphous silicon carbide films. Journal of Applied Physics 1998;83:4968.

[54] Bell, F. G. and Ley L. Photoemission study of SiO_x ($0 \le x \le 2$) alloys. Physical Review B 1988;37:8383.

[55] Maex K., Baklanov M. R., Shamiryan D., Iacopi F., Brongersma S. H., Yanovitskaya Z. S. Low dielectric constant materials for microelectronics. Journal of Applied Physics 2003;93:8793.

[56] Dehan E., Temple-Boyer P., Henda R., Pedroviejo J. J. and Scheid E. Optical and structural properties of SiO_x and SiN_x materials. Thin Solid Films 1995;266:14.

[57] Sun C. Q. A model of bonding and band-forming for oxides and nitrides. Applied Physics Letters 1998;72:6.

[58] Carey J. D., Silva S. R. P. Disorder, clustering, and localization effects in amorphous carbon. Physical Review B 2004;70:235417.

[59] Das G., Mariotto G., Quaranta A. Microstructural evolution of thermally treated low-dielectric constant SiOC:H films prepared by PECVD. Journal of the Electrochemical Society 2006;153:F46.

[60] Fanchini G., Tagliaferro A. Disorder and Urbach energy in hydrogenated amorphous carbon: a phenomenological model. Applied Physics Letters 2004;85:730.

[61] Joannopoulos J. D. and Lucovsky G. The Physics of Hydrogenated Amorphous Silicon II. Springer: Berlin; 1984.

[62] Brodsky M. H. Amorphous Semiconductors. Springer-Verlag: Berlin; 1979.

[63] Wagner H., Beyer W. Reinterpretation of the silicon-hydrogen stretch frequencies in amorphous silicon. Solid State Communications 1983;48:585.

[64] Kumbhar A. S., Bhusari D. M., and Kshirsagar S. T. Growth of clean amorphous silicon–carbon alloy films by hot-filament assisted chemical vapor deposition technique. Applied Physics Letters 1995;66:1741.

[65] Musumeci P., Roccaforte F., Reitano R. Angular distortion of Si clusters in a-SiC. Europhysics Letters 2001;55:674.

[66] Compagnini G., Foti G., Makhtari A. Vibrational analysis of compositional disorder in amorphous silicon carbon alloys. Europhysics Letters 1998;41:225.

[67] Ivashchenko V. I., Shevchenko V. I., Rusakov G. V., Klymenko A. S., Popov, Ivashchenko L. A., Bogdanov E. I. Gap states in a-SiC fromoptical measurements and band structure models. Journal of Physics: Condensed Matter 2002;14:1799.

[68] Nguyen-Tran T., Suendo V., Roca P., and Cabarrocas I. Optical study of disorder and defects in hydrogenated amorphous silicon carbon alloys. Applied Physics Letters 2005;87:011903.

[69] Afanas'ev V. V., Nguyen A. P. D., Houssa M., Stesmans A. , Tőkei Z., and Baklanov M. R. High-resolution electron spin resonance analysis of ion bombardment induced defects in advanced low-κ insulators (κ=2.0–2.5). Applied Physics Letters 2013;102:172908.

[70] Trakhtenberg L. I., Lin S. H., and Ilegbusi O. J. Physico-chemical phenomena in thin films and at solid surfaces. Thin Films and Nanostructures 2007;316:314.

[71] Murayama K., Sano W., Ito T., and Ogiwara C. Excitation energy evolution of photoluminescence spectrum in amorphous hydrogenated silicon. Solid State Communications 2008;146:315.

[72] Lormes W., Hundhausen M., and Ley L. Time resolved photoluminescence of amorphous hydrogenated carbon. Journal of Non-Crystalline Solids 1998;227:570.

[73] Pelant I., and Valenta J. Luminescence Spectroscopy of Semiconductors. Oxford: University Press; 2012.

[74] Giorgis F., Mandracci P., Dal Negro L., Mazzoleni M., and Pavesi P. Optical absorption and luminescence properties of wide-band gap amorphous silicon based alloys. Journal of Non-Crystalline Solids 2000;266:588.

[75] Monroe D. Hopping in exponential band tails. Physical Review Letters 1985;54:146.

[76] Tessler L. R., and Solomon I. Photoluminescence of tetrahedrally coordinated *a*-$Si_{1-x}C_x$:H. Physical Review B 1995;52:10962.

[77] Estes M. J., and Moddel G. Luminescence from amorphous silicon nanostructures. Physical Review B 1996;54:14633.

[78] Robertson J. Recombination and photoluminescence mechanism in hydrogenated amorphous carbon. Physical Review B 1996;53:16302.

[79] Chollon G. Oxidation behaviour of ceramic fibres from the Si–C–N–O system and related sub-systems. Journal of European Ceramics Society 2000;20:1959.

[80] Tayagaki T., Fukatsu S., and Kanemitsu Y. Photoluminescence dynamics and reduced Auger recombination in $Si_{1-x}Ge_x$/Si superlattices under high-density photoexcitation. Physical Review B 2009;79:041301.

[81] Grieshaber W., Schubert E. F., Goepfert I. D., Karlicek R. F., Schurman M. J., and Tran C. Competition between band gap and yellow luminescence in GaN and its relevance for optoelectronic devices. Journal of Applied Physics 1996;80:4615.

Chapter 15

Growth and Characteristics of High-quality InN by Plasma-Assisted Molecular Beam Epitaxy

Chen-Chi Yang, Ikai Lo, Cheng-Hung Shih,
Chia-Hsuan Hu, Ying-Chieh Wang, Yu-Chiao Lin,
Cheng-Da Tsai, Hui-Chun Huang, Mitch M. C. Chou,
Cheng-Chang Yu and Der-Jun Jang

Additional information is available at the end of the chapter

http://dx.doi.org/10.5772/65812

Abstract

The high-quality InN epifilms and InN microdisks have been grown with InGaN buffer layers at low temperatures by plasma-assisted molecular beam epitaxy. The samples were analyzed using X-ray diffraction, scanning electron microscopy, high-resolution transmission electron microscopy, and photoluminescence. The characteristics of the InN epifilms and InN microdisks were studied, and the role of InGaN buffer was evaluated.

Keywords: InN microdisk, InGaN buffer, Molecular beam epitaxy

1. Introduction

III-Nitride semiconductor compounds have been extensively studied for applications in optoelectronic devices, such as solar cells and light emitting diodes (LEDs) [1–5]. The wide direct band-gap gallium nitride (GaN) and aluminum nitride (AlN) compounds, with energy gaps covering the ultraviolet spectrum, are the dominant materials for solid-state lighting devices and have been well studied to date. The molecular beam epitaxy (MBE) technique can be used to grow a thin epifilm in an ultrahigh vacuum (~10^{-10} torr) and low temperature condition [6]. Under such conditions, materials in the effusion cells of the MBE system are heated and they move toward the substrate to form epitaxial high purity films. The low-temperature condition is crucial to grow the compounds with a low volatilized temperature (such as In atom, 650°C). Because of the improvement of InN films grown by MBE, the direct band-gap of the indium

nitride (InN) compound was demonstrated with the value of 0.64 eV rather than 1.9 eV [7, 8]. This important finding indicated that one can tune the band-gap energy to achieve the full-color spectrum (red, green, and blue) devices by changing the III-group alloy ratio without any phosphor. Besides, InN is a high potential material in optoelectronic applications due to its outstanding material properties, such as the smallest effective mass, the highest peak and saturation electron drift velocity, and the largest mobility among the nitride semiconductors [9, 10].

On the other hand, the development of the full-color spectrum micron LED is very important for the high-resolution display. The general method to fabricate micron LED is etching process to reach micro scale. However, it is not easy to downsize to 1–10 μm by etching process. In order to fabricate micron LED, a suitable micron growth base is the top priority. In recent years, the growth and characteristics of InN nanowire on Si (1 0 0) by the vapor-liquid-solid mechanism and on Si (1 1 1) by plasma-assisted molecular beam epitaxy (PA-MBE) were reported [11–13]. The wire diameter was less than 100 nm. In our previous work, we have grown the high-quality self-assembled ***c***-plane GaN ($0\,0\,0\,1^{-}$) hexagonal microdisks with a diameter of 4 μm on γ-$LiAlO_2$ (LAO) substrates. The diameter of microdisk can be adjusted to optimize the quantum effect for nanodevice applications [5]. Besides, we developed a back process to fabricate an electrical contact for the GaN hexagonal microdisk on a transparent p-type GaN template [14]. Consequently, the InN microdisk provides an opportunity to fabricate the InGaN/GaN microdisk quantum well for the application of full-color micron LED without the sapphire substrate, which is mostly used for the bulk GaN-based quantum wells in commercial LEDs but has a large lattice mismatch with InN [1, 2]. In this chapter, we will show the growth of InN ($0\,0\,0\,1^{-}$) hexagonal thin wurtzite microdisks on the γ-LAO substrate by PA-MBE.

2. High-quality InN epifilms

2.1. InGaN buffer layer

When engineering the band structure of III-nitrides, it is difficult to grow high-quality InN thin film due to the low decomposition temperature of InN (<600°C) and the large lattice mismatch between InN and common substrates (e.g., sapphire or silicon) [15]. Therefore, determining an appropriate substrate for the growth of high-quality InN film is one of the main issues in the fabrication of full-color optoelectronic devices. The lattice mismatch between InN (***a*** = 0.3537 and ***c*** = 0.5704 nm) and sapphire (***a*** = 0.4785 and ***c*** = 1.2991 nm) on the ***c***-plane is about 26.1%.

The initial methods prior to InN growth, including substrate nitridation and buffer layer deposition, have very important effects on the growth of high-quality InN films with a flat surface on a sapphire substrate. Xiao et al. grew InN films with 20 min nitridation and a low-temperature InN (LT-InN) buffer layer. By X-ray diffraction (XRD) and room temperature photoluminescence (PL) analyses, it was found that these InN films grown with LT-InN buffer layer have better quality than those without LT-InN buffer layer [16].

Meanwhile, Saito et al. reported the growth of InN films on sapphire with 1 hour nitridation and low-temperature intermediate InN buffer layers, and they found that the growth

http://dx.doi.org/10.5772/65812

of thicker InN with a uniform surface was very difficult without intermediate layers and the electron mobility was improved by improvement of surface flatness [17]. Besides, Lu et al. studied the effect of an AlN buffer layer on the epitaxial growth of InN on the sapphire substrate by MBE and found that by using the AlN buffer layer, the structural and electrical properties of InN could be greatly improved. It was also found that a thicker AlN buffer layer was preferred when growing the InN epilayer, which could lead to better electrical properties and surface morphology [18]. From these studies, we can find that it is helpful to improve the quality of InN thin films by introducing an appropriate buffer layer. In general, a thick GaN film (>4 μm) can be grown on sapphire substrate (0 0 0 1) to form a GaN template. In this chapter, we will show firstly the high-quality epitaxial growth of InN epifilms on GaN template with an appropriate InGaN buffer layer by PA-MBE system. We designed a series of samples to study the effect of InGaN buffer layer with growth-temperature dependence.

2.2. Growth of InN epifilms

Four samples were grown on 2 inch *c*-plane (0 0 0 1) Si-doped GaN/sapphire template substrates that consisted of 3.5 μm intrinsic GaN, 65 nm Si-doped AlGaN and 2 μm Si-doped GaN were grown by metal-organic chemical vapor deposition (MOCVD). The InN thin film was grown on the InGaN buffer layer by the PA-MBE system (Veeco Applied-GEN 930) with standard effusion cells for In- and Ga-evaporation and an rf-plasma cell with 450 W for the N_2-plasma source. Before mounting on a holder, the template substrates were cleaned with acetone (5 min), isopropanol (5 min), and de-ionized water (5 min) in an ultrasonic bath, and then dried with nitrogen gas immediately. After the chemical cleaning, the substrates were out-gassed at 750°C for 10 min in the MBE chamber before epitaxial growth. The temperature was defined by a thermal couple equipped at the backside of the substrates. Thereafter, the substrate temperature was decreased down to growth temperatures. The epitaxial growth of GaN was performed on the GaN template at 700°C with a flux ratio N/Ga = 42.9 represented by beam equivalent pressure (BEP) of evaporative III-group sources from standard effusion cell against that of N_2 source from rf-plasma cell [19] and the duration time of the epitaxial growth for all samples was 10 min. Thereafter, the substrate temperature was ramped to growth temperatures with a flux ratio In/Ga = 2.0, and the duration time of the InGaN buffer layer for all samples was 10 min. Four samples were grown under varied temperatures of InGaN buffer layers: 500, 540, 570, and 600°C. Finally, the substrate temperature was ramped down to growth temperature at 410°C with a flux ratio N/In = 40.0 and the duration time of the InN for all samples was 10 min to grow the InN epifilms.

2.3. Analysis of InN epifilms

The *in situ* reflection high-energy electron diffraction (RHEED) was used to monitor the growth of InN epifilms with 15 kV and 14 mA. The structural properties and crystalline preferred orientations were characterized by an X-ray diffractometer (Bede D1) and a field emission transmission electron microscope (FE-TEM; Phillips Tecnai F-20) with an electron voltage of 200 kV. The cross-sectional TEM specimens were prepared by a focus ion beam (FIB; Seiko SII-3050). The FIB was performed with accelerated voltage of 30 kV to cut the samples roughly

and then refined the sample further by accelerated voltage of 5 kV. The surface morphology was evaluated by the field emission scanning electron microscope (FE-SEM; Seiko SII-3050) and the atomic force microscope (AFM; Dimension 3100). AFM images were taken with tapping mode by silicon probe and the scanning data were characterized by software NanoScope (R) III (Digital Instruments, version 5.12r2). The photoluminescence (PL) measurement was carried out by Ti:sapphire laser (Traix-320) with a light source from 808-nm laser and 208 mW power from room temperature (300 K) to 14 K to investigate the optical emission properties of the InN epifilms.

The crystal structure of all samples was characterized by XRD measurements. **Figure 1** shows the XRD results of all samples and indicates that ***c***-plane InN epifilms were epitaxially grown on GaN templates. From the peaks of X-ray diffraction pattern at 2θ = 32.84°, 33.13°, 33.15°, and 33.76°, we estimated the content of indium of $In_xGa_{1-x}N$ on the basis of Vegard's law to be about 52, 43, 42, and 23%, respectively [20]. The peaks at 2θ = 31.22°, 32.97°, 34.57°, and 34.82° were corresponding to the X-ray diffraction patterns from **c**-plane InN (0 0 0 2), In (1 0 1), GaN (0 0 0 2), and Si-doped AlGaN (0 0 0 2), respectively. These peak positions for the X-ray diffraction patterns were obtained by software Quick Graph (version 2.0) with the Asymmetric Double Sigmoidal linear curve fitting. We can observe that the peak of $In_xGa_{1-x}N$ shifts from left to right with the increasing growth-temperature of the InGaN buffer layer. This shows that the content of indium decreases with the increasing growth temperature, and the diffraction of Indium was observed corresponds to In droplet on the surface of sample 3. In order to eliminate the influence of In drops in further measurements, the acid treatment (H_3PO_4:HNO_3:CH_3COOH:H_2O = 50:2:10:9) was employed for sample 3 to remove the In drops on the surface. As compared to other samples, the interference fringes of InN grown on sample 1 exhibit prominent oscillations. Qualitatively, it shows that sample 1 is a very high-quality and layer-by-layer epitaxial growth InN epifilm. **Figure 2(a** and **b)** shows the rocking curve and full-width at half maximum (FWHM) values of the plane of InN (0 0 0 2) and $In_xGa_{1-x}N$ (0 0 0 2), respectively. The FWHM values of the plane of InN (0 0 0 2) grown on samples 1, 2, 3, and 4 are 435.7, 651.5, 682.6, and 777.1 arc-sec,

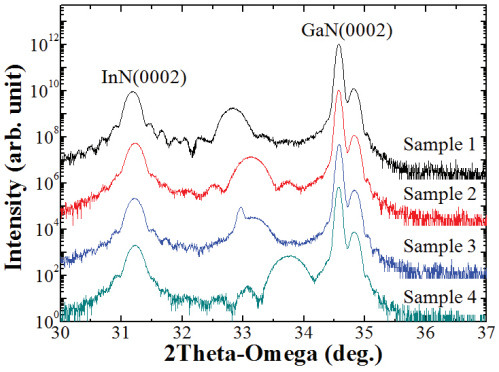

Figure 1. The X-ray 2 Theta-Omega scans of growing samples.

http://dx.doi.org/10.5772/65812

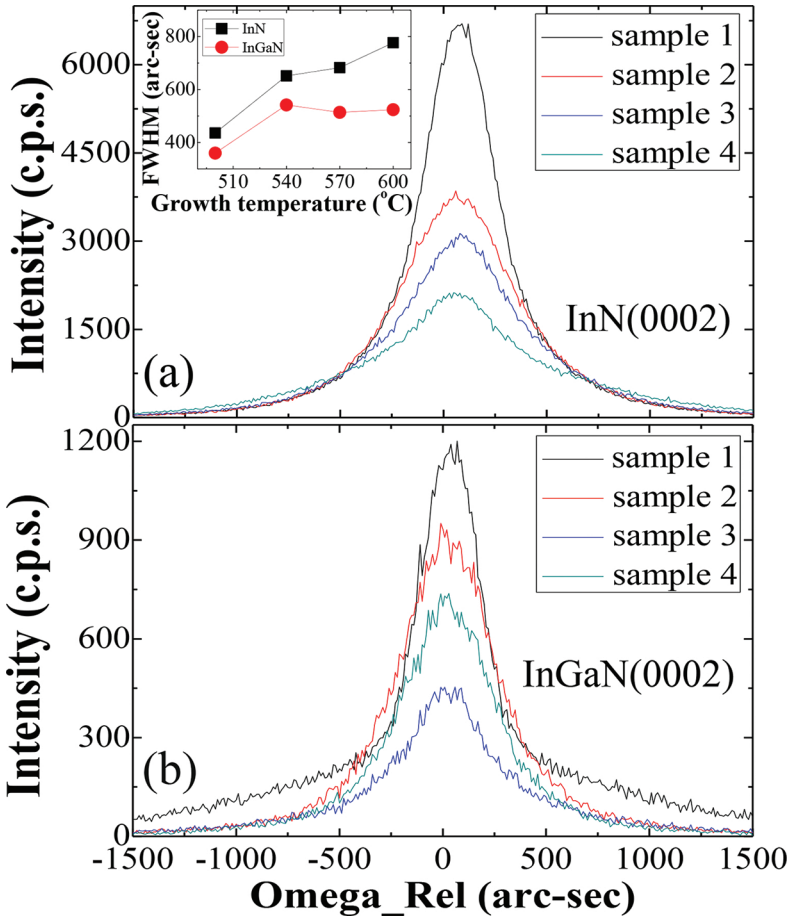

Figure 2. (a) Rocking curve of the plane of InN (0 0 0 2). (b) Rocking curve of the plane of $In_xGa_{1-x}N$ (0 0 0 2). The inset is the FWHM value vs. the growth temperature.

respectively. The FWHM values of the plane of $In_xGa_{1-x}N$ (0 0 0 2) grown on sample 1, 2, 3, and 4 are 359.6, 541.6, 513.7, and 523.8 arc-sec, respectively. It reveals that the intensity value of the plane of InN (0 0 0 2) grown on sample increases and the FWHM value of the plane of InN (0 0 0 2) grown on sample decreases with the decreasing growth temperature of InGaN grown on sample. Therefore, the maximum intensity and minimum FWHM value of the plane of InN (0 0 0 2) grown on sample 1 from **Figure 2(a)** is obtained, which shows that it is helpful to grow high-crystal quality InN epifilms by decreasing the growth temperature of the InGaN buffer layer and the growth parameter of sample 1 is suitable to grow a high-quality InN epifilm.

Figure 3(a–d) shows the surface morphology of *c*-plane (0 0 0 2) InN grown on samples 1, 2, 3, and 4, respectively, obtained by SEM (SII-3050). By comparing the RHEED patterns of InN

grown on samples 1, 2, 3, and 4 along with [1 1¯ 0 0] InN, we found that the RHEED pattern of sample 1 is streaky but others are spotty patterns, indicating that the growth mode of InN on sample 1 was established by the two-dimensional (2D) Frank-van der Merwe epitaxial growth mode. As compared to the XRD results of InN grown on sample 1 with prominent oscillations, sample 1 is a high-quality and layer-by-layer epitaxial 2D-growth sample. From SEM analysis, we observed the flatness of *c*-plane InN epifilm was getting smoother from sample 4 to sample 1 except for sample 3 because of the In drops left on the surface. The surface morphology of samples 1, 2, 3, and 4 were also analyzed by AFM with the root-mean-square (RMS) roughness, as shown in **Figure 4**. The RMS values of samples 1, 2, 3, and 4 are 0.636, 1.537, 9.821, and 1.910 nm, respectively. It shows that the surface of sample 1 is the flattest surface morphology in the samples, and supports the conclusion of XRD, RHEED, and SEM analyses. It also indicates that it is helpful to grow flat InN epifilms by decreasing the growth

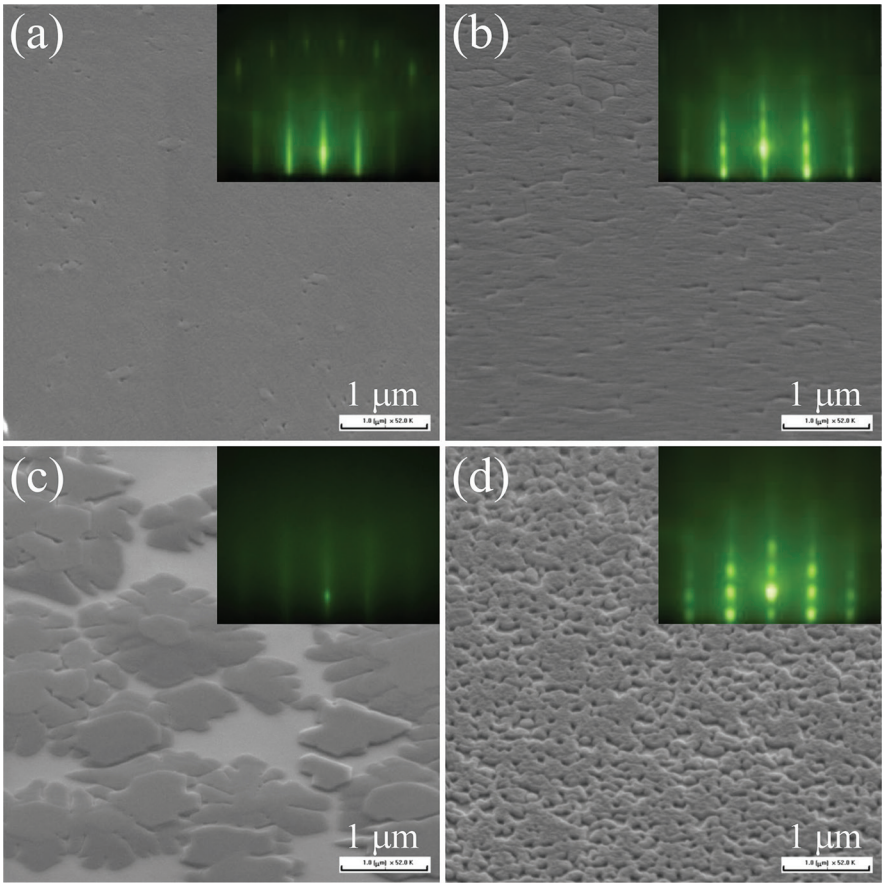

Figure 3. SEM images of *c*-plane InN thin films grown on (a) sample 1, (b) sample 2, (c) sample 3 and (d) sample 4. The scale bar is 1 μm.

http://dx.doi.org/10.5772/65812

temperature of InGaN buffer layer and the growth parameter of sample 1 offers a better condition to grow flat InN epifilms. Sample 1 was then studied in more detail.

Figure 5 shows that PL spectra of sample 1 for different temperatures. The PL measurements were carried out by Ti:sapphire laser (Traix-320) with a light source from 808-nm laser and 208 mW power from 300 to 14 K. When the temperature was changed from 300 to 14 K, the position of major peak shifted from 0.698 to 0.703 eV, in good agreement with the recent data (~0.7 eV) [7, 8]. The intensity of major peak also increased. The major peaks measured at different temperatures were confirmed by a multipeak Gaussian-function curve fitting with the software Origin (Pro. 8.0). The result of the multipeak Gaussian-function curve fitting showed that the major peak was composed by three peaks and all the peak centers shifted to higher energy when the temperature was changed from 300 to 14 K. Among three fitting peaks, only one peak can be described by Varshni's equation [21]:

$$E_g(T) = E_g(0) - \frac{\alpha T^2}{T + \beta}$$

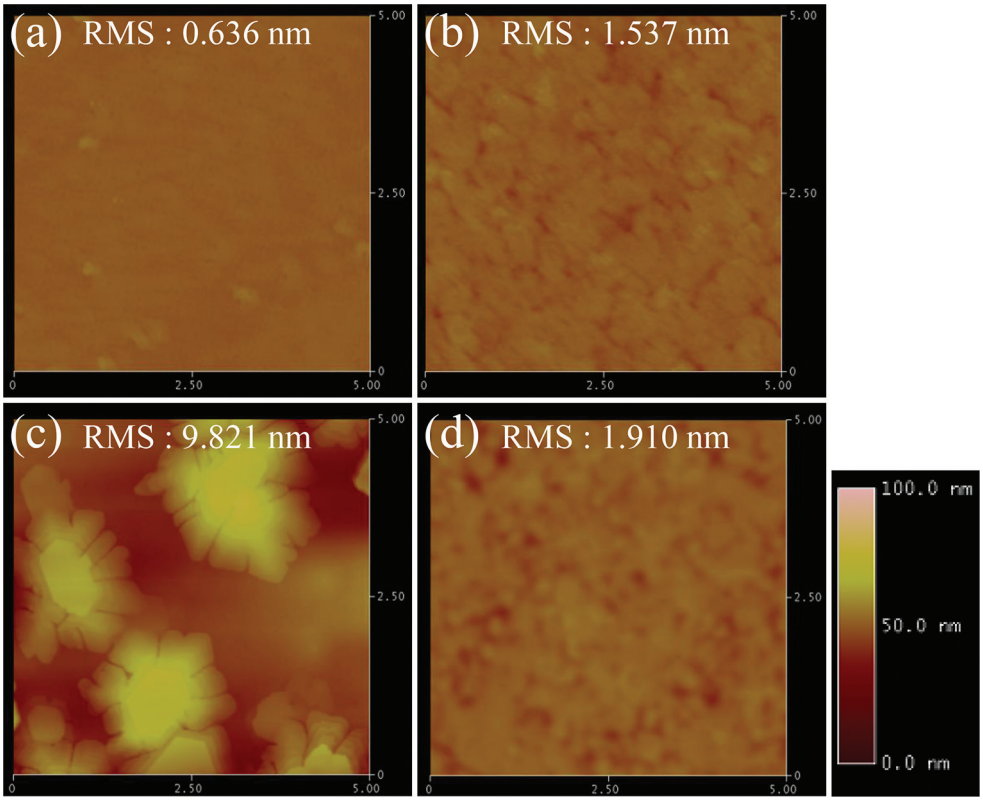

Figure 4. AFM images of surface of growing samples by 5 × 5 μm² scan: (a) sample 1, (b) sample 2, (c) sample 3, and (d) sample 4. The scale bar is 100 nm

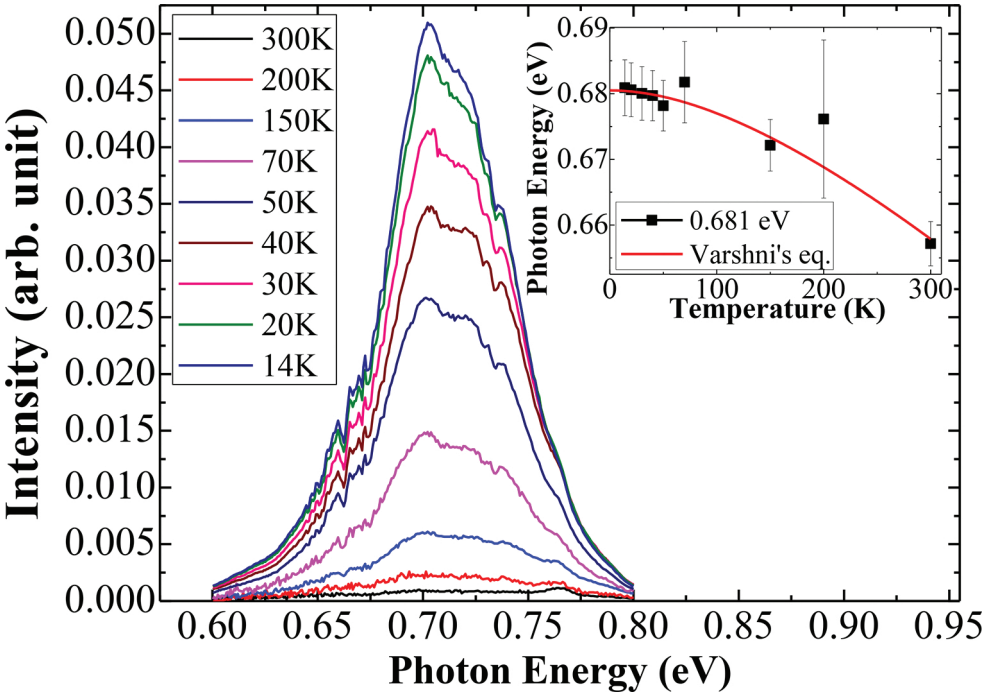

Figure 5. The PL spectra taken at different temperatures. The inset is PL peak energy as a function of temperature. The uncertainty of PL peak position is the result of the multipeak Gaussian-function curve fitting. The red curve is the theoretical fitting to Varshni's equation.

In the inset of **Figure 5**, the theoretical fitting to Varshni's equation is obtained with $E_g(0)$ = 0.681 eV, α = 0.18 meV/K and β = 416 K. As compared to $E_g(0)$ = 0.69 eV, α = 0.41 meV/K and β = 454 K from Wu et al. [8], we find that the values of $E_g(0)$ and β are consistent with the results of Wu et al., within the variation of β. The value of β, Debye temperature at 0 K, is in the range from 370 to 650 K for hexagonal InN, estimated by Davydov et al. [22]. However, the different values of α, the Varshni thermal coefficient, might be due to the different InN thicknesses of the sample used in this study. The other two peaks were nearly independent of temperature, and attributed to the defect levels.

The cross-sectional TEM specimen of sample 1 was prepared by a dual-beam focus ion beam (Seiko SII-3050), with the cleavage plane along the [1 1$^-$ 0 0] direction on the *c*-plane InN (0 0 0 1) and carbon was used as a preservation layer to avoid the damage from the Ga-ion beam during the preparation. The microstructure of sample 1 was analyzed by the field emission transmission electron microscope (FE-TEM; Phillips Tecnai F-20) with an electron voltage of 200 kV. From the TEM bright field image with [1 1 2$^-$ 0] zone axis in **Figure 6(a)**, we deduced the selective area diffraction (SAD) pattern for sample 1, as shown in **Figure 6(b)**. It shows three distinguishing rectangular diffraction spots in the SAD pattern, indicating that sample 1 was formed by the high-quality GaN, InGaN buffer layer and InN crystals. All of the spots

http://dx.doi.org/10.5772/65812

are very clear and with no distortion. It shows that there are few stacking-faults in sample 1. The ***d*-spacing** of {0 0 0 1} and {[1 1¯ 0 0]} planes of GaN were measured to be (d_{0001} = 0.5109 nm and d1 1¯ 0 0=0.2753 nm). The ***d*-spacing** of {0 0 0 1} and {[1 1¯ 0 0]} planes of InGaN were measured to be (d_{0001} = 0.5371 nm and d1 1¯ 0 0=0.2821 nm). The ***d*-spacing** of {0 0 0 1} and {[1 1¯ 0 0]} planes of InN were measured to be (d_{0001} = 0.5634 nm and d1 1¯ 0 0=0.3043 nm). This indicates that the In content of $In_xGa_{1-x}N$ in Sample 1 is, about 50% determined from these d_{0001} data, which is consistent with the XRD analysis. The scanning transmission electron microscope (STEM) measurement will show the high contract images among GaN, InGaN, and InN layers. We show the STEM result for sample 1 in **Figure 6(c)**. It clearly exhibits, with a high-resolution STEM image, that the InN epifilm was well formed on the InGaN buffer layer and the InGaN buffer layer was well established on GaN template. The thicknesses of

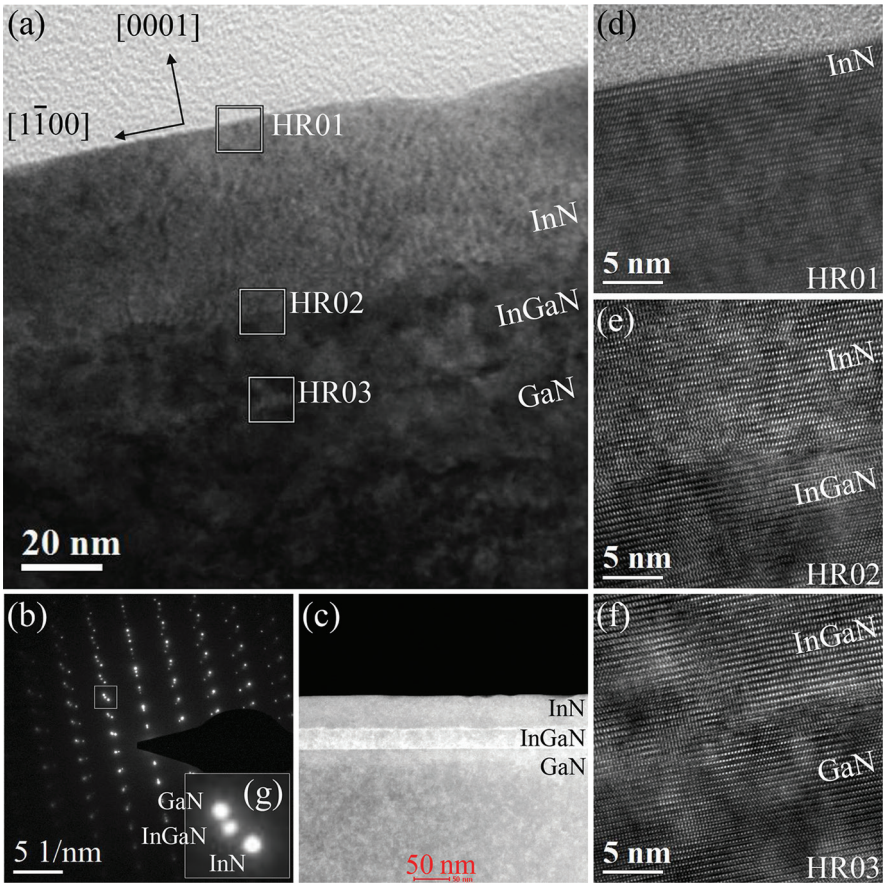

Figure 6. TEM analysis of sample 1: (a) the bright field image of TEM, the scale bar is 20 nm, (b) the selective area diffraction patterns, the scale bar is 5 (1/nm), (c) the STEM image, the scale bar is 50 nm. (d)–(f) the high-resolution TEM images of InN, InN-InGaN interface, and InGaN-GaN interface, respectively, the scale bar is 5 nm, (g) the enlarged SAD pattern of the square in (b).

InN and InGaN buffer layer were evaluated from the STEM image to be about 50 and 30 nm, respectively. The high-quality crystalline microstructures of InN, InGaN and GaN layers were also confirmed by the high-resolution TEM images. **Figure 6(d–f)** showed that InGaN buffer layer was well-stacked on GaN and high-quality InN epifilm was well-stacked on the InGaN buffer layer with some minor structural defects (e.g., dislocations or stacking faults) occurred in InN and InGaN layers.

2.4. Characteristics of InN epifilms

From the crystal structural analyses by XRD and TEM, we found that the crystal quality was significantly improved by decreasing the growth temperature of InGaN buffer layer. From the SEM images and AFM analyses, we also found that the surface of InN epifilm became smoother by decreasing the growth temperature of the InGaN buffer layer. From the PL measurements, we showed that the energy of 0.681 eV emitted from the InN epifilm of sample 1 (the growth temperature of InGaN buffer layer is 500°C) by the fitting to Varshni's equation. Finally, it is suggestive that one can grow high-quality and flat InN epifilms by decreasing the growth temperature of the InGaN buffer layer. Therefore, the influence of InGaN buffer layer is very effective to grow high-quality InN epifilms and InN microstructures as well. We therefore grow InN hexagonal microdisks on the LAO substrate with the InGaN buffer layer.

3. InN hexagonal microdisks

3.1. Growth of InN microdisks

The two-orientation growth of GaN nanopillars on the LAO substrate has been reported in our previous papers [23, 24]. In this paper, we applied the two-orientation growth to grow the 2D *M*-plane InN epifilm and 3D ***c***-plane InN hexagonal microdisks on the LAO substrate with the InGaN buffer layer at low-growth temperature (470°C). The sample was grown on a high-quality 1 × 1 cm^2 LAO (1 0 0) substrate with the InGaN buffer layer by a low-temperature PA-MBE system (Veeco Applied-GEN 930). The LAO substrate was cut from the crystal ingot, which was fabricated by the traditional Czochralski pulling technique. Then, we grew InN hexagonal microdisks with an InGaN buffer layer on the γ-$LiAlO_2$ substrate by plasma-assisted molecular beam epitaxy. The details of growth parameters can be obtained from the previous paper [25].

3.2. Analysis of InN microdisks

The crystal structure of the microdisk sample is characterized by the high-resolution X-ray diffraction (XRD; Bede D1) measurement and is shown in **Figure 7**. From the peak of X-ray diffraction pattern at $2\theta = 31.69°$, we estimated the content of indium of $In_xGa_{1-x}N$ on the basis of Vegard's law to be about 20% [20]. The peaks at $2\theta = 29.07°$, 31.31°, 32.29°, and 34.69° represent the X-ray diffraction patterns from **M**-plane InN ($1\,1^{-}\,0\,0$), ***c***-plane InN ($0\,0\,0\,2^{-}$),

M-plane GaN (1 1^{-} 0 0) and LAO (1 0 0), respectively. By the asymmetric double sigmoidal linear curve fitting with the software Quick Graph (version 2.0), these XRD peak positions were obtained that agreed with those data of the standard wurtzite structure bulk InN (JCPDS file No. 50-1239). The ***d*-spacing** between {0 0 0 2^{-}} planes of InN was evaluated to be d_{0002} = 0.28216 nm from the Bragg's law ($2d\sin\theta = n\lambda$) with Cu K_{α} wavelength λ = 0.1540562 nm. The lattice constant of wurtzite InN microdisk is smaller than that of bulk InN by 1.09%, as compared with the value on JCPDS file, d_{0002} = 0.28528 nm.

The surface morphology of the sample was evaluated by the field emission scanning electron microscope (FE-SEM, SII-3050). **Figure 7(a)** showed the top-view SEM image of the sample. The morphology of the sample exhibited that 3D *c*-plane InN hexagonal microdisks and 2D *M*-plane InN epifilm were grown on the LAO substrate. **Figure 7(b)** showed the tilt-view SEM image of the InN microdisk shown in the center of **Figure 7(a)**, and the diameter of the InN microdisk was 0.60 μm. The micrographic image of the sample showed that the 3D *c*-plane InN hexagonal microdisks and nanopillars were grown atop an anionic hexagonal basal plane of LAO, while the 2D *M*-plane InN epifilm were developed along with the lateral orientation [112^{-}0]InN//[001]LAO.

The microstructure of the sample was analyzed by a field emission transmission electron microscope (FE-TEM; Phillips Tecnai F-20) at an electron voltage of 200 kV. The cross-sectional TEM specimen was prepared by a dual-beam focus ion beam (FIB; Seiko SII-3050), on the

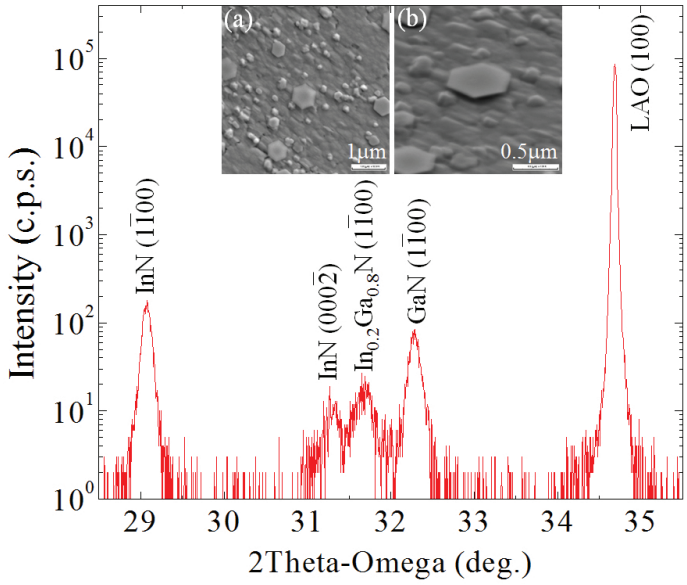

Figure 7. The X-ray 2 Theta-Omega scan of the sample. In the inset of (a) the top-view SEM image of the sample, the scale bar is 1 μm. (b) Enlarged SEM image with a tilted angle of InN hexagonal thin disk, the scale bar is 0.5 μm.

cleavage plane along [11¯00] direction of the *c*-plane InN hexagonal thin disk. **Figure 8(a)** showed the bright field image with [112¯0]InN//[001]LAO zone axis. The thicknesses of *M*-plane InN, *M*-plane InGaN and *M*-plane GaN were measured to be about 265, 51, and 137 nm, respectively. The height for the *c*-plane InN hexagonal thin disk from neck to top was about 188 nm. The high-resolution TEM images with [112¯0]InN//[001]LAO zone axis were performed in the areas HR01 and HR02 of the sample, as shown in **Figure 8(a)**. From high-resolution TEM analyses, we found the staking faults at the boundary between *M*-plane and *c*-plane GaN, which released the strains between the misfit *M*-plane and *c*-plane wurtzite structures of GaN and InGaN. The *c*-plane wurtzite structure was followed up to the neck area and formed a uniform *c*-plane InGaN pyramid-shaped structure. The wave-shaped InN was produced by the staking faults between the misfit *c*-plane wurtzite structures of InGaN and InN. In **Figure 8(b)**, the wave-shaped InN became uniform in the area HR01 and followed further to form the InN hexagonal thin disk structure. In **Figure 8(c)**, the high-quality crystalline structure of the InN thin disk is shown in the area HR02. **Figure 8(d–i)** shows the selective area diffraction (SAD) patterns taken along the growth direction from the bottom to the top (labeled from DP01 to DP06), which covered *c*-plane GaN, *M*-plane GaN, *c*-plane InN, and *M*-plane InN. **Figure 8(d)** simply shows one clear single rectangular diffraction pattern (white) at the location of DP03, indicating that the hexagonal thin disk was uniquely formed by the *c*-plane wurtzite InN crystal. The ***d*-spacing** between {0 0 0 1¯} planes and {1 1¯ 0 0} planes of InN hexagonal thin disk were measured to be ***dc*** = 0.5687 nm and ***dM*** = 0.3025 nm, respectively. Compared with the values given in JCPDS file No. 50-1239 which are 0.5703 and 0.30647 nm, respectively, the difference between wurtzite InN thin disk and bulk InN for ***dc*** and ***dM*** are 0.28 and 1.24%, respectively, revealing that the

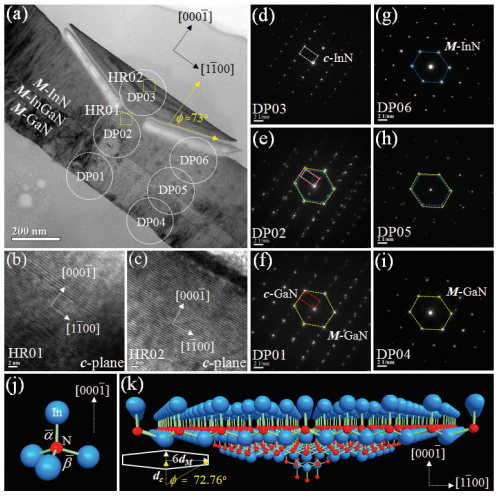

Figure 8. TEM analyses of the InN hexagonal thin disk: (a) the bright field image with [1 1 2¯ 0]InN//[0 0 1]LAO zone axis. The high-resolution TEM images taken at the points shown in (a) are presented in (b) and (c), the scale bar is 2 nm. The selective area diffraction patterns taken at the points shown in (a) are presented in [(d) – (i)], the scale bar is 2 (1/nm). The ball-stick model for InN epilayer: (j) the chemical bonds of (0 0 0 1¯) surface, (k) the hexagonal thin disk.

http://dx.doi.org/10.5772/65812

lattice constant of InN thin disk is smaller than that of bulk InN. The result is consistent with the XRD analysis. In **Figure 8(e)**, the SAD patterns showed the overlapping diagram of two rectangles and two hexagons at the neck area of the disk (location of DP02), indicating that a ***c***-plane InN (white rectangle) was formed in addition to the ***c***-plane GaN (red rectangle), ***M***-plane InN (blue hexagon), and ***M***-plane GaN (yellow hexagon) at the neck area. We checked the ***M***-plane InN (blue hexagon) and ***M***-plane GaN (yellow hexagon) by the SAD patterns, as shown in **Figure 8(g–i)**. These two hexagons are identical to those shown in **Figure 8(h)**, indicating that the ***M***-plane wurtzite InN and ***M***-plane wurtzite GaN were grown in the same crystalline direction. From the analyses of SAD patterns, we found that the ***c***-plane wurtzite nanocrystal was embedded between ***M***-plane wurtzite nanocrystal areas at the beginning of nucleation when GaN was grown on the LAO substrate. We demonstrated a ball-stick model for the self-assembled InN hexagonal thin disk to establish the growth mechanism of the InN hexagonal thin disk. The ball-stick model for the standard wurtzite InN (JCPDS file No. 50-1239) with $\boldsymbol{a} = \boldsymbol{b} = 0.3537$ nm, $\boldsymbol{c} = 0.5703$ nm, and $u=\alpha^{-}/c= 3/8$ was used to simulate the ***c***-plane InN thin disk in **Figure 8(j)**, where blue balls and red balls represented In atoms and N atoms, respectively. In our previous paper, we showed that the GaN $(0\,0\,0\,1^{-})$ microdisk with a tilted angle of $\theta = \tan^{-1}(\boldsymbol{dM}/\boldsymbol{dc}) = 28°$ was established with the capture of N atoms by the β^{-}-dangling bonds of the most-outside Ga atoms for each ***dc*-spacing** during the GaN lateral overgrowth [5]. In the case of InN thin disk, when the growth temperature was lowered to 470°C, the ***c***-plane InN $(0\,0\,0\,1^{-})$ hexagonal thin disk was built up with the capture of N atoms by the β^{-}-dangling bonds of the most-outside In atoms and then the lateral overgrowth occurred; by capture of In atoms by β^{-}-dangling bonds of N atoms, to form the thin disk. The lateral overgrowth along the $(1\,1^{-}\,0\,0)$ direction was extended to six ***dM*-spacings** for each ***dc*-spacing**, resulting in the angle of 73 off the ***c***-axis. Based on the ball-stick model, the edge was then tilted off the *c*-axis $[0\,0\,0\,1^{-}]$ direction by the angle of $\varphi = \tan^{-1}(6\boldsymbol{dM}/\boldsymbol{dc}) = 72.76°$ as shown in **Figure 8(k)**. We also calculated the angle from the measured SAD data at the InN hexagonal thin disk in **Figure 8(d)**, and obtained that the *d*-spacing between $\{0\,0\,0\,1^{-}\}$ planes was $\boldsymbol{dc} = 0.5687$ nm and the ***d*-spacing** between $\{1\,1^{-}\,0\,0\}$ planes was $\boldsymbol{dM} = 0.3025$ nm, resulting in $\varphi = \tan^{-1}(6\boldsymbol{dM}/\boldsymbol{dc}) = 72.60°$, which was in good agreement with the model predicted.

3.3. Characteristics of InN microdisks

We have grown InN hexagonal thin microdisks on the LAO substrate with the InGaN buffer layer by PA-MBE. From the SEM images and TEM analyses, we found that ***c***-plane wurtzite was established at the nucleation of GaN on the LAO substrate and ***c***-plane InN hexagonal thin disks were built up at low temperature (470°C) after insetting the InGaN buffer layer. The ***c***-plane InN $(0\,0\,0\,1^{-})$ hexagonal thin disk was produced with the capture of N atoms by the β^{-}-dangling bonds of the most-outside In atoms, and then laterally over-grown along $[1\,1^{-}\,0\,0]$ direction by six ***dM*-spacings** for each ***dc*-spacing**. The oblique angle of InN hexagonal thin disk was formed by the lateral overgrowth of the wurtzite structure. Based on the standard wurtzite InN, the angle of $\varphi = \tan^{-1}(6\boldsymbol{dM}/\boldsymbol{dc}) = 72.76°$ was evaluated. The oblique angle of InN hexagonal thin disk can be examined directly from the SAD pattern and high-resolution TEM analyses to be 72.60° and about 73°, respectively.

4. Conclusion

In this paper, we have reported the growth and characteristics of 2D ***c***-plane InN (0 0 0 1) epifilms and 3D ***c***-plane InN (0 0 0 1^{-}) hexagonal thin microdisks with InGaN buffer layers at low temperatures by PA-MBE. By decreasing the growth temperature of the InGaN buffer layer, we can grow high-quality and flat InN epifilms. Besides, InGaN buffer layer can also provide the growth base to form InN hexagonal thin microdisks. By introducing InGaN buffer layers, the high-quality InN epifilms and microstructures can be grown under suitable growth conditions. Consequently, the InN hexagonal thin microdisk provides an opportunity to fabricate the InGaN/GaN microdisk quantum well for the application of full-color micron LED.

Acknowledgements

The project was supported by the Ministry of Science and Technology of Taiwan and the Core Facilities Laboratory for Nanoscience and Nanotechnology in Kaohsiung and Pintung Area.

Author details

Chen-Chi Yang[1,2], Ikai Lo[1,2]*, Cheng-Hung Shih[1,2], Chia-Hsuan Hu[1,2], Ying-Chieh Wang[1,2], Yu-Chiao Lin[1,2], Cheng-Da Tsai[1,2], Hui-Chun Huang[1,2], Mitch M. C. Chou[1,2], Cheng-Chang Yu[1,2] and Der-Jun Jang[1,2]

*Address all correspondence to: ikailo@mail.phys.nsysu.edu.tw

1 Department of Physics, Center for Nanoscience and Nanotechnology, National Sun Yat-Sen University, Kaohsiung, Taiwan

2 Department of Materials and Optoelectronics Science, National Sun Yat-Sen University, Kaohsiung, Taiwan

References

[1] S. Nakamura, M. Senoh, N. Iwasa, S. I. Nagahama, T. Yamada, and T. Mukai. Super-bright green InGaN single-quantum-well-structure light-emitting diodes. Japanese Journal of Applied Physics. 1995;**34**(Part 2, Number 10B):L1332-L1335. DOI: 10.1143/JJAP.34.L1332

[2] S. Nakamura, S. Pearton, and G. Fasol, editors. The Blue Laser Diode: The Complete Story. Berlin: Springer Science & Business Media; 20 0 0 . 367 p. DOI: 10.1007/978-3-662-04156-7

[3] I. Lo, J. K. Tsai, W. J. Yao, P. C. Ho, L. W. Tu, T. C. Chang, S. Elhamri, W. C. Mitchel, K. Y. Hsieh, J. H. Huang, H. L. Huang, and W. C. Tsai. Spin splitting in modulation-doped

Al_xGa_{1-x} N/GaN heterostructures. Physics Review B. 2002;**65**:161306. DOI: 10.1103/PhysRevB.65.161306

[4] I. Lo, W. T. Wang, M. H. Gau, J. K. Tsai, S. F. Tsay, and J. C. Chiang. Gate-controlled spin splitting in GaN/AlN quantum wells. Applied Physics Letters. 2006;**88**:082108. DOI: 10.1063/1.2178505

[5] I. Lo, C. H. Hsieh, Y. C. Hsu, W. Y. Pang, and M. C. Chou. Self-assembled GaN hexagonal micropyramid and microdisk. Applied Physics Letters. 2009;**94**:062105. DOI: 10.1063/1.3079078

[6] A. Y. Cho, and J. R. Arthur. Molecular beam epitaxy. Progress in Solid State Chemistry. 1975;**10**, Part 3:157-191. DOI: 10.1016/0079-6786(75)90 0 0 5-9

[7] J. Wu, W. Walukiewicz, K. M. Yu, J. W. Ager III, E. E. Haller, H. Lu, W. J. Schaff, Y. Saito and Y. Nanishi. Unusual properties of the fundamental band gap of InN. Applied Physics Letters. 2002;**80**:3967. DOI: 10.1063/1.1482786

[8] J. Wu, W. Walukiewicz, W. Shan, K.M. Yu, J.W. Ager, S.X. Li, E.E. Haller, H. Lu, and W.J. Schaff. Temperature dependence of the fundamental band gap of InN. Journal of Applied Physics. 2003;**94**:4457-4460. DOI: 10.1063/1.1605815

[9] S. K. O'Leary, B. E. Foutz, M. S. Shur, U. V. Bhapkar, and L. F. Eastman. Electron transport in wurtzite indium nitride. Journal of Applied Physics. 1998;**83**:826-829. DOI: 10.1063/1.366641

[10] Z. Y. Fan and N. Newman. Experimental determination of the rates of decomposition and cation desorption from AlN surfaces. Material Science Engineering: B. 2001;**87**:244-248. DOI: 10.1016/S0921-5107(01)00720-6

[11] C. H. Liang, L. C. Chen, J. S. Hwang, K. H. Chen, Y. T. Hung, and Y. F. Chen. Selective-area growth of indium nitride nanowires on gold-patterned Si(1 0 0) substrates. Applied Physics Letters. 2002;**81**:22-24. DOI: 10.1063/1.1490636

[12] T. Stoica, R. Meijers, R. Calarco, T. Richter, and H. Luth. MBE growth optimization of InN nanowires. Journal of Crystal Growth. 2006;**290**:241-247. DOI: 10.1016/j.jcrysgro.2005.12.106

[13] Y. L. Chang, F. Li, A. Fatehi, and Z. Mi. Molecular beam epitaxial growth and characterization of non-tapered InN nanowires on Si (1 1 1). Nanotechnology. 2009;**20**:345203. DOI: 10.1088/0957-4484/20/34/345203

[14] I. Lo, Y. C. Wang, Y. C. Hsu, C. H. Shih, W. Y. Pang, S. T. You, C. H. Hu, M. M. C. Chou, and G. Z. L. Hsu. Electrical contact for wurtzite GaN microdisks. Applied Physics Letters. 2014;**105**:082101. DOI: 10.1063/1.4894080

[15] K. Xu and A. Yoshikawa. Effects of film polarities on InN growth by molecular-beam epitaxy. Applied Physics Letters. 2003;**83**:251-253. DOI: 10.1063/1.1592309

[16] H. Xiao, X. Wang, J. Wang, N. Zhang, H. Liu, Y. Zeng, J. Li, and Z. Wang. Growth and characterization of InN on sapphire substrate by RF-MBE. Journal of Crystal Growth. 2005;**276**:401-406. DOI: 10.1016/j.jcrysgro.2004.12.001

[17] Y. Saito, T. Yamaguchi, H. Kanazawa, K. Kano, T. Araki, Y. Nanishi, N. Teraguchi, and A. Suzuki. Growth of high-quality InN using low-temperature intermediate layers by RF-MBE. Journal of Crystal Growth. 2002;237-239:1017-1021. DOI: 10.1016/S0022-0248(01)02119-4

[18] H. Lu, W. J. Schaff, J. Hwang, H. Wu, G. Koley, and L. F. Eastman. Effect of an AlN buffer layer on the epitaxial growth of InN by molecular-beam epitaxy. Applied Physics Letters. 2001;79:1489-1491. DOI: 10.1063/1.1402649

[19] J-K. Tsai, I. Lo, K-L. Chuang, L-W.Tu, J-H. Huang, C-H. Hsieh, and K-Y. Hsieh. Effect of N to Ga flux ratio on the GaN surface morphologies grown at high temperature by plasma-assisted molecular-beam epitaxy. Journal of Applied Physics. 2004;**95**:460. DOI: 10.1063/1.1634388

[20] A. R. Denton and N. W. Ashcroft. Vegard's law. Physical Review A. 1991;**43**:3161-3164. DOI: 10.1103/PhysRevA.43.3161

[21] Y.P. Varshni. Temperature dependence of the energy gap in semiconductors. Physica. 1967;34:149-154. DOI: 10.1016/0031-8914(67)90062-6

[22] V. Yu. Davydov, V. V. Emtsev, I. N. Goncharuk, A. N. Smirnov, V. D. Petrikov, V. V. Mamutin, V. A. Vekshin, S. V. Ivanov, M. B. Smirnov and T. Inushima. Experimental and theoretical studies of phonons in hexagonal InN. Applied Physics Letters. 1999;**75**:3297-3299. DOI: 10.1063/1.125330

[23] C. H. Hsieh, I. Lo, M. H. Gau, Y. L. Chen, M. C. Chou, W. Y. Pang, Y. I. Chang, Y. C. Hsu, M. W. Sham, J. C. Chiang, and J. K. Tsai. Self-assembled c-plane GaN nanopillars on γ-$LiAlO_2$ substrate grown by plasma-assisted molecular-beam epitaxy. Japanese Journal of Applied Physics. 2008;**47**:891-895. DOI: 10.1143/JJAP.47.891

[24] I. Lo, C. H. Hsieh, Y. L. Chen, W. Y. Pang, Y. C. Hsu, J. C. Chiang, M. C. Chou, J. K. Tsai, and D. M. Schaadt. Line defects of M-plane GaN grown on g-$LiAlO_2$ by plasma-assisted molecular beam epitaxy. Applied Physics Letters. 2008;**92**:202106. DOI: 10.1063/1.2924288

[25] C. C. Yang, I. Lo, C. H. Hu, H. C. Huang, and M.M. C. Chou. Growth of InN hexagonal microdisks. AIP Advances. 2016;**6**:085015. DOI: 10.1063/1.4961699

Chapter 16

Chemical Solution Deposition Technique of Thin-Film Ceramic Electrolytes for Solid Oxide Fuel Cells

Mridula Biswas and Pei-Chen Su

Additional information is available at the end of the chapter

http://dx.doi.org/10.5772/66125

Abstract

Chemical solution deposition (CSD) technique is recently gaining momentum for the fabrication of electrolyte materials for solid oxide fuel cells (SOFCs) due to its cost-effectiveness, high yield, and simplicity of the process requirements. The advanced vacuum deposition techniques such as sputtering, atomic layer deposition (ALD), pulsed laser deposition (PLD), metallo-organic chemical vapor deposition (MOCVD) are lacking in scalability and cost-effectiveness. CSD technique includes a variety of approaches such as sol-gel process, chelate process, and metallo-organic decomposition. The present chapter discusses briefly about the evolution of CSD method and its subsequent entry to the field of SOFCs, various solution methods associated with different chemical compositions, film deposition techniques, chemical reactions, heat treatment strategies, nucleation and growth kinetics, associated defects, etc. Examples are cited to bring out the history dating back to the discovery of amorphous zirconia film through the successful fabrication of the crystalline fluorite-type films such as yttria-stabilized zirconia (YSZ), scandia-doped ceria (SDC), and crystalline perovskite-type films such as yttria-doped barium zirconate (BZY) and yttria-doped barium cerate (BCY), to name a few.

Keywords: chemical solution deposition, solid oxide fuel cell, ceramic electrolyte, thin films

1. Introduction

The high-temperature solid oxide fuel cells (HTSOFCs, ≥750°C) are yet to find widespread commercialization due to its high cost and short lifetime associated with its high-temperature operation. Thus, the demand for low-cost solid oxide fuel cells (SOFCs) has stimulated

research to develop low-temperature SOFCs (LTSOFCs, ≤500°C) [1]. Since the high performance of SOFCs requires high operating temperature to activate electrochemical reactions and charge transport processes, reduction in operating temperature will sacrifice performance of SOFCs. Therefore, attempts have been made to find new materials and fabrication technologies for LTSOFCs so that performance remains the same or gets enhanced. One of the main challenges in decreasing the operating temperature is the lower electrolyte conductivity, which resulted in high ohmic resistance, and deteriorates the fuel cell performance. Efforts have been made to enhance performance via reducing the thickness of ceramic electrolyte [2–8]. As the resistance of ionic charge transportation across the electrolyte obeys Ohm's law, thinner film offers less resistance to the ionic conduction and provides lower area-specific resistance. Various thin-film fabrication methods have been developed to date including vacuum-based [9–15] and non-vacuum-based methods [16–18]. Among them, chemical solution deposition (CSD) technique has been a promising technique for its high yield, versatility, and low investment cost. Moreover, the characteristic of CSD method allows easy deposition of the film over the large area up to several square meters [19]. The following paragraphs will be discussing the progress of the concept of thin film and discovery and progress of CSD method.

1.1. The concept of thin-film electrolyte and its progress

The concept of the thin-film electrolyte was first introduced with the fabrication of 400 μm thick stabilized zirconia (SZ) electrolyte in the 1960s [20]. The trend continued with the development of 30 μm thick yttria-stabilized zirconia (YSZ) electrolyte which, for the first time, successfully demonstrated the remarkable reduction of ohmic resistance from 1 to 3×10^{-3} Ω owing to minimization of the thickness of electrolyte from 1 mm to 30 μm [16]. In 1977, one electrochemical experiment, for the first time, achieved 0.91 V of open-circuit voltage (OCV) at 400°C with 0.05–1.7 μm thick calcia-stabilized zirconia (CSZ) film [10], which is a major breakthrough for LTSOFCs. With the progress in the R&D sector, Westinghouse Electric Corporation first launched cathode-supported tubular cell with 50 μm thick electrolyte, which was the first appearance of SOFC with a film electrolyte in the commercial sector [14]. All these developments were carried out with the vacuum-based methods (i.e., electrochemical vapor deposition, physical vapor deposition, chemical vapor deposition, sputtering, etc.) which lack in scalability and cost-effectiveness. As the alternative to those methods, slurry and solution-based methods were adopted. They are atmospheric or vacuum plasma spraying [21], spray pyrolysis [22], slurry coating [23, 24], and CSD [17, 18]. Although these methods are successful for micrometer thick film, the thickness of the electrolyte could not be brought down to the sub-micrometer level. With the miniaturization of SOFCs, demand for sub-micrometer thin electrolyte has been generated. CSD-based method has recently demonstrated its ability to produce films with sub-micrometer thickness.

1.2. Discovery and progress of CSD

The CSD method was introduced with the discovery of silica (SiO_2) gel from silicon alkoxide in humidified atmosphere in the middle of the nineteenth century [25]. The potential of this technique was realized with the application of single and multilayered coating of titania

http://dx.doi.org/10.5772/66125

(TiO_2), zirconia (ZrO_2), alumina (Al_2O_3), etc. on SiO_2 glass in the 1950s, and henceforth commercialization followed [26–28]. The development of YSZ film fabrication method started with the invention of amorphous coating of ZrO_2 film in the Central Glass and Ceramic Research Institute, India, in 1984 [17]; the Lawrence Berkeley National Laboratory took a pioneering role to develop crack-free, smooth crystalline 0.1–2 μm thin YSZ electrolyte film with sufficiently high conductivity at a temperature of 450°C [29]. Gastightness of YSZ film was demonstrated for the first time with the achievement of promising open-circuit voltage (OCV) of 0.85 V at 600°C [30]. This optimistic result casts light on the rapid progress of CSD method in the field of SOFCs. In 1912, Korea Institute of Science and Technology, South Korea, reported the fabrication of a dense and gastight bilayer electrolyte of YSZ/gadolinia-doped ceria (GDC) with thickness of 100/400 nm. The success of this process was established with the achievement of 1.0 V OCV at 650°C [31]. Numerous significant progresses across the globe are discussed in various articles [3, 32–46].

The fabrication strategies were extended from binary to ternary oxide electrolytes. The fabrication of multiple oxide electrolytes faced difficulties with single-phase formation because of the presence of several oxides and their different crystallization kinetics. The possibility of developing a single-phase ternary oxide thin film was advanced with the successful fabrication of lead zirconate titanate (PZT) film via metallo-organic decomposition (MOD) and sol-gel route in the 1980s [18, 47, 48]. For the first time, phase-pure ternary oxide electrolyte film of Yb-doped strontium zirconate (YDSZ) was successfully obtained via sol-gel method [49]. Our group from Nanyang Technological University, Singapore, has recently reported the fabrication of a dense and crack-free yttria-doped barium zirconate (BZY) thin film by modified CSD technique along with various sintering strategies [38, 40, 50–52] at remarkably low sintering temperature of 800–1000°C. The following sections will give the detail about the various solution preparation strategies and sintering methods.

2. CSD methods

CSD techniques are specially characterized by its mass transport process (**Figure 1**) which maintains liquid phase as the mass transport media for the transportation of precursors from the source to the substrate. The major advantages of CSD method are homogeneity of the product and lower processing temperature compared to the temperature for solid-state sintering [29]. Morphological control over the deposited film can be gained through varying composition, viscosity, pH, concentration of the solution, etc.

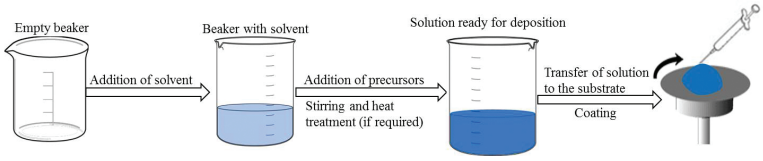

Figure 1. Chemical solution deposition technique.

Based on various requirements of different film morphology, CSD process can be categorized into three major groups: sol-gel process, chelate process, and MOD technique [53]. In this section, the CSD methodologies will be reviewed, with an emphasis on the underlying chemical aspects of the solution. The characteristics of the main three methods have been summarized in **Table 1**.

Method	Precursors and solvents	Control of chemistry	Simplicity
Sol-gel	• Metal alkoxides as precursors	High	Low
	• Alcohols as solvents		
	• Acid or base as catalyst		
	• Water for polymerization		
Chelate	• Metal carboxylate, alkoxide, and β-diketonate as precursors	Moderate	Moderate
	• Acetylacetonate and acetic acid as chelating agent and solvents		
Metallo-organic decomposition (MOD)	• Long-chain metal carboxylates such as 2-ethylhexanoate, dimethoxy dineodecanoate, and neodecanoate as precursors	Low	High
	• Xylene as solvent (inert)		

Table 1. The comparison among three major CSD processes.

2.1. Sol-gel process

A classical sol-gel process typically involves metal alkoxides and alcohols ($M(OR)_x$ and ROH). Common alcohols are methanol and ethanol; 2-methoxyethanol and 1,3-propanediol are also widely used [54, 55]. The selection of cationic components and solvent is crucial for controlling subsequent hydrolysis and condensation reaction, which is the basis for the development of short polymeric species and metal-oxygen-metal (M–O–M) bond upon heat treatment. The reactions are described below [56]:

Hydrolysis:

$$M(OR)_x + H_2O \rightarrow M(OR)_{x-1}(OH) + ROH \tag{1}$$

Condensation (alcohol elimination):

$$2M(OR)_{x-1}(OH) + M_2O(OR)_{2x-3}(OH) + ROH \tag{2}$$

http://dx.doi.org/10.5772/66125

Condensation (water elimination):

$$2M(OR)_{x-1}(OH) + M_2O(OR)_{2x-2} + H_2O \tag{3}$$

The primarily evolution of inorganic networks occurs through the generation of small particle resulting into colloidal suspension (sol), followed by the formation of continuous network in liquid matrix (gel) [57, 58]. The formation of sol and gel is aided by addition of water, base, and acid [59]. Base and acid act as catalysts. Upon drying and heating, the gel gets converted into amorphous film along with densification. With further heating, amorphous film ceramizes and rate of densification slows down.

In case of multicomponent system, all the alkoxide precursors may not have equal tendency to get dissolved in the same solvent because of their different polarity and ionicity/covalency. Those alkoxides are sometimes pre-hydrolyzed so that the final solution becomes compositionally homogeneous.

Hydrolysis of a particular M–O–R bond depends on its polarity. As the bond polarity increases, the tendency of being hydrolysis also increases. This character plays an important role in determining the processing window which gives an amount of the ratio of reagent to water and precursor concentration. Addition of water to the solution should be controlled to hinder precipitation. Otherwise, powder formation will take place. There are two major strategies to address the problem of hydrolysis associated with polar compounds: alcohol exchange reaction and chelation. In both processes, susceptibility of the reactants toward water is reduced. The alcohol exchange reaction is described below [59]:

$$M(OR)_x + xR'OH \rightarrow M(OR')_x + xROH \tag{4}$$

or

$$M(OR)_x + xR'OH \rightarrow M(OR)_{x-1}(OR') + ROH + (x-1)R'OH \tag{5}$$

The alcohol, 2-methoxyethnol, is widely used for alcohol exchange reaction due to its bidentate nature. Hence, the newly generated alkoxide is less prone to hydrolysis, thereby allowing easy formation of gel instead of precipitate [35]. As for example, 2-methoxyethanol was used to dissolve Ba metal and partially substitute propoxide of zirconium propoxide for the fabrication of epitaxial BZY film. Acetic acid is used for chelation. In some typical film fabrication method, both the acetic acid and 2-methoxyethanol are used together [60]. As 2-methoxyethnol does not change the solution pH, it is often used for the dilution of solution.

2.2. Chelate process

This is a specialized process of sol-gel technique which employs chelation reaction as the key process in the preparation of the precursor solution. This process with a wide range of application and variety of chemical compositions has opened a separate branch called chelate process. The process aims at the reduction in over-reactive tendency of alkoxides via addition of acetylacetonate or diethanolamine. In most compositions, metal carboxylate, β-diketonate, and alkoxides are used as precursors [59]. Mostly, transition metal alkoxides show polarity with high tendency toward rapid hydrolysis and condensation, requiring complexing or chelating ligands to limit uncontrolled reactions. Acetic acid and acetylacetone are added to the precursor solution to alleviate the issue. Acetic acid can act as both chelating and bridging agent, while acetylacetone only acts as chelating agent. This chelating agent blocks hydrolysis site with the replacement of reactive alkoxide ligand. A typical reaction with acetic acid is described below:

$$M(OR)_n + xCH_3COOH \rightarrow M(OR)_{n-x}(CH_3COO)_x + xROH \tag{6}$$

This typical reaction states that the species contains both the acetate and alkoxide ligands. Being bidentate in nature [61] and sterically larger than alkoxy group, the acetate ligands are not much susceptible to hydrolysis. In addition to this, acetylacetone plays the role of stabilizer of colloidal solution as well since it prevents aggregation of colloidal particles by creating steric hindrance [62]. In a typical chelate process, YDSZ was prepared via chelate route using acetylacetone [49]. This chelate process has been widely used to fabricate YSZ and BZY films for SOFC electrolytes [36, 40, 50–52, 63].

2.3. Metallo-organic decomposition (MOD)

This method involves high molecular weight precursors such as water-insensitive carboxylates and 2-ethylhexanoates. This process is less common than the other methods [59, 64]. This method is straightforward without necessitating precise control of the chemistry. Long-chain carboxylate compounds such as lead 2-ethylhexanoate, titanium dimethoxy dineodecanoate, zirconium neodecanoate, etc. are used as precursors, whereas the common solvent is xylene. The method involves simply dissolution of the metallo-organic compounds in a common solvent. The organic moieties of long-chain length compounds enhance dissolution tendency and concomitantly hinder hydrolysis tendency. They are normally dissolved in common solvent such as xylene [59, 64–66]. As these precursors are water insensitive and nonreactive to one another, they do not undergo any structural or chemical change [56]. This process is the simplest one among the three methods since no skill for controlling the hydrolysis and condensation is necessary. Still, this process suffers from several limitations. First, the large organic chains may cause crack during its decomposition upon heat treatment. Second, modification of the solution properties is limited; hence, the microstructure of the thin film cannot be tailored. This method has been applied specially for the ferroelectric materials [56]. The application of this method is not so popular in the field of SOFCs.

2.4. Other processing routes

Although the abovementioned three processes have found extensive application, there are several other routes such as Pechini method (old method), aqueous solution, citrate, nitrate routes, etc. [56, 59]. Pechini method is an aqueous chemical route which involves dissolution of metal cations and hydroxycarboxylic acid (such as citric acid, etc.) and ethylene glycol in deionized water. Till date, simple Pechini method has not shown any remarkable progress in the field of SOFC electrolytes. Pechini method modified with ethylenediaminetetraacetic acid (EDTA) has been proved to be an efficient technique for the fabrication of nonporous thin-film gadolinia-doped barium cerate (BCG) for SOFC [67]. Citrate process is also similar to the Pechini method [56] without involving ethylene glycol. This method modified with EDTA as chelating agent successfully produced electrolyte film without through-film crack [38]. Aqueous method includes dissolution of metal nitrates or chlorides and other polymerizing agents such as polyvinylpyrrolidone (PVP) in deionized water [34]. A SOFC cell with 0.5 μm thick crack-free YSZ electrolyte film was fabricated via this method. YSZ thin films obtained by both the aqueous and the nonaqueous processes are identical as per the surface morphology, which gives the direction toward the development of aqueous method in future.

2.5. Combined colloidal CSD method

The limitation of sol-gel, chelate, and MOD processes lies in obtaining film thicker than 0.5 μm with the application of single-layer coating [68]. Therefore, the multi-coating approach was required to obtain thicker film. Still, there is limitation for obtaining crack-free film thicker than 10 μm due to the constraining effect of the substrate. Hence, combined colloidal CSD method was introduced [32, 63, 68, 69]. This method involves addition of pre-synthesized nano-powder to CSD solution. This newly formed system consists of precursors, nano-powder (either synthesized via sol-gel route or commercially purchased), and at least one solvent [69]. Nanoparticles are introduced in the chemical solution to encounter the external constraint due to the presence of substrate and reduce the extent of differential densification in the planar dimension. As the metal-oxide network shrinks faster than the substrate, shrinkage mismatch occurs between the film and the substrate. Since the nanoparticles are supposed to sinter at a significantly lower rate than the metal-oxide framework [31], nanoparticles were added to the solution. To date, there are several significant research works on the YSZ thin film and doped ceria with the thickness ranging from nanometer to several micrometer via CSD method or combined CSD method [32–34, 39, 60, 63, 68, 70–72]. Several groups have already made micro-SOFCs based on CSD techniques [39, 70, 72].

3. Deposition techniques

The precursor solution is deposited over the substrate via a number of coating techniques. The most widely used coating techniques are spin coating, dip coating, and spray coating, as illustrated in **Figure 2**. In this section, the film deposition techniques and their application to SOFC electrolytes will be discussed.

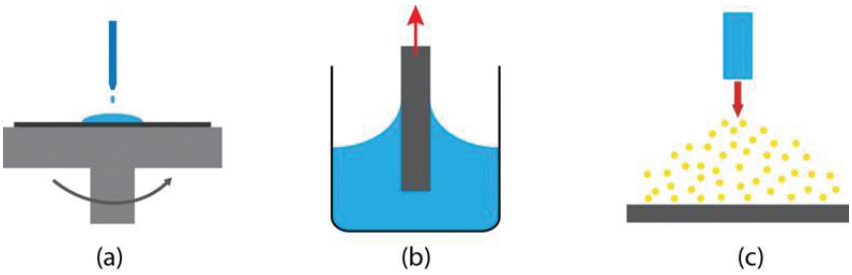

Figure 2. Schematic diagrams of (a) spin, (b) dip, and (c) spray coating.

3.1. Spin coating

Spin coating is a simple process to deposit uniform thin films on relatively flat substrates (**Table 2**). Typically, the substrate to be coated is held in place by vacuum chuck, and the coating solution is dispensed onto the substrate. The substrate is then accelerated to the desired rotation speed for certain duration to obtain desirable film thickness. The excess liquid is spread out from the substrate due to the action of centrifugal force, leaving a thin uniform coating on the surface of the substrate. The major advantages of spin coating are reproducibility, uniformity, simplicity, ability to use different substrate materials, and low cost. The main disadvantage of the method is the requirement of the smooth and flat substrate.

Technique	Description	Advantages	Disadvantages	Application
Spin coating	Evenly coats the substrates with CSD solution due to the rotation of the substrate placed on vacuum chuck	• Simplicity • Thin and uniform coating • Low cost	• Relatively low throughput • Requirement of smooth and flat substrate	• Semiconductors • Photoresist • Insulators • Organic semiconductors • SOFC electrolyte and cathode, etc.
Dip coating	Immersion of a substrate into CSD solution and its subsequent removal	• Simplicity • Controllable film thickness • Coating on irregular and complex shaped substrates	• Variation in film thickness • Coating on the both sides of the substrate simultaneously	• Flat or cylindrical substrates • Optical coating on glass, etc.
Spray coating	Deposition of the aerosol of CSD solution, via a nebulizer or a nozzle, on the substrate	• Uniform coating even on highly structured surfaces	• Expensive	• Coating on dielectrics • Coating for corrosion protection, etc.

Table 2. Three coating techniques used for CSD processes.

http://dx.doi.org/10.5772/66125

The thickness of the coating film is influenced by the spinning speed and time as well as the solution viscosity. According to the empirical equation, the film thickness (t) is inversely proportional to the square root of the spin speed (ω: angular velocity) [73]:

$$t \propto \frac{1}{\sqrt{\omega}} \tag{7}$$

Spinning speed of 2000–3000 rpm is usually used for depositing SOFC electrolyte thin films. The film thickness of 30–100 nm is obtained after one layer deposition depending on the viscosity of the solution and duration of spinning. Typical film thicknesses of SOFC electrolytes are kept usually below 1 μm [31, 34, 38, 44, 74–76]. Several works on electrolyte fabrication with spin coating technique have been reported in the field of SOFCs [31, 38, 76].

3.2. Dip coating

Dip coating is a simple, flexible, and cost-effective solution deposition technique that allows coating on both large area and complex shaped substrates. The process involves immersion of substrate in the solution and subsequent removal. A coherent liquid film is entrained on the withdrawal of the substrate from the coating fluid, and the film is subsequently consolidated by drying and accompanying chemical reactions. Typical film thickness obtained is in the micrometer range.

The process of film formation follows fluid mechanical equilibrium between the entrained film and the receding liquid. The equilibrium is governed by several forces. Viscous drag and gravitational forces play the most significant role. Other forces like surface tension, inertial force, or disjoining pressure also play an important role [77]. A competition between these forces in the film deposition region governs the thickness of the film. The film thickness is given by the Landau-Levich equation [78, 79]:

$$t = 0.94 \frac{\eta U^{2/3}}{\gamma^{1/6} \rho g^{1/2}} \tag{8}$$

where η is the liquid viscosity, U is the withdrawal speed, γ is the surface tension, and ρ is the liquid density. This technique is not applied for electrolyte fabrication of SOFCs because this technique aids in the formation of film on both sides of the substrate.

3.3. Spray coating

The spray coating technique is based on the transformation of a liquid precursor solution into a fine aerosol by atomizer or nebulizer [80]. These fine droplets are then deposited on a substrate surface either with carrier gas or with an electrostatic field or by gravity. The substrate may be at room temperature or above. The different spray techniques are mainly distinguished by the method of atomization [81] and, hence, produce different morphologies of the film. For

example, YSZ thin films deposited using electrostatic spray deposition (ESD) and pressurized spray deposition (PSD) on the substrate [82] showed different morphologies from dense to porous. Other parameters such as flow rate, substrate temperature, and deposition time also influence the morphology of the deposited film. The flow rate should not exceed a certain value for a particular composition of the solution and associated parameters; otherwise, cracks may form. Spray pyrolysis has also been applied for the deposition of SOFC electrolyte thin films [71, 83, 84]. To mention a significant work, a gastight bilayer electrolyte fabricated via spray coating technique demonstrated a power density of 750 mW/cm^2 with the achievement of 1.01 V OCV at 770°C [84].

4. Solution chemistry

The chemistry of the solution determines the morphology of the film. A wide knowledge of chemistry is required to formulate workable solution. Attention must be paid to several issues such as reactivity among the precursors and solvent, homogeneity of the solution, solvent vapor pressure, wettability of the solvent to the substrate surface, reaction products, pH and viscosity of the solution, etc.

The hydrolysis and condensation reaction needs to be controlled carefully to tailor the morphology of the film. Precursors with more than two hydrolysis sites are highly sensitive toward hydrolysis and form three-dimensional networks during gelation, which provides rigidity to the M–O–M network and inhibits densification of the final sintered film. Water, chelating agent, and modifying ligand are added to block the hydrolysis sites of the precursors. Precursors with two unblocked sites form linear structure, which facilitates almost stress-free densification in all directions.

Transition metal alkoxide precursors require special attention because of their high reactivity and inclination toward coordination expansion. Due to their coordination expansion, these metals become coordinatively unsaturated. In order to satisfy their coordination, they sometimes get integrated with water and subsequently undergo precipitation. These highly sensitive alkoxides need to be handled in glove box initially. Diethanolamine (DEA) and triethanolamine (TEA) are generally used to stabilize alkoxides of transition metals [85]. Stabilization also occurs via chelation and alcohol exchange method. After modification, they do not react with moisture in air.

Compositional homogeneity is desirable for the successful fabrication of film without any defect. Striation is a very common problem associated with heterogeneous solution. Striation is a series of ridges resulting into variation in thickness throughout the film [86]. Heterogeneity is associated with the separation of polymer-rich and polymer-deficient portion of the solution due to the presence of both polar and nonpolar precursors in a multicomponent system. Therefore, a single solvent with both the characters is desirable to maintain homogeneity. For example, 2-methoxyethanol having both the characters is a widely used solvent. Heterogeneous solution also results from the mixture of the solvents of different characters such as specific gravity. Phase separation is another issue associated with the heterogeneous solution, which

occurs due to the different rate of the hydrolysis of different components. Refluxing treatment is carried out to address the issue. This treatment helps in random combination of cations [87].

Solvent vapor pressure is one important parameter because solvent determines the film thickness and its rigidity. The short-chain alcohols are generally used for thinner film, while the long-chain alcohols are for thicker films [88, 89]. Short-chain alcohols have higher tendency to leave film faster because of its higher vapor pressure. Higher vapor pressure generates higher capillary force, which drives precursors in greater proximity, thereby causing higher cross-linking among metal-oxide precursors. This cross-link offers rigidity to the film, producing crack in the film [29]. On the other hand, the solvents with low vapor pressure hinder cross-linking reaction, resulting into the crack-free film.

The solution pH and the product generated during condensation reaction have immense influence over the rate of condensation reaction [90, 91]. The reaction products are alcohol and water. Alcohol is eliminated during deposition, which forces the condensation reaction to shift toward the forward direction. Thus, more M–O–M cross-linked network forms. The presence of water in the solution or in the ambient atmosphere slows down the condensation process. The early work showed that the density of the film was enhanced with the presence of more water [91].

Viscosity and concentration of the solution are other variables to control the thickness and the initiation of the crack throughout the film. Early work demonstrated that the higher concentration of the solution produced the thicker film with crack. As per the literature report, the critical thickness limit for the film is governed by the following equation [92]:

$$h = \frac{K_{IC}}{\sigma \Omega_C(\Sigma)} \tag{9}$$

where h is the critical thickness, K_{IC} is the critical stress intensity factor, σ is the tensile stress in the film, and $\Omega_c(\Sigma)$ is the ratio of Young's modulus of the film to that of the substrate.

Solution properties	Effects
Polar and nonpolar character of the solvent	Striation: variation of film thickness
Vapor pressure of solvent	Cracking, dewetting
Concentration and viscosity	Film thickness, crack formation, and uniformity of film
Modifying ligand	Possible formation of 2D network instead of 3D network
Long-chain polymer	Low tensile stress in the film
Presence of water	Slower condensation reaction
Presence of alcohol	Faster condensation reaction

Table 3. Solution properties.

The equation describes the dependence of the critical thickness on the tensile stress exerted on it. Critical thickness decreases with the increase in tensile stress. The critical thickness of film can be increased with the use of longer-chain solvents [89]. Another approach to deal with this issue is to increase the adhesion between the substrate and film [29]. During shrinkage, formation of crack occurs due to the large mismatch of thermal expansion coefficients of the film and the substrate. The strain energy is relieved via the formation of crack, but this strain energy can be balanced by the strength of adhesion of the film to the substrate. Excellent substrate-film adhesion may provide relaxation for the fabrication of thicker film. Therefore, modification of substrate surface before deposition has significance. The properties of solution and their effects are summarized in **Table 3**.

5. Heat treatment

5.1. Physical changes occurring during heat treatment

Several phenomena occur after deposition of film. They are hydrolysis, drying, condensation, gelation, and densification [93]. Generally, gelation and drying phenomena occur simultaneously during deposition and continue afterward. The deposited film acts as a viscoelastic solid, which is an inorganic framework with organic moieties entrapping solvent [94]. These organics are removed with heat treatment via either pyrolysis or thermolysis process. Pyrolysis occurs in the presence of oxygen, whereas thermolysis occurs in the absence of oxygen. Followed by organic removal, crystallization occurs. Partial densification takes place in the amorphous stage, while the final densification occurs after crystallization.

Hydrolysis-condensation reaction generally occurs in the temperature range of 80 to 400°C. This reaction generates water and alcohols, which are removed via drying process. During drying or organic removal process, a gas-liquid interface is generated within the pores because of the evaporation of liquid. In addition to this, gas-solid and solid-liquid interfaces also exist. These interfaces generate pressure, which gives birth to capillary contraction. The magnitude of capillary contraction depends on the specific energies across these interfaces, nature of the liquid, and pore size. This capillary contraction is responsible for producing the driving force to the collapse of the amorphous network. This driving force is proportional to the pore diameter. At this stage, the film might be prone to crack because of the pressure differential occurring due to the presence of pores with different diameters. The total stress due to drying, capillary contraction, and network consolidation is normally around 100 MPa [95].

Gelation occurs due to the continuous removal of water and organics. During gelation, M–O–M network starts forming. With the heat treatment, a good number of M–O–M linkages form and densification proceeds. Skeletal densification occurs with the structural rearrangement of M–O–M bond. The structure approaches to the state of metastable liquid in the temperature range of 400–600°C. With the increase in temperature, viscous flow occurs [51], followed by crystallization above 600°C. However, crystallization starts after complete removal of organics. Crystallization kinetics depends on its own nature of crystallization (i.e., glass formers have slow rate of crystallization, while other oxides show

http://dx.doi.org/10.5772/66125

moderate to high rate of crystallization) and the heating schedule. Structural relaxation occurs during crystallization process. The presence of organic groups delays structural relaxation and crystallization to a higher temperature. Following this principle, crystallization is purposefully delayed so that densification gets over before crystallization [50]. All the processes overlap one another. There is no distinct temperature range. Depending on the solution chemistry, the processes may occur faster or slower.

5.2. Phase transformation

After completion of pyrolysis, liquid film transforms to the metastable amorphous stage. With further heat treatment to the higher temperature, the amorphous film transforms to the crystalline stage via nucleation and growth process. Thermodynamic driving force plays a role behind this transformation. This force comes from the difference between the free energies of those two states. **Figure 3** describes the phenomena. The driving force for transformation to the final stage depends on the crystallization temperature and the free energy associated with both stages of the films.

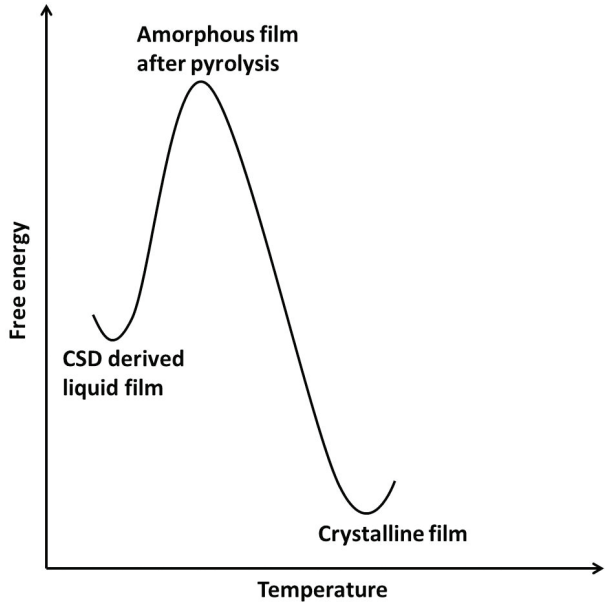

Figure 3. Thermodynamic driving force associated with phase transformation.

Crystallization kinetics starts with the nucleation, which is quite similar to the transformation from amorphous glassy to crystalline phase. The different features of CSD-derived film are associated with the presence of residual hydroxyl group, excess surface area associated with the porosity, and skeletal density. However, the nucleation and growth theory applicable for glass-ceramic science also applies to the transformation of the CSD-derived film [96]. Gibb's

free energy (ΔG) associated with the driving force for crystallization is expressed by the following equation:

$$\Delta G = -\frac{4}{3}\pi r^3(\Delta G_v) + 4\pi r^2\sigma \tag{10}$$

where ΔG_v and σ are Gibb's free energies associated with unit volume and surface, respectively, and r is the radius of the nucleus formed during nucleation. The equation gives rise to the concept of critical radius. A critical radius (r^*) is the minimum required radius for the formation of stable nucleus. The derivative of the above equation with respect to radius gives the relationship between the critical radius (r^*) and the energy barrier (ΔG^*) required to be overcome to form a stable nucleus, which is described by the following equation:

$$\Delta G^{\star} = \frac{16\pi\sigma^3}{3(\Delta G_v)^2} \tag{11}$$

This equation holds good for homogeneous nucleation where the amorphous film does not encounter any nucleation site. Heterogeneous nucleation occurs when the amorphous material can rest on nucleation site, i.e., any surface such as impurity, substrate, grain boundaries, etc. In case of heterogeneous nucleation, the above equation is modified by the contact angle term, $f(\theta)$, associated with the substrate surface (roughness) and the crystal:

$$\Delta G^*_{hetero} = \frac{16\pi\sigma^3}{3(\Delta G_v)^2} f(\theta) \tag{12}$$

where

$$f(\theta) = \frac{2 - 3cos\theta + cos^3\theta}{4} \tag{13}$$

where θ is the contact angle between the substrate surface and the crystal. Heterogeneous nucleation is always energetically favorable because of the lower energy barrier due to the presence of the preferential nucleation sites.

Rates of nucleation and growth with respect to the temperature coordinate are important factors for tailoring microstructure of the film. Higher nucleation rate gives finer microstructure, while

http://dx.doi.org/10.5772/66125

higher rate of growth with lower nucleation gives coarse microstructure. The relationship among temperature, nucleation density (number of nuclei in a cubic meter volume), and free energy barrier is governed by the following equation:

$$n^* \infty \exp\left(-\Delta \frac{G^*}{RT}\right) \tag{14}$$

As the temperature is raised, higher energy is provided to overcome the nucleation barrier. Therefore, the rate of nucleation increases. After nucleation rate reaches the maximum height, it declines with further increase of temperature. Driving force for crystallization gets reduced as the material approaches its melting temperature [94] and barrier height to nucleation increases. This type of phenomena gives rise to a bell-shaped curve. The same kind of curve is also applicable for the growth rate. A typical curve is presented in **Figure 4**.

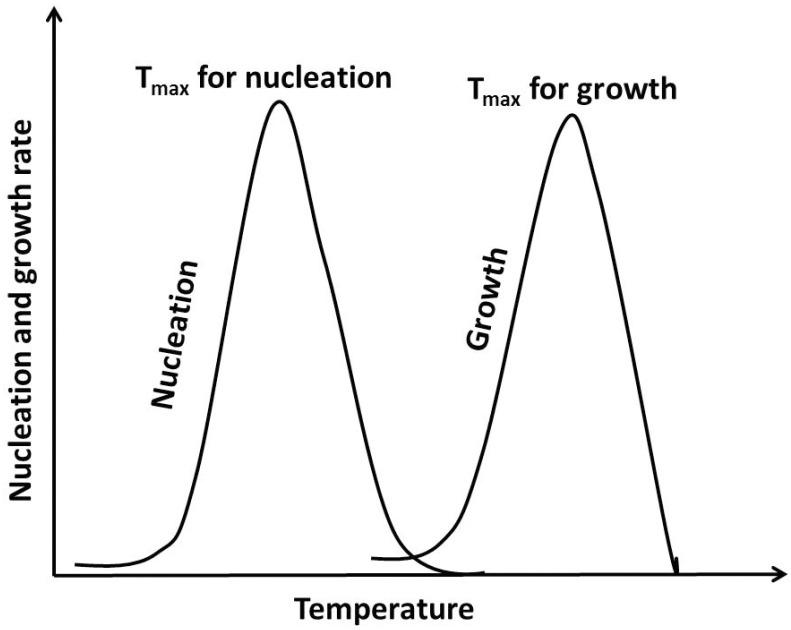

Figure 4. Schematic of nucleation and growth locus in temperature coordinate for homogeneous nucleation (ideal case).

The nucleation curve is followed by the growth rate curve on the temperature coordinate, and they overlap to some extent. The area of the overlapped region depends on chemical composition of the solution, fabrication procedure, and prior heat treatment history. The representation in **Figure 4** is applicable for the homogeneous nucleation [97] as the apex of the growth rate curve lies at higher temperature than that of the nucleation rate curve. Based

on the calculation, the maximum nucleation rate may be located at higher temperature than the maximum growth rate in case of heterogeneous nucleation. The schematic representation of these phenomena is depicted in **Figure 5**.

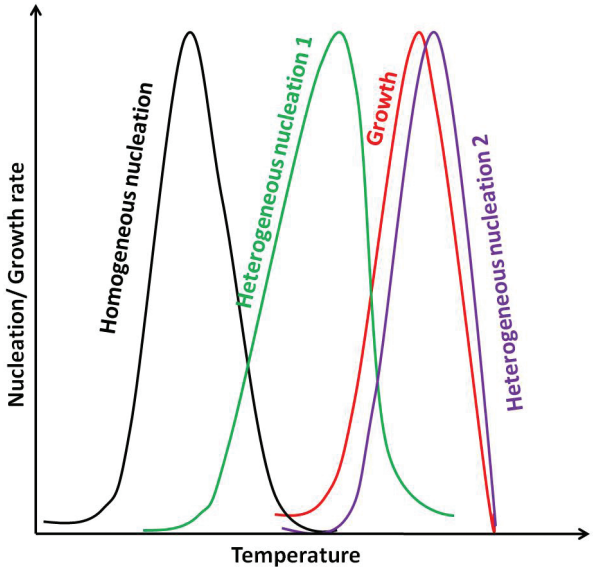

Figure 5. Schematic of nucleation and growth locus in temperature coordinate for heterogeneous nucleation and homogeneous nucleation with low interfacial energy.

In case of the film on the substrate, crystallization is affected due to the presence of two separate nucleation events. One is the surface nucleation of the film which is homogeneous in nature, and the other one is the interfacial nucleation on the substrate. Nucleation occurs on both the substrate and film surfaces, as represented in **Figure 6**.

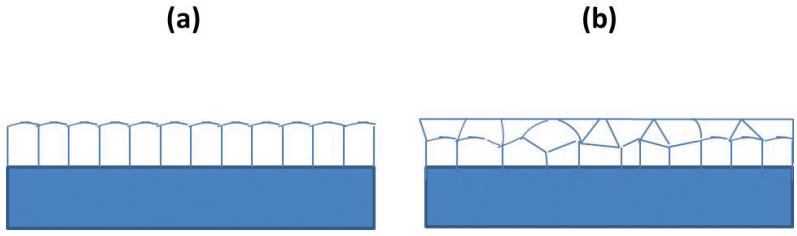

Figure 6. Kinetic competition between two nucleation events on the interface and on the surface of the film: (a) nucleation at the interface only and (b) nucleation at both interface and surface of the film.

Heterogeneous nucleation occurs at the substrate first, while homogeneous nucleation and growth event occur on the surface of the film; growth direction is opposite to each other. The

density of nucleus is higher at the interface than at the surface of the film. The dominance of one process over the other depends on the crystallization temperature of the film. The film with lower crystallization temperature shows smaller difference in the kinetics of two nucleation events, than the film with higher crystallization temperature [98].

5.3. Salient features

Heating rate also has impact over the kinetics of these processes. Various heating schedules with several heating rates are used to keep control over the microstructure of the film. Keddie and Giannelis experimented on the effect of heating rate (0.2–8000°C/min) for the densification of TiO_2 film as model system [99] and found that the thinnest film was obtained with the highest heating rate. Rapid thermal annealing (RTA) and isothermal heat treatment at high temperature are two useful processes for thin-film fabrication [50, 99].

Effect of the substrate is another important issue for the orientation of thin film. A highly oriented phase-pure barium zirconate ($BaZrO_3$) film fabricated via sol-gel route was epitaxially grown on (100) plane on strontium titanate ($SrTiO_3$) at 800°C, while the same solution deposited on $LaAlO_3$ substrate had produced film with random structure [35].

6. Conclusion

The CSD method combined with right sintering strategy is the blessing in the sector in SOFC manufacturing. The growth of the SOFC technologies is restricted mostly to the R&D sector because suitable position in the market of clean energy sources is yet to be achieved. The hurdle behind commercialization of intermediate to low-temperature SOFCs arises from its high manufacturing cost. The CSD method has proved to be a potential technique in this field. Although this method did not find application for over a century after its discovery, now it is progressing exponentially with time in all the sectors of thin film. The fabrication of crystalline YSZ and YDSZ film has initiated a new era in the manufacturing of SOFCs, which ensures the rapid commercialization of SOFCs in the near future. This technology requires low investment cost while demanding a good command over chemistry. Therefore, CSD technology is facing several difficulties related to the fabrication strategies. The major issues are preparation of homogeneous solution for multicomponent system, preservation of the solution for a considerable duration without aging, handling with highly reactive precursors, controlling the hydrolysis-condensation reaction, gelation kinetics, solvent evaporation, choice of environment-friendly chemicals without compromising necessary properties, selection of appropriate deposition technique, right heating schedule and environment, determination of critical thickness limit, etc. Many challenges have been successfully dealt with, while a good number of issues need more attention. However, recent success stories predict the bright future of this technology. Presently, effort is also given to the water-based CSD method.

Author details

Mridula Biswas and Pei-Chen Su*

*Address all correspondence to: peichensu@ntu.edu.sg

School of Mechanical and Aerospace Engineering, Nanyang Technological University, Singapore, Singapore

References

[1] Hong S, Bae J, Koo B, Kim YB. High-performance ultra-thin film solid oxide fuel cell using anodized-aluminum-oxide supporting structure. Electrochemistry Communications. 2014;47:1–4.

[2] Su PC, Chao CC, Shim JH, Fasching R, Prinz FB. Solid oxide fuel cell with corrugated thin film electrolyte. Nano Letters. 2008;8(8):2289–2292.

[3] Shim JH, Chao CC, Huang H, Prinz FB. Atomic layer deposition of yttria-stabilized zirconia for solid oxide fuel cells. Chemistry of Materials. 2007;19(15):3850–3854.

[4] Huang H, Nakamura M, Su P, Fasching R, Saito Y, Prinz FB. High-performance ultrathin solid oxide fuel cells for low-temperature operation. Journal of The Electrochemical Society. 2007;154(1):B20–B24.

[5] Huang H, Gür TM, Saito Y, Prinz F. High ionic conductivity in ultrathin nanocrystalline gadolinia-doped ceria films. Applied Physics Letters. 2006;89(14):3107.

[6] Su PC, Prinz FB. Nanoscale membrane electrolyte array for solid oxide fuel cells. Electrochemistry Communications. 2012;16(1):77–79.

[7] Chao CC, Hsu CM, Cui Y, Prinz FB. Improved solid oxide fuel cell performance with nanostructured electrolytes. ACS Nano. 2011;5(7):5692–5696.

[8] Choi H, Cho GY, Cha SW. Fabrication and characterization of anode supported YSZ/GDC bilayer electrolyte SOFC using dry press process. International Journal of Precision Engineering and Manufacturing-Green Technology. 2014;1(2):95–99.

[9] Greene J, Wickersham C, Zilko J, Welsh L, Szofran F. Morphological and electrical properties of rf sputtered Y_2O_3-doped ZrO_2 thin films. Journal of Vacuum Science & Technology. 1976;13(1):72–75.

[10] Croset M, Schnell JP, Velasco G, Siejka J. Composition, structure, and ac conductivity of rf-sputtered calcia-stabilized zirconia thin films. Journal of Applied Physics. 1977;48(2):775–780.

[11] Isenberg A. Energy conversion via solid oxide electrolyte electrochemical cells at high temperatures. Solid State Ionics. 1981;3:431–437.

[12] Nakagawa N, Kuroda C, Ishida M. Preparation of thin-film zirconia electrolyte fuel-cell by rf-sputtering. Denki Kagaku. 1989;57(3):215–218.

[13] Negishi A, Nozaki K, Ozawa T. Thin-film technology for solid electrolyte fuel cells by the rf sputtering technique. Solid State Ionics. 1981;3:443–446.

[14] Srivastava P, Quach T, Duan Y, Donelson R, Jiang S, Ciacchi F, et al. Electrode supported solid oxide fuel cells: Electrolyte films prepared by dc magnetron sputtering. Solid State Ionics. 1997;99(3):311–319.

[15] Uhlenbruck S, Nédélec R, Sebold D, Buchkremer HP, Stöver D. Electrode and electrolyte layers for solid oxide fuel cells applied by physical vapor deposition (PVD). ECS Transactions. 2011;35(1):2275–2282.

[16] Maskalick N, Sun C. Sintered zirconia electrolyte films in high-temperature fuel cells. Journal of The Electrochemical Society. 1971;118(8):1386–1391.

[17] Ganguli D, Kundu D. Preparation of amorphous ZrO_2 coatings from metal-organic solutions. Journal of Materials Science Letters. 1984;3(6):503–504.

[18] Fukushima J, Kodaira K, Matsushita T. Preparation of ferroelectric PZT films by thermal decomposition of organometallic compounds. Journal of Materials Science. 1984;19(2): 595–598.

[19] Schwartz RW, Schneller T, Waser R. Chemical solution deposition of electronic oxide films. Comptes Rendus Chimie. 2004;7(5):433–461.

[20] Jagannathan K, Tiku S, Ray H, Ghosh A, Subbarao EC. Solid electrolytes and their applications. In: Technological Applications of Solid Electrolytes. Springer; US. 1980. pp. 201–259.

[21] Chiodelli G, Magistris A, Scagliotti M, Parmigiani F. Electrical properties of plasma-sprayed yttria-stabilized zirconia films. Journal of Materials Science. 1988; 23(4):1159–1163.

[22] Setoguchi T, Sawano M, Eguchi K, Arai H. Application of the stabilized zirconia thin film prepared by spray pyrolysis method to SOFC. Solid State Ionics. 1990;40:502–505.

[23] de Souza S, Visco SJ, De Jonghe LC. Reduced-temperature solid oxide fuel cell based on YSZ thin-film electrolyte. Journal of The Electrochemical Society. 1997; 144(3):L35–L37.

[24] Charpentier P, Fragnaud P, Schleich D, Gehain E. Preparation of thin film SOFCs working at reduced temperature. Solid State Ionics. 2000;135(1):373–380.

[25] Ebelmen J. Sur les éthers siliciques. Comptes Rendus de l'Académie des Sciences. 1844;19:398–400.

[26] Dislich H. Sol-gel: Science, processes and products. Journal of Non-Crystalline Solids. 1986;80(1):115–121.

[27] Schroeder H. Properties and applications of oxide layers deposited on glass from organic solutions. Optica Acta. 1962;9:249.

[28] Dislich H, Hussmann E. Amorphous and crystalline dip coatings obtained from organometallic solutions: Procedures, chemical processes and products. Thin Solid Films. 1981;77(1):129–140.

[29] Kueper TW, Visco SJ, De Jonghe L. Thin-film ceramic electrolytes deposited on porous and non-porous substrates by sol-gel techniques. Solid State Ionics. 1992;52(1):251–259.

[30] Mehta K, Xu R, Virkar AV. Two-layer fuel cell electrolyte structure by sol-gel processing. Journal of Sol-Gel Science and Technology. 1998;11(2):203–207.

[31] Oh EO, Whang CM, Lee YR, Park SY, Prasad DH, Yoon KJ, et al. Extremely thin bilayer electrolyte for solid oxide fuel cells (SOFCs) fabricated by chemical solution deposition (CSD). Advanced Materials. 2012;24(25):3373–3377.

[32] Courtin E, Boy P, Piquero T, Vulliet J, Poirot N, Laberty-Robert C. A composite sol-gel process to prepare a YSZ electrolyte for solid oxide fuel cells. Journal of Power Sources. 2012;206:77–83.

[33] Bailly N, Georges S, Djurado E. Elaboration and electrical characterization of electro-sprayed YSZ thin films for intermediate temperature-solid oxide fuel cells (IT-SOFC). Solid State Ionics. 2012;222:1–7.

[34] Chen YY, Wei WCJ. Processing and characterization of ultra-thin yttria-stabilized zirconia (YSZ) electrolytic films for SOFC. Solid State Ionics. 2006;177(3):351–357.

[35] Paranthaman M, Shoup SS, Beach DB, Williams RK, Specht ED. Epitaxial growth of $BaZrO_3$ films on single crystal oxide substrates using sol-gel alkoxide precursors. Materials Research Bulletin. 1997;32(12):1697–1704.

[36] Schneller T, Schober T. Chemical solution deposition prepared dense proton conducting Y-doped $BaZrO_3$ thin films for sofc and sensor devices. Solid State Ionics. 2003;164(3):131–136.

[37] Groß B, Engeldinger J, Grambole D, Herrmann F, Hempelmann R. Dissociative water vapour absorption in $BaZr_{0.85}Y_{0.15}O_{2.925}/H_2O$: Pressure-compositions isotherms in terms of fermi-dirac statistics. Physical Chemistry Chemical Physics. 2000;2(2):297–301.

[38] Xie H, Su PC. Fabrication of yttrium-doped barium zirconate thin films with sub-micrometer thickness by a sol-gel spin coating method. Thin Solid Films. 2015; 584:116–119.

[39] Rupp JL, Infortuna A, Gauckler LJ. Thermodynamic stability of gadolinia-doped ceria thin film electrolytes for micro-solid oxide fuel cells. Journal of the American Ceramic Society. 2007;90(6):1792–1797.

[40] Biswas M, Xie H, Su PC. Low temperature synthesis of sub-micrometer yttria-doped barium zirconate thin films by modified chemical solution deposition technique. ECS Transactions. 2015;68(1):481–488.

[41] Matsuzaki Y, Hishinuma M, Yasuda I. Growth of yttria stabilized zirconia thin films by metallo-organic, ultrasonic spray pyrolysis. Thin Solid Films. 1999;340(1):72–76.

[42] Butz B, Störmer H, Gerthsen D, Bockmeyer M, Krüger R, Ivers-Tiffée E, et al. Microstructure of nanocrystalline yttria-doped zirconia thin films obtained by sol-gel processing. Journal of the American Ceramic Society. 2008;91(7):2281–2289.

[43] García-Sánchez M, Peña J, Ortiz A, Santana G, Fandiño J, Bizarro M, et al. Nanostructured ysz thin films for solid oxide fuel cells deposited by ultrasonic spray pyrolysis. Solid State Ionics. 2008;179(7):243–249.

[44] Abakevičienė B, Žalga A, Tautkus S, Pilipavičius J, Navickas E, Kareiva A, et al. Synthesis of YSZ thin films by the novel aqueous sol-gel citrate-precursor method. Solid State Ionics. 2012;225:73–76.

[45] Zhang L, Yang W. High-performance low-temperature solid oxide fuel cells using thin proton-conducting electrolyte with novel cathode. International Journal of Hydrogen Energy. 2012;37(10):8635–8640.

[46] Chung BW, Chervin CN, Haslam JJ, Pham AQ, Glass RS. Development and characterization of a high performance thin-film planar SOFC stack. Journal of the Electrochemical Society. 2005;152(2):A265–A269.

[47] Budd KD, Key S, Payne D, Steele BCH. Sol-gel processing of $PbTiO_3$, $PbZrO_3$, PZT and PLZT thin films. In: British Ceramics Proceedings. Institute of Ceramics; Stoke-on-Trent, England. 1985.

[48] Dey S, Budd KD, Payne DA. Thin-film ferroelectrics of PZT of sol-gel processing. IEEE Transactions on Ultrasonics, Ferroelectrics, and Frequency Control. 1987;35(1):80–81.

[49] Eschenbaum J, Rosenberger J, Hempelmann R, Nagengast D, Weidinger A. Thin films of proton conducting $SrZrO_3$-ceramics prepared by the sol-gel method. Solid State Ionics. 1995;77:222–225.

[50] Xie H, Biswas M, Fan L, Li Y, Su PC. Rapid thermal processing of chemical-solution-deposited yttrium-doped barium zirconate thin films. Submitted to Surface and Coating Technology. 2016.

[51] Biswas M, Xie H, Baek JD, Su PC. Fabrication of yttria-doped barium zirconate electrolyte with submicrometer thickness via low temperature viscous flow sintering. Submitted to Surface and Coating Technology. 2016.

[52] Biswas M, Xie H, Baek JD, Su PC. Low temperature sintering of gas-tight yttria-doped barium zirconate electrolyte with sub-micrometer thickness. submitted to Journal of American Ceramic Society. 2016.

[53] Tuttle B, Schwartz R. Solution deposition of ferroelectric thin films. MRS Bulletin. 1996;21(06):49–54.

[54] Schwartz RW, Reichert TL, Clem PG, Dimos D, Liu D. A comparison of diol and methanol-based chemical solution deposition routes for PZT thin film fabrication. Integrated Ferroelectrics. 1997;18(1–4):275–286.

[55] Ramamurthi SD, Payne DA. Structural investigations of prehydrolyzed precursors used in the sol-gel processing of lead titanate. Journal of the American Ceramic Society. 1990;73(8):2547–2551.

[56] Schwartz RW. Chemical solution deposition of perovskite thin films. Chemistry of Materials. 1997;9(11):2325–2340.

[57] Brinker CJ, Scherer GW. Sol → gel → glass: I. Gelation and gel structure. Journal of Non-Crystalline Solids. 1985;70(3):301–322.

[58] Esquivias L, Kallala M, Sanchez C, Cabane B. Advanced materials from gels SAXS study of gelation and precipitation in titanium-based systems. Journal of Non-Crystalline Solids. 1992;147:189–193.

[59] Brinker CJ, Scherer GW. Sol-Gel Science: The Physics and Chemistry of Sol-Gel Processing. Academic Press, Inc.; New York. 2013.

[60] Veldhuis SA, George A, Nijland M, ten Elshof JE. Concentration dependence on the shape and size of sol-gel-derived yttria-stabilized zirconia ceramic features by soft lithographic patterning. Langmuir. 2012;28(42):15111–15117.

[61] Doeuff S, Henry M, Sanchez C, Livage J. Hydrolysis of titanium alkoxides: Modification of the molecular precursor by acetic acid. Journal of Non-Crystalline Solids. 1987;89(1): 206–216.

[62] Chatry M, Henry M, Livage J. Synthesis of non-aggregated nanometric crystalline zirconia particles. Materials Research Bulletin. 1994;29(5):517–522.

[63] Courtin E, Boy P, Rouhet C, Bianchi L, Bruneton E, Poirot N, et al. Optimized sol-gel routes to synthesize yttria-stabilized zirconia thin films as solid electrolytes for solid oxide fuel cells. Chemistry of Materials. 2012;24(23):4540–4548.

[64] Joshi V, Dacruz C, Cuchiaro J, Araujo C, Zuleeg R. Analysis of C-V and I-V data of BST thin films. Integrated Ferroelectrics. 1997;14(1–4):133–140.

[65] Vest RW, Jiejie X. $PbTiO_3$/films from metalloorganic precursors. IEEE Transactions on Ultrasonics, Ferroelectrics, and Frequency Control. 1988;35(6):711–717.

[66] Cui T, Markus D, Zurn S, Polla D. Piezoelectric thin films formed by MOD on cantilever beams for micro sensors and actuators. Microsystem Technologies. 2004;10(2):137–141.

[67] Agarwal V, Liu M. Preparation of barium cerate-based thin films using a modified pechini process. Journal of Materials Science. 1997;32(3):619–625.

[68] Barrow D, Petroff T, Sayer M. Thick ceramic coatings using a sol gel based ceramic-ceramic 0–3 composite. Surface and Coatings Technology. 1995;76:113–118.

[69] Zhao H, Li X, Ju F, Pal U. Effects of particle size of 8 mol% Y_2O_3 stabilized ZrO_2 (YSZ) and additive Ta_2O_5 on the phase composition and the microstructure of sintered YSZ electrolyte. Journal of Materials Processing Technology. 2008;200(1–3):199–204.

[70] Muecke UP, Beckel D, Bernard A, Bieberle-Hütter A, Graf S, Infortuna A, et al. Micro solid oxide fuel cells on glass ceramic substrates. Advanced Functional Materials. 2008;18(20):3158–3168.

[71] Rupp JL, Drobek T, Rossi A, Gauckler LJ. Chemical analysis of spray pyrolysis gadolinia-doped ceria electrolyte thin films for solid oxide fuel cells. Chemistry of Materials. 2007;19(5):1134–1142.

[72] Rupp JL, Solenthaler C, Gasser P, Muecke U, Gauckler LJ. Crystallization of amorphous ceria solid solutions. Acta Materialia. 2007;55(10):3505–3512.

[73] Tummala R. Fundamentals of Microsystems Packaging. McGraw-Hill Professional; New York. 2001.

[74] Pan Y, Zhu J, Hu MZ, Payzant EA. Processing of YSZ thin films on dense and porous substrates. Surface and Coatings Technology. 2005;200(5):1242–1247.

[75] Lin JM, Hsu MC, Fung KZ. Deposition of ZrO_2 film by liquid phase deposition. Journal of Power Sources. 2006;159(1):49–54.

[76] Rørvik PM, Haavik C, Griesche D, Schneller T, Lenrick F, Wallenberg LR. Chemical solution deposition of thin films for protonic ceramic fuel cells. Solid State Ionics. 2014;262:852–855.

[77] Scriven L. Physics and applications of dip coating and spin coating. In: MRS Proceedings. Cambridge University Press; USA 1988.

[78] Brinker C, Frye G, Hurd A, Ashley C. Fundamentals of sol-gel dip coating. Thin Solid Films. 1991;201(1):97–108.

[79] Schunk PR, Hurd AJ, Brinker CJ, Kistler SF, Schweizer PM. Liquid film coating. In: Free-Meniscus Coating Processes. Springer; Netherland 1997. pp. 673–708.

[80] Perednis D, Gauckler LJ. Thin film deposition using spray pyrolysis. Journal of Electroceramics. 2005;14(2):103–111.

[81] Beckel D, Bieberle-Hütter A, Harvey A, Infortuna A, Muecke U, Prestat M, et al. Thin films for micro solid oxide fuel cells. Journal of Power Sources. 2007;173(1):325–345.

[82] Perednis D, Wilhelm O, Pratsinis S, Gauckler L. Morphology and deposition of thin yttria-stabilized zirconia films using spray pyrolysis. Thin Solid Films. 2005; 474(1):84–95.

[83] Somroop K, Pornprasertsuk R, Jinawath S. Fabrication of Y_2O_3-doped $BaZrO_3$ thin films by electrostatic spray deposition. Thin Solid Films. 2011;519(19):6408–6412.

[84] Perednis D, Gauckler L. Solid oxide fuel cells with electrolytes prepared via spray pyrolysis. Solid State Ionics. 2004;166(3):229–239.

[85] Takahashi Y, Matsuoka Y. Dip-coating of TiO_2 films using a sol derived from Ti(Oi-Pr)$_4$-diethanolamine-H_2O-i-PrOH system. Journal of Materials Science. 1988;23(6): 2259–2266.

[86] Haas D, Birnie D, Zecchino M, Figueroa J. The effect of radial position and spin speed on striation spacing in spin on glass coatings. Journal of Materials Science Letters. 2001;20(19):1763–1766.

[87] Bradley D, Mehrotra R, Gaur D. Metal Alkoxides. Academic Press, London; 1978.

[88] Brennecka GL, Tuttle BA. Fabrication of ultrathin film capacitors by chemical solution deposition. Journal of Materials Research. 2007;22(10):2868–2874.

[89] Tu Y, Milne S. Processing and characterization of $Pb(Zr,Ti)O_3$ films, up to 10 μm thick, produced from a diol sol-gel route. Journal of Materials Research. 1996;11(10):2556–2564.

[90] Brinker CJ, Clark DE, Ulrich DR. Better ceramics through chemistry II. In: MRS Symposium Proceedings. Cambridge University Press; USA. 1986.

[91] Glaser P, Pantano CG. Effect of the H_2O/TEOS ratio upon the preparation and nitridation of silica sol/gel films. Journal of Non-Crystalline Solids. 1984;63(1):209–221.

[92] Garino TJ. The cracking of sol-gel films during drying. In: MRS Proceedings. Cambridge University Press; USA. 1990.

[93] Schmidt H. Chemistry of material preparation by the sol-gel process. Journal of Non-Crystalline Solids. 1988;100(1):51–64.

[94] Schneller T, Waser R, Kosec M, Payne D. Chemical Solution Deposition of Functional Oxide Thin Films. Springer-Verlag Wien; Heidelberg. 2013.

[95] Garino TJ, Harrington M. Residual stress in PZT thin films and its effect on ferroelectric properties. In: MRS Proceedings. Cambridge University Press; USA. 1991.

[96] Chiang YM, Kingery WD, Birnie DP. Physical Ceramics: Principles for Ceramic Science and Engineering. John Wiley & Sons; New York. 1997.

[97] Schmelzer JW, Abyzov AS, Fokin VM, Schick C, Zanotto ED. Crystallization of glass-forming liquids: Maxima of nucleation, growth, and overall crystallization rates. Journal of Non-Crystalline Solids. 2015;429:24–32.

[98] Schwartz R, Voigt J, Tuttle B, Payne D, Reichert T, DaSalla R. Comments on the effects of solution precursor characteristics and thermal processing conditions on the crystal-

lization behavior of sol-gel derived lead zirconate titanate thin films. Journal of Materials Research. 1997;12(2):444–456.

[99] Keddie JL, Giannelis EP. Effect of heating rate on the sintering of titanium dioxide thin films: Competition between densification and crystallization. Journal of the American Ceramic Society. 1991;74(10):2669–2671.

Chapter 17

Modern Technologies for Creating Nanostructures in Thin-Film Solar Cells

Yang Tang

Additional information is available at the end of the chapter

http://dx.doi.org/10.5772/64611

Abstract

Most photovoltaic devices (solar cells) sold in the market today are based on silicon wafers, so-called first-generation technology. There is an argument whether the market at present is on the verge of switching to a "second generation" of thin-film solar cell technology. Thin-film photovoltaic device technology relies on light management to enhance light absorption in thin absorber layers. The use of the ZnO nanorods in the thin-film solar cells is an effective way to decrease the reflection. The variation of the geometrical parameters of the ZnO nanorods, such as the diameter, the height and the density, can lead to an optimum, which results in the maximal absorption in the absorber.

Keywords: thin film, solar cell, nanostructure, electrodeposition, efficiency

1. Introduction

The solar energy as one of the new energy sources and a regenerated energy is abundant and pollution free. Most photovoltaic devices (solar cells) sold in the market today are based on silicon wafers, so-called first-generation technology. There is an argument that whether the market at present is on the verge of switching to a "second generation" of thin-film solar cell technology. Nowadays three types of the thin-film solar cells have realized industrialization. They are copper indium gallium selenide (CIGS) solar cells, CdTe solar cells and a-Si solar cells. CIGS-based thin-film photovoltaic devices show the highest efficiency among the various thin-film technologies, having recently reached a record value of 22.6% for the laboratory scale [1]. CdTe-based thin-film solar cells have got a record lab efficiency of 22.1% [2]. Some of the technologies have already entered the stage of mass production with commercial modules that provide stable efficiencies in the 13–14% range. There is still a large gap between the lab-scale

efficiency and the module efficiency indicating the great potential of the technologies. It is vitally important to further develop the innovative thin-film technologies using environmentally friendly and sustainable approaches with lower costs and higher efficiencies.

2. Nanostructured thin-film solar cells

This section starts with a brief introduction on ZnO fundamental properties and the definition of nanostructures. The structures of the thin-film photovoltaic devices are depicted. Then the nanorod meets the solar cell. The applications of the ZnO nanorods in thin-film photovoltaic devices are given. It is followed by the results on the efficiency boost of the thin-film solar cells implanted with ZnO nanorods.

2.1. Implantation of the nanostructures

ZnO is a wide direct bandgap II–VI semiconductor. In last decade, the ZnO material ranging from its thin films to nanostructures has been widely investigated for their applications in various electronic and optoelectronic devices. ZnO is not really a newly discovered material. Research on ZnO has continued for many decades with interest. In terms of its characterization, reports go back to 1935 or even earlier. For example, lattice parameters of ZnO were investigated for many decades [3–7].

Most of the group II–VI binary compound semiconductors crystallize in either cubic zinc blende or hexagonal wurtzite structure where each anion is surrounded by four cations at the corners of a tetrahedron and vice versa. Three kinds of crystal structures are shared by ZnO, which are rocksalt, zinc blende and wurtzite [8]. The zinc blende ZnO structure can be stabilized only by growth on cubic substrates, and the rocksalt structure may be obtained at relatively high pressures [8].

In a variant of the cell structure the nontransparent rear metal contact can be replaced by a transparent conductive oxides (TCO) film. For conventional CIGS thin-film solar cells, metallic Mo back electrodes are commonly used, making it impossible for light to pass through the metal electrode layer. It is possible to reverse the cell structure by starting with the deposition of the transparent contact (superstrate configuration). ZnO nanorod arrays are embedded between the TCO layer and the absorber layer serving as a buffer role. Optionally, an additional buffer layer can be inserted between the ZnO nanorods and the absorber in the superstrate solar cells. The light enters the cell through the superstrate, which has the advantage that the module can be encapsulated with nontransparent material of lower mass and lower cost. Moreover, if the other contact electrode were replaced by a TCO contact, the cell would be illuminated by both sides. In addition, the ZnO nanorod arrays have been incorporated into a superstrate or a bifacial cell structure of the other thin-film photovoltaic devices such as dye-sensitized solar cells [9], quantum dye-sensitized solar cells [10] and organic solar cells [11].

2.2. Efficiency boost of the nanostructured thin-film solar cells

The ZnO nanorods electrodeposited on fluorine doped tin oxide (FTO) substrates have a typical bottom diameter of 220 nm and a top diameter of 120 nm. The ZnO nanorod arrays' density is 6.8×10^8 1/cm^2. The simulation of the nanostructured structure started with the

http://dx.doi.org/10.5772/64611

ZnO nanorod arrays possessing this typical morphology and geometry. The modeling results including reflectance, transmission and absorption were weighted with the AM 1.5 solar spectrum. The optical modeling results on the structure of glass/SnO_2:F/ZnO nanorods/Cu(In,Ga)Se_2. The optical constants of the Cu(In,Ga)Se_2 is derived from the layer. At first, The ZnO nanorod arrays' densities were varied while the other parameters such as the diameters and lengths are fixed. **Table 1** and **Figure 1** show the modeling results. The densities are varied from 4.2×10^8 to 3.2×10^9 1/cm^2. Correspondingly, the percentage site coverages of the ZnO nanorods on the FTO surface are varied from 13.2 to 100%. As shown in the table, an increase in the ZnO nanorods' density leads to a considerable decrease in the reflection. The reflection is decreased from 12.07 to 5.60% by increasing the ZnO nanorods' density from 4.2×10^8 1/cm^2 (site coverage 13.2%) to 3.2×10^9 1/cm^2 (site coverage 100%). An increase in the ZnO nanorods' density results in an increase in the transmission. With increasing the ZnO nanorods' density from 4.2×10^8 1/cm^2 (site coverage 13.2%) to 3.2×10^9 1/cm^2 (site coverage 100%), the transmission is increased from 3.33 to 4.36%. The reason for the increase of the transmission in the range between 900 and 1200 nm is that ZnO nanorods work as a waveguide for the infrared light. As a result of the rise in the ZnO nanorods' density from 4.2×10^8 1/cm^2 (site coverage 13.2%) to 3.1×10^9 1/cm^2 (site coverage 97.5%), the absorption in SnO_2:F descends from 12.15 to 11.09%. However, the absorption in the SnO_2:F ascends from 11.09 to 11.58% with increasing the ZnO nanorods' density from 3.1×10^9 1/cm^2 (site coverage 97.5%) to 3.2×10^9 1/cm^2 (site coverage 100.0%). An increase in the ZnO nanorods' density leads to a continuous increase of the absorption in ZnO nanorods. Owing to the decrease of the reflection and the SnO_2:F absorption with increasing the ZnO nanorods' density from 4.2×10^8 1/cm^2 (site coverage 13.2%) to 3.1×10^9 1/cm^2 (site coverage 97.5%), the absorption in Cu(In,Ga)Se_2 is boosted from 63.30 to 68.13%. An increase in the ZnO nanorods' density over 3.1×10^9 1/cm^2 results in a reduction in the absorption of Cu(In,Ga)Se_2. Therefore, the structure with the ZnO nanorods' density of 3.1×10^9 1/cm^2 (site coverage 97.5%) has the maximum absorption in Cu(In,Ga)Se_2.

Sample	ZnO nanorods' height (mm)	Reflection (%)	Transmission (%)	Absorption in Sn_2O_3:F (%)	Absorption in ZnO nanorods (%)	Absorption in Cu(In,Ga)Se_2 (%)
1	–	13.18	3.47	12.27	–	62.20
2	50	8.30	3.54	11.75	1.01	66.52
3	90	5.97	3.77	11.34	1.45	68.59
4	100	5.88	3.83	11.28	1.48	68.65
5	110	5.86	3.90	11.24	1.50	68.62
6	200	5.93	4.08	11.18	1.73	68.20
7	300	5.70	4.31	11.09	1.89	68.13
8	400	5.72	4.64	10.98	2.02	67.76
9	700	5.65	5.39	10.88	2.31	66.89
10	1000	5.74	6.02	10.95	2.58	65.83

Table 1. The optical modeling results on the structure of glass/SnO_2:F/ZnO nanorods/Cu(In,Ga)Se_2. The simulated ZnO nanorod has a bottom diameter of 220 nm and a top diameter of 120 nm. The density of the nanorods is 3.1×10^9 1/cm^2 with the site coverage of 97.5%. The heights of the ZnO nanorods are varied.

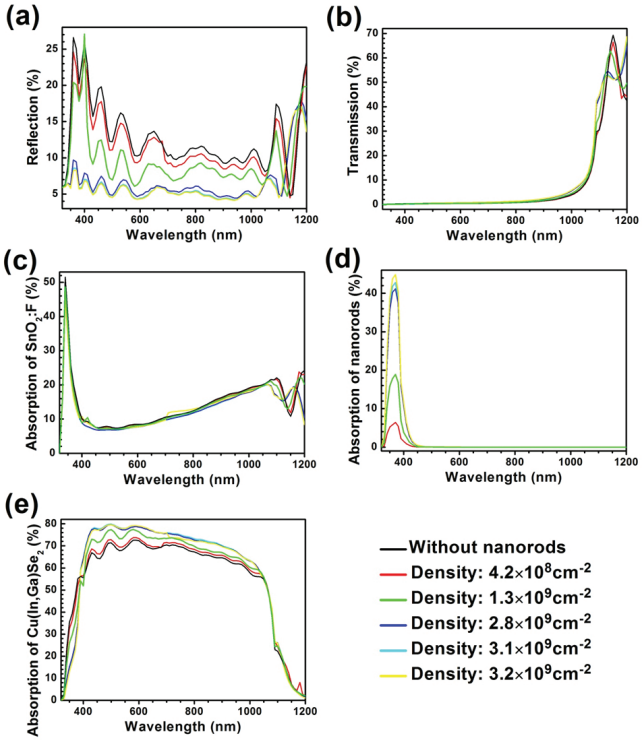

Figure 1. The simulated optical spectra of the structure of glass/SnO_2:F/ZnO nanorods/Cu(In,Ga)Se_2. The simulated ZnO nanorod has a bottom diameter of 220 nm and a top diameter of 120 nm. The nanorod's height is 300 nm. The densities of the ZnO nanorod arrays are varied. Correspondingly the percentage site coverages of the ZnO nanorods on the SnO_2:F surface are varied.

Since the ZnO nanorods' density has been optimized to be 3.1 × 10^9 1/cm^2 (site coverage 97.5%), the other morphological parameters of the ZnO nanorods would be varied to achieve the maximum absorption in Cu(In,Ga)Se_2. Thus, the ZnO nanorods' heights are varied while the other parameters such as the diameters and densities are fixed. **Table 2** and **Figure 2** show the modeling results. The nanorods' heights are varied from 50 to 1000 nm. By increasing the ZnO nanorods' height from 50 to 110 nm, the reflection of the structure is decreased from 8.30 to 5.86%, which is diminished by 29.4%. An increase in the ZnO nanorods' heights from 110 to 1000 nm does not induce a significant change of the structures' reflections and the reflections vary in a small range between 5.65 and 5.93%. As shown in **Table 2**, an increase in the ZnO nanorods' height leads to a considerable increase of the structure's transmission. The transmission is boosted from 3.57 to 6.02% by increasing the ZnO nanorods' height from 50 to 1000 nm, which is enlarged by 68.6%. As shown in **Figure 2**, the increase in the transmission is in the range from 900 (1.38 eV) to 1200 nm (1.03 eV), because ZnO nanorods work as a waveguide enhancing the infrared transmission. An increase in the ZnO nanorods' height from 50 to 700 nm induces a slight decrease of the absorption in SnO_2:F from 11.75 and 10.88%, which is diminished by 7.4%. However, the absorption in the SnO_2:F ascends from 10.88 to 10.95% with increasing the ZnO nanorods' height from 700 to 1000 nm. An

increase in the ZnO nanorods' height leads to a continuous increase of the absorption in ZnO nanorods. The absorption in ZnO nanorods ascends from 1.01 to 2.58% as a result of the increase in the nanorods' height from 50 to 1000 nm. Owing to the decrease of the reflection and the SnO_2:F absorption with increasing the ZnO nanorods' height from 50 to 100 nm, the absorption in Cu(In,Ga)Se_2 is boosted from 66.52 to 68.65%. As a consequence of the boost in the transmission and the ZnO nanorod absorption, an increase in the ZnO nanorods' height over 100 nm results in a reduction in the absorption of Cu(In,Ga)Se_2. Therefore, the nanostructured thin-film solar cells with the ZnO nanorods' height of 100 nm has the maximum absorption in Cu(In,Ga)Se_2.

Sample	ZnO nanorods' bottom diameter (nm)	Nanorod site coverage (%)	Reflection (%)	Transmission (%)	Absorption in Sn_2O_3:F (%)	Absorption in ZnO nanorods (%)	Absorption in Cu(In,Ga)Se_2 (%)
1	–	–	13.18	3.47	12.27	–	62.20
2	120	29.9	10.31	3.66	11.81	0.43	64.91
3	160	53.2	8.39	3.73	11.56	0.89	66.55
4	200	89.7	6.55	3.81	11.35	1.31	68.10
5	210	94.2	6.18	3.82	11.31	1.38	68.43
6	220	97.5	5.88	3.83	11.28	1.48	68.65

Table 2. The optical modeling results on the structure of glass/SnO_2:F/ZnO nanorods/Cu(In,Ga)Se_2. The simulated ZnO nanorod has a top diameter of 120 nm and a length of 100 nm. The density of the ZnO nanorod arrays is 3.1×10^9 1/cm^2. The bottom diameters of the ZnO nanorod are varied. Correspondingly the percentage site coverages of the ZnO nanorods on the SnO_2:F surface are varied.

First, the ZnO nanorods' bottom diameters are varied while the other parameters such as the top diameter, length and density are fixed. **Table 3** and **Figure 3** show the modeling results. The nanorods' bottom diameters are varied from 120 to 220 nm. Correspondingly, the percentage site coverage of the ZnO nanorods on the FTO surface is varied from 29.9 to 97.5%. As shown in the table, the ZnO nanorod possessing the same size of the bottom and top diameters has the hexagonal prism morphology and shows a high reflection of 10.31%. An increase in the ZnO nanorods' bottom diameter leads to a considerable decrease in the reflection. By increasing the ZnO nanorods' bottom diameter from 120 (site coverage 29.9%) to 220 nm (site coverage 97.5%), the reflection is decreased from 10.31 to 5.88%, which is reduced by 43.0%. With increasing the ZnO nanorods' bottom diameter from 120 (site coverage 29.9%) to 220 nm (site coverage 97.5%), the transmission is slightly increased from 3.66 to 3.83%. As a result of the rise in the ZnO nanorods' bottom diameter from 120 (site coverage 29.9%) to 220 nm (site coverage 97.5%), the absorption in SnO_2:F descends from 11.81 to 11.28%. An increase in the ZnO nanorods' bottom diameter leads to a continuous increase of the absorption in ZnO nanorods. Owing to the decrease of the reflection and the SnO_2:F absorption with increasing the ZnO nanorods' bottom diameter from 120 (site coverage 29.9%) to 220 nm (site coverage 97.5%), the absorption in Cu(In,Ga)Se2 is boosted from 64.91 to 68.65%. Therefore, the nanostructured thin-film solar cells with the ZnO nanorods' bottom diameter of 220 nm (site coverage 97.5%) has the maximum absorption in Cu(In,Ga)Se_2.

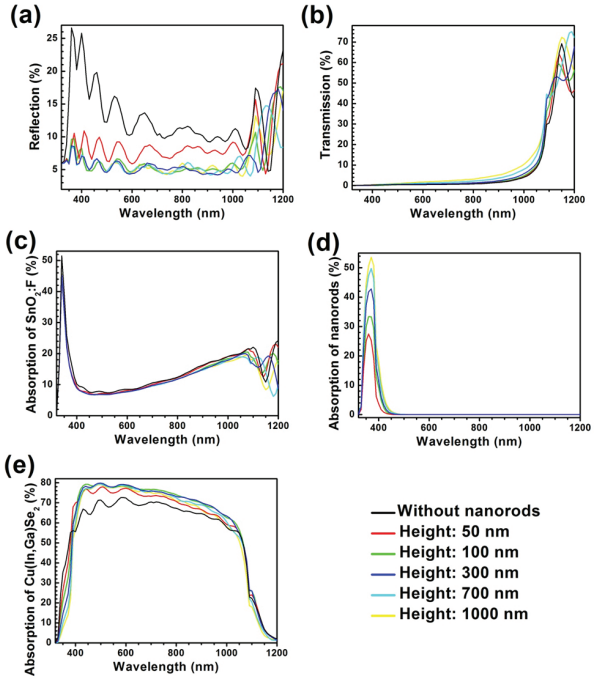

Figure 2. The simulated optical spectra of the structure of glass/SnO_2:F/ZnO nanorods/Cu(In,Ga)Se_2. The simulated ZnO nanorod has a bottom diameter of 220 nm and a top diameter of 120 nm. The density of the nanorods is 3.1×10^9 1/cm^2 with the site coverage of 97.5%. The heights of the ZnO nanorod are varied.

Since the ZnO nanorods' bottom diameter has been optimized to be 220 nm, the top diameter of the ZnO nanorods would be varied to achieve the maximum absorption in Cu(In,Ga)Se_2. **Table 4** and **Figure 4** show the modeling results. The nanorods' top diameters are varied from 80 to 160 nm. With increasing the ZnO nanorods' top diameter from 80 to 150 nm, the reflection of the structure is decreased from 6.85 to 5.64%, which is diminished by 17.7%. As shown in **Table 4** an increase in the ZnO nanorods' top diameter over 150 nm results in a slight increase in the reflection. The reflection of the structure with the ZnO nanorods possessing a top diameter of 160 nm is 5.65%. By increasing the ZnO nanorods' top diameter from 80 to 160 nm, the transmission is increased from 3.67 to 3.96%. As a result of the rise in the ZnO nanorods' top diameter from 80 to 160 nm, the absorption in SnO_2:F descends from 11.48 to 11.18%. An increase in the ZnO nanorods' top diameter leads to a continuous increase of the absorption in ZnO nanorods. Owing to the decrease of the reflection and the SnO_2:F absorption with increasing the ZnO nanorods' top diameter from 80 to 140 nm, the absorption in Cu(In,Ga)Se_2 is boosted from 67.84 to 68.76%. By increasing the ZnO nanorods' top diameter from 140 to 150 nm, the absorption in Cu(In,Ga)Se_2 keeps constant. An increase in the ZnO nanorods' top diameter over 150 nm results in a reduction in the absorption of Cu(In,Ga)Se_2. Therefore, the nanostructured thin-film solar cells with the ZnO nanorods' top diameter of 150 nm has the maximum absorption in Cu(In,Ga)Se_2. Compared with the structure without using the ZnO nanorods, the absorption of Cu(In,Ga)Se_2 in the nanorod-integrated structure is boosted from 62.20 to 68.76%, which is enlarged by 9.5%.

http://dx.doi.org/10.5772/64611

Sample	ZnO nanorods' top diameter (nm)	Reflection (%)	Transmission (%)	Absorption in Sn_2O_3:F (%)	Absorption in ZnO nanorods (%)	Absorption in Cu(In,Ga)Se_2 (%)
1	–	13.18	3.47	12.27	–	62.20
2	60	6.85	3.67	11.48	1.28	67.84
3	80	6.48	3.73	11.41	1.34	68.16
4	100	6.15	3.78	11.35	1.40	68.44
5	120	5.88	3.83	11.28	1.48	68.65
6	130	5.77	3.87	11.25	1.51	68.72
7	140	5.69	3.90	11.22	1.55	68.76
8	150	5.64	3.93	11.20	1.59	68.76
9	160	5.65	3.96	11.18	1.62	68.71

Table 3. The optical modeling results on the structure of glass/SnO_2:F/ZnO nanorods/Cu(In,Ga)Se_2. The simulated ZnO nanorod has a bottom diameter of 220 nm and a height of 100 nm. The density of the ZnO nanorod arrays is 3.1×10^9 1/cm^2. The top diameters of the ZnO nanorods are varied.

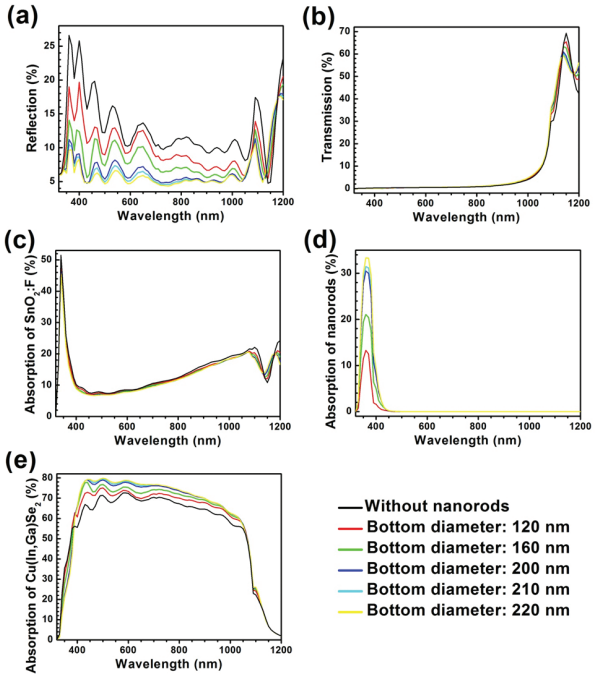

Figure 3. The simulated optical spectra of the structure of glass/SnO_2:F/ZnO nanorods/Cu(In,Ga)Se_2. The simulated ZnO nanorod has a top diameter of 120 nm and a height of 100 nm. The density of the ZnO nanorod arrays is 3.1×10^9 1/cm^2. The bottom diameters of the ZnO nanorod are varied. Correspondingly the percentage site coverages of the ZnO nanorods on the SnO_2:F surface are varied.

Sample	ZnO nanorods' top diameter (nm)	Reflection (%)	Transmission (%)	Absorption in Sn_2O_3:F (%)	Absorption in ZnO nanorods (%)	Absorption in $Cu(In,Ga)Se_2$ (%)
1	–	13.18	3.47	12.27	–	62.20
2	60	6.85	3.67	11.48	1.28	67.84
3	80	6.48	3.73	11.41	1.34	68.16
4	100	6.15	3.78	11.35	1.40	68.44
5	120	5.88	3.83	11.28	1.48	68.65
6	130	5.77	3.87	11.25	1.51	68.72
7	140	5.69	3.90	11.22	1.55	68.76
8	150	5.64	3.93	11.20	1.59	68.76
9	160	5.65	3.96	11.18	1.62	68.71

Table 4. The optical modeling results on the structure of glass/SnO_2:F/ZnO nanorods/$Cu(In,Ga)Se_2$. The simulated ZnO nanorod has a bottom diameter of 220 nm and a height of 100 nm. The density of the ZnO nanorod arrays is 3.1×10^9 1/cm^2. The top diameters of the ZnO nanorods are varied.

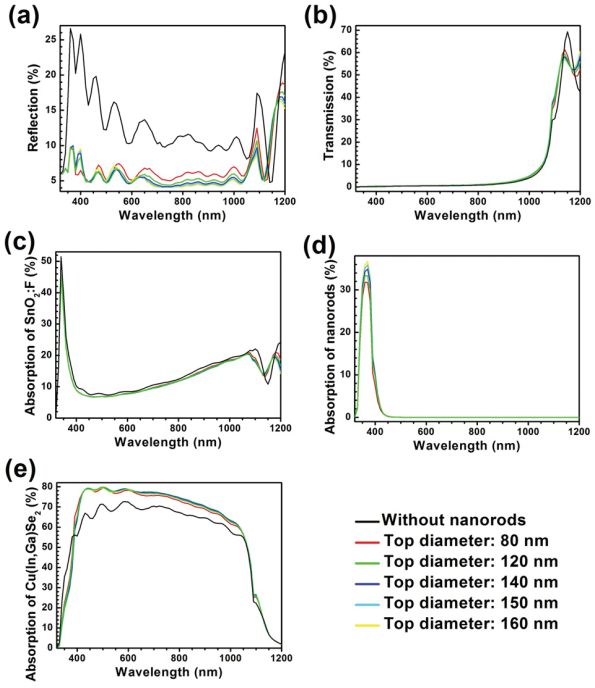

Figure 4. Current versus time transients obtained on FTO substrate at potential of −1.39 V.

http://dx.doi.org/10.5772/64611

3. Growth of ZnO nanorod arrays

The solution-based fabrication routes including hydrothermal method and electrochemical deposition (ECD) method are the ways to grow ZnO nanostructures at a low temperature down to the range between 60 and 90°C [12–23]. Meanwhile the growth can be achieved over large areas up to 30 × 30 cm. A two-stage electrodeposition method for tailoring the ZnO nanostructures is presented.

3.1. Nucleation and crystal growth

For the electrolyte recipe of ZnO nanostructures, there are two choices for the Zn source in the solution: $ZnCl_2$ [12] or $Zn(NO_3)_2$ [13]. In order to provide the oxygen source, one would have to bubble O_2 into the electrolyte during electrodeposition if $ZnCl_2$ were used [12]. The oxygen source is from the reduction of NO_3^- for the electrolyte using $Zn(NO_3)_2$. The formations of ZnO by NO_3^- precursors were described in Eqs. (1)–(4) as follows [13].

$$Zn\left(NO_3\right)_2 \rightarrow Zn^{2+} + 2NO_3^- \quad (1)$$

$$NO_3^- + 2e + H_2O \rightarrow 2OH^- + NO_2^- \quad (2)$$

$$Zn^{2+} + 2OH^- \rightarrow Zn(OH)_2 \quad (3)$$

$$Zn(OH)_2 \rightarrow ZnO + H_2O \quad (4)$$

During the ECD process, the electrodeposited products are deposited on one of the electrodes. The electrode with the deposited materials is the working electrode (WE). However, the WE is not adequate for the complete ECD process. At least another electrode should be installed for allowing current to flow. In the simplest case, a two-electrode cell is used for ECD. In order to measure the accurate WE potential, a three-electrode cell containing a WE, a counter electrode (CE) and a reference electrode (RE) is more common. A current flows between the WE and CE, while the potential of the WE is measured against the RE. The glass substrates are used as the WE. The electrochemical cell was placed in a thermoregulated bath. The liquid electrolyte contains the salts regarding the recipes. A schematic illustration of the set up for the ECD process is shown in **Figure 5**. The electrochemical process is controlled and recorded by a potentiostat/galvanostat.

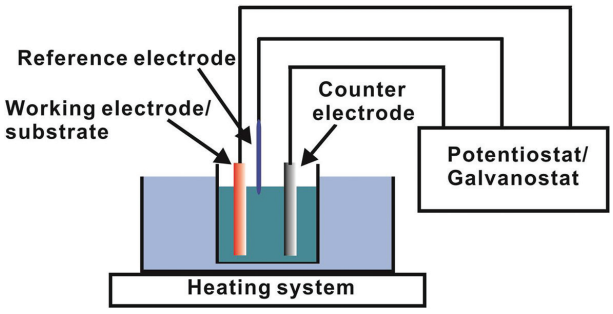

Figure 5. The scheme of the electrochemical deposition system.

Figure 6 shows a typical curve for current vs transit time obtained in the electrodeposition process of the ZnO nanorods. At the beginning of the potential step, there is a rapid surge of the current. The potential difference between the FTO surface and the electrolyte leads to the accumulation of excess charges near the surface. As a result, the electric double layer is formed at the phase boundary [24]. The initial surge corresponds to the electric double layer charging at the onset of the potential step [25]. After the surge, current decays abruptly as cations are reduced and the anions are oxidized in the close vicinity of the electrode [26, 27]. The nucleation forms in this stage. As fresh cations and anions diffuse, the current began to increase. The internal hexagonal structure of ZnO favors the anisotropic growth along the c-axis direction, which leads to the formation of the nanorods [28, 29]. During the nanorods' growth process, the surface area of the nanorods is increasing continuously. Therefore, the transient current density cannot be determined except for monitoring the in situ growth of the nanorods and collecting the information of the nanorods' morphological changes during the electrodeposition process.

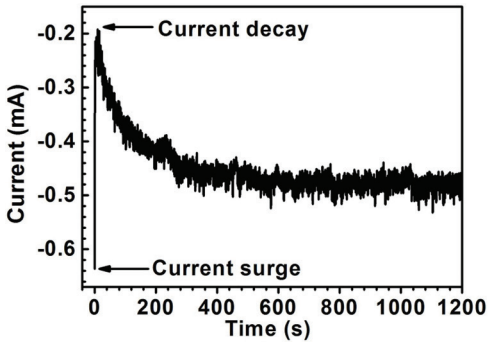

Figure 6. Current versus time transients obtained on FTO substrate at potential of −1.39 V.

3.2. Two-stage electrodeposition

Since the growth of ZnO nanostructures greatly depends on the nucleation process, it is possible to control the ZnO nanostructures' growth and properties by adjusting the amperage in the nucleation process. We developed a two-stage electrodeposition method to control the electrodeposited ZnO nanostructures' morphology and geometry. The samples were prepared from an aqueous solution: 7 mM $Zn(NO_3)_2.6H_2O$ and 7mM NH_4NO_3. The method was divided into two stages. A galvanic current (galvanic control) was applied during the first stage and then it was switched to a potentiostatic mode (−1.39V) (potentiostatic control) for the following growth stage. In order to investigate the influence of the galvanic current on the ZnO nanorods' growth and properties, we prepared one sample by using potentiostatic method (−1.39V) and the other samples by using two-stage electrodeposition method with the galvanic current ranging from −0.2 to −2 mA. All the FTO substrates were cut into small 2.5 cm^2 rectangles and then cleaned in an ultrasonic bath of acetone and ethanol with subsequent rinsing in distilled water. After preparation, the samples were washed with distilled water to remove any residual salt. By using this new method, the packing density of ZnO nanorods on bare FTO can be adjusted.

3.3. Control of ZnO nanorod arrays' density

Since the growth of ZnO nanorods greatly depends on the nucleation process, it is possible to control the ZnO nanostructures' growth and properties by adjusting the current density in the nucleation process. We developed a new method, that is, two-stage electrodeposition method to control the packing density and diameter of the electrodeposited ZnO nanorods. The two-stage eletrodeposition method was divided into two stages. A galvanic current was applied during the first stage and then it was switched to a potentiostatic mode for the following growth stage. In order to investigate the influence of the galvanic current density on the ZnO nanorods' growth and properties, we prepared one sample by using potentiostatic method with a potential of −1.39V and the other samples by using galvanic current ranging from −0.2 to −2 mA/cm^2.

The average density, average diameter the average length in five ZnO nanorods samples were estimated from a statistical evaluation and are summarized in **Table 5**. The diameter and height dispersion in five ZnO nanorod samples are shown in **Figure 7**. It shows that the ZnO nanorods' density in samples prepared by using two-stage eletrodeposition method with a high galvanic current density (−0.5 to −2 mA/cm^2) is larger than that of sample prepared under a low galvanic current density (−0.2 mA/cm^2). Therefore, it is clear that an increase in galvanic current density leads to a considerable increase of the ZnO nanorods' density. By increasing the galvanic current density from −0.2 to −2 mA/cm^2, the density of ZnO nanorods was boosted from 4.2×10^8 to 1.3×10^9 1/cm^2, which is enlarged by ∼200%. According to the formations of ZnO by NO_3^- precursors described in Eqs. (1)–(4), an increase in a current raises the yields of OH^- ions. As a result, the nucleation sites were boosted in the initial nucleation process. The mechanism is illustrated in **Figure 8**. The ZnO nanorods' density was increased in the following process under the potentiostatic mode.

Galvanostatic stage: current density (mA/cm^2)	Potentiostatic stage: potential (V)	Average diameter (nm)	Average height (nm)	Density (10^8/cm^2)
0	−1.39	166	619	6.8
−0.2	−1.39	317	625	4.2
−0.5	−1.39	82	625	9.1
−1.2	−1.39	82	622	13.0
−2	−1.39	74	620	12.9

Table 5. Growth parameters of two stages, average diameter, average height and density of the ZnO nanorods.

In order to investigate the nucleation process at the galvanic stage, four samples were prepared under a galvanic mode with the galvanic current density ranging from −0.2 to −2 mA/cm^2, and the process was stopped before the following potentiostatic stage. The densities of the nucleation sites in these samples were shown in **Table 6**. The size of nuclei sites in the sample prepared under −0.2 mA/cm^2 was too small to be observed in the measurements. By increasing the galvanic

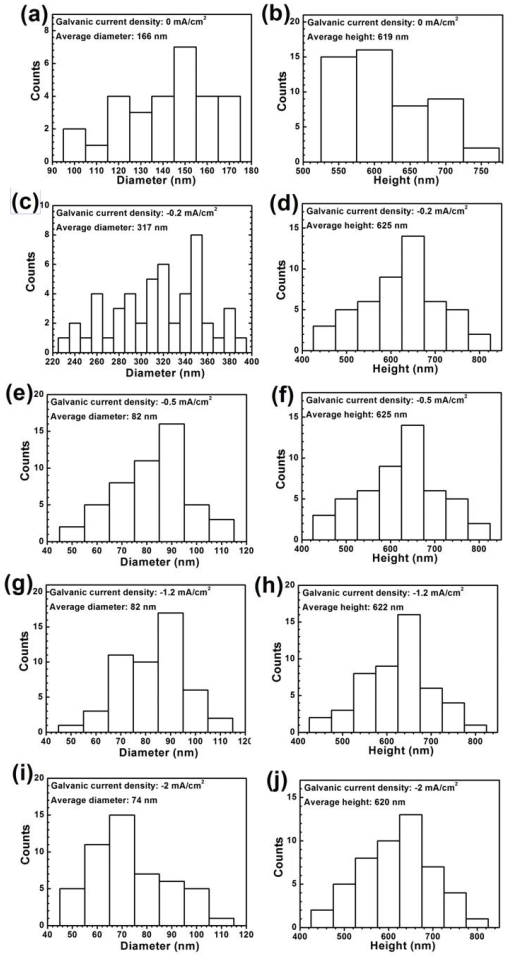

Figure 7. The diameter and height dispersion of the ZnO nanorods prepared by using two-stage electrodeposition method with the galvanic current density of 0 mA/cm² (a), (b); −0.2 mA/cm² (c), (d); −0.5 mA/cm² (e), (f); −1.2 mA/cm² (g), (h) and −2 mA/cm² (i), (j).

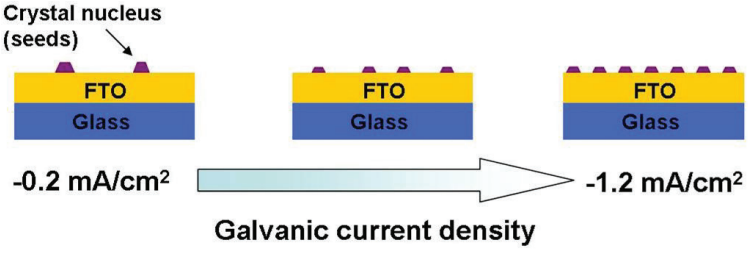

Figure 8. The sketch of the ZnO nanorods' nucleation mechanism under different galvanic current densities.

current density, the density of the nucleation sites was boosted from 1.5×10^9 to 2.4×10^9 1/cm^2. These nucleation sites assisted the following growth of ZnO nanorods with a higher density.

An increase in the galvanic current density, on the other hand, induced a significant decrease of the ZnO nanorods' average diameter. The average diameter of ZnO nanorods was reduced from 317 to 74 nm as the galvanic current density was increased from −0.2 to −2 mA/cm^2. The size of ZnO nanorods' diameter depended on the nucleation sites at the initial stage. Since the yields of OH^- ions is higher than Zn^{2+} ions in the initial process under a higher galvanic current density, the fact that the rate of OH^- generation is larger than the diffusion rate of Zn^{2+} ions to the cathode suppresses the lateral growth of the nucleation sites. As a consequence, the size of the nanorods' diameter was decreased by using a higher galvanic current density. The galvanic current did not lead to a significant variation of the ZnO nanorods' average length and the ZnO nanorods keep a virtually constant average length around 620 nm.

Galvanic current density (mA/cm^2)	Time (s)	Density (10^9/cm^2)
−0.2	40	–
−0.5	40	1.5
−1.2	40	2.7
−2	40	2.4

Table 6. Growth parameters and density of the samples prepared under a galvanostatic mode.

4. Conclusion

Thin-film photovoltaic device technology relies on light management to enhance light absorption in thin absorber layers. The use of the ZnO nanorods in the thin-film solar cells is an effective way to decrease the reflection. The variation of the geometrical parameters of the ZnO nanorods, such as the diameter, the height and the density can lead to an optimum, which results in the maximal absorption in the absorber. An approach of a rigorous modeling is presented to simulate and optimize the light absorption in the Cu(In,Ga)Se_2 absorbers with ZnO nanorods.

ZnO nanorod arrays were fabricated by using an electrochemical deposition method. A two-stage electrodeposition method for adjusting the ZnO nanorods' density on bare SnO_2:F substrates has been described and analyzed. The ZnO nanorods' density arrays were adjusted from 4.2×10^8 to 1.3×10^9 1/cm^2 by increasing the galvanic current density from −0.2 to −2 mA/cm^2. An increase in the galvanic current density induced a significant decrease of the ZnO nanorods' average diameter.

In this chapter, the modeling results show that the use of the ZnO nanorod arrays lead to an increase of the absorption in the absorber layer. After that, the growth of the ZnO nanorod arrays is tailored towards the optimized shape and geometry of the nanorod arrays. The opening questions and further research suggestions are outlined as follows.

The nanorods in the simulation are vertically aligned on the substrate. However, the real ZnO nanorods grown on FTO substrates are randomly oriented. It is suggested to run simulation on a tilted nanorod, which reflects the average orientation situation of the nanorod arrays. It is suggested to develop more effective ways to tailor the morphology and geometry of the ZnO nanorod arrays. Besides the use of the nanorods in the traditional thin-film solar cells, there are other possible methods for improving the light management in the thin-film solar cells. For example, some metal nanoparticles such as silver and gold nanodots can be incorporated into the solar cells. Due to the surface plasmonic effects of the nanoparticles, light will be efficiently coupled into the solar cells. In addition, a nanostructured antireflective coating layer can be coated on the surface of the cover glass in the thin-film solar modules. The antireflective coating layer will decrease the reflection between the glass and the air resulting in the boost of the light harvesting in the internal solar cells. The modern technology of the light management of the thin-film solar cells is now developing rapidly and the combination of the nanostructures and thin films will show the power.

Acknowledgements

This work was supported by the National Natural Science Foundation of China under Grant No. 61404007 and the Beijing Talents Fund (2015000021223ZK38).

Author details

Yang Tang

Address all correspondence to: tangy118@hotmail.com

National Institute of Clean-and-Low-Carbon Energy, Future Science & Technology City, Beijing, People's Republic of China

References

[1] ZSW, Press release, June 15, 2016.

[2] First Solar, Press release, February 23, 2016.

[3] C. W. Bunn, Proc. Phys. Soc. London 47, 835, 1935.

[4] R. B. Heller, J. McGannon, and A. H. Weber, J. Appl. Phys. 21, 1283, 1950.

[5] T. J. Gray, J. Am. Ceram. Soc. 37, 534, 1954.

[6] G. P. Mohatny and L. V. Azaroff, J. Chem. Phys. 35, 1268, 1961.

[7] R. R. Reeber, J. Appl. Phys. 41, 5063, 1970.

[8] Ü. Özgür, Y. I. Alivov, C. Liu, et al., J. Appl. Phys. 98, 041301, 2005.

[9] M. Law, L. E. Greene, J. C. Johnson, et al., Nat. Mater. 4, 455–459, 2005.

[10] X. W. Sun, J. Chen, J. L. Song, D. W. Zhao, W. Q. Deng, and W. Lei, Opt. Expr. 18(2), 1296–1301, 2010.

[11] D. C. Olson, S. E. Shaheen, R. T. Collins, et al., J Phys. Chem. C. 111, 16670–16678, 2007.

[12] M. Izaki and T. Omi, Appl. Phys. Lett. 68, 2439–2440, 1996.

[13] M. Izaki and T. Omi, J. Electrochem. Soc. 143, L53–L55, 1996.

[14] C. J. Lan, H. Y. Cheng, R. J. Chung, J. H. Li, K. F. Kao, and T. S. Chin, J. Electrochem. Soc. 154, D117–D121, 2007.

[15] J. Yang, Y. Qiu and S. Yang, Cryst. Growth Des. 7, 2562–2567, 2007.

[16] J. Chen, L. Ae, Ch. Aichele, and M. Ch. Lux-Steiner, Appl. Phys. Lett. 92, 161906, 2008.

[17] L. Vayssieres, K. Keis and S. E. Lindquist, J. Phys. Chem. B, 105, 3350, 2001.

[18] L. Schmidt-Mende and J. L. MacManus-Driscoll, Mater. Today, 10, 40, 2007.

[19] M. N. R. Ashfold, R. P. Doherty, N. G. Ndifor-Angwafor, D. J. Riley, Y. Sun, Thin Solid Films, 515, 8679, 2007.

[20] K. Govender, D. S. Boyle, P. B. Kenway, and P. O'Brien, J. Mater. Chem. 14, 2575, 2004.

[21] L. E. Greene, M. Law, and J. Goldberger, Angew. Chem. Int. Ed. 42, 3031–3034, 2003.

[22] Y. Tak and K. Yong, J. Phys. Chem. B, 109, 19263–19269, 2005.

[23] C-C Lin, H-P Chen, H-C Liao, et al. Appl. Phys. Lett. 86, 183103, 2005.

[24] V. S. Bagotsky, Fundamentals of Electrochemistry, John Wiley & Sons, Inc., New Jersey, 2006, Second edition, p. 22.

[25] S. B. Sadale, P. S. Patil, Solid State Ionics. 167, 273–283, 2004.

[26] A. I. Inamdar, Y. S. Kim, J. S. Sohn, H. Im, H. Kim, D.-Y. Kim, R. S. Kalubarme, C. J. Park, J. Korea Phys. Soc. 59, 145–149, 2011.

[27] A. I. Inamdar, S. H. Mujawar, S. B. Sadale, A. C. Sonavane, M. B. Shelar, P. S. Shinde and P. S. Patil, Sol. Energy Matar. Solar Cells. 91, 864, 2007.

[28] Y. Lin, J. Yang, X. Zhou, Appl. Surf. Sci. 258, 1491–1494, 2011.

[29] L. Vayssieres, K. Keis, S.-E. Lindquist, A. Hagfeldt, J. Phys. Chem. B, 105, 3350–3352, 2001.

Chapter 18

Close-Spaced Sublimation (CSS): A Low-Cost, High-Yield Deposition System for Cadmium Telluride (CdTe) Thin Film Solar Cells

Nowshad Amin and Kazi Sajedur Rahman

Additional information is available at the end of the chapter

http://dx.doi.org/10.5772/66040

Abstract

Semiconductors are the key materials in many of our modern day devices, such as sensors, integrated circuits, energy harvesting devices, optoelectronics and so on. However, apart from two known elemental semiconductors that are silicon and germanium, we have been using many of the synthesized ones since the microelectronic revolution known as invention of transistor. Numerous compound semiconductors since then have been synthesized, grown, deposited or simply fabricated by numerous processes in the scientific community. To avoid associated chemical disposals or keep safe from toxic or combustible gas usages in any semiconductor fabrication facilities, many researchers choose physical vapor deposition as the simplest method. One of such processes is called Close-Spaced Sublimation (CSS), which is a kind of thermal evaporation by nature. This chapter would give a comprehensive outline on CSS as one of the most advantageous semiconductor deposition processes for many compound semiconductors having relatively low evaporation temperature. Cadmium telluride (CdTe) is one of the examples utilized for solar cell absorber materials since the early 1980s using CSS technique. Therefore, growth of CdTe thin films by CSS and its utilization in thin film solar cells will be discussed to comprehend the ultimate benefits of the close-spaced sublimation (CSS) process.

Keywords: semiconductors, thin films, close-spaced sublimation, temperature profile, CdTe thin film solar cells

1. Introduction

Close-spaced sublimation (CSS) is one of the simplest methods in physical vapor deposition. Materials especially semiconductors that evaporate below 800°C can be coated on substrates like glass in both vacuum and atmospheric pressure. The target materials have to be in the form of solid in either chunk or powder form [1–3]. As for example, compound semiconductor like cadmium telluride (CdTe) can be deposited at around 600°C with a thickness of 1–10 μm within 10 min of deposition time, which is one of the fastest deposition times among other physical vapor deposition (PVD) methods. Needless to mention, CSS and binary compound material cadmium telluride (CdTe) are densely interrelated due to extensive usage of CSS in the growth of CdTe thin film [4, 5]. The binary compound CdTe has been recognized as one of the promising thin film photovoltaic materials owing to its near optimum bandgap of 1.44 eV and high absorption coefficient over 10^5/cm. CdTe, therefore, absorbs over 90% of available photons ($h\nu > 1.44$ eV) in 1 μm thickness, and hence, films of only 1–3 μm are sufficient for solar cells [6, 7]. Several types of CdTe solar cells such as Schottky barrier, homojunction, heterojunction, and p-i-n have been investigated to date [8–10]. Among all, the most successful configurations are the heterojunctions where a wide bandgap semiconductor can be used as the heterojunction partner or "window." However, cadmium sulfide (CdS) has been the most widely studied and most appropriate window material for CdTe solar cells to date. Most recent development in CdTe thin film solar cells has found noteworthy improvements in small area conversion efficiencies. A number of techniques such as atomic layer epitaxy, spraying, electrodeposition (ED), and close-spaced sublimation (CSS) have been employed for the fabrication of CdTe thin film solar cells with significant efficiencies of over 20% with various configurations. It is quite notable that even though important dissimilarities exist, the performances achieved are independent to processing demonstrating the versatility of CdTe and its superior status in the photovoltaic technologies.

The deposition method for CdTe thin films differs widely and can considerably affect the material properties and device performance. Since CdTe has high absorption coefficient hence thicknesses for CdTe thin films are limited within 2–10 μm [11, 12]. There are various methods to deposit CdTe, which includes close-spaced sublimation (CSS), vapor transport deposition (VTD), electrodeposition (ED), physical vapor deposition (PVD), sputtering, etc. [13–15]. Among all the deposition methods, the highest efficient CdTe thin film solar cell was obtained by close-spaced sublimation (CSS). The substrate temperature is one of the crucial parameters for CdTe deposition as it could be observed that most of the deposition techniques demonstrated has substrate heating. Higher growth temperature not only enhances the deposition rate, but it also determines the quality of junction formation. Moreover, some research studies illustrated that CdTe deposited at higher temperature exhibits better performance. Therefore, the resistivity of the CdTe films decreases with an increase in substrate temperature.

http://dx.doi.org/10.5772/66040

2. Deposition of CdTe thin films by close-spaced sublimation (CSS) technique

The CSS technique is particularly attractive for the deposition of CdTe films since it offers high deposition rates and can be simply scaled up for manufacturing purposes. CSS equipment can be constructed with a wide variety of options such as vacuum, temperature, spacing between source and substrate. One can design first based on required material to be coated on substrates. As for example, the source and substrate in case of CdTe are kept at a close distance of 2 mm in our case, which can also be changed by some simple techniques like increasing spacer of certain thickness. Now, top and bottom heaters can be chosen according to the temperature needed to evaporate either in atmospheric pressure or evacuating to the range of millitorr, filling with certain gas like Ar or N_2. There is a need for good temperature controller which can be programmable in steps such as increment or hold time. Finally, natural cooling is followed to let the temperature falls back to room temperature. Interestingly, the whole CSS deposition takes place within only 10 min, excluding the evacuation or purging time. We have successfully grown a required thickness of 1 micron for CdTe to be used in solar cells, which is the most challenging part in CSS to learn temperature profiles for various thickness with the best coating or film properties needed in each application.

The main design prerequisite for the close-spaced sublimation (CSS) equipment is to minimize the influence of extrinsic impurities that could be incorporated from ambient to the deposited films. This requirement minimizes the number of impurity sources that would be heated to high temperatures together with the number of wires required to feed through the chamber. Sublimation illustrates the direct phase transition between a solid and gas state. A close-spaced sublimation is dependent on the following factors:

- Sublimation process at the surface of the source
- Transport of the gas from the source to the substrate surface
- Sublimation process at the surface of the substrate

Phase diagrams of CdTe demonstrate a very narrow composition where the CdTe binary compound exists as a solid without any other phases, with an atomic percentage of tellurium equal to approximately 50%. The melting point of the material is also a maximum at this point and equal to 1099°C [16]. Greenberg calculated the range of tellurium concentration over which the material is in a purely solid phase to be 49.996 to 50.012 atomic percent [17]. A pressure phase temperature diagram of CdTe has also been published, which indicates the boundary of a solid to vapor transition [18]. The sublimation of CdTe occurs in the region where the CdTe is in a pure solid phase as calculated by Greenberg. This region is defined by the solid-liquid-vapor transition as the upper limit, the sides are defined by the limits of Cd and Te saturation in CdTe, and the bottom is defined by the line of stoichiometric congruent sublimation where the vapor has the same composition as the solid [19]. The sublimation reaction happens in the following equation [20]:

$$2\ CdTe\ (s) \leftrightarrows 2\ Cd\ (g)\ +\ Te_2(g) \tag{1}$$

The consequence of manipulating certain deposition parameters on the growth rate has also been reported earlier. Alamri demonstrated two distinct growth rate regions when increasing the source and substrate distance for a series of depositions [21]. This would specify a change in the growth mechanism, apparently from a sublimation limited to diffusion limited case. The growth rate was found to be independent of the substrate temperature (over a 100°C region), for temperatures significantly lower than source temperature and with a low deposition chamber pressure (10^{-5} mbar). This result does not emerge to agree with the theory for any sublimation limited cases suggested by others groups. No reason for this disagreement can be found from the experimental detail provided. As the distance between the source and substrate increased at low pressures, the growth rate was reported to decrease due to the divergence of the gas. Research works by Nagayoshi and Suzuki observed that the deposition rate increased as the source temperature increased for a deposition under vacuum, in agreement with a sublimation limited case [22]. They also varied the substrate temperature showing for a source temperature of 650°C and a substrate temperature of 520°C, the growth rate reached maximum in that case. The incidence of a maximum deposition rate for a series of experiments where only the substrate temperature was varied would imply varying this parameter changed the deposition mechanism. Work by Anthony et al. showed the composition of the environment gas also has an effect on the diffusion limited process. They recommend that the faster growth rate in a helium environment compared to argon was due to the small molecular weight and diameter of the helium [23].

2.1. Close-spaced sublimation (CSS) system

CSS technique has been mainly emphasized for the deposition of CdTe films on foreign substrates. This technique has been extensively investigated because of the relatively high efficiency of solar cells prepared from CSS grown CdTe films. Deposition by reaction condensation from vapor generated from direct sublimation of the compounds has produced the highest efficiency devices. A schematic diagram of the CSS apparatus is shown in **Figure 1**.

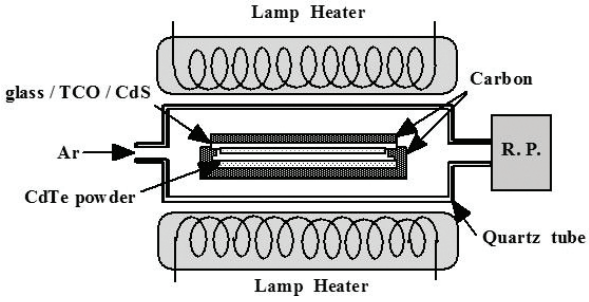

Figure 1. Schematic view of close-spaced sublimation (CSS) apparatus.

http://dx.doi.org/10.5772/66040

The substrate and source, separated by a small distance (1 mm for instance) and placed on appropriate holders, are enclosed in a fused silica tube with gas inlet and outlet tubes to keep controlled environment inside. The system is maintained at desired temperatures by using infrared radiation, and thermocouples inserted into the sample holders are used to monitor their temperatures. The important process parameters are the temperatures of the source and the substrate, the nature of the atmosphere, the pressure in the reaction tube, and the composition of the source material. These parameters are inter-related. For example, the partial pressure of Cd and Te_2 in the reaction tube is important in determining the rate of deposition, and these pressures, or the dissociation pressure of CdTe, depend exponentially on temperature. At a given source temperature, the sublimation rate increases rapidly as the pressure in the chamber is reduced from the atmospheric pressure. At low pressures, such as 1 Torr, the mean free path of the gaseous species in the reaction tube increases, and the condensation process is no longer limited to the space between the substrate and the source material. The effect of the nature of the ambient gas is related mainly to its thermal conductivity. In case of fixed source-substrate spacing, high thermal conductivity of the ambient gas tends to increase the substrate temperature, thus reducing the growth rate. High deposition rate of CdTe films (up to 10 μm/min) is therefore a special feature of the CSS process that benefits the thin film growth in a short span of time.

Deposition pressures between 1 and 30 Torr, substrate temperature from 500 to 600°C, and source temperatures between 700 and 800°C are commonly used for CSS. Sublimation of the compounds produces monatomic Cd and diatomic group VI (Te_2 or S_2) vapor, which recombines by the reverse reaction on the relatively cool substrate. Essentially, the coating process is a chemical vapor deposition with locally generated vapor (sublimation) and a reverse reaction (deposition) evolving no by-products. Due to high vapor pressures of the elements relative to the compounds, depositions of CdTe at temperatures above 500°C result in single phase films with stoichiometry to better than 100 ppm. **Table 1** provides a summary in the range of conditions used for the deposition of the CdTe films.

Substrate temperature	550–620°C
Source temperature	565–625°C
Pressure	1–2 Torr (Ar gas atmosphere)
Spacing	2 mm

Table 1. Deposition conditions used in the CSS growth of CdTe films.

In this study, the substrate temperature is varied in the range of 550–620°C. The source temperature, the total pressure, and spacing are adjusted to result in deposition rates of about 1.0–5.0 μm/min. However, for some films, the pressure during the deposition is kept at 2 Torr. One of the important efforts of this study is to control the film thickness toward stable pinhole free CdTe films of thickness <5 μm. By keeping other deposition parameters constant, the temperature profile is changed according to the desired film thickness. The chamber is

evacuated several times and then is kept at 1.8 Torr of Ar gas to create the appropriate atmosphere for deposition.

2.2. Sintering of source material

Sintering is the procedure of compacting and forming a solid mass of material by heat and/or pressure without melting it to the point of liquefaction. In CSS process, sintering is usually executed to prepare the source material, while fine-powdered CdTe or other materials are used. In cases of chunks, one can skip the sintering process. In sintering, CdTe powder is first put on the empty well on the bottom holder. Then, the powder is heated at specific pressure and temperature to make the powder compact as well as to form solid as shown in **Figure 2**.

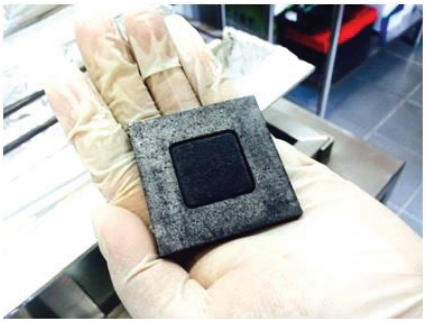

Figure 2. CdTe source material as sintered for CSS process.

The source material on the graphite box is exhausted for each experiment, so the volume of the material decreases after each sublimation process. CdTe is also deposited on the inside wall of the chamber in regions where the temperature is cooler than the graphite blocks. This means that more than just the amount of CdTe deposited on the sample is released from the source material during each experiment. The parameters used during the sintering are given in **Table 2**.

CSS sintering parameters	Value
Source temperature	700°C
Spacing	1 mm
Pressure	10 Torr (Ar gas atmosphere)
Heating time	30 min

Table 2. CdTe sintering parameters used in CSS.

The chamber has a rotary vacuum pump attached to one flange with the choice to allow gas to flow into the other flange. To control the pumping rate, a valve is positioned between the

http://dx.doi.org/10.5772/66040

pump and deposition chamber, a pipe which bypassed the valve has a smaller diameter to limit the flow of gas. The pressure in the chamber is normally measured by pressure gauges. Argon and nitrogen gases are attached to the system. The argon gas is used as a deposition gas. Nitrogen is generally used for purging and venting the chamber to open the quartz tube (**Figure 3**).

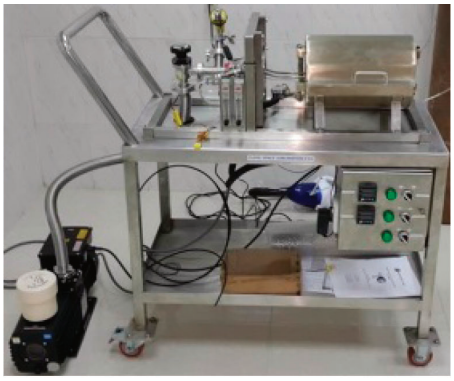

(a)

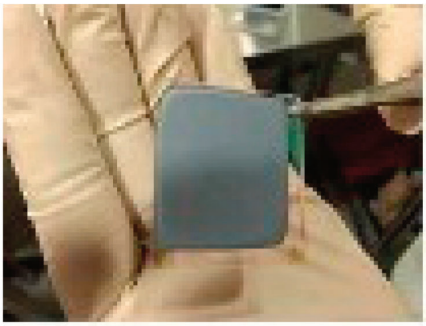

(b)

Figure 3. (a) CSS deposition system and (b) CSS grown CdTe thin film on glass.

In general, the CSS chamber is left under vacuum between experiments. When it is needed to open the chamber, gas is fed inside to bring the pressure up to atmosphere. The end flange with the gas inlet can be removed, and the graphite blocks can also be removed from the chamber. The sample is placed in the substrate block, and two glass samples are kept on top working as heat spreaders. The graphite blocks are then placed at the end of the tube, and the thermocouples are positioned within the blocks. The blocks are then pushed into the centre of the quartz tube, and the chamber is pumped to a vacuum. After a vacuum has been reached, the gas pressure gauge could then be adjusted to acquire the desired pressure within the chamber after a few purging of ambient inside. When the environment is stabilized, the heating

sequence starts, and the temperature monitoring begins. The superstrate configuration is basically used to deposit CdTe on top of CdS deposited films. The system is maintained at the set temperatures by means of radiative heating using a total of 2 kW halogen lamps on top and bottom. The thermocouples are inserted into the graphite holders to monitor the growth temperatures (**Figure 4**).

Figure 4. Inside view of the CSS chamber with spacers placed on top of bottom holder.

2.3. Significance of temperature profiles

The substrate temperature of CdTe thin films during the growth is an essential parameter to obtain high-quality films ultimately resulting in high-efficiency CdTe/CdS thin film solar cells. During the fabrication of CdTe/CdS full cell, high temperature is required for CdTe thin films for inter-diffusion of CdS and CdTe to form $CdS_{1-x}Te_x$ layer. The formation of a $CdS_{1-x}Te_x$ mixed crystal layer modifies the electrical junction into the CdTe improving the electrical and photovoltaic characteristics of the junction [24]. The extent of inter-diffusion depends on the rate of deposition and the substrate temperature [25].

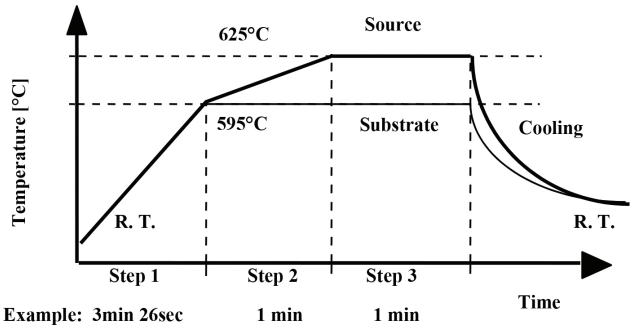

Figure 5. A typical temperature profile for CdTe growth of 5 μm and above.

http://dx.doi.org/10.5772/66040

In many literatures, it is found that the high conversion efficiencies obtained from CSS CdTe films have been attributed to the high substrate temperature. The use of high substrate temperatures is considered to uphold the interface reaction between the CdS and CdTe. Considering all the above facts, the temperature profile (described as heat profile in some literatures) is highlighted strongly. In order to achieve high efficiency, it is more significant to attain high-quality CSS CdTe films. Several temperature profiles have been utilized to differentiate the cell performance. The temperature profile of the growth process is illustrated in **Figure 5**.

2.4. High-efficiency CdTe solar cells (>5 μm) from CSS technique

Although a number of important factors in CSS growth, which are supposed to bear significant roles in overall performance, are demonstrated earlier, the most important issue is to grow high-quality CdTe film regardless of its growth technique. To study as well as to make an effort in achieving such high-quality CdTe films, several temperature profiles were adopted during the growth by CSS here. All these temperature profiles were evaluated from their related results such as solar cell characteristics. In general, it has been noticed that the temperature profiles have important effect on the crystallinity as well as the thickness of the CdTe layer (**Figure 6**).

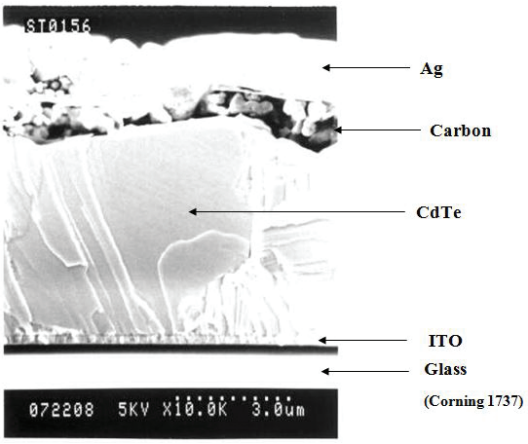

Figure 6. FESEM cross-sectional view of CdTe solar cell grown by CSS.

The most common temperature profile, which is recommended by the leading comrades in this field of CdTe solar cell fabrication, consisted of three steps with all high temperatures is shown in **Figure 5**. After the initial ramp-up step, the second step is supposed to have a great role in the crystallization of CdTe. The third step is important for stabilizing the microcrystals and the gaining the growth of CdTe layer. A part of the study also found unintentional growth of CdTe during the rise of temperature at the first step of the temperature profile. Even at low temperatures, small seed grains of CdTe were observed. Therefore, investigations have been

carried out for all possible temperature profiles in high temperature region and finally proposed the optimum one, as shown earlier in **Figure 5**, for better quality CdTe films (5–7 μm thick). The key point of this temperature profiles lies in the reverse mode during temperature rise as substrate temperature gets higher than the source temperature at any time dimension until the set temperature. Once the substrate temperature reaches its set point (e.g., 595°C), the source temperature increases until its set point (e.g., 625°C) and then both of them keep the set temperature constant, thus create a temperature difference of 30°C viable for CdTe growth in this case. This type of reverse mode in temperature rise could control the unintentional growth of CdTe at lower temperatures, which (CdTe) is suspected to be lower in quality with pinholes etc. In the modified temperature profile, the unexpected CdTe growth was suppressed to as low as 0.15 μm when the temperature rise of both source and substrate was stopped at the set point of substrate temperature. These CdTe films are then used to make full solar cell devices with the configuration of glass/ITO/CdS/CdTe/C:Cu/Ag. The conversion efficiency of 15.31% with open-circuit voltage (Voc) of 0.811 V, short-circuit current (Jsc) of 26.3 mA/cm^2, fill factor (F.F.) of 0.718 was achieved for the best cell as the highest to date found in the current configuration and process. The thickness of CdTe layer was about 7 μm, and the effective area of the cell was 1 cm^2. The current-voltage (J-V) characteristics are shown in **Figure 7**.

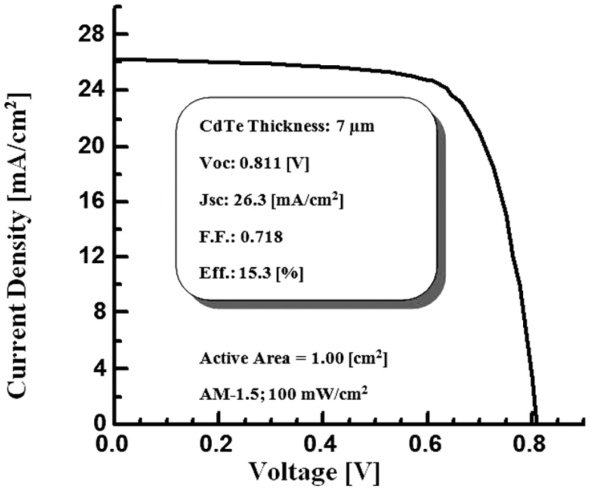

Figure 7. J-V characteristics of the CdTe thin film solar cell.

2.5. Thickness reduction in CdTe by low-temperature growth

The key concern is to obtain high-quality CdTe films regardless of the growth technique. Typically, the temperature corresponds to the source temperature of 625°C and substrate temperature of 595°C for high-efficiency cells, where 5-μm-thick CdTe is grown in this profile.

http://dx.doi.org/10.5772/66040

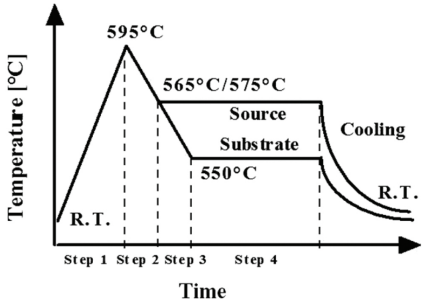

Figure 8. Temperature profile for low-temperature growth of CdTe.

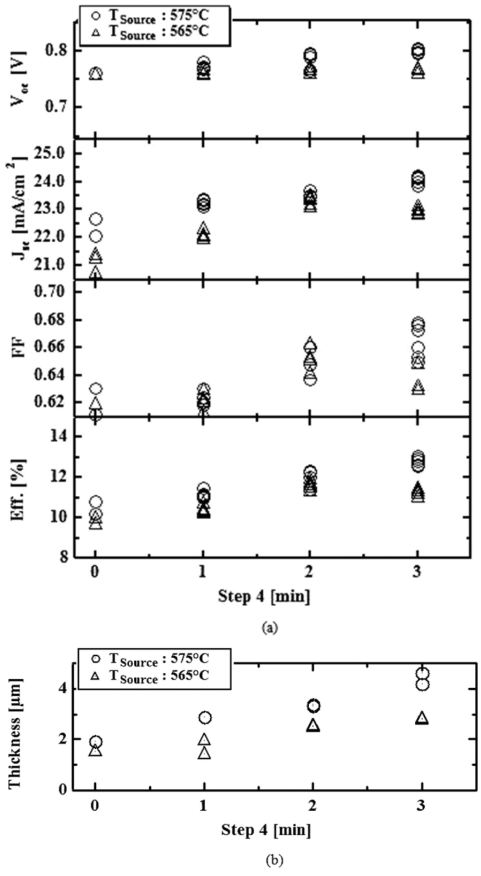

Figure 9. Effect of growth time on the (a) solar cell performance and (b) thickness of CdTe films, grown at low temperature.

Therefore, the temperature reduction in both the source and the substrate was carried out with the aim of obtaining a high-quality, as well as thinner, CdTe layer. No CdTe growth was observed until the source temperature of 530°C and substrate temperature of 500°C were maintained. In the profile shown in **Figure 8**, both the source and the substrate were first heated to a high temperature of 595°C for surface cleaning and then lowered to 575 or 565°C in the case of the source and 550°C in the case of the substrate. Controlling the time in step 4, thickness control (reduction) of the CdTe layer to 1.5 and 2 μm was achieved for source temperatures of 565 and 575°C, respectively.

Figure 9 illustrates the effect of growth time in step 4 on the thickness of the CdTe layer, as well as on the overall performance of solar cells. Thickness could be controlled down to 1.5 μm with a conversion efficiency of 10.4% (Voc: 0.76 V, Jsc: 22 mA/cm^2, F.F.: 0.62, area: 1 cm^2) at a source temperature of 565°C. Meanwhile, if the source temperature is increased to 575°C while keeping the substrate temperature unchanged at 550°C, the growth rate remarkably increases. However, the thickness can be controlled down to 2 μm with this profile, with an efficiency of 10.8% (Voc: 0.76 V, Jsc: 22.7 mA/cm^2, F.F.: 0.63, area: 1 cm^2). Therefore, a low-growth temperature demonstrates lower possibility of achieving thin CdTe films (1 μm) with high efficiency.

2.6. Control of CdTe thickness by reducing temperature difference

With the aim of achieving high-quality thin films and considering the results presented in previous section, the temperatures of the source and the substrate were increased to 600 and 595°C, respectively. The temperature profile is shown in **Figure 10**.

Moreover, the temperature difference between the two was set to 5°C to reduce the thickness. Thickness control down to 2 μm was possible with an efficiency of 11% (Voc: 0.77 V, Jsc: 23.7 mA/cm^2, F.F.: 0.60, area:1 cm^2). The overall performance deteriorated with the decrease in thickness but showed an improvement compared to the cells grown at lower temperatures as can be found in **Figure 11**. Regardless of the temperature profiles, all the cell performances were affected with the decrease in CdTe film thickness.

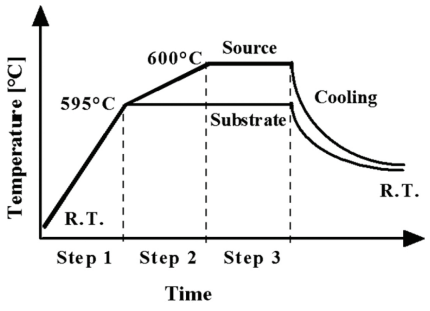

Figure 10. Temperature profile for CdTe growth in CSS with minimal temperature difference between source and substrate.

http://dx.doi.org/10.5772/66040

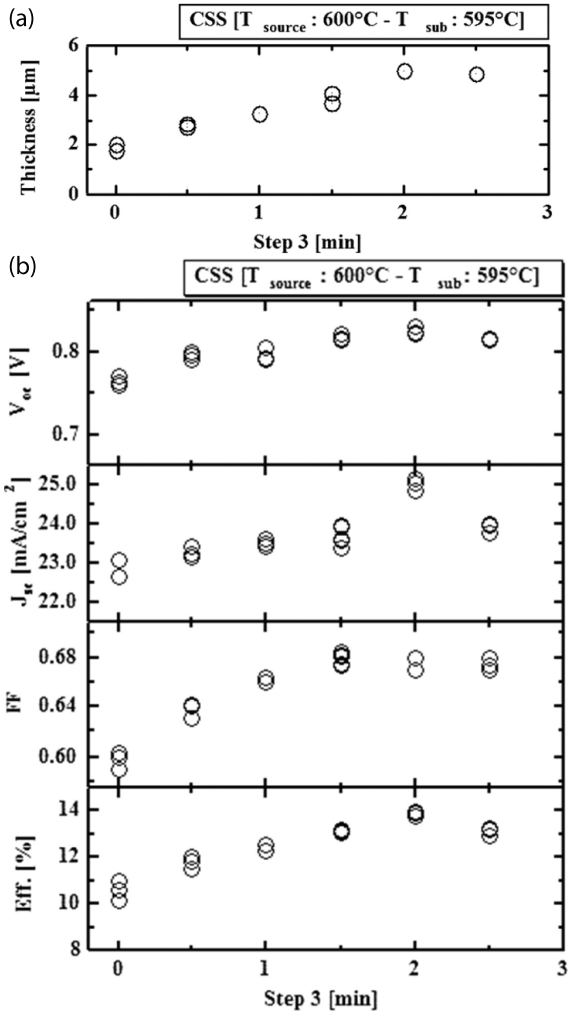

Figure 11. Characteristics of CdTe solar cells (a) and thickness of CdTe films (b), deposited using minimal temperature difference between source and substrate in CSS.

2.7. Growth of 1 μm-CdTe thin films by CSS

As described in earlier sections, several temperature profiles have been used during CSS growth of CdTe to determine the effect of temperature. It has become apparent that temperature plays a significant role in thickness control. Following the temperature profile shown in **Figure 12**, the temperatures of both the substrate and the source were raised together to several peak temperatures, and it was possible to grow thin CdTe layers with thickness from 0.5 to 1.5 μm for peak temperatures from 595 to 620°C.

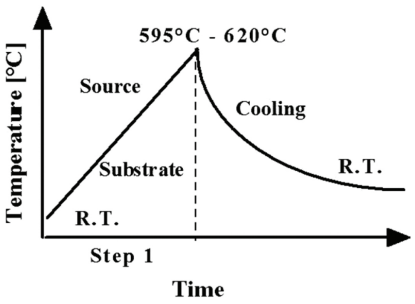

Figure 12. Temperature profile of 1-μm-thick CdTe thin film growth by CSS.

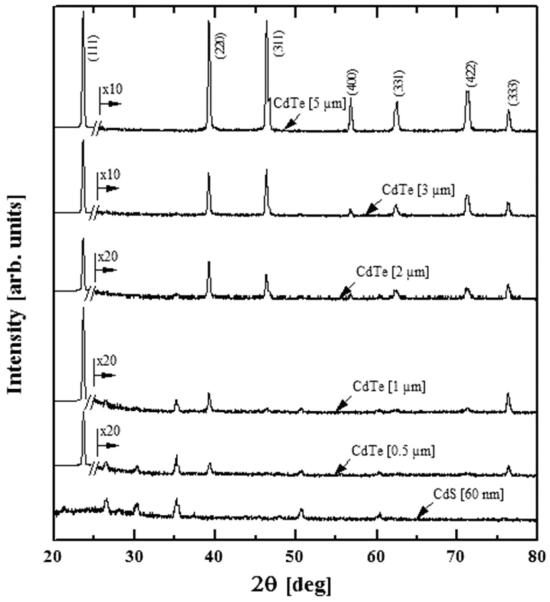

Figure 13. XRD patterns of CdTe films of different thicknesses.

To determine the performances of solar cells with various CdTe layer thicknesses, the I-V characteristics, spectral response, and reflectance were measured, and scanning electron microscope (SEM) and AFM images were taken to evaluate the quality of the films. From the XRD measurement, significant difference among the CdTe films from 5 to 1 μm thick can be observed, as shown in **Figure 13**. In the case of 1 μm films, some other peaks, probably from ITO or CdS, were found. Compared to thicker films, all the 1-μm-thick films showed strong preferential orientation in the (111) direction. SEM images of the 1-μm-thick CdTe surface shown in **Figure 14(a)** exhibit the larger grain size of the films. Differently shaped grains have been found in the case of thicker CdTe films.

http://dx.doi.org/10.5772/66040

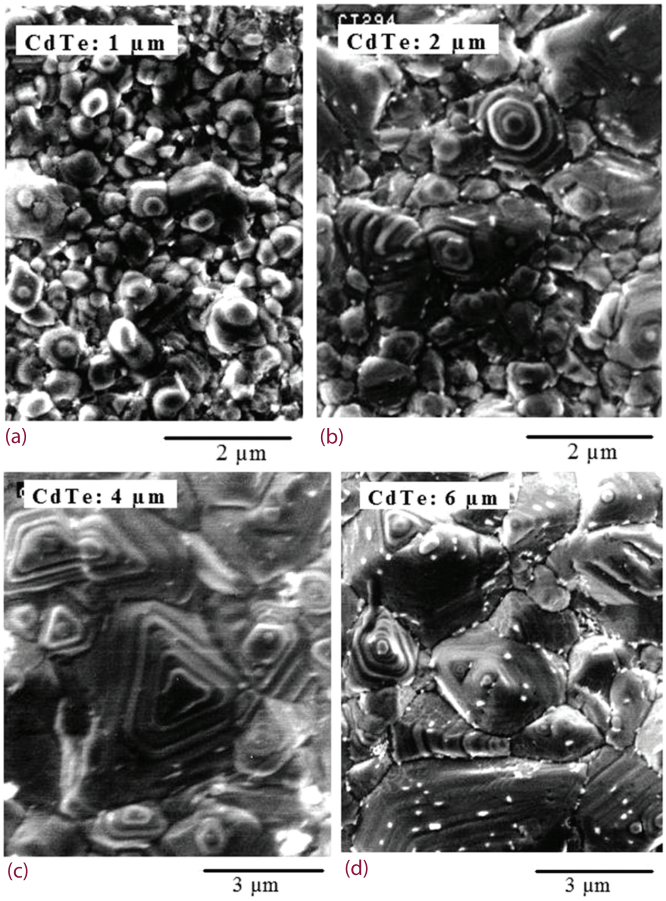

Figure 14. SEM micrographs of the surfaces of (a) 1 µm, (b) 2 µm, (c) 4 µm and (d) 6 µm-thick CdTe films [24].

Films deposited at substrate temperatures of 550–620°C exhibited preferential orientation along the (111) direction as indicated by X-ray diffraction studies. Scanning electron microscope (SEM) images also revealed the high quality of the deposited films of CdTe. The microstructure of CdTe films depends on the substrate temperature, source-substrate temperature gradient, and the crystallinity of the substrate. In general, the grain size increases with the increasing substrate temperature and film thickness.

An efficiency of 8.3% (Voc: 0.73 V, Jsc: 20.2 mA/cm^2, F.F.: 0.57, area: 1 cm^2) was achieved for cells with 0.5-µm-thick CdTe, whereas 9.9% (Voc: 0.75 V, Jsc: 22 mA/cm^2, F.F.: 0.6, area: 1 cm^2) and 11.4% (Voc: 0.77 V, Jsc: 23.7 mA/cm^2, F.F.: 0.63, area: 1 cm^2) were achieved for solar cells with 1- and 1.5-µm-thick CdTe, respectively. The most significant achievement of this effort was the establishment of the growth technique of such thin, high-quality CdTe films, along with reproducibility.

2.8. Overall optimization of CSS grown CdTe solar cells

To be used as a working device, optimization is needed. In order to form an ohmic contact to CdTe thin films, Cu-doped graphite carbon paste was screen-printed, and then, the resulting stacks were subjected to annealing in controlled atmospheres. One related study showed that Cu is distributed as effective acceptors in the CdTe layer, rendering it p-type after annealing. Despite having optimum data for 5-μm-thick CdTe layers, optimization of the annealing temperature was carried out. Significant improvement was found in comparatively low-temperature regions. An excellent improvement in efficiency to 11.2% (Voc: 0.77 V, Jsc: 23.1 mA/cm^2, F.F.: 0.63, area: 1 cm^2) was achieved at the annealing temperature of 345°C. The current-voltage (I-V) characteristic is shown in **Figure 15**. Copper, which is believed to have diffused into the CdTe layer from the carbon layer, functioned as an effective acceptor after annealing at the optimum temperature. Supported by the spectral response data where the cells treated at high temperature exhibit a significant shift near the CdTe absorption edge suggests a possible inter-diffusion of CdS into the CdTe and causes the bandgap of this material to decrease slightly. Since the junction is exposed to such high temperatures, excessive inter-diffusion (which forms CdS_xTe_{1-x}) is believed to occur, which leads to almost complete consumption of the 1-μm-thick CdTe layer grown during CSS. Therefore, it can be concluded that the uncontrolled formation of such CdS_xTe_{1-x} alloy in 1-μm-thick CdTe solar cells can adversely affect the cell performance, which is not possible to overcome by merely treating the stack of layers in any optimum conditions. Therefore, growth during CSS has to be carefully controlled by temperature profiles to achieve high-quality films in terms of grain size, defects, uniformity or homogeneity.

2.9. Conclusion

Close-spaced sublimation (CSS) is one of the most cost-efficient, high-throughput semiconductor coating techniques that offers industrial scalability as well. We developed our custom-

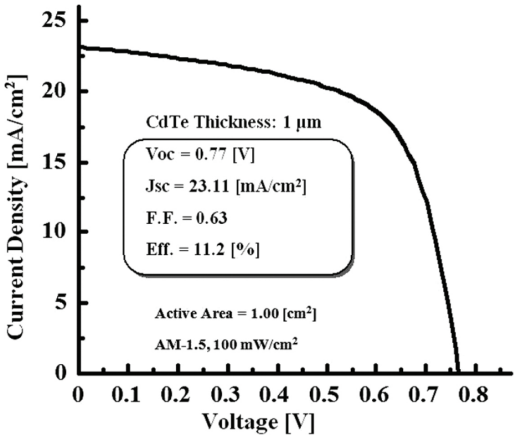

Figure 15. J-V characteristics of 1 -μm-thick CdTe solar cell (top record to date) [24].

http://dx.doi.org/10.5772/66040

ized close-spaced sublimation (CSS) apparatus and achieved growth of our material of interest, such as group II-VI compound semiconductor, that is, CdTe for solar cell application. By controlling the temperature profile in steps, thickness of the CdTe film is controlled over 7 to 1 μm without any pinholes in order to realize material conservation as well as to improve the performance through controlling the carrier recombination loss in relatively thicker CdTe absorption layers. The films are investigated by all possible means of thin film characterization like XRD, SEM, UV-Vis, and so on to find its optimized usage in thin film solar cell. The growth of 1-μm-thick CdTe films was achieved by controlling the temperature profile during CSS growth, with reproducibility. Gradual improvements were found in the glass/ITO/CdS/CdTe solar cells as conversion efficiencies of 15.3% for 7-μm-thick, 14.3% for 5-μm-thick, 11.4% for 1.5-μm-thick, and 9.9% for 1-μm-thick CdTe films grown by CSS. Moreover, after a rigorous optimization in post-deposition and back electrode formation annealing profiles, conversion efficiency of 11.2% in the case of 1-μm-thick CdTe was achieved, in air mass 1.5 without antireflection coating as the best value to date. All the results have shown successful deposition of CdTe by this customized close-spaced sublimation (CSS) technique and therefore verify its implication to similar kind of semiconductors for solar cells or other purposes.

Acknowledgements

The authors would like to acknowledge and appreciate the contribution of The National University of Malaysia (Universiti Kebangsaan Malaysia) through the research grants with code DIP-2015-021 and GUP-2016-042.

Author details

Nowshad Amin* and Kazi Sajedur Rahman

*Address all correspondence to: nowshad@ukm.edu.my

The National University of Malaysia, Universiti Kebangsaan Malaysia, Bangi, Selangor, Malaysia

References

[1] Romeo, N., Bosio, A., Romeo, A. An innovative process suitable to produce high-efficiency CdTe/CdS thin-film modules. Solar Energy Materials and Solar Cells. 2010; 94(1): 2–7.

[2] McCandless, B. E., Dobson, K. D. Processing options for CdTe thin film solar cells. Solar Energy. 2004; 77(6): 839–856.

[3] Ferekides, C. S., Marinskiy, D., Viswanathan, V., Tetali, B., Palekis, V., Selvaraj, P., Morel, D. L. High efficiency CSS CdTe solar cells. Thin Solid Films. 2000; 361: 520–526.

[4] Britt, J., Ferekides, C. Thin film CdS/CdTe solar cell with 15.8% efficiency. Applied Physics Letters. 1993; 62: 2851–2852.

[5] Ferekides C., Britt J., Ma Y., Killian L. High efficiency CdTe solar cells by close spaced sublimation. Proceedings of 23rd IEEE Photovoltaic Specialists Conference, New York, USA, 1993, p. 389–393.

[6] Chu, T. L., Chu, S. S. Recent progress in thin-film cadmium telluride solar cells. Progress in Photovoltaics: Research and Applications. 1993; 1(1): 31–42.

[7] Chu, T. L., Chu, S. S., Britt, J., Chen, G., Ferekides, C., Schultz, N., Wang, C., Wu, C. Q. High efficiency thin film cadmium telluride solar cells. Photovoltaic Advanced Research and Development Project. 1992; 268: 88–93.

[8] Anthony, T. C., Fahrenbruch, A. L., Peters, M. G., Bube, R. H. Electrical properties of CdTe films and junctions. Journal of Applied Physics. 1985; 57: 400–410.

[9] Chu, T. L., Chu, S. S., Ang, S. T. Electrical properties of CdS/CdTe heterojunctions. Journal of Applied Physics. 1988; 64(3): 1233–1237.

[10] Fahrenbruch, A. L., Bube, R. H. Fundamentals of Solar Cells (Academic, New York), 1983, p. 231–234.

[11] Chu, T., Chu, S., Ferekides, C., Britt, J., Wu, C. Thin-film junctions of cadmium telluride by metal organic chemical vapor deposition. Journal of Applied Physics. 1992; 71: 3870.

[12] Albright, S. P., Singh, V. P., Jordan, J. F. Junction characteristics of CdS-CdTe solar cells. Solar Cells. 1998; 24: 43–56.

[13] McCandless, B. E., Moulton, L. V., Birkmire, R. W. Recrystallization and sulfur diffusion in CdCl2 treated CdTe/CdS thin films. Progress in Photovoltaics: Research and Applications. 1997; 5(4): 249–260.

[14] Ringel, S. A., Smith, A. W., MacDougal, M. H., Rohatgi, A. The effects of CdCl2 on the electronic properties of molecular-beam epitaxially grown CdTe/CdS heterojunction solar cells. Journal of Applied Physics. 1991; 70(2): 881–889.

[15] Singh, V. P., Brafman, H., McClure, J. C. Characterization of thin film CdS/CdTe solar Cells. Solar Cells. 1991; 31: 23–38.

[16] Massalski, T. B., Okamoto, H., Subramanian, P. R., Kacprzak, L. Binary Alloy Phase Diagrams (2nd Edition). ASM International, Materials Park, Ohio, USA, 1990.

[17] Greenberg, J. H. P-T-X phase equilibrium and vapor pressure scanning of non-stoichiometry in CdTe. Journal of Crystal Growth. 1996; 161: 1–11.

[18] Greenberg, J. H., Guskov, V. N., Lazare, V. B. P-T-X phase diagram cadmium-tellurium. Materials Research Bulletin. 1992; 27: 997–1001.

http://dx.doi.org/10.5772/66040

[19] Guskov, V. N., Izotov, A. D. Thermodynamic principles of the synthesis of CdTe, ZnTe, and CdZnTe solid solutions. Inorganic Materials. 2008; 44: 1409–1433.

[20] De Largy, B., Finch, A., Gardner, P. J. Thermodynamic functions for the congruent sublimation of cadmium telluride. Journal of Crystal Growth. 1983; 61: 194–198.

[21] Alamri, S. N. The growth of CdTe thin film by close space sublimation system. Physica Status Solidi (A). 2003; 200: 352–360.

[22] Nagayoshi, H., Suzuki, K. Growth of thick CdTe films by close-space-sublimation technique. IEEE Nuclear Science Symposium Conference Record, Rome, Italy, 2004, vol. 1–7, p. 4411–4414.

[23] Anthony, T. C., Fahrenbruch, A. L., Bube, R. H. Growth of CdTe films by close-spaced vapor transport. Journal of Vacuum Science and Technology A. 1984; 2: 1296–1302.

[24] Amin, N., Isaka, T., Okamoto, T., Yamada, A., Konagai, M. Prospects of thickness reduction of the CdTe layer in highly efficient CdTe solar cells towards 1 μm. Japanese Journal of Applied Physics. 1999; 38: 4666–4672.

[25] Wu, X., Coutts, T. J., Mulligan, W. P. Properties of transparent conducting oxides formed from CdO and ZnO alloyed with SnO_2 and In_2O_3. Journal of Vacuum Science and Technology A. 1997; 15(3): 1057–1062.

Effects of $CdCl_2$ Treatment on Physical Properties of CdTe/CdS Thin Film Solar Cell

Nazar Abbas Shah, Zafran Rabeel,
Murrawat Abbas and Waqar Adil Syed

Additional information is available at the end of the chapter

http://dx.doi.org/10.5772/67191

Abstract

We report CdTe, CdS, and ITO thin films on glass substrates for solar cell fabrication by closed space sublimation and chemical bath deposition. CdTe and CdS thin films were sublimated to chemical treatment at 25°C in a saturated $CdCl_2$ solution (1.04 g/100 ml methanol) and heat treated at 400°C for 30 minutes. Indium tin oxide and tellurium films were analyzed by spectrophotometer and scanning electron microscopy. It has been observed that solar cell performance can be improved by depositing a $CdCl_2$ layer on the CdTe/CdS layers. The optical, structural, and morphological changes of CdTe and CdS surfaces on CdTe/CdS/ITO/glass solar cells due to $CdCl_2$ solution treatment followed by annealing for 400°C were studied. Optical analysis showed about 15% decrease in transmittance after $CdCl_2$ heat treatment in case of CdTe thin film, whereas CdS thin film demonstrated an increase of about 10–15% transmittance after $CdCl_2$ heat treatment. Similarly, a decrease in band gap values was found for both CdTe and CdS thin films after $CdCl_2$ heat treatment. XRD and SEM results of $CdCl_2$ heat-treated CdTe and CdS samples showed recrystallization, reorientation, and progressive increase in grain size. The grain sizes of CdTe and CdS samples demonstrated an increase of about 0.2 μm.

Keywords: $CdCl_2$, cadmium sulfide, cadmium telluride, heat treatment, morphological, optical, structural

1. Introduction

Considering the high absorption coefficient, near optimum band gap, and manufacturability of cadmium telluride (CdTe), it can quite easily be regarded as one of the most favorable photovoltaic materials realizable for use as high-efficiency and low-cost thin film solar cell. Typically, a

CdTe solar cell structure consists of Au/CdTe/CdS/ITO/glass. It has a direct band gap of 1.45 eV and only 1 μm CdTe can absorb more than 90% of the photons having energy greater than 1.45 eV that is why it is well suited for solar cell applications. CdTe is stable up to 500°C. CdTe has lattice constant of 0.68 nm at 300 K. The thermal conductivity of CdTe is 6.2 W m/m^2 K at 293 K. The specific heat capacity is about 210 J/kg K at 293 K. In solar cell fabrication CdTe is used as a p-type semiconductor which has a junction with cadmium sulfide (CdS) as an n-type semiconductor. Infrared detector material (HgCdTe) is manufactured when CdTe is alloyed with mercury. An important application of CdTe is as a radiation detector that is used to detect X-ray and alpha, beta, and gamma rays, and for this purpose, CdTe is doped with chlorine. CdTe has electron affinity of 4.3 eV. The work function is 5.5 eV for p-type CdTe. It can be doped both as p-type as well as n-type semiconductors [1–3].

A II-VI semiconductor compound cadmium sulfide (CdS) has much importance because of its many applications in several heterojunction photovoltaic thin film devices of CdTe, copper indium gallium diselenide ($Cu(In_xGa_{1-x})Se_2$), or copper indium gallium sulfide (CIGS) and solar cells. Many other devices in the fields of electronics, optics, and infrared are also fabricated by using CdS [1–3]. The CdS is a suitable n-type material, which can be fabricated by a variety of fabrication techniques like sol-gel technique [4], close spaced sublimation (CSS), chemical bath deposition (CBD), thermal evaporation, chemical vapor deposition, molecular beam epitaxy, and spray pyrolysis. Each and every deposition process provides different optical, structural, electrical, and morphological properties [5–10].

First solar cell has reported CdS deposited by high rate vapor transport deposition (HRVTD). CdS is called window layer due to its higher rate of light transmission [11–14]. CdS thin films are very suitable for so many other semiconductor devices and radiation detectors. CdS thin films with wide band gap are highly used for photovoltaic devices. Since CdS is used as window layer in solar cell, it should be fabricated very thin and high amount of light should pass through CdS and be absorbed in CdTe. The CdS thin film must be continuous to reduce the effect of short circuit in the cell. The CdS thin films deposited by CBD can fulfill these requirements. So the thickness of CdS has much importance for the high-efficiency of solar cell [15–17]. CdS (CBD) thin films are grown by cadmium chloride, ammonium nitrate, and potassium hydroxide. After heating to a specific temperature, thiourea is added to start the fabrication process [18–20].

CBD is a very easy process for the fabrication of CdS thin films on ITO glass. For the fabrication of thin film solar cell, one needs a very thin film up to 60–80 nm. It is a very suitable process especially for solar cell point of view. It is a process in which substrate is placed in a hot chemical solution stirring vigorously for a specific time, positive and negative ions will reach and meet on the substrate and thin film is grown. The advantage of this technique is that neither vacuum and nor very high temperature is required for CBD [5, 21].

CdS thin films fabricated by the CSS are also another moderate temperature fabrication technique in a vacuum chamber. More than 20% efficiency has been achieved by using CdTe/CdS heterojunction thin film solar cell by this technique. CSS is a moderate temperature procedure so it provides better results in some cases [22, 23]. The CSS technique is one of the techniques that have produced encouraging results [15] mainly because it is a

http://dx.doi.org/10.5772/67191

simple deposition apparatus and high transport efficiency and deposition can be done in low vacuum at moderate temperatures. There is minimum use of material in the CSS system as compared to other methods. As the substrate is close to the source materials in the CSS technique, roughness increases in the thin films and has high absorption, which makes it a suitable material for solar cell applications. The CSS has a disadvantage as one cannot introduce a thickness monitor.

The general working properties of solar cells can be best described by three parameters: short circuit current (I_{SC}), open circuit voltage (V_{OC}), and fill factor (FF). Postdeposition processing of polycrystalline CdTe/CdS heterojunction thin film solar cells with cadmium chloride ($CdCl_2$) heat treatment has been demonstrated to improve the short circuit current and open circuit voltage of CdTe/CdS thin film solar cell, by recrystallization, reorientation, and grain enhancement of films for photovoltaic operation [24–26]. Heat treatment with $CdCl_2$ has been known to be a key step in high quality CdTe/CdS solar cells preparation [27–31]. Irrespective of the method being used for deposition of CdTe and CdS layer, $CdCl_2$ treatment has become a customary and vital process in fabrication of high-efficiency CdTe/CdS-based photovoltaic devices. Three different methods of $CdCl_2$ treatment are widely known to be used; solution $CdCl_2$ treatment, evaporated $CdCl_2$ treatment, and vapor $CdCl_2$ treatment [12]. $CdCl_2$ treatment is basically known to activate a chemical reaction between CdTe and CdS, which is the driving force for the bulk and grain-boundary inter-diffusion of CdTe and CdS [13]. However, regardless of the $CdCl_2$ treatment method being used, the basic mechanism by which $CdCl_2$ effects CdTe and CdS can be expected as a similar process [12–15].

The optical, structural, and morphological properties of CdTe and CdS thin films are mainly subjective to the preparation route. Hence, a variety of methods have been applied for the synthesis of such materials, e.g., thermal evaporation [16], chemical pyrolysis deposition (CPD) [17], metal organic chemical-vapor deposition (MOCVD) [18–20], closed space sublimation (CSS) [21] and chemical bath deposition (CBD) [22–25]. CSS and CBD are known to produce optimal and encouraging results for CdTe/CdS based solar cells. Both the techniques have many advantages for production of photovoltaic devices under controlled conditions, such as exceptional uniformity and reproducibility of film thickness even for a large-scale module [26, 27].

There are different materials being used for the manufacturing of thin film solar cells. The silicon photovoltaic cells are covering more than 70% of the world market. Silicon solar cells containing amorphous, polycrystalline, crystalline, and now a days silicon thin film solar cells are being used. Thin film solar cells (TFSC) containing (II–VI) and (III–V) semiconductor materials have high efficiencies. These include copper indium gallium sulfide (CIGS), GaAs, Cu $(InGa)Se_2$, and CdTe/CdS. The selection of material depends upon the band gap, absorbing ability of material, and cost of fabrication process.

CdTe is very suitable for thin film solar cells because it has direct band gap at room temperature. In the world PV market, the CdTe based solar cells have attained 16.5% efficiency. It has very good match with CdS on ITO glass substrate. CdS is used as a window layer; it means more than 70% of light will pass through the first n-type layer of solar cells. Different techniques can be used for the manufacturing of thin film CdTe based solar cells [19–26].

It has some native defect cation vacancies (Vcd) that can behave as double accepters and anion vacancies (VTe) can behave as double donors. These vacancies can be formed with other extrinsic impurities [5, 6]. A problem of CdTe is that it is toxic if ingested and if its powder is inhaled. If properly processed, manufactured, and encapsulated, then it may be harmless. It is observed that elemental cadmium is more toxic than CdTe. It is also studied that CdTe quantum dots causes extensive reactive oxygen damage to cell membrane, mitochondria, and cell nucleus.

If it is to be used at large scale commercialization of solar panels then exposure and long term safety of CdTe will be serious issue. So attempts are being made to overcome all these issues. The BNL has given the research that CdTe large-scale PV modules have neither any health risks nor any threats for environment. These modules can be recycled. These modules do not produce any pollutants during their working for long term [7, 8]. Major issue for the CdTe PV modules is the availability of tellurium. Actually, tellurium is an extremely rare element (1–5) parts per billion in the earth's crust. Manufacturing of CdTe PV solar panels at large-commercial scale will cause depletion of tellurium [9].

In the present work, effects of $CdCl_2$ thermal treatment on physical properties of CdTe/CdS heterojunction solar cells, fabricated using CSS and CBD, have been investigated. Correspondingly, the results have demonstrated that performance of solar cell can be improved significantly after this treatment. In this regard, optical properties such as film thickness, refractive index, absorption, and optical band gap, crystallographic properties such as crystallite size and plane orientation, and morphological properties such as grain size, have been investigated using UV-VIS-IR spectrophotometer, X-ray diffraction (XRD) and scanning electron microscopy (SEM), respectively, at room temperature (25°C) [28–31].

2. Why thin films

Thin film technology is well known technology for physics and engineering applications. It is projected to be one of the major processing techniques to fabricate electronic, optical, and magnetic data storage devices, solar cells, light emitting diodes (LED), etc.

Thin film science and technology play a crucial role in the high-tech industries that will bear the main burden of future, while the major exploitation of thin films are in microelectronics, communications, optical electronics, coatings of all kinds, and energy generation. Thin films of various materials are currently in use as protective and optical coatings, electronics, antireflection films, polarizers, radiation detectors, and solar energy converters.

It is not only thickness that is defining a film but also the way of fabrication which is responsible for the uniformity, structure, and other properties of the film. The optical, structural, and electrical properties of thin film are different from the bulk materials; it is the reason these are being used. Characterization and fabrication of thin films is very easy. The structural, chemical and physical properties depend on the deposition parameters and thickness of the thin film. The electrical, optical, and mechanical behavior of thin film also depends on microstructure,

http://dx.doi.org/10.5772/67191

surface morphology, purity, and homogeneity. These things are strongly dependent on the fabrication methods and selected parameters and post depositions treatments also.

Stable, accurate, efficient, reliable low-cost electronic, insulating, sensors, and many other industrial devices with minimum use of material are possible due to thin film technology. Thin film devices are easy to manufacture, especially suitable for flexible solar cells.

Thin films are layers of ferromagnetic, semiconductor or ceramic materials. It ranges from fractions of a nanometer to several micrometers in thickness (usually 100 A-1 μm). It is a microscopically thin layer of material that is deposited onto a metal, ceramic, semiconductor or plastic base. Thin Films can be conductive or dielectric (non-conductive) and are used in myriad applications. Thin films have almost a two dimensional structure, so they give a better insight into the structural properties of the material. The earliest of what might be called latest thin film optics was discovered by Robert Boyle and Robert Hooke, independently of the phenomenon now known of older material even without any visible signs of tarnish, was too low. One possible explanation which he suggested was the formation on the surface of the thin layer from the underlying material.

Dennis Taylor, in 1891, published the first edition of his famous book on the adjustment and testing of telescopic objectives. In fact Taylor developed method of artificially producing the tarnish by chemical etching. Kollmorgen followed this work and developed the chemical process for different types of glass. In Nineteenth century at the same time a great deal of progress was made in the field of interferometry. The most significant development from thin film point of view was the Fabry-Perot inferometer described in 1899 which became one of the basic structures of thin film filters. Development became more rapid in the 1930s, an indeed it is in this period that we can recognize the beginning of the modern thin film optical coating. In 1932, Rouard observed that very thin metallic film reduced the internal reflectance of the glass plate, although the external reflectance was increased. In 1934, Bauer in the course of fundamental investigations of optical properties of halides produced reflection-reducing coatings and pfund evaporated zinc sulfide layers to make low loss beam splitters for Michelson interferometers. Noting incidentally that titanium dioxide could be a better material. In 1936, John Strong produced anti-reflection coatings by evaporation of fluorite to give inhomogeneous films which reduced the reflectance of glass to visible light to as much as 89% a most impressive figure. Then in 1939, Geffcken constructed the first thin film metal-dielectric interference filters. The most important factor in this sudden expansion of thin film coatings was the manufacturing process. Although sputtering was discovered by the middle of nineteenth century and vacuum evaporation in the beginning of twentieth century, these were not considered as useful manufacturing proccesses. The main difficulty was the lack of suitable pumps and it was not until the early 1930s that the works of CR Burch on diffusion pump oil made it possible for this process to be used satisfactorily. Since the tremendous trades have been made particularly in last few years, filters with greater than 100 layers are not uncommon and uses have been found for them in almost every branch of science and technology.

Much research has been done on the mechanism of thin film growth with evaporated films. It has been found by observation of films evaporated directly in the viewing field of an electron

microscope that film growth may be divided into certain stages. Pashley et al. distinguished four stages of growth process: nucleation and island structure, coalescence of islands, channel filling, and formation of continuous film. Nucleation is the initial stage of a film. The particles which have been evaporated from the evaporation source and have reached the substrate, on which a thin film is to deposit, generally lose part of their energy on impingement. Therefore, the mobility of the atoms or molecules on the surface decreases as the atoms give up their energy to the substrate. The effect of elevated substrate temperature is to permit the atoms to retain sufficient energy to make the movements necessary for the accommodation on the substrate and among them. Most of the flux arrives at the substrate in atomic form. These ad-atoms diffuse around the substrate and their diffusivities are dependent on the interaction between the ad-atoms (adsorbed atoms) and the substrate and the temperature of the substrate. Any defects or crystallographic variations on the substrate surface acts as a potential well and the atoms have to overcome this potential barrier to keep moving around. Occasionally, they succeed so well that they are re-evaporated. In diffusing randomly they come across other atoms and join them to form doublets, which have lower diffusivities. Beyond a critical nucleus size (on the order of 10–100 Å), the larger nuclei grow at the expense of the smaller ones, and so the number of nuclei on the substrate is continually decreasing during growth. The initial nucleation is enhanced by the presence of defects on the substrate. At this stage the individual crystallites (about 100 Å in diameter) are quite perfect structurally. As more flux arrives at the surface, the nuclei sizes grow and eventually islands are formed. During this stage of film growth some islands come into mutual contact and coalescence ensues. The coalescence phase is critical for the formation of grain boundaries and dislocations. As the larger nuclei (perhaps several thousand atoms in size) combine, the amount of disorder at the merging boundary depends on the orientation of each nucleus before contact. If the nuclei are aligned (as in epitaxial growth on a well-matched substrate lattice), either a twin boundary or none at all is formed. If the islands are not aligned before contact (as in growth on an amorphous substrate or growth at low temperature), a grain boundary is formed. As the nuclei become large, the energy of the aggregate becomes smaller so the larger nuclei have less ability to hold to each other as they combine.

It is believed that certain energy is liberated by coalescence, which is sufficient to affect a temporary melting of the crystallites in contact. After coalescence, the temperature drops and newborn island occurs again. It has been established that when two islands which are of different sizes and crystallographic orientation coalescence, the resultant crystallite assumes the orientation of larger one. As the islands grow, there is a decreasing tendency for them to become completely rounded after coalescence. Large shape changes still occur, but these are confined mainly to the regions in the immediate vicinity of junction of the islands. Consequently, the islands become elongated and join to form a continuous network structure in which the deposit material is separated by long, irregular, and narrow channels of width 50–200 Å. As deposition continues, secondary nucleation occurs in these channels, and the nuclei are incorporated into the bulk of the film as they grow and touch the sides of the channel. At the same time, channels are bridged at some points and fill in rapidly in liquid like manner. Eventually, most of the channels are eliminated and the film is continuous but contains many small irregular holes. Secondary nucleation takes place on substrate with in holes,

http://dx.doi.org/10.5772/67191

which are produced during channel filling stage. The hole contains many secondary nuclei which coalesce with each other to form secondary islands which then touch edge of hole and coalesce with the main film to leave a clean hole. Further, secondary nuclei then form, and the process is repeated until the hole finally fills. The liquid like behavior of the deposit persists until a complete film is obtained. These processes are substantially complete before appreciable growth in thickness occurs.

3. Deposition techniques for thin films

The process by which thin film is deposited onto a substrate or onto a previously deposited layer is called thin film deposition. The process will be followed according to the requirements and economic conditions. There are some major techniques used for thin film fabrication such as physical vapor deposition (PVD), closed space sublimation (CSS), chemical vapor deposition (CVD), chemical bath deposition (CBD), pulsed laser deposition (PLD), electro-deposition (ED), sputtering technique, and atomic layer epitaxy (ALE) [16–18]. So many techniques can be used for the CdTe. It is the versatility of the CdTe because it provides many ways for its deposition. The method of deposition should be economical, easily scalable, and easy to handle and can give good conversion efficiency of the device. The method should be easily applicable at large industrial level. The deposition technique will be preferred which have maximum conversion efficiency, low cost, and high deposition rate. Many techniques have efficiency up to 12% in laboratory but not at the industrial level. There should be such kind of deposition techniques that will give good conversion efficiency in laboratory as well as at industrial level [10].

3.1. Physical vapor deposition (PVD)

It is the process in which material is sublimated from solid or liquid source and condensed upon the substrate; mostly the whole process is done in a vacuum. The deposition rate for physical vapor deposition is approximately from 1 to 10 nm per second. This deposition technique is used for the deposition of alloys, elements, and compounds by the reactive deposition. In reactive deposition, a gas environment is used which has a reaction with the source material (depositing material) to form a compound, the gas environment may be a nitrogen gas or some other gas.

The physical vapor deposition can be categorized as:

(i) vacuum evaporation, (ii) sputter deposition, and (iii) molecular beam epitaxy.

Physical vapor deposition is a technique whereby physical processes, such as evaporation, sublimation or ionic impingement on a target, facilitate the transfer of atoms from a solid or molten source onto a substrate. Evaporation and sputtering are the two most widely used processes and PVD method is used for depositing films. Important factors in controlling the structure of a growing film are growth flux or deposition rate, substrate temperature, source temperature, and evaporation time.

The ratio of the substrate temperature to the melting temperature of the film material is an important factor in determining the structure of a polycrystalline film. These factors determine the degree to which ad-atoms are able to seek out minimum energy positions and grain boundaries are able to adopt morphologies of minimum energy. The driving force for grain growth is the reduction in the total grain boundary surface area and the attendant reduction in the total energy associated with grain boundary surfaces. Another mechanism for the development of structure in polycrystalline films involves recrystallization, the driving force for which is the minimization of energy associated with defects, such as pre-existing dislocations, in addition to grain boundary energy. Minimization of stored elastic energy arising from intrinsic and mismatch strains in the film can also serve as an additional factor contributing to grain growth and recrystallization.

The factors that control the very early stages of growth of a thin film on a substrate are described in atomistic terms. The process begins with a clean surface of the substrate material, which is at substrate temperature Ts, exposed to a vapor of a chemically compatible film material, which is at the vapor temperature TV.

To form a single crystal film, atoms of the film material in the vapor must arrive at the substrate surface, adhere to it, and settle into possible equilibrium positions before structural defects are left behind the growth front.

To form an amorphous film, on the other hand, atoms must be prevented from seeking stable equilibrium positions once they arrive at the growth surface. In either case, this must happen in more or less the same way over a very large area of the substrate surface for the structure to develop. At first sight, this outcome might seem unlikely, but such films are produced routinely.

Atoms in the vapor come into contact with the substrate surface where they form chemical bonds with atoms in the substrate. The temperature of the substrate must be low enough so that the vapor phase is supersaturated in some sense with respect to the substrate, an idea that will be made more concrete below. There is a reduction in energy due to formation of the bonds during attachment. Some fraction of the attached atoms, which are called ad-atoms, may return to the vapor by evaporation if their energies due to thermal fluctuations are sufficient to occasionally overcome the energy of attachment. High energy ad-atoms stick on the growth surface where they arrive, and the film tends to grow with an amorphous or very fine-grained polycrystalline structure. The growth surface invariably has some distribution of surface defects crystallographic steps, grain boundary traces, and dislocation line terminations, for example which provide sites of relatively easy attachment for ad-atoms. For semiconductor films, the epitaxial structure is essential to the electronic performance of the material. For metal films, on the other hand, the electrical conductivity of a polycrystalline film is nearly as large as that of a single crystal film.

In the vacuum evaporation process, source material is evaporated thermally inside the vacuum and its vapors are condensed at the substrate. The vacuum has a benefit of controlling the contaminations and reducing the melting temperature of the source material. Vacuum also increases the mean free path for the motion of deposited species. The vacuum required for deposition is from 10^{-5} to 10^{-10} Torr. Thermal evaporation is obtained by thermal heating

http://dx.doi.org/10.5772/67191

sources such as tungsten coils. The vacuum evaporation technique is used for fabrication of decorative coating, corrosion protective coatings, and electrically conducting films [13]. The sputter deposition is done by physical sputtering. It is the process in which material is not heated thermally so it is a non-vaporizing process. Material from target is ejected and then deposits onto a substrate. When energetic particles like ions are bombarded on the sputtering target, a plume of material is released and deposits onto a substrate just like a shower of sand when a golf ball lands in the bunker. The bombarding particles are usually gaseous ions accelerated from plasma. The sputtering gas is often an inert gas like argon gas. The spacing between source and substrate is less than vacuum deposition.

The plasma pressure for sputter deposition is from 5 to 30 mTorr. The sputtered particles are thermalized by gas phase collision before they reach substrate surface. The ions are generated from local plasma (diode or planar magnetron sputtering) or a separate ion beam source (ion beam deposition) [13, 14], as shown in **Figure 1**.

In molecular beam epitaxial (MBE) growth, the fabrication of crystalline thin film can be grown epitaxial above the other crystalline substrate with the beam of molecules or atoms.

This method required an ultra-high vacuum up to (10^{-8}) pa for the film deposition. The rate of deposition is very slow which is 1 μm/h. The materials are then evaporated and reach the substrate individually on the wafer and reaction takes place between these vapors. This method can give high-purity epitaxial layers of compound semiconductors. The word "beam" shows that sublimated atoms of the material do not interact with each other and with vacuum chamber until reach the wafer, due to long mean free path of atoms. The crystalline film is fabricated on the substrate of the same material which is called as homoepitaxy. So this epitaxy is done with only single material. Heteroepitaxy is performed with different materials. In heteroepitaxy, crystalline thin film is fabricated on the substrate of a different material. The disadvantage of this method is that it is very expensive. In MBE technique; vapor phase, liquid phase, and solid phase methods can be used [16].

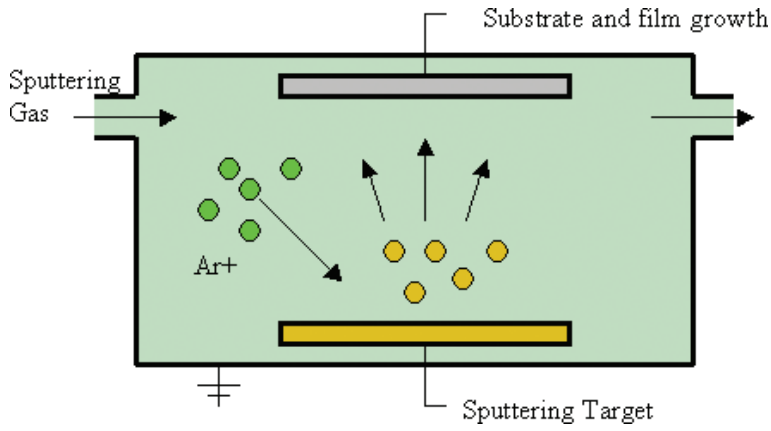

Figure 1. Sputtering apparatus.

3.2. Close spaced sublimation (CSS) technique for thin film deposition

Close space sublimation is a type of thermal evaporation technique. Advantage of CSS process is simplified deposition and high transport efficiency conducted under low vacuum conditions at moderate temperatures. In CSS technique, desired source material is placed in powder form in a graphite boat which is being heated by halogen lamps [5]. The substrate is placed in a mica sheet, which acts as a thermal gradient between the source and the substrate. The material starts to sublimate and deposit on substrate. The source is maintained at higher temperature than substrate. The deposited film presents a high crystallographic orientation and adequate opto-electrical properties for photovoltaic applications.

The CSS is a process for a thin film deposition of materials in a vacuum as shown in **Figure 2**. The material is sublimated by heating and its vapors condensed onto a substrate which is placed above the source material. The basic phenomenon of thin film deposition based on dissociation at high temperature.

Before the fabrication of thin film by close spaced sublimation, the substrate needs a proper cleaning by these methods like acetone, isopropyl alcohol, a rinse with distilled water, and ultrasonic cleaning.

The quality of thin films, material transport and deposition rate depends upon the fabrication parameters [17, 18].

It is observed that high substrate temperature of CdTe provides good performance of solar cell devices. Resistivity of CdTe decreases by increasing the substrate temperature and grain size reduces by increasing substrate temperature. Deposition rate also improved at high substrate

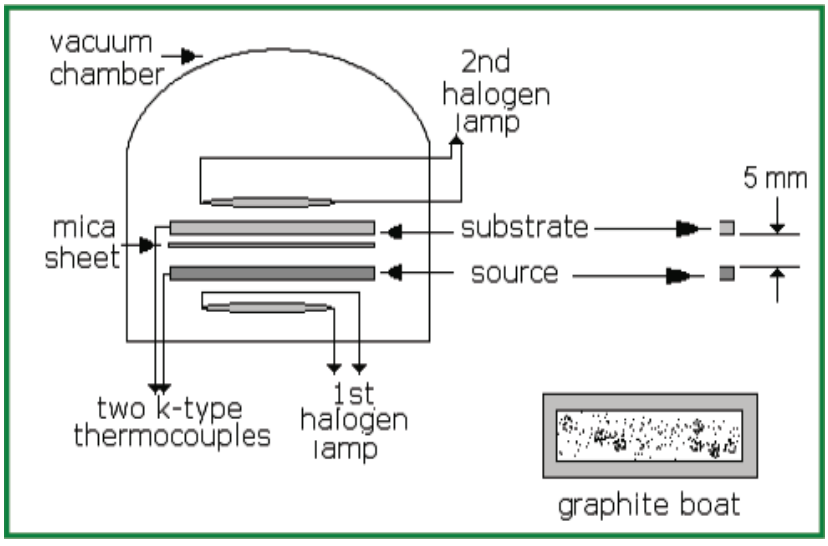

Figure 2. Schematic diagram of CSS designed at CIIT.

http://dx.doi.org/10.5772/67191

temperature [19]. The pacing between source and substrate is inversely proportional to the rate of deposition. Vacuum level for CdS and CdTe deposition is from 10^{-3} to $10^{-}5$ mbar.

Annealing of the films provides improvement of surface morphology and it reduces roughness of surface of CdS and CdTe films. Recombination centers reduce by annealing. The crystallinity of film also improves by the annealing process. Open circuit voltage also increased by increasing annealing temperature. Spectral response especially in the range of 500–600 nm is also improved by annealing temperature. Hence efficiency of solar cell can be improved [20–22].

The particles movement from higher concentration to lower concentration is called diffusion. The distance particles can travel without any collision is called mean free path. Diffusion of one kind of particles into other kind of material can change its characteristics like a semiconductor material can be converted into an n-type or a p-type. The advantages of CSS are as follows: (1) the evaporation source and substrate are heated directly by halogen lambs and their temperature is controlled using temperature controllers; (2) the source and substrate are separated by a mica sheet of about 1–3 mm. In this way, the source vapors are confined to closed space, leading to less wastage of evaporated material as compared to other methods. The mica sheet maintains the source and substrate at different temperatures, due to which the evaporating materials will always have better access to the substrate; (3) the films deposited by this method present a high crystallographic orientation and adequate opto-electrical properties for photo voltaic applications; (4) the system is very simple and easy to use; and (5) it has high transport efficiency conducted under low vacuum conditions at moderate temperature. There are also some limitations: (1) the main limitation of CSS deposition system is that there is no quartz crystal to monitor the growth rate and thickness of the film deposited; and (2) this method can only be used for limited number of materials, i.e., materials which can be sublimated at moderate temperatures.

Thermal evaporation method for preparing thin films is becoming very popular since 30 years or so. In this method the pressure of gas in chamber is reduced to value as low as possible, this is called creating vacuum. Generating vacuum properly is very important because when evaporation is performed in poor vacuum or close to the atmospheric pressure, the resulting deposition is generally non-uniform. The purity of deposited films also depends on the quality of vacuum and on the purity of source material. Vacuum is created by different pumps for example we have rotary vane pump and oil diffusion pump. In our vacuum coating unit, these pumps create different vacuum ranges, 10^{-3} to 10^{-6} mbar. In this vacuum chamber, source material is evaporated by heating at suitable temperature for particular time. In this method one must make sure that in order to deposit a material, the evaporation system must be able to sublimate it and also pressure of gas in chamber is low enough so that mean free path of the atoms of evaporated material is larger than source-substrate distance.

3.3. Chemical vapor deposition (CVD)

CVD is a chemical process used to produce high-purity and high-performance solid materials. The process is often used in the semiconductor industry to produce thin films. In a typical CVD process, the wafer (substrate) is exposed to one or more volatile precursors, which react and/or decompose on the substrate surface to produce the desired deposit. Frequently, volatile by-products are also produced, which are removed by gas flow through the reaction chamber.

Micro fabrication processes widely use CVD to deposit materials in various forms, including: nanocrystalline, polycrystalline, amorphous, and epitaxial. These materials include: silicon, carbon fiber, carbon nanofibers, filaments, carbon nanotubes, SiO_2, silicon-germanium, tungsten, silicon carbide, silicon nitride, silicon oxynitride, titanium nitride, and various high-k dielectrics. The CVD process is also used to produce synthetic diamonds. It is a chemical reaction which transforms gas molecules into the solid material and then into thin film or powder form, on the substrate surface. CVD is widely used to fabricate semiconductor devices.

Atomic layer epitaxy (ALE), or atomic layer chemical vapor deposition (ALCVD), now a days is known as atomic layer deposition (ALD) technique used for the production of high quality and thin solid films of specific crystal structures or orientations. This method provides very fine control of film thicknesses to one atomic layer. It has a wide range of applications in areas such as thin film ceramics, gas sensors, radiation detectors, optical/infrared filters, surface hardening, and fiber optical materials. The term *epitaxy* comes from the Greek roots *epi*, meaning "above", and *taxis*, meaning "in ordered manner". It can be translated "to arrange upon". It is a method that is based on sequential use of gas phase chemical process. Mostly in (ALE) two chemicals are used called precursors. Chemical reaction takes place between these precursors with surface one at a time in sequential manner. Using ALE alternating monolayers of two different elements can be deposited onto a substrate. In this technique material amount deposited in each cycle is constant. This method provides crystalline and uniform films especially if very thin film is required. In the laboratory of advanced energy systems, ALE used to grow both CdS and CdTe layers in a single process. ALE reactor with four individually controlled sources to control inside solid reactants, and has number of sources for external inert gas flow and liquid reactants. The spacing between two substrates is 1–3 mm.

The deposition of a substance on an electrode by the process of electrolyses is another CVD method. It is a technique in which electric current is passed through a chemical solution and ionization occurs then these ions deposit on the substrate.

Electrolytic deposition-cathodic film is also a versatile method of depositing film on an electrode (cathode) of the cell in which electrode is placed in a solution and the ions in that solution are impelled to the electrodes by an electric anodization was used as electrolyte in the middle of nineteenth century. A few years later, sulfuric acid bath was used in same process. This technique can be related to that of electrolytic deposition method. Same apparatus is used for both, but in this case, the thin film is formed at the anode or positive electrode rather than at cathode.

4. Fabrication of CdS thin film by chemical bath deposition (CBD) and (CSS) techniques

A II–VI semiconductor compound cadmium sulfide (CdS) has much importance because of its so many applications in several heterojunction photovoltaic thin film devices of CdTe, copper indium gallium diselenide ($Cu(In_xGa_{1-x})Se_2$), or copper Indium Gallium sulfide (CIGS), and solar cells. Many other devices in the fields of electronics, optics, and infrared are also fabricated by using CdS [1–3]. The CdS is a suitable n-type material, can be fabricated by a

http://dx.doi.org/10.5772/67191

variety of fabrication techniques like sol-gel technique [4], close spaced sublimation (CSS), chemical bath deposition (CBD), thermal evaporation, chemical vapor deposition, molecular beam epitaxy and spray pyrolysis. Each and every deposition process provides different optical, structural, electrical, and morphological properties [5–10].

First, solar cell has reported CdS deposited by high rate vapor transport deposition (HRVTD). CdS is called window layer due to its higher rate of light transmission [11–14]. CdS thin films are very suitable for so many other semiconductor devices and radiation detectors. CdS thin films with wide band gap are highly used for photovoltaic devices. Since CdS used as window layer in solar cell so it should be fabricated very thin, high amount of light should pass through CdS and absorb in CdTe. The CdS thin film must be continuous to reduce the effect of short circuit in the cell. The CdS thin films deposited by CBD can fulfill these requirements. So the thickness of CdS has much importance for the high efficiency of solar cell [15–17]. CdS (CBD) thin films are grown by cadmium chloride, ammonium nitrate, and potassium hydroxide. After heating to a specific temperature, thiourea is added to start the fabrication process [18–20]. CBD is very easy process for the fabrication of CdS thin films on ITO glass. For the fabrication of thin film solar cell, one needs a very thin film up to (60–80) nm. It is very suitable process especially from solar cell point of view. It is a process in which substrate is placed in a hot chemical solution stirring vigorously for specific time, positive and negative ions will reach and meet on the substrate and thin film is grown. The advantage of this technique is that neither vacuum and nor very high temperature is required for CBD [5, 21].

Thin films of CdS were deposited on microscope glass sides and ITO glass sides. Two fabrication procedures were used for CdS deposition for the first time in our lab. Firstly, CdS thin films were fabricated by CBD technique. For fabrication of thin film for solar cells, we need a very thin film up to (60–80) nm. In this process substrate was placed in a hot chemical solution stirring vigorously for 10–30 minutes with magnetic stirring at 3 Hz at 75°C by combining positive and negative ions on the substrate thin film was grown. The advantage was that neither vacuum nor very high temperature is required for CBD. The chemical solutions of (0.02 M) about 80 ml solution of cadmium chloride ($CdCl_2$), (1.5 M) about 80 ml solution of ammonium nitrate (NH_4NO_3), and (0.5 M) about 200 ml solution of potassium hydroxide (KOH) were made in a beaker. When temperature reached at 75°C, thiourea of (0.2 M) about 80 ml solution was added to start fabrication. The films were fabricated with magnetic stirring of 3 Hz for 10–30 min at 75°C as described in [5]. It is a process in which substrate is placed in a hot chemical solution stirring vigorously for specific time, positive and negative ions will reach and meet on the substrate and thin film is grown. The advantage of this technique is that neither vacuum and nor very high temperature is required for CBD [24]. Substrate was cleaned by using detergent then rinsed in distilled water then again clean with acetone and rinsed in distilled water then clean with isopropyl alcohol (IPA).

These three solutions are added to the beaker. The substrates are fixed inside the solution with the help of a substrate holder. The beaker is placed on the hot magnetic plate with magnetic stirrer inside. A pH meter and thermometer is also dipped in the solution to measure pH and temperature, respectively. Provide heat to solution up to temperature of 75°C. The solution is provided by stirring continuously throughout the experiment.

When temperature reached at 75°C add the thiourea about 0.2 M (80 ml).

As thiourea is added to the solution, the reaction starts suddenly. So thiourea is the last component which is added to the solution. The CdS deposition starts when thiourea is added. Use stop watch now and substrates will be taken out after the 10, 20, and 30 min, respectively.

Films are retired from the solution according to the specific deposition time and rinsed immediately with distilled water into an ultrasonic cleaner. The CdS deposited films with pale yellow color are obtained. The CdS film is deposited on both sides of the ITO glass. So film from glass side is cleaned by using 10% hydrochloric acid (HCl) solution. It needs much care when using HCl acid on glass side for cleaning because drops of HCl can remove film from ITO sides as well. After deposition, these CdS films will be annealed at 400°C for 30 min [25–27].

CdS thin films fabricated by the CSS are also another moderate temperature fabrication technique in a vacuum chamber. More than 20% efficiency has been achieved by using CdTe/CdS heterojunction thin film solar cell by this technique. CSS is moderate temperature procedure so it provides in some cases better results [22, 23]. The CSS technique is one of the techniques that have produces encouraging results [15] mainly because it is simple deposition apparatus and high transport efficiency and deposition can be done in low vacuum at moderate temperatures. There is minimum use of material in the CSS system as compared to other methods. As the substrate is close to the source materials in the CSS technique, roughness increases in the thin films and has high absorption, which makes it suitable material for solar cell applications. The CSS has a disadvantage that one cannot introduce thickness monitor.

CdS (CSS) fabrication was carried out in a vacuum chamber of approximately 4×10^{-1} mbar. The CdS sigma Aldrich powder 99.999% pure was used. Substrate temperature was maintained at 400°C and source temperature was in between (500–600)°C. Source material was heated by 1000 W halogen lamp and substrate was heated by a 500 W halogen lamp. Time of deposition was about (3–5) min as shown in **Figure 2**. The film was fabricated after collected after cooling. It is very easy process for the fabrication of CdS thin films on ITO glass. The disadvantage of closed spaced sublimation is that thickness cannot be controlled. For the fabrication of thin film solar cell we need a very thin film up to 60–80 nm, which is not easily possible by using close spaced sublimation process. It is very suitable process especially from solar cell point of view. CdS thin films were deposited on ITO glass substrate by CBD technique as shown in **Figure 3** using $CdCl_2$, ammonium nitrate (NH_4NO_3), potassium hydroxide (KOH), and thiourea as starting materials. ITO coated glass was used as available from sigma-Aldrich. Deposition was carried out with magnetic stirring at 3 Hz for 30 min at 75°C. The resulting CdS layer was annealed at 400°C for 30 min in a vacuum chamber at 4×10^{-2} mbar, and its thickness was found to be 800 nm. The CdTe layer was deposited on CdS by CSS technique under vacuum of 4×10^{-1} mbar. Deposition time was kept as 3–5 min. The substrate and source temperature were maintained at 400 and 530°C, respectively. A 500 W halogen lamp was used to heat the CdS/ITO/glass substrate, whereas a graphite boat was used to heat the source material with a 1000 W halogen lamp. The source and substrate spacing was measured as 4–5 mm. CdTe film thickness was measured as 5 μm. To enhance the p-type properties of CdTe, tellurium (Te) layer (400 nm) was deposited on CdTe by CSS technique under vacuum of 4×10^{-2} mbar. Deposition time was kept as 5 min, whereas, source and substrate temperatures were kept as 350 and 200°C, respectively. Resulting Te layer was annealed at 200°C for 1 h.

http://dx.doi.org/10.5772/67191

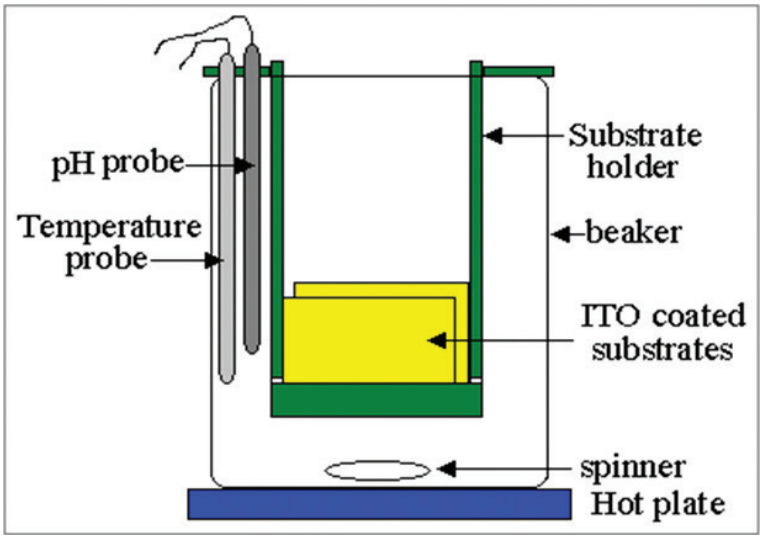

Figure 3. Chemical bath deposition apparatus.

1.04 g $CdCl_2$ was dissolved in 50 ml methanol at 65°C with constant magnetic stirring at 3 Hz for 10 min $CdCl_2$/methanol solution was then allowed to cool down at room temperature (25°C). The CdS/ITO/glass and the CdTe/CdS/ITO/glass structures were soaked in the $CdCl_2$ solution for 7 s. After drying at room temperature, the structures were annealed in a tube furnace for 30 min at 400°C with constant flow of argon gas (30 ml/min).

Transmission spectra, X-ray diffraction (XRD), and scanning electron microscope (SEM) with energy dispersive X-ray (EDX) investigations were carried out in order to understand the optical, crystallographic, and morphological effects of $CdCl_2$ treatment on CdTe and CdS films. Optical analysis using UV-VIS-NIR spectrophotometer was also used to study the thickness of films. Rutherford back scattering (RBS) analysis was used to identify the elemental composition of CdS thin films and further confirm their thickness. Rutherford back scattering spectrometry with an accuracy of 7% was used. High energy alpha particles were bombarded on the CdS film. Backscattered He^{2+} ion energy distribution and yield at a given angle were measured. Backscattered ions were detected by using a surface barrier detector with 17 keV resolution kept at a scattering angle of 160°. Since cross section of backscattering for each element is known, it is possible to get a quantitative compositional analysis from the RBS spectrum. Silver (Ag) paste was used for ohmic contact formation in the ITO/CdS/CdTe solar cells structure.

5. Comparative analysis of optical properties of thin films

(UV-VIS-IR) spectrophotometer was used to study optical properties of CdS (CBD) and CdS (CSS) thin films. The transmission for (CBD) films starts after 300 nm wavelength but in case of (CSS) transmission starts after 500 nm. So in CdS (CSS), blue portion of light was absorbed.

Transmission increased especially above 550 nm wavelength region. In the region of 600–800 nm the transmission was more than 70% for both (CBD) and (CSS), so light transmission through (CBD) films was higher than (CSS). Due to this high transmission characteristic which showed that CdS a good window layer for the thin film solar cells of many kinds, fabricated by both of the techniques. The Swanepoel model provided calculations about thickness and refractive index. Energy values were calculated by plotting a graph between energy and $(\alpha h\nu)^2$. Formula for refractive index (n) is given in Eqs. (1)–(3).

$$d = \frac{M \lambda_{max} \lambda_{min}}{4n(\lambda_{max} - \lambda_{min})} \tag{1}$$

where M is the number of oscillations between maximum and minimum transmission wavelengths λ_{max} and λ_{min}, respectively. The obtained thickness of CdTe films was 5 μm. n can be calculated using the relation:

$$n = \frac{[N + (N^2 - 4s^2)^{\frac{1}{2}}]}{2} \tag{2}$$

$$\text{Where, } N = 1 + s^2 + 4s\left(\frac{T_M - T_m}{T_M T_m}\right) \tag{3}$$

Here, the refractive index of glass, s = 1.52, T_{max} and T_{min} are the maximum and minimum transmissions, respectively. The values of d and n are calculated from Eqs. (1) and (2). The optical properties demonstrate a slight increase in absorption in IR region. Consequently, the transmittance is seen to slightly decrease after $CdCl_2$ heat-treatment. The band gap can be determined using the following relation:

$$\alpha h\nu = A(h\nu - E_g)^{N/2} \tag{4}$$

Here A is a constant, $h\nu$ is the photon energy, E_g is the optical energy band gap. N depends on the nature of the transition (N = 1 for direct band gap, while N = 4 for indirect band gap transition). $h\nu$ can be calculated by

$$h\nu(\text{eV}) = 1.24/\lambda(\mu\text{m}) \tag{5}$$

The band gap can be obtained by extrapolating $(\alpha h\nu)^2$ versus the incident photon energy ($h\nu$) plot. $CdCl_2$ heat-treatment results showed a slight decrease in band gap values as well. The band gap values extracted from these plots are 1.50 eV for as-deposited and 1.49 eV for $CdCl_2$ heat-treated sample.

5.1. Optical properties of CdTe by closed space sublimation (CSS)

The optical measurements using the spectrophotometer can provide the information about the transmittance, thickness, refractive index, absorption coefficient, and energy band gap. The as-deposited CdTe films have a high absorption in the visible and near-infrared regions, which did not change significantly after the CdCl treatment. The transmission in the as-deposited sample is about 80% at higher wavelength. The same is improved to above 85% in the heat-treated sample while the CdCl2 treated sample has about 80% transmission in higher wavelength region as shown in **Figure 4**.

The crystallographic orientation of CdTe samples was investigated by X-ray diffraction. The main reflections of the samples are the same and can be indexed according to fcc CdTe lattice.

http://dx.doi.org/10.5772/67191

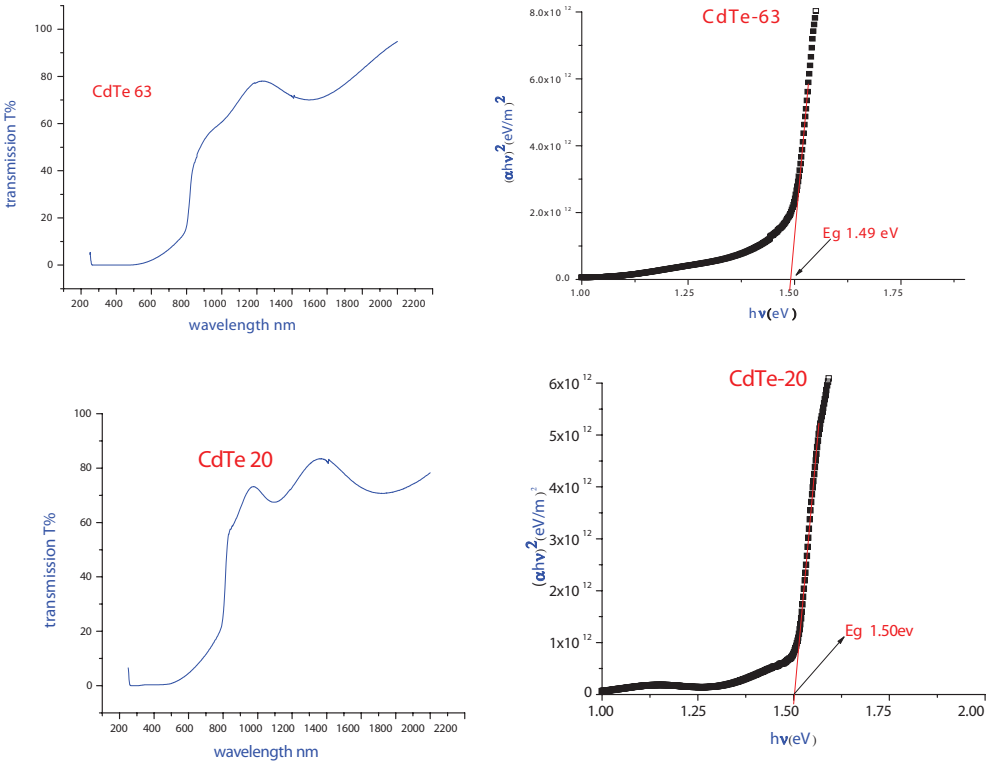

Figure 4. Transmittance vs. wavelength and energy band gap of CdTe samples.

The data analysis gave the lattice constant as 6.395 Å, which agreed with the reported value of 6.410 Å for the as-deposited and $CdCl_2$ lattice constant (ASTM Cards 15-0770, 75-2086). Two values of the lattice constant are attributed to the recrystallized lattice. The strongest (1 1 1) reflection in the as-deposited sample indicates that a preferential orientation of (1 1 1) matches well with the observation earlier reported. The loss in the texture of CdTe is exhibited in $CdCl_2$-treated sample. However, the intensity of the (1 1 1) peak is lower in $CdCl_2$-treated sample CdTe-63, implying that the samples are losing (1 1 1) texture and at the same time reorienting themselves in the (2 2 0) direction. The structure of CdTe is Cubic. The nature of deposited film is polycrystalline as shown in **Figure 5**.

5.2. Scan electron microscopy (SEM) of CdTe samples CdTe-20 and CdTe-63, CdTe-20 and CdTe-63

The morphology of the as-deposited heat-treated and $CdCl_2$ -treated samples CdTe-20 and CdTe-63 show the change in the shape and size of the CdTe grains as in **Figure 6**. The average grain size of the as-deposited sample is under 01.7 μm and 0.86 μm in the heat-treated sample respectively while some of the bigger grains divide into smaller grains and reorient themselves, which results into an entirely different microstructure. The SEM images support the XRD results.

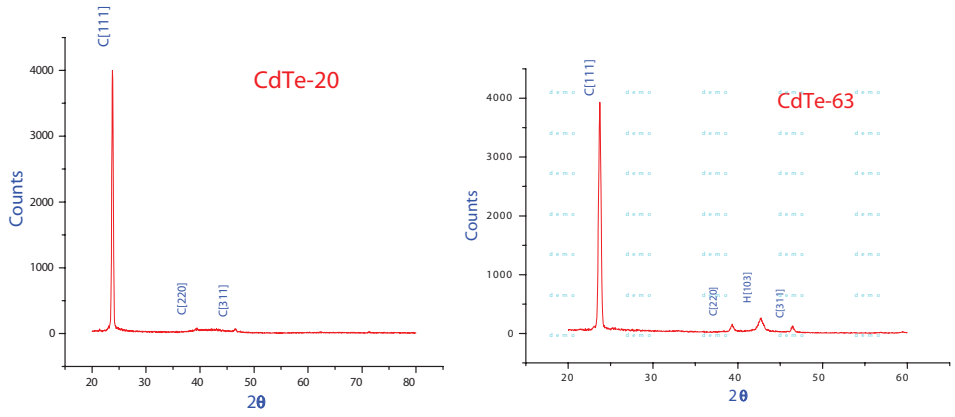

Figure 5. X-ray diffraction spectrum for CdTe samples.

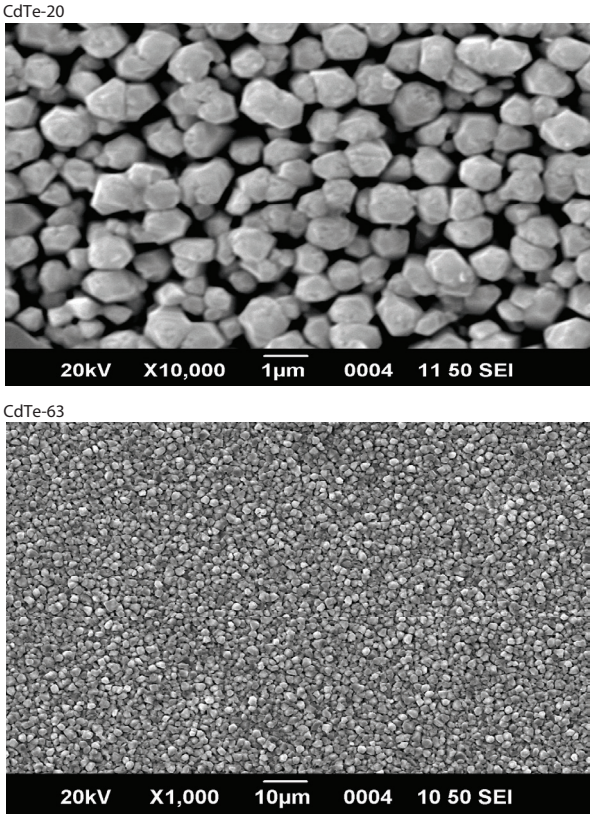

Figure 6. SEM micrographs of CdTe-20 and CdTe-63 samples.

http://dx.doi.org/10.5772/67191

5.3. Optical analysis of CdS thin film by chemical bath deposition

The CdS layer has good transmittance especially above 550 nm wavelength region as shown in **Figure 7**. Transmission starts after 300 nm by CBD process. In the region of 600–800 nm, the transmission is more than 70% in samples CdS 21 and CdS/CBD 23. This is the characteristic which shows that CdS is good window layer for the thin film solar cells of many kinds.

The band gap can be obtained by extrapolating $(\alpha h\nu)^2$ versus the incident photon energy $(h\nu)$ plot. CdS 23 and CdS 24 samples fabricated by chemical bath deposition results showed a slight decrease in band gap values as well. The band gap values extracted from these plots are 2.36 eV and 2.33 eV.

5.4. Structural analysis of CdS by chemical bath deposition (CBD)

Structural properties were studied by X-ray diffraction using CuKα radiations of 1.5418 Å. The data analysis provided lattice constant as 6.50 Å for as-deposited sample. The lattice parameter can be calculated by using the relation for only cubic structure.

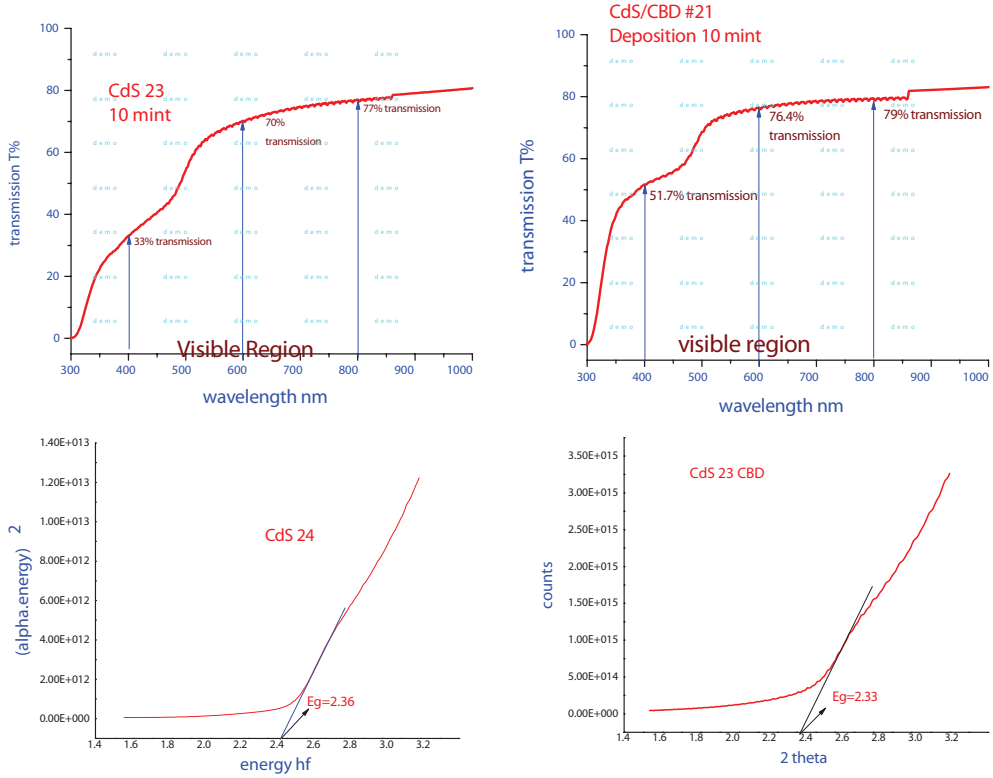

Figure 7. Transmittance vs. wavelength and energy band gap of CdS samples.

$$a = d\,(h^2 + k^{2+} l^2)^{1/2} \tag{6}$$

where h, k, and l are Miller indices, for hexagonal structure formula for "d" is

$$1/d^2 = 4/3\left((h^2 + hk + k^2) + \frac{l^2}{c^2}\right) \tag{7}$$

By using the Scherer formula, crystalline size can be calculated

$$\text{Crystalline size} = \frac{0.9\lambda}{\beta \cos\theta} \tag{8}$$

λ is X-rays wavelength, 0.9 is a constant shape factor, β is full width half maxima in radians, θ is Bragg's angle [25]. Peaks relating to CdS can be identified by using standard card JCPDS-00-041-1049. The d-spacing values were compared with standard values of ASTM cards to find the structure. It was observed in this experimental work that CdS thin films had a mixed structure of H (0 0 2) and C (1 1 1) for both techniques. So CdS has a polycrystalline behavior [20–22, 30–39]. Preferred orientation is (0 0 2) and structure is hexagonal as shown in **Figure 8**.

5.5. Optical analysis of CdS thin film by close sublimation technique (CSS)

The CdS deposited by close spaced sublimation have transmission for light above 550 nm then it again decreases for infrared region as shown in **Figure 9**. So if we consider only visible spectrum as for the solar cell point of view then it can be observed that from 600 to 800 nm, the transmission is more than 60% which shows that CdS is a good and efficient window layer for the visible spectrum or solar spectrum exclusively. The energy band gap is also showing the 2.44 and 2.38 eV for samples CdS 13 and CdS 318, respectively.

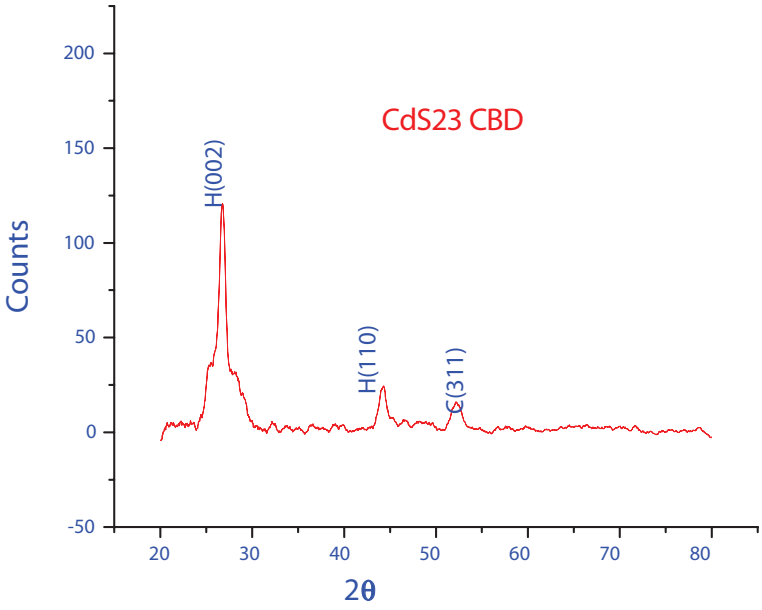

Figure 8. X-ray diffraction spectrum for CdTe samples.

http://dx.doi.org/10.5772/67191

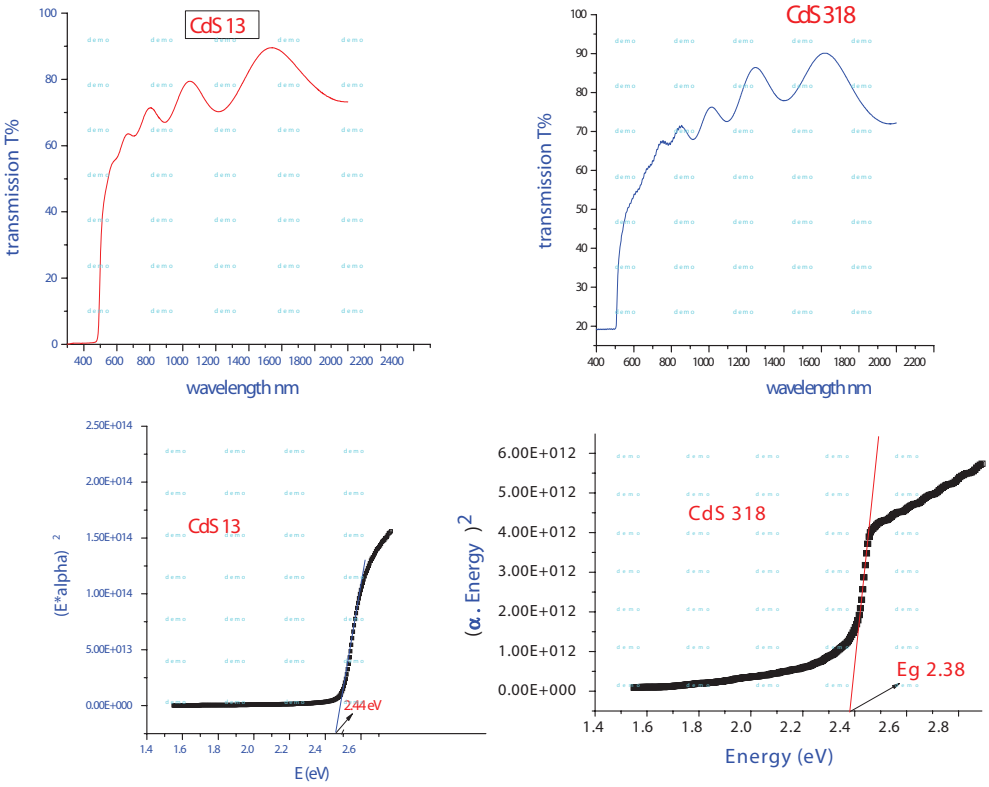

Figure 9. Transmittance vs. wavelength and energy band gap of CdS samples.

5.6. Structural analysis of CdS by close sublimation technique (CSS)

The XRD spectra were taken scanning the values of 2θ from 20 to 80° as shown in **Figure 10**. In CdS (CSS) high intensity planes were grown during the film growth due to high temperature. In CdS (CSS) strong peaks C (1 1 1), and H(0 0 2) were for two samples 317 and 318 as observed, which proved the polycrystalline behavior of CdS thin films. The height of peak/intensity for CdS (CBD) was only up to 200, 150, and 400, first strong peak was H (0 0 2) for two samples and C (1 1 1) for third sample at 2θ value of (26.49, 25.19, 26.74) degree of angle. In our research work for both CBD and CSS techniques, first hexagonal strong peak was dominant. The size of grains was different for different fabrication techniques this may be due to film thickness, temperature or different nucleation of CdS for different deposition methods.

5.7. SEM analysis of CdS (CBD) and CdS (CSS)

Surface morphology was studied by using scanning electron microscopy (SEM), and grain size for CdS (CSS) was measured to be 300–400 nm as shown in **Figure 11**.

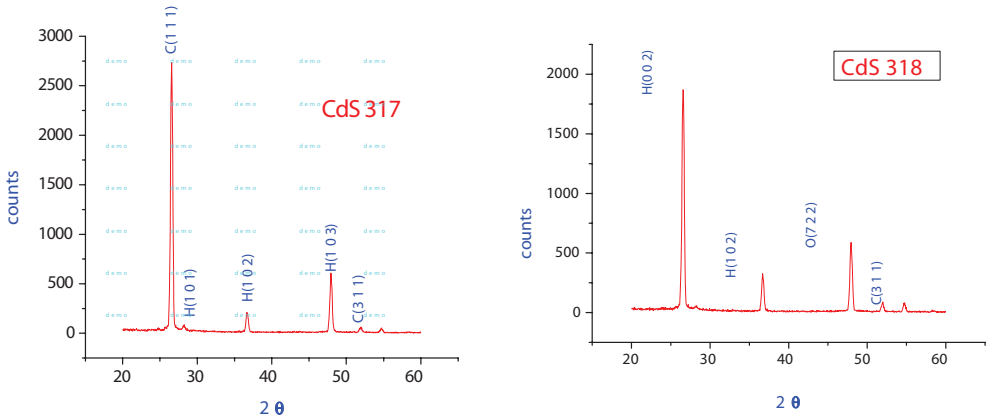

Figure 10. X-ray diffraction spectrum for CdS samples.

The surface of CBD films was slightly nonuniform but CdS (CSS) structure was fine with better crystallinity. SEM analysis showed that CBD-CdS thin films grain size approximately was found to be (50–100) nm and CSS-CdS films grain size was approximately (200–300) nm. It was also observed that at high source temperature, grain size was bigger in the CSS technique. It is reported in the literature that even less crystalline and non-uniform films of CBD process gave high-efficiency as compared to CSS [5, 40–42].

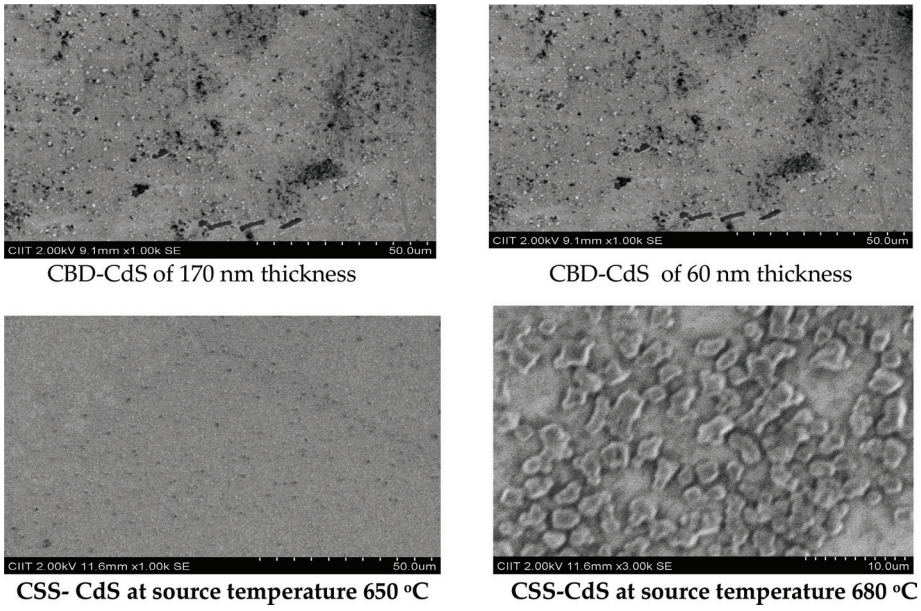

Figure 11. SEM micrographs of CBD-CdS and CSS-CdS samples.

http://dx.doi.org/10.5772/67191

The transmission spectra of ITO coated thin films and ITO/CdS films shows more than 90% light is passes in the visible as well as near infrared regions shown in **Figure 12**. Since a CdS thin film (100–200 nm) is used for solar cells, the CdS film is well suited as the TCS for CdTe solar cells.

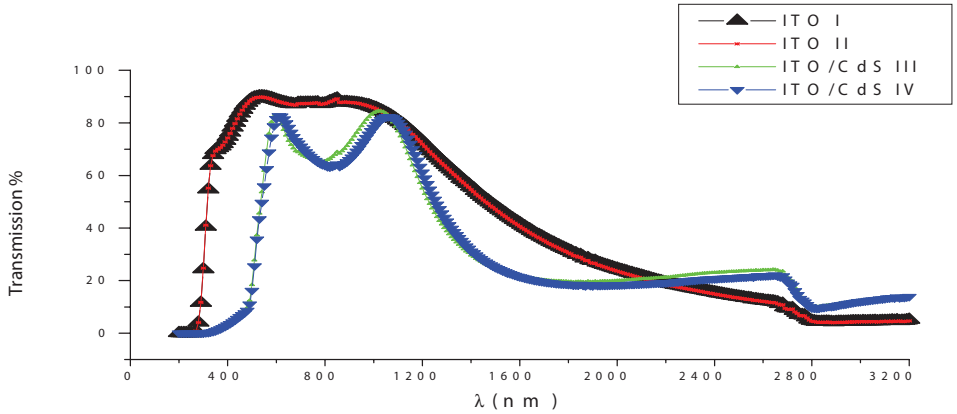

Figure 12. Transmission as a function of wavelength of ITO substrates and ITO/CdS thin films.

6. Conclusions

An ITO/CdTe/CdS/glass solar cell was successfully prepared using CSS and CBD techniques. Optical analysis of ITO demonstrated transmittance of over 85% for whole wavelength. The effects of $CdCl_2$ immersion and heating on the optical, structural, and morphological properties of CdTe and CdS surfaces were studied with an effort to promote recrystallization, reorientation, and progressive increase in grain size. Structural properties investigated by using XRD exhibited shift in 2θ diffraction angles of peaks, change in crystalline size, change in intensity of preferred orientation, and change in the total number of peaks, which indicates toward recrystallization and reorientation. The optical results after $CdCl_2$ heat-treatment showed a decrease in transmittance in the case of CdTe thin film and increase in the case of CdS thin film. Similarly, band gap values were also observed to decrease after the $CdCl_2$ heat-treatment. Surface morphology of CdTe thin films was affected by $CdCl_2$ heat-treatment as well. The SEM micrographs assisted in investigating the changes. A grain size of CdTe as-deposited sample was found to improve after the $CdCl_2$ heat-treatment. Similarly, a grain size of CdS as-deposited sample was found to improve after the $CdCl_2$ heat-treatment. In conclusion, the significant improvement to the CdTe/CdS films solar cell performance can be achieved when annealed at 400°C in the presence of $CdCl_2$ on the free surfaces of CdTe and CdS. These results can be used in turn to improve the short circuit current and open circuit voltage of solar cells.

Author details

Nazar Abbas Shah[1]*, Zafran Rabeel[2], Murrawat Abbas[3] and Waqar Adil Syed[4]

*Address all correspondence to: nabbasqureshi@yahoo.com

1 Thin Films Technology Research Laboratory, Department of Physics, COMSATS Institute of Information Technology, Islamabad, Pakistan

2 Higher Education Department, Punjab, Lahore, Pakistan

3 Federal Urdu University of Arts & Science, Islamabad, Pakistan

4 Islamic International University, Islamabad, Pakistan

References

[1] Werthen, JG, Anthony, TC, Fahrenbruch, AL, Bube, RH, 16th IEEE Photovoltaic Specialists Conference, p. 1138, 1982.

[2] Tyan, YS, Perez-Albuerne, EA, 16th IEEE Photovoltaic Specialists Conference, p. 794, 1982.

[3] Chakrabarti, R, Dutta, J, Maity, AB, Chaudhuri, S, Pal, AK, "Photoconductivity of CdTe Films." Thin Solid Films, 32, 288 (1996). doi:10.1016/S0040-6090(96)08801-3.

[4] Touskova, J, Kindl, D, Tousek, J, ''Preparation and Characterization of CdS/CdTe Thin Film Solar Cells.'' Thin Solid Films, 293, 272 (1997). doi:10.1016/S0040-6090(96)09113-4.

[5] Matsumoto, H, Kuribayashi, K, Komatsu, Y, Nakano, A, Uda, H, Ikegami, S, ''30 × 30 cm^2 CdS/CdTe Single Substrate Module Prepared by Screen Printing Method.'' Japan. Journal of Applied Physics, 22, 891 (1983). doi:10.1143/JJAP.22.891.

[6] Wu, X, Keane, JC, Dhere, RG, Dehart, C, Albin, DS, Duda, A, Gessert, TA, Asher, SD, Levi, H, Sheldon, P, "Seventeenth European Photovoltaic Solar Energy Conference." Proceedings from the International Conference, Vol. 1, p. 995. WIP Munich and ETA-Florence, 2001.

[7] Abbas Shah, N, Ali, A, Ali, Z, Maqsood, A, Aqili, AKS, ''Properties of Te-Rich Cadmium Telluride Thin FilmsFabricated by Closed Space Sublimation Technique.'' Journal of Crystal. Growth, 284, 477 (2005). doi:10.1016/j.jcrysgro. 08.005 2005.

[8] Nakayama, N, Matsumoto, H, Nakano, A, Ikegami, S, Uda, H, Yamashita, T, ''Ceramic Thin Film CdTe Solar Cell.'' Journal of Applied Physics, 19, 703 (1980). doi:10.1143/JJAP.19.703.

[9] Khan, MA, Shah, NA, Ali, A, Basharat, M, Hannan, MA, Maqsood, A, ''Fabrication and Characterization of Cd Enriched CdTe Thin Films by Close Spaced Sublimation.'' Journal of Coatings Technology and Research 6, 251–256 (2009).

[10] Menezes, CA, ''Low Resistivity CdTe-Te Films by a Combined Hot-Wall-Flash Evaporation Technique.'' ECS Journal of Solid-State Science and Technology, 127, 155 (1980).

[11] Huber, W, Lopez-Otero, A, ''The Electrical Properties of CdTe Films Grown by Hot Wall Epitaxy.'' Thin Solid Films, 58, 21 (1979). doi:10.1016/0040-6090(79)90201-3.

[12] Humenburger, J, Sitter, H, Huber, W, Sharma, NC, Lopez Otero, A, ''Hot-Wall Epitaxy of II–VI Compounds: Cadmium Sulfide and Cadmium Telluride.'' Thin Solid Films, 90, 101 (1982). doi:10.1016/0040-6090(82)90081-5.

[13] Cohen, ML, Chelikowsky, JR, ''Electronic Structure and Optical Properties of Semiconductor.'' In: Cardona, M, Fulde P, von Klitzing, K, Queisser, HJ (eds.) Springer book *Series in Solid State Science*, Vol. 75, p. 80. 1988.

[14] McCandless, BE, Dobson, KD, ``Processing Options for CdTe Thin Film Solar Cells''. Solar Energy, 77(6), 839 (2004).

[15] Cha, D,. Kim, S, Huang, NK, "Study on electrical properties of CdS films prepared by chemical pyrolysis deposition." Journal of Material Science and Engineering, B, 106, 63–68 (2004).

[16] Moutinho, HR, Al-Jasim, MM, Abufoltuh, FA, Levi, DH, Dippo, PC, Dhere, RG, Kazmerski, LL, "IEEE 26th Photovoltaic Specialists Conference, 1997 Treatment on the Morphology and Structural Properties of CdTe Thin Films Deposited by the CSS Method.'' Surface Review and Letters, 9, 1681 (2002). doi:10.1142/S0218625X02004219.

[17] Hiroshi, U, Hideo, Y, Yoshikazu, O, Manabu, K Hajimu, S, "Thin CdS Films prepared by metalorganic chemical vapor deposition." Solar Energy Materials and Solar Cells, 75 (1–2), 219-226 (2003).

[18] Abbas Shah, N, Ali, A, Maqsood, A, ''Preparation and Characterization of CdTe for Solar Cells, Detectors and Related Thin Film Materials.'' Journal of Electronic Materials, 37 (2), 145–151 (2008). doi:10.1007/s11664-007-0338-7.

[19] Swanepoel, R, ''Determination of the Thickness and Optical Constants of Amorphous Silicon.'' Journal of Physics E: Scientific Instruments,16, 1214–1222 (1983). doi:10.1088/0022-3735/16/12/023.

[20] Shah, NA, Ali, A, Aqili, AKS, Maqsood, A, ''Physical Properties of Ag Doped Cadmium Telluride Thin Films Fabricated by Closed Space Sublimation Technique.'' Journal of Crystal Growth, 290, 452–458 (2006). doi:10.1016/j.jcrysgro. 2006.01.051.

[21] Mendoza-Perez, R., Sastre-Hernandez, J, Puente, G, Vigil-Galan, O, "CdTe solar cell degradation studies with the use of CdS as the window material." Solar Energy Materials and Solar Cells, 93, 79 (2009).

[22] Mehmood, W, Abbas, NA, "Study of cadmium sulfide thin films as a window layers. In the Proceedings of the 2012 AIP Conference, 1476, 178 (2012).

[23] Ali, Z, Aqili, KSA, Maqsood, A, Akhtar, SMJ, "Properties of Cu-Doped Low Resistive ZnSe Flms Deposited by Two-Sourced Evaporation." Vacuum, 80, 302–309 (2005).

[24] Bonnet, D, "Manufacturing of CSS CdTe solar cells." Thin Solid Films, 361, 547 (2000).

[25] Birkmire, RW, "Recent progress and critical issues in thin film polycrystalline solar cells and modules." IEEE Photovoltaics: 26th Conference. Proceedings. pp. 295–300, 1997.

[26] Chopra, KL, "Thin Film Phenomena." 1969 (New York: McGraw-Hill).

[27] Laks, DB, Van de Walle, CG, Neumark, GF, Pantelides, ST, "Role of native defects in wide-band-gap semiconductors." Physical Review Letters, 66, 648–651 (1991).

[28] Chegaar, M, Ouennoughi, Z, Guechi, F, Langueur, H, ``Determination of Solar Cells Parameters under Illuminated Conditions'', Journal of Electronic Devices, 2, 17–21 (2003).

[29] Salinger, J, ``Measurement of Solar Cell Parameters with Dark Forward I-V Characteristics'', Journal of Acta Polytechnica, 46, 25-27 (2006).

[30] Green, MA, "Solar Cell Fill Factors: General Graph and Empirical Expressions", Journal of Solid-State Electronics, 24, 788–789 (1981).

[31] Shah, NA, Ali, A, Hussain, S, ``$CdCl_2$ Treated CdTe Thin Films Deposited by CSS Method'', Journal of Coatings Technology and Research, 7, 105–110 (2010).

[32] Shah, NA, Adil, WA, Atta, MA, ``Characterization of II–VI Semiconductor Thin Films Fabricated by Close Spaced Sublimation'', Nanoscience and Nanoletters, 1, 62–65 (2009).

[33] Shah, NA, Ali, A, Maqsood, A, Characterization of CdTe Thin Films Fabricated by Close Spaced Sublimation Technique and a Study of Cu Doping by Ion Exchange Process''. Journal of Non-Crystalline Solids Elsevier, 355, 1474 (2009).

[34] Kaydanov, VI, Ohno, TR, Studies of Basic Electronic Properties of CdTe-Based Solar Cells and Their Evolution during Processing and Stress, Final Technical Report 16 October 2001—31 August 2005 Colorado School of Mines Golden, Colorado.

[35] Fthenakis, VM, ``Life Cycle Impact Analysis of Cadmium in CdTe PV Production''. Elsevier Renewable & Sustainable Energy Reviews, 8, 303–334 (2004).

[36] Kumar, V, ``Characterization of Large Area Cadmium Telluride Films and Solar Cells Deposited on Moving Substrates by Close Spaced Sublimation'', MS thesis, University of south Florida, USA (2003).

[37] Ferekides, CS, "Thin Films and Solar Cells of Cadmium Telluride and Cadmium Zinc Telluride", Ph.D. Dissertation, University of South Florida, USA (1991).

[38] Khrypunova, G, Romeo, A, Kurdesauc, F, Bätzner, DL, Tiwarie, AN, ``Recent Developments in Evaporated CdTe Solar Cells'', Solar Energy Materials and Solar Cells, 90, 664–677 (2006).

[39] Alvin Compaan, D, Gupta, A, Lee, S, Wang, S, Drayton, J, ``High Efficiency, Magnetron Sputtered CdS/CdTe solar Cells, Solar Energy, 77, 815–822 (2004).

[40] Feuillet, M, Charleux, G, Mariette, M, Pub, H, ``Atomic Layer Epitaxy of CdTe and MnTe Hartmann'', Journal of Applied Physics,79, 3035 (1996).

http://dx.doi.org/10.5772/67191

[41] Dluzewski, P, ``TEM Characterization of MBE Grown CdTe/ZnTe Axial Nanowires'', Journal of Microscopy, 237, 337–340, (2010).

[42] Romeo, N, Bosio, A, Canevari, V, Podesta, A, ``Recent Progress on CdTe/CdS Thin Film Solar Cells'', Solar Energy, 77, 665–994 (2004).

Chapter 20

Silver-Based Low-Emissivity Coating Technology for Energy-Saving Window Applications

Guowen Ding and César Clavero

Additional information is available at the end of the chapter

http://dx.doi.org/10.5772/67085

Abstract

Low-emissivity (low-E) technology is a unique and cost-effective solution to save energy in buildings for different climates. Its development combines advances in materials science, vacuum deposition, and optical design. In this chapter, we will review the fundamentals of energy saving window coatings, the history of its application, and the materials used. The current low-E coating technologies are overviewed, especially silver-based low-E technologies, which comprise more than 90% of the overall low-E market today. Further, the advanced understanding of generating high-quality silver thin films is discussed, which is at the heart of silver-based low-E product technology development. How the silver thin film electrical, optical, and emissivity properties are influenced by their microstructure, thickness, and by the materials on neighboring layers will be discussed from a theoretical and an experimental perspective.

Keywords: low-E, emissivity, silver, coating, glass, window, optical, materials

1. Introduction to low-E applications

The growing awareness of global warming has intensified efforts to make buildings and vehicles more energy efficient. "Building heating, ventilation, and air conditioning (HVAC) accounted for 14% of primary energy consumption in the United States in 2013" [1]. Windows are often considered the least energy-efficient component in a building. Efficiency upgrades that improve the energy efficiency of windows are among the most promising and cost-effective energy technology options available now. A National Academy of Sciences study concluded that, "by an order of magnitude, the largest apparent benefits [of the technologies examined] were realized as avoided energy costs in the buildings sector in energy efficiency"[2].

Modern coating technologies provide architectural window coatings with adequate illumination levels in building interiors, while controlling energy transfer to save either cooling or heating energy. In 2003, 95% typical new windows in U.S. were double-glazed windows, and 50% have a low-E coating [3].Thus, energy saving windows are very popular in developed countries.

1.1. Why low-E coating windows are needed

Typical commercial buildings waste 30% of the energy they consume, mostly by heat and cooling loss through the building envelope (windows, doors, roofs, etc.) [4]. Losses through windows alone are estimated to cost U.S. consumers roughly $40 billion each year [2]. Radiation losses occur through the window glass and represent about 60% of the total heat loss in a standard window [4]. How can the heat transfer through windows be effectively controlled? One cost-effective solution today is through low-emissivity (low-E) coatings.

1.2. What is low-emissivity coating?

To understand low-emissivity coatings, let us first define emissivity. Emissivity is the ratio of heat emitted from a given material compared to that from a blackbody, from zero to one. A blackbody would have an emissivity of 100% and a perfect reflector would have zero value. The emissivity of the surface of a material is its effectiveness in emitting energy as thermal radiation. The typical common materials emissivity is listed below in **Table 1**.

When the emissivity of a window coating is low, the window coating is called low-E coating. The standard varies for different countries. Pyrolytic low-E coating for single-pane glass normally can achieve around 20% emissivity, while silver-based sputter coatings can achieve 8–2% emissivity, which represents currently 90% of the low-E market. These two types of low-E coatings will be discussed in more detail in the later sections.

Materials surface**	Thermal emissivity
Aluminum foil	0.03
Asphalt	0.88
Brick	0.9
Concrete, rough	0.91
Glass, smooth (uncoated)	0.91
Limestone	0.92
Marble, Polished or white	0.89–0.92
Marble, Smooth	0.56
Paper, roofing or white	0.88–0.86
Plaster, rough	0.89
Silver, polished	0.02

Table 1. Emissivity of common materials [39].

http://dx.doi.org/10.5772/67085

1.3. How can low-E coating windows save energy?

Let us first review a few common terminologies in the low-E field according to Ref. [5]:

Insulating glass unit (IGU) commonly consists of double or triple panes of glass separated by a vacuum or gas-filled space and sealed together at the edge to reduce the heat transfer of the buildings. The common insulating filled gas are air, argon, or krypton. There are four surfaces for double-paned IGUs, commonly labeled as surface 1–4 from exterior to interior, as shown in **Figure 1** [5].

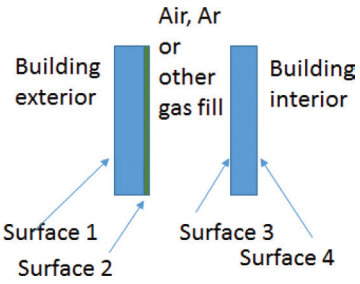

Figure 1. The structure of IGU.

Visible light transmittance (Tvis) is the transmitted percentage of visible light (380–780 nm) through glass, (or insulating glass unit, IGU).

Solar heat gain coefficient (SHGC) is the percentage of the solar energy passing through the window over the incident solar energy (including direct solar transmittance and indirect reradiation).

U-factor is a measure of air-to-air heat transmission (loss or gain) in indoor and outdoor temperatures of a 1-m high glazing due to the thermal conductance and the difference. It is an overall coefficient of heat transfer, the lower the U-factor, the better the insulating properties of the windows.

Second, let us explain how low-E coating could save energy, which is discussed in two climate conditions:

a. In cold climates, there are three functions desired for windows: (1) prevent heat loss (which requires blocking IR spectra), (2) inspire good human feelings, which requires transparency to visible light with friendly colors, and (3) let as much solar heat as possible into the room, which requires transparency to whole solar spectrum up to 2500 nm.

b. In hot climates, the third item is the opposite. We wish to block solar heat (SHGC) as much as possible, which usually contradicts the high-visible transmittance requirement of the item (2). Thus, the ratio of visible-light transmittance to the SHGC ratio

concept is needed, and it is called LSG (light-to-solar gain ratio). We desire LSG to be as high as possible and current highest LSG window product in the market is around 2.4.

In the spectra level, the ideal low-E coating spectra for cold and hot climates were illustrated from reference [6] as in **Figure 2**.

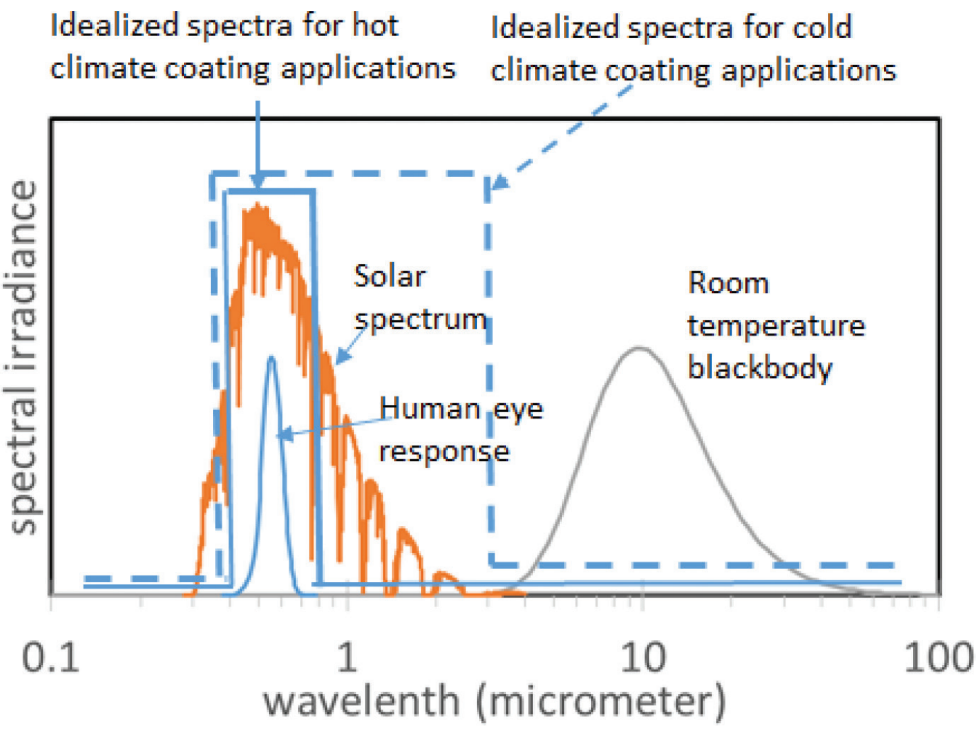

Figure 2. The idealized low-E coating spectra for hot or cold climates.

1.4. Examples of low-E windows in saving energy cost

The energy savings by installing low-E window are solid. Guardian Industries demonstrated two examples at the 2012 AIA National Convention and Design Exposition [7]: Two similar buildings were located in Chicago and Miami, respectively. The floor area of the six stories buildings were 120,000 square feet for both, with floor-to-floor height of 12 feet; slab on grade foundation, strip-type windows, window area 20,000 square feet, R-13 wall insulation, natural gas for heat, and electric power A/C. Several Guardian window products were installed as listed below (the IGU configuration were 6 mm glass/12 mm space/6 mm glass, and coating was at #2 surface) (**Table 2**).

http://dx.doi.org/10.5772/67085

Glazing	Type	%Tvis	SHGC	U-value
Clear glass	Mono	89%	81.8%	1.1
No coating	I.G.U	80%	71.3%	0.48
SN 68	I.G.U	68%	37.4%	0.29
Nu 50	I.G.U	50%	39.2%	0.34
AC 43	I.G.U	43%	29.6%	0.31
NU 40	I.G.U	40%	31.3%	0.33
silver 20	I.G.U	18%	20.0%	0.41

Table 2. Several typical glass product and their basic parameters [7] .

The annual cost for cooling and heating was calculated in comparison to clear glass (without low-E coating) as shown below. The savings purely from heating and cooling could be $8000 annually in the Chicago building, and double in the Miami building, as shown in **Figure 3**. The reason for the reduction of heating and cooling cost is not only due to the low-E window preventing the heat transfer to make the room warm at night and cool at day time, but also due to a significant reduction of the solar IR heat through the windows.

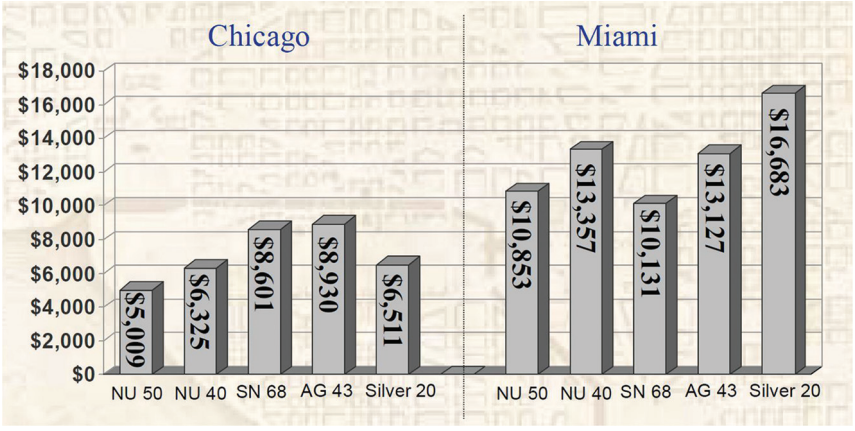

Figure 3. Comparison of annual heating and cooling saving cost for a building in Chicago and Miami [7].

In addition, the cooling and heating system capacity could be reduced too, so that one-time savings from reduction in HVAC system cooling capacity was calculated in comparison to a noncoating unit, as shown in **Figure 4**. That cost reduction could be $30,000 for the buildings.

Considering a 10-year period, the cost saving is very attractive: $100,000 in Chicago, and double that amount in Miami ($200,000). The exact number with different low-E product is showed in **Figure 5**, in comparison with clear glass windows (without low-E coatings).

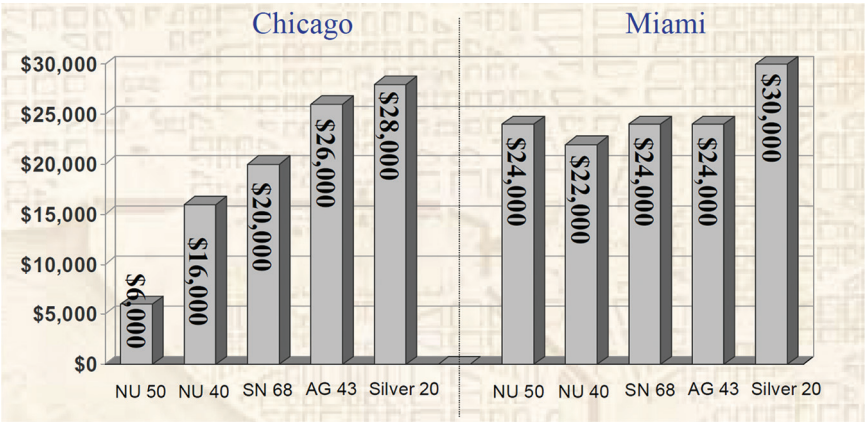

Figure 4. One-time savings from reduction in HVAC system cooling capacity (compared to a noncoating unit) [7].

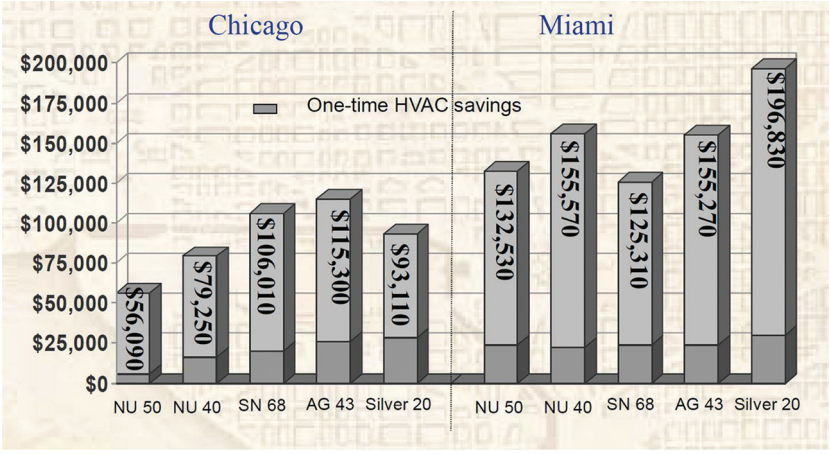

Figure 5. Ten-year savings including heating/cooling cost saving and one-time saving from reduction in HVAC system cooling capacity (compared to a noncoating unit) [7].

2. Low-E coating technology

2.1. Brief history of low-E coating technology

Low-E coating technology's roots can be traced back more than 100 years ago, from Drude, Hagen, and Rubens's theories. The first glass coating that was able to selectively reflect radiation can be traced back to 1958, when Holland and Siddall [8] demonstrated a gold coating on glass with high-transmittance and high-heat reflections. In the 1960s, a product called "Stop Ray" was first released in the market for solar control glass to reduce the cooling cost of the

http://dx.doi.org/10.5772/67085

building. Later, a product called "Infrastop" was also introduced to the market. In the 1970s and 1980s, another type of low-E glass appeared, called "K-Glass," which demonstrated high environmental and chemical durability, and also reduced the solar IR heat transfer. In the 1980s, the silver coating breakthrough was demonstrated, with higher transmittance, much lower emissivity, and friendly color. Quickly, silver coating low-E became the dominant low-E product in the market. Today, silver coatings can be further developed with multiple silver blocks, known as double silver and triple silver products. A brief history of low-E is covered in **Table 3** [9, 10].

2.2. What materials can be used for low-E window coating

Around the 1900s, the German physicist Paul Drude explained the optical behavior of free electrons in a solid based on the kinetic theory of free electrons in a metal. This theory is still widely used in literature today. In the early twentieth century, physicists Hagen and Rubens found that the heat emission from bulk metals described by their emissivity, ε, correlates strongly with their conductivity, σ, i.e., with the concentration of free electrons [11]. Based on the Drude model, they derived a formula to connect conductivity σ and emissivity:

$$\varepsilon = \sqrt{\frac{8\,\varepsilon_0\,\omega}{\sigma}} \tag{1}$$

Thus, the higher the conductivity, the lower the emissivity. In the low-E industry, there are a few practical estimations on the relationship of emissivity and sheet resistivity, such as $\varepsilon = 0.0106\,R_{\square}$, where $R_{\square}$ is the film sheet resistivity [11]. This is the reason why film-sheet resistivity is a very important parameter in qualifying low-E products, and it is easily measured by a four-point probe. In addition, Ref. [12] found a way to estimate the optical properties of silver (refractive index) at near IR by resistivity measurements [12].

There are two types transparent low-E coatings in today's market: (1) semiconductive coatings, e.g., ITO (indium tin oxide) and FTO (fluorine-doped tin oxide) and (2) metallic coating. Some common low-E materials are listed in **Table 4** for comparison.

2.3. Major industry Low-E window coating technologies

Although there are many thin film coating methods available for glass coatings, such as sol-gel, PECVD, ALD, and E-beam evaporation, there are only two major low-E window coating technologies in today's market: sputtered coating and pyrolytic coating, which provide cost-effective, high durablility, excellent uniformity on jumbo glass (3 m or more wide glass). The two technologies are discussed in the following:

1. Chemical vapor deposition (CVD) coating, or called pyrolytic coating, is a low-E coating technology that appeared in the market in the 1970s. This method deposits films directly on the hot glass while it is still on the float line, so it is also called online low-E. The layout is shown in **Figure 6**. The CVD process is chosen right after the float/tin bath on the production line with around 600°C. Because the substrate glass moves about 1 ft/s as it travels down the float line, only 1–1.5 s are available for the coating to form. The precursor compounds (both gases and liquids) are vaporized in a reactor that spreads the resulting gas mixture uniformly over an advancing, newly formed glass ribbon. Chemical reactions occur in the gas above the glass and on the growing surface of the deposited film. Temperature

	1950s	1960s	1960s	1970s	1974	1975–1980s	1980s	1981	1988	1990s	2006
Notes	Market for heat reflection glass	First solar control glass to reduce the cooling cost of the building		Heat insulating glass units of building	1st energy crisis				Asymmetrical silver layer system	Double silver	Tripple silver
Firm:	BOC Edwards	Flaverbel	Heraeus / DETAG	Philips (NL)		Flashglass / DELOG	Pilkington	Interpane	Interpane	Cardinal, etc.	PPG
Film stack	**BiOx/Au/BiOx**	**BiOx/Au**	**ZnS/Au/ZnS**	**Tin oxide**		**BiOx/Au, IGU filled Ar**	**Tin oxide**	**BiOx/ PbOx/ Ag/PbOx/ BiOx**	**Silver-based coating**	**Oxide / Ag/oxide /Ag/ oxide**	**3 cycles of Oxide/Ag/ oxide**
Trade name		"Stop ray"	"Infrastop"	Thermoplus		Thermoplus	k-Glass	Iplus neutral			Solarban glass
New features	High transmittance/ high heat reflection	High IR reflection, low thermal emissivity, good transmittance	High IR reflection, low thermal emissivity, good transmittance	High transmittance low-e coating		Transmission form 40==>60%, U: 1.3W/m 2 k, Jumbo glass	Highly durable chemical/ mechanical resistance	Aging resistant and color neutral better than greenish/ pinkish color by Au/Cu coating	Higher transmission, better neutral color	Better solar gain control, higher LSG, >1.7	Better solar gain control, higher LSG >2.2
Deposition method	Sputter/ evaporation	Sputter	Evaporation	Pyrolysis / APCVD		Sputter	Pyrolysis/ APCVD	Sputter	Sputter	Sputter	Sputter

Table 3. Brief history of low-E technology, data obtained from [9, 10].

http://dx.doi.org/10.5772/67085

control is easier because the large thermal mass of the system also keeps the temperature relatively uniform across the ribbon. Strongly adhered coatings maintain their integrity when the product is bent and tempered [13].

Technical specifications of the transparent conductive coating	Indium oxide (ITO) coatings	Tin oxide (FTO) coatings	Gold layer systems	Silver layer systems
Layer thickness (nm)	>20	>20	>6	>6
Sheet resistance R (Ω)	>8	>8	>5	>1
Light transmittance (%)	>80	>80	>25	>85
Abrasion resistance	Very good	Very good	Good	Good
Chemical resistance	Good	Very good	Adequate	Adequate
Thermal stability to technical parameters	Adequate	Adequate to good	Adequate	Good
Adherence to the glass surface	Very good	Very good	Good	Good
Preferred coating technique for deposition onto flat glass	Sputter process	APCVD Pyrolytic process	Sputter process	Sputter process
Pane thickness for coating (mm)	>0.3	>2	>0.3	>0.3
Planes of coated pane	As uncoated flat glass	Poorer than uncoated flat glass	As uncoated flat glass	As uncoated flat glass

Table 4. The common low-E materials comparison, data obtained from Ref. [11] .

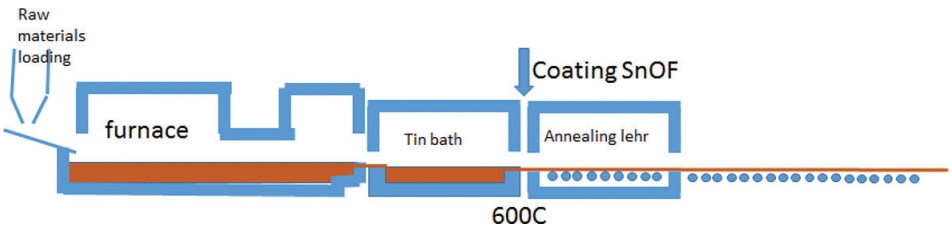

Figure 6. Schematic of a float bath production line used to deposit fluorine-doped tin oxide. Simplified from Ref. [13].

The typical deposition materials by pyrolytic method is fluorine-doped tin oxide (FTO). Their extinction coefficient k is very small (0.01 at 550 nm), so that the typical thickness is of μm scale, whose transmittance of >80% is acceptable. The refractive index is typically around 2. This kind of coating shows extremely good environmental and chemical resistance. Thus, sometimes it is called hard-low-E coating.

2. Today, more than 90% of the low-E window coatings are manufactured by sputtered coaters. Worldwide, billions of square meters per year of glass is coated by sputtering method and this amount is increasing steadily. Metallic low-E coating is conveniently manufactured by a sputtering method, because it provides a cost-effective solution and excellent coating uniformity; in addition, it also provides rich products with variety of choices on color, transmittance, solar heat gain, etc. The sputtering coater provides improved emissivity (below 0.08), therefore better heat radiation control, better solar heat control, and better optical performance. In addition, the price for current low-E coating products is very affordable, below \$1/ft^2 for single silver coating on 3 mm soda-lime glass.

Sputtering coater could process many different types of materials including:

- *Metal materials*: most metal could be deposited by sputtering method. The most widely used metallic low-E coatings are silver or gold. The extinction coefficient k is very high for such metals, such as 3.5 for sliver and 2.6 for gold at wavelength of 550 nm, so only thin films such as 20 nm are acceptable for good transmittance.
- *Semiconductor*: such as indium-doped tin oxide (ITO), aluminum-doped zinc oxide (AZO), etc.
- *Dielectric materials*: such as bismuth oxide, tin oxide, zinc oxide, titanium oxide, silicon oxide, silicon nitride, etc

The typical metal sputter deposition coater layout is shown in **Figure 7**.

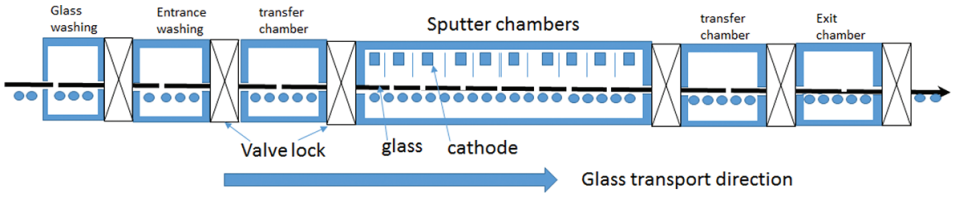

Figure 7. Schematic of a continuous-batch sputter-coating reactor, simplified from Ref. [13].

The sputtering coater is typically independent of the glass production, so it is also called offline low-E coating. The coater line starts with a glass washer, and an entrance chamber to pump down to vacuum condition. The glass travels through each chamber for different layers of material deposition, finally passing through the exit chamber to the ambient condition. Being an offline process, sputtering process allows for a high level of flexibility, such as flexible layer system, the scale of production, etc. Also, it is generally regarded to be environmentally safe, without waste products. Thus, the sputter coating is the most used technology in the low-E coating industry today.

3. Silver-based low-E coating technology overview

Among the sputtered low-E coating products, silver-based low-E is dominant. There are three major categories of silver-based low-E products: single-silver, double-silver, and triple-silver products [14]. The structures are similar, with single-silver structure being the simplest one. A typical structure is as follows (**Figure 8**).

http://dx.doi.org/10.5772/67085

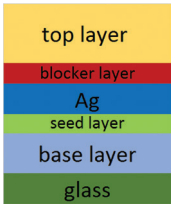

Figure 8. Typical single-silver coating layer structure.

It has been reported that the electrical/optical properties of Ag thin film strongly depend on its microstructure, such as crystallite size [15], grain size [16], grain boundaries [17], and surface roughness [18, 19], and also on the microstructure of the dielectric under-layers [20–22]. Thus, the R&D direction for the low-E industry has been focused on how to improve silver-thin film microstructure for better optical and thermal performance. Generating high-quality silver thin films is at the center of the technological development of silver-based low-E products. This will be further discussed in Section 3. The base and top layers are typically transparent dielectric materials layers, which are critical to the visible optical performance. Seed and blocker layers are very important to the emissivity properties, and they will be discussed in the following sections.

3.1. Seed layer

Using a seed layer is a common deposition technique to promote thin-film microstructure, and to enhance the thin-film properties, such as optical and mechanical properties. It is often reported that the ZnO seed layer can enhance silver thin film crystallite size and grain size, so that its resistivity and absorption is greatly reduced [22, 23]. Arbab et al. [23] have demonstrated that ZnO seed layer is better than other oxides, such as zinc stannate, as shown in **Figures 9** and **10**. The well-crystallized Ag (111) atop of ZnO (002) basal plane induced lower resistivity than that of polycrystalline Ag atop of zinc stannate. ZnO is a material that crystallizes very easily at room temperature even at very thin thickness such as 5 nm. The ZnO lattice sites are at the corners and center of a hexagon. Three silver atoms at alternate fourfold hollow sites form the unit cell of a (111) plane of silver, with 2.6% lattice mismatch between the ZnO and Ag layers [23], thus, the crystallized ZnO lattice promote the silver growing at (111) direction.

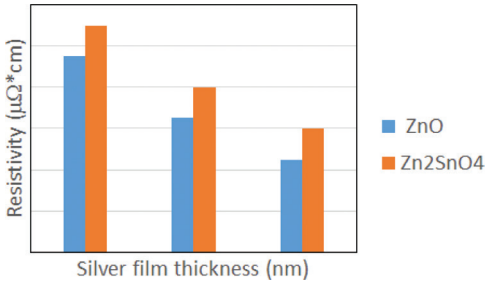

Figure 9. Well-crystallized Ag (111) atop of ZnO (002) basal plane induced lower resistivity than that of polycrystalline Ag atop of zinc stannate.

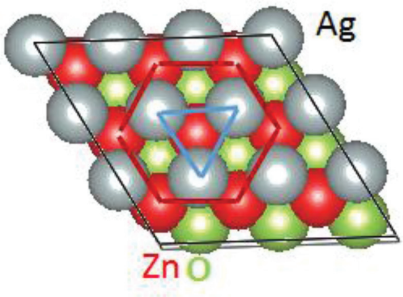

Figure 10. Ag (111) growth atop of ZnO (002).

3.2. Blocker layer

The blocker layer is extremely important in silver-based low-E coating. Treichel et al. [24] gave a good description of blocker layer functions by noting that the typical top layer is comprised by oxide materials, such as SnO_2, TiO_2, or ZnO. Without a blocker layer, the deposition of the top layer takes place directly on top of the unprotected silver film. In such a case, the silver layer meets a highly reactive sputter process, with the presence of oxygen radicals. The silver crystal lattice will be damaged and the silver atoms will agglomerate, until the top layer forms close to the surface, preventing further reacting species from reaching the silver [24]. Since the quality of the low-E coating is mainly determined by the crystallized silver, an additional barrier, the blocker layer, becomes necessary for high-quality low-E coating. In the study shown below, the metal titanium was chosen. In low-E applications, emissivity and resistivity is in nearly linear relationship. When the blocker is too thin, no close protecting layer formed yet, the emissivity/resistivity (from silver) is high, which is called region 1. As the blocker thickness is increased, the emissivity/resistivity reaches a minimum, called region 2. Further increasing the thickness, called region 3, leads to emissivity/resistivity flat or increasing slightly, as shown in **Figure 11**.

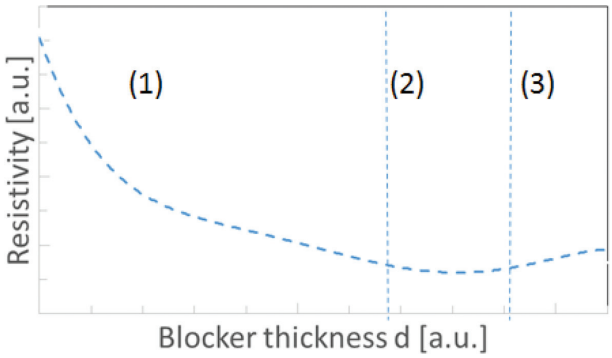

Figure 11. The resistivity of single-silver stack is dependent on the blocker thickness.

http://dx.doi.org/10.5772/67085

The optimized blocker layer consists of two portions: a metallic portion close to the silver layer and a region with higher oxidization ratio close to the top layer. The typical blocker layer thickness is below 10 nm [24].

3.3. Double silver and triple silver

The coating stack in **Figure 8** can now be used as a building block for multi-low-E stacks. Introducing a sequence of two blocks in **Figure 8** leads to double silver stacks, which will enhance low-E coating with higher selectivity between IR and visible. The typical structure is illustrated in **Figure 12**.

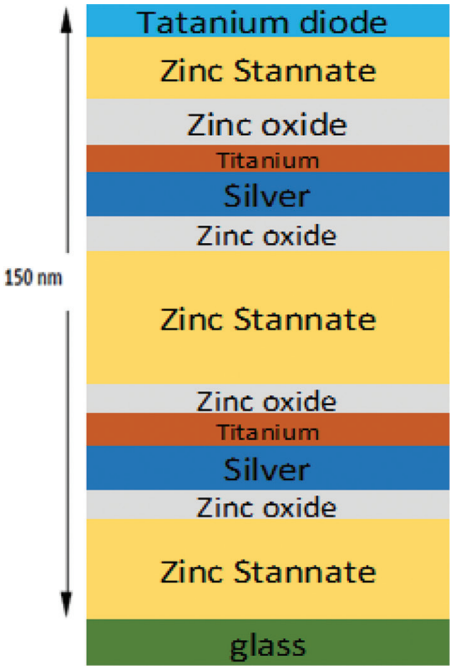

Figure 12. The double silver stack layout from PPG products with the data obtained from Ref. [25].

In this case, the dielectric material is zinc stannate, the seed layer is zinc oxide, and the blocker layer is titanium. The zinc stannate layer in the middle has a thickness roughly equal to the total thickness of the base and the top layer of the single silver. The typical double low-E coating glass spectra is shown in **Figure 13**, with transmittance around 70%, and reflectance from film and glass sides below 10% in the visible region. However, the transmittance is near zero at the IR region (λ > 1000 nm), and the reflectance for IR is very high >90% (for λ > 1000 nm).

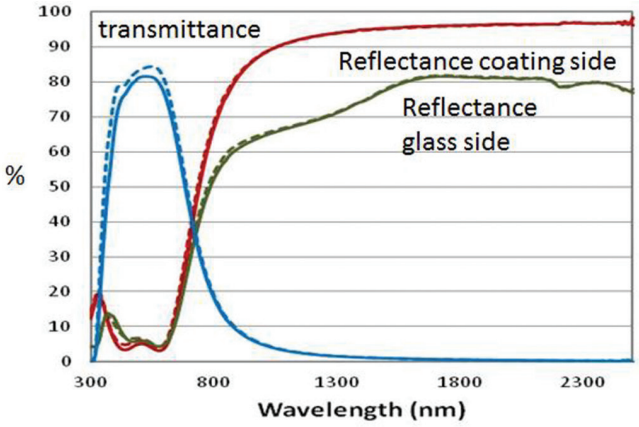

Figure 13. The typical double silver spectra of transmittance and reflectance from film side and glass side [26].

Further, if the three blocks of single silver of **Figure 8** were put together [13], it would make a triple silver stack which is shown in **Figure 14**. The selectivity of IR and visiblity is the best in today's market, however, the cost is higher.

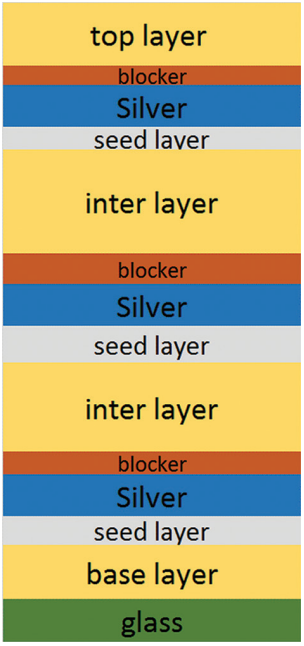

Figure 14. A typical triple silver stack.

http://dx.doi.org/10.5772/67085

4. Advanced understanding of silver-based low-E coatings: thin film silver properties

Silver-based low-E window coating currently accounts for 90% of the market. The thin film silver properties are key in low-E coating technology. Thus, a separate section is used to focus on the thin film silver properties from practice to theory.

There is a hundred years of research history on electric conduction and optical response in metals [27–29]. The Drude model [30] describes two main parameters governing the electronic response: (i) the electron collision time τ, a statistical parameter describing the mean time between collisions, and (ii) the plasma frequency ω_p, mainly determined by the concentration of carriers. Lorentz analyzed the electronic behavior using the dynamical theory of gases [31]. These theories gave a reasonable optical response of metals [32]. In addition, surface electronic scattering effects are extremely important, and the optical response of metal nanoparticles with the interfaces were reported [33–35].

The low-E industry history started with gold thin film then shifted to silver thin film, and the transition significantly improve the window color appearance, and the energy-saving efficiency, and the cost. Materials innovation is the key to low-E coating performance. The following figure clearly shows the silver benefit in optical absorption in comparison with those of gold and copper with 15 nm thin film, although they are all excellent conductors and are shown in **Figure 15** [11].

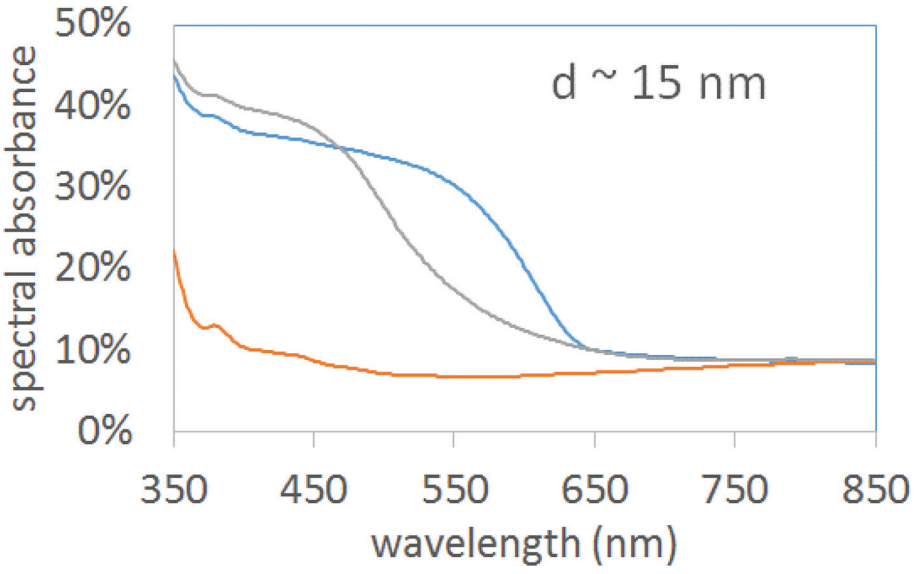

Figure 15. The spectral absorbance for 15 nm thin film of Ag, Au, and Cu.

4.1. Silver thickness effect in the electrical properties

The thin film silver thickness effects on its electrical properties were studied in many literatures, and Ref. [12] gave a good comparison of the theoretical and experimental results. **Figure 16** shows experimental resistivity values (ρ) decreased as Ag films with thicknesses ranging from 3 to 74 nm and the theoretical model predictions [12]. The silver was either directly deposited on the glass or was deposited in a stack with seed and blocker layers. There are two models used in the fitting of the experiments:

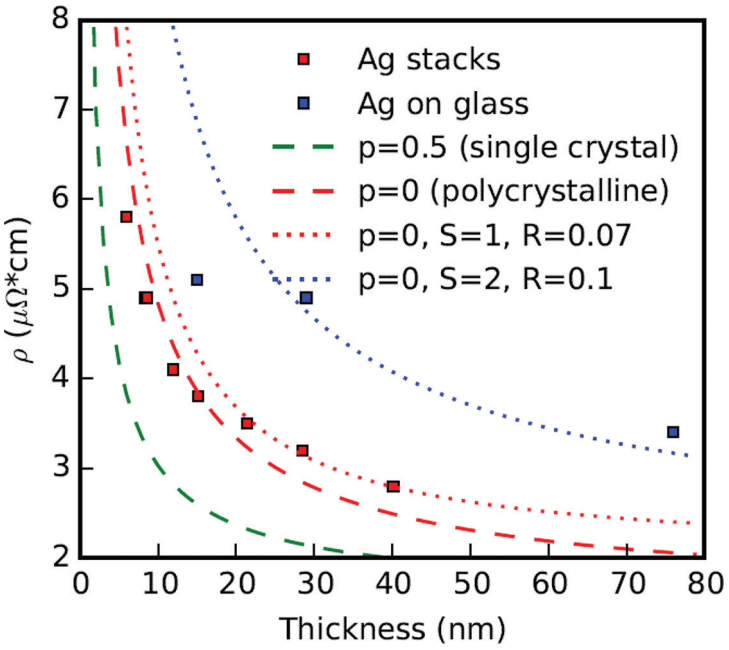

Figure 16. Experimental electrical resistivity for Ag stacks (red dots), Ag on glass (blue dots), and calculated values using Fuchs-Sondheimer's theory for polycrystalline films ($p = 0$) and single crystal films ($p = 0.5$). The dotted lines show how roughness and intergrain scattering affect resistivity using the Rossnagel and Kuan formalism [12].

(i) First is the Fuchs-Sondheimer theory [31], considering electronic scattering by the interfaces, and the resistivity of metal thin films model used in the fitting is shown below:

$$\rho = \rho_i \left[1 - \frac{3}{2\kappa}(1-p)\int_1^{\infty}\left(\frac{1}{t^3}-\frac{1}{t^5}\right)\frac{1-e^{-\kappa t}}{1-p\,e^{-\kappa t}}\,dt\right]^{-1} \quad (2)$$

where $\kappa = d/l$, with d is the thin film thickness, l is the electronic mean free path, ρ_i is the bulk resistivity, t is an integration parameter, and p is the probability that an electron will be specularly reflected upon scattering from one of the surfaces (p). Typical values for p are 0 for polycrystalline films and 0.5 for single crystal films. The electrical and optical properties of Ag thin films exhibit a marked dependence with thickness when this is comparable to the electronic mean free path.

http://dx.doi.org/10.5772/67085

(ii) The nonoptimum growth of Ag on glass leads to rougher films and agglomeration in the lower thickness limit. Mayadas et al. [36, 37] extended Fuchs-Sondheimer theory in Eq. (1) to consider electronic scattering by grain boundaries. Furthermore, Rossnagel and Kuan [38] revised this model and extended it to take into account surface roughness and grain size as

$$\rho = \rho_i \left[1 + \frac{0.375(1-p)Sl}{d} + \frac{1.5\,Rl}{(1-R)\,g}\right] \tag{3}$$

where S is the roughness parameter that equals 1 in perfect, atomically flat interfaces, and increases as roughness does so. R is the scattering coefficient, illustrating the scattering of electrons at the grain boundaries. Finally, g is the average grain size, which is shown in **Figure 17**. These parameters clearly illustrate how thickness, grain size, and surface roughness affect the films reflectivity.

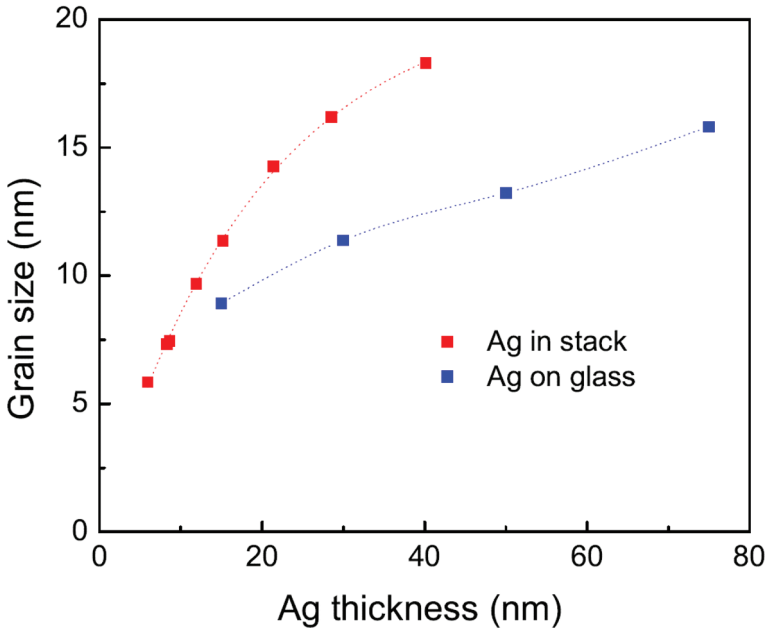

Figure 17. Ag grain size measured for the case of films deposited on glass and in stack configuration [12].

4.2. Silver thickness effect in the optical properties

Ref. [10] provided a good model and experiments on the silver thickness effect in the optical properties. **Figure 18(a)** shows the refractive index (n) and extinction coefficient (k) for Ag thin films deposited on glass with thickness ranging from 15.3 to 74.3 nm [12]. A progressive reduction in n is observed as the Ag films get thicker, achieving values close to bulk for thicknesses around 74.3 nm [36]. On the other hand, the extinction coefficient (k) was found to remain almost identical for all the thicknesses.

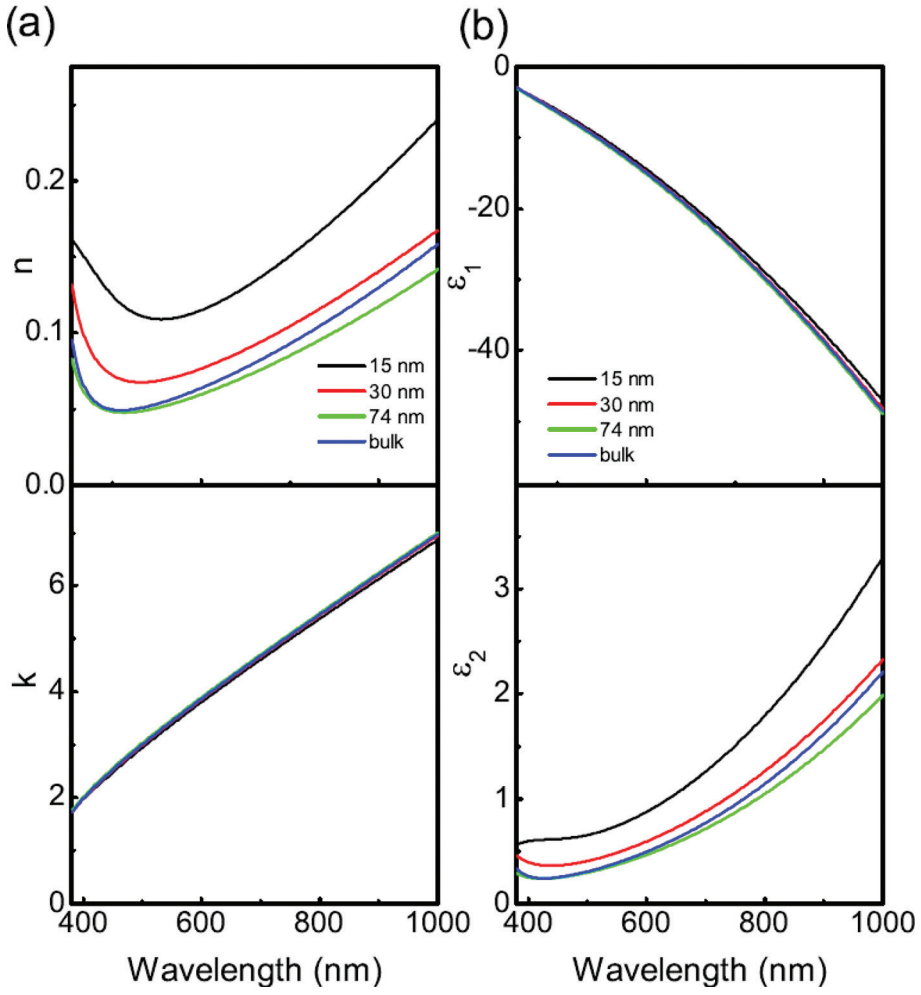

Figure 18. (a) Refractive index (n) and extinction coefficient (k) and (b) real and imaginary parts of the dielectric function for Ag thin films deposited on glass [12].

Using the ellipsometry method, the electron scattering times τ for the Ag films can be calculated. It is interesting to find that the product $\tau \times \rho$ also remains constant, as shown in **Figure 19**, and the theory behind it have been discussed in the literature [12]. Further, a new model was developed to predict the silver refractive index as shown in **Figure 20**.

$$n \approx \frac{\rho}{2\varepsilon_0(\rho\tau)^2\omega^3 k} = \frac{\rho}{2\varepsilon_0 C^2 \omega^3 k} \tag{4}$$

where C is the product $\rho \times \tau$, with the value 59 ± 2 μΩ cm fs [10], independent of the wavelength, and k is nearly a constant for the silver film.

http://dx.doi.org/10.5772/67085

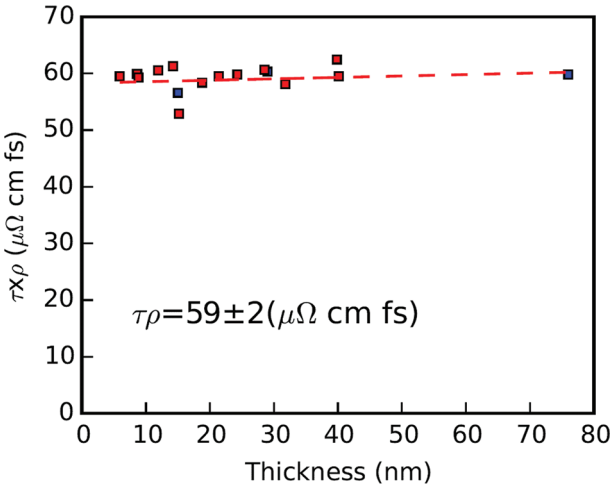

Figure 19. The product $\tau \times \rho$ remains constant within the thicknesses range studied with silver directly deposited on glass, and with silver in the stack between seed and blocker layer [12].

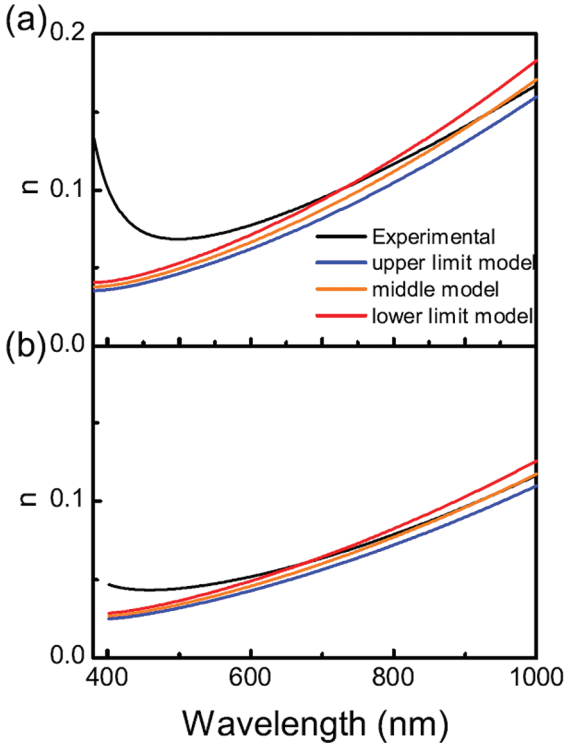

Figure 20. Experimental refractive index spectra for Ag films (a) 29 nm and (b) 74 nm thick along with calculations using three values of the constant *C*, i.e., 59 μΩ cm fs as middle point, and 57 and 61 μΩ cm fs as lower and upper limits, respectively [12].

4.3. Emissivity dependence with silver thickness

Low-emissivity coatings have important applications in energy-efficient windows and thermal coatings. **Figure 21** shows experimental emissivity values for Ag thin films with thicknesses ranging from 3 to 40 nm [12]. A progressive increase in emissivity is observed as the films get thinner, which means their ability to reflect infrared radiation decreases.

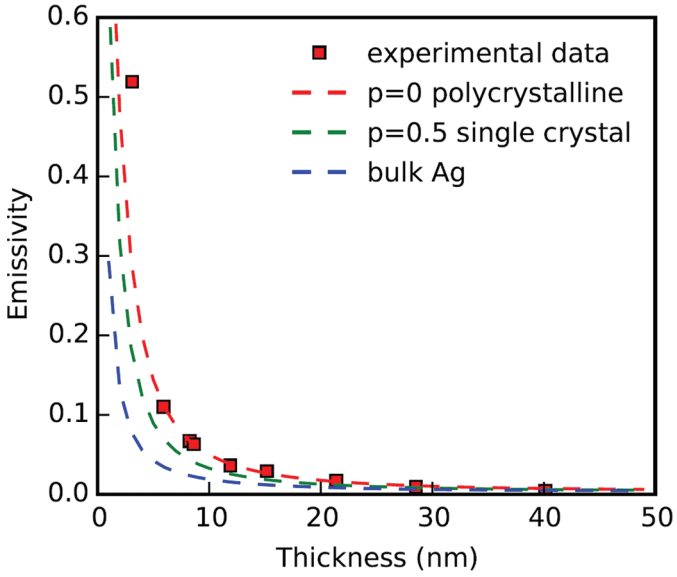

Figure 21. Emissivity versus thickness for Ag thin films. Calculations correspond to bulk Ag optical constants considering no dependence with thickness (blue line), considering the evolution of the electron collision time predicted for polycrystalline films $p = 0$ (red line) and single crystal films $p = 0.5$ (green line) [12].

The optical model could calculate the reflectivity by using silver's optical constants with different silver film thicknesses, which can be used for simulating silver emissivity [12]

$$\epsilon = \frac{\sum_{i=1}^{m}(1 - R_{\lambda i})\, E_{bi}\, \Delta\lambda_i}{\sum_{i=1}^{m} E_{bi}\, \Delta\lambda_i} \tag{5}$$

where R_λ is the reflectivity at wavelength λ and $E_{b\lambda}$ is the radiation emitted by blackbody at wavelength λ, and R_λ can be calculated from the refractive index n, k, which can be calculated from the modeling for polycrystalline and single crystal. These results are compared with experimental results in **Figure 21**, which implied that the most experimental silver film results are agreed with the polycrystalline model.

5. Conclusion

Stronger legislations are helping to improve the energy efficiency of new buildings, so low-E technology, especially silver-based low-E technology, has developed very fast in the last 30

years. Silver-based low-E technology is reviewed on its application background, history, and on how technically to generate high-quality, silver thin films; further on how the silver thin film's electrical, optical, and emissivity properties are influenced by their microstructure, thickness, and by the materials on neighboring layers through a theoretical and an experimental perspective. Low-E window coating is one of the fastest growing sectors in the glass industry, and sputtered silver-based low-E will continue to grow in the near future globally.

Acknowledgement

The authors would like to thank low-E group members' support at Intermolecular Inc.

Author details

Guowen Ding* and César Clavero

*Address all correspondence to: gding@intermolecular.com; dingguowen@yahoo.com

Intermolecular, Inc., San Jose, CA, USA

References

[1] U.S. Department of Energy, Advanced Research Projects Agency – Energy (ARPA-E). Program review, No. DE-FOA-0001425, [Internet]. [Updated: 2016]. Available from: http://arpa-e.energy.gov/sites/default/files/documents/files/SHIELD_ProgramOverview.pdf

[2] Board on Energy and Environmental Systems. Energy Research at DOE: Was It worth It? Energy Efficiency and Fossil Energy Research 1978 to 2000. [Internet]. National Academies Press. 2001. Available from: http://www.nap.edu/catalog.php?record_id=10165 [Accessed: 12/17/12]

[3] S. Selkowitz. High Performance Windows and Glazings Technologies, Systems and Tools in the U.S. In: IEA Building Envelope Technologies and Policies Workshop; 17/11/2011; Paris.

[4] J. Rissman, H. Kennan. Low-Emissivity Windows Case Studies on the Government's Role in Energy Technology Innovation. [Internet]. American Energy Innovation Council 2014 Available from: http://energyinnovation.org/wp-content/uploads/2014/06/Low-E-Windows-Case-Study.pdf

[5] PPG Technology. Understanding Insulating Glass Units [Internet]. 2015. Available from: http://www.ppgresidentialglass.com/window_glass/understanding_IGU.aspx

[6] The Florida Solar Energy Center (FSEC). How Window Work [Internet]. 2014. Available from: http://www.fsec.ucf.edu/en/consumer/buildings/basics/windows/how/solar_gain.htm

[7] J. Wilson. The Evolution of Glass and High-Performance Coatings. In: AIA 2012 National Convention and Design Exposition; May17–19, 2012; Walter, Washington, DC; 2012.

[8] L. Holland, G. Siddall. Heat-reflecting windows using gold and bismuth oxide films. J. Appl. Phys. 1958;**9**:359–361.

[9] H.J. Gläser. AGC Interpane. History of the Development and Industrial Production of Low-e Coatings for High Heat Insulating Glass Units [Internet]. 19 December. 2006. Available from: http://www.interpane.com/m/en/history_of_low-e_coatings_123.87.html

[10] Glassonweb.com. Industry's First Triple-Silver Glass [Internet]. 27 October 2016. Available from: https://www.glassonweb.com/news/industrys-first-triple-silver-glass

[11] H.J. Gläser. "Large area glass coating." Von Ardenne Anlagen Technik GMBH: Germany; 2000. ISBN-10: 3000049533, ISBN-13: 978-3000049538, ASIN: B001L9LH42

[12] G. Ding, C. Clavero, D. Schweigert, M. Le. "Thickness and microstructure effects in the optical and electrical properties of silver thin films." American Institute of Physics Advances. 2016;**5**:17234.

[13] R.J. McCurdy. Flat Glass. In: Coating on Glass Technology Roadmap Workshop; Jan 18–19; Livermore, California; 2000.

[14] Von Ardenne Anlagentechnik/Architecture article, Glass on web. "Continued Process Improvements in Architectural Glass Coating" [Internet]. 2012. Available from: http://www.glassonweb.com/articles/article/785/

[15] K. Kato, H. Omoto, A. Takamatsu. Vacuum. 2009;**84**:587–591.

[16] A.M. Kazakos, D.E. Fahnline, R. Messier, L.J. Pilione. J. Vaccum Sci. Technol. A. 1992; **A10**:3445–3450.

[17] E. Gerlach. Phys. Stat. Sol. B. 1996;**195**:159–166.

[18] E.Z. Luo, S. Heun, M. Kennedy, J. Wollschlager, M. Henzler. Phys. Rev. B. 1994;**49**(7): 4858–4865.

[19] K. Kato, H. Omoto, A. Takamatsu. Adv. Mater. Res. 2010;**117**:69–74.

[20] Y. Tsuda, H. Omoto, K. Tanaka, H. Ohsaki. Thin Solid Films. 2006;**502**:223–227.

[21] S. Ulrich, A. Pflug, K. Schiffmann, B. Szyszka, Phys. Stat. Sol. C. 2008;5:1235–1239.

[22] K. Kato, H. Omoto, A. Takamatsu, Vacuum. 2008;84:606–609.

[23] M. Arbab, Thin Solid Films, 2001;381:15–31.

[24] O. Treichel, V. Kirchhoff, G. Brauer. 2000 Society of Vacuum Coaters, 43rd Annual Technical Conference Proceedings, April 15–20; Denver; 2000.

[25] J. Finley, PPG Industries, Inc. The future high performance Glazing in commercial buildings [Internet]. Available from: http://www.lehigh.edu/imi/teched/SolarWS/T6f_Finley.pdf

[26] G. Ding, J. Cheng, T. Ju, M. Le, D. Schweigert, G. Zhang. Color shift of high LSG low emissivity coating after heat treatment. US Patent No. 9279910 B2; Mar. 8, 2016.

[27] M. Fox, Optical Properties of Solids. Oxford University Press, Oxford Master Series in Physics (Book 3); Oxford University Press; 2 edition: Britain (May 20, 2010) 2001;416. ISBN-10: 0199573379, ISBN-13: 978-0199573370

[28] D.E. Aspnes, *Handbook of Optical Constants of Solids*, edited by E.D. Palik, Academic Press, Burlington; 1997. pp. 89–112.

[29] L. Azaroff, Introduction to Solids. TMH Edition, Tata McGraw-Hill Publishing Company Limited.

[30] P. Drude, Ann. Phys. 1990;**306**(3):566–613.

[31] E.H. Sondheimer, Adv. Phys. 1952;**1**(1):1–42.

[32] P.B. Johnson, R.W. Christy, Phys. Rev. B 1972;**6**(12):4370–4379.

[33] U. Kreibig, M. Vollmer, Optical Properties of Metal Clusters. Springer-Verlag, Berlin; 1995.

[34] C. Clavero, A. Cebollada, G. Armelles, Y. Huttel, J. Arbiol, F. Peiro, A. Cornet, Phys. Rev. B 2005;**72**(2):024441.

[35] C. Clavero, Ph.D. Thesis, Universidad Autónoma de Madrid, 2007.

[36] A.F. Mayadas, M. Shatzkes, J.F. Janak, Appl. Phys. Lett. 1969;**14**(11):345–347.

[37] A.F. Mayadas, M. Shatzkes, Phys. Rev. B 1970;**1**(4):1382–1389.

[38] S.M. Rossnagel, T.S. Kuan, J. Vacuum Sci. Technol. B 2004;**22**(1):240–247.

[39] 2009 ASHRAE Handbook: Fundamentals. IP Edition. American Society of Heating, Refrigerating and Air-Conditioning Engineers; 2009. ISBN 978-1-933742-56-4